Proceedings of the Workshop
"Fermi meets Jansky: AGN in Radio and Gamma-Rays"

held in Bonn
June 21st-23rd 2010

Edited by
Tuomas Savolainen[1]
Eduardo Ros[1,2]
Richard W. Porcas[1]
J. Anton Zensus[1]

1: Max-Planck-Institut für Radioastronomie
2: Universitat de València

Cover illustration: Matthias Kadler

(Collage showing gamma-ray emission observed by the Large Area Telescope (LAT) onboard NASA's *Fermi Gamma-Ray Space Telescope* in its first-flight all-sky image (Credit: NASA/DOE/International LAT Team) and associations of the brightest point sources with powerful parsec-scale jets in AGN from the MOJAVE Very Long Baseline Array program. Image courtesy of M. Kadler, Sternwarte Bamberg (Univ. Erlangen), the MOJAVE- and *Fermi*/LAT-teams.)

Cover design: Eduardo Ros

Table of Contents

VLBI Observations of Gamma-Ray AGN

Jet Physics

Non-Blazar Gamma-Ray AGN

Preface

This volume contains the papers to be presented at the Workshop "Fermi meets Jansky: AGN in Radio and Gamma-Rays", held at the Max-Planck-Institut für Radioastronomie in Bonn on June 21–23 2010. Around 70 scientists from around the world will come together to discuss the recent rapid advances in the field of active galactic nuclei (AGN) research, triggered by the first results from the *Fermi Gamma-ray Space Telescope*. The number of scientists interested in the topic was significantly greater than the number which could be accommodated. We offer our apologies to all those who therefore could not be admitted to the workshop.

It is not known whether Enrico Fermi, one of the eminent physicists of the 20th century, and Karl Jansky, the father of radio astronomy, ever met. Fermi emigrated to the United States 12 years before Jansky's death, thus creating a chance for an encounter, but at this point Jansky was not pursuing astronomical research any more. Most likely the two did not have professional contact during their lifetimes, but today their scientific legacies, particle physics and radio astronomy, are tightly inter-twined in the field of high energy astrophysics. Radio synchrotron radiation is a tell-tale sign of highly energetic particles in our Universe, particles which may have gained their energy via acceleration processes named after Fermi.

The highly relativistic particles found in AGNs are not only radio-emitters, but they also generate copious amounts of radiation throughout the whole electromagnetic spectrum up to TeV γ-rays. Since the EGRET instrument on-board the *Compton Gamma-ray Observatory* opened up the γ-ray sky, the origin of the prominent high energy radiation from AGNs has been one of the major open questions in modern astrophysics. It is fair to say that this discovery strongly influenced the field of AGN studies.

Despite the seminal discoveries made by EGRET, its sensitivity was not great and the resulting γ-ray light curves were too poorly sampled to be able to decisively select among the various models that were proposed to explain the AGN γ-ray emission, thus creating a long-lasting controversy amongst the proponents of different hypotheses. Now, two decades after the launch of *CGRO*, we are at a turning point. The MeV-GeV γ-ray sky is currently being observed with unprecedented sensitivity by two new satellites, AGILE and *Fermi*. At the same time the latest generation of ground-based atmospheric imaging Cherenkov telescopes is detecting new TeV-emitting AGN at an ever increasing rate. In particular, *Fermi* has revolutionised γ-ray studies due to its high sensitivity, wide energy range, large field-of-view, and an observing mode that allows continuous all-sky monitoring. Equipped with these state-of-the-art instruments, astrophysicists are now able to draw a comprehensive picture of the γ-ray emitting AGN population.

The emission from the high-energy particles in AGN is, however, a broadband phenomenon, and it has been clear for a while that, in order to understand the physics behind the high

energy emission, a multi-wavelength approach is necessary. Since the EGRET era there have been indications that the γ-ray brightness of AGN is linked to their radio–mm-wavelength properties, and the first results from joint *Fermi* γ-ray and radio studies have now confirmed this. The connection is there, and one big question now is how intimate it is. Are the radio–mm-wavelength properties and the γ-ray brightness correlated just because the radiation at both extremes of the spectrum is emitted from a relativistic jet? Or are the two emission processes more tightly knit with a possibly co-spatial production of both? The goal of the "Fermi meets Jansky" workshop is to bring together experts from both the radio and γ-ray communities to discuss our understanding of high energy physics in AGN. One of the central themes will be the location of the γ-ray emitting region. How close is it to the central black hole? We hope that the workshop serves to converge the views about this and other open questions or at least helps to outline what observations are needed to settle the long-standing debates.

To maximise the usefulness of these proceedings it was decided that they be published before the workshop, so that the proceedings can serve as a reference during the discussions at the meeting and that they may help foster further interaction among scientists soon after the meeting. We thank the authors for their co-operation in delivering publication-ready electronic manuscripts and for meeting the strict deadlines. It is highly gratifying that—except for a handful—almost all of the 55 presentations could be included in this book.

The editorial work was limited to copy editing and to some amount of language editing in order to improve the readability of the book. No refereeing regarding the scientific content of the contributions was performed. The editors take responsibility for any errors generated in the papers by their editorial work.

In Bonn, on the 11$^{\text{th}}$ of June 2010,
Tuomas Savolainen
Eduardo Ros
Richard W. Porcas
J. Anton Zensus

List of Participants

IVÁN AGUDO
Boston University
iagudo@bu.edu

HUGH D. ALLER
University of Michigan
haller@umich.edu

MARGO F. ALLER
University of Michigan
mfa@umich.edu

EMMANOUIL ANGELAKIS
MPI für Radioastronomie
eangelakis@mpifr.de

TIGRAN G. ARSHAKIAN
MPI für Radioastronomie
tigar@mpifr-bonn.mpg.de

PETER BIERMANN
MPI für Radioastronomie
plbiermann@mpifr-bonn.mpg.de

ROGER BLANDFORD
Stanford University
rdb3@stanford.edu

MORITZ BÖCK
Dr. Remeis-Observatory and ECAP,
Bamberg
moritz.boeck@sternwarte.uni-erlangen.de

MARKUS BÖTTCHER
Ohio University
boettchm@ohio.edu

SILKE BRITZEN
MPI für Radioastronomie
sbritzen@mpifr-bonn.mpg.de

CHIN-SHIN CHANG
MPI für Radioastronomie
cschang@mpifr.de

CHI C. CHEUNG
Naval Research Laboratory
ccheung@milkyway.gsfc.nasa.gov

FILIPPO D'AMMANDO
INAF-IASF Palermo
dammando@ifc.inaf.it

JUSTIN FINKE
Naval Research Laboratory
justin.finke.ctr@nrl.navy.mil

CHRISTIAN M. FROMM
MPI für Radioastronomie
cfromm@mpifr-bonn.mpg.de

LARS FUHRMANN
MPI für Radioastronomie
lfuhrmann@mpifr-bonn.mpg.de

KRISZTINA EVA GABANYI
Hungarian Academ Res. Groupy of Sci-
ences, Phys. Geodesy and Geodynamics
Res. Group
gabanyik@sgo.fomi.hu

DARIO GASPARRINI
Agenzia Spaziale Italiana
dario.gasparrini@asdc.asi.it

GABRIELE GIOVANNINI
Astronomy Dept. - Bologna University
ggiovann@ira.inaf.it

MARCELLO GIROLETTI
INAF Istituto di Radioastronomia
giroletti@ira.inaf.it

PHILIP HARDEE
University of Alabama
phardee@bama.ua.edu

TALVIKKI HOVATTA
Purdue University
thovatta@purdue.edu

FAITH HUNGWE
HartRAO
faith@hartrao.ac.za

SVETLANA J. JORSTAD
Boston University
jorstad@bu.edu

MATTHIAS KADLER
Dr. Remeis Sternwarte, Bamberg
matthias.kadler@sternwarte.uni-erlangen.de

KENNETH I. KELLERMANN
National Radio Astronomy Observatory
kkellerm@nrao.edu

MOTOKI KINO
National Astronomical Observatory of
Japan
motoki.kino@nao.ac.jp

YURI Y. KOVALEV
Astro Space Center of Lebedev Physical
Institute
yyk@asc.rssi.ru

THOMAS P. KRICHBAUM
MPI für Radioastronomie
tkrichbaum@mpifr-bonn.mpg.de

ANNE LÄHTEENMÄKI
Aalto University Metsähovi Radio Ob-
servatory
alien@kurp.hut.fi

JONATHAN LEÓN-TAVARES
Aalto University Metsähovi Radio Ob-
servatory
leon@kurp.hut.fi

MATTHEW L. LISTER
Purdue University
mlister@purdue.edu

ANDREI P. LOBANOV
MPI für Radioastronomie
alobanov@mpifr.de

BENOIT LOTT
CENBG/IN2P3/CNRS
lott@cenbg.in2p3.fr

MAXIM LYUTIKOV
Purdue University
lyutikov@purdue.edu

ELIZABETH MAHONY
The University of Sydney
emahony@physics.usyd.edu.au

FRANCO MANTOVANI
Istituto di Radioastronomia - INAF
fmantovani@ira.inaf.it

ALAN P. MARSCHER
Boston University
marscher@bu.edu

MARIA MASSI
MPI für Radioastronomie
mmassi@mpifr-bonn.mpg.de

WALTER MAX-MOERBECK
California Institute of Technology
wmax@astro.caltech.edu

WILLIAM McCONVILLE
Univ. of Maryland
wmcconvi@umd.edu

CORNELIA MÜLLER
Dr. Remeis-Observatory and ECAP, Bamberg
cornelia.mueller@sternwarte.uni-erlangen.de

HIROSHI NAGAI
National Astronomical Observatory of Japan
hiroshi.nagai@nao.ac.jp

KRZYSZTOF NALEWAJKO
Nicolaus Copernicus Astronomical Center
knalew@camk.edu.pl

ELINA NIEPPOLA
Metsähovi Radio Observatory
eni@kurp.hut.fi

ROOPESH OJHA
NVI / USNO
rojha@usno.navy.mil

MONICA ORIENTI
INAF - Bologna
orienti@ira.inaf.it

TIMOTHY J. PEARSON
California Institute of Technology
tjp@astro.caltech.edu

RICHARD W. PORCAS
MPI für Radioastronomie
porcas@mpifr-bonn.mpg.de

RAY PROTHEROE
University of Adelaide
rprother@physics.adelaide.edu.au

TAPIO PURSIMO
Nordic Optical Telescope
tpursimo@not.iac.es

ALEXANDER B. PUSHKAREV
MPI für Radioastronomie
apushkar@mpifr.de

JÖRG RACHEN
MPI for Astrophysics
jprachen@mpa-garching.mpg.de

ANTHONY C.S. READHEAD
California Institute of Technology
acr@astro.caltech.edu

PATRIZIA ROMANO
INAF/IASF Palermo
romano@ifc.inaf.it

EDUARDO ROS
Univ. Valencia and MPI für Radioastronomie
Eduardo.Ros@uv.es

TUOMAS SAVOLAINEN
MPI für Radioastronomie
tsavolainen@mpifr-bonn.mpg.de

JEFFREY D. SCARGLE
NASA Ames Research Center
Jeffrey.D.Scargle@nasa.gov

FRANK K. SCHINZEL
MPI für Radioastronomie
schinzel@mpifr.de

REINHARD SCHLICKEISER
Ruhr-University Bochum
rsch@tp4.rub.de

KIRILL SOKOLOVSKY
MPI für Radioastronomie
ksokolov@mpifr-bonn.mpg.de

MERJA TORNIKOSKI
Aalto University Metsähovi Radio Observatory
Merja.Tornikoski@tkk.fi

GINO TOSTI
University of Perugia and INFN Perugia
tosti@pg.infn.it

SASCHA TRIPPE
IRAM Grenoble
trippe@iram.fr

TASSO TZIOUMIS
CSIRO, ATNF
tasso.tzioumis@csiro.au

ESKO VALTAOJA
Tuorla Observatory, University of Turku
valtaoja@utu.fi

STEFANO VERCELLONE
INAF/IASF Palermo
stefano@ifc.inaf.it

STEPHANE VINCENT
University of Utah
svincent@physics.utah.edu

JÖRN WILMS
Dr. Remeis-Observatory and ECAP, Bamberg
joern.wilms@sternwarte.uni-erlangen.de

MOHAMMAD ZAMANINASAB
MPI für Radioastronomie
zamani@ph1.uni-koeln.de

J. ANTON ZENSUS
MPI für Radioastronomie
azensus@mpifr-bonn.mpg.de

ZHIBIN ZHANG
Guizhou University
z_b_zhang@sina.com

Scientific Organising Committee

CHARLES D. DERMER
Naval Research Laboratory

MATTHIAS KADLER
Dr. Remeis Sternwarte, Bamberg

ALAN P. MARSCHER
Boston University

JULIE MCENERY
NASA Goddard Space Flight Center

ANTHONY C.S. READHEAD
California Institute of Technology

EDUARDO ROS
University of Valencia and MPI für Radioastronomie

TUOMAS SAVOLAINEN (chair)
MPI für Radioastronomie

GINO TOSTI
INFN Perugia & University of Perugia

ESKO VALTAOJA
University of Turku

STEFANO VERCELLONE
INAF Palermo

ROBERT WAGNER
MPI für Physik

J. ANTON ZENSUS
MPI für Radioastronomie

General Properties of Fermi/LAT Blazars

B. Lott[1] on behalf of the *Fermi*/LAT Collaboration

Centre d'Etudes Nucléaires de Bordeaux Gradignan, CNRS/IN2P3, Université de Bordeaux, Centre d'Etudes Nucléaires Bordeaux Gradignan, UMR 5797, Gradignan, 33175, France

Abstract. The First Catalog of Blazars and other AGNs detected by the *Fermi*/LAT includes over 700 sources, only about 100 of which were previously known as γ-ray emitters. The general properties (redshift, luminosity, spectral hardness, variability...) for the different populations classified according to the strength of their emission lines (FSRQs, BL Lacs) or the estimated position of the synchrotron peak are reviewed.

1. Introduction

Since its launch in June 2008, the *Fermi*/LAT has opened a new era in high-energy astrophysics. Its unprecedented sensitivity, almost uniform at high galactic latitude, makes it very suitable to study populations of extragalactic objects. In survey mode, the sky is scanned every 3 hours, enabling alerts to be issued shortly after transient or new flaring sources are detected. The continuous survey has allowed source monitoring and variability studies on time scales ranging from months down to a few hours. Another breakthrough arises from the *Fermi*/LAT large energy range extending into the 10-100 GeV domain, which was previously little explored. This feature has allowed new spectral features at high energy to be discovered and has also enabled the identification of potential candidates of TeV sources, effectively leading to several discoveries by ground-based Cherenkov detectors.

As EGRET demonstrated that the extragalactic γ-ray sky was dominated by blazars, there were great expectations concerning progress in blazar and AGN science from the *Fermi*/LAT . Many of these expectations have been or are about to be fulfilled. In the following, I will discuss recent advances concerning *Fermi*/LAT blazar populations and their different properties. M. Giroletti (in these proceedings) will discuss the γ-radio connection and C.C. Cheung will present non-blazar sources detected by the *Fermi*/LAT .

2. Blazar Populations

2.1. Census

The First Catalog of Active Galactic Nuclei Detected by the *Fermi*/LAT (Abdo et al. 2010a), referred to as 1LAC in the following is a spinoff of the *Fermi*/LAT First Source Catalog (1FGL, Abdo et al. 2010b) based on data accumulated over the first 11 months of sky survey. A first list of *Fermi*/LAT -detected AGNs using 3 months of data and including 106 high-confidence sources, called the LAT Bright AGN Sources (LBAS, Abdo et al. 2009a) was released in early 2009. Thanks to the *Fermi*/LAT performance closely matching expectations and its essentially flawless operation, the actual detection limit is very close to pre-launch predictions, i.e., F(E>100 MeV)$\simeq 7.5 \times 10^{-9}$ ph cm^{-2}s^{-1} (high galactic latitude, photon index=2.2, 11 months of operation). This detection limit is higher for lower galactic latitudes and for softer sources. The 1FGL catalog includes 1451 sources with test statistic greater than 25, 1049 being located at $|b| > 10°$. The mean 95% containment radius is 0.15° for the high-latitude 1FGL sources. The association of a given source with an AGN is based on spatial coincidence following a Bayesian approach similar to that used for EGRET (Mattox et al. 2001). Three main catalogs were used for this purpose: the Combined Radio All-sky Targeted Eight GHz Survey (CRATES, Healey et al. 2007), the Candidate Gamma-Ray Blazar Survey (CGraBs, Healey et al. 2008) and the Roma-BZCat (Massaro et al. 2009). For each catalog, the prior was adjusted so that the posterior probabilities (calculated for all candidate sources in the parent catalogs) fulfill the condition: $N_{\text{false}} \approx \sum_{i=1}^{k}(1 - P_i)$ where the number of false positives N_{false} is estimated from Monte-Carlo simulations. This procedure leads to the association of 709 sources ($P_i > 0.5$) corresponding to 671 distinct γ-ray sources. A total of 663 are associated with $P_i > 0.8$ and constitute the "high-confidence sample". Finally, 559 sources belong to the "clean sample" meeting the following conditions: high confidence association, no double associations, no anomaly observed in the association or detection procedures. Only 11 associations are expected to be spurious in that sample. The validity of the procedure is confirmed by the good agreement of the actual distribution of angular separation between γ-ray sources and their AGN counterparts with theoretical expectations.

The classification in terms of Flat-Spectrum Radio Quasars (FSRQs) and BL Lac-type objects (BL Lacs) is conventionally based on the strength of the emission lines. This classification has been used in the 1LAC. In addition, a more refined classification based on the source spectral energy distribution (SED) and dealing with the location of the synchrotron peak ν_{syn} has been carried out by us-
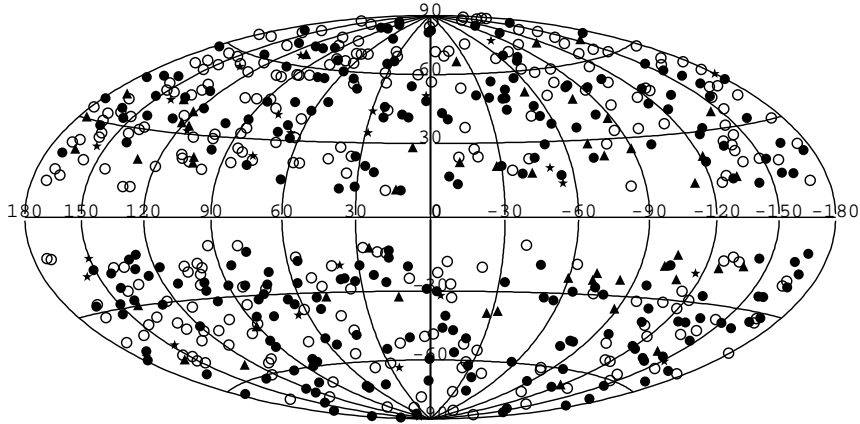
Fig. 1. Locations of the sources in the 1LAC clean sample. Solid circles: FSRQs, open circles: BL Lacs, stars: radio galaxies, triangles: AGNs of unknown type.

ing archival data at lower wavelengths, more precisely α_{ro} and α_{ox}, the radio-to-optical and optical-to-X-ray spectral slopes. The empirical relation between $(\alpha_{ro}, \alpha_{ox})$ and ν_{syn} was derived from a set of 48 high-quality, simultaneous SEDs of γ-ray blazars (Abdo et al. 2010e). Sources were classified as low-, intermediate- or high-synchrotron peaked sources (referred to as LSPs, ISPS, HSPs respectively) if $\log(\nu_{syn}){<}14$, $14{<}\log(\nu_{syn}){<}15$ or $\log(\nu_{syn}){>}15$ respectively, where ν_{syn} is in Hz.

The census of sources in the 1LAC high-confidence sample is as follows: 281 FSRQs, 291 BL Lacs (141 of which have a measured redshift), 30 other AGNs, 61 of unknown type. The nearly equal numbers of BL Lacs and FSRQs is in sharp contrast with the situation encountered with EGRET (Hartman et al. 1999) where FSRQS outnumbered BL Lacs by a factor $\simeq 3$. This is probably primarily related to the larger sensitivity at high energy of the LAT, as most BL Lacs have harder spectra than FSRQs as discussed below. Moreover, the LAT is far more sensitive to multi-GeV photons than was EGRET, which lost sensitivity above several GeV due to self-vetoing effects.

In addition to blazars, 3 radio-galaxies were detected early on: Cen A (Abdo et al. 2009a), NGC 1275 (Abdo et al. 2009a), and M 87 (Abdo et al. 2009c). In the 1LAC, five more sources are classified as misaligned AGNs: three radio galaxies (NGC 1218 = 3C 78, PKS 0625−35, and NGC 6251) and two steep-spectrum radio quasars (3C 207 and 3C 380). The properties of radio-galaxies and steep-spectrum radio sources detected by the LAT will be presented later during this conference by C. C. Cheung. Five other 1LAC sources (Abdo et al. 2009d) have flat or nearly flat radio spectra between ∼1 GHz and 8.4 GHz and strong emission lines in their optical spectra, but these lines are narrow, in contrast to the broad emission features seen in FSRQs. Under the standard AGN unification paradigm,

this is interpreted as an indication that the jet axis is at a larger angle to the line of sight than for a typical FSRQ. This causes the broad-line region to be obscured by the dusty torus surrounding the central black hole, leaving only narrow lines in the resulting spectrum, and such sources are commonly described as narrow-line radio galaxies (NLRGs). The NLRGs appearing in the 1LAC are 4C +15.05, PKS 1106+023, CGRaBS J1330+5202, 4C +15.54, and CGRaBS J2250−2806.

All (except for 4) FSRQs for which ν_{syn} can be estimated from archival data are of the LSP type. For BL Lacs, the breakdown is 67 LSPs, 44 ISPs, and 117 HSPs. Following the trend already observed in the BL Lac/FSRQ ratio, HSPs are highly overrepresented as compared to the EGRET sample.

Although the fraction of identification of high-galactic sources is fairly large ($\simeq 65\%$), some identifications are clearly missed as a significant asymmetry between northern and souther galactic hemisphere is observed (18% for BL Lacs and 4% for FSRQs, while little asymmetry is observed for the whole 1FGL sources), manifesting the incompleteness of the parent catalogs. This is partly supported by the similarity of the γ-ray properties, including flux and photon spectral index, of the unidentified sources to those of the 1LAC blazars.

2.2. Redshift distribution

All figures and statistics in the following will refer to the clean sample.

The redshift distributions for FSRQs and BL Lacs in the clean sample are presented in Fig. 2 along with the corresponding ones for the *WMAP* blazars (Hinshaw et al. 2007), which constitute a flux-limited all-sky sample above 1 Jy in the central *WMAP* observing band (Q band, 41 GHz). Note that only 141 out of 291 (42%) high-confidence 1LAC BL Lacs have measured red-
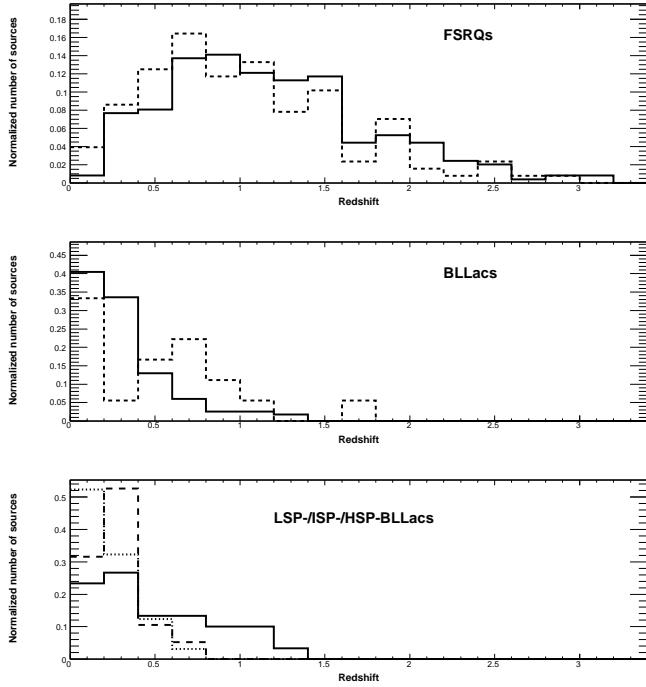
Fig. 2. Top: Normalized redshift distribution for the FSRQs in the clean sample (solid histogram). The redshift distribution for FSRQs in the *WMAP* catalog is also shown for comparison (dashed histogram). Middle: The same for BL Lacs. Bottom: Redshift distributions for LSP-BL Lacs (solid), ISP-BL Lacs (dashed), HSP-BL Lacs (dotted) in the clean sample.

Fig. 3. Flux ($E > 100$ MeV) vs. photon spectral index for the sources in the clean sample. The solid curves represents the $TS = 25$ flux limit estimated for a Galactic position (l, b) = (40°, 40°). FSRQs (solid circles), BL Lacs (open circles).

shifts. This is notably worse than for LBAS, in which 29 out of 42 (69%) BL Lacs had measured redshifts. The redshift distributions of γ-ray–detected blazars—both for FSRQs and for BL Lacs—are fairly similar to those for *WMAP*, peaking around $z = 1$ for FSRQs and at a lower redshift for BL Lacs (the lowest-redshift 1LAC BL Lac has $z = 0.030$). The distributions are very similar to those of the bright sources in the LBAS sample. The highest redshift for a high-confidence 1LAC FSRQ is $z = 3.10$. For comparison, the maximum redshift in both CGRaBS and Roma-BZCAT is for an FSRQ with $z > 5$. No strong evidence for a new population of misaligned FSRQs emerging at lower redshifts is found.

It is interesting to compare the redshift distribution of the LAT blazars (in particular, the FSRQs) with that of the objects detected by BAT on *Swift* (Ajello et al. 2009). Despite a fourfold increase in exposure time with respect to the LBAS sample and a consideration of γ-ray sources with $TS > 25$ in the 1LAC compared with $TS > 100$ in LBAS, the number of LAT-detected blazars still drops sharply at $z \sim 2.5$, and only two of the high-confidence 1LAC blazars have $z > 3$ (keeping in mind biases from the lack of redshift measurements). This is very different from the BAT survey, in which half of all FSRQs have $z > 2$, and the distribution extends to $z \sim 4$. This behavior may be indicative of a shift in the SED peak frequencies toward lower values (i.e., a "redder" SED) for blazars at

high redshifts. Indeed, the jets of the high-redshift BAT blazars are found to be more powerful than those of the LAT blazars and are among the most powerful known (Ghisellini et al. 2010). The peak of the inverse Compton flux for these objects, estimated to be in the MeV or even sub-MeV range, is located closer to the BAT band than to the LAT band, and the LAT instead samples the cutoff region of the inverse Compton spectrum.

3. Flux and Spectral properties

3.1. Flux

The 11-month average photon spectral index is plotted against the flux ($E > 100$ MeV) estimated from a power law fit in Fig. 3 for blazars in the clean sample. As the figure shows, the limiting flux corresponding to $TS = 25$ depends fairly strongly on the photon spectral index; the solid curve corresponds to a simple analytical estimate FSRQs (solid circles in Fig. 3) mostly cluster in the soft spectral index region, while BL Lacs (open circles) primarily occupy the hard spectral index region, confirming the trend seen for the LBAS sources (Abdo et al. 2009a). This implies that the limiting flux is different for FSRQs and BL Lacs. The mean fluxes are 8.5×10^{-8} photons cm^{-2} s^{-1} and 2.9×10^{-8} photons cm^{-2} s^{-1} for FSRQs and BL Lacs respectively. The faintest BL Lacs are about a factor of 3 fainter than the faintest FSRQs.

The high-flux ends of the EGRET and *Fermi*/LAT flux distributions are found in reasonable agreement, while the peak fluxes observed by EGRET are substantially higher than those observed for the brightest 1LAC sources. The main reason for the different peak fluxes observed by EGRET and the LAT is probably the different time spans over which the observations were conducted (4.5 years for EGRET vs. 11 months for the LAT), enabling the sources to explore a wider range of different states during the EGRET era.
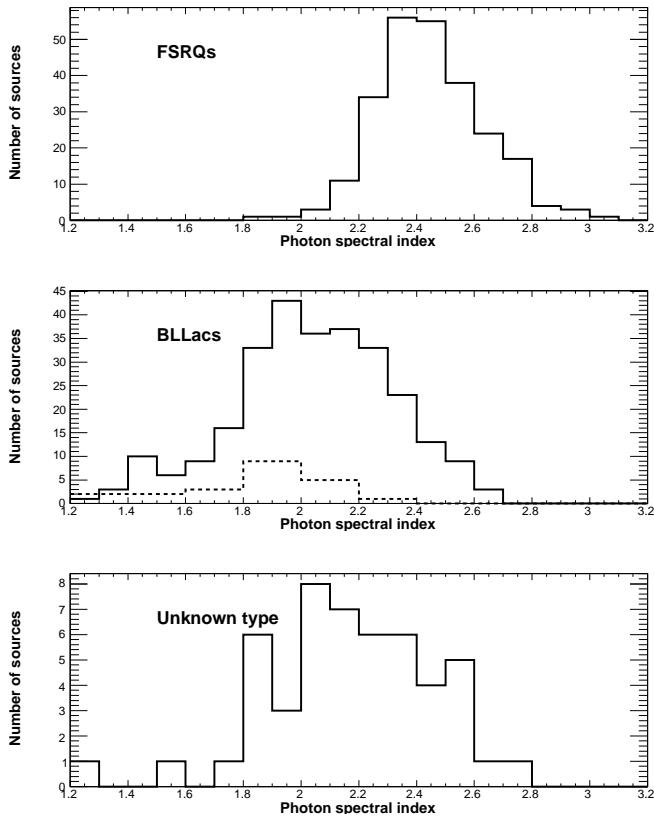
Fig. 4. Photon spectral index distributions for the FSRQs (top), BL Lacs (middle), and AGNs of unknown type (bottom) in the clean sample. For BL Lacs, the dashed histogram corresponds to the TeV-detected sources.
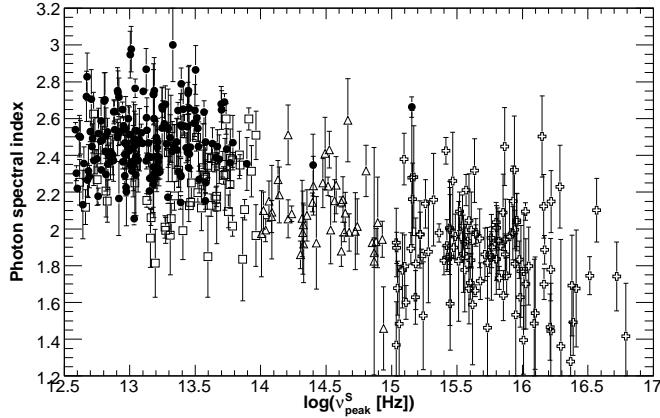
Fig. 5. Photon spectral index vs. peak frequency of the synchrotron component of the SED for FSRQs (solid circles) and BL Lacs (squares: LSPs, triangles: ISPs, crosses: HSPs) in the clean sample.

3.2. Photon index

The photon spectral index distributions for the clean sample, shown in Fig. 4, confirm the trend found for the LBAS sources (Abdo et al. 2009a) and alluded to above, with a clear difference between FSRQs and BL Lacs. Only 7% of
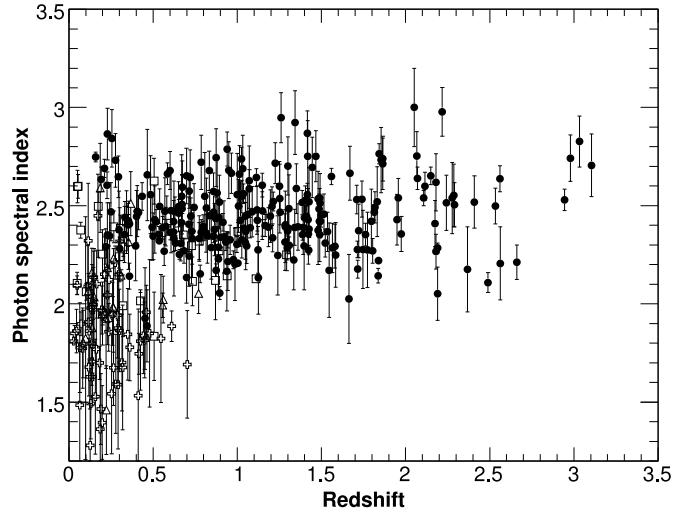
Fig. 6. Photon spectral index vs. redshift for the FSRQs (solid circles) and BL Lacs (squares: LSPs, triangles: ISPs, crosses: HSPs) in the clean sample.

FSRQs (17/231) have a photon spectral index $\Gamma < 2.2$, and only two FSRQs have $\Gamma < 2$ (with uncertainties of $\sim$0.2). Thus, it is quite clearly established that LAT-detected FSRQs exhibit soft γ-ray spectra. The 1LAC BL Lac distribution is broader than that observed for LBAS; it shows a larger overlap with the FSRQ distribution. In Abdo et al. (2010c), the BL Lacs with $\Gamma > 2.2$ were found to be mostly LSP sources. This trend is also confirmed for the 1LAC sources, as illustrated in Fig. 5, which shows Γ vs. $\nu_{\mathrm{peak}}^{\mathrm{S}}$. Abdo et al. (2010c) also point out that the BL Lac photon spectral index distribution suffers from a bias since the high-spectral-index (i.e., soft) end is cut off somewhat due to the TS threshold. The completeness of the sample is discussed elsewhere (Tosti, in these proceedings). As expected, the TeV sources present in the 1LAC have fairly hard spectra. Their photon index distribution is depicted in Fig. 4 (middle panel, dashed histogram).

The photon spectral index is plotted against redshift in Fig. 6. For FSRQs, no significant evolution is visible. This behavior is compatible with what was previously observed for LBAS. The attenuation effect of the extragalactic background light (EBL) would tend to introduce spurious evidence of evolution, but the soft spectra of FSRQs and the common presence of spectral breaks at a few GeV (Abdo et al. (2010c)) both minimize this effect. A stronger evolution is seen for BL Lacs: hard sources are mostly located at low redshifts, while most high-redshift sources are softer than average (though it is important to bear in mind that most BL Lacs do not have measured redshifts). This trend was less clear for the LBAS BL Lacs Abdo et al. 2009a due to lower statistics. The photon spectral index distributions for sources with $z < 0.5$ and $z > 0.5$ are notably different. This provides some insight into the properties of BL Lacs without measured redshifts. The distribution of BL Lacs with unknown redshifts includes notably fewer hard sources than that for
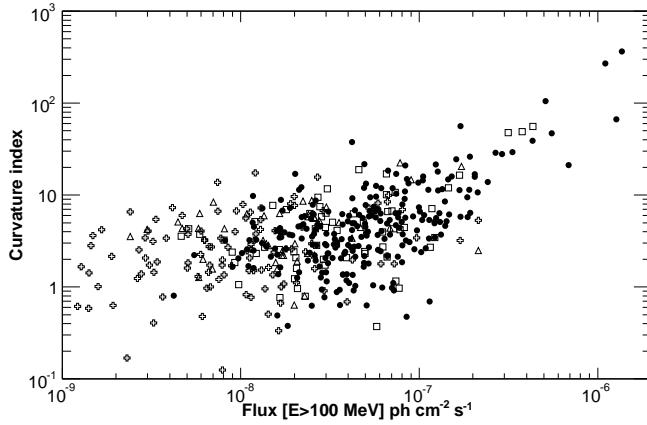
Fig. 7. Spectral curvature index vs. flux for FSRQs (solid circles) and BL Lacs (squares: LSPs, triangles: ISPs, crosses: HSPs) in the clean sample.

BL Lacs with known redshifts. The distribution of BL Lacs with unknown redshifts is similar to that of BL Lacs with $z > 0.5$ (K-S probability of 0.54 that the two distributions are drawn from the same underlying population) supporting the idea of some bias toward higher redshifts for this class of objects.

3.3. Spectral break

While all AGNs spectra measured with EGRET were consistent with single power law distributions, the extended energy range covered by the *Fermi*/LAT has enabled to discover the presence of a spectral break at a few GeV for bright LBAS FSRQs and some LSP-/ISP-BL Lacs (Abdo et al. (2010c)). So far, no break has ever been found in the spectrum of any bright HSP-BL Lacs, while if present it would have easily be detectable given the relative hardness of these sources. The first evidence for such feature was found in 3C 454.3 (Abdo et al. 2009e), which is still so far the best studied case thanks to its high current brightness. The best model to the data accumulated over 6 months of operation is a broken power law with a break energy of 2.5 GeV and a change in spectral slope of 1.2. The break origin is still unknown, several possibilities (feature of the underlying electron energy distribution, Klein-Nishina effect, intrinsic absorption within the emitting blob...) are being actively discussed.

The departure of the spectrum from a power-law shape can be estimated via a simple χ^2 test on the five fluxes, referred to as the curvature index (Abdo et al. 2010b). Figure 7 displays the curvature index vs flux for the 1LAC sources. The trend found for the LBAS sources is of course confirmed with the larger sample. One must keep in mind that in order to show a high curvature index a source needs both to have a spectrum deviating from a power-law distribution and be bright enough so that the observed deviation is statistically significant. Thus no conclusion can be drawn for fainter sources.
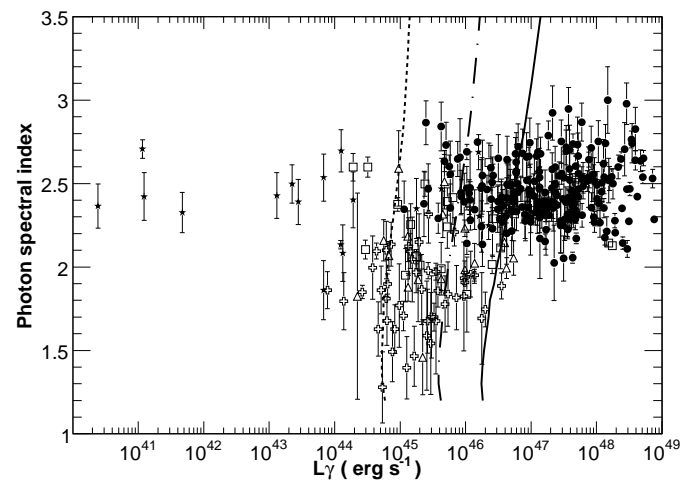
Fig. 8. Photon spectral index vs. γ-ray luminosity for the different AGN classes (solid circles: FSRQs, squares: LSP-BL Lacs, triangles: ISP-BL Lacs, crosses: HSP-BL Lacs, stars: radio galaxies) in the clean sample. The curves represent approximate instrumental limits for $z = 0.2$ (dashed), $z = 0.5$ (dot-dashed), and $z = 1$ (solid).

4. Luminosity Distributions

The γ-ray luminosity L_γ is calculated as $L_\gamma = 4\pi d_L^2 S(E_1, E_2)/(1 + z)^{\Gamma-2}$ where d_L is the luminosity distance, Γ is the photon spectral index, S is the energy flux, and E_1 and E_2 are the lower and upper energy bounds (taken here to be 100 MeV and 100 GeV) respectively.

Figure 8 shows the photon spectral index plotted against the γ-ray luminosity. It is important to bear in mind two issues when interpreting this correlation: the higher flux limit for soft sources and the difference in redshift distributions between FSRQs and BL Lacs. Given their relative softness (and thus, high flux limit), FSRQs are excluded from the soft-faint region. BL Lacs are also partly excluded because of their relatively low fluxes. Luminosity limits calculated for different redshifts are displayed for reference in Fig. 8 and illustrate somewhat the effect of the Malmquist bias (sources located at larger distances appear more luminous than closer ones since fainter sources are below the detection threshold).

Furthermore, as noted by Ghisellini et al. (2009) and seen in Fig. 8, the γ-ray blazars detected with the *Fermi*-LAT separate into hard-spectrum, low-luminosity sources, primarily consisting of BL Lac objects, and high-luminosity, soft-spectrum sources, primarily consisting of FSRQs and LSP-BL Lacs. Compared with the LBAS sample, the blazar divide now displays an extension of the sample toward low-luminosity objects in each of the blazar subclasses. In addition, we identify a third branch consisting of radio galaxies, which are distinguished from the aligned blazars by their soft spectra and very low γ-ray luminosities.

The finding that FSRQs in the 1LAC almost all have soft ($\Gamma \gtrsim 2.2$) γ-ray spectra suggests a connection between the presence of strong emission lines and the non-thermal electron maximum Lorentz factor or spectral shape. It is consistent with scenarios (Ghisellini et al. 1998; Böttcher & Dermer 2002) in which the strong ambient radiation fields, as revealed by the presence of emission lines, affects the acceleration and cooling of particles and controls the formation of the blazar SED. The luminosity dependence of the γ-ray spectral hardness is also consistent with the blazar sequence (Ghisellini et al. 1998; Fossati et al. 1998; Ghisellini & Tavecchio 2008), in which the frequencies of the synchrotron and Compton peaks are inversely correlated with the apparent isotropic luminosities of the blazars. This behavior has been interpreted in terms of an evolution of FSRQs into BL Lac objects as the supply of matter fueling the accretion disk declines, the surrounding external radiation fields become less intense, and the jet weakens (Böttcher & Dermer 2002, Cavaliere & D'Elia 2002, Ghisellini & Tavecchio 2008).

Important caveats must, however, be considered before drawing firm conclusions about the blazar sequence from the 1LAC sources. First, identification of the blazars used to construct the blazar sequence is biased by the flux limits and frequency ranges of the underlying radio and X-ray samples (Giommi et al. 1999, Padovani et al. 2003), and different conclusions about its validity can be drawn depending on the catalogs used to examine the sequence. Second, specific sources that do not conform to the sequence have been identified (e.g., Caccianiga & Marchä). Third, the 1LAC is significance-limited rather than flux-limited, which results in preferential detection of lower-flux, harder-spectrum sources. This means that there is a strong bias against detecting weak, soft-spectrum γ-ray sources from low-luminosity LSP blazars that might violate the sequence. On the other hand, hard-spectrum HSP sources should be more easily detected, but there are no high-luminosity HSP sources detected in the LAT band (see Fig. 8), as all high-luminosity objects have SEDs of the LSP type. This may, however, reflect the difficulty of measuring the redshifts of BL Lacs. Even for sources associated with AGNs with high probabilities, a large fraction of BL Lacs lack redshift measurements. It is possible that a number of distant, high-luminosity HSP-BL Lacs are included in the 1LAC sample. According to our SED classification, $\sim$20 BL Lacs with unknown redshifts are already classified as HSPs. If they were all at high redshift (e.g., $z = 2$), and excluding those already detected at very high energy (which indicates a low redshift due to a lack of EBL absorption), $\sim$7 objects could have γ-ray luminosities $L_\gamma \gtrsim 10^{48}$ erg s^{-1}.

The existence of such sources, though quite rare, would be contrary to expectations from the blazar sequence (Ghisellini et al. 1998, Fossati et al. 1998, Ghisellini & Tavecchio 2008). In the absence of redshift measurements of possible high-luminosity, hard-spectrum sources, we can only conclude that the *Fermi* results seem compatible with the sequence. Identifying hard-spectrum
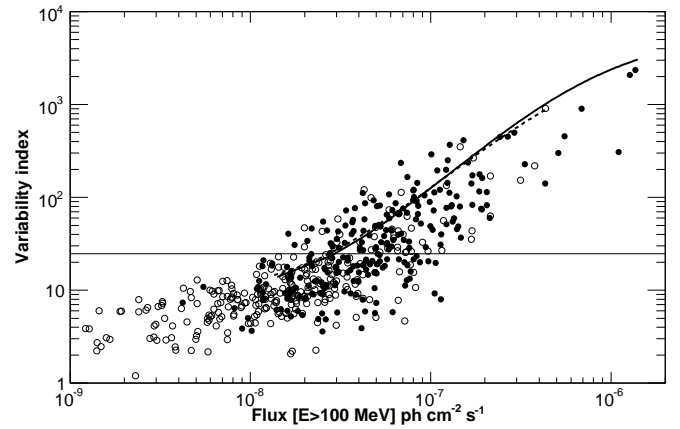
Fig. 9. Variability index versus flux for FSRQs (solid circles) and BL Lacs (open circles) in the clean sample. The curves display the evolution of the variability index for the FSRQ 3C 454.3 (solid) and the BL Lac object AO 0235+164 (dashed) that would be observed for the same temporal variation but lower mean fluxes.

blazar sources at high redshifts is also important for studies of the cosmological evolution of the extragalactic background light, which are hampered by their absence.

5. Variability

One of the defining characteristics of AGNs is their variability, measured at all time scales and at all wavelengths. Through 2010 Jan 20, 43 1LAC sources (and one at low latitude) have been the subjects of ATels from the LAT team. They comprise 32 FSRQs (with redshifts as high as $z = 2.534$, for B3 1343+451), 10 BL Lacs, and one AGN of another type (CGRaBS J2250−2806, a narrow-line radio galaxy). Doubling flux time scales as short as 6 hours have been reported for bright FSRQs as 3C454.3 and PKS1502+106 in the *Fermi*/LAT band.

In the LBAS sample, 46 sources (35 FSRQs, 10 BL Lacs, and one blazar of unknown type) were flagged as variable based on the results of a χ^2 test applied to weekly light curves covering the first three months of the LAT sky survey. Recently, Abdo et al. (2010d) detected variability in 64 LBAS sources by analyzing weekly light curves over a period of 11 months. The 1FGL catalog also lists a variability index V, obtained using a simple χ^2 test, that can be used to determine the probability that a source is variable. Sources for which $V > 23.21$ have a 99% probability (for 10 degrees of freedom) of being variable. Figure 9 shows the the variability index plotted vs flux for blazars (BL Lacs and FSRQs) in the clean sample . For the same reasons as for the curvature index, in order for a source to be associated with a high variability index, it has to be both variable and sufficiently bright. 189 blazars in the clean sample are found to be variable. They comprise 129 FSRQs (68%), 46 BL Lacs (24%), five AGNs of other types (NGC 1275, B2 0321+33B, 4C +15.54, B2 1722+40, and CGRaBS J2250−2806), and nine blazars of unknown

type. The 46 variable BL Lacs include 24 LSPs, nine ISPs, 10 HSPs, and three BL Lacs (CRATES J0058+3311, CGRaBS J0211+1051, and CRATES J1303+2433) for which there are not enough multi-wavelength data to permit an SED classification. These are quite bright sources observed at energies higher than the peak energies of their SEDs, where the amplitude of the variability is generally larger. No significant differences in the variability of FSRQs and BL Lacs are observed for sources at comparable fluxes.

6. Sources detected at other bands

6.1. EGRET sources

Ten years after EGRET, it is interesting to look at the fraction of the AGNs that were active in the EGRET era and are detected again by the LAT with a comparable flux. We consider two sources to be "positionally coincident" when the separation between their positions is less than the quadratic sum of their 95% error radii. In the 1LAC sample, 63 AGNs are positionally coincident with 3EG sources. Of these, the 3EG catalog lists 51 sources as AGN identifications and four as AGN associations. The 3EG catalog listed a total of 62 sources as AGN identifications, so there are 11 identified EGRET AGN that are not positionally coincident with 1LAC sources. 45 sources from the 1LAC have positions compatible with the revised EGRET catalog (Casandjian & Grenier 2008), while 22 sources are positionally coincident with sources from the high-energy EGRET catalog. In all, 75 1LAC sources have coincident detections from one or more of these three EGRET catalogs.

6.2. AGILE sources

11 of the sources in this catalog are included in the first year *AGILE* catalog (Pittori et al. 2009). All 11 are identified as blazars by *AGILE*, and indeed, these 11 comprise the total sample of blazars in the 1AGL catalog. Only two of these *AGILE*-detected sources do not have similar EGRET detections. In all, 77 1LAC sources have been cataloged by other GeV instruments. These AGNs are composed of 49 FSRQs, 21 BL Lacs, four AGNs of other types, and three AGNs of unknown types.

During its 4.5-year mission, EGRET found few sources with flux ($E > 100$ MeV) less than 10×10^{-8} photons cm^{-2} s^{-1}. A large number of the 1LAC sources have fluxes well below this value; such sources would not have been visible to EGRET. Some sources, such as 1FGL J0428.6−3756 (associated with PKS 0426−380) and 1FGL J2229.7−0832 (associated with PKS 2227−08), have flux values well above the EGRET threshold but were not seen by EGRET and yet are not noted as being variable in the 1FGL data. These examples continue to demonstrate that long-duration variability is evident in AGN γ-ray flux.

All of the EGRET sources seen at 10σ significance and associated with flaring blazars have been detected by the LAT and appear with blazar associations.

6.3. Hard X-ray sources

The Swift-BAT and INTEGRAL-IBIS instruments have been conducting surveys at hard X-ray energies, drastically improving our knowledge of the source populations in this energy band; the most recent catalogs are the fourth IBIS catalog (Bird et al. 2010) of 723 sources detected at 17–100 keV and the 54-month Palermo BAT catalog (Cusumano et al. 2009) of 1049 sources detected at 14–150 keV. An initial comparison between the LBAS sources and the fourth IBIS catalog by Ubertini et al. 2009 showed that only a small subset of the >250 *INTEGRAL* AGNs, of which 19 are blazars, was detected by the LAT.

Restricting the catalogs to $|b| > 10°$, there are 291 IBIS sources and 736 BAT sources. If we consider all of the 1LAC sources with associated counterparts that fall within the error circles of the hard X-ray catalogs, 50 of the 1LAC sources can be associated with known hard X-ray sources. Of these 50 sources, one appears only in the fourth IBIS catalog, 16 appear in both the fourth IBIS catalog and the 54-month Palermo BAT catalog, and the remaining 35 are detected only in the 54-month Palermo BAT catalog. This is still a very small subset of AGNs despite the depth of the LAT catalog and the sky coverage of the BAT catalog.

The high-confidence 1LAC AGNs detected in hard X-rays contains 27 FSRQs, 16 BL Lacs, and seven AGNs of other types. Most of the AGNs (54%) detected in hard X-rays are FSRQs; this is expected since the external Compton peak of these high-luminosity objects reaches a maximum at MeV energies and declines in the hard X-rays, maintaining a substantial fraction of the emitting power. The difference in the spectral shapes of BL Lacs and FSRQs observed in hard X-rays indicates that this energy range probes the high-energy tail of the synchrotron peak in BL Lacs and the ascending part of the Compton peak in FSRQs.

6.4. TeV sources

Of the TeV AGNs, 28 are detected by *Fermi* as 1FGL sources, with a mean photon spectral index of $\langle\Gamma_{\mathrm{GeV}}\rangle = 2.02 \pm 0.01$. Taking only the subsample of 25 GeV–TeV BL Lacs, the mean index is $\langle\Gamma_{\mathrm{GeV}}\rangle = 1.92 \pm 0.01$ ($\sigma_\Gamma = 0.26$), compared with 2.07 ± 0.01 ($\sigma_\Gamma = 0.28$) for the larger sample of *Fermi* BL Lacs, illustrating that the TeV sources are among the hardest BL Lacs in the GeV regime. The measured spectra of the majority of the GeV–TeV BL Lacs are well described by power laws in both regimes. For many of the sources, the photon spectral index of the GeV emission differs significantly from that of the TeV emission, which may be an indication of the presence of a break in the γ-ray spectrum between the two regimes.

However, most of the TeV spectra have not been measured simultaneously with the GeV spectra, and caution is advised when comparing the spectra in detail. The largest such break, consistent with $\Delta\Gamma \equiv \Gamma_{\mathrm{TeV}} - \Gamma_{\mathrm{GeV}} \sim 2$, is evident in the spectra of 1ES 1101+496, H 1426+428 and PG 1553+113. By contrast, the spectra of the nearby radio galaxies M 87 and Cen A show no evidence of a spectral break. The mean break index is $\langle\Delta\Gamma\rangle$=1.3. An apparent deficit of sources with small $\Delta\Gamma$ is observed at high redshift which may partly be the effects of pair production with the EBL, which is expected to introduce a redshift-dependent steepening into the TeV spectra of extragalactic objects.

The four TeV AGNs not detected thus far by *Fermi* are RGB J0152+017, 1ES 0229+200, 1ES 0347−121 and PKS 0548−322, all HSP-BL Lacs. Extrapolating the measured power-law TeV spectra from all the TeV AGNs down to 200 GeV, it is evident that these four have among the smallest fluxes of all TeV AGN at this energy.

7. Conclusion

The 1LAC catalog has paved the way to a better understanding of γ-ray blazars. The main results are:

- an increase by 5 of the number of known GeV blazars
- a low number of misaligned blazars, 6 radio galaxies
- redshift distributions peaking at z≃1 for FSRQs and at low redshift for BL Lacs with known redshifts
- a high BL Lac/FSRQ ratio, close to unity
- a high HSP/LSP ratio among BL Lacs
- a fairly strong correlation between photon spectral index and blazar class for the detected sources

By now, about twice as many *Fermi*/LAT data have been accumulated. The 2LAC catalog should be released in the Fall of 2010.

References

Abdo, A. A. et al. 2009a, ApJ, 700, 597
Abdo, A. A. et al. 2009b, ApJ, 707, 1310
Abdo, A. A. et al. 2009c, ApJ, 707, 55
Abdo, A. A. et al. 2009d, ApJL, 707, L142
Abdo, A. A. et al. 2009e, ApJ, 699, 817
Abdo, A. A. et al. 2010a, ApJ, 715, 429
Abdo, A. A. et al. 2010b, accepted by ApJS, [arXiv: 1002.2280]
Abdo, A. A. et al. 2010c, ApJ, 710, 1271
Abdo, A. A. et al. 2010d, [arXiv: 1004.0348]
Abdo, A. A. et al. 2010e, accepted by ApJ, [arXiv: 0912.2040]
Ajello, M., et al. 2009, ApJ, 699, 603
Bird, A. J., et al. 2010, ApJS, 186, 1
Böttcher, M., & Dermer, C. D. 2002, ApJ, 564, 86
Caccianiga, A., & Marchä, M. J. M. 2004, MNRAS, 348, 937
Casandjian, J., & Grenier, I. A. 2008, A&A, 489, 849
Cavaliere, A., & D'Elia, V. 2002, ApJ, 571, 226
Cusumano, G., et al. 2009, A&A, in press; [arXiv:0906.4788]
Fossati, G., Maraschi, L., Celotti, A., Comastri, A., & Ghisellini, G. 1998, MNRAS, 299, 433
Ghisellini, G., Celotti, A., Fossati, G., Maraschi, L., & Comastri, A. 1998, MNRAS, 301, 451
Ghisellini, G., & Tavecchio, F. 2008, MNRAS, 387, 1669
Ghisellini, G., Maraschi, L., & Tavecchio, F. 2009, MNRAS, 396, L105
Ghisellini, G., et al. 2010, MNRAS, submitted; [arXiv:0912.0001]
Giommi, P., Menna, M. T., & Padovani, P. 1999, MNRAS, 310, 465
Hartman, R. C. et al. 1999, ApJS, 123, 79
Healey, S. E. et al. 2007, , ApJS, 171, 61
Healey S. E. et al. 2008, ApJS, 175, 97
Hinshaw G. et al. 2007, ApJ, 170, 288
Massaro E. et al. 2009, A&A, 495, 691
Mattox, J. R. et al. 2001, ApJS, 135, 155
Padovani, P., Perlman, E. S., Landt, H., Giommi, P., & Perri, M. 2003, ApJ, 588, 128
Pittori, C., et al. 2009, A&A, 506, 1563
Ubertini P. et al. 2009, ApJL, 706, L7

The radio gamma-ray connection in AGNs in the era of Fermi/LAT

M. Giroletti[1], A. Reimer[2], L. Fuhrmann[3], V. Pavlidou[4], J. L. Richards[4]
on behalf of the *Fermi*/LAT collaboration, and
E. Angelakis[3]

[1] INAF Istituto di Radioastronomia, via Gobetti 101, I-40129, Bologna, Italy
[2] Institut für Astro- und Teilchenphysik and Institut für Theoretische Physik, Leopold-Franzens-Universität Innsbruck, A-6020 Innsbruck, Austria
[3] Max-Planck-Institut für Radioastronomie, Auf dem Hügel 69, 53121 Bonn, Germany
[4] California Institute of Technology, Owens Valley Radio Observatory, USA

Abstract. Radio and gamma-ray emission from active galactic nuclei (AGN) are thought to share a common origin, related to the ejection phenomena in the vicinity of supermassive black holes. Thanks to its sensitivity, surveying capability, and broad energy range, the Large Area Telescope (LAT) onboard the *Fermi* Gamma-ray Space Telescope has permitted us to discover and characterize several hundreds extragalactic gamma-ray sources. These sources are typically associated with blazars, characterized by significant radio emission and flat spectrum. The radio luminosity distribution is extended over 7 orders of magnitudes, with flat spectrum radio quasars clustered at higher powers and BL Lacs more scattered. We present here a comparison of the gamma-ray and radio emission properties during year 1 of the Fermi-LAT observations, using both archival and simultaneous radio observations. We remark the need to consider different case studies (dividing by source class, origin of radio data, gamma-ray energy band) and to discuss the statistical significance of the results with the use of Monte Carlo simulations.

1. Introduction

Around 10% of active galactic nuclei (AGN) are strong sources of radio emission. This includes radio galaxies, radio quasars (flat or steep spectrum), and BL Lac type objects. All these sources are generally referred to as radio loud (RL) AGN, whereas flat spectrum radio quasars (FSRQ) and BL Lac objects are collectively known as *blazars*. Interestingly, the vast majority of identified extragalactic sources in the third EGRET catalog (3EG, Hartman et al., 1999) belong to the blazar class.

RL AGN, and blazars in particular, are by far the most numerous and most luminous class of extragalactic gamma-ray sources. Since these sources are bright in both gamma-ray and radio, it is natural to expect a connection between the emission processes in the two energy bands. Radio emission from blazars (and RL AGN in general) is generally accepted to be synchrotron radiation emitted by relativistic electrons, while the physical processes responsible for the γ-ray emission are much less well constrained. The presence of non-thermal synchrotron emission implies the existence of a population of relativistic electrons. In the presence of low energy seed photons and relativistic beaming, Inverse Compton (IC) up-scattering of the photons is frequently invoked to explain the γ-ray emission.

Indeed, in the well known *blazar sequence* (Fossati et al., 1998; Ghisellini et al., 1998; Donato et al., 2001), it is proposed that the synchrotron and inverse Compton mechanisms give rise to a connection between the radio luminosity and the peak frequencies and relative intensities

of the characteristic two-humped spectral energy distribution (SED) of blazars. On the other hand, evidence for a direct correlation between radio and γ-ray flux density or luminosity with EGRET data has been widely debated (e.g., Stecker et al., 1993; Salamon & Stecker, 1994; Taylor et al., 2007; Bloom, 2008) but not conclusively demonstrated, when all the relevant biases and selection effects are considered (e.g., Mücke et al., 1997).

The Large Area Telescope (LAT) onboard the *Fermi Gamma-ray Space Telescope*, with its large field of view and unprecedented sensitivity, is now putting us in the condition of a better understanding of the extragalactic γ-ray source population. In anticipation of the launch of *Fermi*, large projects in the radio band have been undertaken (e.g., Healey et al., 2007; Fuhrmann et al., 2007; Richards et al., 2009; Lister et al., 2009). The results of these projects can now be exploited to gain insights into the radio properties of this population (see also Max-Moerbeck et al., 2009) and into the relation between radio and gamma-ray properties. Indeed, a number of papers (e.g., Abdo et al., 2009b; Kovalev et al., 2009) have appeared discussing this topic as soon as the first list of bright sources was announced (Abdo et al., 2009c); a few more (Giroletti et al., 2010; Mahony et al., 2010; Ghirlanda et al., 2010) have then addressed the same issue considering the sources in the 1 year *Fermi*/LAT catalog (1FGL, Abdo et al., 2010b).

We report in Sect. 2 the main results obtained after three months of sky-survey operation (LAT Bright AGN
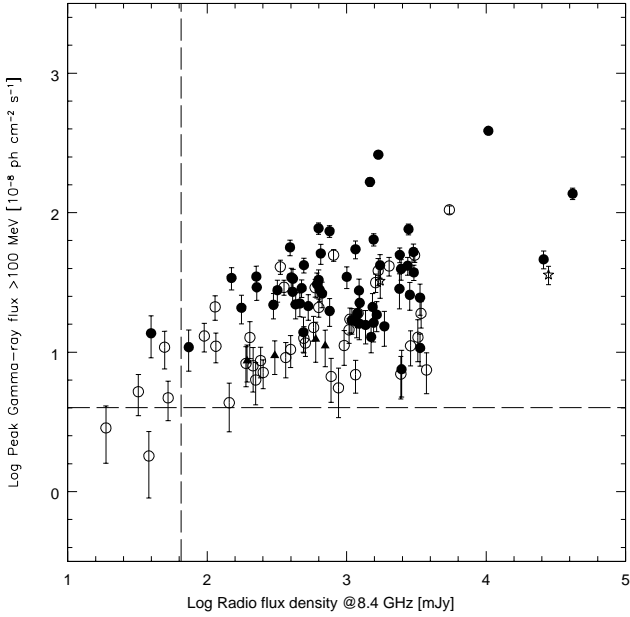
Fig. 1. Peak gamma-ray flux vs. radio flux density at 8.4 GHz for LBAS sources; the dashed lines show the CRATES flux density limit and the typical LAT detection threshold in three months. Filled circles: FSRQs; open circles: BL Lacs; triangles: blazars of unknown type; stars: radio galaxies.

Sample, LBAS, Abdo et al., 2009b). Some analysis performed on the 1 year catalog sources is presented in Sect. 3. A discussion and the conclusions so far are given in Sect. 4, along with our future plans. We use a ΛCDM cosmology with $h = 0.71$, $\Omega_{\mathrm{m}} = 0.27$ and $\Omega_{\Lambda} = 0.73$, where the Hubble constant $H_0 = 100h$ km s^{-1} Mpc^{-1} and define radio spectral indices α such that the flux density $S(\nu) \propto \nu^{-\alpha}$.

2. Radio/gamma-ray connection in the LBAS

In its first three months of sky-survey operation, the LAT has revealed 125 non-pulsar bright sources at $|b| > 10°$ with test statistic greater than 100 ($TS > 100$, corresponding to a detection significance of $\sim 10\sigma$); 106 of these sources have high-confidence associations with known AGN, 10 have lower-confidence associations, and only 9 remain un-associated. Therefore, the fraction of high-latitude bright γ-ray sources associated with radio loud AGN turns out to be as high as 93%! Of the 106 LBAS sources, 104 are blazars, consisting of 58 FSRQs (including one narrow-line Seyfert 1, J0948+0022, Abdo et al., 2009a); 42 BL Lacs; four blazars with unknown classification; and two radio galaxies (Centaurus A and NGC 1275).

By combining data in the radio archives and the LAT measurements, the properties of the LBAS sources at low and high energy were compared. The basic radio properties were obtained from the radio catalogs used for the associations, i.e., CRATES (Healey et al., 2007) and BZCat
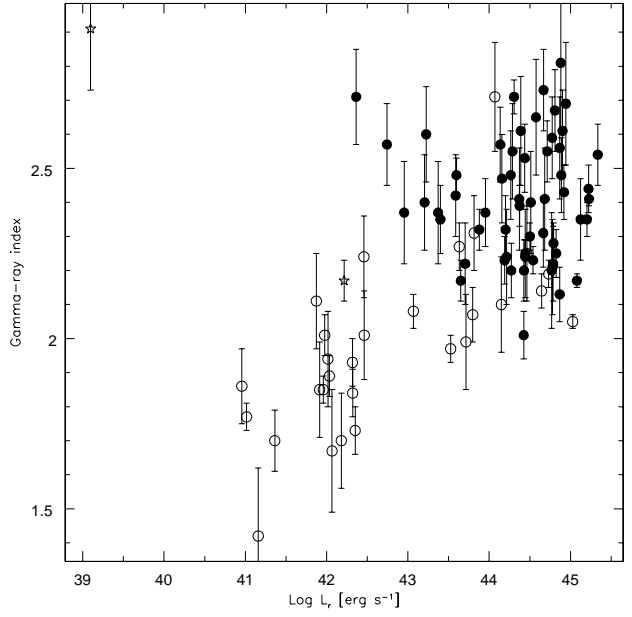
Fig. 2. Gamma-ray photon index vs. radio luminosity for LBAS sources. Symbols as in Fig. 1. The object in the top left corner is the gamma-ray source associated to Cen A.

(Massaro et al., 2009). CRATES provides 8.4 GHz VLA data for sources brighter than $S_{4.8\,\mathrm{GHz}} = 65$ mJy, typically with sub-arcsecond resolution. BZCat is a multi-frequency catalog giving low frequency radio data, typically from the NVSS.

Using these data, we show the peak γ-ray flux vs. the radio flux density in Fig. 1 and the radio luminosity vs. γ-ray spectral index plane in Fig. 2. These plots are also discussed in detail in Abdo et al. (2009b). The calculation of a simple Spearman's rank correlation coefficient ρ for the distribution in the flux-flux plane (Fig. 1) of the 106 objects yields $\rho = 0.42$. When FSRQs and BL Lacs are considered separately, however, quite different results are obtained ($\rho_{\mathrm{FSRQ}} = 0.19$, $\rho_{\mathrm{BL\,Lac}} = 0.49$). The other relevant plot for the comparison of radio and γ-ray properties is the radio luminosity vs. γ-ray spectral index plane (see Fig. 2). The broad LAT energy range permits to readily reveal the separation between BL Lacs and FSRQs, with FSRQs at largest L_r and softer indices and BL Lacs at lower L_r and harder indices. As far as the two radio galaxies are concerned, NGC 1275 is similar to BL Lacs, while Cen A is well displaced, having a much softer γ-ray spectral index than other low-power radio sources.

3. Radio/gamma-ray connection in the 1LAC

After more than 1 year of scanning the gamma-ray sky, the LAT First Year catalog[1] (Abdo et al., 2010b), including more than 1400 sources, has been made public. About half of these sources belong to the AGN class (1LAC, Abdo et al., 2010a) with most of them identified via radio catalogs

---

[1] http://fermi.gsfc.nasa.gov/ssc/data/access/lat/1yr_catalog/
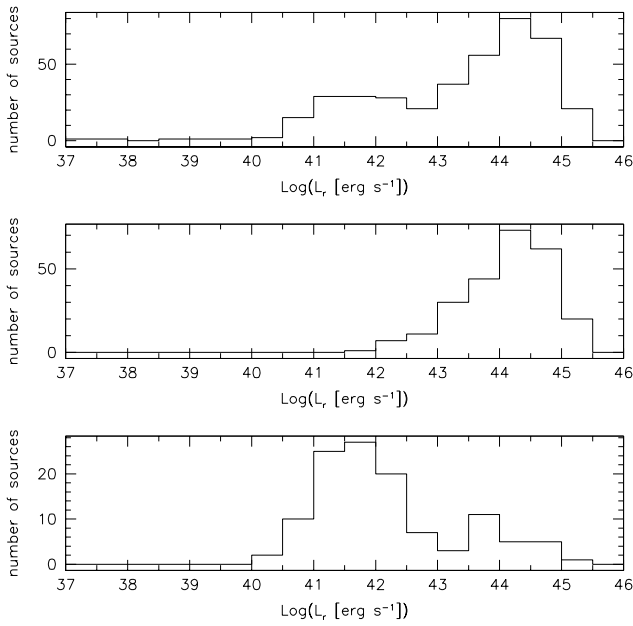
Fig. 3. Histogram of radio luminosity distribution for sources in the 1LAC catalog. Top panel: all sources; middle: FSRQs; bottom: BL Lacs.

Fig. 4. Preliminary distribution of 1-yr LAT sources in the gamma-ray photon flux at $E > 1\,\mathrm{GeV}$ vs. $8\,\mathrm{GHz}$ radio flux density plane. Symbols as in Fig. 1.

as for the LBAS. In particular, 599 high latitude 1FGL sources have a single high confidence association with an AGN, including 248 FSRQs and 275 BL Lacs. In the following, we consider this set of sources (also known as the *1LAC clean sample*) for our analysis.

Whereas the LBAS results were based on sources with $TS > 100$ in three months of survey, the 1LAC clean sample considered here is selected with $TS > 25$ (significance about 5σ). As a consequence, the explored space of parameters becomes significantly larger: thanks to the *great sensitivity* and *broad energy range* of the LAT, *Fermi* has already been successful in revealing faint γ-ray sources and in the characterization of their diverse photon indices.

However, although several gamma-ray sources are associated to blazars as weak as a few tens mJy, the radio properties of the 1LAC sources remain overall similar to those found for the LBAS sources. For example, the different distributions for the radio luminosity of FSRQs and BL Lacs are confirmed, with $\log L_{\mathrm{r,FSRQ}}\ [\mathrm{erg\,s^{-1}}] = 44.2 \pm 0.7$ and $\log L_{\mathrm{r,BL\,Lac}}\ [\mathrm{erg\,s^{-1}}] = 42.2 \pm 1.2$, respectively (see Fig. 3). In particular, the BL Lacs remain spread over a wider interval of radio luminosities, reaching as low luminosities as $L_r = 10^{40}$ erg s^{-1}.

As far as the radio spectral properties are concerned, the vast majority of sources have a flat spectrum ($\langle \alpha \rangle = 0.06\pm0.23$), including sources as weak as a few tens of mJy. However, a small but significant tail of steeper spectrum sources is also present, which are described in more detail in dedicated works, such as the one on misaligned AGNs by Abdo et al. (2010c).

Finally, the radio flux density vs. mean γ-ray flux plane becomes more populated, as shown in Fig. 4. The

Spearman's rank correlation coefficient for the full sample changes to $\rho = 0.39$. Of course, the remarks noted above still apply: different source classes sample different regions of the plane, data are not simultaneous, and observational biases could be present. For these reasons, we have considered both archival and simultaneous radio data. The simultaneous radio data are available from the Owens Valley Radio Observatory (OVRO) monitoring program (Richards et al., 2009) for 199 sources, while the archival radio data are from CRATES (Healey et al., 2007) or CRATES-like programs, such as CLASS (Myers et al., 2003).

For each of the two samples, we have also compared the radio flux density to the 1-yr gamma-ray photon flux in various energy bands, considering only the sources that are significant in a given one. Moreover, we tested the two populations of FSRQs and BL Lacs separately, since they have different spectral properties and showed different behaviors in the preliminary analysis (Abdo et al., 2009b; Giroletti et al., 2010).

Indeed, FSRQs and BL Lacs continue to reveal different behaviors, with BL Lacs displaying larger values of ρ than FSRQs. For example, in the $E > 1\,\mathrm{GeV}$ energy band, we find $\rho = 0.49$ for BL Lacs and $\rho = 0.34$ for FSRQs, which bracket the value obtained considering all the 599 sources ($\rho = 0.39$). Moreover, in FSRQs the correlation coefficient increases with the energy range, while BL Lacs behave on the contrary.

4. Discussion and an outlook

The correlation coefficients reported in the previous section provide information about its apparent strength, but a quantitative evaluation of its statistical significance can only be obtained with Monte-Carlo tests. Pavlidou et al. (2010) have devised a method to investigate how frequently a sample of objects with intrinsically uncorrelated gamma/radio flux densities will yield an apparent correlation as strong as the one seen in the data, when subjected to the same distance effects as the sample actually under consideration.

While, we defer to other papers the details of the method and its applications to the 1LAC sample (Pavlidou et al., 2010; Abdo et al., 2010d), we just highlight one result that shows the relevance of the effect of the redshift range on the probability distribution of ρ for the uncorrelated cases. Since BL Lacs have a much more limited redshift range than FSRQs, FSRQs exhibit the effect of an induced correlation by the d_L^2 factor in a much more pronounced way in our statistical tests. As a consequence, and not simply because ρ_{FSRQ} is actually lower, it is harder to demonstrate a statistically robust correlation for FSRQs. On the other hand, several BL Lacs lack a measured redshift and including them in the statistical test requires assumptions that have to be carefully pondered.

All in all, thanks to its unique capabilities, *Fermi* has revealed that the bright gamma-ray extragalactic sky is dominated by radio loud AGN, and blazars in particular, even more than it could be probed during the EGRET era. The presence of a correlation between the observed radio and gamma-ray flux density for the *Fermi* sources seems to hold, as also discussed by Kovalev et al. (2009), Mahony et al. (2010), and Ghirlanda et al. (2010). However, a statistically sound assessment of its significance – as well as an understanding of its possible physical implications – can only be explored with Monte-Carlo simulations (Pavlidou et al., 2010; Abdo et al., 2010d).

References

Abdo, A. A., Ackermann, M., Ajello, M., et al. 2009a, ApJ, 699, 976

Abdo, A. A., Ackermann, M., Ajello, M., et al. 2009b, ApJ, 700, 597

Abdo, A. A., Ackermann, M., Ajello, M., et al. 2009c, ApJS, 183, 46

Abdo, A. A., Ackermann, M., Ajello, M., et al. 2010a, ApJ, 715, 429

Abdo, A. A., Ackermann, M., Ajello, M., et al. 2010b, ApJS, 188, 405

Abdo, A. A., Ackermann, M., Ajello, M., et al. 2010c, ApJ submitted (misaligned AGNs)

Abdo, A. A., et al. 2010d, in preparation

Bloom, S. D. 2008, AJ, 136, 1533

Donato, D., Ghisellini, G., Tagliaferri, G., & Fossati, G. 2001, A&A, 375, 739

Fossati, G., Maraschi, L., Celotti, A., et al. 1998, MNRAS, 299, 433

Fuhrmann, L., Zensus, J. A., Krichbaum, T. P., et al. 2007, AIPC, 921, 249

Ghirlanda, G., Ghisellini, G., Tavecchio, F., & Foschini, L. 2010, submitted to MNRAS, arXiv:1003.5163

Ghisellini, G., Celotti, A., Fossati, G., et al. 1998, MNRAS, 301, 451

Giroletti, M., Reimer, A., Fuhrmann, L., Pavlidou, V., & Richards, J. L. 2010, in 2009 Fermi Symposium, eConf Proceedings C091122, arXiv:1001.5123

Hartman, R. C., Bertsch, D. L., Bloom, S. D., et al. 1999, ApJS, 123, 79

Healey, S. E., Romani, R. W., Taylor, G. B., et al. 2007, ApJS, 171, 61

Kovalev, Y. Y., Aller, H. D., Aller, M. F., et al. 2009, ApJ, 696, L17

Lister, M. L., Aller, H. D., Aller, M. F., et al. 2009, AJ, 137, 3718

Mahony, E. K., Sadler, E. M., Murphy, T., Ekers, R. D., Edwards, P. G., & Massardi, M. 2010, submitted to ApJ, arXiv:1003.4580

Massaro, E., Giommi, P., Leto, C., et al. 2009, A&A, 495, 691

Max-Moerbeck, W., et al. 2009, in 2009 Fermi Symposium, eConf Proceedings C091122 arXiv:0912.3817

Mücke, A., Pohl, M., Reich, P., et al. 1997, A&A, 320, 33

Myers, S. T., Jackson, N. J., Browne, I. W. A., et al. 2003, MNRAS, 341, 1

Pavlidou, V., Richards, J. L., Max-Moerbeck, W., et al. 2010, ApJ submitted

Richards, J. L., Max-Moerbeck, W., Pavlidou, V., et al. 2009, in 2009 Fermi Symposium, eConf Proceedings C091122 arXiv:0912.3780

Stecker, F. W., Salamon, M. H., & Malkan, M. A. 1993, ApJ, 410, L71

Salamon, M. H., & Stecker, F. W. 1994, ApJ, 430, L21

Taylor, G. B., Healey, S. E., Helmboldt, J. F., et al. 2007, ApJ, 671, 1355

Identifying Fermi–LAT AGN using high-frequency radio surveys

E. K. Mahony[1,2], E. M. Sadler[1], T. Murphy[1,3], R. D. Ekers[2], P. G. Edwards[2], and M. Massardi[4] on behalf of the AT20G team

[1] Sydney Institute for Astronomy, School of Physics, University of Sydney, NSW 2006, Australia
[2] Australia Telescope National Facility, CSIRO, P.O Box 76, Epping, NSW 1710, Australia
[3] School of Information Technologies, The University of Sydney, NSW 2006, Australia
[4] INAF, Osservatorio Astronomico di Padova, Vicolo dell'Osservatorio 5, I−35122 Padova, Italy

Abstract. The high-frequency radio sky, like the gamma-ray sky surveyed by the Fermi satellite, is dominated by flat-spectrum radio quasars and BL-Lac objects at bright flux levels. To investigate the relationship between radio and gamma-ray emission in extragalactic sources, we have cross-matched the Australia Telescope 20 GHz survey catalogue (AT20G; Murphy et al. 2010) with the Fermi-LAT 1-year Point Source Catalogue (1FGL; Abdo et al. 2010a). The AT20G survey is a blind radio survey of the southern sky (excluding the Galactic plane at $|b| < 1.5°$) down to a limiting flux density of 40 mJy at 20 GHz. Observations for this survey were carried out using the Australia Telescope Compact Array from 2004–2008. The high-frequency selection provides a clean catalogue to search for extragalactic gamma-ray sources observed in the southern hemisphere, and as such provides a useful database in identifying gamma-ray counterparts as the Fermi mission continues to discover many more of these objects.

1. Introduction

The recent release of the First Fermi-LAT (1FGL; Abdo et al. 2010a) catalogue provides an unprecedented view of the gamma-ray sky. Many of these high energy sources (particularly those at high Galactic latitudes) are attributed to active galactic nuclei (AGN), where the gamma-ray emission is thought to originate from collimated jets close to the core (Blandford & Rees, 1978). As a result, flat spectrum radio-loud QSOs (FSRQs) and BL-Lac objects, where the jet is more closely aligned with our line of sight, dominate the population of extragalactic sources selected in gamma-ray surveys. Further properties of the AGN detected by Fermi are presented in more detail in the First LAT AGN catalogue (1LAC; Abdo et al. 2010b).

The 1FGL catalogue lists AGN associations for 41% of Fermi sources with $|b| > 1.5°$, but there are many that remain unidentified. The relatively large uncertainty in the Fermi positions (typically 540 arcsec) makes it necessary to search at other wavelengths to identify the correct astronomical source, and the Fermi team have used a Bayesian analysis method to cross-match the 1FGL with a range of catalogues (Abdo et al. 2010a).

Searching high-frequency radio catalogues provides an alternative and potentially more direct way to identify the extragalactic Fermi sources. The dominant emission at high radio frequencies originates from the radio jets close to the central core, so provides a snapshot of the most recent AGN activity (Mattox et al. 2001). This is very different from lower radio frequencies near 1.4 GHz, where extended radio lobes, built up over large periods of time, dominate the emission. The source density of high-frequency radio sources on the sky is also lower, greatly reducing the number of spurious radio sources within a Fermi error box. Since most Fermi sources are expected to have a flat radio spectrum, this makes radio identification with a high-frequency catalogue much more straightforward and reliable.

This was recognized by Healey et al. (2008), who assembled an all-sky catalogue of 8 GHz measurements of candidate blazars (selected on the basis of their radio spectral index at 1–5 GHz) to help identify Fermi sources. The 20 GHz AT20G catalogue, which has no spectral pre-selection, provides an independent check of radio–gamma-ray associations for southern sources.

This talk is based on a publication which is in press at the time of writing (Mahony et al. 2010, ApJ, 716 in press).

2. The Australia Telescope 20 GHz (AT20G) Survey

The Australia Telescope 20 GHz (AT20G) survey (Murphy et al. 2010) is a blind radio survey of the southern sky (excluding the Galactic plane at $|b| < 1.5°$) down to a limiting flux density of 40 mJy at 20 GHz. Observations for this survey were carried out using the Australia Telescope Compact Array from 2004–2008. Most objects south of $\delta < −15°$ also have near-simultaneous flux density measurements at 4.8, 8.4 and 20 GHz providing accurate radio spectral information not affected by variability.

Prior to this survey, the radio sky above 5 GHz was largely unexplored. Figure 1 shows the sensitivity limits of a number of other large-area radio surveys. AT20G provides the most sensitive, large area survey at high-radio
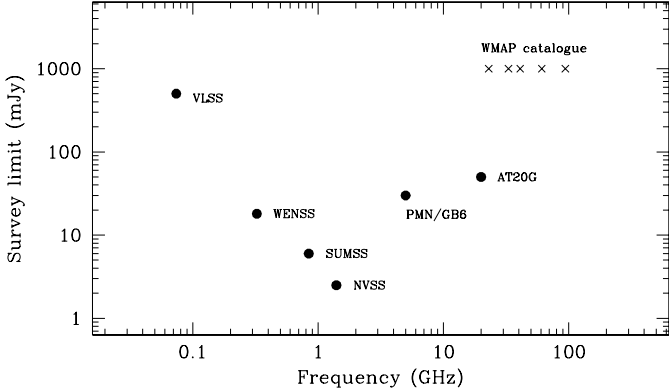
Fig. 1. Sensitivity limits of surveys covering at least a quarter of the sky. The only other high-frequency large-area survey is the WMAP Point Source Catalogue (Bennett et al. 2003; Hinshaw et al. 2007) which is flux-limited at 1 Jy at 23 GHz. Figure from Sadler et al. (2008); see this paper for more details.

frequencies to date. There are many reasons for wanting to complete a high-frequency radio survey. It is vital for future CMB missions, such as the *Planck* satellite, in identifying contaminating foreground sources. It also provides much needed calibrators for future millimetre telescopes such as ALMA. In addition, the 20 GHz source population is different to that seen at lower frequencies, and furthermore, cannot be predicted from low radio-frequency data making it scientifically interesting in its own right.

Due to the high-frequency selection, the AT20G catalogue is dominated by flat spectrum radio sources (Sadler et al. 2006; Massardi et al. 2010, in preparation) which is ideal in searching for Fermi counterparts. Whilst the radio data provides a unique sample of objects, these data alone are insufficient to completely constrain models of radio source properties and the evolution of radio galaxies. The AT20G radio positions are accurate to ~ 1 arcsec, allowing us to make optical identifications in a reliable way, providing vital multi-wavelength information.

3. Cross-matching 1FGL with the AT20G catalogue

Since the AT20G catalogue only covers the southern sky, we used a subset of 1FGL sources south of the equator (and excluding the Galactic plane $|b| < 1.5°$) for the cross-matching. In addition, since the AT20G catalogue is best-suited to identifying extragalactic AGN, sources classified as Galactic[1] in the 1FGL catalogue were removed from the sample.

Using this set of Fermi sources (referred to here as the 1FGL–South dataset), we then searched the AT20G catalogue for radio sources within the 95% confidence ellipse given in the 1FGL catalogue. This resulted in 233 (43%) Fermi sources with AT20G counterparts. The majority of these identifications are in agreement with the 1LAC catalogue, with an addition of eight sources which are newly

---

[1] We also excluded six sources in the LMC and SMC fields.
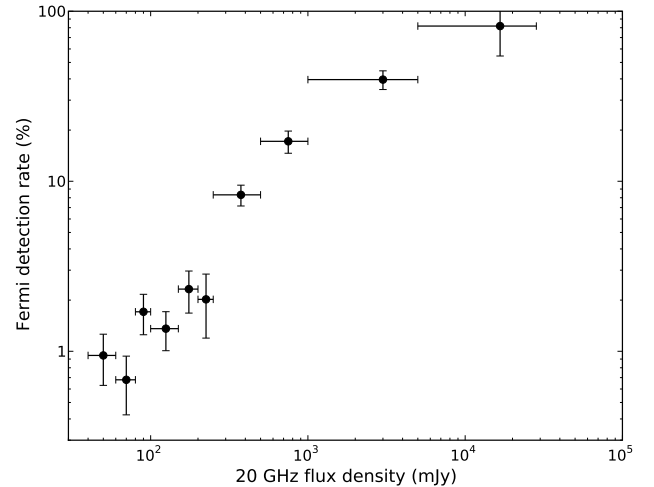
Fig. 2. Fermi detection rate of AT20G radio sources as a function of 20 GHz flux density. The vertical error bars show the counting errors for each bin while the horizontal error bars indicate the bin size. Figure from Mahony et al. (2010).

identified as potential gamma-ray AGN. We did not search for matches outside the 95% Fermi confidence region, since our priority was to make a reliable set of matches which provides a 'clean' sample. Monte Carlo testing revealed that 4.4% could be chance associations. This results in our final list of Fermi–AT20G matches being 95% complete and at least 95% reliable.

The Fermi detection rate for AT20G sources increases with increasing 20 GHz flux density, as shown in Fig. 2. Here we binned the AT20G catalogue in flux density and plotted the percentage of AT20G sources detected in the 1FGL–South dataset for each bin plotted.

A total of 110 of the sources in the 1FGL–South dataset are classified as variable in gamma-rays, with a less than 1% probability of being a steady source (Abdo et al. 2010a). Of these, 96 (87%) are detected at 20 GHz. On the other hand, only 138 (32%) of the non-variable gamma-ray sources are detected in AT20G.

4. Radio–Gamma-ray Flux comparison

To investigate any correlations between the radio and gamma-ray properties we plotted the 20 GHz flux density against the gamma-ray flux density as shown in Fig. 3, revealing a trend of increasing gamma-ray flux density with increasing 20 GHz flux density. A similar trend has also recently been noted by Ghirlanda et al. (2010). Some additional scatter may be introduced due to the fact that the AT20G observations were taken up to 2–5 years previous to the Fermi observations. This figure also shows that the variable Fermi sources have higher gamma-ray fluxes than the non-variable sources. This can account for the higher AT20G detection rate for the variable sources mentioned in Section 3, as the correlation between gamma-ray and 20 GHz flux implies that a larger fraction of the brighter gamma-ray sources will be above the 40 mJy flux limit of the AT20G survey.
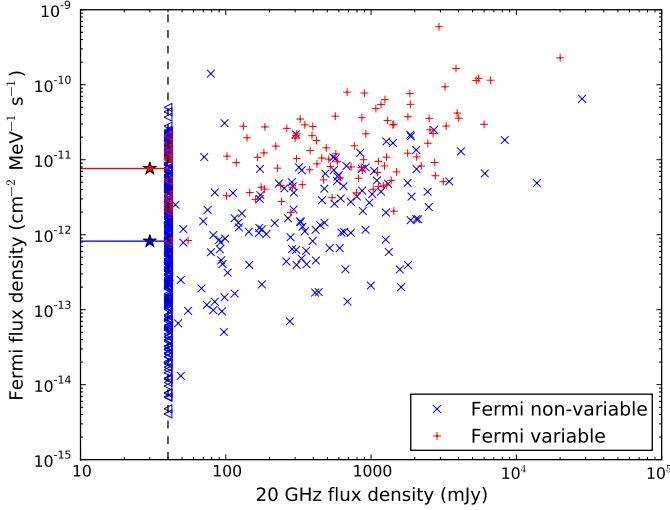
Fig. 3. 20 GHz flux density against Fermi flux density for sources classified as variable in 1FGL ('+') and those not classified as variable ('×'). The Fermi sources not detected in AT20G are shown as triangles at the 40 mJy flux limit of the survey (also shown by the dashed line). The median gamma-ray fluxes for the upper limits are denoted by the stars, but it should be noted that these upper limits include a mixture of populations and are not limited to AGN. Figure from Mahony et al. (2010).

Table 1. Results from spearman-rank correlation tests comparing the 20 GHz flux with the gamma-ray flux density. The second column is the correlation coefficient (ρ) and the third column is the probability of finding these coefficients by chance (P). For comparison the results reported in Abdo et al. (2009) using the Fermi–LAT Bright AGN Sample (LBAS) are also listed which used the 8.4 GHz flux and the peak gamma-ray flux above 100 MeV.

Subset	Fermi–AT20G		LBAS	
	ρ	P	ρ	P
All	0.49	7.5×10^{-16}	0.42	4.5×10^{-6}
variable	0.44	9.0×10^{-6}	-	-
non-variable	0.46	1.5×10^{-8}	-	-
FSRQ	0.31	0.0006	0.19	0.080
BL-Lacs	0.43	0.002	0.49	0.00055

Spearman-rank correlation tests show that these correlations are statistically significant. Results for the variable and non-variable sources, along with the FSRQ and BL-Lacs are shown in Table 1. The correlation coefficients and corresponding probabilities given in Abdo et al. (2009) for the Fermi–LAT Bright AGN Sample are also given for comparison.

These results indicate that the basic emission mechanism for the radio and gamma-rays is coupled, with both related to the relativistic jets of the AGN. The radio emission results from synchrotron emission by relativistic electrons while the gamma-ray emission is thought to be created by inverse Compton scattering of photons by similar, or possibly the same, high energy particles (Maraschi et al. (1992), Ghisellini & Madau (1996), Bloom & Marscher (2006)). A similar correlation between
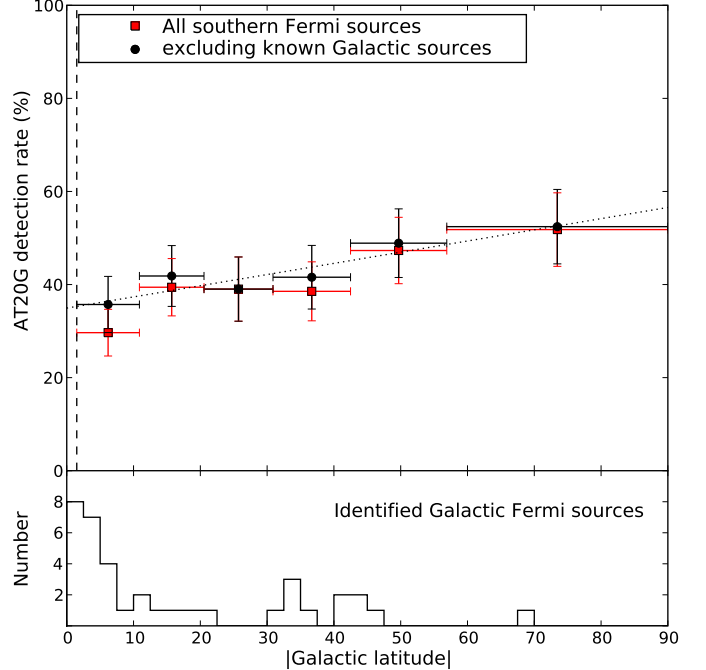
Fig. 4. AT20G detection rate binned in Galactic latitude. The circles show the detection rate of AT20G sources in the 1FGL–South dataset (where known Galactic sources have been removed) while the squares show the detection rate when these sources are included. The lower plot shows the histogram of sources defined as Galactic in the 1FGL catalogue that have been added when plotting the squares. The dotted line denotes the linear fit to the circles. The dashed line at $|b| = 1.5°$ indicates the limit of the AT20G survey and lower latitudes have been excluded from this analysis. Figure from Mahony et al. (2010).

the gamma-ray and high-radio frequency fluxes was found in Kovalev et al. (2009), which compared the average 100 MeV–1 GeV photon flux with quasi-simultaneous VLBI 15 GHz flux measurements for objects in the Fermi–LAT Bright Source Catalogue. There is also the possibility that the Doppler boosting effects are similar in both the radio and gamma-ray regimes. This could account for the strength of the correlation seen in Fig. 3 given that the observations were not simultaneous.

5. AT20G detection rate as a function of Galactic latitude

Figure 4 shows the AT20G detection rate of sources in the 1FGL–South dataset binned by Galactic latitude. Due to the much smaller area of sky at $b > 0$ in the southern hemisphere, the data were binned in $|b|$ rather than b to improve the statistics. We also removed 37 1FGL sources which are associated with Galactic objects such as pulsars and pulsar wind nebulae (none of these 37 Galactic Fermi sources are detected in the AT20G survey). This Figure shows that the AT20G detection rate of 1FGL sources is *not* constant with Galactic latitude, but decreases at lower Galactic latitudes. Here a linear regression fit has
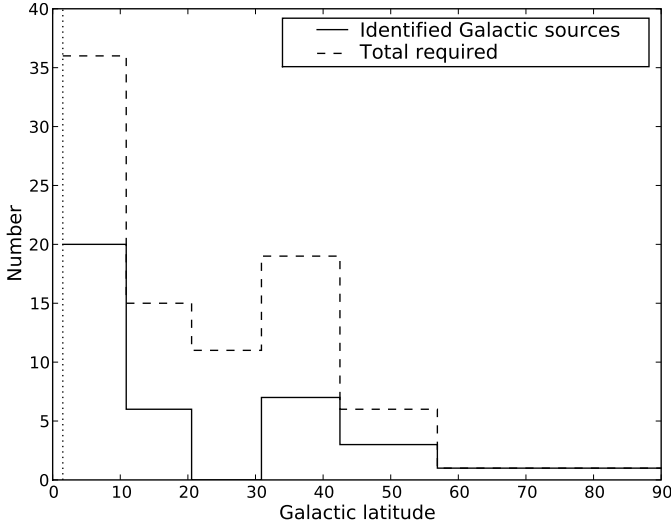
Fig. 5. The minimum number of Galactic Fermi sources needed to make the AT20G detection rate constant with Galactic latitude. Figure from Mahony et al. (2010).

a slope of 0.23 and we can rule out that the slope is flat at the 99% confidence level. This strongly suggests that the 1FGL catalogue contains a mixture of extragalactic and (unidentified) Galactic sources, whose relative numbers change with $|b|$. The squares in Fig. 4 show the detection rate when the known Galactic sources are added back in to the 1FGL–South sample.

To calculate the minimum number of Galactic sources still unidentified, we assumed that there were no unidentified Galactic sources towards the Galactic poles. Taking the detection rate of 52% given in the last bin in Fig. 4 to be the expected AT20G detection rate across the whole sky means that there are at least 50 high-latitude ($|b| > 1.5°$) Galactic gamma-ray sources in the southern hemisphere that still remain to be identified. The estimated distribution of these sources is shown in Fig. 5. Here the total number of sources in each bin is the amount needed to make the AT20G detection rate constant with Galactic latitude (Fig. 4). The Galactic sources already identified are shown by the solid line.

6. Conclusions

In summary, a blind survey at high radio frequencies (such as AT20G) is an ideal catalogue to search for extragalactic gamma-ray counterparts as, like the gamma-ray sky, it is dominated by flat spectrum radio sources (either quasars or BL-Lacs).

Cross-matching the 1FGL catalogue with the AT20G catalogue resulted in 233 (43%) associations within the 95% Fermi confidence ellipse. Monte Carlo tests show that we expect 4.4% to be chance associations meaning that the final catalogue of Fermi–AT20G matches is 95% complete and 95% reliable. The detection rate of Fermi sources in the AT20G catalogue increases strongly with 20 GHz flux density. It ranges from approximately 1% at 100 mJy to almost 100% at 20 GHz fluxes above 10 Jy. The majority

of these matches are in agreement with the Fermi AGN source association. There are eight AT20G sources that are newly identified as potential Fermi counterparts, all at low Galactic latitude.

This confirms that the majority of gamma-ray sources have flat radio spectra as the AT20G survey provides an unbiased sample with no spectral pre-selection. It also verifies that there is not a missing gamma-ray population of steep spectrum radio sources. We find a trend of increasing gamma-ray flux density with 20 GHz flux density which is slightly stronger for the non-variable Fermi sources.

The distribution of AT20G detections as a function of Galactic latitude reveals that the percentage of AT20G matches decreases towards the Galactic plane. We calculate that there are at least 50 unidentified Galactic gamma-ray sources in the southern hemisphere at latitudes above $|b| = 1.5°$, as the AGN detection rate should not vary with Galactic latitude.

The AT20G survey provides a clean catalogue to search for extragalactic gamma-ray sources observed in the southern hemisphere. As such it provides a useful database in identifying gamma-ray counterparts as the Fermi mission continues to discover many more of these objects.

References

Abdo, A. A. et al. 2010, e-print arXiv:1002.2280
Abdo, A. A. et al. 2010, ApJ, 715, 429
Abdo, A. A. et al. 2009, ApJ, 700, 597
Bennett C. L. et al., 2003, ApJ, 583, 1
Blandford, R. D., & Rees, M. J. 1978, in Pittsburgh Conf. on BL Lac Objects, ed. A. M. Wolfe (Pittsburgh: Univ. Pittsburgh Press) 328
Bloom, S. D., & Marscher, A. P. 1996, ApJ, 461, 657
Ghirlanda, G. et al. 2010, e-print arXiv:1003.5163
Ghisellini, G., & Madau, P. 1996, MNRAS, 280, 67
Healey S. E. et al. 2008, ApJS, 175, 97
Hinshaw G. et al., 2007, ApJS, 170, 288
Kovalev, Y. Y., et al. 2009, ApJ, 696, L17
Mahony, E. K. et al. 2010, ApJ, 716, in press
Maraschi, L., Ghisellini, G., & Celotti, A. 1992, ApJ, 397, L5
Mattox, J. R., Hartman, R. C., & Reimer, O. 2001, ApJS, 135, 155
Murphy, T. et al. 2010, MNRAS, 402, 2403
Sadler, E. M. et al. 2006, MNRAS, 371, 898
Sadler, E. M. et al. 2008, MNRAS, 385, 1656

The γ-ray properties of radio-selected extragalactic jets

M. Böck[1], M. Kadler[1,2,3], G. Tosti[4,5], T. H. Burnett[6], C. Müller[1], R. Ojha[7,8] on behalf of the LAT collaboration, and J. Wilms[1]

[1] Dr. Karl Remeis-Observatory & ECAP, Universität Erlangen-Nürnberg, Sternwartstr. 7, 96049 Bamberg, Germany
[2] CRESST/NASA Goddard Space Flight Center, Greenbelt, MD 20771, USA
[3] Universities Space Research Association, 10211 Wincopin Circle, Suite 500 Columbia, MD 21044, USA
[4] Istituto Nazionale di Fisica Nucleare, Sezione di Perugia, I-06123 Perugia, Italy
[5] Dipartimento di Fisica, Università degli Studi di Perugia, I-06123 Perugia, Italy
[6] Department of Physics, University of Washington, Seattle, WA 98195-1560, USA
[7] U.S. Naval Observatory, 3450 Massachusetts Ave. NW, Washington DC 20392, USA
[8] NVI, Inc., 7257 Hanover Parkway, Greenbelt, MD 20770, USA

Abstract. Most extragalactic jets in radio-loud Active Galactic Nuclei are bright and variable γ-ray sources, which are continuously monitored with *Fermi*/LAT. We present the γ-ray properties of the MOJAVE and TANAMI AGN samples of radio-loud AGN. Both programs provide properties of the parsec-scale radio jets using Very Long Baseline Interferometry (VLBI) techniques. This information is important to understand the broad-band emission mechanism of these sources. In this work we compare the radio and γ-ray properties of the two samples and present upper limits on the γ-ray flux of the radio-brightest jet sources not yet detected by *Fermi*/LAT.

1. Introduction

Most extragalactic jets in radio-loud Active Galactic Nuclei (AGN) are bright and variable γ-ray sources. The high luminosity and variability of blazars is explained by a jet orientated close to the line of sight, in which charged particles are moving with relativistic speed, thus the emission is Doppler boosted (Blandford & Rees, 1978; Maraschi et al., 1992). This model is supported by the apparent superluminal motion which is typically found in the inner radio-jets of blazars (Lister et al., 2009b, , and therein).

Since 2008 August 11, the sky is monitored at γ-ray energies in the range from $\sim$20 MeV to >300 GeV with the Large Area Telescope (LAT), which is a pair conversion detector on board the *Fermi Gamma-Ray Space Telescope* (Atwood et al., 2009). *Fermi*/LAT scans the whole sky every three hours and its sky-survey mode is optimized to obtain a uniform exposure on longer time scales (> weeks). A large number of AGN were detected and monitored with *Fermi*/LAT (709 AGN during the first year of operation, Abdo et al., 2010b).

In this work, we present the γ-ray properties of two samples from the two largest ongoing Very Long Baseline Interferometry (VLBI) AGN monitoring survey programs: Tracking Active Galactic Nuclei with Austral Milliarcsecond Interferometry (TANAMI; Ojha et al., 2010) and Monitoring Of Jets in Active galactic nuclei with VLBA Experiments (MOJAVE; Lister et al., 2009a). The two samples are described in Sect. 2. For our analysis we use data obtained during the first year of *Fermi* operations.

The combined analysis of radio and γ-ray properties is still in progress. The detailed presentation of the upper limit analysis, a discussion of tentative new detections and individual sources is in work and will be published in an upcoming paper (Abdo et al., in prep.).

2. Sample

In our study, we investigate the γ-ray properties of two samples of extragalactic jets: the MOJAVE 1 and the TANAMI samples. MOJAVE 1 is a purely radio-selected sample of all AGN at declinations $\delta > -20°$, whose 15 GHz radio flux density has exceeded 1.5 Jy (2 Jy for sources with $\delta < 0°$) at any epoch between 1994 and 2004 (Lister et al., 2009a). In total, the MOJAVE 1 sample is comprised of 135 AGN: 101 quasars, 22 BL Lac objects, 8 galaxies, and 4 unclassified objects. About two thirds of the sources in the MOJAVE 1 sample have been monitored since 1994 as part of the VLBA 2 cm Survey (Kellermann et al., 1998) with the Very Long Baseline Array (VLBA; Napier et al., 1994). Since 2002, the MOJAVE 1 sample has been observed with the VLBA as part of the MOJAVE program[1] (see Lister et al., these proceedings, p. 159).

TANAMI is a radio VLBI monitoring program of currently 75 extragalactic jets south of $-30°$ declination. The observations are performed approximately every two months with the telescopes of the Australian Long Baseline Array (LBA; Norris, 1988) in combination with telescopes in South Africa, Antarctica and Chile. A detailed discussion of the TANAMI program including a description of the initial source sample, explanations of

---

[1] `http://www.physics.purdue.edu/astro/MOJAVE/`

Table 1. Total number N of the MOJAVE 1 and TANAMI sources and the number of those detected with *Fermi*/LAT.

Class	MOJAVE 1 N	detected	TANAMI N	detected
Quasar	101	61	32	24
BL Lac	22	19	10	10
Galaxy	8	3	11	2
Unclassified	4	2	22	17

the observation and data reduction procedures, and brief notes on the individual sources are given by Ojha et al. (2010). TANAMI contains a radio-selected and a γ-ray selected sub-sample (see Ojha et al., 2010, for details). The radio selected sub-sample supplements the MOJAVE 1 sample south of $-30°$ declination. TANAMI observations are made at 8.4 GHz and 22 GHz yielding spectral indices of parsec-scale jet features (Müller er al., these proceedings, p. 229).

3. Analysis

To find associations of the AGN in the MOJAVE 1 and TANAMI sample with *Fermi*/LAT-detected γ-ray sources we performed a positional-association analysis. For each radio position of the sources in the sample we selected the closest sources in the "Fermi Large Area Telescope First Source Catalog" (Abdo et al., 2010a) inside the position uncertainty region of the γ-ray source. This approach yielded unique results for the majority of sources. A comparison with the results of the automatic source association pipeline of the LAT team (Abdo et al., 2009), in which the class and physical expectations of the association is taken into account, confirmed these results.

We used a maximum likelihood analysis (Cash, 1979; Mattox et al., 1996) to analyze those AGN which could not be associated with γ-ray catalog sources. For the calculation of upper limits on the γ-ray flux and the test statistic (TS) measuring the significance we used data in the range 100 MeV to 100 GeV obtained in the first year of *Fermi*/LAT.

We used the standard *Fermi*/LAT *Science Tools* and the methods described by Böck et al. (2009) to obtain the flux, photon index, and test statistic of each unassociated source. For sources with TS $<$ 25 we calculated upper limits on the flux. Sources with TS $\geq$ 25 were considered as tentative new detections and in this case we modeled the flux and the spectral index. For the sources with TS $<$ 1 the upper limits can be underestimated, thus we do not consider these sources in this work. Results for a Bayesian approach following Abdo et al. (2010a) will be presented in a following paper.

4. Results

Table 1 shows the number of quasars, BL Lacs, and galaxies in the MOJAVE 1 and TANAMI sample which are associated with γ-ray sources in the *Fermi*/LAT 1-year source list (Abdo et al., 2010a). 85 out of the 135 AGN in the MOJAVE 1 sample are detected with *Fermi*/LAT during its first year of operation. With a detection rate of 19/22 most BL Lac objects in the sample are detected. 61/101 quasars are detected and 2/4 unclassified objects. At 3/8, the detection rate of the galaxies is the lowest. In the TANAMI sample 24 out of 32 quasars are detected with *Fermi*/LAT. The detection rates of unclassified sources is substantially higher in the TANAMI sample than in the MOJAVE 1 sample. This is most likely due to the inclusion of a γ-ray selected sub-sample and the addition of sources detected by *Fermi*/LAT after three months (Abdo et al., 2009). The detection rates for the radio-selected TANAMI sub-sample consisting of 21 AGN are: 9/13 Quasars, 3/3 BL Lac objects and 2/5 Galaxies, which is comparable to the MOJAVE 1 sample.

For the analysis of the associated sources we used the photon spectral indices from the *Fermi*/LAT first source catalog calculated in the range of 0.1–100 GeV, since this value can be obtained even for relatively weak sources (Abdo et al., 2010b). Fig. 1 shows the distribution of flux and photon spectral index averaged over 11 months. In addition to the catalog values we present the values we obtained for the tentative new detections.

Fig. 1 indicates a difference between the MOJAVE 1 and the TANAMI sample which is caused by the different selection criteria. The γ-ray selected TANAMI sub-sample contains several hard sources, i.e., sources with relatively small γ-ray photon spectral index, including many BL Lac objects and unassociated sources. BL Lac objects tend to have on average harder γ-ray spectra than the quasars (Abdo et al., 2009, 2010b).

Hard sources can be better localized with *Fermi*/LAT. Thus the limiting photon flux for a TS $>$ 25 detection is significantly lower for BL Lac objects than for quasars with softer spectra (Abdo et al., 2010b, Fig. 10). In Fig. 2 this effect is not visible as the hardest sources in the sample do not reach a photon spectral index of $\Gamma < 1.5$ as it is the case for the sources discussed by Abdo et al. (2010b). In addition, they consider the photon flux above 100 MeV instead of 0.1–100 GeV, which increases the photon flux for soft sources significantly.

The distribution of spectral indices (Fig. 3) confirms that BL Lac objects exhibit harder γ-ray spectra than quasars and shows that the majority of the spectral indices of the tentatively new detected sources is softer than that of the associated sources, which is consistent with the difficulty to detect soft weak sources with *Fermi*/LAT.

It is worth noting that all three BL Lac objects in the radio-selected TANAMI sub-sample and the majority of BL Lac objects in the MOJAVE 1 sample have γ-ray spectral indices $\Gamma > 2.2$. Abdo et al. (2010c) found that BL Lacs with $\Gamma > 2.2$ are mostly low synchrotron peaked (LSP) BL LACs (see also Abdo et al., 2010b, Fig. 14). It might be expected that a radio-selected sample contains more LSP BL Lacs than high synchrotron peaked ones, as the LSP type is brighter at the radio frequencies used for the selection.
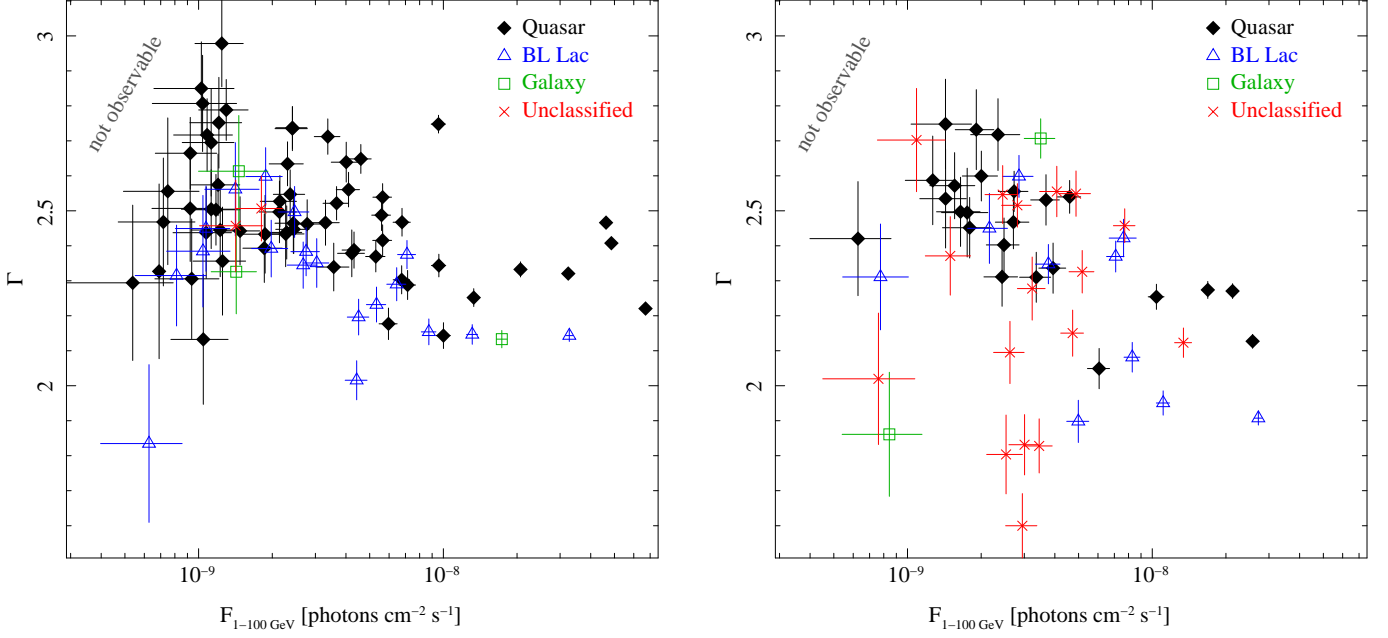
Fig. 1. Distribution of flux and photon spectral indices of the associated sources in the MOJAVE 1 (left) and TANAMI (right) samples. The flux is given in units of photons cm^{-2} s^{-1} in the energy range 1–100 GeV. In the top left corners *Fermi*/LAT cannot detect sources.
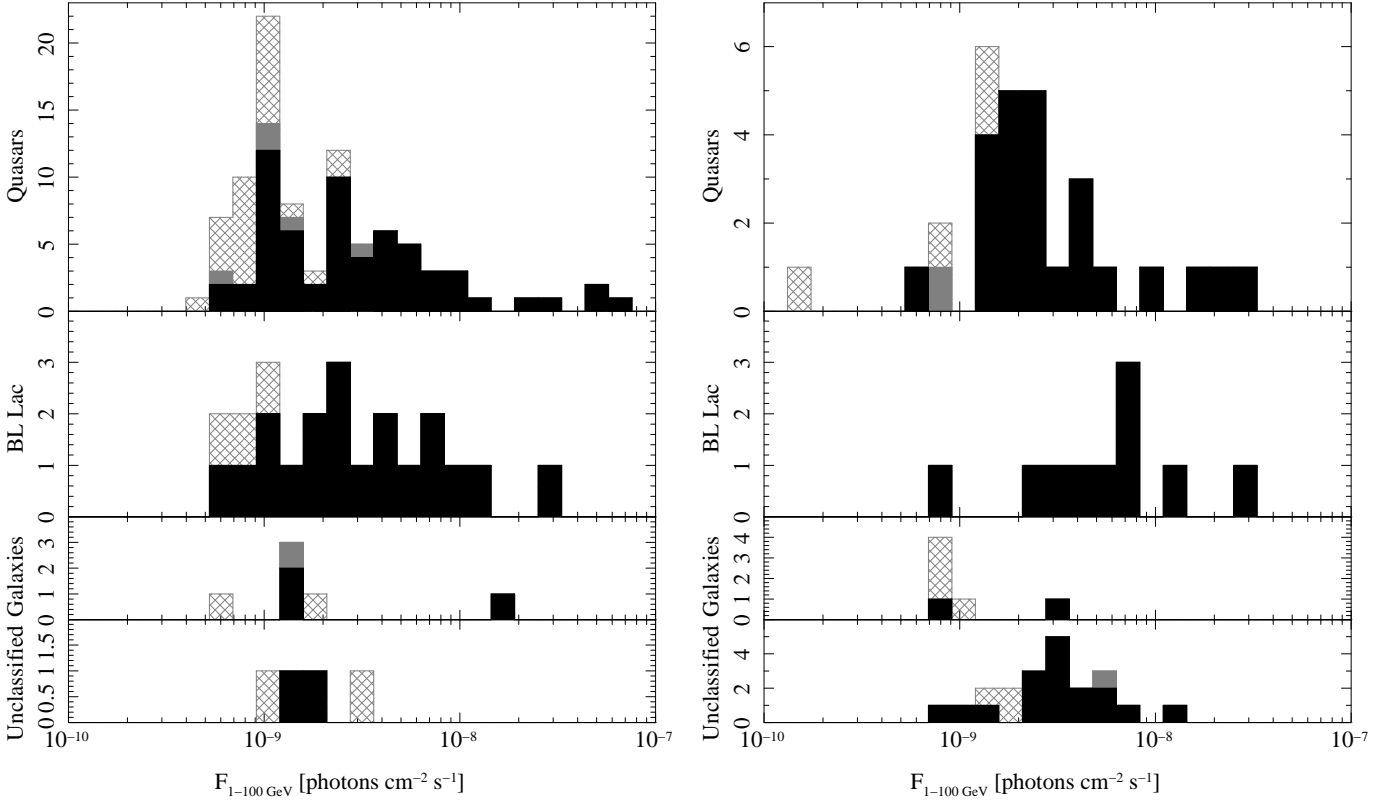
Fig. 2. Distribution of the flux of the associated sources in the MOJAVE 1 (left) and TANAMI (right) samples. Sources associated with catalog sources are shown in black, the tentative new detections in gray and the upper limits are shown cross hatched.

5. Summary

The γ-ray properties of the MOJAVE 1 and TANAMI AGN samples were analyzed. The detection rates with *Fermi*/LAT depend on the source class. For the radio-selected MOJAVE 1 sample and the radio-selected TANAMI sub-sample BL Lac objects have the highest detection rates, followed by the quasars, whereas only a small fraction of the radio galaxies in the samples are seen by *Fermi*/LAT. With a maximum likelihood analysis on
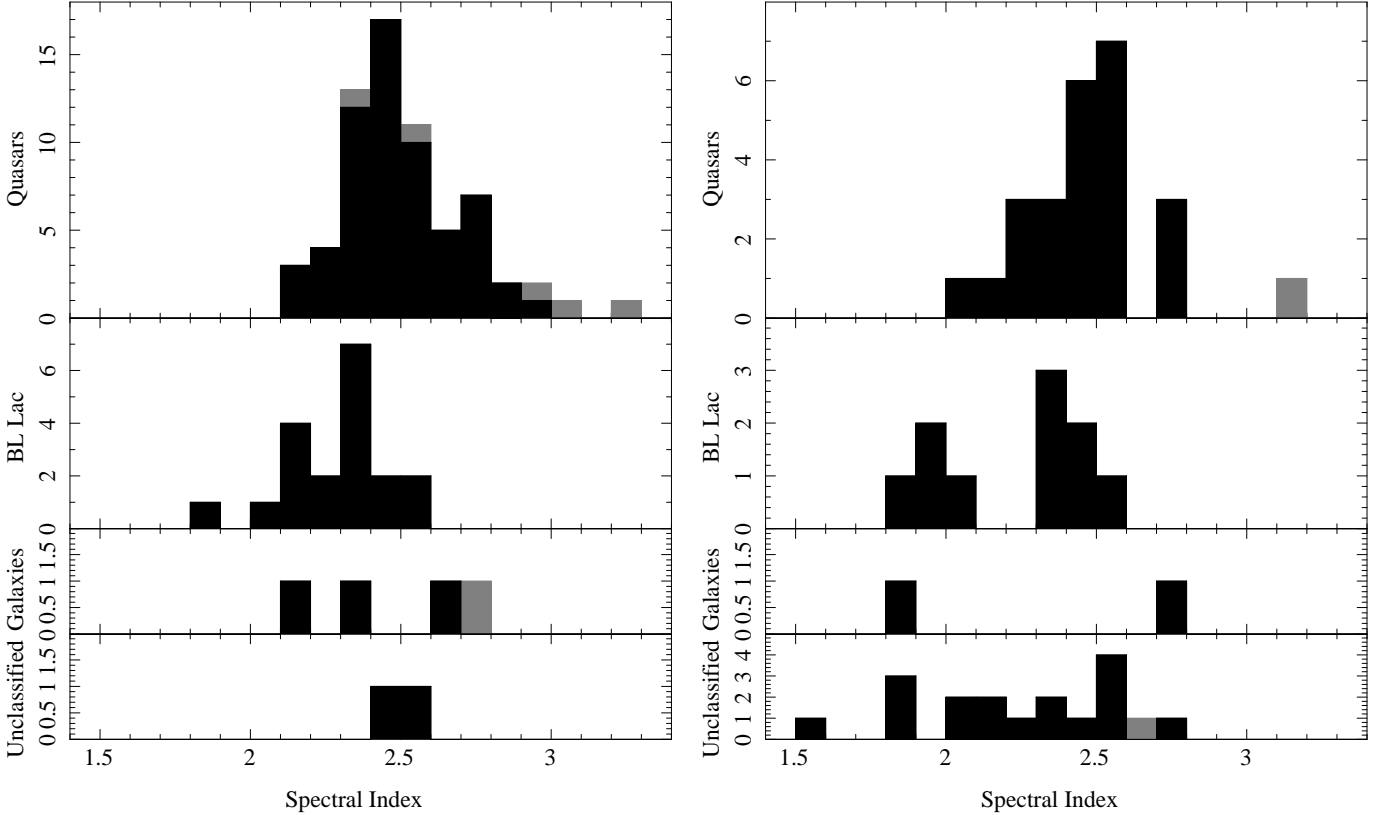
Fig. 3. Distribution of the spectral index of the associated sources in the MOJAVE 1 (left) and TANAMI (right) samples. The tentative new detections are shown in gray.

sources which were not associated with γ-ray sources in the *Fermi*/LAT First Source Catalog, we obtained upper limits on the γ-ray flux of these sources and found tentative new detections.

The analysis of the upper limits and the tentative new detections will be discussed in an upcoming paper.

References

Abdo A. A., Ackermann M., Ajello M., et al., 2010a, ApJS 188, 405

Abdo A. A., Ackermann M., Ajello M., et al., 2010b, ApJ 715, 429

Abdo A. A., Ackermann M., Ajello M., et al., 2009, ApJS 183, 46

Abdo A. A., Ackermann M., Ajello M., et al., 2010c, ApJ 710, 1271

Atwood W. B., Abdo A. A., Ackermann M., et al., 2009, ApJ 697, 1071

Blandford R. D., Rees M. J., 1978, In: A. M. Wolfe (ed.) BL Lac Objects., p.328

Böck M., Kadler M., Tosti G., et al., 2009, eprint arXiv:0912.4192

Cash W., 1979, ApJ 228, 939

Kellermann K. I., Vermeulen R. C., Zensus J. A., & Cohen M. H., 1998, AJ 115, 1295

Lister M. L., Aller H. D., Aller M. F., et al., 2009a, AJ 137, 3718

Lister M. L., Cohen M. H., Homan D. C., et al., 2009b, AJ 138, 1874

Maraschi L., Ghisellini G., & Celotti A., 1992, ApJL 397, L5

Mattox J. R., Bertsch D. L., Chiang J., et al., 1996, ApJ 461, 396

Napier P. J., Bagri D. S., Clark B. G., et al., 1994, IEEE Proceedings 82, 658

Norris R.P., 1988, In: M. J. Reid & J. M. Moran (ed.) The Impact of VLBI on Astrophysics and Geophysics, Vol. 129. IAU Symposium, p.485

Ojha R., Kadler M., Böck M., et al., 2010, eprint arXiv:1005.4432

Study of a microwave selected sample at gamma-ray energies

D. Gasparrini,[1,3] E. Cavazzuti[1,2], P. Giommi[1,2], C. Pittori[1,3], S. Colafrancesco[1,2] on behalf of the
Fermi/LAT collaboration

[1] Agenzia Spaziale Italiana (ASI) Science Data Center, I-00044 Frascati (Roma), Italy
[2] Agenzia Spaziale Italiana, I-0100, Roma, Italy
[3] INAF- Osservatorio Astronomico di Roma, I-00040 Monteporzio Catone, Italy

Abstract. Blazars are a small fraction of all extragalactic sources but, unlike other objects, they are strong emitters across the entire electromagnetic spectrum. Recent data in the microwave region of the electromagnetic spectrum have become available to allow for systematic studies of blazars over large cosmological volumes. This frequency band is indeed particularly suited for the selection of blazars since at these frequencies the contamination from radio extended components with steep spectra is no longer present and the emission from the accretion process is negligible. In our study we investigate the possible relation between the microwave and gamma-ray emission for the *Fermi*/LAT AGNs detected in the first year and belonging to *WMAP* 7th year bright source catalogue and the study of the gamma-ray upper limits for the WMAP7 sources not yet detected in the *Fermi* AGN catalogue. We discuss some properties of the sample to understand if the non- detected sources by *Fermi*/LAT are different from the detected ones. The absence of strong differences could imply that *Fermi* is still detecting flaring sources or could be a hint of a multicomponent model for blazar emission.

1. Introduction

Blazars are rare extragalactic objects as they are a subset of radio loud QSOs, which in turn are only ≈10% of radio-quiet QSOs and Seyfert galaxies that are found in large numbers at optical and at X-ray frequencies. Despite that, the strong emission at all wavelengths that characterizes blazars, makes them the dominant type of extragalactic sources in those energy windows where the accretion onto a supermassive black hole, or other thermal mechanisms, do not produce significant radiation. For instance, in the microwave band, Giommi et al. (2009) showed that blazars are the largest population of extragalactic objects (see also Toffolatti et al. (1998)). The same is true in the γ-ray band as seen in Abdo et al. (2009), Abdo et al. (2010a) and at TeV energies where BL Lac objects are the most frequent type of sources found in the high Galactic latitude sky.

Although blazars have been known and studied in different energy windows for over 40 years, many questions still remain open about their physics and demographics.

We investigate these problematics using a multi-wavelength approach through *Wilkinson Microwave Anisotropic Probe* (*WMAP*) (μ-wave) and *Fermi* (γ-ray) observations.

Primordial photons are redshifted to μ-wave frequencies due to the Universe expansion and we see these photons as cosmic background in μ-wave band. Tiny inhomogeneities in the early universe left their imprint on the CMB in the form of small anisotropies in its temperature. These anisotropies contain information about basic cosmological parameters (e.g., total energy density and curvature of the universe). The ability of the present and upcoming CMB experiments to determine the cosmological parameters requires a careful cleaning of the CMB maps from the galactic and extra-galactic foregrounds . This cleaning produces very useful bright source catalogs useful to our scopes.

The microwave frequency range is, moreover, likely the best region of the electromagnetic spectrum to pursue statistical studies of blazars since it is less affected by the superposition of spectral components of different nature like e.g., steep radio emission from the extended part of the jet, non-nuclear optical emission from the host galaxy or optical/UV and soft X-ray emission from an accretion disk.

We have already studied a μ-wave selected sample and its X-ray properties in Giommi et al. (2007) and verified that the μ-wave flux is tightly correlated with the X-ray one. Given the currently accepted emission mechanisms, such as Synchrotron Self Compton, as responsible for the broad-band blazar emission, we would like to investigate a possible relation among μ-wave and γ-ray fluxes.

Our strategy consists in building a complete sample of blazars selected in the μ-wave band, starting from the *WMAP* bright source catalogues periodically released by the *WMAP* Team. Than we study the properties of this μ-wave selected sample of jet-dominated AGN looking for synchrotron peak distribution of the sources, possible relations between μ-wave fluxes and X-ray, γ-ray duty cycle, $\alpha_{\mu\gamma}$. As in Pittori et al. (2007), we take into account the constraints from the observed extragalactic gamma-ray background on the maximum duty cycle allowed for the selected sample of *WMAP* Blazars.

2. Instruments

The *WMAP* satellite (Bennet et al. (2003)) provides an all-sky survey of the millimeter-wave sky and its point source catalogs are valuable for the study of flat-spectrum radio sources. In this work we use the seven-year catalogue of 471 foreground sources (WMAP7) (Gold et al. (2010)). We define the complete sample as including all sources in the WMAP7 catalogue with flux at 41 GHz higher than 0.9 Jy.

We define a flux limited sample using the source fluxes as observed in the *WMAP* 41 GHz channel as compromise between sensitivity, completeness and the need to use a high frequency band, to avoid the steep radio components. Highest frequency channels in *WMAP* survey (61, 94 GHz) have less objects and are less deep in flux with respect to lower frequencies (23, 33, and 41 GHz).

The *Fermi Gamma-Ray Space Telescope* is an international mission dedicated for the study of γ-ray emission in the Universe. The LAT, the primary instrument, is an imaging, wide field-of-view telescope, covering the energy range from below 20 MeV to more than 300 GeV with a sensitivity that exceeds EGRET by a factor of 30 or more. *Fermi* satellite commonly observes the sky in scanning mode: on a given orbit, the LAT will sweep the sky 35 degree away from the orbital plane, covering 75% of the sky. At the end of the orbit, *Fermi* will rock to 35 degree on the other side of the orbital. Therefore the entire sky is covered every three hours providing an uniform sky coverage within few orbit (Atwood et al. (2009)). Thanks to the improved instrument performance (point spread function, effective area, large field of view, broad energy range) blazar observations with *Fermi*/LAT are advancing our understanding of blazars and AGNs.

The First LAT Active galaxies Catalog (1LAC, Abdo et al. (2010a)) presents a wide study of the population of AGNs in data set from the first year of *Fermi* scientific operations. 1LAC includes 671 γ-ray sources located at high Galactic latitudes ($|b_{\mathrm{II}}| > 10°$) that are detected with a test statistic greater than 25 and associated statistically with AGNs. We use this catalog to find the gamma-ray counterparts of the microwave selected sources.

3. WMAP-7 and Fermi/LAT 1LAC samples cross-correlation

As in Giommi et al. (2009), we have carried out an extensive search to identify the counterparts of all the microwave foreground sources listed in the *WMAP* 7-year catalogue using literature and archival data. Our results allow us to define a flux limited sample of 267 high Galactic latitude microwave sources ($f_{41\,\mathrm{GHz}} \geq 0.9$ Jy, $|b_{\mathrm{II}}| > 10°$) which is virtually complete. From the analysis of classification in this complete sample we note that there is a dominance of blazars (88%).

Most of these are Low Synchrotron Peaked blazars (LSP, mainly FSRQ, 85% of the complete sample). This is what we expect from a sample selected in microwave

band, in fact High Synchrotron Peaked Blazars (HSP) are less frequent and are usually found in deeper samples. We estimate the frequency of the synchrotron peak from the values of the multi wavelength indexes α_{ro}, α_{ox} as indicated in Abdo et al. (2010b)

We perform a spatial cross-correlation between the WMAP7 sample and the *Fermi*/LAT 1LAC, exploiting the fact that 1LAC provides the coordinates of the radio counterparts . We obtain 131 WMAP7 objects with known microwave emission that are detected in the first year of *Fermi* data acquisition. As expected, blazars make up about 96% of this sample. In our work we use the integrated gamma-ray flux evaluated in the energy range 1–3 GeV, where are detected the vast majority of the LAT photons.

This result shows that *Fermi*-LAT in one year has detected 50% of the sources selected in microwave band. For the other 136 sources in the WMAP7 complete sample we compute the gamma-ray flux upper limit, using the 11 months dataset. The upper limit calculation makes use of the profile likelihood method described in details in Rolke et al.(2005). If the test Statistic of the source is lower than 0 we used the method described in Helene(1983) optimized for *Fermi*/LAT .

4. Detected vs Undetected sample properties

Are the WMAP7 sources undetected by *Fermi*-LAT different from the detected ones? We compare the two subsamples properties (e.g., redshift, ν_{peak} etc.) looking for differences.

The redshift distributions of the two subsamples are reported in Fig. 1. Undetected sources show lower redshifts than the detected ones, however a Kolmogorov-Smirnov test on these samples gives a probability of 96% that they belong to the same parent distribution.

Looking at the position of the synchrotron peak frequency (Fig. 2), we see that the two distributions are very
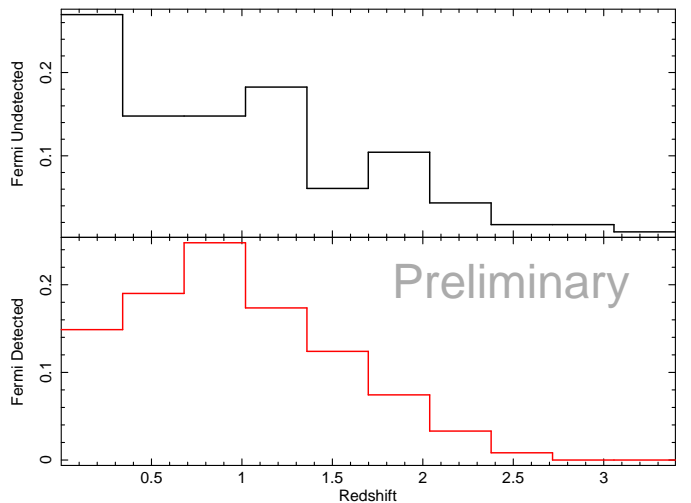
Fig. 1. Redshift distributions of Undetected (above) and Detected (below) by *Fermi* -LAT
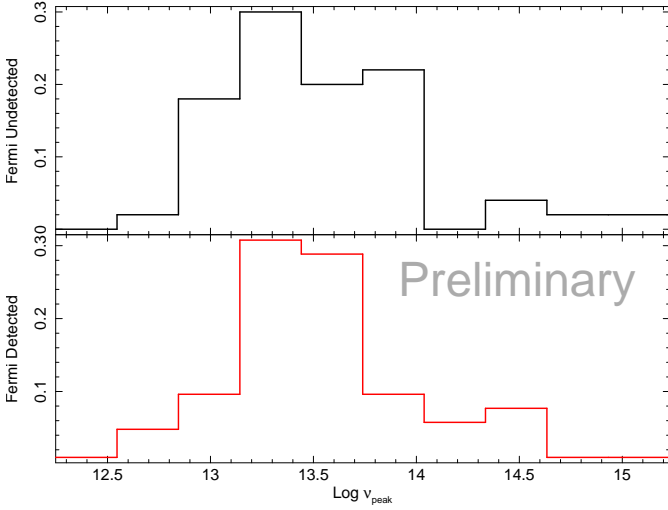
Fig. 2. ν_{peak} distributions on Undetected (above) and Detected (below) by *Fermi*-LAT

similar, the detected sources seem to have a narrower distribution but the result of the K-S test does not give us a proper indication on the parent population ($P = 67\%$).

The next property we investigate is the microwave flux at 41 GHz. Figure 3 shows an excess in the detected distribution at 1.7 Jy. Moreover, stronger microwave sources seem favorite for a gamma-ray detection, being the high flux side of the detected-sources distribution more sampled.

To better understand this, we plot the microwave flux versus gamma-ray flux (Fig. 4). Crosses are the *Fermi*/LAT detections while arrows represent the gamma-ray flux upper limit. We don't see any strong correlation between the two energy bands. However, in a recent paper Kovalev et al. 2009 found a correlation between high frequency radio (15 GHz) and γ-ray fluxes. In this work the set of radio observations were quasi simultaneous to
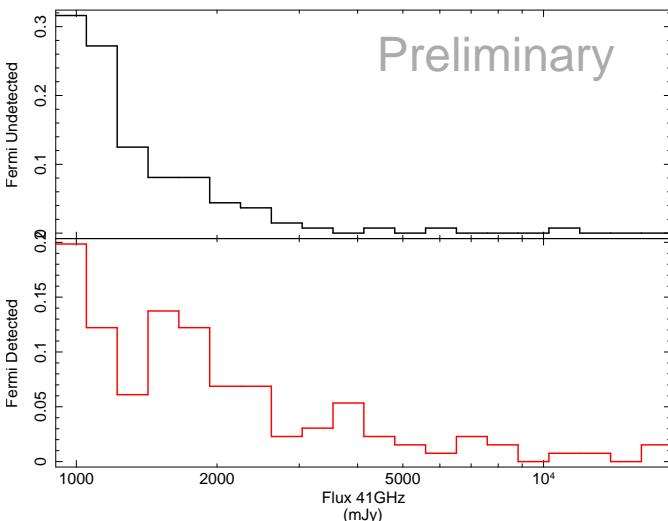
Fig. 3. Flux at 41 GHz distributions on Undetected (above) and Detected (below) by *Fermi*-LAT

Fermi γ-ray ones. We are considering the possibility that the γ-ray high variability of blazars blurs the correlation with the μ-wave band. The upper limits are distributed at low gamma-ray fluxes as expected but some of the faint gamma-ray sources are indeed strong microwave emitters. These sources can have a strong cutoff of the spectrum at MeV energies and therefore not yet detected due the sensitivity of *Fermi*/LAT in the first year of observation.

5. Conclusions

Fermi is detecting a significant number of powerful microwave emitters. The μ-wave to γ-ray correlation is blurred by large γ-ray variability of blazars, specially with non-simultaneous data. No strong differences in the studied properties are found. This could imply that, after 1 year of *Fermi* data taking, we are still detecting mainly those LSP sources which undergone strong flares, or show multiple components which allow them to be detected in the GeV energy range, leading to the same conclusions already showed in Abdo et al. (2010b). In other words, *Fermi*/LAT is detecting those objects which show additional features with respect to a simple homogeneous SSC and those 50% undetected could be driven by simple SSC processes.

Planck data along with *Fermi* one, being both operated in survey mode, will give us unprecedented set of real simultaneous data.

These two energy bands (μ-waves and γ-rays) are indeed best suited to study blazars as their emission at these frequencies is largely dominated by non-thermal radiation. The combined study of blazars in the μ-wave and in the γ-ray energy bands will probably offer a unique opportunity to understand many of the physical details of this class of black hole-dominated cosmic structures.

References

Abdo, A.A., Ackermann, M., Ajello, A., et al. 2009, ApJ 700, 597

Fig. 4. γ-ray Flux (1–3 GeV) vs μ-wave flux density at 41 GHz.

Abdo, A.A., Ackermann, M., Ajello, M., et al. 2010, ApJ 715, 429

Abdo, A.A., Ackermann, M., Agudo, I., et al. 2010, ApJ 716, 30

Atwood, W.B., Abdo, A.A., Ackermann, M., et al. 2009, ApJ 697, 1071

Bennet, C.L., Bay, M., Halpern, M., et al. 2003, ApJ 583, 1

Giommi, P., Colafrancesco, S., Padovani, P., et al. 2009 A&A, 508, 107

Giommi, P., Capalbi, M., Cavazzuti, E., et al. 2007 A&A, 468, 571

Gold, B., et al. 2010, submitted to ApJS arXiv:1001.4555

Helene, O. 1983, Nuclear Instruments and Methods in Physics Research, 212, 319

Kovalev, Y.Y., Aller, H.D., Aller, M.F., et al. 2009, ApJ 696, L17

Pittori, C., Cavazzuti, E., Colafrancesco, S., & Giommi, P., 2007, Ap&SS 309, 89

Rolke, W.A., López, A.M., & Conrad, J. 2005, Nuclear Instruments and Methods in Physics Research A, 551, 493

Toffolatti, L., Argueso Gomez, F., de Zotti, G., et al. 1998 MNRAS 297, 117

Multi-band properties of superluminal AGN detected by Fermi/LAT

T.G. Arshakian[1]⋆, J. León-Tavares[2], J. Torrealba[3], and V.H. Chavushyan[4]

[1] Max-Planck-Institut für Radioastronomie, Auf dem Hügel 69, 53121 Bonn, Germany
   e-mail: `t.arshakian@mpifr-bonn.mpg.de`
[2] Aalto University Metsähovi Radio Observatory, Metsähovintie 114, FIN-02540, Kylmälä, Finland
   e-mail: `leon@kurp.hut.fi`
[3] Instituto de Astronomía, Universidad Nacional Autónoma de México, Apartado Postal 70-264, 04510 México
   D.F., México, e-mail: `cjanet@astroscu.unam.mx`
[4] Instituto Nacional de Astrofísica Óptica y Electrónica, Apartado Postal 51 y 216, 72000 Puebla, Pue, México
   e-mail: `vahram@inaoep.mx`

Abstract. We perform a multi-band statistical analysis of core-dominated superluminal active galactic nuclei (AGN) detected with *Fermi* Large Area Telescope (LAT). The detection rate of γ-ray jets is found to be high for optically bright AGN. There is a significant correlation between the γ-ray luminosity and the optical nuclear and radio (15 GHz) luminosities of AGN. We report a well defined positive correlation between the γ-ray luminosity and the radio-loudness for quasars and BL Lacertae type objects (BL Lacs). The slope of the best-fit line is significantly different for quasars and BL Lacs. The relations between the optical and radio luminosities and the γ-ray loudness are also examined, showing a different behavior for the populations of quasars and BL Lacs. Statistical results suggest that the γ-ray, optical and radio emission is generated at different locations and velocity regimes along the parsec-scale jet.

1. Introduction

Extreme optical variability was a clear signature for some blazars detected at γ-ray energies during the EGRET era (Fitchel et al. 1994). Using the *Fermi*/LAT improved sensitivity, recent multi-wavelength variability studies on individual sources have confirmed the tight connection among the γ-ray and optical variable emission (e.g. 3C 273 in Abdo et al. 2010a). So far there was no attempt to compare optical continuum properties among γ-ray blazars. In this manuscript we take advantage of the unprecedented sensitivity provided by the first bright source catalogue (1FGL; Abdo et al. 2010b) to study the multi-band correlations between optical, radio, and γ-ray emission in superluminal AGN detected by *Fermi*/LAT during its first 11 months of operation. We adopt a flat cosmology with $H_0 = 71$ km s^{-1} Mpc^{-1}, $\Omega_m = 0.27$, and $\Omega_\Lambda = 0.73$.

2. The MOJAVE sample

The sample consists of core-dominated AGN from the MOJAVE (Monitoring of Jets in AGN with VLBA Experiments) program. The MOJAVE-2 sample contains about 250 core-dominated AGN (Kovalev et al. 2009) most of which are currently monitored with the Very Large Baseline Array (VLBA) at 15 GHz (for a detailed description of the sample see Lister et al. 2009). The 1FGL catalogue includes about 190 sources from the MOJAVE-2 sample. Optical nuclear fluxes and redshift measurements

⋆ Speaker
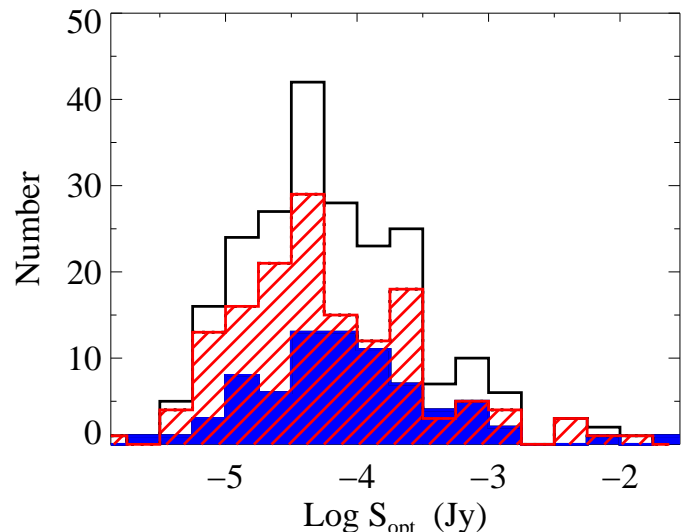
Fig. 1. Distributions of optical nuclear fluxes for AGN from the MOJAVE-2 sample (full line), 102 AGN detected as the gamma-ray source (filled histogram) and non-detected with *Fermi*/LAT during the 1FGL period (shaded histogram).

were available for a sample of 102 MOJAVE-2 sources (Arshakian et al. 2010a) identified by *Fermi*/LAT (hereafter, M2-1FGL sample). Seventy six out of 102 sources in the M2-1FGL sample are part of the statistically complete MOJAVE-1 sample. We will refer to these 76 sources as the M1-1FGL sample. The Kolmogorov-Smirnov (K-S) test shows that the distribution of redshifts in the
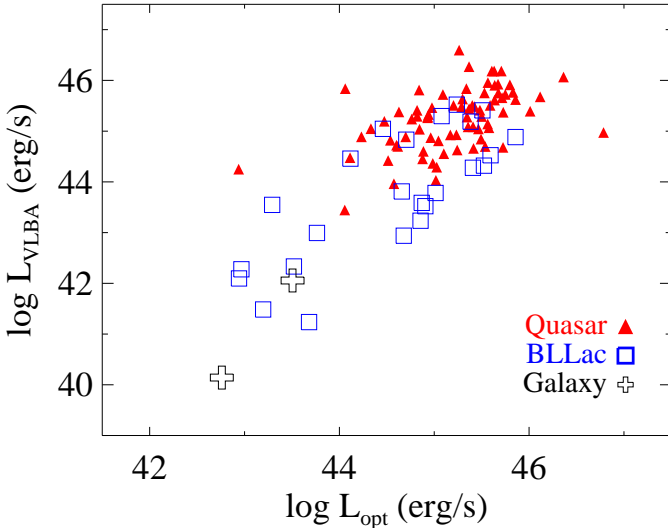
Fig. 2. Radio luminosity at 15 GHz against optical nuclear luminosity at 5100 Å.

MOJAVE-1 sample and the M1-1FGL sample are drawn from the same parent population indicating that the M1-1FGL sample is not biased by redshift.

The M2-1FGL sample consists of 76 quasars, 24 BL Lacs, and two radio galaxies which are excluded from further statistical tests. We use the non-parametric Kendall's τ test to analyze correlations between independent variables, and the partial Kendall's τ test to account for the common dependence on redshift in the correlations between luminosities. Throughout the paper we assume a correlation to be significant if a chance probability $P < 0.05$.

3. Interplay between γ-ray, optical and radio properties of superluminal AGN

The distribution of optical nuclear fluxes for the MOJAVE-2 AGN detected and non-detected with *Fermi*/LAT is presented in Figure 1. At first glance, the *Fermi*/LAT detected sources seem to have higher optical fluxes than those with no-detection. This is further supported by the K-S statistical test: there is a significant difference (at a confidence level of 99.9%) between the distributions of optical fluxes of AGN detected and non-detected by *Fermi*/LAT. When using the M1-1FGL sample, the difference is significant at a confidence level of 96%. We conclude that the detection rate of γ-ray AGN is high for sources having high optical nuclear fluxes.

We derive the optical nuclear luminosities (L_{opt}), total VLBA luminosities (L_{VLBA}), and the rest-frame radio-loudness ($R \propto S_{VLBA}/S_{opt}$) using the fluxes given in Arshakian et al. (2010a). γ-ray luminosities were computed using the Eq. (1) in Ghisellini et al. (2009), where $S_\gamma(\nu_1, \nu_2)$ is the energy flux between 0.1 GeV and 100 GeV from the 1FGL catalogue. Note that the γ-ray, optical, and radio luminosities are estimated from non-simultaneous observations.
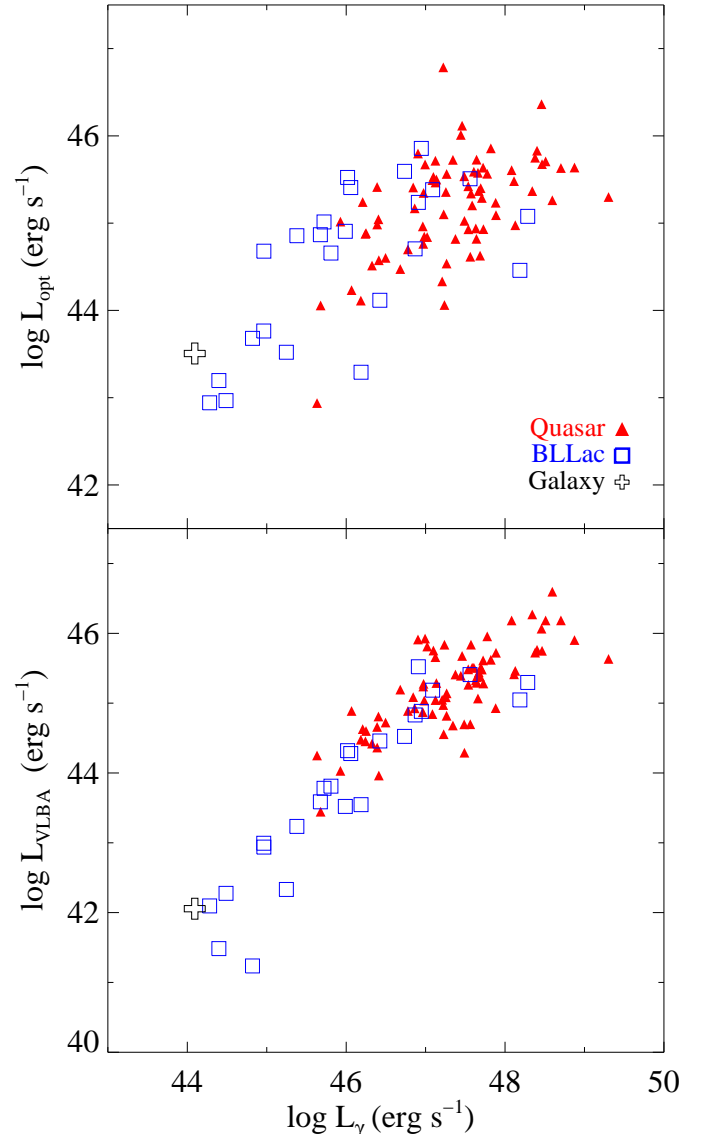
Fig. 3. Optical nuclear luminosity against γ-ray luminosity (top panel), and radio (15 GHz) luminosity against γ-ray luminosity (bottom panel) for AGN from the M2-1FGL sample. Objects are symbol coded by optical spectral type, and the labels in the top panel denote the corresponding population.

Optical–Radio emission. Arshakian et al. (2010a) found a positive correlation in the $L_{opt} - L_{VLBA}$ relation plane for AGN from the MOJAVE-1 sample. They concluded that the correlation is due to the population of quasars and that the optical emission is non-thermal and generated in the parsec-scale jet. This is supported by studies of individual radio galaxies, 3C 390.3 and 3C 120 (Arshakian et al. 2010b and León-Tavares et al. 2010) for which the link between optical continuum variability and kinematics of the parsec-scale jet was found. It was interpreted in terms of optical continuum flares generated at sub-parsec-scales in the innermost part of a relativistic jet rather than in the accretion disk. We confirm the $L_{opt} - L_{VLBA}$ positive correlation for a larger sample of
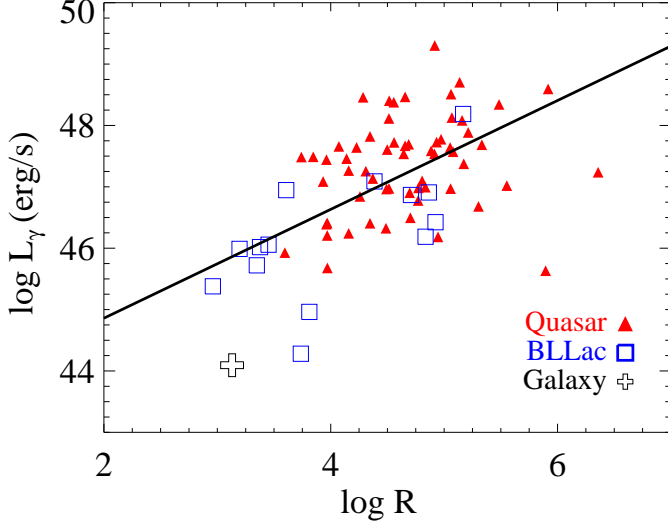
Fig. 4. γ-ray luminosity (L_γ) versus radio-loudness (R) for M2-1FGL AGN. The solid line represents the ordinary least-square fit to the data.

M2-1FGL quasars as well as no-correlation for BL Lacs (see Fig. 2 and Tables 1 and 2).

Gamma-ray–Optical emission. We find a positive correlation between L_γ and $L_{\rm opt}$ (Figure 3). The correlation is significant for quasars from the M2-1FGL and M1-1FGL samples and it is stronger for M1-1FGL quasars (Tables 1 and 2), suggesting for a single production mechanism for γ-ray and optical nuclear emission.

Gamma-ray–Radio emission. Kovalev et al. (2009) reported a significant correlation between γ-ray and radio VLBA (8 GHz) emission for sample of $\sim$30 AGN. This correlation holds at high confidence level ($> 99.9\%$; Figure 3) for non-simultaneous measurements and a larger sample (M2-1FGL) of AGN. This suggests that the powers averaged over the long time scales are correlated and, hence, the Doppler-factors of the parsec-scale jet in the gamma and radio domains are not changing substantially on a timescale of a few years. Pushkarev et al. (these proceedings) found that the γ-ray emission leads the radio emission of the parsec-scale jet at 15 GHz with time delay of few months. They interpreted the observed time lag as a result of synchrotron opacity in the jet: the radio and γ-ray emission are generated in the same region (perturbation in the jet?) and become observable with some time delay due to the opacity effects. If this scenario is correct then the variable optical emission is also generated in the perturbation moving upstream the jet, and we should expect that the optical emission leads the radio emission and delays with respect to the γ-ray emission.

The correlation in the $L_{\rm VLBA} - L_\gamma$ relation plane is apparently stronger than that in the $L_{\rm opt} - L_\gamma$ (Figure 3). One may think that the corrected optical nuclear emission of some AGN (Arshakian et al. 2010a) might be contaminated by contribution of a stellar component thus causing the large dispersion in the $L_{\rm opt} - L_\gamma$ diagram. Contamination should be stronger in radio galaxies and

weaker in quasars and BL Lacs for which the contribution of optical nuclear emission is dominant. The large dispersion in the $L_{\rm opt} - L_\gamma$ relation plane can be due to non-simultaneous optical/γ-ray observations and stronger variability in the optical regime than that in the radio, and/or wider range of Doppler factors in the optical regime compared to the range of Doppler factors of the jet at 15 GHz, if the bulk of optical emission is generated in the relativistic jet and it is Doppler boosted.

We report a significant positive correlation ($> 99\%$) between L_γ and radio-loudness for quasars and BL Lacs (see Fig. 4 and Table 1). The solid line in Figure 5 represents the best fit to the data,

$$\log L_\gamma = (0.95 \pm 0.11)\log R + (42.76 \pm 0.25). \qquad (1)$$

The $L_\gamma \propto R$ relation suggests that the strong γ-ray jets have progressively high Doppler factors (or faster speeds) in the radio domain compared to those in the optical regime. For quasars, the regression line is fitted by

$$\log L_\gamma = (0.33 \pm 0.14)\log R + (45.8 \pm 0.32), \qquad (2)$$

while for BL Lacs the best fit is,

$$\log L_\gamma = (0.98 \pm 0.21)\log R + (42.29 \pm 0.44). \qquad (3)$$

It is noticeable that the slope derived for quasars is shallower than the slope fitted for BL Lacs. The $L_\gamma - R$ correlation is still significant for all AGN ($> 99\%$), quasars and BL Lacs (99%) of the M1-1FGL sample (Table 2). The best-fit parameters for the later sample are almost unchanged.

Table 1. Kendall's τ correlation analysis between emission characteristics of AGN from the M2-1FGL sample. A1 and A2 are the independent variables for which the Kendalls τ correlation analysis is performed, τ is the correlation coefficient, and P is the probability of a chance correlation. The correlations are considered to be significant if the chance probability $P < 0.05$ (or confidence level $> 95\%$).

A1	A2	All τ	All P	Quasars τ	Quasars P	BL Lacs τ	BL Lacs P
$L_{\rm VLBI}$	$L_{\rm opt}$	0.2	7×10^{-3}	0.2	2×10^{-2}	0.1	0.4
L_γ	$L_{\rm opt}$	0.1	4×10^{-2}	0.1	5×10^{-2}	0.1	0.3
L_γ	$L_{\rm VLBA}$	0.4	6×10^{-8}	0.3	7×10^{-5}	0.5	7×10^{-4}
L_γ	R	0.4	3×10^{-9}	0.2	8×10^{-3}	0.4	1×10^{-4}
$L_{\rm opt}$	$S_\gamma/S_{\rm VLBA}$	-0.3	1×10^{-5}	0.2	4×10^{-2}	0.5	1×10^{-3}

Gamma-ray loudness. We define the γ-optical loudness and γ-radio loudness as the $S_\gamma/S_{\rm opt}$ and $S_\gamma/S_{\rm VLBA}$, respectively. We find that the radio luminosity is independent of γ-optical loudness (Figure 5, left panel). On the other hand, there is a negative correlation in the $L_{\rm opt} - S_\gamma/S_{\rm VLBA}$ relation plane (Figure 5, right panel), which is much stronger for BL Lacs (confidence level $\gtrsim 99.9\%$; Tables 1 and 2). For the M2-1FGL AGN, the best-fit regression line is represented by $L_{\rm opt} \propto (S_\gamma/S_{\rm VLBA})^{-0.57}$. We interpret this relation as the optically weaker jets to
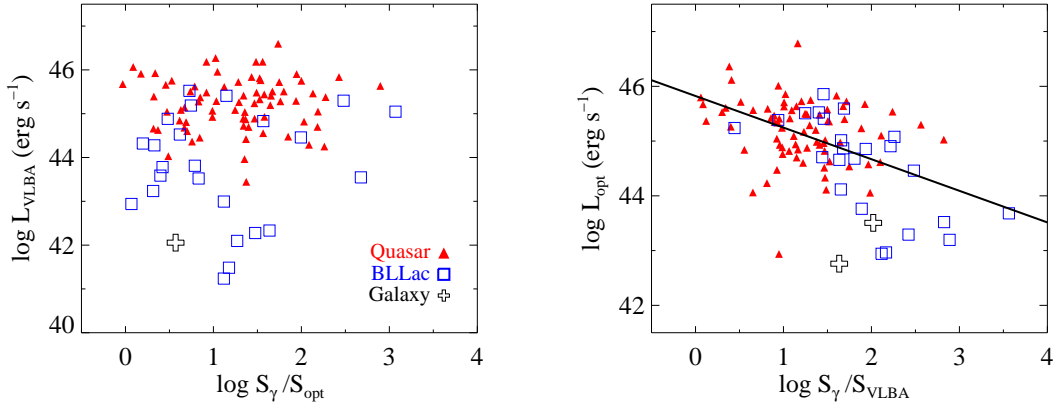
Fig. 5. L_{VLBI} − $S_\gamma/S_{\mathrm{opt}}$ (left panel) and L_{opt} − $S_\gamma/S_{\mathrm{VLBI}}$ (right-panel). The solid line represents the ordinary least-square fit to the data

Table 2. Kendall's τ correlation analysis between emission characteristics of AGN from the M1-1FGL sample.

A1	A2	All τ	All P	Quasars τ	Quasars P	BL Lacs τ	BL Lacs P
L_{VLBA}	L_{opt}	0.2	1×10^{-2}	0.2	2×10^{-2}	0.1	0.6
L_γ	L_{opt}	0.2	2×10^{-2}	0.2	1×10^{-2}	0.1	0.7
L_γ	L_{VLBA}	0.4	1×10^{-6}	0.3	1×10^{-4}	0.4	$5 \times 10-2$
L_γ	R	0.4	3×10^{-6}	0.2	1×10^{-2}	0.6	1×10^{-2}
L_{opt}	$S_\gamma/S_{\mathrm{VLBA}}$	−0.3	1×10^{-4}	0.2	4×10^{-2}	0.5	2×10^{-3}

have higher Doppler factors (or Lorentz factors if outflows radiating in optical and γ-ray bands have the same viewing angle) in the gamma domain compared to those in the radio domain. The slope of the best-fit line is steeper for BL Lacs (-0.89 ± 0.21) than for quasars (-0.24 ± 0.1) and the difference is statistically significant. We suggest that, on the average, the ratio between the Doppler factors in gamma and radio regimes varies slower for quasars than for BL Lacs, indicating for different velocity regimes in their jets.

The significant differences found between quasars and BL Lacs are supported in recent studies (e.g. Ghisellini et al. 2009, Sambruna et al. 2010, Tornikoski et al., in these proceedings) suggesting the presence of different physical conditions along the jet in quasars and BL Lacs. This and other insights into the relationship between the γ-ray, radio, and optical emission will be pursued in a more detail in further studies.

4. Summary

Using the sample of 100 superluminal quasars and BL Lacs detected by *Fermi*/LAT, we investigate relations between their optical, radio, and γ-ray emission available from non-simultaneous observations. Our main results are summarized as follows:

- The detection rate of γ-ray superluminal AGN is high for optically bright AGN.
- The known positive correlation between L_{opt} and L_{VLBA} holds for the M2-1FGL quasars at a confidence level of 98 %. The known correlation between γ-ray flux and radio flux density (measured quasi-

simultaneously) is also valid for non-simultaneous measurements of L_γ and L_{VLBA} for quasars. The L_γ − L_{VLBA} correlation is significantly stronger than that in the L_γ − L_{opt} relation plane.

- There is a correlation between L_{opt} and L_γ which exclusively holds for quasars. The correlation is significant for the M2-1FGL quasars (at a confidence level of 99 %) and marginally significant for quasars from the M1-1FGL sample (c.l. 95 %).
- We report a statistically significant positive correlation (c.l. > 99 %) between γ-ray luminosity and radio-loudness for both, quasars and BL Lacs. The slope of the L_γ − R relation is found to be steeper for the population BL Lacs.
- We find that the radio luminosity at 15 GHz is independent of the γ-radio loudness ($S_\gamma/S_{\mathrm{VLBA}}$) for quasars and BL Lacs. The γ-optical loudness ($S_\gamma/S_{\mathrm{opt}}$) and optical nuclear luminosity are negatively correlated for quasars (c.l. 96 %) and BL Lacs (c.l. 99.9 %) with the slope of the later being steeper.

References

Abdo, A. A., Ackermann, M., Ajello, M., et al. 2010a, Nature, 463, 919

Abdo, A. A., Ackermann, M., Ajello, M. et al. 2010b, submitted to ApJS, `arXiv:1002.2280`

Arshakian, T. G., Torrealba, J., Chavushyan, V. H., et al. 2010a, A&A, in press, `arXiv:1003.2577`

Arshakian, T. G., León-Tavares, J., Lobanov, A. P., et al. 2010b, MNRAS, 401, 1231

Fitchel, C. E., Bertsch, D. L., Chiang, J., et al. 1994, ApJS, 94, 551

Ghisellini, G., Maraschi, L., & Tavecchio, F. 2009, MNRAS, 396, L105

Kovalev, Y. Y., Aller, H. D., Aller, M. F., et al. et al. 2009, ApJ, 696, L17

León-Tavares, J., Lobanov, A. P., Chavushyan, V. H., et al. 2010, ApJ, 715, 355

Lister, M. L., Aller, H. D., Aller, M. F., et al. 2009, AJ, 137, 3718

Sambruna, R. M., Donato, D., Ajello, M., et al. 2010, ApJ, 710, 24

Young radio sources: a radio-gamma perspective

M. Orienti[1,2] and G. Migliori[3]

[1] Dipartimento di Astronomia, Universitá di Bologna, via Ranzani 1, I-40127, Bologna, Italy
[2] Istituto di Radioastronomia - INAF, via Gobetti 101, I-40129, Bologna, Italy
[3] SISSA/ISAS, via Bonomea 265, I-34136, Trieste, Italy

Abstract. The evolutionary stage of a powerful radio source originated by an AGN is related to its linear size. In this context, compact symmetric objects (CSOs), which are powerful and intrinsically small ($< 1\,$kpc) radio sources with a convex synchrotron radio spectrum that peaks around the GHz regime, should represent a young stage in the individual radio source life. Their radio jets expand within the dense and inhomogeneous interstellar medium of the host galaxy, which may influence the source growth. The radio emission is expected to evolve as a consequence of adiabatic expansion and radiative and inverse Compton losses. The role played by the different mechanisms in the radio and gamma regimes is discussed.

1. Introduction

Powerful ($L_{1.4\mathrm{GHz}} > 10^{25}\,\mathrm{W\,Hz}^{-1}$) and intrinsically compact (linear size LS < 1–$20\,$kpc) extragalactic radio sources are considered to represent an early stage in individual radio source evolution. Their main characteristic is the rising synchrotron radio spectrum which turns over at frequencies from a few hundred MHz up to the GHz regime. The mechanism responsible for the spectral peak is synchrotron self-absorption (SSA; Snellen et al. 2000), although an additional contribution from free-free absorption (FFA) is present in the most compact objects (Orienti & Dallacasa 2008, Kameno et al. 2000).

When imaged with the high spatial resolution provided by radio interferometers, these objects resemble a scaled-down version of the classical edge-brightened FR II radio galaxies (Fanaroff & Riley 1974). Given their compact and two-sided structures, Wilkinson et al. (1994) termed these sources "Compact Symmetric Objects" (CSO) and suggested a possible evolutionary connection with the larger radio galaxies. Conclusive evidence of the genuine *youth* of this class of objects came from the determination of both kinematic (Polatidis & Conway 2003) and radiative (Murgia 2003, Murgia et al. 1999) ages, which were shown to be in the range of 10^3–10^5 years.

Several studies of samples of compact radio sources (O'Dea & Baum 1997) show an anti-correlation between the peak frequency and the linear size: the higher the peak frequency ν_{p}, the smaller the source is. This anti-correlation agrees well with an evolutionary scenario where the peak, caused by SSA, moves to lower frequencies as the source adiabatically expands. In this context we can draw an evolutionary path linking the different stages of source evolution: the smaller sources (LS < 1–$50\,$pc), with ν_{p} above a few GHz and known as high frequency peakers (HFP), will evolve into the GHz-peaked spectrum (GPS) sources, with LS $\sim 1\,$kpc and $\nu_{\mathrm{p}} \sim 1\,$GHz, which will become compact steep spectrum (CSS) objects (LS ~ 1–$20\,$kpc, and $\nu \sim 100\,$MHz), i.e. the progenitors of FRIIs.

Several evolutionary models (i.e Fanti et al. 1995, Kaiser & Alexander 1997) have been developed to describe the various steps of the source growth. Given the compact sizes, these objects reside entirely within the host galaxy, enshrouded by the dense and inhomogeneous interstellar medium (ISM), where jet-cloud interaction may play a role in the source growth (Jeyakumar 2009).

In this contribution we describe the role played by the various mechanisms in the source evolution, such as adiabatic expansion, energy losses, and their effects on the source spectrum, in particular in the radio and gamma regimes. Throughout this paper we assume $H_0 = 71\,\mathrm{km\,s^{-1}\,Mpc^{-1}}$, $\Omega_{\mathrm{M}} = 0.27$, $\Omega_{\Lambda} = 0.73$, in a flat Universe. The spectral index is defined as $S(\nu) \propto \nu^{-\alpha}$.

2. Physical properties

The knowledge of the magnetic field has crucial implications to the determination of radio source evolution. The models developed so far consider that the radio sources are in a minimum energy condition, which corresponds to equipartition between the particle energy and the magnetic field (Pacholczyk 1970). However, there is no *a-priori* reason why a radio source must be in equipartition.

A direct way to measure the magnetic field is based on observational parameters. In fact, in the case that the spectral peak is produced by SSA, the magnetic field H can be computed from the peak frequency ν_{p}, peak flux density S_{p}, and angular size θ by the relationship (Kellermann & Paulinity-Toth 1981):

$$H \sim f(\alpha)\theta^4\nu_{\mathrm{p}}^5 S_{\mathrm{p}}^{-2}(1+z)^{-1}\,, \tag{1}$$

where $f(\alpha)$ is a function weakly dependent on the spectral index ($f_{\alpha}=8$ for $\alpha=0.5$), and z is the redshift. The region considered in Eq. 1 is assumed to be homogeneous and

deviations from this assumption introduce uncertainties. Studies of a few CSS sources carried out at low frequencies (i.e., close to their peak frequency) were subject to substantial uncertainties on the component size. The high spatial resolution and the frequency coverage of the VLBA match well the requirements for a proper study of the most compact HFP sources, whose spectrum is reasonably fitted by self-absorbed synchrotron emission from a homogeneous component. The magnetic field derived for a sample of very young and compact HFP (Orienti & Dallacasa 2008) has been found in good agreement with the equipartition magnetic field, with values around a few tens of mG.

In the presence of such high magnetic fields, the radiative losses are very severe, making the lifetime of the relativistic electrons responsible for the radio emission very short, and causing a marked cut-off in the optically-thin part of the spectrum. If the particle injection stops, the radio spectrum rapidly shifts towards low frequencies, becoming undetectable by conventional observations, since only low-energy electrons will be able to survive longer in such high magnetic fields.

It should be noted that in a few source components, the magnetic field computed directly from the observational parameters is very different from the equipartition value. In these cases the analysis of their radio spectra indicates that the optically-thick regime is too inverted to be due to SSA (see Sect. 3), and an additional contribution from FFA is needed. This implies that the magnetic field derived from observational parameters is physically meaningless.

3. The ambient medium

The onset of radio emission is thought to be related to merger or accretion events which feed the central active galactic nucleus (AGN). For this reason, the interstellar medium of galaxies hosting a radio source is rather dense and inhomogeneous. Statistical studies of atomic hydrogen in absorption of a sample of young radio sources (Pihlström et al. 2003, Gupta et al. 2006) have shown an anti-correlation between the linear size and the HI column density (N_{HI}): the larger the source, the smaller the HI column density is. This can be explained assuming that the neutral hydrogen is settled in a circumnuclear torus/disk: the HI absorption is detected against the receding jet when our line of sight passes through the disk/torus along its way toward the radio emission. This interpretation is based on observations with poor spatial resolution. When pc-scale VLBI observations have been performed, it has been noted that in some compact sources, like 4C +12.50 (Morganti et al. 2005) the HI absorption is not produced by an organized circumnuclear structure, but it probably comes from an unsettled off-nuclear cloud located where the jet bends.

Other evidence of an inhomogeneous medium enshrouding the radio sources arises from the distribution of the ionized medium. VLBI studies of the compact HFP sources OQ 208 (Kameno et al. 2000), J0428+3259, and J1511+0518 (Orienti & Dallacasa 2008) could locate FFA against one lobe only, indicating an asymmetric distribution of the ionized gas. Given their intrinsically small linear size, young radio sources reside completely within such a dense and inhomogeneous environment, where jet-ISM interaction may influence the source evolution. Various studies of young radio sources have pointed out that in a large number of objects the brightest lobe is also the closest to the core (Saikia et al. 2003, Orienti et al. 2007). Such asymmetries are better interpreted in terms of jet-ISM interaction instead of projection effects. Furthermore, the detection of HI in absorption against only the brightest (and closest to the core) lobe of 3C 49 and 3C 268.3 (Labiano et al. 2006) strongly supports this interpretation. During the time the jet is piercing the cloud, its velocity is considerably slowed down. The interaction prevents adiabatic expansion and the radio luminosity is enhanced by strong radiative losses.

4. High energy emission

Although young radio sources are preferentially studied in the radio band, knowledge of their high energy emission is crucial in providing us information on the central region of the AGN and on their total energy distribution, i.e., a key element in understanding the source fate.

X-ray detections of GPS/CSSs registered a drastic increase with the advent of the *XMM-Newton* and *Chandra* observatories. Observational campaigns on GPS and CSS galaxies (Guainazzi et al. 2006, Vink et al. 2006, Tengstrand et al. 2009) and quasars (Siemiginowska et al. 2008) have been performed for the first time with detection fractions of nearly 100% of the selected subsamples. However, for most of the cases, the extreme compactness of the sources combined with the spatial resolution of the X-ray observatories ($\sim 1''$ in the best case with *Chandra*) prevents resolving the X-ray morphology and locating the site of origin of the high-energy emission. Therefore, these studies rely mainly on analysis of the X-ray spectral properties (presence of an intrinsic absorber, evaluation of X-ray intrinsic luminosities), but the identification of the various spectral features is often controversial. As a consequence, the origin of the X-ray and high-energy emission remains still a matter of debate. Thermal high energy/X-ray emission is expected from the accretion disk's hot corona or it could arise from interactions between the expanding radio source and the interstellar medium (Reynolds et al. 2001, Bicknell & Sutherland 2006). A significant contribution to the total X-ray flux can be given by the extended components, namely jet, hot spots and lobes, overpressured and powerful at the initial stages. In this case, the mechanism at the basis of high energy emission may be inverse Compton (IC) of either the thermal UV/IR photons from the accretion disk/circumnuclear torus by the lobes' relativistic electrons (Stawarz et al. 2008, Ostorero et al. 2010), or synchrotron photons by a dominant jet component (Migliori et al., in prep.). IC emission from the lobes should most
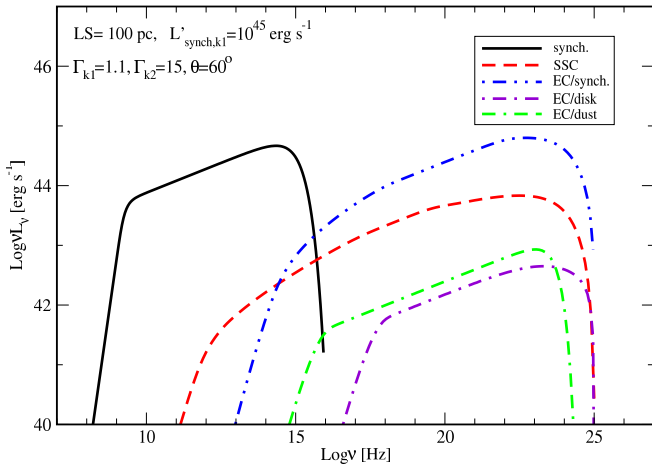
Fig. 1. Modeled SED for a knot located at $100\,\mathrm{pc}$ from the core (see text). The different curves show the modeled components: synchrotron emission (synch., *black solid line*), SSC emission (SSC, *red dashed line*), comptonized disc and torus photons (EC/disk and EC/dust *violet dot-dashed line* and *green dot-double dashed line* respectively), and IC emission of external synchrotron photons from a blazar-like component (EC/synch., *blue double-dot-dashed line*).

likely be dominant in GPS galaxies, where projection effects should be marginal, while IC emission from jet components is favored in more powerful GPS and CSS quasars. In the former case, the intensity of the IC emission for a given jet kinetic power, strictly depends on both the lobe size (i.e. its compactness), and the thermal photons arising from the dense and inhomogeneous nuclear ambient medium embedding the radio source. In the latter case, the ingredients at the basis of the high-energy emission are both the velocity of the emitting region, namely a jet knot, and its direction (approaching or moving away) relative to the source of the external thermal/non-thermal photon seeds. We note that while IC emission from the lobes is isotropic, the emission from the jet can be strongly beamed. More complexity is added when we consider a jet with a velocity structure, either axial (see e.g., Ghisellini et al. 2005) or radial (Celotti et al. 2001, Georganopoulos & Kazanas 2003), and synchrotron photons of the fast moving component are up-scattered by the electrons in the slower one.

As an example, we show in Fig. 1 the results for a synchrotron and IC modeled SED for a knot located at $100\,\mathrm{pc}$ from the nuclear region, emitting an intrinsic integrated luminosity $L'_{\mathrm{syn.,k1}} = 10^{45}\,\mathrm{erg\,s^{-1}}$. The expected IC emission produced by the knot electrons with the local synchrotron photons (synchrotron self Compton, SSC), and the external Compton with UV/disc (EC/disc) and IR/torus (EC/torus) photons are calculated. The bolometric disc luminosity is $L'_{\mathrm{disc}} = 10^{46}\,\mathrm{erg\,s^{-1}}$ and about 10% of the disc luminosity is reprocessed in the torus. The knot is moving with a bulk motion $\Gamma_{\mathrm{k1}} = 1.1$, and the elec-

tron energy distribution is described by a simple power law ($N(\gamma) \propto \gamma^{-p}$) with an energy spectral index $p = 2.6$ and extremes $\gamma_{\min} = 10$ and $\gamma_{\max} = 10^5$. A second knot, which releases an intrinsic integrated synchrotron luminosity of $L'_{\mathrm{syn.,k2}} = 10^{43}\,\mathrm{erg\,s^{-1}}$, is located at the jet base and it has a highly relativistic motion ($\Gamma_{\mathrm{k2}} = 15$). The synchrotron photons coming from this internal blazar-like component are up-scattered by the electrons in the slow-moving outer knot, (EC/synch., see Celotti et al. 2001 for a complete description of the model). The jet axis has an inclination of 60 degrees with respect to the observer line of sight. The dominant contribution to the high energy emission is provided by the EC/synch. emission. Thus, the presence of a velocity gradient along the jet seems to play a determining role in the production of the high energy emission.

4.1. Non-thermal γ-ray emission

An interesting aspect of the non-thermal scenarios, both for lobes in galaxies and jets in quasars, is that compact sources are also expected to be important γ-ray emitters. Observations in the γ-ray band could be important for several aspects:

- they should allow us to discriminate genuinely young/compact sources from projected sources/blazars. In particular, simultaneous, multi-wavelength (radio to γ-ray) observations carried out at various epochs, are a powerful tool to catch the elusive variability typical of blazars.
- they should be a decisive confirmation of the non-thermal hypothesis, since high-energy thermal emission is expected to rapidly drop in the MeV-GeV energy bands. Anyway, on this regard it is worth noting that at the current *Fermi*/LAT sensitivity only the most powerful and near objects may be detected. Certainly this introduces a fundamental bias, especially for the quasar class on average located at relatively high redshifts.
- γ-ray emission from the jet could allow us to shed light on the jet dynamics during the initial stages, whether there is a single velocity or a more complex structure. In this case, a comparison with the giant counterparts detected by *Fermi*/LAT could also be important to better understand the general evolutionary path.

5. Conclusions

Intrinsically compact radio galaxies represent a high fraction (15%–30%) of the sources selected in flux-limited radio catalogues. Their compactness, together with their two-sided morphology, suggests that their radio emission is still in a young phase and it will likely evolve into the large, edge-brightened radio galaxies. This class of objects is characterized by their peaked synchrotron spectrum, likely produced by SSA. Their physical properties indicate that they are in equipartition conditions with typical values of the magnetic fields from a few mG to a few hun-

dred mG in the most compact and brightest components. Such high magnetic fields cause severe energy losses for the relativistic electrons, thus producing steep optically-thin spectra. The ambient medium enshrouding these radio sources is quite dense and inhomogeneous, where jet-cloud interaction may take place and influence the source growth, for example impeding the jet expansion.

Although these sources are mainly studied in the radio band, their X-ray emission has been detected with the advent of *Chandra* and *XMM-Newton* observatories. However, the insufficient spatial resolution prevented us from constraining the site of the X-ray emission, since both thermal and non-thermal models are degenerate in the X-ray band. Non-thermal inverse Compton produced by relativistic electrons from lobes or jet components with either thermal photon seeds from the ambient medium (i.e., disc/torus), or non-thermal synchrotron photons from a relativistic jet knot, may be at the origin of the high-energy emission. *Fermi*/LAT observations in the γ-ray regime will help us in defining the actual region responsible for the high-energy emission, as well as the structure of the newly born radio jets.

References

Bicknell, G. V.& Sutherland, R. S. 2006, AN 327, 235

Celotti, A., Ghisellini, G., & Chiaberge, M. 2001, MNRAS, 321, 1

Fanaroff, B. L. & Riley, J. M. 1974, MNRAS, 167, 31

Fanti, C., Fanti, R., Dallacasa, D., et al. 1995, A&A, 302, 31

Georganopoulos, M. & Kazanas, D. 2003, ApJ, 594L, 27

Ghisellini, G., Tavecchio, F., & Chiaberge, M. 2005, A&A, 432, 401

Guainazzi, M., Siemiginowska, A., Rodriguez-Pascual, P., & Stanghellini, C. 2004, A&A, 421, 461

Gupta, N., Salter, C. J., Saikia, D. J., Ghosh, T., & Jeyakumar, S. 2006, MNRAS, 373, 972

Jeyakumar, S. 2009, AN, 330, 287

Kaiser, C. R. & Alexander, P. 1997, MNRAS, 286, 215

Kameno, S., Horiuchi, S., Shen, Z.-Q., et al. 2000, PASJ, 52, 209

Kellermann, K. I. & Pauliny-Toth, I. I. K. 1981, ARA&A, 19, 373

Labiano, A., Vermeulen, R. C., Barthel, C. P., et al. 2006, A&A, 447, 481

Morganti, R., Tadhunter, C. N., & Oosterloo, T. A. 2005, A&A, 444, 9

Murgia, M., Fanti, C., Fanti, R., et al. 1999, A&A, 345, 769

Murgia, M. 2003, PASA, 20, 19

O'Dea, C. P. & Baum, S. A. 1997, AJ, 113, 148

Orienti, M., Dallacasa, D., & Stanghellini, C. 2007, A&A, 461, 923

Orienti, M. & Dallacasa, D. 2008, A&A, 487, 885

Ostorero, L., Moderski,R., Stawarz, Ł, et al. 2010, ApJ, 715, 1071

Pacholczyk, A. G. 1970, Radio Astrophysics, Freeman & Co., San Francisco

Pihlström, Y. M., Conway, J. E., & Vermeulen, R.C. 2003, A&A, 404, 871

Polatidis, A. G. & Conway, J. E. 2003, PASA, 20, 69

Reynolds, C. S., Heinz, S., & Begelman, M. C. 2001, ApJ, 549, 179

Saikia, D. J., Jeyakumar, S., Mantovani, F., et al. 2003, PASA, 20, 50

Siemiginowska, A., LaMassa, S., Aldcroft, T.L., Bechtold, J., & Elvis, M. 2008, ApJ, 684, 811

Snellen, I. A. G., Schilizzi, R. T., Miley, G. K., et al. 2000, MNRAS, 319, 445

Stawarz, Ł., Ostorero, L., Begelman, M. C., et al. 2008, ApJ, 680, 911

Tengstrand, O., Guainazzi, M., Siemiginowska, A., et al. 2009, A&A, 501, 89

Vink, J., Snellen, I., Mack, K.-H., & Schilizzi, R. 2006, MNRAS, 367, 928

Wilkinson, P. N., Polatidis, A. G., Readhead, A. C. S., et al. 1994, ApJ, 432, 87

Redshift Properties of MASIV sources

T. Pursimo[1], R. Ojha[2], D.L. Jauncey[3], J.E.J. Lovell[4], B.J. Rickett[5], J.-P. Macquart[6], H.E. Bignall[6], L. Kedziora-Chudczer[7], M. Dutka[8], C. Senkbeil[4], and S. Shabala[9]

[1] Nordic Optical Telescope, E-38700 Santa Cruz de La Palma, Spain
[2] NVI Inc./United States Naval Observatory, 3450 Massachusetts Ave., NW, Washington DC 20392, USA
[3] Australia Telescope National Facility, CSIRO, PO Box 76, Epping, NSW 1710, Australia
[4] School of Mathematics & Physics, Private Bag 37, University of Tasmania, Hobart TAS 7001, Australia
[5] Department of Electrical and Computer Engineering, University of California, San Diego, La Jolla, CA 92093, USA
[6] ICRAR/Curtin University of Technology, Bentley, WA, 6102, Australia
[7] School of Physics, University of Sydney, NSW 2006, Australia
[8] The Catholic University of America, 620 Michigan Ave., N.E., Washington, DC 20064, USA
[9] Oxford Astrophysics, Denys Wilkinson Building, Keble Road, Oxford OX1 3RH, United Kingdom

Abstract. The MASIV 5 GHz VLA flat-spectrum radio source variability survey of the northern sky has discovered that more than half of its 475 targets exhibited interstellar scintillation (ISS) at one or more of the four survey epochs. We present the first results of the spectroscopic identifications of the sample. For 253 sources the spectroscopic identification is obtained and evaluated from the literature. For 76 sources in the RA range 13^h -24^h we use data from our own observations with the Nordic Optical Telescope and the Palomar Hale Telescope. Based on their optical spectrum and luminosity, the majority of the sources are QSOs. However there are many BL Lac objects and some narrow line/weak AGN in the sample. The BL Lac fraction appears to be much higher amongst the ISS than non-ISS sources and most other type of AGN than BL Lac or FSRQ are non-ISS sources, which indicates a higher incidence of bright, compact cores in BL Lacs. Our results show that ISS sources have a flat redshift distribution in comparison to the non-ISS sources. Particularly intriguing is a lack of $z >2$ ISS sources in the MASIV sample, which may be explained by the scattering properties of the Intergalactic Medium. The radio and optical luminosities of ISS and non-ISS sources are similar. Finally, we find that about 50% of the ISS sources with $S_{5\,GHz} > 0.3$ Jy are LAT-detected in comparison to a 25% detection rate of the non-ISS sources.

1. Introduction

There is now considerable evidence that Short-Timescale Variability (STV) results primarily from scintillation in the turbulent ionized interstellar medium of our Galaxy. This conclusion emerges from two lines of observational evidence. Time delays have been detected between the arrival times of the intensity fluctuations from STV sources at two widely-spaced telescopes (e.g Bignall et al. 2006). Further, annual cycles have been detected in the timescale of STV sources (Jauncey et al. 2003), a periodic modulation that most plausibly results from the change in the relative velocity of the Earth and the scattering medium through the course of a year. Though questions remain (Jauncey et al. 2001 & Krichbaum et al. 2002), interstellar scintillation is the only reasonable explanation of these observations.

Though an extrinsic (as opposed to intrinsic) origin for STV points to less extreme physical conditions for the sources that exhibit this phenomenon, scintillators are still among the most extreme and active radio AGN known. For a source to scintillate its angular size must be comparable to that of the first Fresnel zone (Narayan 1992) which implies microarcsecond angular sizes for screen distances of tens to hundreds of parsecs. Further, brightness temperatures of some scintillators are well in excess of 10^{14} K (Macquart 2000) which implies Doppler factors of several hundred or more (Readhead 1994) which is significantly higher than seen in VLBI surveys (e.g., Zensus et al. 2003). Thus, an investigation of the properties of AGN that exhibit STV is of considerable astrophysical interest.

In order to construct a large sample of scintillating extragalactic sources with which to examine microarcsecond structure, parent population and the spatial distribution of scintillators, and to probe the turbulent ISM responsible for the scintillation, the Microarcsecond Scintillation-Induced Variability (MASIV) survey was undertaken (Lovell et al. 2003).

2. The sample

The MASIV sample has its roots in two radio catalogues CLASS (Cosmic Lens All Sky Survey; Myers et al. 1995) and JVAS (Jodrell Bank VLA Astrometric Survey; e.g., Wilkinson et al. 1998). Compact sources, unresolved at 8.4 GHz with the VLA, and having a flat-spectrum (CLASS/JVAS vs NVSS catalog (NRAO VLA Sky Survey; Condon et al. 1998) with a spectral index lower limit of -0.3 ($S \propto \nu^{\alpha}$) were chosen. The sample was next reduced into strong ($S_{8.4\,GHz} > 0.6 Jy$) and weak

subsamples ($S_{8.4\,GHz} < 0.13Jy$) of about 300 sources each. Finally, the sources were selected to have uniform sky distribution in order to have the best possible coverage for the Very Large Array (VLA) at 5 GHz observations (see Lovell et al. 2003 for details). After removing sources with the presence of structure or confusion we are left with the final sample of 475 point sources common to all four epochs of MASIV observations. Lovell et al. (2008) presented the statistical analysis of the VLA data and found that the STV properties are consistent with the ISS. About 43% of the sources were variable in more than two epochs. The majority of the scintillators appear to be "episodic" (varying only in some epochs) rather than "persistent" (varying at all epochs) and "Rapid" scintillators with short intra-hour timescales are remarkably rare. For the analysis below, we compare the optical and radio properties to the STV. Following Lovell et al. (2008), we label sources which show STV in 'X' epochs, 'STVX' where 'X' is zero for non-STV sources and 1, 2, 3 or 4 for source that met the MASIV variability criteria for one, two, three or all four epochs and finally sources with two or more time showing STV are grouped as ISS-sources.

3. Optical data

The main goal of this work is to present the spectroscopic identifications and redshifts of the MASIV sample. The majority of the radio strong sample sources have observed spectroscopically and the results collected in NED (68%). However this is not the case with the weak sample (22%). In order to define the sample for optical spectroscopy and select appropriate observing resources accurate optical identification was a prerequisite.

For optical identification we used mainly the Sloan Digital Sky Survey (SDSS DR 5 Adelman-McCarthy et al. 2007) and GSC 2.3 (Lasker et al. 2008). 165 sources were identified from the SDSS DR5, which is complete down to $r=22.5$ ($\lambda_{eff} \sim 6230$Å) with astrometric accuracy about $0.''1$ (Pier et al. 2003) and covers ~ 8000 square degrees, essentially the Galactic gap and some smaller patches. For 223 sources we used GSC 2.3 which is scans of the POSS-II plates, and have F magnitudes ($\lambda_{eff} \sim 6500$Å) down to 20.5 with poorer photometric (~ 0.15 mag) and astrometric accuracy ($0.''3$) than the SDSS.

The new redshift were obtained using the 2.56 m Nordic Optical Telescope (NOT) which is located at La Palma and the 5 m Palomar Hale Telescope. Most of the NOT data was obtained during two observing runs (July 2005 and July 2006) supplemented by a few additional nights. The Hale data was obtained during an observing run on August 2007. At NOT, low resolution (dispersion of 3Å/pixel) spectra were obtained using ALFOSC with grism 4 with practical wavelength coverage about 3800 - 8000Å. At Hale, the Double Spectrograph (DBSP) was used with continuous wavelength coverage from ~ 3400 to 9500 Å, with dispersion of ~ 1Å and ~ 4.9Å per pixel for blue and red arms respectively.
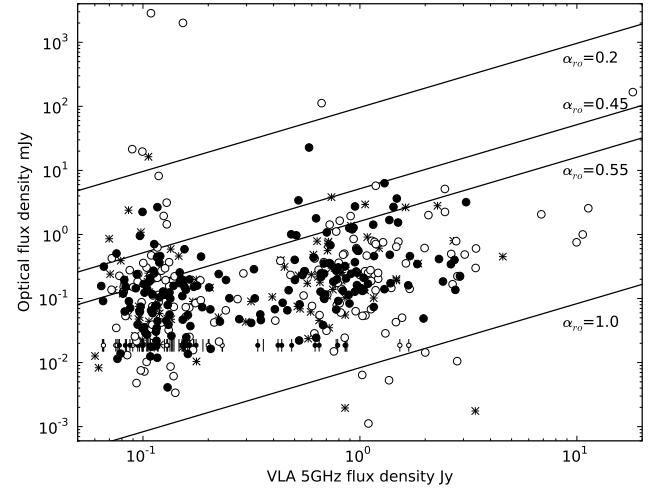
Fig. 1. VLA versus galactic extinction corrected R-band flux density. The diagonal lines indicate constant radio-optical flux ratio where open symbols are non-ISS sources, crosses STV1 and filled ISS sources. The vertical line indicates upper limit.

The redshifts were determined from the narrow emission lines whenever possible or, in most cases, broad emission lines. On the basis of the optical spectrum the sources have been divided into three main groups: weak line objects (mainly BL Lacs), objects with strong and broad lines (mainly FSRQ) and objects with strong and narrow lines (mainly Seyfert 2's). Our spectroscopic classification scheme is adapted from previous works e.g., Caccianiga et al. (2002a).

4. Results, Sample properties

The optical identification rate is 86% (215) for the radio "strong" and 77% (197) for the "weak" sample. The apparent magnitudes are similar amongst the STV-groups and there is no evidence of an STV apparent optical brightness correlation. Figure 1 shows the optical versus radio flux density with diagonal lines indicating constant radio-optical flux ratio, suggesting that the "weak" sample has a broader range of SEDs than the "strong" one.

We have measured 70 new redshifts with spectroscopic identification and 6 new featureless spectrum BL Lacs from our own observations. In addition we include 232 redshifts and 21 BL Lac objects from the literature. The majority (79%, 261) of the sources have broad emission lines (FSRQs, some Sy1s) the next largest group is BL Lac objects (15%, 48) and the remaining 6% (20) are low luminosity AGNs (Sy2, PEG, LINER) and galaxies. There is only little difference in the spectroscopic identification between the radio "strong" and "weak" samples. At redshift $z < 0.2$, most of the "strong" sample objects are BL Lacs or have broad emission lines in contrast to the "weak" sample, where most low-z objects have narrow emission lines or "galaxy" type of spectrum. Interestingly, only one of the ISS sources has a narrow emission line spectrum, all the others have broad or no emission lines.
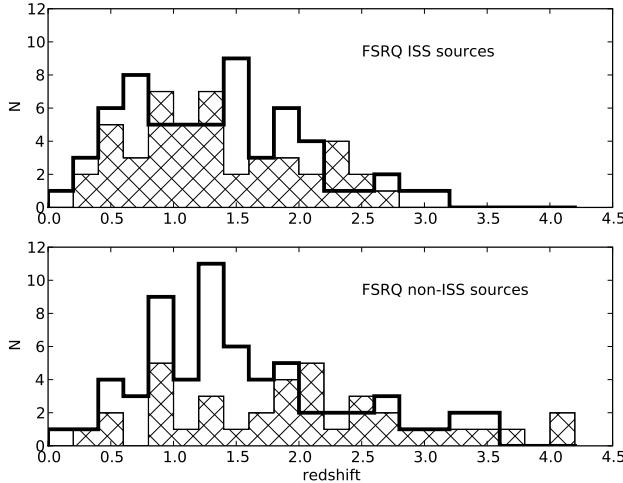
Fig. 2. Redshift distributions of the FSRQs. The open histogram shows the radio "strong" and hatched "weak" sample.

There are 71 *Fermi*/LAT detected sources of which 65 have $S_{5GHz} > 0.3$Jy. The LAT detection rate of the radio "strong" ISS sources is higher the non-ISS sources (38% vs 21%), however for the BL Lac-FSRQ fractions are similar between the full and ISS samples. Of the BL Lac objects 10% showed no STV, 70% are ISS-sources and of the featureless spectrum sources ~ 50% are STV4 sources. The fraction of BL Lacs increases from 6% of the non-variable to 40% of the STV4 sources and this is seen in both "strong" and "weak" samples. Finally, only ~ 40% of the BL Lacs have emission line redshift.

The median redshift of the full sample has only a modest increase from "strong" to "weak" sources (1.23 and 1.29). However the redshift distribution depends on the spectroscopic identification of the object, radio flux limit and the STV properties. The median redshift of the radio "strong" FSRQ sample is only slightly lower than that of the radio "weak" (1.33 vs 1.46) . These values are similar to the mean redshifts from previous studies e.g., FSRQs from 1 J, S4 and DXRBS samples (Landt et al 2001).

Inspecting the redshift distributions and the STV properties (Figure 2) it appears that the distributions of the variable and non-variable are different. The radio "strong" sample has similar median redshifts for ISS and non-ISS sources ($z_{med} =1.30$ vs 1.36), however this is not the case for radio "weak" sample ($z_{med} =1.24$ vs 1.94). The Kolmogorov-Smirnov test suggests that there is a 0.5% chance that the radio "weak" FSRQ ISS and non-ISS samples are drawn from the same parent population.

In Figure 3 we plot the optical and radio luminosities. FSRQ have $P_r= 10^{25.4-29}$ W/Hz, BL Lac objects and Seyfert 1/2 type have P_r between 10^{25-27} W/Hz and and PEG, galaxy, Liner type objects are weaker than 10^{25} W/Hz. The absolute magnitude range from -22 to -30 for the FSRQs and between -20 to -26 for the rest of the objects. At similar redshift ISS and non-ISS FSRQs have similar radio power and optical luminosity with Kolmogorov-Smirnov and Student's t-test indicating that the two sam-

ples are drawn from the same parent population. The source distributions are overlapping with an apparent radio power optical luminosity correlation. However, the apparent correlation is much weaker when selecting only redshift 1.0-2.0 FSRQs (Figure 3), when the slope is -1.2 with Pearson correlation coefficient of -0.49 with high statistical significance. This suggests that correlation between radio and optical luminosities is mild at best.

5. Discussion

Fossati et al. (1998) found for blazars a tight correlation between optical and radio luminosity and also that the SED is a function of radio power. This, so called 'blazar sequence', predicts that low radio power sources have higher SED peak frequency than a high radio power source, due to radiative cooling. The low radio power sources should have their SED peak at X-rays and high power sources at infrared. The correlation has been disputed (see a review e.g., Padovani (2007a), but see also the revised model by Ghisellini & Tavecchio (2008) We found only weak correlation between the radio power and optical luminosities, when reducing the selection effects such as the object, redshift-luminosity correlation and k-correction effects.

We found about the same fraction of FSRQs, BL Lacs and AGNs as has been found from Candidate Gamma-Ray Blazar Survey (CGRaBS, Healey et al. 2008) and Deep X-Ray Radio Blazar Survey (DXRBS, Padovani et al. 2007b). By the selection, "The CLASS blazar survey" (CBS, Marcha et al 2001, Caccianiga et al 2002a) is closest to MASIV however it also has weak ($S_{8.6GHz} \sim$1mJy), but only optically bright (R$\leq$17.5) sources. This results more low redshift ($z < 0.15$) and narrow-line sources than the MASIV survey. Also, optically less luminous but powerful radio sources (Figure 3, where $M_R > -23$ and Log$P >$26) are missing from the CBS.

It is interesting to note that STV4 is one of the most effective preselection to find BL Lac objects. In comparison, radio–X-ray selection results 18-25% BL Lacs (DXRBS Padovani et al. 2007b and XB-REX, Caccianiga, et al. 2002b) however, 50% of the γ-ray selected blazars are BL Lacs (Abdo et al. 2010).

Our results suggest that the selection criteria of persistent STV strongly favours BL Lac objects as 43% of the sources showing STV in all four epochs are BL Lac objects. The compact radio structure seems to give similar source distribution as radio/X-ray selection. However there are fewer low radio power objects and the number of objects with featureless optical spectrum is greater amongst compact radio core objects. Also compact radio structure removes mainly Type 2 objects and favours FSRQs and rejects low redshift sources. Similarly having fainter magnitude limit the fraction of FSRQs increases and Type 2 decreases. However this might be due to the fact at fainter magnitudes FSRQs with strong emission lines are easier to identify than BL Lacs and Type 2 targets with weak or no emission lines.
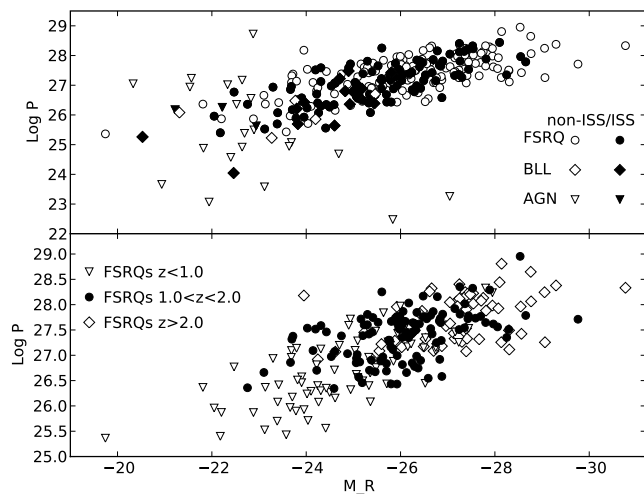
Fig. 3. Absolute optical R-magnitude vs radio power. The circles indicate FSRQs, stars BL Lac objects and triangles Type 2 objects and galaxies. In the top panel filled symbol indicates ISS source and open non-ISS sources. The bottom panel shows different redshift ranges for FSRQs.

Lovell et al. (2008) found that at redshift 2 the number of ISS sources decreases. Using the present data with spectroscopic identifications the trend has been confirmed for the FSRQs with high statistical level. In addition, we found that at similar redshift ISS and non-ISS sources have similar radio and optical luminosities. This suggests that the two type sources are similar and we argue that the difference is extrinsic to the source rather than intrinsic.

Based on 1043 γ-ray sources Abdo et al. (2010) found among other things, that most 1LAC sources are blazars, the redshift distributions the 1LAC FSRQs peak at $z \sim 1$ with maximum redshift $z = 3.1$ and that about 50% of the 1LAC blazars are BL Lac objects. These properties are surprisingly close to the MASIV ISS sources, where all but one of the ISS sources have broad/no lines, the redshift distributions of the ISS sources are similar for the 'strong' and 'weak' radio sources with $z_{median}=1.2$ and $z_{max}=3.1$ and the fraction of BL Lacs increases with the STV so that 40% of STV4 sources are BL Lacs.

Our results are consistent with previous study of the STV properties with the Pearson-Readhead compact extragalactic radio sources (Lister et al 2001) if the BL Lac objects and FSRQs are studied as one sample. They have found that STV sources have smaller emission line widths and lower 5GHz luminosities than the non-STV sources. Finally, we note that although MASIV sources probe finer scales then e.g., VLBI, our "resolution" for the most nearby ISS source (Mkn 421) is about $\sim 7 \times 10^{16}$cm, more than hundred times the estimate of the size of an X-ray emission region.

6. Summary

We have presented the optical and spectroscopic identification of a new sample of 475 compact flat spectrum radio sources. About half of these sources show STV. We have spectroscopic identifications and redshifts for 329 source, comprising $\sim$90% the radio "strong" ($S_{5Ghz} >0.3$ Jy) and 50% complete radio "weak" sample($0.3< S_{5Ghz} <0.06$ Jy).

● About 80% of the "strong" and 60% of the "weak" sources have an optical counter part with $R <20$ magnitude.

● Almost 80% of the MASIV sources are identified as FSRQs, $\sim$13% BL Lacs and $\sim$7% narrow-line objects or galaxies. The spectroscopic identifications are similar for radio "strong" and "weak" samples. Our results suggest that the compact radio structure favours FSRQs and BL Lacs amongst flat spectrum sources.

● Of the ISS sources 25% are BL Lacs, and the rest are almost exclusively FSRQs. The fraction of BL Lacs increases with the STV and 40% of the persistent STV sources are BL Lac objects.

● Radio and optical luminosities of the ISS and non-ISS FSRQs are similar at a given redshift, suggesting intrinsically similar SEDs.

● The redshift distribution of the ISS FSRQs appears to be independent of the radio flux in contrast to the non-ISS. Taking into account similar luminosities this suggests that lack of high redshift ISS sources is related to the environment of the source rather than being intrinsic.

References

Abdo, A.A., et al 2010, ApJ, 715, 429
Adelman-McCarthy, J.K., et al. 2007 ApJS, 172, 634
Bignall, H. E. et al. 2006 ApJ, 652, 1050
Caccianiga, A., et al., 2002a MNRAS, 329, 877
Caccianiga, A., et al., 2002b ApJ, 566, 181
Condon, J.J, et al 1998 AJ, 115, 1693
Fossati G., et al. 1998 MNRAS, 299, 433
Ghisellini, G, & Tavecchio, F. 2008, MNRAS, 387, 1669
Healey, S.E., et al. 2008 ApJS, 171, 61
Jauncey, D.L., et al, 2001 Ap&SS 278, 87
Jauncey, D.L., et al, 2003 Ap&SS 288, 63
Krichbaum, T.P. et al, 2002 PASA, 19, 14
Landt et al. 2001 MNRAS 323, 757
Lasker, B.M., et al 2008 AJ, 136, 735
Lister et al. 2001 ApJ, 546, 964
Lovell, J.E.J, et al. 2003 AJ, 126, 1699
Lovell, J.E.J, et al. 2008 ApJ, 689, 108
Marcha, M.J.M, et al. 2001 MNRAS, 326, 1455
Macquart, J.-P., et al., 2000 ApJ, 538, 623
Myers, S.T., et al., 1995 ApJ, 447, L5
Narayan, R. 1992, RSPTA, 341, 151
Padovani, P. 2007 Ap&SS, 309, 63
Padovani, P., et al. 2007 ApJ, 662, 182
Pier, J.R., et al. 2003, AJ, 125, 1559
Readhead, A.C.S. 1994 ApJ, 426, 51
Wilkinson, P.N, et al, 1998 MNRAS, 300, 790
Zensus, J.A., et al. 2003 ASP Conf. Ser. 300 Radio Astronomy at the Fringe, ed. . A. Zensus, M. H. Cohen, & E. Ros, 27

The first IRAM/PdBI polarimetric millimeter survey of AGN[*]

S. Trippe, R. Neri, M. Krips, A. Castro-Carrizo, M. Bremer, V. Piétu, and A.L. Fontana

Institut de Radioastronomie Millimétrique (IRAM), 300 rue de la Piscine, F-38406 Saint Martin d'Hères, France

Abstract. We have studied the linear polarization of 86 active galactic nuclei (AGN) in the observed frequency range 80–267 GHz (3.7–1.1 mm in wavelength), corresponding to *rest-frame* frequencies 82–738 GHz, with the IRAM Plateau de Bure Interferometer (PdBI). The large number of measurements, 441, makes our analysis the largest polarimetric AGN survey in this frequency range to date. We extracted polarization parameters via earth rotation polarimetry with unprecedented median precisions of ~0.1% in polarization fractions and ~1.2° in polarization angles. For 73 of 86 sources we detect polarization at least once. The degrees of polarization are as high as ~19%, with the median over all sources being ~4%. Source fluxes and polarizations are typically highly variable, with fractional variabilities up to ~60%. We find that BL Lac sources have on average the highest level of polarization. There appears to be no correlation between degree of polarization and redshift, indicating that there has been no substantial change of polarization properties since $z \simeq 2.4$. Our polarization and spectral index distributions are in good agreement with results found from various samples observed at cm/radio wavelengths; thus our frequency range is likely tracing the signature of synchrotron radiation without noticeable contributions from other emission mechanisms. The "millimeter-break" located at frequencies $\gtrsim 1$ THz appears to be not detectable in the frequency range covered by our survey.
— The results outlined here have been published in: Trippe, S., et al. 2010, A&A, in press (arXiv:1003.3205).

1. Introduction

Active galactic nuclei (AGN) have been studied extensively in the wavelength range from cm-radio to γ radiation in the last decades (see, e.g., Kembhavi & Narlikar 1999, or Krolik 1999, and references therein for a review). There is overwhelming observational evidence that the main source of their emission is accretion onto supermassive black holes (SMBH) with masses $M_\bullet \simeq 10^{6...9} M_\odot$ (e.g., Ferrarese & Ford 2005, and references therein). However, the properties of AGN at millimeter wavelengths are comparatively poorly known.

The linear polarization of AGN contains important information on the physics of galactic nuclei. Polarization fractions and angles provide details on synchrotron emission, the geometry of emission regions, strength and orientation of magnetic fields, and (via Faraday rotation and/or depolarization) on particle densities and matter distributions of the surrounding or outflowing matter (see, e.g., Saikia & Salter 1988, and references therein). This makes a detailed overview of the polarization properties of AGN in the millimeter wavelength range highly valuable. However, existing studies are usually limited to a few selected sources (e.g., Hobbs et al. 1978; Rudnick et al. 1978; Stevens et al. 1996, 1998; Attridge 2001), the work of Nartallo et al. (1998), which covers 26 sources, being a notable exception. One might also count similar studies of the black hole in the center of the Milky Way, Sgr A* (e.g., Marrone et al. 2006), and other local low-luminosity AGN (LLAGN; e.g., Bower, Falcke & Mellon 2002) in this context. Very recently, Agudo et al. (2010) analyzed a large sample of 145 AGN at 86 GHz using the IRAM 30-m telescope at Pico Veleta, Spain.

Like other radio astronomical observatories, the PdBI uses AGN as phase and amplitude calibrators. We have used this fact to conduct a polarimetric survey of 86 sources observed from January 2007 to December 2009. The scope of this survey is to provide for the first time an overview of the polarimetric properties of AGN in the mm/radio domain based on a large number of targets.

2. Observations and Data Analysis

In January 2007 (January 2008 for the 2 mm-band), the antennas of the IRAM Plateau de Bure Interferometer (PdBI) were equipped with dual linear polarization Cassegrain focus receivers. Since then, it is possible to observe both orthogonal polarizations – "horizontal" (H) and "vertical" (V) with respect to the antenna frame – simultaneously. Observations can be carried out non-simultaneous in three atmospheric windows located around wavelengths of 1.3 mm, 2 mm, and 3 mm. Each of these bands covers a continuous range of frequencies; these ranges are 201–267 GHz for the 1.3 mm band, 129–174 GHz for the 2 mm band, and 80–116 GHz for the 3 mm band. Within a given band, any frequency is available for observations (Winters & Neri 2008)[1].

The PdBI is not (yet) equipped for observations of all Stokes parameters. We collect linear polarization data on point sources via earth rotation polarimetry, i.e., we monitor the fluxes in the H and V channels as functions of parallactic angle ψ. For assessing the polarization of a source, we calculate the parameter

$$q(\psi) = \frac{V-H}{V+H}(\psi) = \frac{Q}{I}\cos(2\psi) + \frac{U}{I}\sin(2\psi) \tag{1}$$

from the fluxes $H(\psi)$ and $V(\psi)$. The second equality means that $q(\psi)$ provides full information on linear polarization (see,

---

[1] http://www.iram.fr/IRAMFR/GILDAS/doc/pdf/pdbi-intro.pdf

e.g., Sault, Hamaker & Bregman 1996; Thompson, Moran & Swenson 2001) if a sufficient range of ψ is observed.

Due to the nature of polarized light and the fact that the PdBI receivers are located in the Cassegrain foci, observing a polarized target results in $q(\psi)$ being a sinusoidal signal with a period of 180°. The functional form of $q(\psi)$ is thus

$$q(\psi) \equiv m_L \cos[2(\psi - \chi)] \tag{2}$$

Here m_L is the fraction of linear polarization (ranging from 0 to 1; in the following, we will express m_L in units of %) and χ is the polarization angle (ranging from 0° to 180°.

Our targets are PdBI calibration sources with flux densities $\gtrsim 0.2\,$Jy at 90 GHz. During each standard PdBI observation, one or two (spatially not resolved) AGN are monitored in parallel to the primary science target(s) for the purpose of phase and amplitude calibration. The AGN observations are thus a by-product of the standard interferometer operation; this makes it possible to conduct a large AGN survey without the need for dedicated observing time.

3. Results

3.1. Data and Accuracies

We included all PdBI calibration source data obtained from January 2007 to December 2009 in our analysis. We collected 441 polarization measurements for 86 AGN, resolved in time and frequency. Our analysis covers the *observed* frequency range 80–267 GHz (3.7–1.1 mm in wavelength).

For 78 out of our 86 AGN, redshifts z are available from the literature. We collected these values from the NASA/IPAC Extragalactic Database (NED)[2] and the MOJAVE Survey Data Archive[3] (Lister et al. 2009). These data are a mix of photometric and spectroscopic redshifts with varying accuracies; in any case, the accuracies are good enough for our purpose. Our AGN sample spans a wide range in redshift, from $z = 0.02$ (0316+413 = 3C84) to $z = 2.69$ (0239+108) with the peak of the distribution located at $z \simeq 0.7$. This means that our survey covers a *rest-frame* frequency range of 82–738 GHz (as far as known).

Thanks to the high sensitivity of the PdBI and the fact that $q(\psi)$ is a relative parameter, our survey is highly precise. The median *statistical* errors δ in m_L and χ are

$\delta m_L = 0.32\%$ and $\delta \chi = 1.9°$ for the 1.3 mm band,
$\delta m_L = 0.16\%$ and $\delta \chi = 1.5°$ for the 2 mm band,
$\delta m_L = 0.10\%$ and $\delta \chi = 1.1°$ for the 3 mm band.

These numbers reveal a level of precision that is unprecedented (compare, e.g., Stevens et al. 1996; Nartallo et al. 1998).

3.2. Polarization Levels

We actually detected polarization in 316 (out of 441) measurements; the remaining 125 were non-detections resulting in polarization fraction upper limits. Out of our 86 AGN, we found

---
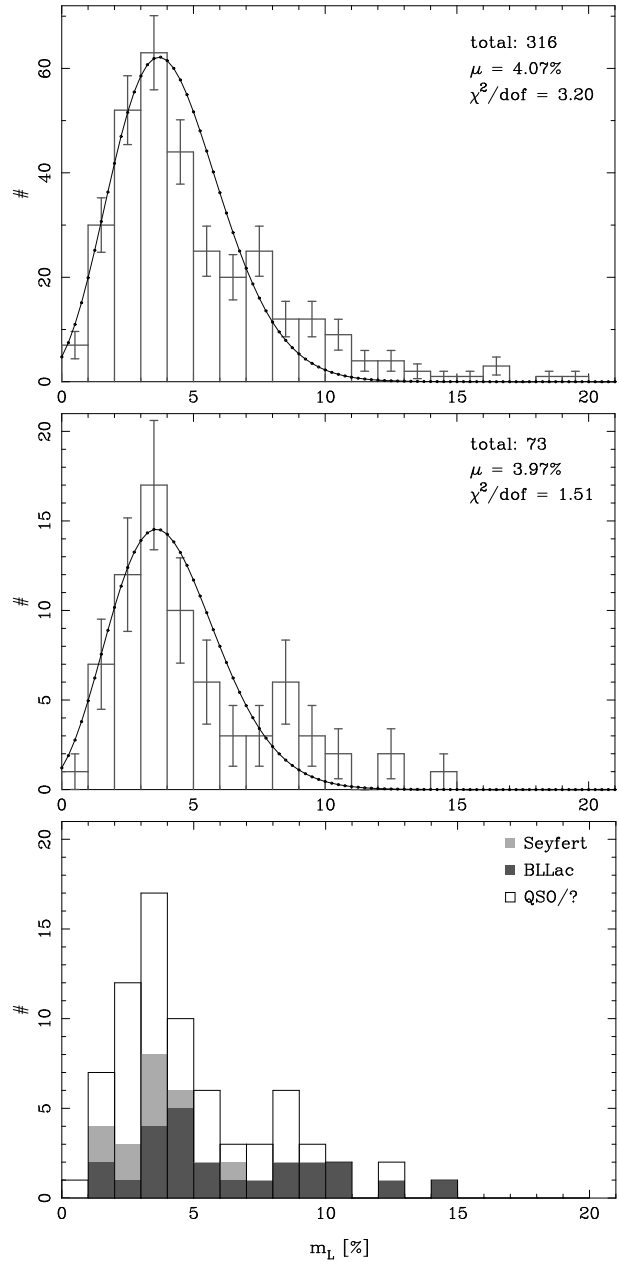
Fig. 1. Histograms of fractional linear polarization. *Top panel*: all measurements which detected linear polarization. *Center panel*: one value, averaged over both time and frequency, per source. *Bottom panel*: same as center panel, but separating the contributions of different source types. Error bars are binomial errors. The black curves indicate the best-fitting Poissonian profiles; the corresponding $\chi^2/$dof values are given in the plots. The median values are $\mu \simeq 4.1\%$ and $\mu \simeq 4.0\%$ respectively; we find polarization fractions up to $\approx 19\%$.

for 73 of them significant polarization at least once; the remaining 13 objects remained unpolarized (within errors) during our monitoring campaign. For 45 sources we detect polarization at least twice; for seven sources, the number of positive measurements exceeds ten. This corresponds to high detection rates: for ~72% of all measurements (~85% of all sources) we actually see polarized emission. The polarization fractions we find range from 0.6% (1928+738 at 93.2 GHz in November 2009)

to 19.4% (1005+066 at 83.3 GHz in January 2008) with a median of ~4.1%.

In Fig. 1 we present the polarization distributions. In both histograms there is a marginal trend towards a pronounced tail (maybe even bimodality) of the distributions. This may indicate a systematic difference between source types.

In order to investigate this quantitatively, we grouped our sources into Seyfert galaxies, BL Lacertae (BL Lac) objects, and QSOs (the last group including sources of unknown type or unclear classification). Like the redshifts, we took the source classifications from the NED and the MOJAVE archive. From all 73 AGN with detected polarization, 24 are of type BL Lac, 10 are Seyfert galaxies, and 39 are QSOs/unclear. The *average* degrees of polarization are

$m_L = 6.5 \pm 0.7\%$ for BL Lac,

$m_L = 3.4 \pm 0.4\%$ for Seyferts,

$m_L = 4.5 \pm 0.4\%$ for QSO/unclear.

Errors are standard errors $\sigma_m/\sqrt{N}$. Although these numbers are limited by low-number statistics, they reveal a trend for BL Lac objects to be the most polarized AGN in the mm wavelength range (see Fig. 1, bottom panel). In particular, there are no Seyfert galaxies with polarization fractions above 7%.

3.3. Polarization vs. Spectral Index

Combining our polarization data with flux information can provide valuable physical information. For this study we make use of flux data from the PdBI calibrator flux monitoring program (Krips et al. *in prep.*). As for many sources the PdBI flux monitoring provides frequency-resolved flux density information, we computed spectral indices where possible. For this we made use of the standard assumption that the flux density S_ν is related to the frequency ν via a power law $S_\nu \propto \nu^{-\alpha}$ with α being the spectral index. We computed α for 55 sources for which we had enough data at hand.

In order to test a potential relation between spectral index and polarization properties, we inspected the source-averaged polarization fraction $\langle m_L \rangle$ as function of α. The corresponding diagram is presented in Fig. 2. We find a Pearson correlation coefficient $r_P = -0.299$; this indicates that there is no strict correlation between spectral index and polarization fraction. However, this value points out a trend towards sources with lower α having larger polarization fractions. This is actually visible by eye: for $\alpha < 0.5$, the data span a range in polarization fractions up to ~12.5%; for $\alpha > 0.5$, there are no data beyond $\langle m_L \rangle = 7.5\%$. We do not see a relation between source class (Seyfert, BL Lac, QSO) and location in the diagram (except for the – already discussed – fact that BL Lac objects tend to be those with the highest polarization).

3.4. Polarization vs. Frequency and Redshift

We also examined possible correlations between polarization levels, frequency (both rest-frame and observed), and redshift. We do not find any relation; these parameters appear to be uncorrelated.
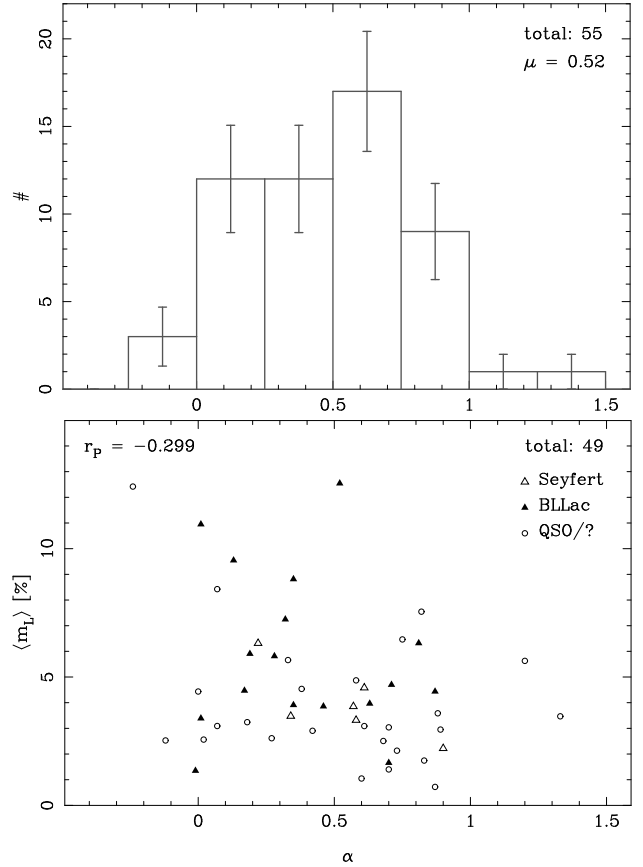
Fig. 2. *Top panel*: Histogram of spectral indices α for 55 of our AGN. The index is defined via $S_\nu \propto \nu^{-\alpha}$. The distribution ranges from -0.2 to $+1.3$ with a median value $\mu = 0.52$. Error bars indicate binomial errors. *Bottom panel*: Source-averaged degree of linear polarization $\langle m_L \rangle$ vs. spectral index α. The Pearson correlation coefficient $r_P = -0.299$ indicates that there is no strict correlation between spectral index and degree of polarization, but that there is a trend towards sources with lower values of α having higher polarization levels.

4. Discussion

Our survey provides an overview of the polarimetric properties of AGN at millimeter wavelengths. In order to put our results into context, one needs to take into account that our source sample is biased with respect to brightness. As our targets serve as calibrators, there is a preferential selection of bright AGN located close to primary PdBI targets. Our sources are mm/radio-bright ($S_\nu \gtrsim 0.2\,$Jy at 3 mm) and have (as far as known) spectra that are consistent with power law spectra. We therefore assume here that the emission we observe is fully non-thermal.

For synchrotron emission from an ensemble of homogeneous and isotropic relativistic electrons moving in a uniform magnetic field (B-field), the degree of linear polarization can be calculated analytically. If the energy distribution of the electrons follows a power law with index Γ, then $\Gamma = 2\alpha + 1$ and

$$m_L = \frac{\Gamma + 1}{\Gamma + 7/3} \qquad (3)$$

(e.g., Pacholczyk 1970) for optically thin sources. For flat-spectrum sources with $\alpha \sim 0$ (i.e., $\Gamma \sim 1$), one finds degrees of polarizations $m_L \sim 60\%$; if $\alpha > 0$, m_L increases even further.

Obviously, our observations find much smaller values (see e.g., Fig. 1); even our highest value, $m_L \simeq 19\%$, is more than a factor of three below the theoretical number. Clearly, the AGN we observe are far away from being "ideal" synchrotron emitters at mm wavelengths. Instead, the superposition of emission from various components (cores, lobes, jets) not resolved by the PdBI (within its present range of baselines) seems to average out most of the polarization signal. For a given component, e.g., a jet, averaging due to non-uniform B-field geometries can be expected to reduce the observed polarization signal further. This is in good agreement with earlier results (e.g., Nartallo et al. 1998), and, more recently, Agudo et al. (2010). An additional explanation may be that some emission regions are actually optically thick. In this case,

$$m_L = \frac{1}{2\Gamma + 13/3} \qquad (4)$$

(e.g., Pacholczyk 1970). For $\alpha \sim 0$, one finds $m_L \sim 16\%$. If α increases, the polarization level *decreases* further, resulting in values located in the m_L range we actually observe.

The distribution of the source-averaged polarization fractions (see Fig. 1) provides two conclusions. First, we do see a trend that BL Lac sources have higher intrinsic polarization levels. Second, there is no obvious segregation of source types; the distributions show a large amount of overlap, indicating a smooth transition between source types.

The absence of a correlation between redshift and (source-averaged) degree of polarization provides interesting constraints on the time evolution of AGN. As we observe polarized emission in 65 sources with $z \lesssim 2.4$, our sample probes a substantial part of the age of the universe. From this we can conclude that the properties of polarized mm radiation from AGN have not evolved substantially since $z \simeq 2.4$.

The spectral indices of our sources are located in the range $\alpha \simeq -0.2...1.3$ (see Fig. 2). This indicates that our sample actually provides a mix of core-dominated ($\alpha \lesssim 0.5$) and outflow (lobe/jet)-dominated ($\alpha \sim 0.5 - 1$; e.g., Krolik 1999) sources. On the one hand, the absence of a clear correlation between spectral index and degree of polarization (see Fig. 2) suggests that (at least at mm wavelengths) the polarization levels of AGN cores and outflows are of the same order of magnitude. On the other hand, there is a marginal trend towards higher polarization in core-dominated sources; this leaves room for systematically higher polarization levels in AGN cores compared to outflows by factors ≈ 2.

Our results are in good agreement with AGN properties observed in the centimeter wavelength range, with respect to the distributions of polarization fractions and spectral indices obtained from various samples. The surveys by Altschuler & Wardle (1976, 1977) and Aller et al. (1985) found maximum polarizations of $\sim 15\%$ in the frequency range 2–14.5 GHz, with "typical" degrees of polarization being $\lesssim 5\%$. This is especially interesting as our survey probes the high-frequency end of the "pure synchrotron" domain of the AGN spectral energy distribution. At frequencies above ~ 1 THz, other radiation processes like Compton scattering in the accretion zone around the central black hole can contribute substantially to the emission (e.g., Krolik 1999 and references therein). Observationally, this transition expresses itself in the "millimeter-break" located at $\nu \gtrsim 1$ THz (e.g., Elvis et al. 1994). We find for our frequency range the same characteristic radiation properties – in terms of polarization and distribution of spectral indices – as for the cm wavelength range. From this we can conclude that the rest-frame frequency range up to 738 GHz traces – like the cm/radio continuum domain – the signatures of "pure" synchrotron emission without noticeable contributions from other emission mechanisms. The mm-break appears to be not detectable in the frequency range covered by our survey.

We find that substantial variations in the degree of polarization (up to $\sim 60\%$ in fractional standard deviation) on timescales from weeks to years are a common feature throughout our AGN sample. This is the case also for the source fluxes that show variabilities at a similar level. High variabilities in both, fluxes and polarization fractions, point towards strong variations in source activities, accretion flows, B-field geometries, and/or outflows (jets) on the timescales of our survey. The most common explanation of such violent behaviour is shocks occurring in relativistic jets, possibly accompanied by jet bending and changes in B-field configurations (e.g., Stevens et al. 1998; Nartallo et al. 1998). Other, more recent models propose the orbital motion of plasma concentrations ("hotspots") in the accretion disks of supermassive black holes in order to explain flux and polarization variations on timescales from hours to weeks (e.g., Broderick & Loeb 2006). In any case, our results indicate that these processes are a frequent phenomenon for luminous AGN.

References

Agudo, I., et al. 2010, ApJSS, submitted
Aller, H.D., et al. 1985, ApJSS, 59, 513
Altschuler, D.R. & Wardle, J.F.C. 1976, MNRAS, 82, 1
Altschuler, D.R. & Wardle, J.F.C. 1977, MNRAS, 179, 153
Attridge, J.M. 2001, ApJ, 553, L31
Bower, G.C., Falcke, H. & Mellon, R.R. 2002, ApJ, 578, L103
Broderick, A.E. & Loeb, A. 2006, MNRAS, 367, 905
Elvis, M., et al. 1994, ApJSS, 95, 1
Ferrarese, L. & Ford, H. 2005, SSR, 116, 523
Hobbs, R.W., Maran, S.P. & Brown, L.W. 1978, ApJ, 223, 373
Kembhavi, A.K. & Narlikar, J.V. 1999, *Quasars and Active Galactic Nuclei*, Cambridge University Press, ISBN 0-521-47989-4
Krolik, J.H. 1999, *Active Galactic Nuclei*, Princeton University Press, ISBN 0-691-01152-4
Lister, M.L., et al. 2009, AJ, 137, 3718
Marrone, D.P., et al. 2006, ApJ, 640, 308
Nartallo, R., et al. 1998, MNRAS, 297, 667
Pacholczyk A.G. 1970, *Radio Astrophysics*, Freeman, ISBN 0-7167-0329-7
Rudnick, L., et al. 1978, ApJ, 225, L5
Saikia & Salter 1988, ARA&A, 26, 93
Sault, R.J., Hamaker, J.P. & Bregman, J.D. 1996A&AS, 117, 149
Stevens, J.A., Robson, E.I. & Holland, W.S. 1996, ApJ, 462, L23
Stevens, J.A., et al. 1998, ApJ, 502, 182
Thompson, A.R., Moran, J.M. & Swenson, G.W. 2001, *Interferometry and Synthesis in Radio Astronomy*, 2nd ed., Wiley-Interscience, ISBN 0-471-25492-4
Winters, J.M. & Neri, R. 2008, *An Introduction to the IRAM Plateau de Bure Interferometer*, public IRAM document, version 4.0-10

Models for the Spectral Energy Distributions and Variability of Blazars

M. Böttcher

Astrophysical Institute, Department of Physics and Astronomy, Ohio University, Athens, OH, USA

Abstract. In this review, recent progress in theoretical models for blazar emission will be summarized. The salient features of both leptonic and lepto-hadronic approaches to modeling blazar spectral energy distributions will be reviewed. I will present sample modeling results of spectral energy distributions (SEDs) of different types of blazars along the blazar sequence, including *Fermi* high-energy γ-ray data, using both types of models. Special emphasis will be placed on the implications of the recent very-high-energy (VHE) γ-ray detections of non-traditional VHE γ-ray blazars, including intermediate and low-frequency-peaked BL Lac objects and even flat-spectrum radio quasars. Due to the featureless optical spectra of BL Lac objects, the redshifts of several BL Lacs remain unknown. I will briefly discuss possible constraints on their redshift using spectral modeling of their SED including *Fermi* + ground-based VHE γ-ray data. It will be shown that in some cases, spectral modeling with time-independent single-zone models alone is not sufficient to constrain models, as both leptonic and lepto-hadronic models are able to provide acceptable fits to the overall SED. Subsequently, recent developments of time-dependent and inhomogeneous blazar models will be discussed, including detailed numerical simulations as well as a semi-analytical approach to the time-dependent radiation signatures of shock-in-jet models.

1. Introduction

Blazars (BL Lac objects and γ-ray loud flat spectrum radio quasars [FSRQs]) are the most extreme class of active galaxies known. They have been observed at all wavelengths, from radio through VHE γ-rays. The broadband continuum SEDs of blazars are dominated by non-thermal emission and consist of two distinct, broad components: A low-energy component from radio through UV or X-rays, and a high-energy component from X-rays to γ-rays (see, e.g., Figure 1).

Blazars are sub-divided into several types, defined by the location of the peak of the low-energy (synchrotron) SED component. Low-synchrotron-peaked (LSP) blazars, consisting of flat-spectrum radio quasars and low-frequency peaked BL Lac objects (LBLs), have their synchrotron peak in the infrared regime, at $\nu_s \leq 10^{14}$ Hz. Intermediate-synchrotron-peaked (ISP) blazars, consisting of LBLs and intermediate BL Lac objects (IBLs) have their synchrotron peak at optical – UV frequencies at 10^{14} Hz $< \nu_s \leq 10^{15}$ Hz, while High-synchrotron-peaked (HSP) blazars, almost all known to be high-frequency-peaked BL Lac objects (HBL), have their synchrotron peak at X-ray energies with $\nu_s > 10^{15}$ Hz (Abdo et al. (2010b)). This sequence had first been identified by Fossati et al. (1998), and associated also with a trend of overall decreasing bolometric luminosity as well as decreasing γ-ray dominance along the sequence FSRQ $\rightarrow$ LBL $\rightarrow$ HBL. According to this classification, the bolometric power output of FSRQs is known to be strongly γ-ray dominated, in particular during flaring states, while HBLs are expected to be always synchrotron dominated. However, while the overall bolometric-luminosity trend still seems to hold, recently, even HBLs seem to undergo episodes of strong γ-ray dominance. A prominent example was the recent joint *Fermi* + HESS observational campaign on the HBL PKS 2155-304 (Aharonian et al. (2009)).

Figure 1 shows examples of blazar SEDs along the blazar sequence, from the FSRQ 3C 279 (a), via the LBL BL Lacertae (b) and the IBL 3C 66A (c), to the HBL RGB J0710+591 (d). The sequence of increasing synchrotron peak frequency is clearly visible. However, the *Fermi* spectrum of the LBL BL Lacertae indicates a γ-ray flux clearly below the synchrotron level, while the SED of the IBL 3C 66A is clearly dominated by the *Fermi* γ-ray flux, in contradiction with the traditional blazar sequence.

The emission from blazars is known to be variable at all wavelengths. In particular the high-energy emission from blazars can easily vary by more than an order of magnitude between different observing epochs (von Montigny et al. (1995), Mukherjee et al. (1997), Mukherjee et al. (1999)). However, high-energy variability has been observed on much shorter time scales, in some cases even down to just a few minutes (Aharonian et al. (2007), Albert et al. (2007a)). The flux variability of blazars is often accompanied by spectral changes. Typically, the variability amplitudes are the largest and variability time scales are the shortest at the high-frequency ends of the two SED components. In HBLs, this refers to the X-ray and VHE γ-ray regimes. Such differential spectral variability is sometimes associated with inter-band or intra-band time lags as well as variability patterns which can be characterized as spectral hysteresis in hardness-intensity diagrams (e.g.,Takahashi et al. (1996), Kataoka et al. (2000),
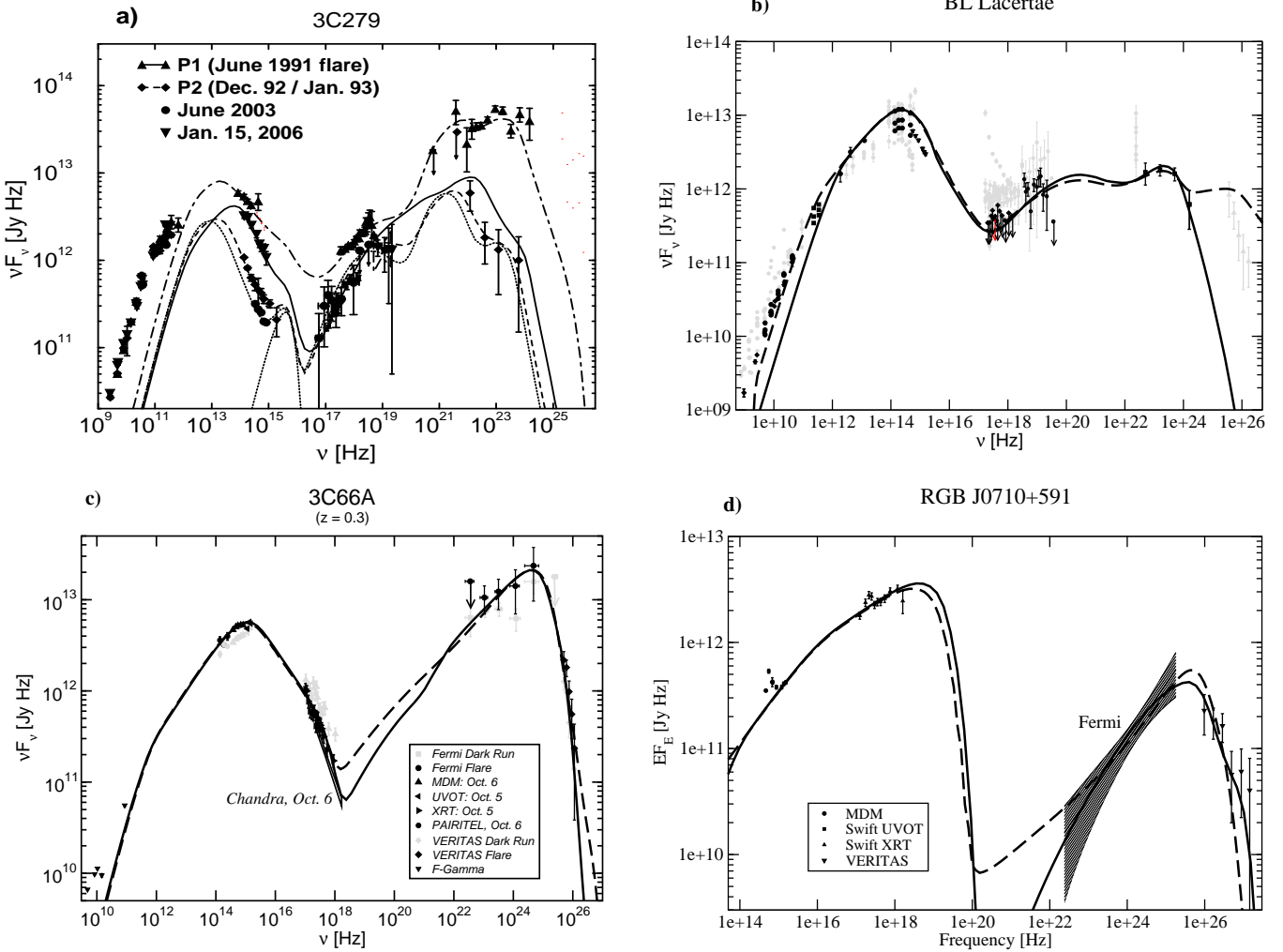
Fig. 1. Spectral energy distributions of four sub-classes of blazars: a) the FSRQ 3C 279 (from Collmar et al. (2010)), b) the LBL BL Lacertae, (data from Abdo et al. (2010b)), c) the intermediate BL Lac 3C 66A (data from Acciari et al. (2010c)), and d) the HBL RGB J0710+591 (data from Acciari et al. (2010b)). In Panel a) (3C 279), lines are one-zone leptonic model fits to SEDs at various epochs shown in the figure. In all other panels, heavy solid lines are fits with a leptonic one-zone model; heavy long-dashed lines are fits with a one-zone lepto-hadronic model.

Fossati et al. (2000), Zhang et al. (2002)). However, even within the same object this feature tends not to be persistent over multiple observations. Also in other types of blazars, hints of time lags between different observing bands are occasionally found in individual observing campaigns (e.g., Böttcher et al. (2007), Horan et al. (2009)), but the search for time-lag patterns persisting throughout multiple years has so far remained unsuccessful (see, e.g., Hartman et al. (2001) for a systematic search for time lags between optical, X-ray and γ-ray emission in the quasar 3C 279).

2. Basic features of leptonic and lepto-hadronic models

The high inferred bolometric luminosities, rapid variability, and apparent superluminal motions provide compelling evidence that the non-thermal continuum emission of blazars is produced in $\lesssim 1$ light day sized emis-

sion regions, propagating relativistically with velocity $\beta_\Gamma c$ along a jet directed at a small angle $\theta_{\rm obs}$ with respect to our line of sight (for details on the arguments for relativistic Doppler boosting, see Schlickeiser (1996)). Let $\Gamma = (1 - \beta_\Gamma^2)^{-1/2}$ be the bulk Lorentz factor of the emission region, then Doppler boosting is determined by the Doppler factor $D = (\Gamma[1 - \beta_\Gamma \cos\theta_{\rm obs}])^{-1}$. Let primes denote quantities in the co-moving frame of the emission region, then the observed frequency $\nu_{\rm obs}$ is related to the emitted frequency through $\nu_{\rm obs} = D\nu'/(1+z)$, where z is the redshift of the source, and the energy fluxes are connected through $F_{\nu_{\rm obs}}^{\rm obs} = D^3 F_{\nu'}'$. Intrinsic variability on a co-moving time scale $t_{\rm var}'$ will be observed on a time scale $t_{\rm var}^{\rm obs} = t_{\rm var}'(1+z)/D$. Using the latter transformation along with causality arguments, any observed variability leads to an upper limit on the size scale of the emission region through $R \lesssim c\, t_{\rm var}^{\rm obs} D/(1+z)$.

While the electron-synchrotron origin of the low-frequency emission is well established, there are two funda-

mentally different approaches concerning the high-energy emission. If protons are not accelerated to sufficiently high energies to reach the threshold for $p\gamma$ pion production on synchrotron and/or external photons and to contribute significantly to high-energy emission through proton-synchrotron radiation, the high-energy radiation will be dominated by emission from ultra-relativistic electrons and/or pairs (leptonic models). In the opposite case, the high-energy emission will be dominated by cascades initiated by $p\gamma$ pair and pion production as well as proton, $\pi^{\pm}$, and $\mu^{\pm}$ synchrotron radiation, while primary leptons are still responsible for the low-frequency synchrotron emission (lepto-hadronic models). The following sub-sections provide a brief overview of the main radiation physics aspects of both leptonic and lepto-hadronic models.

2.1. Leptonic models

In leptonic models, the high-energy emission is produced via Compton upscattering of soft photons off the same ultra-relativistic electrons which are producing the synchrotron emission. Both the synchrotron photons produced within the jet (the SSC process: Marscher & Gear (1985), Maraschi et al. (1992), Bloom & Marscher (1996)), and external photons (the EC process) can serve as target photons for Compton scattering. Possible sources of external seed photons include the accretion disk radiation (e.g., Dermer et al. (1992), Dermer & Schlickeiser (1993)), reprocessed optical – UV emission from circumnuclear material (e.g., the BLR; Sikora et al.(1994), Blandford & Levinson (1995), Ghisellini & Madau (1996), Dermer et al. (1997)), infrared emission from a dust torus (Błażejowski et al. (2000)), or synchrotron emission from other (faster/slower) regions of the jet itself (Georganopoulos & Kazanas (2003), Ghisellini & Tavecchio (2008)).

The relativistic Doppler boosting discussed above allows one to choose model parameters in a way that the $\gamma\gamma$ absorption opacity of the emission region is low throughout most of the high-energy spectrum (i.e., low compactness). However, at the highest photon energies, this effect may make a non-negligible contribution to the formation of the emerging spectrum (Aharonian et al. (2008)) and re-process some of the radiated power to lower frequencies. Also the deceleration of the jets may have a significant impact on the observable properties of blazar emission through the radiative interaction of emission regions with different speed (Georganopoulos & Kazanas (2003), Ghisellini et al. (2005)) and a varying Doppler factor (Böttcher & Principe (2009)). Varying Doppler factors may also be a result of a slight change in the jet orientation without a substantial change in speed, e.g., in a helical-jet configuration (e.g., Villata & Raiteri (1999)). In the case of ordered magnetic-field structures in the emission region, such a helical configuration should have observable

synchrotron polarization signatures, such as the prominent polarization-angle swing recently observed in conjunction with an optical + *Fermi* γ-ray flare of 3C 279 (Abdo et al. (2010a)).

In the most simplistic approaches, the underlying lepton (electrons and/or positrons) distribution is ad-hoc pre-specified, either as a single or broken power-law with a low- and high-energy cut-off. While leptonic models under this assumption have been successful in modeling blazar SEDs (e.g., Ghisellini et al. (1998)), they lack a self-consistent basis for the shape of the electron distribution. A more realistic approach consists of the self-consistent steady-state solution of the Fokker-Planck equation including a physically motivated (e.g., from shock-acceleration theory) acceleration of particles and all relevant radiative and adiabatic cooling mechanisms (e.g., Ghisellini & Tavecchio (2009), Acciari et al. (2009b), Weidinger et al. (2010)). The model described in Acciari et al. (2009b), based on the time-dependent model of Böttcher & Chiang (2002), has been used to produce the leptonic model fits shown in Fig. 1.

In order to reproduce not only broadband SEDs, but also variability patterns, the time-dependent electron dynamics and radiation transfer problem has to be solved self-consistently. Such time-dependent SSC models have been developed by, e.g., Mastichiadis & Kirk (1997), Kataoka et al. (2000), Li & Kusunose (2000), Sokolov et al. (2004). External radiation fields have been included in such treatments in, e.g., Sikora et al. (2001), Böttcher & Chiang (2002), Sokolov & Marscher (2005).

Leptonic models have generally been very successfully applied to model the SEDs and spectral variability of blazars. The radiative cooling time scales (in the observer frame) of synchrotron-emitting electrons in a typical $B \sim 1$ G magnetic field are of order of several hours – ~ 1 d at optical frequencies and $\lesssim 1$ hr in X-rays and hence compatible with the observed intra-day variability. However, the recent observation of extremely rapid VHE γ-ray variability on time scales of a few minutes poses severe problems to simple one-zone leptonic emission models. Even with large bulk Lorentz factors of ~ 50, causality requires a size of the emitting region that might be smaller than the Schwarzschild radius of the central black hole of the AGN (Begelman et al. (2008)). As a possible solution, it has been suggested (Tavecchio & Ghisellini (2008)) that the γ-ray emission region may, in fact, be only a small spine of ultra-relativistic plasma within a larger, slower-moving jet. Such fast-moving small-scale jets could plausibly be powered by magnetic reconnection in a Poynting-flux dominated jet, as proposed by Giannios et al. (2009).

2.2. Lepto-hadronic models

If a significant fraction of the jet power is converted into the acceleration of relativistic pro-

tons in a strongly magnetized environment, reaching the threshold for $p\gamma$ pion production, synchrotron-supported pair cascades will develop (Mannheim & Biermann (1992), Mannheim (1993)). The acceleration of protons to the necessary ultra-relativistic energies ($E_p^{\max} \gtrsim 10^{19}$ eV) requires high magnetic fields of several tens of Gauss to constrain the Larmor radius $R_L = 3.3 \times 10^{15} B_1^{-1} E_{19}$ cm, where $B = 10 B_1$ G, and $E_p = 10^{19} E_{19}$ eV, to be smaller than the size of the emission region, typically inferred to be $R \lesssim 10^{16}$ cm from the observed variability time scale. In the presence of such high magnetic fields, the synchrotron radiation of the primary protons (Aharonian (2000), Mücke & Protheroe (2000)) and of secondary muons and mesons (Rachen & Mészáros (1998), Mücke & Protheroe (2000), Mücke & Protheroe (2001), Mücke et al. (2003)) must be taken into account in order to construct a self-consistent synchrotron-proton blazar (SPB) model. Electromagnetic cascades can be initiated by photons from π^0-decay ("π^0 cascade"), electrons from the $\pi^\pm \to \mu^\pm \to e^\pm$ decay ("$\pi^\pm$ cascade"), p-synchrotron photons ("p-synchrotron cascade"), and μ-, π- and K-synchrotron photons ("$\mu^\pm$-synchrotron cascade").

Mücke & Protheroe (2001) and Mücke et al. (2003) have shown that the "π^0 cascades" and "$\pi^\pm$ cascades" from ultra-high energy protons generate featureless γ-ray spectra, in contrast to "p-synchrotron cascades" and "$\mu^\pm$-synchrotron cascades" that produce a two-component γ-ray spectrum. In general, direct proton and $\mu^\pm$ synchrotron radiation is mainly responsible for the high energy bump in blazars, whereas the low energy bump is dominated by synchrotron radiation from the primary e^-, with a contribution from secondary electrons.

Hadronic blazar models have so far been very difficult to investigate in a time-dependent way because of the very time-consuming nature of the required Monte-Carlo cascade simulations. In general, it appears that it is difficult to reconcile very rapid high-energy variability with the radiative cooling time scales of protons, e.g., due to synchrotron emission, which is $t_{sy}^{obs} = 4.5 \times 10^5 (1 + z) D_1^{-1} B_1^{-2} E_{19}^{-1}$ s (Aharonian (2000)), i.e., of the order of several days for ~ 10 G magnetic fields and typical Doppler factors $D = 10 D_1$. However, rapid variability on time scales shorter than the proton cooling time scale may be caused by geometrical effects.

In order to avoid time-consuming Monte-Carlo simulations of the hadronic processes and cascades involved in lepto-hadronic models, one may consider a simplified prescription of the hadronic processes. Kelner & Aharonian (2008) have produced analytic fit functions to Monte-Carlo generated results of hadronic interactions using the SOFIA code (Mücke et al. (2000)). Those fits describe the spectra of the final decay products, such as electrons, positrons, neutrinos, and photons from π^0 decay. The use of those functions requires a prior knowledge of the target photon field (in the SPB model

the electron-synchrotron photon field) as well as the proton spectrum. Once the first-generation products are evaluated, one still needs to take into account the effect of cascading, as the synchrotron emission from most of the electrons (and positrons) as well as π^0 decay γ-rays are produced at $\gg$ TeV energies, where the emission region is highly opaque to $\gamma\gamma$ pair production. A quasi-analytical description of the cascades can be found as follows.

We start with the injection rates of first-generation high-energy γ-rays, $\dot{N}_\epsilon^0$, and pairs, $Q_e(\gamma)$, from the analytical fit functions of Kelner & Aharonian (2008). The cascades are usually well described as linear cascades so that the optical depth for $\gamma\gamma$ absorption, $\tau_{\gamma\gamma}(\epsilon)$ can be pre-calculated from the low-energy radiation field. Under these conditions, the spectrum of escaping (observable) photons can be calculated as

$$\dot{N}_\epsilon^{esc} = \dot{N}_\epsilon^{em} \left(\frac{1 - e^{-\tau_{\gamma\gamma}[\epsilon]}}{\tau_{\gamma\gamma}[\epsilon]} \right) \tag{1}$$

where $\dot{N}_\epsilon^{em}$ has contributions from the first-generation high-energy photon spectrum and synchrotron emission from secondaries, $\dot{N}_\epsilon^{em} = \dot{N}_\epsilon^0 + \dot{N}_\epsilon^{sy}$. A fairly accurate evaluation of the synchrotron spectrum is achieved with a single-electron emissivity of the form $j_\nu \propto \nu^{1/3} e^{-\epsilon/\epsilon_0}$ with $\epsilon_0 = b\gamma^2$, where $b \equiv B/B_{crit}$ and $B_{crit} = 4.4 \times 10^{13}$ G. The electron distribution, $N_e(\gamma)$ will be the solution to the isotropic Fokker-Planck equation in equilibrium ($\partial \langle . \rangle / \partial t = 0$):

$$\frac{\partial}{\partial \gamma} (\dot{\gamma} N_e[\gamma]) = Q_e(\gamma) + \dot{N}_e^{\gamma\gamma}(\gamma) + \dot{N}_e(\gamma)^{esc}. \tag{2}$$

For the high magnetic fields of $B \gtrsim 10$ G, as required for hadronically dominated γ-ray emission, electron cooling will be dominated by synchrotron losses, i.e., $\dot{\gamma} = -\nu_0 \gamma^2$ with $\nu_0 = (4/3) c \sigma_T u_B / (m_e c^2)$. We are only interested in high-energy particles emitting synchrotron radiation at least at X-ray energies. For those particles, the synchrotron cooling time scale is expected to be much shorter than the escape time scale so that the escape term in Eq. 2 may be neglected. $\dot{N}_e^{\gamma\gamma}(\gamma)$ in Eq. 2 is the rate of particle injection due to $\gamma\gamma$ absorption, to be evaluated self-consistently with the radiation field. In the $\gamma\gamma$ absorption of a high-energy photon of energy ϵ, one of the produced particles will assume the major fraction, f_γ of the photon energy. Hence, an electron/positron pair with energies $\gamma_1 = f_\gamma \epsilon$ and $\gamma_2 = (1 - f_\gamma) \epsilon$ is produced. Furthermore realizing that every non-escaping photon (according to Eq.1) will produce an electron/positron pair, we can write the pair production rate as

$$\dot{N}_e^{\gamma\gamma}(\gamma) = f_{abs}(\epsilon_1) \left(\dot{N}_{\epsilon_1}^0 + \dot{N}_{\epsilon_1}^{sy} \right) + f_{abs}(\epsilon_2) \left(\dot{N}_{\epsilon_2}^0 + \dot{N}_{\epsilon_2}^{sy} \right) \tag{3}$$

where $\epsilon_1 = \gamma/f_\gamma$, $\epsilon_2 = \gamma/(1 - f_\gamma)$ and $f_{abs}(\epsilon) \equiv 1 - (1 - e^{-\tau_{\gamma\gamma}[\epsilon]})/\tau_{\gamma\gamma}[\epsilon]$. With this approximation, we find an implicit solution to Equation 2:

$$N_e(\gamma) = \frac{1}{\nu_0 \gamma^2} \int_\gamma^\infty d\tilde{\gamma} \left\{ Q_e(\tilde{\gamma}) + \dot{N}_e^{\gamma\gamma}(\tilde{\gamma}) \right\} \tag{4}$$

The solution (4) is implicit in the sense that the particle spectrum $N_e(\gamma)$ occurs on both sides of the equation as $\dot{N}_e^{\gamma\gamma}$ depends on the synchrotron emissivity, which requires knowledge of $N_e(\tilde{\gamma})$, where pairs at energies of $\tilde{\gamma}_1 = \sqrt{\gamma/(f_\gamma b)}$ and $\tilde{\gamma}_2 = \sqrt{\gamma/([1 - f_\gamma] b)}$ provide the majority of the radiative output relevant for pair production at energy γ. However, for practical applications, one may use the fact that generally, γ, the argument on the l.h.s., is much smaller than $\tilde{\gamma}_{1,2}$. This condition is fulfilled if there is no pion-induced pair injection at energies above $\gamma_{\mathrm{crit}} = 4.4 \times 10^{13} ([1 - f_\gamma] B_G)^{-1}$ or $E_{\mathrm{e,crit}} = 2.3 \times 10^{19} ([1 - f_\gamma] B_G)^{-1}$ eV. In a usual synchrotron-proton-blazar model setup, no substantial pair injection above $E_{\mathrm{e,crit}}$ is expected. Therefore, Eq. 4 may be evaluated progressively, starting at the highest pair energies for which $Q_0(\gamma) \neq 0$ or $\dot{N}_{\epsilon_{1,2}}^0 \neq 0$, and then using the solution for $N_e(\gamma)$ for large γ as one progresses towards lower values of γ.

Once the equilibrium pair distribution $N_e(\gamma)$ is known, it can be used to evaluate the synchrotron emissivity and hence, using Eq. 1 the observable photon spectrum.

Example model fits to several blazar SEDs using a simplified lepto-hadronic model based on the Kelner & Aharonian (2008) fit functions and the above cascade description are shown in Fig 1, b) – d) and compared to leptonic models of the same SEDs. As the low-frequency component is electron-synchrotron emission from primary electrons, it is not surprising that virtually identical fits to the synchrotron component can be provided in both types of models. In the high-frequency component, strongly peaked spectral shapes, as, e.g., in 3C 66A and RGB J0710+591 require a strong proton-synchrotron dominance with the cascading of higher-energy ($\gg$ TeV) emission only making a minor contribution to the high-energy emission. This, in fact, makes it difficult to achieve a substantial extension of the escaping high-energy emission into the > 100 GeV VHE γ-ray regime. In objects with a smoother high-energy SED, e.g., BL Lacertae in Fig. 1b, a substantially larger contribution from cascade emission (and leptonic SSC emission) is allowed to account for a relatively high level of hard X-ray / soft γ-ray emission. This also allows for a substantial extension of the γ-ray spectrum into the VHE regime.

3. Spectral fits along the blazar sequence

In the framework of leptonic models, the blazar sequence FSRQ $\rightarrow$ LBL $\rightarrow$ IBL $\rightarrow$ HBL is often modeled through a decreasing contribution of external radiation fields to radiative cooling of electrons and production of high-energy emission (Ghisellini et al. (1998)). In this sense, HBLs have traditionally been well represented by pure synchrotron-self-Compton models, while FSRQs often require a substantial EC component. This interpretation is consistent with the observed strong emission lines in FSRQs, which are absent in BL Lac objects. At the same time, the denser circumnuclear environment in quasars might also lead to a higher accretion rate and hence a more
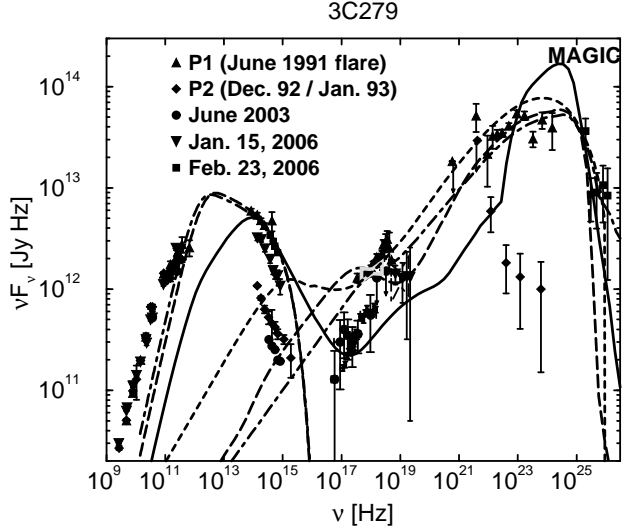
Fig. 2. Fits to the SED of 3C 279 during the time of the MAGIC detection (Albert et al. (2008)). The heavy solid curve is an attempt of a leptonic model with EC-dominated γ-ray emission, while the dotted curve is an SSC fit to the X-ray through γ-ray spectrum. The dashed and dot-dashed curves are hadronic model fits.

powerful jet, consistent with the overall trend of bolometric luminosities along the blazar sequence. This may even be related to an evolutionary sequence from FSRQs to HBLs governed by the gradual depletion of the circumnuclear environment (Böttcher & Dermer (2002)).

However, in this interpretation, it would be expected that mostly HBLs (and maybe IBLs) should be detectable as emitters of VHE γ-rays since in LBLs and FSRQs, electrons are not expected to reach $\sim$ TeV energies. This appears to contradict the recent VHE γ-ray detections of lower-frequency peaked objects such as W Comae (Acciari et al. (2008)), 3C 66A (Acciari et al. (2009a)), PKS 1424+240 (Acciari et al. (2010a)), BL Lacertae (Albert et al. (2007b)), S5 0716+714 (Anderhub et al. (209), and even the FSRQs 3C 279 (Albert et al. (2008)) and PKS 1510−089 (Wagner & Behera (2010))).

The overall SEDs of IBLs detected by VERITAS could still be fit satisfactorily with a purely leptonic model. Fitting the SEDs of the IBLs 3C 66A and W Comae with a pure SSC model, while formally possible, would require rather extreme parameters. In particular, magnetic fields several orders of magnitude below equipartition would be needed, which might pose a severe problem for jet collimation. Much more natural fit parameters can be adopted when including an EC component with an infrared radiation field as target photons (Acciari et al. (2009b), Acciari et al. (2010c)).

In Böttcher et al. (2009) it has been demonstrated that the VHE γ-ray detection of the FSRQ 3C 279 poses severe problems for any variation of single-zone leptonic jet model. The SED with the MAGIC points is shown in Fig. 2, along with attempted leptonic as well as hadronic

model fits. The fundamental problem for the leptonic model interpretation is the extremely wide separation between the synchrotron and γ-ray peak frequencies. In a single-zone SSC interpretation this would require a very high Lorentz factor of electrons at the peak of the electron distribution and, in turn, an extremely low magnetic field. In an EC interpretation (the solid curve in Fig. 2) the SSC component, usually dominating the X-ray emission in leptonic fits to FSRQs like 3C 279, is too far suppressed to model the simultaneous RXTE spectrum. As an alternative, the optical emission could be produced in a separate emission component. A pure SSC fit to the X-ray and γ-ray component (the short-dashed curve in Fig. 2) is technically possible, but also requires a far sub-equipartition magnetic field. Much more natural parameters could be achieved in a fit with the synchrotron-proton-blazar model (Mücke et al. (2003)), as illustrated by the long-dashed and dot-dashed model curves in Fig. 2.

4. Redshift constraints from blazar SED modeling

BL Lac objects are defined by the absence of broad emission lines in their optical spectra. This makes the determination of their redshifts, and hence distances, very difficult, and in many cases even impossible. Photometric redshifts, estimated under the assumption that the host galaxies of BL Lac objects are nearly standard candles (e.g., Sbarufatti et al. (2005)), are still highly uncertain, and optical spectroscopy often yields only lower limits on redshifts (e.g., Finke et al. (2007)).

An alternative method of estimating BL Lac redshifts exploits the fact that high-energy and VHE γ-rays are absorbed through $\gamma\gamma$ pair production on the Extragalactic Background Light (EBL), see, e.g., Dwek & Krennrich (2005), Stecker et al. (2006), Franceschini et al. (2008), Gilmore et al. (2009), Finke et al. (2010). Substantial progress has been made in the last few years so that the accepted models of the EBL spectrum are now converging to an EBL level near the lower limit set by direct galaxy counts (e.g., Aharonian et al. (2006), Abdo et al. (2010c)).

Exploiting this improved knowledge of the EBL spectrum and intensity, limits on VHE γ-ray blazars can now be set from the expectation that the intrinsic (unabsorbed by the EBL) HE to VHE γ-ray spectra of blazars are not becoming harder towards higher energies. A robust upper limit to the source redshift can therefore be found by considering a straight power-law extrapolation of the best-fit *Fermi* power-law spectrum into the VHE γ-ray regime, and attributing the change in spectral slope towards the measured VHE spectrum purely to EBL absorption (e.g., Georganopoulos et al. (2010), Acciari et al. (2010a)). A somewhat more realistic approach has been suggested by Prandini et al. (2010), taking into account the expected intrinsic softening of the VHE γ-ray spectrum, based on a sample of blazars with known redshifts detected both by *Fermi* and ground-based VHE γ-ray observatories.
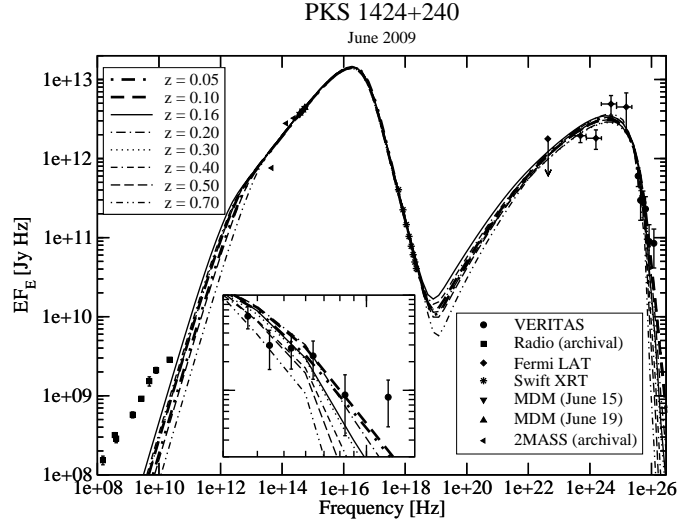
Fig. 3. Fits to the SED of PKS 1424+240, assuming a range of plausible redshifts (from Acciari et al. (2010a)). All SEDs have been corrected for $\gamma\gamma$ absorption by the EBL using the model of Gilmore et al. (2009). The inset shows a zoom-in on the VHE γ-ray spectrum. The spectral fits favour a source redshift of $z < 0.4$.

If the SED of a blazar with unknown redshift is well sampled, the EBL absorption effect can be exploited in an even more sophisticated way by constraining models through the SED from the optical to GeV γ-rays and varying the redshift to yield the best fit to the measured VHE γ-ray spectrum. This procedure has been carried out in detail for the recent VERITAS detections of PKS 1424+240 (Acciari et al. (2010a)) and 3C 66A (Acciari et al. (2010c)).

In the case of PKS 1424+240, only very unreliable redshift estimates were available. Fig. 3 shows our suite of models for a wide range of plausible redshifts. While a straight power-law extrapolation of the *Fermi* spectrum yields an upper limit of $z < 0.6$, our spectral model (leptonic SSC) clearly favors a redshift of $z < 0.4$. The redshift of 3C 66A is usually quoted as $z = 0.444$, but is actually highly uncertain as well (Bramel et al. (2005)). A scan through redshifts yielded a preferred redshift of $z \sim 0.2 - 0.3$ for this object, in good agreement with the estimate found by Prandini et al. (2010). The leptonic model fit to 3C 66A shown in Fig. 1c is based on a redshift of $z = 0.3$.

5. Inhomogeneous jet models

The complicated and often inconsistent variability features found in blazars provide a strong motivation to investigate jet models beyond a simple, spherical, one-zone geometry. The idea behind phenomenological multi-zone models like the spine-sheath model of Tavecchio & Ghiselini (2008) or the decelerating-jet model of Georganopoulos & Kazanas (2003) was that differential relativistic motion between various emission zones will lead to Doppler boosting of one zone emission into the rest frame of another zone. This can reduce the
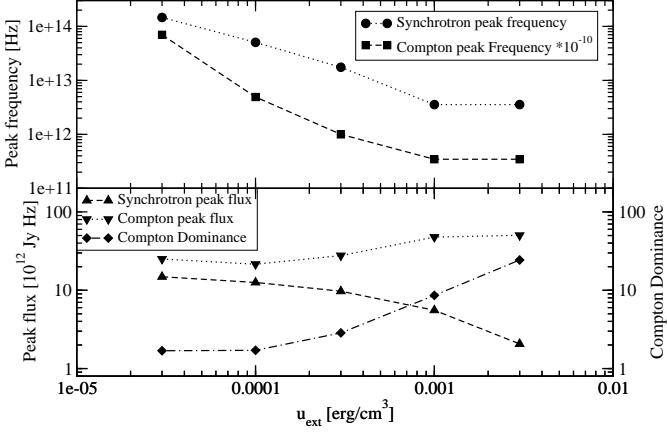
Fig. 4. Dependence of the SED characteristics of time-averaged spectra from the internal-shock model, on the external radiation energy density u_{ext}.

Fig. 5. Dependence on inter-band cross correlations and time lags on the external radiation energy density.

requirements of extreme bulk Lorentz (and Doppler) factors inferred from simple one-zone leptonic modeling of rapidly variable VHE γ-ray blazars, such as Mrk 501 or PKS 2155-304, and has led to successful model fits to the SEDs of those sources with much more reasonable model parameters.

However, the models mentioned above do not treat the radiation transport and electron dynamics in a time-dependent way and do therefore not make any robust predictions concerning variability and inter-band cross-correlations and time lags. In order to address those issues, much work has recently been devoted to the investigation of the radiative and timing signatures of shock-in-jet models, which will be summarized in the following sub-section.

5.1. Shock-in-jet models

Early versions of shock-in-jet models were developed with focus on explaining radio spectra of extragalactic jets, e.g., by Marscher & Gear (1985). Their application to high-energy spectra of blazars was proposed by Spada et al. (2001). Detailed treatments of the electron energization and dynamics and the radiation transfer in a standing shock (Mach disk) in a blazar jet were developed by Sokolov et al. (2004), Mimica et al. (2004), Sokolov & Marscher (2005), Graff et al. (2008). The internal-shock mode discussed in Joshi (2009) assumes that the central engine is intermittently ejecting shells of relativistic plasma at varying speeds, which subsequently collide. Such models have had remarkable success in explaining SEDs and time lag features of generic blazars.

The realistic treatment of radiation transfer in an internal-shock model for a blazar requires the time-dependent evaluation of retarded radiation fields originating from all parts of the shocked regions of the jet. The model system is therefore highly non-linear and can generally only be solved using numerical simulations (e.g., Sokolov et al. (2004), Mimica et al. (2004), Graff et al. (2008)). As the current detailed internal-shock
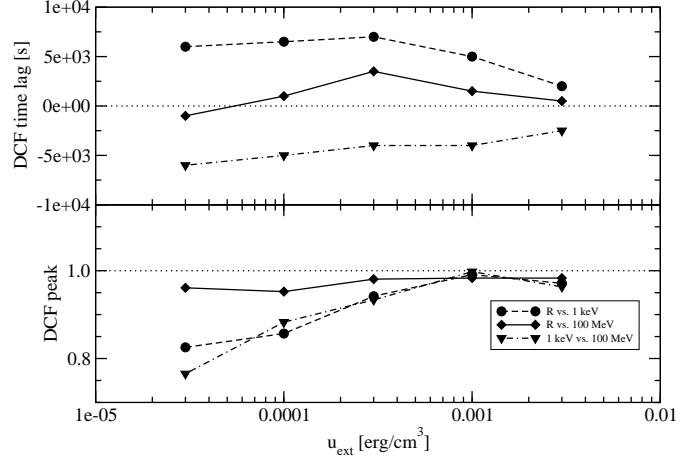
models employ either full expressions or accurate approximations to the full emissivities of synchrotron and Compton emission, a complete simulation of the time-dependent spectra and light curves is time-consuming and does therefore generally not allow to efficiently explore a large parameter space. General patterns of the SED, light curves and expected time lags between different wavelength bands have been demonstrated for very specific, but observationally very poorly constrained, sets of parameters.

To remedy this aspect, Böttcher & Dermer (2010) have developed a semi-analytical internal-shock model for blazars. In this model, the time- and space-dependent electron spectra, affected by shock acceleration behind the forward and reverse shocks, and subsequent radiative cooling, is calculated fully analytically. Taking into account all light travel time effects, the observed synchrotron and external-Compton spectra are also evaluated fully analytically, using a δ-function approximation to the emissivities. The evaluation of the SSC emission still requires a two-dimensional numerical integration.

This semi-analytical model allowed the authors to efficiently scan a substantial region of parameter space and discuss the dependence on the characteristics of time-averaged SEDs, as well as cross-band correlations and time lags. As an example, Fig. 4 shows the dependence of the SED characteristics on the external radiation field energy density, u_{ext}. In the classical interpretation of the blazar sequence, an increasing u_{ext} corresponds to a transition from BL Lac spectral characteristics to FSRQ-like characteristics. The decreasing synchrotron peak frequency and increasing Compton dominance found in the parameter study are reproducing this effect.

From the internal-shock simulations, energy-dependent light curves could be extracted. Using the standard Discrete Correlation Function (DCF: Edelson & Krolik (1988)) analysis, inter-band time lags could be extracted for any set of parameters. Fig. 5 shows the dependence of the inter-band time lags between

optical, X-ray and *Fermi*γ-ray light curves (top panel) and the quality of the cross correlation, characterized by the peak value of the DCF (bottom panel) as a function of the external radiation energy density.

One of the most remarkable results of this study was that only slight changes in physical parameters can lead to substantial changes of the inter-band time lags and even a reversal of the sign of the lags. This may explain the lack of consistency of lags even within the same source.

References

Abdo, A. A., et al., 2010, Nature, 463, 919

Abdo, A. A., et al., 2010b, ApJ, 716, 30

Abdo, A. A., et al., 2010c, ApJ, submitted `arXiv:1005.0996`

Acciari, V. A., 2008, ApJ, 684, L73

Acciari, V. A., 2009a, ApJ, 693, L104

Acciari, V. A., 2009b, ApJ, 707, 612

Acciari, V. A., et al., 2010a, ApJ, 708, L100

Acciari, V. A., et al., 2010b, ApJ, 715, L49

Acciari, V. A., et al., 2010c, in preparation

Aharonian, F. A., 2000, New Astron., 5, 377

Aharonian, F. A., 2006, Nature, 440, 1018

Aharonian, F. A., et al., 2007, ApJ, 664, L71

Aharonian, F. A., Khangulyan, D., & Costamante, L., 2008, MNRAS, 387, 120

Aharonian, F. A., et al., 2009, A&A, 502, 749

Albert, J., et al., 2007a, ApJ, 669, 862

Albert, J., et al., 2007b, ApJ, 66, L17

Albert, J., et al., 2008, Science, 320, 1752

Anderhub, H., et al., 209, ApJ, 704, L129

Begelman, M. C., Fabian, A. C., & Rees, M. J., 2008, MNRAS, 384, L19

Blandford, R. D., & Levinson, A., 1995, ApJ, 441, 79

Blażejowski, M., et al., 2000, ApJ, 545, 107

Bloom, S. D., & Marscher, A. P., 1996, 461, 657

Böttcher, M., & Chiang, J., 2002, ApJ, 581, 127

Böttcher, M., & Dermer, C. D., 2002, ApJ, 564, 86

Böttcher, M., et al., 2007, ApJ, 670, 968

Böttcher, M., Reimer, A., & Marscher, A. P., 2009, ApJ, 703, 1168

Böttcher, M., & Dermer, C. D., 2010, ApJ, 711, 445

Böttcher, M., & Principe, D., 2009, ApJ, 692, 1374

Bramel, D. A., et al., 2005, ApJ, 629, 108

Collmar, W., et al., 2010, A&A, submitted

Dermer, C. D., Schlickeiser, R., & Mastichiadis, A., 1992, A&A, 256, L27

Dermer, C. D., & Schlickeiser, R., 1993, ApJ, 416, 458

Dermer, C. D., Sturner, S. J., & Schlickeiser, R., 1997, ApJS, 109, 103

Dwek, E., & Krennrich, F., 2005, ApJ, 618, 657

Edelson, R. A., & Krolik, J. H., 1988, ApJ, 333, 646

Finke, J. D., et al., 2007, A&A, 447, 513

Finke, J. D., Razzaque, S., & Dermer, C. D., 2010, ApJ, 712, 238

Fossati, G., et al., 1998, MNRAS, 299, 433

Fossati, G., et al., 2000, ApJ, 541, 166

Franceschini, A., Rodighiero, G., & Vaccari, M., 2008, A&A, 487, 837

Georganopoulos, M., & Marscher, A. P., 1998, ApJ, 506, 621

Georganopoulos, M., & Kazanas, D., 2003, ApJ, 594, L27

Georganopoulos, M., Finke, J. D., & Reyes, L. C., 2010, ApJ, 714, L157

Giannios, D., Uzdensky, D. A., & Begelman, M. C., 2009, MNRAS, 395, L29

Ghisellini, G., & Madau, P. 1996, MNRAS, 280, 67

Ghisellini, G., et al., 1998, MNRAS, 301, 451

Ghisellini, G., Tavecchio, F., & Chiaberge, M., 2005, A&A, 432, 401

Ghisellini, G., & Tavecchio, F., 2008, MNRAS, 386, L28

Ghisellini, G., & Tavecchio, F., 2009, MNRAS, 397, 985

Gilmore, R. C., et al., 2009, MNRAS, 399, 1694

Graff, P. B., Georganopoulos, M., Perlman, E. S., & Kazanas, D., 2008, 689, 68

Hartman, R. C., et al., 2001, ApJ, 558, 583

Horan, D., et al., 2009, ApJ, 695, 596

Joshi, M., 2009, Ph.D. Thesis, Ohio University

Kataoka, J., et al., 2000, ApJ, 528, 243

Kelner, S. R., & Aharonian, F. A., 2008, Phys. Rev. D., 78, 034013

Kirk, J. G., et al., 2000, ApJ, 542, 235

Kusunose, M., Takahara, F., & Li, H., 2000, ApJ, 536, 299

Li, H., & Kusunose, M., 2000, ApJ, 536, 729

Mannheim, K., & Biermann, P. L., 1992, A&A, 253, L21

Mannheim, K., 1993, A&A, 221, 211

Maraschi, L., Celotti, A., & Ghisellini, G., 1992, ApJ, 397, L5

Marscher, A. P., & Gear, W. K., 1985, ApJ, 298, 114

Mastichiadis, A., & Kirk, J. G., 1997, A&A, 320, 19

Mimica, P., Aloy, M. A., Müller, E., & Brinkmann, W., 2004, A&A, 418, 947

Mücke, A., et al., 2000, Comp. Phys. Comm., 124, 290

Mücke, A., & Protheroe, R. J., 2000, AIP Conf. Proc., 515, 149

Mücke, A., & Protheroe, R. J., 2001, Astropart. Phys., 15, 121

Mücke, A., et al., 2003, Astropart. Phys., 18, 593

Mukherjee, R., et al., 1997, ApJ, 490, 116

Mukherjee, R., et al., 1999, ApJ, 527, 132

Prandini, E., et al., 2010, MNRAS, in press (arXiv:1003.1674)

Rachen, J., & Mészáros, P., 1998, Phys. Rev. D, 58, 123005

Sbarufatti, B., Treves, A., & Falomo, R., 2005, ApJ, 635, 173

Schlickeiser, R., 1996, A&AS, 120, 481

Sikora, M., Begelman, M., & Rees, M. 1994, ApJ, 421, 153

Sikora, M., et al., 2001, ApJ, 554, 1

Sokolov, A., Marscher, A. P., & McHardy, I. A., 2004, ApJ, 613, 725

Sokolov, A., & Marscher, A. P., 2005, ApJ, 629, 52

Spada, M., Ghisellini, G., Lazzati, D., & Celotti, A., 2001, MNRAS, 325, 1559

Stecker, F. W., Malkan, M. A., & Scully, S. T., 2006, ApJ, 648, 774

Takahashi, T., et al., 1996, ApJ, 470, L89

Tavecchio, F., & Ghisellini, G., 2008, MNRAS, 385, L98

Villata, M., & Raiteri, C. M., 1999, A&A, 347, 30

von Montigny, C., et al., 1995, ApJ, 440, 525

Wagner, S., & Behera, B., 2010, 10th HEAD Meeting, Hawaii (BAAS, 42, 2, 07.05)

Weidinger, M., Rüger, M., & Spanier, F., 2010, Astrophys. & Space Sciences Transactions, vol. 6, Issue 1, p. 1 `arXiv:1001.2145`

Zhang, Y. H., et al., 2002, ApJ, 572, 762

Combined synchrotron and nonlinear synchrotron-self-Compton cooling of relativistic electrons

R. Schlickeiser[1], M. Böttcher[2], U. Menzler[1], M. Zacharias[1]

1 Institut für Theoretische Physik, Lehrstuhl IV: Weltraum- und Astrophysik, Ruhr-Universität Bochum, 44780 Bochum, Germany

2 Astrophyiscal Institute, Department of Physics and Astronomy, Clippinger 339, Ohio University, Athens, OH 45701, USA

Abstract. The broadband SEDs of blazars exhibit two broad spectral components which in leptonic emission models are attributed to synchrotron radiation and SSC radiation of relativistic electrons. During high state phases the high-frequency SSC component often dominates over the low-frequency synchrotron component implying that the inverse Compton SSC losses of electrons are at least equal to or greater than the synchrotron losses of electrons. The linear synchrotron cooling, usually included in radiation models of blazars, then has to be replaced by the SSC cooling. Here, we present an analytical solution to the kinetic equation of relativistic electrons subject to the combined synchrotron and non-linear synchrotron self-Compton cooling for monoenergetic injection. We calculate the time-dependent fluxes and time-integrated fluences resulting from monoenergetic electrons cooling via synchrotron and SSC, and suggest this as a model for the broadband SED of Compton-dominated blazars.

1. Introduction

The broadband continuum spectra of blazars are dominated by nonthermal emission and often consist of two distinct broad components. In leptonic emission models (for review see Böttcher 2007) synchrotron radiation from highly relativistic electrons generates the low-energy component whereas the high-energy component results from Compton interactions of the same relativistic electron population. In most modeling works reproducing the SEDs of blazars, a single or broken power-law distribution of electrons is assumed to produce both the synchrotron and Compton emission. Comparing the required parameters for modeling FSRQs and LBLs in such a framework, many authors concluded that these Compton dominated blazars are more plausibly represented by γ-ray emission being dominated by Comptonization of external radiation fields, e.g., from the accretion disk or the broad line region (e.g., Madejski et al. 1999, Böttcher & Bloom 2000). Since this conclusion depends on the assumption of an underlying power-law electron distribution, we here re-visit this problem by investigating the radiative signatures of the injection and subsequent, self-consistent synchrotron and SSC cooling of monoenergetic electrons, including the case of SSC dominated radiative output.

The dominance of the SSC component over the synchrotron component in this case implies that the inverse Compton SSC losses of electrons are at least equal or greater than the synchrotron losses of electrons, even more when the intergalactic deabsorption of the TeV emission from the cosmic infrared background is accounted for. The ratio of the observed SSC to synchrotron photon luminosity from the same population of electrons $n(\gamma)$

$$\frac{L^*_{SSC}}{L^*_{sy}} = \frac{\int dV \int_1^\infty d\gamma \, n(\gamma)|\gamma \dot{S}_{SC}|}{\int dV \int_1^\infty d\gamma \, n(\gamma)|\dot{\gamma}_S|} \tag{1}$$

directly reflects the ratio of the corresponding loss rates, because of the identical Doppler boosting factors (Dermer and Schlickeiser 2002) of synchrotron and SSC emission.

In the case of the dominance of the first-order SSC component over the synchrotron component, Schlickeiser (2009 – hereafter referrred to as paper S) has pointed out that then the linear synchrotron cooling rate, included standardly in radiation models of blazars, has to be replaced by the nonlinear SSC cooling rate. In the Thomson limit (hereafter referred to as SST-losses) the SST energy loss rate of a single electron

$$|\dot{\gamma}|_{\rm SST} \simeq A_0 \gamma^2 \int_0^\infty d\tilde{\gamma} \, \tilde{\gamma}^2 n(\tilde{\gamma}, t) \,, \quad A_0 = \frac{3\sigma_T c_1 P_0 R \epsilon_0^2}{mc^2} \tag{2}$$

depends on the energy integral of the actual electron spectrum $n(\gamma, t)$, reflecting that the energy integral determines the number density of the target synchrotron photons in the source. The dependence on the energy integral is a collective effect completely different from the linear synchrotron energy loss rate of a single electron in a constant magnetic field

$$|\dot{\gamma}|_S = D_0 \gamma^2, \quad D_0 = \frac{4}{3}\frac{c\sigma_T}{mc^2}U_B = 1.29 \cdot 10^{-9}b^2 \text{ s}^{-1}, \tag{3}$$

which is solely determined by the magnetic field strength $B = b$ Gauss and the electron Lorentz factor γ. The notation in Eqs. (2) and (3) is the same as in paper S:

$P_0 = 3.2 \cdot 10^{12} \, \mathrm{eV^{-1}s^{-1}}$, $\epsilon_0 = 1.16 \cdot 10^{-8} b \, \mathrm{eV}$, R is the radius of the spherical source, c denotes the speed of light, $\sigma_T = 6.65 \cdot 10^{-25} \, \mathrm{cm^2}$ is the Thomson cross section and $c_1 = 0.684$.

The competition between the instantaneous injection of ultrarelativistic electrons ($\gamma_0 \gg 1$) at the rate $Q(\gamma, t) = q_0 \delta(\gamma - \gamma_0)\delta(t)$ at time $t = 0$ and the combined synchrotron and SST radiative losses is described by the time-dependent kinetic equation for the volume-averaged relativistic electron population inside the radiating source (Kardashev 1962):

$$\frac{\partial n(\gamma, t)}{\partial t} - \frac{\partial}{\partial \gamma}\left[\gamma^2 n(\gamma, t)\left(D_0 + A_0 \int_0^\infty d\tilde{\gamma}\,\tilde{\gamma}^2 n(\tilde{\gamma}, t)\right)\right]$$
$$= q_0 \delta(\gamma - \gamma_0)\delta(t), \tag{4}$$

where $n(\gamma, t)$ denotes the volume-averaged differential number density.

2. Solution of electron kinetic equation for combined synchrotron and SST cooling

Using the method of Schlickeiser and Lerche (2007) the solution of the kinetic equation (4) is

$$n(\gamma, T) = q_0 \gamma^2 \delta(\gamma^{-1} - T - \gamma_0^{-1})\left(H[T] - H[T - \gamma^{-1}]\right) \tag{5}$$

in terms of the implicit time variable

$$K_0 y = T - \sqrt{\frac{q_0}{K_0}}\left[\arctan\left(\sqrt{\frac{K_0}{q_0}}[\gamma_0^{-1} + T(y)]\right)\right.$$
$$\left. - \arctan\left(\sqrt{\frac{K_0}{q_0}}\gamma_0^{-1}\right)\right] \tag{6}$$

where $K_0 = D_0/A_0$ and $y = A_0 t$. Unfortunately, this dependence $y(T)$ cannot be directly inverted to infer the general dependence $T(t)$. However, an approximate but reasonably accurate inversion is possible by using the asymptotic expansions of the arctan-function for small and large arguments compared to unity.

2.1. Injection parameter

The argument of the arctan-function is always larger than $\alpha^{-1} = (K_0/q_0\gamma_0^2)^{1/2}$. Therefore, we consider the two cases $\alpha \gg 1$ and $\alpha \ll 1$, respectively. The parameter α depends on the energy density of the initially injected relativistic electrons and can be written as

$$\alpha = \frac{q_0^{1/2}\gamma_0}{K_0^{1/2}} = \frac{\gamma_0}{\gamma_B} = 46\frac{\gamma_4 N_{50}^{1/2}}{R_{15}} \tag{7}$$

with the characteristic Lorentz factor

$$\gamma_B = \frac{K_0^{1/2}}{q_0^{1/2}} = \frac{106}{R_{15}^{1/2} q_5^{1/2}} = \frac{217 R_{15}}{N_{50}^{1/2}} \tag{8}$$

for standard blazar parameters $q_0 = 10^5 q_5 \, \mathrm{cm^{-3}}$, $R = 10^{15} R_{15}$ cm and the total number of instantaneously injected electrons $N = 4\pi R^3 q_0/3 = 10^{50} N_{50}$, where we scale the electron injection Lorentz factor $\gamma_0 = 10^4 \gamma_4$. Obviously, the more compact the source is, and the more electrons are injected, the smaller the characteristic Lorentz factor γ_B is. If the injection Lorentz factor γ_0 is higher (smaller) than γ_B, the injection parameter α will be larger (smaller) than unity. For a compact sources with a large number of injected relativistic electrons the injection parameter α is much larger than unity.

Schlickeiser et al. (2010) demonstrated that for small values of the injection parameter $\alpha \ll 1$, corresponding to $\gamma_0 \ll \gamma_B$, the time evolution of the electron distribution function is solely determined by the linear synchrotron losses, and is given by

$$n(\gamma, \gamma_0, t) = \frac{q_0}{\gamma^2}H[\gamma_0 - \gamma]\delta\left(\gamma^{-1} - \gamma_0^{-1} - D_0 t\right)$$
$$= q_0 H[\gamma_0 - \gamma]\delta\left(\gamma - \frac{\gamma_0}{1 + D_0\gamma_0 t}\right), \tag{9}$$

which agrees with the standard linear synchrotron cooling solution.

For large injection parameters $\alpha \gg 1$, corresponding to $\gamma_0 \gg \gamma_B$, we obtain for small times

$$n_1(\gamma, \gamma_0, t < t_c) =$$
$$q_0 H[\gamma_0 - \gamma]H[t_c - t]\delta\left(\gamma - \frac{\gamma_0}{(1 + 3q_0\gamma_0^3 A_0 t)^{1/3}}\right), \tag{10}$$

which agrees with the nonlinear SST solution of paper S, his equation (28). At late times

$$n_2(\gamma, \gamma_0, t \geq t_c) =$$
$$q_0 H[\gamma_B - \gamma]H[t - t_c]\delta\left(\gamma - \frac{\gamma_B}{\frac{1+2\alpha^3}{3\alpha^3} + \gamma_B K_0 A_0 t}\right), \tag{11}$$

which is a modified linear cooling solution. Note that both solution show that at the transition time

$$t_c = \frac{\alpha^3 - 1}{3\alpha^3 \gamma_B D_0} \simeq \frac{1.2 \cdot 10^6 N_{50}^{1/2}}{R_{15} b^2} \, \mathrm{s} \tag{12}$$

the electrons have cooled to the characteristic Lorentz factor γ_B.

Provided electrons are injected with Lorentz factors much higher than γ_B, given in Eq. (8), they initially cool down to the characteristic Lorentz factor γ_B by nonlinear SST-cooling until time t_c. At later times they further cool to lower energies according to the modified cooling solution (11). If the electrons are injected with Lorentz factors much smaller than γ_B they undergo only linear synchrotron cooling at all energies with no influence of the SST cooling. The characteristic Lorentz factor γ_B is only determined by the injection conditions, whereas the time scale t_c also depends on the magnetic field strength. This different cooling behaviour for large and small injection energies affects the synchrotron and SSC intensities and fluences.

3. Intrinsic synchrotron radiation fluences

The optically thin synchrotron intensity from relativistic electrons with the volume-averaged differential density $n(\gamma, t)$ is given by

$$I(\epsilon, t) = R j_S(\epsilon, t) = \frac{R}{4\pi} \int_0^\infty d\gamma \, n(\gamma, t) p_S(\epsilon, \gamma), \qquad (13)$$

where $p_s(\epsilon, \gamma)$ denotes the synchrotron power of a single electron.

In order to collect enough photons, intensities are often averaged or integrated over long enough time intervals. For rapidly varying photon intensities this corresponds to fractional fluences which are given by the time-integrated intensities

$$F_f(\epsilon, t_f) = \int_0^{t_f} dt \, I(\epsilon, t) = \frac{1}{3 A_0 q_0 \gamma_0^3} \int_0^{\tau_f} d\tau \, I(\epsilon, \tau) \qquad (14)$$

with $\tau_f = 3 A_0 q_0 \gamma_0^3 t_f$. The total fluence spectra result in the limit $t_f \to \infty$

$$F(\epsilon) = F_f(\epsilon, t_f = \infty) = \frac{1}{3 A_0 q_0 \gamma_0^3} \int_0^\infty d\tau \, I(\epsilon, \tau) \qquad (15)$$

For small injection energy $\alpha \ll 1$ the total synchrotron fluence is

$$F_s(\epsilon) \simeq F_{0S} \begin{cases} c_0 \left(\frac{E_0}{\epsilon}\right)^{1/2} & \text{for } \epsilon \ll E_0 \\ \left(\frac{E_0}{\epsilon}\right) \exp\left(-\epsilon/E_0\right) & \text{for } \epsilon \gg E_0 \end{cases} \qquad (16)$$

where $c_0 = 0.95302$ and $E_0 = 1.74 b \gamma_4^2$ eV denotes the intial characteristic synchrotron photpon energy.

For the high injection energy case $\alpha \gg 1$ the total synchrotron fluence varies as

$$F_h(\epsilon) \simeq$$

$$F_{0h} \begin{cases} c_0 \alpha^2 \left(\frac{E_0}{\epsilon}\right)^{1/2} & \text{for } \epsilon \ll E_0/\alpha^2 \\ c_2 \left(\frac{E_0}{\epsilon}\right)^{3/2} & \text{for } E_0/\alpha^2 \ll \epsilon \ll E_0 \\ \left(\frac{E_0}{\epsilon}\right) \exp\left(-\epsilon/E_0\right) & \text{for } \epsilon \gg E_0 \end{cases} \qquad (17)$$

Fig. 1 shows the fluence SEDs $N(x) \propto x F(x)$ for small ($\alpha_s = 0.1$) and high ($\alpha_h = 100$) injection conditions in terms of the normalized synchrotron photon energy $x = \epsilon/E_0$.

At high synchrotron photon energies ($\epsilon \gg E_0$) the total synchrotron fluences for small and high injection energy exhibit the same exponential cut-off. However, at low energies ($\epsilon \ll E_0$) we find markedly different power law behaviours for the two injection cases:

D1) In the high injection case the synchrotron SED peaks at a photon energy which is a factor $2 x_B = 1.4 \alpha_h^2 = 1.4 \cdot 10^{-4}$ smaller than the peak in the small injection case.

D2) The high injection energy peak value decreases at small times $t < \alpha t_s/3$ more rapidly than the small injection energy peak value.

D3) The high injection SED is a broken power law with spectral indices $+0.5$ below and -0.5 above the peak energy $x_B \ll 1$, respectively, and it cuts-off exponentially
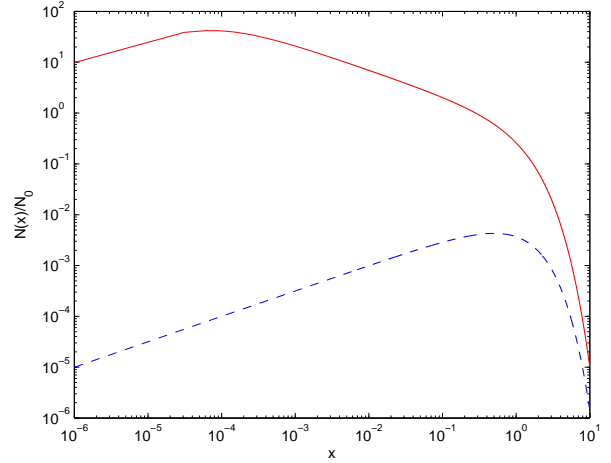
Fig. 1. Total synchrotron fluence SED $N(x)$ for high ($\alpha_h = 100$, full curve) and small ($\alpha_s = 0.1$, dashed curve) injection conditions calculated for $\gamma_0 = 10^4$. From Schlickeiser et al. (2010).

at photon energies $x > 1$. Below the peak energy x_B the time of maximum synchrotron intensity decreases as $t_{\max} \propto \epsilon^{-1/2}$, whereas above the peak energy x_B it decreases more rapidly as $t_{\max} \propto \epsilon^{-1/2}$ due to the severe additional SST losses.

D4) The small injection SED is a single power law with spectral index $+0.5$ below the peak energy $x_p = 0.5$, and it cuts-off exponentially at photon energies $x > 1$. Here the time of maximum synchrotron intensity decreases as $t_{\max} \propto \epsilon^{-1/2}$ at all energies $x < 1$ because in the small injection case the SST-losses do not contribute.

4. Synchrotron and SSC fluence SEDs from numerical radiation code

In Fig. 2 and 3 we show the synchrotron and SSC fluence SEDs calculated with the numerical radiation code of Böttcher et al. (1997) using a magnetic field strength $b = 1$ and an injection Lorentz factor $\gamma_0 = 10^4$ for the high ($\alpha_h = 100$) and small ($\alpha_s = 0.1$) injection cases. Both numerical synchrotron SEDs are in remarkable agreement with the analytical SEDs shown in Fig. 1. In particular, the numerical SEDs confirm all four predicted differences listed in the last section.

The good agreement of the numerically and analytically calculated synchrotron radiation fluence distributions confirms a posteriori the validity of the assumptions made in the analytical calculations, in particular the neglect of higher order SSC losses for the high injection case.

The radiation code also yields the SSC fluence SEDs. We note from Figs. 2–3 that for the high injection case the SSC SED has a much higher amplitude than the synchrotron SED, whereas the opposite holds for the low and intermediate injection cases. Moreover, all SSC SEDs peak at the same photon energy, although the SSC peak value
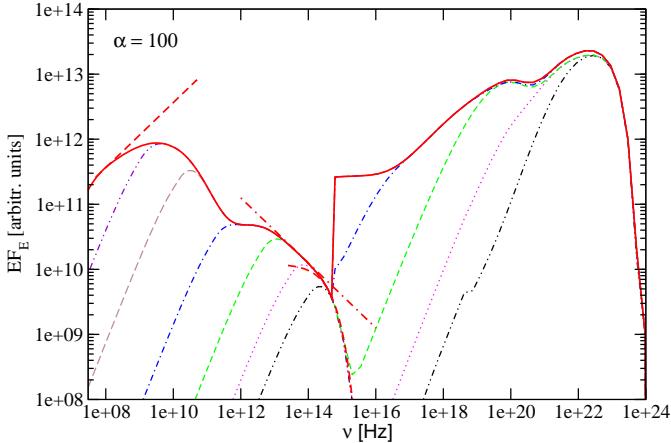
Fig. 2. Numerically calculated fractional and total synchrotron and SSC fluence SEDs for high ($\alpha_h = 100$) injection conditions calculated for $\gamma_0 = 10^4$. The full curves show the total fluence SEDs. The dashed, and dot-dashed lines show the asymptotic behaviour of the total synchrotron flunce according to Eq. (17). The fractional fluences are shown at approximately logarithmically spaced times. Note that the SSC emission has been artificially cut off at low frequencies as it would otherwise overwhelm the high-energy end of the synchrotron emission. From Schlickeiser et al. (2010).
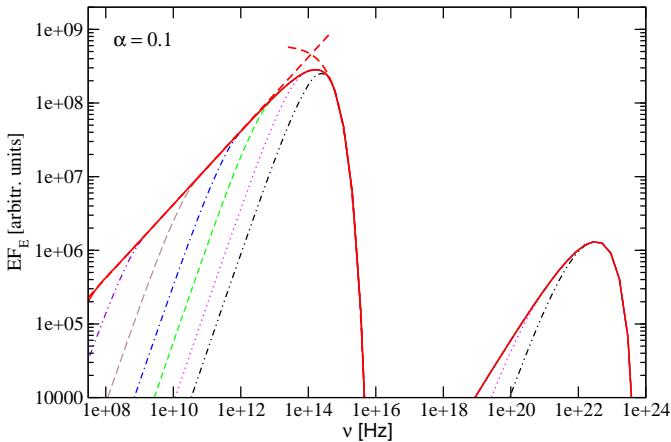
Fig. 3. Numerically calculated fractional and total synchrotron and SSC fluence SEDs for small ($\alpha_s = 0.1$) injection conditions calculated for $\gamma_0 = 10^4$. The full curves show the total fluence SEDs. The dashed lines show the asymptotes according to Eq. (16). From Schlickeiser et al. (2010).

in the high injection case is a factor $2 \cdot 10^7$ larger than in the small injection case.

5. Summary and conclusions

We have presented an analytical solution to the synchrotron and non-linear synchrotron-self-Compton cooling in the Thomson regime (SST) of monoenergetic electrons. Based on our analytical solution, we evaluated the time-dependent synchrotron emissivity and time-integrated fluences. We find qualitatively different results depending on whether electron cooling is initially Compton dominated (high injection energy parameter α) or it is al-

ways synchrotron dominated (low α). In the low-α case, the resulting fluence spectrum exhibits a simple exponentially cut-off power-law behaviour, $S_\nu \propto \nu^{1/2} e^{-\nu/\nu_0}$. In contrast, in the high-α case, we find a broken power-law with exponential cutoff, parametrized in the form $S_\nu \propto \nu^{1/2} \frac{\nu_B}{\nu + \nu_B} e^{-\nu/\nu_0}$. The analytically calculated synchrotron fluence SEDs and light curve peak times agree well with the corresponding numerically calculated quantities using the radiation code of Böttcher et al. (1997). Based on our analysis we propose the following interpretation of multiwavelength blazar SEDs:

Blazars, where the γ-ray fluence is much larger than the synchrotron fluence, are regarded as high injection energy sources. Here, the synchrotron fluence should exhibit the symmetric broken power law behaviour Eq. (17) around the synchrotron peak energy that is a factor $(\alpha_h \gamma_0)^2$ smaller than the SSC peak energy. Below and above ν_B the synchrotron light curve peak times exhibit different frequency dependences $t_{\max}(\nu < \nu_B) \propto \nu^{-1/2}$ and $t_{\max}(\nu > \nu_b) \propto \nu^{-3/2}$, respectively, resulting from the additional severe SST-losses at $\nu > \nu_B$.

Blazars, where the γ-ray fluence is much smaller than the synchrotron fluence, are regarded as small injection energy sources. Here, the synchrotron fluence exhibits the single power law behaviour (D4) up to a higher synchrotron peak energy that is a factor γ_0^2 smaller than the SSC peak energy. In this case the synchrotron light curve peak time exhibits the standard linear synchrotron cooling decrease $t_{\max}(\nu) \propto \nu^{-1/2}$ at all frequencies.

If the injection Lorentz factor γ_0 and the size of the source are the same, different values of the injection parameter α result from different total numbers of instantaneously injected electrons. E.g., the high injection case $\alpha_h = 100$ results for $N_{50} = 4.7$, whereas the low injection case $\alpha_s = 0.1$ needs $N_{50} = 4.7 \cdot 10^{-6}$.

References

Böttcher, M., 2007, Astroph. & Space Sci. 309, 95
Böttcher, M., Mause, H., Schlickeiser, R., 1997, A&A 324, 395
Böttcher, M., & Bloom, S. D., 2000, AJ, 119, 469
Dermer, C. D., Schlickeiser, R., 2002, ApJ 575, 667
Kardashev, N. S., 1962, Sov. Astron. J. 6, 317
Madejski, G., Sikora, M., Jaffe, T., et al. 1999, ApJ, 521, 145
Schlickeiser, R., 2009, MNRAS 398, 1483 (S)
Schlickeiser, R., Lerche, I., 2007, A&A 476, 1
Schlickeiser, R., Böttcher, M., Menzler, U., 2010, A&A, in press

Electromagnetic cascade in the vicinity of a supermassive black hole

S. Vincent and S. LeBohec

Physics Department, University of Utah, Salt Lake City, UT 84112, USA

Abstract. In the recent years, radio galaxies have emerged as a new class of extragalactic very high energy γ-ray emitters (VHE; E>300 GeV). The proximity and the multi-wavelength campaigns of these sources make possible unique studies of acceleration processes in the immediate surroundings of supermassive black holes (BHs). The recently fast variabilities of TeV γ-rays from M 87 on a timescale of days, strongly constrains the size of the possible sites of particle acceleration responsible to the TeV emission, while the VLBA radio observations can probe regions down to the milli-arcsecond scale and suggest the core of M 87 as the most likely source of VHE emission. In this study, it is shown that TeV γ-ray production can take place in the vicinity of a BH, threaded by externally magnetic field lines, in a process similar to that of pulsar electrodynamics.

1. Introduction

Recent discoveries of VHE emission from the radio-galaxies M 87 and Centaurus A opened up a new source class for studies. Radio-galaxies belong to the active galactic nuclei (AGN) class, but their jets make a larger angle to the line of sight and therefore the emission is less boosted. The most nearby AGN are radio galaxies and the detection of VHE emission from these sources enable unique studies of the spatial origin of the VHE emission.

In February 2008, a joint HESS-MAGIC-VERITAS campaign observed a VHE flare from M 87 over a 4-day time span. Such detection with fast-variability on timescale of days implies compact emission regions with a characteristic linear size $R \leq R_{\mathrm{var}} = ct_{\mathrm{var}}\delta/(1 + z) \sim 10^{15}\mathrm{cm}(\delta/10)(t_{\mathrm{var}}/1h)$, where δ is the Doppler factor of the VHE emitting region. The VHE gamma-ray telescopes cannot provide images with a sufficient resolution to localize the sites of the γ-ray production but, shortly after, the *Chandra* X-ray observatory detected an excess from the core of M 87 at a historical maximum while the flux from the nearby knot HST-1 remained quiescent. Over at least the following two months, until the VLBA monitoring project ended, the radio flux increases from a region within 70 Schwarzschild radius of the core. These results imply that charged particles are accelerated to VHE in the immediate vicinity of the black hole.

Theoretical studies of BH magnetosphere have shown that the electromagnetic field can be used to extract the rotational energy of BHs. Blandford & Znajek (1977) pointed out that electrons can be accelerated and reach enough energy to radiate VHE photons by synchrotron radiation and inverse Compton scattering. These photons can encounter thermal photons and create electron-positron pair which will in turn be accelerated leading to a cascade.

The vicinity of the black hole has been invoked to explain high energy radiation from BHs (Beskin et al. 1992; Hirotani & Okamoto 1998; Levinson 2000; Neronov & Aharonian 2007). And, the purpose of this study is to further extend the previous analysis, to clarify more quantitatively the micro process of interaction of radiation-pair creation. A Monte-Carlo technique is used for treating the full cascade process. The calculation follows the development of the cascade initiated by a primary electron, the conversion of the synchrotron and inverse Compton photons and the subsequent photons by the secondary pairs.

2. Outline of the simulation

In this section, we briefly describe how a pair production cascade proceeds in a thin gap in the force-free magnetosphere. We also describe the Monte-Carlo simulation and the physical processes, the input parameters and the criteria for the simulation to stop.

In the inner region near the hole, the magnetosphere is assumed to be force-free degenerate, i.e., the condition $\rho_e \mathbf{E} + (1/c)\mathbf{j} \times \mathbf{B} = 0$ is satisfied, where ρ_e, $\mathbf{j}$, $\mathbf{E}$ and $\mathbf{B}$ are the charge density, current density and electric and magnetic fields respectively. This means that the role of the plasma particles is just to carry charges and they are treated as if they were massless or inertia-free and the condition

$$\mathbf{E} \cdot \mathbf{B} = 0 \tag{1}$$

is satisfied. The charge density in the force-free magnetosphere is called the Goldreich-Julian charge density by analogy with the charge density in a pulsar magnetosphere. If the local value of the charge density differs significantly from the Goldreich-Julian charge density in any region, the condition (1) is not satisfied and an electric field with a component parallel to the magnetic field provides conditions for particle acceleration to arise.

Two different frames are used to calculate the trajectories. This choice follows the approach introduced by Thorne & MacDonald (1982). One is the Boyer-Lindquist

coordinate frame, which expressed the metric of a rotating (Kerr) black hole and is used to evaluate the photon trajectories. The other coordinate system is the zero angular momentum observer (ZAMO) frame, which is orthonormal and is used to compute the electron trajectories, the synchrotron radiation and the inverse Compton scattering.

A numerical code is developed to track the charged particle trajectories through the magnetosphere. The equation of motion for the electrons in the direct vicinity of the event horizon takes into account of the effects of general relativity. The simulations use the exact cross-section of the full electron-photon cascade involving photon-photon pair production interactions and inverse Compton scattering by electrons of photons of the background radiation. The high-energy particles emerging from an interaction are affected with the same direction as the incident photon or electron. At high energies, this will not introduce any significant error because, in the ZAMOs frame, the emerging particles are highly collimated along the direction of the incident high-energy particle.

The input to the simulation is the energy of the initial charged particle and the initial location in the gap. The mean interaction length in an isotropic photon gas is computed. Then the interaction length is randomly sampled from an exponential distribution with this mean. The equation of motion of the particle is integrated numerically. For the charged particle and at each step of the integration of the trajectory, the energy and power of synchrotron emission is calculated. When the distance traveled is equal to the interaction length then the interaction is treated. The energies of each of the two particles resulting from the interaction are obtained (one electron and one photon from inverse Compton interactions and one electron and one positron from pair production). The 4-momentum and position for the remaining particle is stored in an array and a new interaction point for the emerging particles is then sampled and the interaction is treated as described above.

This proceeds until the particles are outside the infrared region R_{IR}. If the interaction length is greater than R_{IR} or if the condition on the pair energy threshold for a head-on collision ($\theta = \pi$) is not satisfied ($s < 1$), the energy of the particle is output.

3. γ-ray emission from pair cascades: order of magnitude estimates & simulation results

We first present numerical simulations of pair cascades for a maximally rotating BH, i.e., $a/R_G = 1$, with mass $10^8 \, \mathrm{M_\odot}$. The simulation results are then compared to an analytic estimate of the γ-ray spectrum, and the comparison will serve to validate our code.

The electric potential difference generated by a maximally rotating BH is (Thorne et al. 1986)

$$\Delta V \approx 4.4 \times 10^{20} \left(\frac{B}{10^4 \, \mathrm{G}} \right) \left(\frac{M}{10^9 \, \mathrm{M_\odot}} \right) \left(\frac{h}{R_G} \right)^2 \; (\text{in V}) \quad (2)$$

where h is the gap height and $R_G = GM/c^2$ is the gravitational radius. The gap considered in the present section extends along the magnetic field lines from close to the BH's horizon up to the height $h = 0.1 R_G$. Within such a thin gap, the magnetic field can be considered as uniform allowing a direct comparison of the Monte-Carlo simulations with the analytic computations. In the region of interest, the local value of the magnetic field is $B \sim 0.1$ G. In our estimates, we assume the simplest model where the electric field parallel to the magnetic field is given by

$$E_\parallel = \Delta V/h, \quad (3)$$

where ΔV is the potential drop. This means that the typical field in the gap is $E_\parallel = 300 \, \mathrm{V \, m^{-1}}$. Our results can be generalized in a straightforward way to more realistic models of gaps in BH's magnetospheres. Here for the target photon field, the energy distribution is approximated as a δ−function at energy ϵ_0

$$n(\epsilon) = n_r(\epsilon)\delta(\epsilon - \epsilon_0), \quad (4)$$

where n_r is the photon density

$$n_r(\epsilon) = \frac{L}{4\pi R_{\mathrm{IR}}^2 c\epsilon}, \quad (5)$$

and L is the luminosity of the background radiation field. It is assumed that the luminosity of the source comes from matter accreting onto the BH from a region of radius R_{IR} around the BH. The size of the infrared emission region is taken to be $R_{\mathrm{IR}} = 2R_G$. The pulsation of the monochromatic radiation field is $\omega_{\mathrm{IR}} = 10^{14.6} \, \mathrm{rad.s^{-1}}$. The infrared luminosity of the nucleus is $\nu L_\nu = 10^{40} \, \mathrm{erg \, s^{-1}}$. Then the number density of background photon $n_{\mathrm{IR}} \sim 7 \times 10^{13} \, \mathrm{cm^{-3}}$. Table 1 gathers the properties of the model.

Here, the electron is assumed to be initially at rest with respect to the locally inertial observer, and injected at the base of the gap. For each electron propagating in the gap, if the energy loss remains small compared to the gain due to acceleration, then the acceleration is not be radiation reaction limited and the electron's maximum energy is be $E_e = q\Delta V$. If, however, the work done by the gap's electric field is dissipated through the synchrotron and IC radiation, the propagation proceeds in a "loss-saturated" regime. Then the maximum gamma factor from the balance of the acceleration and synchrotron energy loss rates is be $\gamma_{\mathrm{sync}}^{\max} \sim 1.2 \times 10^8$; the maximum gamma factor from IC loss rate is be $\gamma_{\mathrm{IC}}^{\max} \sim 3.6 \times 10^6$. It turns out that, in contrast to the models of pulsar magnetosphere, the IC process is dominant and the maximum energy of the electrons is $E_e^{\max} \sim 3$ erg. The spectrum produced by the synchrotron radiation of a single particle peaks at an energy $E_{\mathrm{sync}}^{\max} \sim 10^{-7}$ erg. Since the total energy must be conserved in the collision, there is an upper limit to the increase in the photon energy and the spectrum produced by IC scattering peaks at an energy $E_{\mathrm{IC}}^{\max} \leq E_e^{\max} \sim 3$ erg. However, the photon-photon pair production has a kinematic threshold for head-on collision $E_{\mathrm{threshold}} \sim 1.65$ erg. Consequently, for the range of parameters considered here,
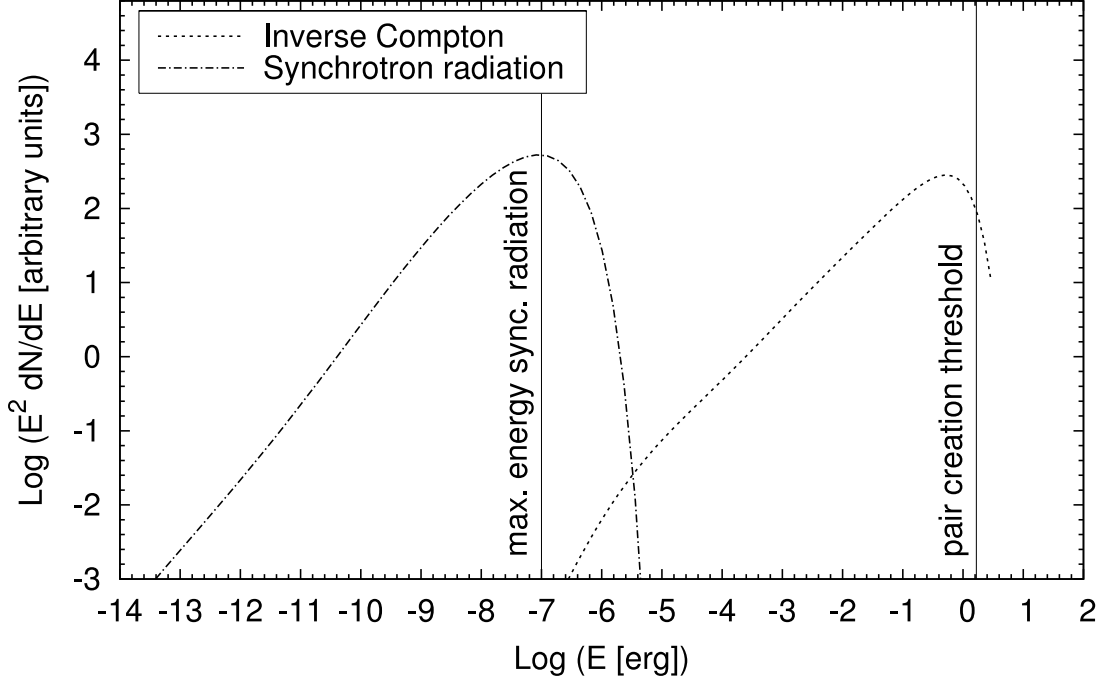
Fig. 1. Spectral energy distribution of emission.

Table 1. Simulation parameters.

BH mass ($M_\odot$)	gap thickness (m)	$E_\parallel$ (V.m^{-1})	B (G)	n_{IR} (cm^{-3})	E_{IR} (erg)
10^8	1.48×10^{10}	300	~ 0.1	7×10^{13}	4.2×10^{-13}

the overall spectrum is expected to peak at the threshold energy.

Figure 1 shows the typical spectrum from the electrons accelerated in the gap close to the BH horizon. The two broad peaks in the spectral energy distribution correspond to synchrotron radiation and inverse Compton scattering of primary and secondary electrons in the infrared region. It can be seen that the synchrotron radiation has a maximum at the energy $E_{\text{sync}}^{\max} \sim 10^{-7}$ erg, and the IC spectrum sharply peaks just below the threshold energy $E_{\text{threshold}} \sim 1.65$ erg. These values, compared with the simple analytical calculations made previously, are in good agreement with the expected maximum value of a Lorentz gamma factor of $\gamma^{\max} = 3.6 \times 10^6$ and a local value of the magnetic field strength of $B \sim 0.1$ G.

Figure 2 shows the differential number spectrum of the high energy photons creating the pairs. The spectrum has a mean value around 2.75 erg agreeing with the upper limit for the photon energy derived previously. The estimate was obtained under the assumption that the IC scattering takes place in the Thomson regime. However, the highest-energy electrons up scatter the background radiation into the Klein-Nishina regime, in which the efficiency of IC scattering is reduced. Hence it is seen that the photon energy may go above 3 erg. The spectrum has a low energy cutoff resulting of the pair creation threshold.

4. Conclusions

In this paper we quantitatively and self-consistently solved the process of pair production cascades in a thin gap in a rotating BH magnetosphere. This model has many similarities to models of particle acceleration in pulsar magnetosphere.

We summarize our results as follows:

1. Under the force-free approximation, there can be regions where an electric field with a component along the magnetic field line, $E_\parallel$, can arise.
2. Once $E_\parallel$ arises, it accelerates charged particles into ultra-relativistic energies.
3. An accelerated e^- scatters background photons to produce γ-ray photons with energies exceeding the threshold condition of pair production.
4. Typically, one of such γ-ray photons collides the background photon to produce an electron-positron pair, which leads to a pair cascade.

As an example of the numerical modeling, we show the spectral energy distribution, the spectrum of γ-ray photons creating pairs and we see that the distributions are in good agreement with the analytical expressions. This comparison enables us to validate our code and, at this stage, this tool can be used to model electron acceleration and γ-ray production in a very compact region close to the
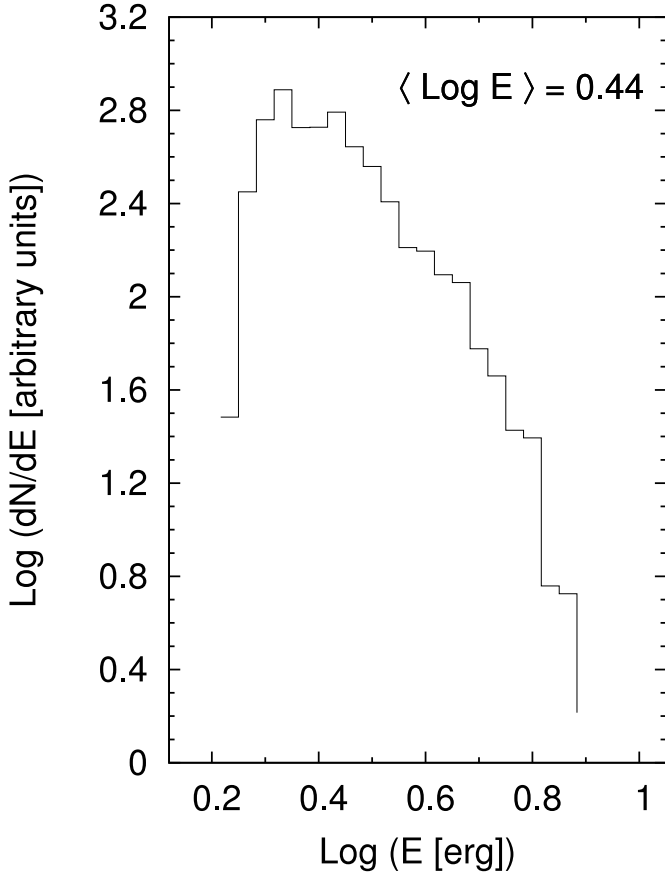
Fig. 2. Differential spectrum of the photons creating pairs.

event horizon of the BH to study the observed variability of TeV γ-rays emission from AGNs.

References

Beskin, V. S., Istomin, Y. N. & Parev, V. I. 1992, Soviet Astronomy, 36, 642
Blandford, R. D. & Znajek, R. L. 1977, MNRAS, 179, 433
Hirotani, K. & Okamoto, I. 1998, ApJ, 497, 563
Levinson, A. 2000, PRL, 85, 912
Neronov, A. & Aharonian, F. A. 2007, ApJ, 671, 85
Thorne, K. S., Price, R. H. & MacDonald, D. A. 1986, Black holes: The membrane paradigm (New Haven, CT, USA: Yale University Press)

Radio–sub-mm flares from blazars in a discontinuous jet model

Jörg P. Rachen[1], Max Häberlein[1][*], Felix Reimold[1][**], and Thomas P. Krichbaum[2]

[1] Max-Planck-Institut für Astrophysik, Karl-Schwarzschild-Str. 1, 85748 Garching, Germany
[2] Max-Planck-Institut für Radioastronomie, Auf dem Hügel 69, 53121 Bonn, Germany

Abstract. We present a model in which AGN jets are described by a dense series of plasma blobs, distributed in masses and velocities. The blobs expand and collide, and ultimately form a continuous jet flow as observed on larger scales. When blobs collide, energetic electrons are produced by first order Fermi acceleration, and emit synchrotron radiation at the radio-optical frequencies with a double-broken power law spectrum. The difference of this model to the well-known Marscher&Gear-model is, that in our model shocks are produced on a range of scales, and exist only temporarily, which causes differences in the prediction for the spectral evolution of flares. We apply our model to radio-submm data obtained for 3C 454.3, and briefly discuss implications for gamma-ray production.

1. Introduction

Based on the work of Marscher & Gear (1985), flares in AGN jets usually modelled by shocks propagating in a continuous plasma jet from its origin to the outside. While the shock continuously energises electrons, synchrotron radiation emitted by it goes through a flare, owing to the competing cooling processes of inverse Compton radiation, dominating in the rise phase, and adiabatic losses in the expanding jet, dominating in the decay phase, with the possibility of a plateau phase in-between, in which synchrotron radiation itself is the dominating cooling process. As the relative strength of cooling processes depends on global jet parameters, which are unlikely to change on a short timescale, all flares should evolve in a similar way, with their rise, plateau and decay timescales being of the same order of magnitude, typically weeks to months. While this fits observations of radio flares quite well, the situation is less clear in the optical and gamma-ray regime. Here, flares appear on a large range of time scales, from less than an hour in some TeV blazars, to weeks for strong blazars in the Fermi regime.

To accommodate the situation in the gamma-ray regime, Spada et al. (2001) suggested a so-called "internal shock model" for blazars, motivated by the model of Rees & Mészáros (1994) for the explanation of rapidly variable gamma-ray burst lightcurves. In this model, shocks are formed in random collisions of shells, and subsequently accelerate electrons to emit synchrotron and inverse Compton radiation. Within the framework of this synchrotron-self Compton (SSC) scenario, Spada et al. (2001) used their model to explain qualitatively the global characteristics of blazar variability at optical to gamma-ray frequencies.

In the current work we revoke the internal shock model for blazars, but focusing on the explanation of flare evolution in the radio-submm regime, which claim to allow us to pinpoint the physical parameters of the jet independent on the assumptions for gamma-ray production. A detailed discussion will be given by Häberlein & Rachen (2010), henceforth referred to as "Paper I". Here we discuss briefly the basic idea and properties of this model, and apply it to a flare observed in the bright blazar 3C 454.3 in 2005.

2. Jets, shocks and plasmons : not a contradiction

Essentially two fundamental mechanisms have been proposed to explain why plasma jets may be launched from accreting black holes: the Blandford & Znajek (1977) process, which is based on electromagnetic extraction of the angular momentum of a rotating black hole in form of a strong Poynting flux, and the Blandford & Payne (1982) process of hydromagnetic extraction of rotating plasma from the corona of the accretion disk. In the recent discussion of AGN and other accreting sources, it is generally assumed that both mechanisms contribute to the jet formation, possibly with different weights depending on the physical properties of the accreting system (e.g., Meier et al. 2001). Although plasma physicists have shown that solutions for the continuous emission of jets exist, all involved physical processes are prone to instabilities, in particular in the highly relativistic regime of accreting black holes. This justifies the assumption that, although jets are observed as continuous plasma flows on larger scales, they are not born like this, but as a dense, random flow of plasma blobs, emitted from a central source similarly to a discharge process.

Let us assume that the blobs are emitted on an average rate $f_* < c/R_S$, if R_S is the Schwarzschild radius of the central black hole, at highly relativistic speeds with a bulk Lorentz factor $\Gamma_* \sim 10$. Being generally unconfined, in their comoving frame the blobs would expand in all directions approximately with their speed of sound, $\beta_s c$, leading to an opening angle of the yet discontinuous jet of $\beta_s \Gamma_*^{-1}$. In the initial phase, where relativistic gas dominates the pressure, the expansion decreases with distance
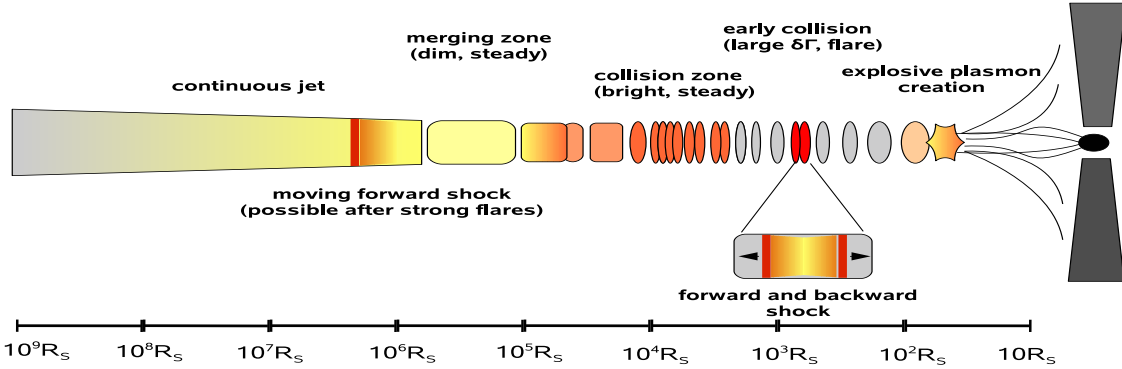
Fig. 1. Illustration of the discontinuous jet model. Plasmons created some $10-100$ Schwarzschild-radii from the black hole collide mostly at around $10^4 R_S$, converting a significant fraction of the bulk Lorentz factor variance into internal energy, and ultimately into radiation. As the "collision region" is quasi-stationary in position and emits most of the radiation in a spectrum averaging out the individual collisions, it might be identified with the bright "millimetre-core" seen in many blazars. Particularly large differences in bulk Lorentz factor may lead to early, strong collisions which appear as flares in the spectrum. As the collision region is leveling out the differences in bulk speed, the jet merges afterwards quite smoothly. A series of fast blobs, e.g., after a surge in the accretion rate, may propagate through the whole system, leading to a series of flares, and ultimately form a moving shock in the continuous jet, explaining VLBI observations as reported by Marscher et al. (2008).

r from the black hole approximately as $\beta_s \propto r^{-1/2}$, leading to an apparent collimation of the jet to angles of less than $1°$. After this, we assume conical expansion with $\beta_s \sim 0.1$. Neglecting velocity differences of the blobs, they would merge rather smoothly after a distance $r_{mrg} \sim \Gamma_*^2 c/f_* \beta_s$, as their expansion has filled up the gaps between them. Of course, a realistic "discharge" process near the black hole will emit the blobs with randomly distributed Lorentz factors $\Gamma_* + \delta\Gamma_i$, with $\langle \delta\Gamma_i \rangle = 0$ and a normalised standard deviation $\sigma_\Gamma = \sqrt{\langle \delta\Gamma_i^2 \rangle}/\Gamma_*$. Inelastic collisions between plasmons will then become frequent at a distance $r_{col} \sim \Gamma_*^2 c/f_* \sigma_\Gamma$, converting on average a fraction $\sigma_\Gamma^2/4$ of the bulk flow into internal energy. Subsequent collisions will lead to more and more elongated "jet-bits", with the spread in Lorentz factor diminishing as $\sigma_\Gamma^{[k]} \sim \sigma_\Gamma^{[0]}/2^k$, if k denotes the number of collisions an individual blob has suffered. Eventually, $\sigma_\Gamma^{[k]} \ll \beta_s$, and blob-expansion is again the dominating process to form the continuous jet at $\gtrsim 10^5 R_S$. Fig. 1 illustrates this process.

We want to emphasise that our plasmons cannot be identified with the observable VLBI components. In our model, there are $\sim \Gamma_*^2/\beta_s \sim 10^3$ plasmons in the discontinuous phase of the jet ($r \lesssim 10^5 R_S$) at any time. They are usually dark, as they are born with extremely high magnetic field cooling down any synchrotron emission on a short timescale. The blobs become bright only after they are re-energised at $\sim 10^4-10^5 R_S$ in collisions. For most blazars, even the best VLBI pictures will not be able to resolve single collisions; rather we expect that the known resolved VLBI features in AGN jets correspond to the distinct zones in our model, as shown and explained in Fig. 1. We also emphasise that, in general, collisions in our model do not correspond to a "flares" in the observed spectrum. As the rate of collisions must be equal to f_* to create a stationary system, that means for $f_* \sim c/10 R_S$ and a $10^8 M_\odot$ black hole several collisions per day. As the syn-

chrotron cooling time scale is much larger, i.e., $f_* t_{syn} \gg 1$, we see at any instant the superposed emission of many plasmon collisions, averaging out their spectral and temporal properties. The average collisions with $\delta\Gamma/\Gamma \lesssim \sigma_\Gamma$ therefore represent what observers call the *quiescent* emission of a blazar; *flares*, on the contrary, are collisions with $\delta\Gamma/\Gamma \gtrsim 3\sigma_\Gamma$, which can have luminosities up to three orders of magnitude higher than the average, as we will show below. In Paper I we present a full scale simulation of the jet, starting from the statistical properties of the central engine and calculating all n-th order collisions on the way to the continuous jet. There we also we demonstrate that the overlay of average "mini-flares" indeed produces a broken power law spectrum with $\alpha \approx 0$ below, and $\alpha \approx 0.7-1.2$ above the break frequency typically in the range $10-300$ GHz, as usually observed in blazars.

3. Flare characteristics in a discontinuous jet

When two plasma blobs, both carrying an energy $\approx Mc^2\Gamma$, collide with a Lorentz factor difference $\delta\Gamma$, two shocks running in opposite directions with speeds $\beta_{sh} \approx \sqrt{2\delta\Gamma/\Gamma}$ (for $\delta\Gamma \ll \Gamma$) are formed, and internal energy $E_{int} \sim \frac{1}{4}Mc^2(\delta\Gamma/\Gamma)^2$ is created. We assume that a significant part of this internal energy is going into turbulence, specifically magnetic field creation in turbulent dynamos, and another significant part into non-thermal particles through the mechanism of first order Fermi acceleration at the shocks. First order Fermi acceleration has the property to *produce* power law particle distributions, and therefore to *explain* the ubiquitous presence of power law spectra in sources known to contain shocks (see Drury 1983 and references therein). We assume in the following the canonical power law index for Fermi-accelerated electrons, i.e., $N(\gamma) = N_e \gamma^{-s}$ with $s = 2$, for the electron Lorentz factor in the range $\check{\gamma} \leq \gamma \leq \hat{\gamma}$. We introduce the pa-

rameters ξ_B and ξ_e by $u_B \equiv B^2/8\pi = \xi_B E_{\rm int}/2V$ and $u_e = N_e m_e c^2 \ln(\hat{\gamma}/\check{\gamma}) = \xi_e E_{\rm int}/2V$, where $V \approx \frac{4}{3}\pi R^3$ is the volume of a "virgin" plasmon. In a conical jet, R related to the distance r from the black hole as $R \approx r\beta_{\rm s}/\Gamma$. As the synchrotron luminosity $L_{\rm syn} \propto R^2 N_e B^2$, we get $L_{\rm syn} \propto R^2 E_{\rm int}^2 \propto (\delta\Gamma/\Gamma)^8$ for constant $\hat{\gamma}/\check{\gamma}$.[1] Therefore, "$3\sigma$-events" in the distribution of collisions can outshine the sum of all average collisions, revealing temporarily the spectral properties of a single emission region with a specific size R, and specific values for plasma properties like N_e or B. This is, what we usually call a *flare*.

The spectrum of a flare is represented as a broken power law with three characteristic frequencies. The first is the synchrotron-self absorption frequency $\nu_{\rm a}$, defined by requiring that the opacity $\tau_{\rm ssa}(\nu_{\rm a}) = 1$, yielding

$$\nu_{\rm a} \approx \left[\frac{\sigma_{\rm T} R u_B u_e}{4 m_e c^2 \ln(\hat{\gamma}/\check{\gamma})}\right]^{\frac{1}{3}} . \tag{1}$$

where $\sigma_{\rm T} = 8\pi r_e^2/3$ is the Thompson cross section. For $\nu < \nu_{\rm a}$, the spectrum is $S_\nu \propto \nu^{5/2}$, for $\nu > \nu_{\rm a}$ we will have $S_\nu \propto \nu^{-\alpha}$ with $\alpha = (s-1)/2 = 0.5$. This spectral index, however, is only correct for $t_{\rm syn}(\nu) > t$, i.e., synchrotron cooling is not yet efficient for the electrons emitting at a characteristic frequency $\nu(\gamma) = 3eB\gamma^2/16 m_e c$ at a time t after the collision. Above a $\tilde{\nu}_{\rm b}(t)$ for which $t_{\rm syn} = t$, the electron spectrum steepens as $s \to s+1$, yielding $S_\nu \propto \nu^{-1}$. Evaluating $\tilde{\nu}_{\rm b}(t)$ for the fully developed flare, i.e., $t \approx R/c\beta_{\rm sh}$, we obtain

$$\nu_{\rm b} \approx \frac{Rc\beta_{\rm sh}^2}{r_e^2}\left[\frac{m_e c^2}{eBR}\right]^3 \tag{2}$$

Finally, the spectrum reaches a maximum frequency at $\nu_{\rm c} = \nu(\hat{\gamma})$, above which it turns into an exponential cutoff. The value of $\hat{\gamma}$ is hereby determined by the relation $t_{\rm acc}(\hat{\gamma}) = t_{\rm syn}(\hat{\gamma})$, where $t_{\rm acc}(\gamma) \approx 3\kappa/c^2\beta_{\rm sh}^2$ is the acceleration time scale for first order Fermi acceleration. Biermann & Strittmatter (1987) connected the diffusion coefficient κ to the plasma turbulence spectrum, and showed that for a Kolmogoroff spectrum known from fully developed hydrodynamical turbulence, $\nu_{\rm c}$ is expected in the infrared to optical regime, as observed for many AGN. In Paper I, we will discuss a slightly modified version of the BS87 approach in more detail; here, we focus on the break frequencies $\nu_{\rm a}$ and $\nu_{\rm b}$, which are more relevant in the radio-submm regime.

We evaluate $\nu_{\rm a}$ and $\nu_{\rm b}$ numerically for the "average" collision, i.e., with $R = r_{\rm col}\beta_{\rm s}/\Gamma_* = \Gamma_* c\beta_{\rm s}/f_*\sigma_\Gamma$, $\beta_{\rm sh} = \sqrt{2\sigma_\Gamma}$, for values $\beta_{\rm s} = 0.1$, $f_* = c/100 R_{\rm S}$, and $\ln(\hat{\gamma}/\check{\gamma}) = 7.5$. If we further assume that the jet power is equal to the Eddington luminosity of the black hole, with mass $10^9 M_9 M_\odot$, we find

$$\nu_{\rm a}' \sim 8 \cdot 10^{13}\,{\rm Hz}\;\sigma_\Gamma^3 \xi_B^{1/3} \xi_e^{1/3} M_9^{-1/3} \to 200\,{\rm GHz}/200\,{\rm GHz} \tag{3}$$

$$\nu_{\rm b}' \sim 1.5 \cdot 10^6\,{\rm Hz}\;\sigma_\Gamma^{-9/2} \xi_B^{-3/2} M_9^{-1/2} \to 150\,{\rm GHz}/1\,{\rm GHz} \tag{4}$$

---

[1] Spada et al. (2001) vary $\check{\gamma}$ rather than N_e to account for constant fraction of non-thermal energy in electrons to total internal energy, which would lead to $L_{\rm syn} \propto (\delta\Gamma/\Gamma)^3$.

We defined $\nu' = D\nu$ to consider that blazar emission is usually Doppler boosted, setting $D = \Gamma_* = 10$. The values after the arrow correspond to $\sigma_\Gamma = 0.3$ and $M_9 = 5$ (as expected for 3C 454.3), the first value for $\xi_B = 0.3$ and $\xi_e = 0.01$, and the second for $\xi_B = 0.01$ and $\xi_e = 0.3$ (see Section 5 for a discussion). We see that for all cases $\nu_{\rm b} < \nu_{\rm a}$, that means we expect in flares a steep spectrum $\propto \nu^{-1}$ above $\nu_{\rm a}$. Note, however, that during the rise phase, $\tilde{\nu}(t) > \nu_{\rm b}$, so that the flare may temporarily exhibit a $\nu^{-0.5}$ spectrum directly above $\nu_{\rm a}$.

Of particular interest is the behaviour of the flux at $\nu_{\rm a}$ during the flare evolution, as this corresponds to the $(\nu_{\rm m}, S_{\rm m})$ plots often used in radio astronomy to describe flare evolution. In our model, B is approximately constant while the shock is active, and R hardly changes during the shock crossing time. Therefore, we expect that $S_{\rm m}$ rises for constant $\nu_{\rm m}$. When the flare decays adiabatically after the shock ceases, the flux in the optically thick region evolves as $S \propto R^2 B^{-1/2}$, as the source function does not depend on the electron spectrum. With $S \propto \nu^{5/2}$ and for $B \propto R^{-2}$, one obtains $S_{\rm m} \propto \nu_{\rm m}^{1.2}$ (one can easily check that $S_{\rm m} \propto \nu_{\rm m}^1$ is obtained for $B \propto R^{-1}$). If synchrotron cooling dominates over adiabatic cooling at $\nu_{\rm a}$, which is normally the case initially as $\nu_{\rm b} \ll \nu_{\rm a}$, one can show that $S_{\rm m} \propto \nu_{\rm m}^{5/2}$, i.e., the flare decays along the spectral edge of self-absorption. This may be compared with the predictions of the Marscher & Gear (1985) model, which are quite different. A more detailed discussion of flare evolution in our model will be given in Paper I.

4. Fitting the 2005 flare in 3C 454.3

To illustrate the capabilities of our approach to reproduce the temporal-spectral evolution of blazar flares, we apply our model to data obtained on the bright blazar 3C 454.3 in a campaign which has been started in 2005 after an initial strong mm-/optical flare. The main goal of the campaign has been to obtain quasi-simultaneous radio-spectra covering the frequency range from 1–300 GHz, which can be used to study the spectral evolution over time.

The Effelsberg 100 m radio-telescope of the Max-Planck-Institut für Radioastronomie with its sequence of secondary focus heterodyne receivers is well suited to measure flux densities quasi-simultaneously within 30-40 mins at 2.7, 5, 8.4, 10.5, 15, 22, 32, and 43 GHz. These measurements were occasionally complemented by flux density measurements at 0.6-1.4 GHz, when the corresponding prime-focus receivers were available. The data were analysed and calibrated in the standard way following similar procedures as described in Fuhrmann et al. (2008) and Angelakis et al. (2008). The Effelsberg radio data were complemented by measurements within a few days of the millimetre flux densities obtained through the regular AGN monitoring program, which is performed at the IRAM 30 m telescope on Pico Veleta (Spain). This instrument provided measurements at 90 GHz and 230 GHz (see Ungerechts et al. (1998) and Agudo et al. (2006) for more details and a description of the data reduction). We fur-
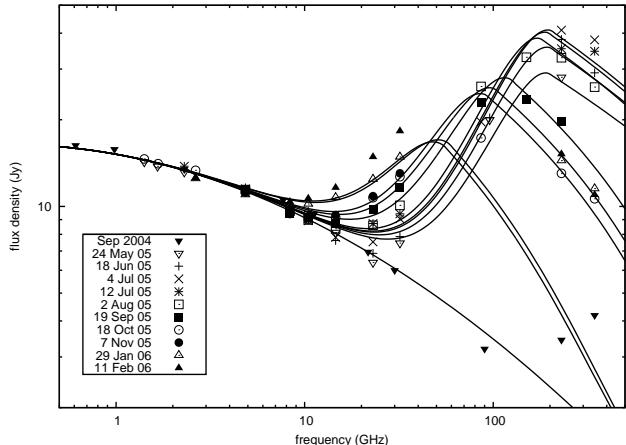
Fig. 2. Fit of a single flare in the discontinuous jet model to data of the 2005/06 flare from 3C 454.3, see also Krichbaum et al. (2006) and the discussion in the text.

ther included 230 GHz and 345 GHz data from the AGN-monitoring of the sub-millimetre array (SMA) on Mauna Kea (Hawaii, see Gurwell et al. (2007) and refs. therein), which are published in part by Villata et al. (2009) and refs. therein.

Fig. 2 shows the data together with spectra simulated from our full model, as described in Paper I. We assumed that two plasmons with $Mc^2 = 7 \cdot 10^{54}$ erg, $\Gamma_1 = 10$ and $\Gamma_2 = 13$ collide at a distance $\sim 10^{19}$ cm from the black hole, consistent with a jet power of 10^{48} erg/sec and $f_* \sim 10^{-6}$ Hz. We further assumed $\beta_s = 0.1$, thus $R \sim 10^{17}$ cm, and a constant viewing angle of $5°$ to calculate the Doppler factor. All parameters have then been optimised in an adaptive method by minimisation of $\sum_t \sum_i \chi_{i,t}^2$ for all data sets taken at the times t as given in the plot, where the simulated flare spectra have been added to a constant underground fitted to the data from September 2004. As the starting time of the flare is unknown, we have identified the data set from July 4th with the maximum of the flare. Frequencies and times have been properly corrected for the redshift of the source, $z = 0.859$. As the best fit parameters, we found $\xi_B \approx 0.3$, and $\xi_e \approx 10^{-3}$. The temporal evolution of the flare is represented quite well, until presumably a new flare arises beginning of February 2006. The discrepancies at the low frequency turnover from the background to the flare spectrum should not surprise, as our model expects the background to change with time. Clearly, data at frequencies above 350 GHz would have been helpful to further constrain our parameters.

5. Implications for gamma-ray emission

In their discontinuous jet model, Spada et al. (2001) included inverse Compton (both SSC and external IC) emission, and determined the necessary jet parameters from the requirement to fit existing gamma-ray data. In contrast, it is our approach to determine the jet parameters from synchrotron emission alone, and keep minds open re-

garding the mechanism of gamma-ray production. We may remind the readership at this point that there are alternatives to inverse Compton models for gamma-ray production. In the so-called "hadronic" scenario, protons are accelerated to extremely high energies, enabling them to produce gamma-rays by pion induced cascades (Mannheim 1993), with a possible admixture of proton-synchrotron radiation (Mücke et al. 2003). As first order Fermi acceleration, which is the base of our model, does not distinguish between protons and electrons in principle, we may state that hadronic models are at least as "natural" as the "leptonic" inverse-Compton scenario. However, hadronic models are very difficult to handle technically, so we abstained from making detailed predictions for the gamma-ray spectra in our model at first; nevertheless it is possible to draw some preliminary conclusions on gamma-ray production from our results.

As discussed by Rachen (2000), leptonic and hadronic models can be distinguished by the required relation of magnetic field to photon density, i.e., by the ratio ξ_B/ξ_e: while leptonic models need $\xi_B \lesssim \xi_e$ (in case of TeV blazars even $\xi_B \ll \xi_e$) to explain gamma-ray data, hadronic models require $\xi_B \sim \xi_p \gg \xi_e$, where ξ_p denotes the fraction of internal energy in relativistic protons. For our fit of the flare of 3C 454.3, $\xi_B \gg \xi_e$ was found. It would be premature to consider this evidence for hadronic origin of gamma rays from 3C 454.3, as our fit method does not really perform a full parameter space search, identifying all allowed and excluded regions. However, it does give confidence in our method to distinguish between hadronic and leptonic models in future, improved applications. This certainly requires to include *all* gamma-ray production methods into our model, and then compare with *both* Fermi gamma-ray, and *detailed* radio-optical data. For the latter, as obvious from the discussion in Section 4, closing the infrared gap in regular blazar monitoring would be highly desirable.

References

Agudo, I., et al. 2006, A&A, 456, 117
Angelakis, E., et al. 2008, Mem. Soc. Astron. Ital., 79, 1042
Biermann, P. L. & Strittmatter, P. A. 1987, ApJ, 322, 643
Blandford, R. D. & Znajek, R. L. 1977, MNRAS, 179, 433
Blandford, R. D. & Payne, D. G. 1982, MNRAS, 199, 883
Drury, L. O'C. 1983, Rep. Prog. Phys., 46, 983
Fuhrmann, L., et al. 2008, A&A, 490, 1019
Gurwell, M. A., et al. 2007, ASP Conf. Ser., 375, 234
Häberlein, M., Rachen, J. P., in prep. Häberlein, M., Diplomarbeit, Max-Planck-Inst. f. Astrophysik, 2010 (**Paper I**).
Krichbaum, T. P., et al. 2006, in Proc. 8th European VLBI Network Symp., eds. A. Marecki et al., 2
Mannheim, K. 1993, A&A, 269, 67
Marscher, A. P., et al. 2008, Nature, 452, 966
Marscher, A. P. & Gear, W. K. 1985, ApJ, 298, 114
Meier, D. L., 2001, ApJ, 549, L9
Mücke, A., et al. 2003, Astropart. Phys., 18, 593
Rees, M. J. & Mészáros, P. 1994, ApJ, 430, L93
Rachen, J. P. 2000, AIP Conf. Ser., 515, 41
Spada M., et al. 2001, MNRAS, 325, 1559
Ungerechts, H., et al. 1998, ASP Conf. Ser., 144, 149
Villata, M., et al. 2009, A&A, 504, 9

Hadronic γ-ray emission from extragalactic mini radio lobes

M. Kino[1]* and K. Asano[2]

[1] National Astronomical Observatory of Japan, Tokyo 181-8588, Japan
[2] Interactive Research Center for Science, Tokyo Institute of Technology, Tokyo 152-88550, Japan

Abstract.
Hadronic emission from parsec size radio lobes in active galactic nuclei (AGN) is discussed. The lobes are composed of shocked jet plasma and expected to be filled with high energy particles. By using a Monte Carlo simulation, we calculate the photon spectra from the lobes including photo-meson interaction processes. When the synchrotron emission from primary electrons is bright, the synchrotron-self-Compton component is dominant in γ-ray bands. The hadronic emission from the lobes can dominate in γ-ray bands when the primary emission is not very bright. The proton synchrotron component arises in the sub MeV band. The synchrotron emission radiated from secondary $e^{\pm}$ pairs produced via photo-meson cascade emerges in $\sim$GeV-TeV energy ranges. These high energy emission signatures provide a test for proton acceleration in young AGN jets.

1. Introduction

The progress of VLBI (Very Long Baseline Interferometry) observations has revealed the existence of compact radio-loud active galactic nuclei (AGN) with linear sizes $LS <$ 1 kpc (e.g., Readhead et al. 1996; O'Dea & Baum 1997). These compact radio sources are currently understood as young progenitors of large radio galaxies (e.g., Fanti 2009 for review). Furthermore, recent investigations have discovered smaller radio lobes with $LS \sim \mathcal{O}(10$ pc) (e.g., Snellen et al. 2004; Orienti et al. 2008). It is well known that recurrent radio sources also possess mini lobes inside them (e.g., Walker et al. 2000). High energy emission from these compact radio sources has been recently explored by some authors (e.g., Stawarz et al. 2008; Kino et al. 2009). However, previous work focuses on the leptonic emission and little is known about adronic emission in them.

Since mini radio lobes with $LS \sim 10$ pc are located close to the AGN core, the lobes are expected to be in dense external radiation fields (Fig. 1). Furthermore, the shocks accelerate protons as well as electrons. Therefore high energy protons are naturally expected to fill the radio lobes although their total amount is still unknown. Therefore $p\gamma$ interaction is inevitable in the mini lobes. Here we examine $p\gamma$ interactions between high energy protons and surrounding target photons. As for external photons, we focus on UV photons from standard accretion disks.

2. Model

Following the standard picture of radio lobe formation in AGNs (e.g., Begelman et al. 1984), here we briefly review the standard picture of radio lobes. When a jet interacts with surrounding ambient matter, most of its kinetic energy is dissipated via strong shocks. The termination point
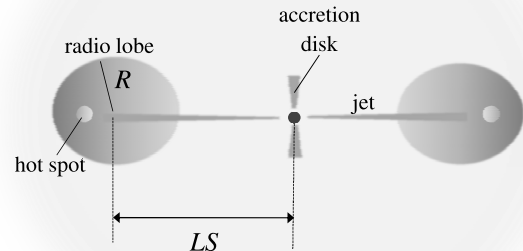
Fig. 1. A cartoon of mini radio lobes immersed in the radiation field due to an accretion disk. In this work we examine the case of $R = 2$ pc, $LS = 10$ pc and $L_{\rm disk} = 3 \times 10^{45}$ erg s^{-1}.

at the tip of the jet is called a hot spot. The hot spot is identified as the reverse shocked region of the decelerated jet. The shocked jet plasma leaks from the hot spot and forms radio lobes. Therefore we can say that the radio lobes are remnants of the decelerated jets which contain relativistic particles. In this work, we examine the case when the lobe contains relativistic protons.

2.1. Proton acceleration and coolings

Hot spots in powerful radio galaxies are one of the promising sights for proton acceleration (e.g., Rachen and Biermann 1993). Here we show that hot spots in mini lobes

* motoki.kino@nao.ac.jp

are also plausible sights for proton acceleration. Hereafter the maximum energy of shock accelerated protons is denoted as $E_{p,\max} = \gamma_p m_p c^2$. The proton acceleration time scale at the hot spots $t_{p,\mathrm{acc,hs}} = \xi_p E_p/(eB_{\mathrm{hs}}c)$ is estimated as

$$t_{p,\mathrm{acc,hs}} \approx 3.5 \; \left(\frac{\xi_p}{100}\right) \left(\frac{E_p}{10^{18}\ \mathrm{eV}}\right) \left(\frac{B_{\mathrm{hs}}}{10^{-1}\ \mathrm{G}}\right)^{-1} \; \mathrm{yr}, \quad (1)$$

where B_{hs} and ξ_p are the magnetic field strength, and the ratio of the acceleration timescale and Larmor timescale for protons at the hot spot, respectively. Although there is no direct estimate for B_{hs}, the magnetic field strengths in mini lobes (B) have been recently estimated as $B \sim 10 - 100$ mG by VLBI observations (Orienti et al. 2008). Since the magnetic field strength at the hot spot B_{hs} should be comparable or larger than B, here we set $B_{\mathrm{hs}} \sim 100$ mG. The value of ξ_p is a free parameter. For blazars it is constrained as $\xi_p > 10$ (Aharonian et al. 2002). There is little constraint on ξ_p for hot spots in mini lobes and we examine the case of $\xi_p = 100$ in this work. The timescale of proton synchrotron is $t_{p,\mathrm{syn,hs}} = (6\pi m_p^4 c^3)/(\sigma_T m_e^2 E B^2) \approx 1 \times 10^4 (E_p/10^{18}\ \mathrm{eV})^{-1}(B_{\mathrm{hs}}/0.1\ \mathrm{G})^{-2}$. The high energy protons escape from the hot spots via sideways expansions and they are injected into the mini lobes. When the escape velocity from the hot spot is $\sim 0.3\ c$, the escape timescale is accordingly $t_{\mathrm{esc,hs}} \sim 3\ (R_{\mathrm{hs}}/10^{18}\ \mathrm{cm})$ years. Therefore, the typical $E_{p,\max}$ is obtained by the relation $t_{p,\mathrm{acc,hs}} \approx t_{\mathrm{esc,hs}}$ and is

$$E_{p,\max} \approx 1 \times 10^{18} \left(\frac{\xi_p}{100}\right)^{-1} \left(\frac{R_{\mathrm{hs}}}{10^{18}\ \mathrm{cm}}\right) \left(\frac{B_{\mathrm{hs}}}{10^{-1}\ \mathrm{G}}\right) \; \mathrm{eV} \quad (2)$$

The Larmor radius of high energy protons with $E_p \sim 10^{18}$ eV is sufficiently smaller than R_{hs}. Hence, the conditions of proton acceleration are satisfied.

Next, high energy protons escape from the hot spot via sideways expansions and they injected in the mini lobes. Then they undergo various coolings in the lobes, i.e, adiabatic loss, $p\gamma$ interaction, and proton synchrotron cooling. Below, we calculate these processes with a Monte Carlo simulation.

3. Monte Carlo simulation

To calculate broadband photon spectra, a Monte Carlo simulation has been performed in this work. The numerical code has been developed by Asano et al. (2008, 2009) and references therein. Therefore we do not repeat it here. Details will be shown in Kino & Asano (in prep.). Distributions of particles and photons are assumed to be isotropic. We include the following physical processes: (1) photo-pion production from protons and neutrons ($p + \gamma \to p/n + \pi^0/\pi^+$), (2) pion decay ($\pi^0 \to 2\gamma$), ($\pi^\pm \to \mu^\pm + \nu$) and muon decay ($\mu^\pm \to e^\pm + \nu$), (3) photon-photon pair production ($\gamma + \gamma \to e^+ + e^-$), (4) Bethe-Heitler pair production ($p + \gamma \to p + e^+ + e^-$), (5) synchrotron and inverse Compton processes of electrons/positrons, protons, pions, muons with Klein-Nishina

cross section, (6) synchrotron self-absorption for electrons/positrons, and (7) adiabatic expansion loss.

4. Results

Figure 2 shows the photon spectra for the case of $L_e = 1 \times 10^{45}$ erg s^{-1}, 1×10^{44} erg s^{-1}, 1×10^{43} erg s^{-1}, 1×10^{42} erg s^{-1}, and 1×10^{41} erg s^{-1} where L_e is the injection power of non-thermal electrons. For electron Gyrofactor, we set $\xi_e = \xi_p = 1 \times 10^2$. The injection index is assumed as $s = 2$ for both electrons and protons. Based on VLBI observations, we set the following parameters as $R = 2$ pc, $R_{\mathrm{hs}} = 0.3$ pc, $B = 0.1$ G, $v_{\mathrm{exp}} = 0.1\ c$, $LS = 10$ pc, and $\gamma_{p,\min} = \gamma_{e,\min} = 10$. For the luminosity and temperature of the standard accretion disk, we assume $L_{\mathrm{disk}} = 3 \times 10^{45}$ erg s^{-1}, and $kT_{\mathrm{disk}} = 10$ eV (e.g., Ostorero et al. 2010). We constrain the injection power of high energy protons L_p to be smaller than total kinetic powers of powerful radio galaxies $\sim 10^{47-48}$ erg s^{-1} (e.g., Ito et al. 2008). We assume $L_p = 5 \times 10^{46}$ erg s^{-1} in this work.

Thin solid lines in Fig. 2 shows the photon spectra without proton injection (i.e. $L_p = 0$). The synchrotron spectra from the primary electrons are well studied by VLBI observations. The turnover frequency is mainly caused by synchrotron self absorption (SSA) (e.g., Snellen et al. 2000). Depending on the synchrotron luminosity of the mini lobe L_{syn}, the observed turnover frequencies of mini lobes show $\nu_{\mathrm{SSA}} \sim 0.1 - 10$ GHz. At the same time, primary electrons suffer from fast synchrotron cooling. Therefore a break frequency due to the synchrotron cooling typically appears comparable to or below ν_{SSA}. This implies that $L_e \approx L_{\mathrm{syn}}$.

Thick solid lines in Fig. 2 represent the photon spectra with proton injection. It is found that the amount of primary electrons controls whether hadronic emission is visible or not. For a lobe with $L_e = 1 \times 10^{45}$ erg s^{-1}, the leptonic emission overwhelm the hadronic emission in all energy domains. As a result, the spectrum with proton injection is almost the same as the one without proton injection. Therefore, the bright lobe is not suitable for testing the existence of high energy protons. As L_e decreases to $L_e \leq 1 \times 10^{44}$ erg s^{-1}, thick and thin lines become separable in the γ-ray energy range because synchrotron emission from secondary electrons is added in the thick lines. For lobes with $L_e < 1 \times 10^{43}$ erg s^{-1}, the proton synchrotron bump appears in the sub-MeV range with the peak at

$$\nu_{p,\mathrm{syn}} \approx 0.7 \left(\frac{E_p}{10^{18}\ \mathrm{eV}}\right)^2 \left(\frac{B}{10^{-1}\ \mathrm{G}}\right) \; \mathrm{MeV}. \quad (3)$$

In the TeV energy range it is shown that TeV-γ photons are significantly attenuated due to soft photons in the lobes.
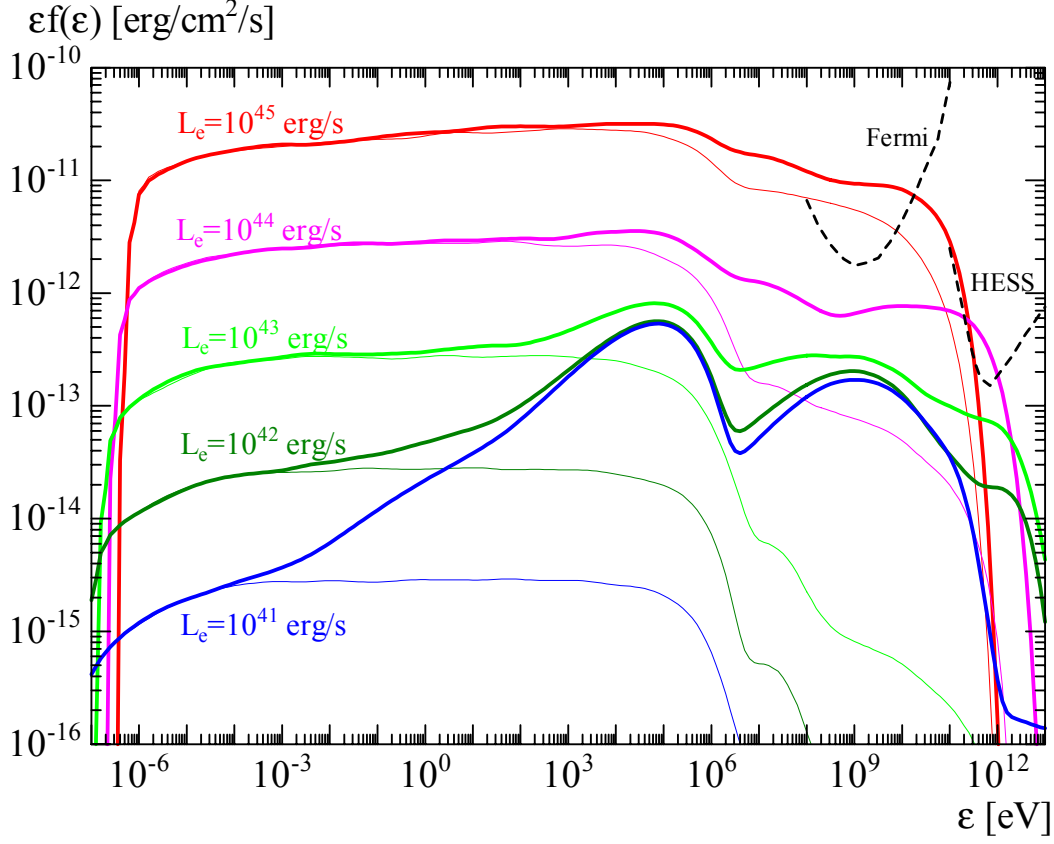
Fig. 2. Predicted broadband spectra from the mini radio lobe for $L_p = 5 \times 10^{46}$ erg s^{-1} and $L_{\rm uv} = 3 \times 10^{45}$ erg s^{-1}. Black, green, yellow, red, and blue lines show the case of $L_e = 1 \times 10^{45}$ erg s^{-1}, 1×10^{44} erg s^{-1}, 1×10^{43} erg s^{-1}, 1×10^{42} erg s^{-1}, and 1×10^{41} erg s^{-1}, respectively. The lobes are located at the distance $D = 100$ Mpc. The proton synchrotron bump is predicted at $\sim$ sub MeV for smaller L_e.

5. Summary

Hadronic emission in extragalactic mini radio lobes is discussed in this work. We calculate broadband photon spectra taking $p\gamma$ interaction and proton synchrotron cooling into account. The powers of standard accretion disk and injected protons are $L_{\rm disk} = 3 \times 10^{45}$ erg s^{-1}, $L_p = 5 \times 10^{46}$ erg s^{-1}, respectively.

For bright lobes with $L_e \sim L_{\rm syn} \sim 10^{45}$ erg s^{-1}, the predicted very high energy emission is detectable with *Fermi*/LAT and HESS. Since it is overwhelmed by the leptonic components in this case, it is hard to figure out whether the γ-ray emission is of hadronic or leptonic origin. For a lobe with $L_e \sim 10^{44}$ erg s^{-1}, secondary $e^{\pm}$ pairs radiate TeV γ synchrotron emission and thus is detectable by the current TeV γ telescopes.

For less luminous radio lobes $L_e \sim L_{\rm syn} < 10^{44}$ erg s^{-1}, the proton synchrotron bump appears in the sub MeV energy band. The synchrotron bump from secondary $e^{\pm}$ pairs created by μ-decay appears at GeV/TeV ranges. If the double bumps due to these hadronic processes are detected, it would be support for the hadronic model since leptonic models do not easily account for such double bumps.

6. Future prospects

We add a comment on the recent radio observation of a mini lobe in 3C 84 which is associated with NGC 1275 ($z = 0.0176$). It shows an outburst around 2005 and a new component C3 emerges with a size smaller than 1 pc (Nagai et al. 2010). *Fermi*/LAT also detected GeV γ-ray emission in the same period (Abdo et al. 2009). Figure 3 displays the actual multi-epoch images of 3C 84 obtained by VERA observations at 22 GHz (Nagai et al. 2010). While the flux of component C3 measured by VERA increases, the GeV γ-ray flux seems to remain constant over the period August 2008 - August 2009 (Kataoka et al. 2010). The difference between the measured flux variations of VLBI and *Fermi*/LAT could indicate a breakdown of the one-zone synchrotron-self Compton model proposed in Abdo et al. (2009). Hadronic emission could partly contribute in γ-ray energy bands, although we did not deal with the specific case of 3C 84 in this work. In order to nail down the real γ-ray emitter, continuous observations by VLBI are quite important.

In the near future, the project of VLBI Space Observatory Programme-2 (VSOP-2) with high angular resolution (Tsuboi et al. 2009) will play a unique role for mini lobe observations. Observations will be made with a 9-m antenna in orbit, together with ground radio telescopes, and will achieve angular resolutions of 40, 80, and 210 microarcsec at 43, 22, and 8 GHz, respectively. In particular, observations at 8 GHz will unveil fine structures of unresolved mini lobes. Furthermore, the era of VSOP-2 will overlap the period in which the next generation TeV γ-ray telescope *CTA* is in operation (http://www.cta-observatory.org/). *CTA* will have a factor of 5-10 improvement in sensitivity in the current energy domain of about 100 GeV to some 10 TeV and an extension of the acces-
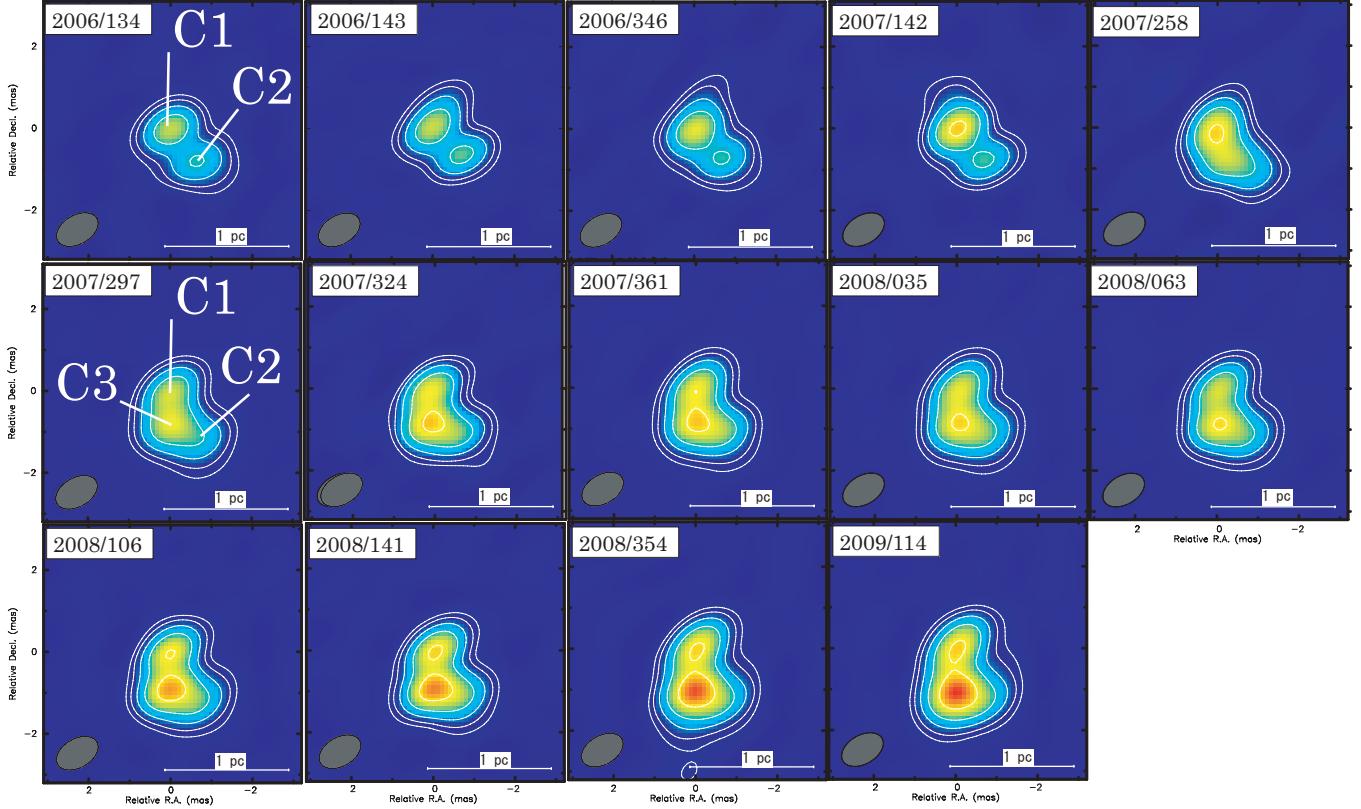
Fig. 3. Multi-epoch VERA images of 3C 84 at 22 GHz. Component C1 is assumed to be the core. Component C3 is the newly born one and it proceeds to the south. The size is still less than 1 pc.

sible energy range to well below 100 GeV and above 100 TeV. Future collaboration between VSOP-2 and *CTA* will be one of the best ways to explore the origin of γ-ray emission from mini radio lobes.

References

Abdo, A. A., et al., 2009, ApJ, 699, 31

Aharonian, F. A., Belyanin, A. A., Derishev, E. V., Kocharovsky, V. V., & Kocharovsky, V. V., 2002, PhRvD, 66, 023005

Asada, K., Kameno, S., Shen, Z.-Q., Horiuchi, S., Gabuzda, D. C., & Inoue, M., 2006, PASJ, 58, 261

Asano, K., & Mészáros, P., 2008, ApJ, 677, L31

Asano, K., Guiriec, S., & Mészáros, P., 2009, ApJ, 705, L191

Begelman, M. C., Blandford, R. D., & Rees, M. J., 1984, RvMP, 56, 255

Fanti, C., AN, 330, 120

Giroletti, M., & Polatidis, A., 2009, AN, 330, 193

Ito, H., Kino, M., Kawakatu, N., Isobe, N., & Yamada, S., 2008, ApJ, 685, 828

Kataoka, J., et al., 2010, ApJ, 715, 554

Kino, M., Ito, H., Kawakatu, N., & Nagai, H., 2009, MNRAS, 395, L43

Nagai, H., et al. 2010, PASJ, 62, L11

O'Dea C. P., Baum S. A., 1997, AJ, 113, 148

Orienti, M., & Dallacasa, D., 2008, A&A, 487, 885

Ostorero, L., et al. 2010, ApJ, 715, 1071 arXiv:0910.3611

Rachen, J. P., & Biermann, P. L., 1993, A&A, 272, 161

Readhead, A. C. S., Taylor, G. B., Pearson, & T. J., Wilkinson, P. N., 1996a, ApJ, 460, 612

Snellen, I.A.G., Schilizzi, R.T., & Miley, G.K. et al. 2000, MNRAS, 319, 445

Snellen, I. A. G., Mack, K.-H., Schilizzi, R. T., & Tschager, W., 2004, MNRAS, 348, 227

Stawarz, Ł., Ostorero, L., Begelman, M. C., Moderski, R., Kataoka, J., & Wagner, S., 2008, ApJ, 680, 911

Tsuboi M., et al., 2009, ASP Conf. Ser. 'Approaching Micro-Arcsecond Resolution with VSOP-2: Astrophysics and Technology', eds. Y. Hagiwara, E. Fomalont, M. Tsuboi, and Y. Murata, 402, 30

Walker, R. C., Dhawan, V., Romney, J. D., Kellermann, K. I., & Vermeulen, R. C., 2000, ApJ, 530, 233

Probing the Physics of Gamma-Ray Blazars with Single-Dish Monitoring Data

M. F. Aller, P. A. Hughes, and H. D. Aller

Department of Astronomy, University of Michigan, Ann Arbor, MI, 48109-1042, USA

Abstract. In the 1990s a comparison of sparse EGRET measurements with single-dish flux density monitoring from the Metsähovi and UMRAO programs established a temporal connection between the onset of flaring at radio band and the occurrence of gamma-ray activity. Correlations between the emergence of new VLBI components from the core, flares in linearly polarized radio flux, and gamma-ray activity in bright EGRET-detected blazars supported a picture in which the gamma-ray and the radio band emission arises in the same shocked region of the jet, with the high energy emission produced via inverse Compton scattering by the synchrotron-emitting electrons in the jet. Quantitative tests of this scenario, however, were hampered by insufficient temporal sampling of the data and the simple nature of the models adopted. The extensive data from *Fermi* coupled with the wealth of well-sampled radio band data from old as well as new programs such as the F-GAMMA project now permit statistical studies for large numbers of sources, including weak HBLs, and detailed analyses of individual highly-active class members. I summarize progress in understanding the origin of the gamma-ray emission using these new measurements. I focus on three areas: attempts to isolate the physical site of the high energy emission using time delay information; investigation of the emission process using the characteristics of the variability; and quantitative tests of the shock model picture using high-time-sampled multi-frequency linear polarization data, VLBP imaging, and new models of propagating oblique relativistic shocks incorporating detailed radiative transfer calculations.

1. Introduction

In spite of the limitation provided by the relative low sensitivity and poor time sampling (detection statistics only) from EGRET, these measurements set the framework for our current understanding of the MeV-to-GeV γ-ray emission from AGN. The enormous increase in sensitivity and the use of large-area sky scan mode rather than pointings made possible by the > 2 sr field of view accessible to the Large Area Telescope (LAT), the principle instrument for studying blazars onboard *Fermi* has resulted in γ-ray light curves with sufficient time sampling to track the variations on intraday time scales during extreme strong flares, and on daily-to-weekly time scales for tens of bright AGN in the energy band $20\,\mathrm{MeV}$ to $> 300\,\mathrm{GeV}$. To match these data, a new generation of radio band monitoring programs has emerged, providing well-sampled light curves for hundreds of sources. These enable investigators to carry out both statistical studies of large samples of AGN to low radio-band flux limit, and detailed studies of individual objects using multi-frequency data provided in support of the *Fermi* mission. Using well-established procedures, including cross-correlations of intra-band data permitting direct comparison of the activity across bands and investigations of the character of the variability itself through analyses which probe the emission process, detailed studies of the variability properties in *both* bands can be carried out. These comparison rely on single-dish monitoring data which provide temporal resolution complementing the spatial resolution provided by monthly-to-less-frequent VLBI imaging measurements. I summarize the current status of these monitoring programs and review what they can tell us about the site of and mechanism for the generation of γ-ray emission from AGN detected by *Fermi*.

2. The EGRET era: setting the stage

The launch of the Compton Gamma Ray Observatory (CGRO) in April 1991 provided us with a new view of familiar blazars. One of the early discoveries from EGRET (the instrument onboard operating above $30\,\mathrm{MeV}$) was the identification of a population of GeV-γ-ray-emitting blazars, positionally associated with well-known radio-bright AGN. Comparison of activity monitored in the millimeter band (37 & $22\,\mathrm{GHz}$) in a sample of ≈ 70 bright sources combined with the EGRET detections in the first EGRET catalogue (Fichtel et al. 1994), the results of an all sky survey carried out from 1991 April to November 1992, established a statistical connection between enhanced radio band activity and detection in the energy band E$>100\,\mathrm{MeV}$ (e.g., Valtaoja & Teräsranta 1995). Note that only a handful of photons were detected by EGRET above $10\,\mathrm{GeV}$ (Thompson 2006), and that much information was extracted based on only a small number of photons in these early studies. Even with the paucity of EGRET data and the relatively small number of sources detected, it became quickly apparent that these γ-ray-detected sources were predominantly radio-bright, compact, core-dominated blazars with high brightness temperatures (Valtaoja & Teräsranta 1996). Further, a temporal association between the occurrence of an EGRET detec-
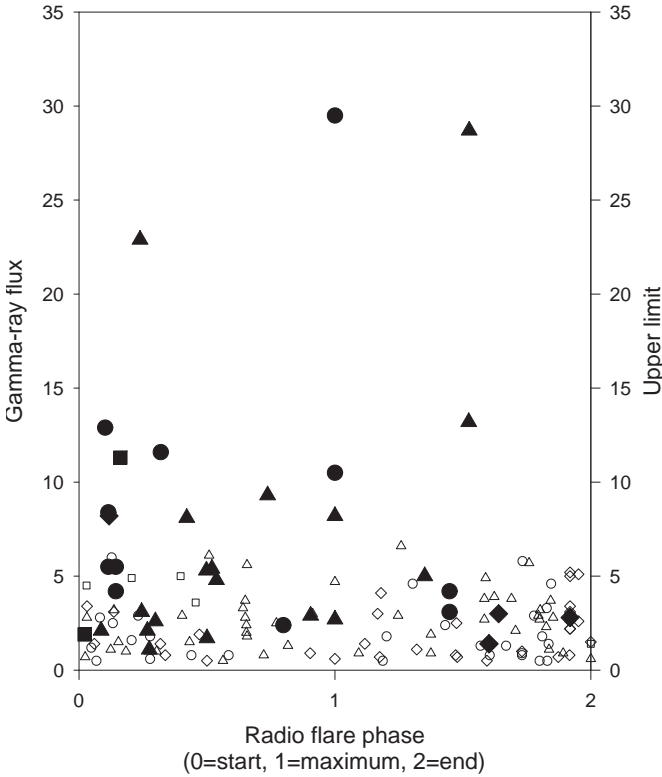
Fig. 1. Time of occurrence of γ-ray detection as a function of flare phase based on Metsähovi data. Figure courtesy A. Lähteenmäki

Fig. 2. γ-ray flux versus Metsähovi peak flare flux. Figure courtesy A. Lähteenmäki.

tion and the rise portion of the radio band flare (start of flare to maximum) was established for individual events using both the millimeter (Valtaoja & Teräsranta 1996) and the centimeter band (Aller, Aller & Hughes 1996) total flux density monitoring data. An example plot illustrating this result is shown in Figure 1 which includes EGRET phase 1+2+3 γ-ray data and Metsähovi monitoring measurements obtained during this time period (see also Lähteenmäki & Valtaoja 1999). Because of the severe undersampling of the EGRET data, however, it was not possible to carry out cross-correlation analyses between the two bands.

Attempts to correlate γ-ray photon flux and radio flare peak flux or radio luminosity yielded mixed results that ranged from no clear correlation (Aller, Aller, & Hughes 1996) to claimed correlations. This discrepancy stemmed from a variety of causes including the use of non-simultaneous data, dependence of the luminosity on redshift, and time delays between the radio and γ-ray activity produced by opacity in the radio jet (Mücke et al. 1996). An example flux-flux correlation is shown in Figure 2 based on detections from EGRET and monitoring observations from the Metsähovi program (see Lähteenmäki et al. 1997).

Studies of a handful of individual, exceptionally-bright sources for which the binned EGRET measurements yielded multiple detections (time-averaged photon flux values as a function of time), in combination with radio band light curves and VLBI imaging data, confirmed the

physical association between flaring in the two bands identified statistically. Analysis of the data for sources such as NRAO 530, confirmed the general trends but found cases of γ-ray detections during declining or constant millimeter-to-centimeter band flux (Bower et al. 1997) which deviated from the general trends.

The link to flaring, and subsequently the identification of a specific flare phase established a connection to the development of individual radio band outbursts. Since the radio band variations are generally attributed to shocks in the radio jet, this connection led investigators to the conclusion that shocks might also play a role in the generation of the γ-ray flaring (e.g., Valtaoja & Teräsranta 1996).

Linear polarization monitoring data track temporal changes in magnetic field structure. In well-resolved events, such data can be used to search for the signature of a shock: a swing in electric vector position angle (hereafter EVPA) and an increase in the fractional linear polarization (hereafter LP). These changes are associated with the compression of the initially tangled magnetic field during the passage of the shock. The 22 & 43 GHz VLBA imaging data for 42 γ-ray-bright blazars obtained from the Jorstad & Marscher program, in combination with UMRAO linear polarization monitoring data, were used to identify a correlation between high γ-ray state and an increase in polarized radio band flux supporting a picture in which the radio emission and the γ-rays originate in the same shocked region of the jet, with the γ-ray emission pro-

duced by inverse Compton scattering in the thin forward region of the shock where the electrons are accelerated (Jorstad 2001). This scenario placed the γ-ray emission site parsecs far from the central engine and downstream of the radio band core.

The majority of the EGRET-detected sources were highly luminous HPQs. With only a few exceptions, these were the very same radio-bright sources which had been included for decades in the Metsähovi and UMRAO flux monitoring programs. We now know that this was a selection effect resulting from the limited sensitivity of EGRET.

3. Single-dish radio band monitoring during the *Fermi* era

In spite of the progress made in understanding the origin of the γ-ray emission using the EGRET data, answers to many questions remain in areas where single-dish monitoring data can provide insights. Specific questions which can be addressed using these data are:

1. Where within the jet is the γ-ray flare produced? This question can be examined using cross identification of flares in the high energy and radio bands. A combination of single-dish monitoring and VLBI imaging can be used to localize the physical site of the high energy emission using the radio core as a fiducial reference point.

2. What emission mechanism is responsible for the generation of the γ-ray emission? This can be explored using SEDs based on contemporaneous broadband measures, including single-dish total flux density data at multiple epochs. These trace the evolution in the νF_ν versus ν plane.

3. What is the mechanism for acceleration of the particles? Tests for the presence of shocks during γ-ray flaring using a combination of data and modeling can be carried out.

4. What special conditions are present in the jet during broadband flaring? Information on jet properties during individual flares and on changes in jet conditions can be derived using single-dish measurements.

Fermi scans the sky every 3 hours providing data which can be analyzed to study the variability in the MeV-GeV band on near-daily to weekly time scales. In support of this program several new programs as well as continuing old ones monitor the total flux density of AGN. The salient features of several of these programs providing data in the centimeter-to-millimeter band for sources north of approximately -30° are summarized in Table 1. The first three entries form the F-GAMMA alliance which works in tight coordination. The OVRO program provides time-sampling at a single frequency, 15 GHz, temporally matched to that attained using *Fermi*. Observations in this band are well-suited for tracking variability since the amplitude of the variability is relatively large compared to that at lower frequencies, and the measurements are relatively free from tropospheric effects which increase with higher frequency. The UMRAO and Metsähovi programs provide long term

Table 1. Current Single-Dish Monitoring Programs

Prog.	freq. (GHz)	sampling	size/advantage
OVRO	15	2–3/week	>1000 many sources; low S
Effsbg.	2.64–43	monthly	≈60 spectra
IRAM	86–270	monthly	≈60 inner jet
UMRAO	4.8, 8, 14.5	1–2/week	35 in core grp. mf; includes LP
Metsähovi	37	monthly	≈100 inner jet
RATAN-600	1–22	2–4/year	600 spectra

histories for smaller numbers of sources and with less-frequent cadence. The AGN population now detected by *Fermi* includes a substantial population of radio-weak sources belonging to the HBL class. These radio-weak sources can only be monitored using single-dish instruments with large collecting areas such as the OVRO 40-m telescope and the Effelsberg 100-m instrument. Spectral data is provided by Effelsberg/IRAM and the RATAN-600 programs. Together the data base of observations includes both temporal and spectral coverage for a large number of sources. Multi-frequency data, including linear polarization measurements, are themselves important for identifying both self-absorption and Faraday effects.

4. Is the broad band activity causally related? Radio band-γ-ray correlations

Evidence in support of a statistically-significant correlation between the fluxes in the two bands would support the hypothesis that the emissions are related. Results based on observations from the OVRO program for 49 sources in the *Fermi* LAT three month catalogue are shown in Figure 3 from the work of Richards et al. (2009). The data shown are averages over the three month period August 4 – October 30, 2008. A correlation is apparent visually. A formal analysis gives a correlation coefficient of r=0.56; Monte Carlo simulations indicate a chance probability of this correlation of only 5×10^{-4}.

Figure 4 shows the flux-flux correlation obtained using results from MOJAVE for sources in the high-confidence 3-month LAT list (Abdo et al. 2009) with radio flux density >0.2 Jy and $\delta \geq$-30 degrees. The 15 GHz fluxes shown include both MOJAVE data (total flux density over the entire VLBA image) and supplementary UMRAO and RATAN-600 fluxes (shown by open circles). This work found a correlation between the γ-ray flux in the first three months of *Fermi* operation and these quasi simultaneous 15 GHz fluxes, and identified that the radio jet was in an
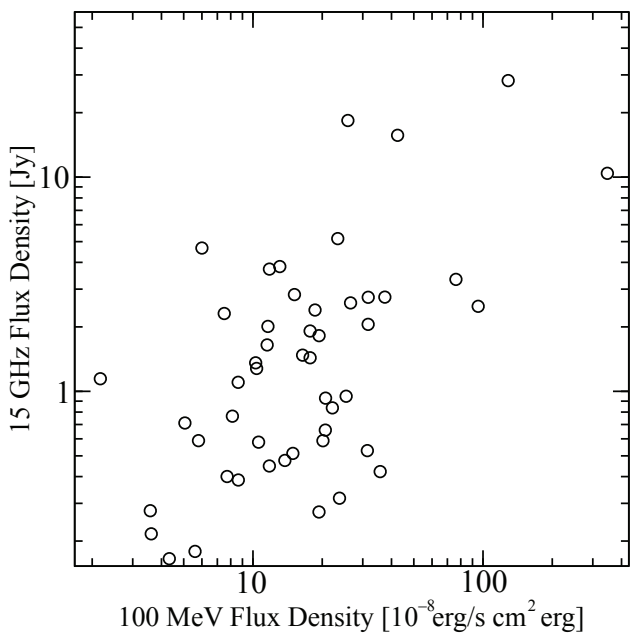
Fig. 3. *Fermi* LAT flux density in the 100 MeV energy band versus OVRO 15 GHz flux density based on data obtained in the first 3 months of operation (Richards et al. 2009).
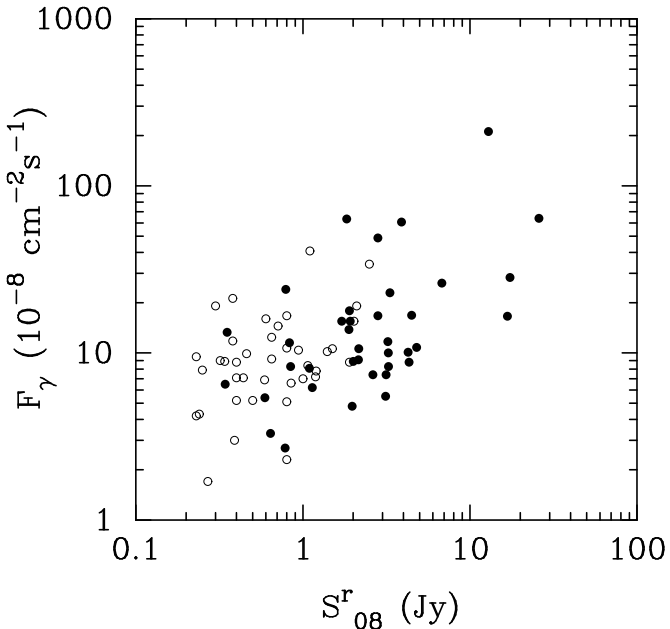

Fig. 4. Average γ-ray photon flux in the 100 MeV–1 GeV energy band versus 15 GHz flux for sources in the MOJAVE sample (from Kovalev et al. 2009).

enhanced state near the time of strong γ-ray emission for sources in this group (Kovalev et al. 2009).

5. Characterization of the Variability

Variability time scales, variability amplitude, quasi-periodicities, and indicators of the noise process producing the variability can be extracted from the detailed study

of light curves. Common analysis tools include structure functions, PDSs, and wavelets. Useful measures of the degree of variability include the fluctuation index and the normalized excess variance. Similar characteristics in the variability of the two bands would support a related origin. However, a sufficiently long data train is required to capture the characteristics of the variability.

5.1. Results

Structure functions, autocorrelations and power spectra are related measures of the distribution of power versus time. Structure functions can provide both a characteristic time scale and a "measure" of the noise process; the former comes from the time lag where the curve plateaus and the latter from the slope of the curve. First order structure functions were computed for the best observed (i.e., most variable) sources in the UMRAO program (Hughes, Aller, & Aller 1992); the turnover yielded a characteristic variability time scale of 2 years while the slope, generally near 1, was consistent with shot noise. Because of the length of the data train in the radio band, several events in each source were captured in general; in a few sources, e.g., 3C 84 and 3C 454.3, the variability was dominated by a single event, and in these cases the slope of the structure function was 1.55 -1.6.

In the case of the γ-ray data, nearly two years of data have accumulated. A study containing light curves of 106 sources showing weekly averages of the data (E>300MeV) obtained over the first 11 months of operation has recently been submitted for publication which includes analysis using structure functions and PDSs. (Abdo et al. 2010c). Characteristic structure function power indices are in the range 1.0 to 1.6. Higher values are found for 0235+164 and 3C 454.3; in these sources the light curves are dominated by a single large event. The light curves of these two objects in the radio band show the same characteristic behavior during this time period.

5.2. Time-Delay Studies

The site of the γ-ray emission can in principle be identified relative to the emission site for the radio emission from time delays by using well-sampled light curves to look for correlated activity. If similar features can be unambiguously identified, the associated time delays, provide information on the location of the γ-ray emission site. In the radio band this can be referenced to the radio core at 43 GHz identified from VLBI imaging. Monitoring observations from the OVRO program have traced the total flux density variability at 15 GHz in hundreds of sources with a time sampling well-matched to that provided by the LAT. Cross-correlation of the OVRO 15 GHz and early *Fermi* data for a few representative cases are presented in Max-Moerbeck (2009). These few examples illustrate that a range of behavior patterns are present in the time delays. While activity is clearly associated across the spectrum,
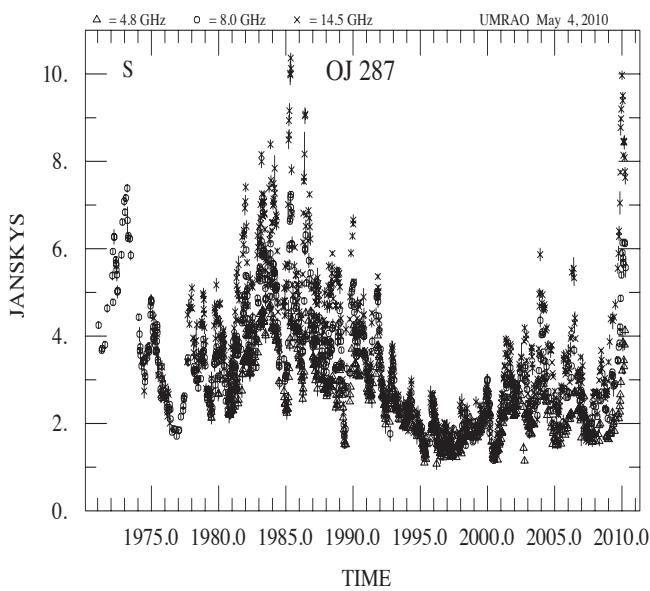
Fig. 5. Weekly averages of the total flux density for OJ 287 from the UMRAO program showing triple-frequency data obtained over 4 decades.

Fig. 6. Evolution of the SED during γ-ray flaring. The filled symbols denote data obtained during the first five days of a sharp γ-ray flare. The unfilled triangles show data obtained about 70 days later during a time when the γ-ray flux was relatively quiescent. In the radio band, the total flux density showed a small systematic decline. The figure was kindly provided by M. Hayashida.

unambiguously identifying individual events across the spectral bands is extremely difficult except during rare, large-amplitude, resolved flares. In other cases, frequency-dependent factors including self-absorption and opacity, differ from source to source and affect the time delay results. An underlying problem in such comparisons is that persistent trends may not exist from source to source, or even in the same source from epoch to epoch; this lack of persistence has recently been quantitatively examined in the optical to γ-ray regime and attributed to variations in a number of parameters which are important in the emission process (Böttcher & Dermer 2010).

5.3. Periodicity

Quasi-periodicities have been identified in several sources observed in the UMRAO program using a variety of analysis tools. The strongest evidence for periodicity in the centimeter band for any source is for OJ 287. Visual inspection of the light curve for this source shown in Figure 5 reveals a long term trend with superimposed flares. Quasi periodic behavior has been identified in this source using wavelets (Hughes, Aller, & Aller 1998). The total flux density amplitude is currently approaching the maximum value attained over the UMRAO multi-decade time period, and the source is also bright at γ-ray band (see Figure 8). No evidence for periodicity has been found (yet) using the *Fermi* light curves over the first 11 months of operation, and it will be very interesting to see what analyses of longer data trains reveal.

6. Emission Process: studies of SEDs using single-dish data

With the high time sampling now available, the evolution of the SED during individual events can be followed; such data can provide insight into the emission mechanism using modeling. The low frequency hump is generally attributed to synchrotron emission produced in the jet, while the second (high frequency) hump is often attributed to a complex mix of components (e.g., Abdo et al. 2010d). An example SED during flaring is shown for 3C 279 (Abdo et al. 2010a) in Figure 6. In the radio band the SEDs at the two epochs overlay, while significant differences in the two time intervals are apparent in all other bands.

7. Mechanism for particle acceleration: Shocks in the radio jet during γ-ray flaring

Independent evidence in support of a scenario in which shocks propagating outward in the jet flows are the origin of the observed blazar activity in the radio through optical spectral regions has come from both model fits of broadband spectral data (e.g., Marscher & Gear 1985) and of fits to centimeter band multi-frequency flux and linear polarization data during outburst using transverse shock models (e.g., Hughes, Aller, & Aller 1989). One possibility for the origin of these disturbances is Kelvin-Helmholtz-induced instabilities. Both detailed hydrodynamical simulations of jet flows and stability analyses have confirmed that such instabilities develop naturally and commonly in the kinetically-dominated portion of the jet; current driven instabilities have also been considered and may dominate in the magnetically dominated regime near the central engine (e.g., Hardee 2006). Shocks have been cited as a means of particle acceleration resulting in flaring in
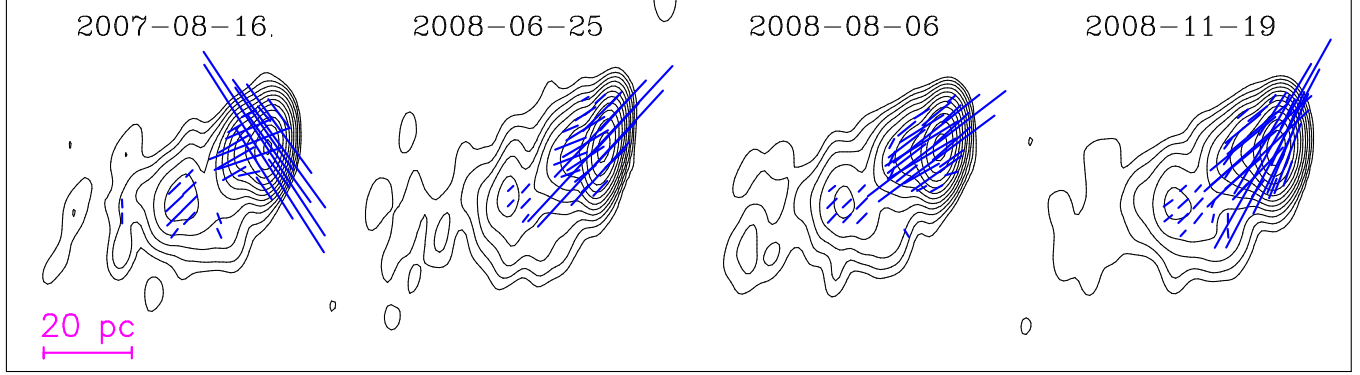
Fig. 7. EVPA swing detected by MOJAVE in 1502+106 at epochs bracketing the 2008 August flare. The most significant changes occurred during the time interval between the first and the second images shown. Figure provided by Y. Y. Kovalev.

the γ-ray band, but searches for specific evidence of shocks during γ-ray flaring have not been widely conducted. In principle, shocks in the parsec scale regime of the jet can be identified by searches for the expected swing in the orientation of the EVPA, apparent in consecutive VLBP images, but in general the VLBI sampling is too sparse to 'detect' these transitions. An example of this kind of flip in EVPA is shown in Figure 7 which displays the MOJAVE 15 GHz images bracketing flaring detected by *Fermi* 'near' to a major flare which occurred in 2008 August (Abdo et al. 2010b). In general the VLBA imaging data is too sparsely sampled to permit following a shock event in detail. Single-dish monitoring of the linear polarization can provide the temporal resolution, but the shock signature will be smoothed out if there are contributions to the emission from many competing, evolving components. In sources dominated by a single or only a few components, the signature of a shock appears in the single-dish monitoring data as as ordered swing in EVPA (through 90 degrees in the special case of a transverse shock) combined with an increase in the degree of linear polarization. In the general case, shocks are expected to be oriented obliquely to the flow direction. The emission properties of such shocks have not been explored in detail in past studies.

As part of the Michigan monitoring program, we are currently obtaining single-dish monitoring observations with a cadence of 1–2 times weekly of both the total flux density and the linear polarization for a small sample of sources known to be flaring in the γ-ray band and sufficiently bright (S≥0.4 Jy) in the radio band to look for a shock signature during times of γ-ray flaring. The program sources (3C 66A, 0235+164, 3C 84, 0420−014, 0454−234, 0528+134, 0716+714, 0727−115, 0805−077, OJ 287, 3C 273, 3C 279, 1308+326, 1502+106, 1510−089, 1633+382, OT 081, 2022−077, BL Lac, CTA 102, & 3C 454.3) are all members of MOJAVE, and 15 of the 21 are in the Boston U. 43 GHz blazar program led by A. Marscher and S. Jorstad. These VLBI data provide crucial complementary information on flow direction relative to the magnetic field orientation and a pattern speed characterizing the jet flow, as well as a means for identify-
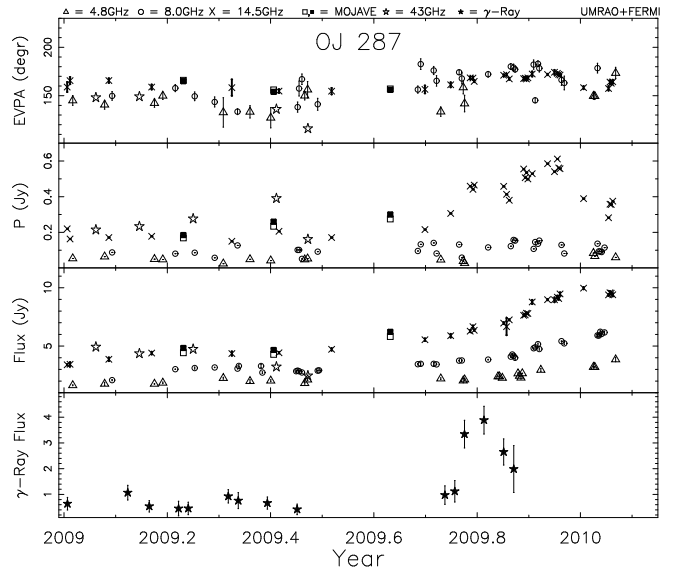
Fig. 8. Shock signature during flaring in OJ 287 in late 2009. From bottom to top weekly-averaged γ-ray photon flux and daily averages of radio band total flux density and LP (fractional linear polarization and EVPA), For comparison VLBA fluxes at 43 GHz (denoted by stars) and a 15 GHz from MOJAVE (source-integrated values filled squares; core only unfilled). γ-ray fluxes (units photons/sec/cm^2×10^{-7}) were kindly provided by S. Jorstad (private communication).

ing sources with relatively simple structure. Example light curves obtained for one of our program sources, OJ 287, are shown in Figure 8. The LP exhibits the expected oblique shock signature – a swing in EVPA through about 40° and an increase in fractional linear polarization from near 0 to a maximum value approaching 8% – temporally associated with the γ-ray flaring in late 2009. The LP swings in EVPA that we have found in this and other sources take place over a time period of order one to two months and require frequent measurements to properly track the variability. In addition to the UMRAO light curves, we show in this figure MOJAVE 15 GHz and BU 43 GHz measurements for comparison. These illustrate the
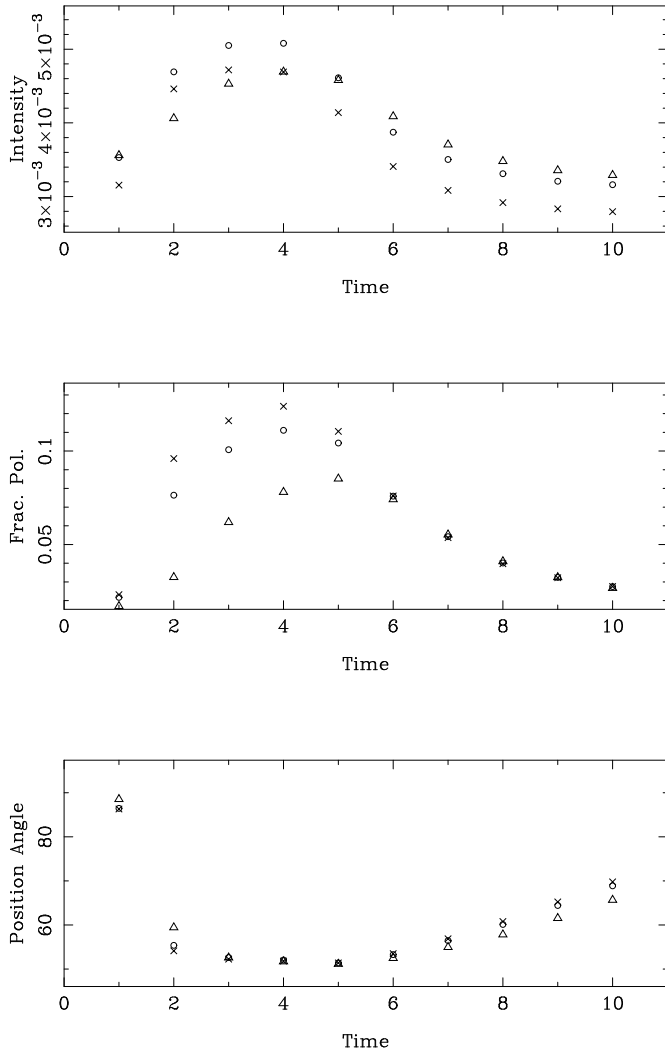
Fig. 9. Simulated light curves from radiative transfer calculations showing from top to bottom total intensity, fractional polarization, and EVPA for three frequencies. The Lorentz factor of the flow=2.5, the Lorentz factor of the shock= 6.7, and the viewing angle=10 degrees. Other model parameters are given in the text.

excellent agreement between the single-dish and VLBA results and graphically show the sampling rate relative to the rapidity of the event itself. Note that in spite of the self-absorption apparent in the UMRAO light curve in the 4.8–14.5 GHz band, that the spectrum is relatively transparent in the 15–43 GHz domain as indicated by the nearly equal flux amplitudes in total flux and linear polarization.

To explore the effect of the various input parameters on the predicted light curves and eventually to use the models to analyze specific events, we have developed new radiative transfer models which incorporate oblique shocks. These models assume an extreme relativistic equation of state and are determined principally by two free parameters: the shock compression and the direction of the shock (forward or reverse). The direction is important for time delay considerations. From modeling of such events, information can be extracted about the conditions in the

jet during γ-ray flaring; changes in these conditions from event to event can be identified and explored as more data accumulates.

We show in Figure 9 representative, simulated light curves from this work. In the example shown, a shock oriented at an obliquity of 45 degrees to the flow direction has been introduced into the relativistic flow at t=0. A forward-moving shock and a compression of 0.7 have been assumed. The model predicts the general features apparent in the data (see Figure 8): a total flux outburst, an increase in the linear polarization to near 10%, a swing in EVPA through about 40 degrees, and the general spectral behavior. Figure 10 contains a series of images showing the evolution of the simulated structure. Images such as these will be generated for comparison with VLBP imaging data to serve as model constraints in the fitting procedure.

8. Future Work

Comparison of the variability detected in the *Fermi* and radio spectral bands continues to support a generic scenario in which the same disturbance is responsible for both the radio band flares and the γ-ray activity, most likely a shock, located near the radio core in the spine of the radio jet (e.g., A. Pushkarev, This Workshop). However, some nagging exceptions to this simple picture remain. For example it does not account for the presence of rapid (hourly) variability in the γ-ray emission detected during strong flares by *Fermi* (Tavecchio et al. 2010), and known from earlier EGRET results. This rapid variability implies a small source size and can most easily be explained by an emission site near the central engine. Such results call into question the completeness of a picture which attempts to explain all emission as originating at one site and by one mechanism. Exceptions to the rule need to be reconciled with the generally-adopted picture.

The specific conditions in the jet leading to γ-ray flaring have not been isolated. These can be examined using a combination of the unique temporal resolution provided by single-dish monitoring, spatial information from VLBI studies, and detailed modeling of the emission patterns. Model development, such as the shock modeling described here, is only in its very early stages. Refinement will include the development of more sophisticated models and fits of these models to specific flares.

Data from large telescopes such as the OVRO 40-m and the Effelsberg 100-m dishes probe the variability properties of pure BL Lacs and the large population of radio-weak HBLs, with sub-weekly cadences which can not be provided by VLBI imaging alone. Detailed analyses of these sources may reveal other properties and behavior patterns which need to be included in the general picture. Recent work from Metsähovi suggests that even the RBLs may have different emission properties characterized by γ-ray photon fluxes which are weak relative to those from other source types and uncorrelated with radio-band flaring (Leon-Tavares, This Workshop).
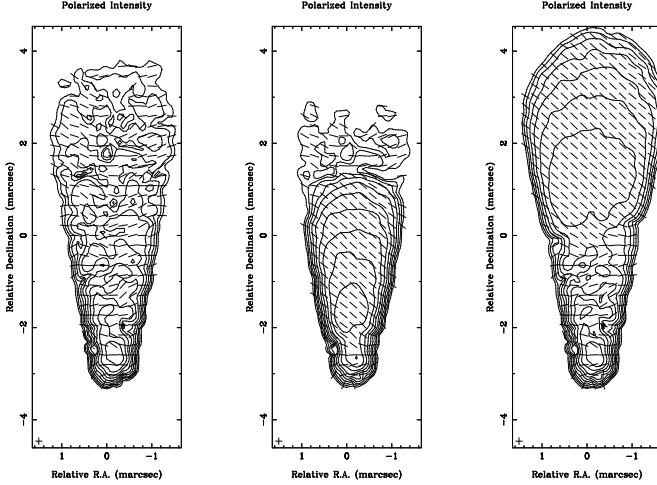
Fig. 10. A sequence of simulated images from radiative transfer calculations showing polarization contours and EVPA orientation as a function of time.

Long-term light curves in both the optical and radio spectral bands, have identified that there are changes in the character of the variability on time scales of several years to decades. Searches for associated changes in the character of the radio band and γ-ray activity as the *Fermi* data accumulates would be further support of an intimate connection between the emission in these two regimes. Such studies will rely on historical data from long-term programs which provide consistently acquired data at a common observing frequency in combination with the data acquired during the operation of *Fermi*.

The first indications of an association between the emission in the radio and γ-ray bands came from observations of a few extreme sources and limited photon statistics by EGRET. This general picture can be refined and filled in using the wealth of data now available from both the single-dish data in the radio band and *Fermi* data. This will not an easy task because of the complexity of the emission patterns and the dependence on many parameters, but exciting, new results will surely result enhancing our understanding of Blazars during the *Fermi* era.

References

Abdo, A. A., et al. 2009, ApJ, 700, 597

Abdo, A. A., et al. 2010a, Nature, 463, 919

Abdo, A. A., et al. 2010b, ApJ, 710, 810

Abdo, A. A., et al. 2010c, ApJ, submitted (astro-ph 1004.0348)

Abdo, A. A., et al. 2010d, ApJ, 716, 30

Aller, M. F., Aller, H. D., & Hughes, P. A. 1996, in Extragalactic Radio Sources, ed. R., Ekers et al. (Kluwer, Dordrecht), 283

Böttcher, M., & Dermer, C. D. 2010, ApJ, 711, 445

Bower, G. C., Backer, D. C., Wright,, M., Forster, J. R. Aller, H. D., & Aller, M. F. 1997, ApJ, 484, 118

Fichtel, C. E., et al. 1994, ApJ Suppl., 94, 551

Hardee, P. E. 2006, in Blazar Variability Workshop II: Entering the GLAST era, ASP Conf. Ser. Vol., 350, 205

Hughes, P. A., Aller, H. D., & Aller, P. A. 1989, ApJ, 341, 68

Hughes, P. A., Aller. H. D., & Aller, M. F. 1992, ApJ, 396, 469

Hughes, P. A., Aller, H. D., & Aller, M. F. 1998, ApJ, 503, 662

Jorstad, S., et al. 2001, ApJ, 556, 738

Kovalev, Y. Y., et al. 2009, ApJ Letters, 696, L17

Lähteenmäki, A., Teräsranta, H., Wiik, K., & Valtaoja, E. 1997, in Proc. of the Fourth Compton Symposium, ed. C. D. Dermer, M. S. Strickman, & J. D. Kurfess, AIP, 1452

Lähteenmäki, A., & Valtaoja, E., 1999, in BL Lac Phenomenon, ASP Conf. Ser. Vol 159, ed. L. O. Takalo & A. Sillanpää, 213

Marscher, A. P., & Gear, W. K. 1985, ApJ, 298, 114

Max-Moerbeck, W. 2009, Fermi Symposium Proceedings, eCong09112 (astro-ph 0912.3817)

Mücke, A., et al. 1996, in Extragalactic Radio Sources, ed. R., Ekers et al. (Kluwer, Dordrecht), 285

Richards, J. L., et al. 2009, Fermi Symposium Proceedings, eConf091122 (astro-ph 0912.3780)

Tavecchio, F., Ghisellini G., Bonnoli, G., & Ghirlanda, G. 2010. MNRAS, online version of article

Thompson, D. J. 2006, in Blazar Variability Workshop II: Entering the GLAST Era, ASP Conf. Ser. Vol. 350, 113

Valtaoja, E., & Teräsranta H. 1995, Astron. Astrophys. 297, L13

Valtaoja, E., & Teräsranta, H. 1996, Astron. Astrophys. Suppl., 120, 491

From EGRET to Fermi: mm-radio data and the origin of gamma-ray emission

E. Valtaoja[1], M. Tornikoski[2], J. León-Tavares[2], E. Nieppola[2], A. Lähteenmäki[2], J. Tammi[2], and T. Hovatta[3]

[1] Tuorla Observatory, Department of Physics and Astronomy, University of Turku, 20100 Turku, Finland
[2] Aalto University, Metsähovi Radio Observatory, Metsähovintie 114, FIN-02540 Kylmälä, Finland
[3] Department of Physics, Purdue University, IN 47907, USA

Abstract. In a series of papers between 1995 and 2006 we have compared the EGRET data with our Metsähovi mm-radio monitoring, seeking clues to the origin of gamma radiation in active galactic nuclei. Our most important conclusion was that at least the strongest gamma-ray flares originate in shocks propagating down the jet, parsecs outside the BLR and the most obvious sources of external seed photons, a result also supported by comparisons with VLBI data. We have now repeated a large fraction of our previous analyses using the wealth of new *Fermi* data. This paper summarizes our results, comparing them to our previous conclusions. The *Fermi* data supports our proposed scenario of gamma-rays originating in shocks, not close to the black hole and the accretion disk as the majority view was during the EGRET era.

1. Introduction

Why are some extragalactic sources gamma-ray bright and others not? What is the mechanism, or mechanisms, responsible for gamma-ray emission? Where in the source does the emission process take place?

The very first EGRET observations gave rise to these fundamental questions about extragalactic gamma-ray sources. Some firm conclusions had been reached by the end of the EGRET era, while others remained highly debated. Very quickly it became obvious that only extragalactic radio sources were gamma-bright; no radio-quiet AGN were detected. Since radio brightness is due to synchrotron emission from relativistic jets, an almost inevitable conclusion was that gamma-rays were created by the inverse Compton process, with relativistic synchrotron-emitting electrons (or, in principle, protons) up-scattering photons to the required energies. However, beyond this the agreement ended. A huge effort of theoretical modelling served to illustrate that many different models and assumptions could reproduce the EGRET observations of a given source; for the best-observed source, 3C 279, up to a dozen significantly different but acceptable model fits were published throughout the years. The EGRET data simply lacked the sensitivity and the time coverage to sufficiently constrain the modelling efforts.

The majority view was that gamma-ray emission occurred close to the most copious sources of photons, the accretion disk and the broad line region, with External Compton (EC) seed photons dominating the process. However, for the TeV BL Lacs synchrotron-self-Compton (SSC) models seemed to give the best fits to the data.

Our research group concentrated on the connections between mm-radio (mainly 37 GHz) and gamma-ray data. This led us to accept a definitely minority view, pre-sented in a series of papers beginning in 1995: at least the strongest gamma-ray flares are produced in the growing shocks in the relativistic jets, parsecs downstream from the radio core and even more distant from the black hole and the accretion disk. Well beyond the BLR, either these gamma-rays had to be SSC or there had to be another source of external seed photons. The main, though not the only, argument in favor of this conclusion was that the strongest gamma-ray flares tended to occur *after* the beginning of the mm-radio flare (e.g., Valtaoja and Teräsranta 1995, 1996; Lähteenmäki and Valtaoja, 2003; Lindfors et al. 2006). A similar conclusion was independently reached by Jorstad et al (2001), who found that strong gamma-ray emission tended to occur a few months after the ejection of a new superluminal component.

With the first eleven months of *Fermi* data, we can now revisit this and other conclusions we reached when comparing the EGRET data to our mm-radio monitoring. In Section 2 we summarize our earlier findings, and in Section 3 we present results from our new analysis, also presented in the contributions by León-Tavares et al., Nieppola et al. and Tornikoski et al. in these proceedings, pp. 93 , 89 , and 85 , respectively)

2. Previous results from comparisons of EGRET and mm-radio data

High radio frequency observations, both continuum and VLBI, are invaluable for gamma-ray studies, because they probe the only regime where we know with certainty both the emission mechanism (synchrotron radiation) and the emission site (shocks propagating downstream from the radio core in a relativistic jet). Thus, if correlations can be established between radio and gamma-ray variations,
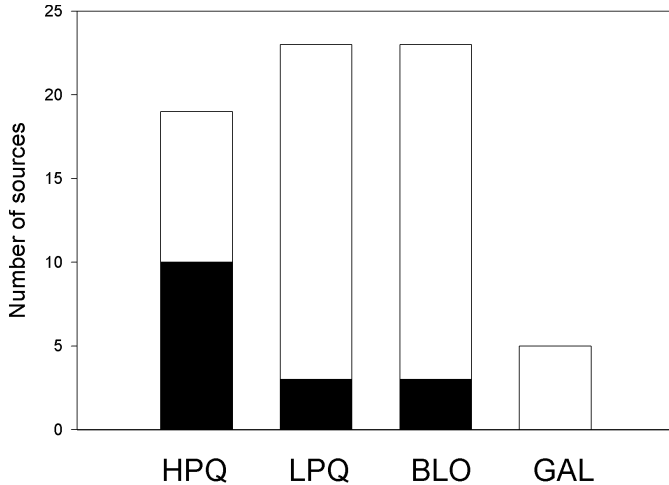
Fig. 1. The fraction of detected sources of the Metsähovi monitoring sample in the EGRET all-sky survey. Adopted from Valtaoja and Teräsranta 1995.

Fig. 2. The fraction of detections during EGRET Phase 1 pointings towards sources in different states of mm-radio activity. INC, increasing radio flux, MAX, close to local maximal radio flux, DEC, decreasing radio flux, MIN, low radio flux. Adopted from Valtaoja and Teräsranta 1995.

Table 1. EGRET gamma-ray observations of 3C 279 versus the time elapsed since the onset of the latest synchrotron flare. Gamma-ray state according to Hartman et al. (2001).

Epoch	Time elapsed (years)	Gamma-ray state
1996.09	0.006	very large flare
1999.07	0.195	high
1996.06	0.206	high
1991.47	0.225	high
1993.86	0.288	moderate
1997.47	0.328	moderate
1993.98	0.409	moderate
1993.00	0.490	low
1997.01	0.924	low
1994.97	0.990	low

they can help to pinpoint the site of gamma-ray emission. In practice, there are several difficulties. There's always a lot going on in the jet, with several overlapping radio continuum flares contributing to the total flux at any given time (e.g., Valtaoja et al. 1999), and, correspondingly, several shocks visible in the VLBI maps, any of which could in principle contribute to the IC component (e.g., Savolainen et al. 2008). Even from EGRET data it was also obvious that radio and gamma-ray variations have different timescales, making straightforward correlation analysis difficult. In consequence, arguments for a radio-gamma correlation need to be statistical.

The only unbiased EGRET data came from Phase 1 all-sky survey; after that, all observations were of preselected sources. This data was analyzed by Valtaoja and Teräsranta (1995, 1996). Figures 1 and 2 show the main results. Strong gamma-ray emitters were overwhelmingly quasars with high optical polarization (HPQs), not "blazars" (an ill-defined class which includes BL Lac objects). Additionally, detections were preferentially made during a rising or peaking mm-radio flare. The crucial fact that gamma-ray flares did not precede radio flares but occurred during their growth led Valtaoja and Teräsranta to suggest that gamma-rays must also originate in the shocks. This conclusion was strengthened by the fact that there seemed to be a correlation also between the gamma-ray flux and both the radio flare flux and radio flare slope (i.e., the Doppler boosting) (Valtaoja and Teräsranta 1996).

Our findings were summarized in Lähteenmäki and Valtaoja (2003). Looking at all the EGRET data, the main conclusions were as follows. (1) Both the EGRET detection probability and the strength of the gamma-ray emission depend on the concurrent radio state of the source in question. (2) There is a clear dependence between source type and gamma-ray emission, with HPQs being the strongest emitters and BL Lacs in generally weaker gamma-ray sources. (3) No convincing correlations

between gamma-ray strength and other source properties were found, with the exception that the so-called gamma dominance, the ratio S_{gamma}/S_{radio} increases with increasing Doppler boosting. However, this dependence vanished after the K-correction was applied to the gamma-ray fluxes. (4) As shown in Figs. 3 and 4, strong gamma-ray flaring occurred preferentially during the rise or peak of the mm-radio flare, indicating a co-spatial origin in the shocks. For weaker gamma-rays the dependence was less clear, and for BL Lacs (all weak gamma-emitters, as a comparison of Figs. 3 and 4 demonstrates) it was not seen. It was suggested that different mechanisms might be dominant in different classes of sources, and in strong vs. weak gamma-ray activity.

Lähteenmäki and Valtaoja also estimated the average delay from the onset of the 37 GHz flare to the strong gamma-ray flares, finding it to be 30–70 days - corresponding to an average distance of 4.9 pc downstream from the radio core, well beyond even the largest BLR. A similar
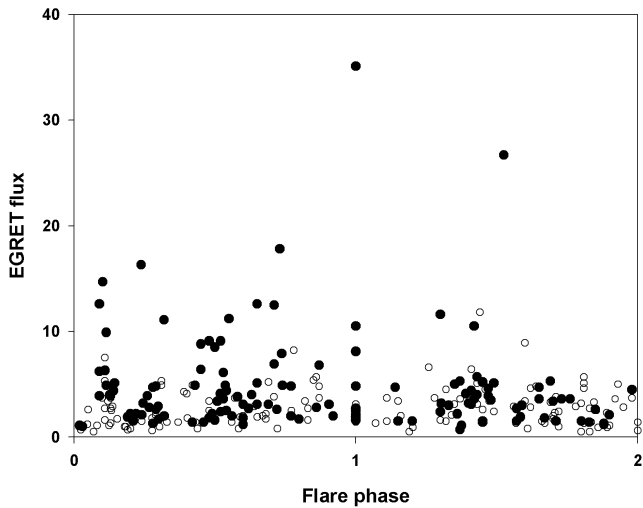
Fig. 3. Observed EGRET flux (during pointed observations) versus flare phase for all quasars monitored in Metsähovi. Flare phase: 1 = beginning, 2 = maximum and 3 = end. Filled dots = detections, open dots = upper limits. Adopted from Lähteenmäki and Valtaoja, 2003.

Fig. 4. Observed EGRET flux (during pointed observations) for all BL Lacs monitored in Metsähovi. See Fig. 3 for details. [Adopted from Lähteenmäki and Valtaoja (2003)]

conclusion was reached by Jorstad et al. from comparisons with VLBI data, who found the gamma-ray emission to occur 52 ± 76 days after the VLBI zero-separation epoch.

Finally, Lindfors et al. (2005, 2006) made a detailed study of the best-observed EGRET source, 3C 279. They modelled the whole multi-frequency behaviour by fitting simultaneously all near-IR to radio data to a succession of outbursts defined according to the shock-in-jet model of Marscher and Gear (1985). A very clear correspondence was found between the time elapsed since the start of the latest outburst and the gamma-ray state during the 10 EGRET observing periods: the longer the time elapsed, the weaker the gamma-ray emission, as shown in Table 1.

In summary, all the available EGRET-era data indicated that at least strong gamma-ray flaring tended to occur after, not before, the onset of a synchrotron flare in the jet. This could only mean that the gamma-rays were indeed coming from the shocks outside the BLR, not upstream of the radio core, very close to the accretion disk and the black hole as virtually all modelling efforts assumed. However, EGRET data was sparse, with large error bars, selection effects and with hardly any temporal information to tie it to events at lower frequencies. We had to wait for *Fermi*.

3. First eleven months of Fermi data

We have compared the data from the *Fermi*/LAT First Source Catalog (Abdo et al. 2010) with the Metsähovi 37 GHz radio monitoring data. We have used both the averaged and the monthly gamma-ray data in the comparisons, looking for correlations with radio-based properties of our sources. Most of the time we have used a complete flux-limited radio sample consisting of 104 sources, 67 of

which were detected by *Fermi*. (For details of the sample, see Tornikoski et al., these proceedings, p. 85 .) We have also compared the 37 GHz flux curves to the monthly averages given in Abdo et al. Most of the results are presented in the contributions by León-Tavares et al. (LT), Nieppola et al. (N) and Tornikoski et al. (T) in these proceedings. Here we briefly summarize the results pertinent to our previous claims based on the EGRET data.

3.1. Correlations between radio and gamma-rays

We find an overall correlation between gamma-ray and 37 GHz data, both with the average fluxes and the monthly fluxes (N, Fig. 1; LT, Fig. 1), but there may be differences in the correlation for different classes of sources. We also find a clear correlation between the estimated peak frequency of the synchrotron SED and the gamma-ray luminosity (N, Fig. 2) an possibly between the gamma dominance and the peak frequency (N, Fig. 4).

3.2. Differences between various classes of AGN

In accordance with our EGRET analysis, we find that the strongest gamma-ray emission comes from HPQs, while BL Lacs are in general weak gamma-ray emitters (LT, Fig. 1; N, Figs. 1 & 2). However, this statement must be qualified by the fact that BL Lacs tend to have much higher SED peak frequencies (both synchrotron and IC peaks), bringing into the play various selection effects and K-corrections. Comparing the relatively few quasars and BL Lacs with similar peak frequencies, we fail to see any clear difference in the gamma dominance (N, Fig. 4).

3.3. What determines the strength of the gamma-ray emission?

Figure 5 shows the gamma dominance for all the sources included in the Metsähovi monitoring sample of Hovatta et al. (2009), with the Lorentz factors and the viewing angles estimated as described in Lähteenmäki et al. (1999). *Fermi*-non-detected sources are also included. There is a tendency for the strongest gamma-ray emitters to be HPQs with high Lorentz factors and small viewing angles, but the overall picture is far from simple. This is also shown by the fact that there is no single property that separates the *Fermi*-detected sources from the non-detected ones (Tornikoski, these proceedings, p. 85). As emphasized by Matt Lister in the *Fermi* Symposium 2009, gamma-ray brightness seems to be a complex combination of viewing angle, Lorentz factor, SED peak frequency and current activity - and likely also something else.

3.4. Different emission mechanisms?

There are hints that quasars and BL Lacs behave differently, with BL Lacs generally exhibiting less correlation with radio flux or its variations. This could be a sign of different dominating emission mechanisms, as suggested by Lähteenmäki and Valtaoja (2003).

3.5. Gamma-rays from shocks?

As Fig. 1 in LT shows, it is impossible to ascertain to which, if any, of the many ongoing radio flares a gamma-ray flare is connected. However, in a statistical sense we recover our earlier results: strongest gamma-ray levels are reached during the rise and the peak of mm-radio flares (LT, Fig. 2). We also find a correlation between monthly averaged gamma-ray and 37 GHz flux levels, which also indicates a co-spatial origin (LT, Fig. 1). Weaker gamma-ray emission is present at all times in many sources; at present it is not possible to say whether it also comes from the ever-present shocks or has a different origin.

4. Conclusions

The new *Fermi* data are in accordance with our earlier conclusions from EGRET. Most importantly, strong gamma-ray emission does seem to occur far away from the black hole and the accretion disk, in shocks parsecs downstream from the radio core and well outside the BLR. Modelling is required for this scenario, incorporating information on the properties of shocks, available from radio data. Since simple SSC models usually fail to produce the observed levels of gamma-ray flux, more sophisticated models should be developed and the possibilities of external seed photon sources outside the BLR should be investigated.
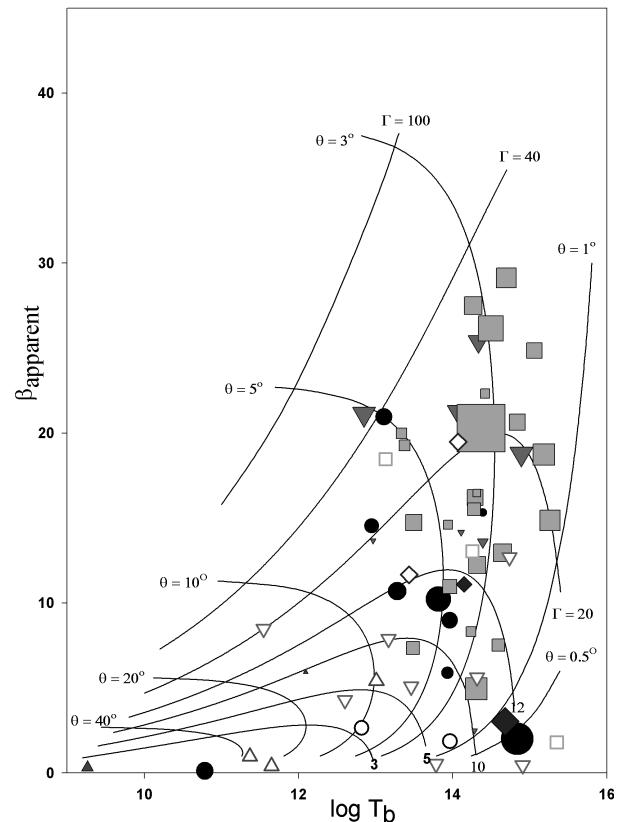
Fig. 5. The gamma dominance, S_{gamma}/S_{radio}. calculated from the 11-month *Fermi* averages for the sources included in the Metsähovi monitoring program and having their Lorentz factors and viewing angles estimated in Hovatta et al. (2009) from the observed variability brightness temperatures T_b and the VLBI speeds β. The areas of the symbols are proportional to S_{gamma}/S_{radio} for the detected sources (filled symbols), while non-detected sources are denoted by open symbols. Black triangles = galaxies, black circles = BL Lacs, black inverted triangles = LPQs, grey squares = HPQs and white diamonds = QSOs without polarization information. The Lorentz factors and the viewing angles are shown by lines in the figure.

References

Abdo, A. A., Ackermann, M., Ajello, M., et al. 2010, ApJS, 188, 405
Hartman, R. C., Villata, M., Balonek, T. J., et al. 2001, ApJ 558, 583
Hovatta, T., Valtaoja, E., Tornikoski, M., & Lähteenmäki, A., 2009, A&A, 494, 527
Jorstad, S. G., Marscher, A. P., Mattox, J. R., et al. 2001, ApJ 556, 738
Lähteenmäki A. & Valtaoja E. 2003, ApJ, 590, 95
Lindfors, E. J., Türler, M., Valtaoja, E., et al. 2005, A&A, 440, 845
Lindfors, E. J., Valtaoja, E., & Türler, M. 2006, A&A, 456, 895
Marscher, A. P & Gear, W. K. 1985, ApJ, 298, 114
Savolainen, T., Wiik, K., Valtaoja, E., Tornikoski, M. 2008, ASP Conf. Ser. Vol 386, 451
Valtaoja, E. & Teräsranta, H. 1995, A&A, 297, L13
Valtaoja, E. & Teräsranta, H. 1996, A&AS, 120, 491
Valtaoja, E., Lähteenmäki, A., Teräsranta, H., Lainela, M. 1999, ApJS, 120, 95

The Relation Between the Radio and Gamma-Ray Emission in Blazars from 15 GHz Monitoring with The OVRO 40 m Telescope and Fermi-GST observations

W. Max-Moerbeck[1], J. L. Richards[1], V. Pavlidou[1], T. J. Pearson[1], A. C. S. Readhead[1], M. A. Stevenson[1], O. King[1], R. Reeves[1], K. Karkare[1], E. Angelakis[2], L. Fuhrmann[2], J. A. Zensus[2], S. E. Healey[3], R. W. Romani[3], and M. S. Shaw[3]

[1] California Institute of Technology, Pasadena, CA, USA
[2] Max-Planck-Institut für Radioastronomie, Bonn, Germany
[3] Stanford University, Stanford, USA

Abstract. A sample of 1158 blazars from the Candidate Gamma Ray Blazar Sample plus additional sources detected by the Large Area Telescope (LAT) on the *Fermi* Gamma-ray Space Telescope are being monitored with the OVRO 40-m Telescope at 15 GHz, making a total of ~ 1500 sources. Using these quasi-simultaneous observations we study the connection between centimeter band behavior as observed by the OVRO 40-m Telescope and the gamma-ray behavior of blazars as detected by *Fermi*. These observations along with Monte Carlo simulations show that there is a statistically significant correlation between the radio and gamma-ray flux densities for the sources in the LAT bright AGN sample. Cross-correlation studies of radio and gamma-ray light curves for the brightest *Fermi* detected sources are being carried out. In addition to presenting preliminary results, we describe a receiver upgrade to increase sensitivity and add radio polarization to our monitoring program. The polarization data will provide important clues about the magnetic field configuration in the radio emission region.

1. Introduction

Among the most notable characteristics of blazars are their broad-band spectral energy distribution and their variability throughout the electromagnetic spectrum. According to the accepted scenario, the low energy emission is produced by synchrotron radiation, and the high energy emission is produced by inverse Compton scattering of some soft photon field by the same electrons producing the low frequency radiation. This can explain the presence of the characteristic double-peaked spectral energy distributions observed in these objects.

Understanding the details of the emission from blazars requires the study of a large sample of sources over a broad frequency range, with adequate cadences to cover the relevant time scales for the flares. The prospect of a large sample of gamma-ray sources detected by the *Fermi* Gamma-Ray Space Telescope (*Fermi*-GST) motivated our group to start a program to monitor a large sample of candidate gamma-ray blazars at 15 GHz using the Owens Valley Radio Observatory 40-meter Telescope (OVRO 40-m). This large sample allows the study of the variability over different populations, their typical time scales and their relation to other physical properties of the central black hole/jet system.

Combining the radio monitoring data with *Fermi*-GST light curves for large samples can inform us about the relation between the radio and gamma-ray emission in these objects, which provides information on the relative location of the radio and gamma-ray emission regions.

This article describes our observing program and its relation to *Fermi*-GST observations. It also presents the first results on the relationship between the radio and gamma-ray flux densities, and gives an update on ongoing technical developments.

2. Observing Program

Monitoring of a large sample of blazars at 15 GHz has been carried out with the OVRO 40-m Telescope since mid-2007. The original sample consisted of all 1158 sources north of declination $-20°$ in the Candidate Gamma Ray Blazar Survey (CGRaBS, Healey et al. 2008). Sources detected by *Fermi*-GST and associated with active galactic nuclei as presented in the "First Large Area Telescope AGN Catalog (1LAC)" (Abdo et al. 2010b) have been added to our monitoring program. All the sources in the 1LAC "clean" sample in our declination range have been added, making the total number of monitored blazars close to 1500.

Observations are made using a dual-beam Dicke-switched system. The individual beams are 2.5' FWHM and are separated by 13'. The cryogenic HEMT receiver has a noise temperature of ~ 30 K and covers the band from 13.5 to 16.5 GHz. The thermal noise floor is about 5 mJy with an additional $\sim 2\%$ contribution from pointing errors. For the observations, the sources are divided into regions no more than $20°$ in diameter. These regions are observed in a sequence chosen to minimize slew times. For each region a pointing correction is obtained from the

first observed source and applied to the other sources on the region. A noise diode signal is measured along with the pointing corrections and used for calibration. Observations of 3C286 are used for absolute flux calibration. A more detailed discussion can be found in Richards et al. (in prep.).

Gamma-ray light curves for the brightest sources can be obtained from the *Fermi*-GST observations. This has been done on weekly time scales for the sources in the LBAS sample (Abdo et al. 2009) using the first 11 months of *Fermi*-GST observations (Abdo et al. 2010a).

We are accumulating more radio data with the goal of extending the analyses presented below to a larger sample of gamma-ray detected sources using longer time series to increase the significance of our results.

3. Radio/Gamma-Ray Flux Correlation

A correlation between the radio and gamma-ray flux densities of blazars would help us understand the relationship between the regions responsible for the emission in these two bands, and also assist in the investigation of the gamma-ray background produced by undetected blazars. Previous studies that have suggested the existence of such a correlation using EGRET data (e.g., Stecker et al. 1993), have used non-simultaneous radio and gamma-ray data, and small samples. More recently Kovalev et al. 2009 have claimed the existence of the correlation using *Fermi* and MOJAVE observations. This study addresses partially the non-simultaneity issue but does not study the effects of possible sample selection or distance biases.

Using our data set we can test this correlation, eliminating the effects associated with non-simultaneity and small samples. Furthermore, we have explored the related issue of the significance of the correlation by examining the effects of the common redshift for the radio and gamma-ray flux densities on the correlation. Complete results and a detailed discussion can be found in Pavlidou et al. (in prep.). The radio and gamma-ray flux densities shown in Fig. 1 have a Pearson product-moment correlation coefficient of $r = 0.56$. Fig. 2 shows the results of the correlation coefficient probability density function estimated using Monte Carlo simulations along with the value obtained for the data presented in Fig. 1. From this test we find a probability of about $P = 5 \times 10^{-4}$ to find as large or larger correlation by chance, indicating the significance of the correlation.

4. Radio/Gamma-Ray Time Lags

The next step in the study of the radio and gamma-ray correlation is the exploration of the relationship between flaring episodes at both wavelengths and their time evolution.

We first explored the presence of variability in the sources detected in both radio and gamma-ray bands regardless of their possible time relation. Using a χ^2 test to evaluate the probability of a constant source producing
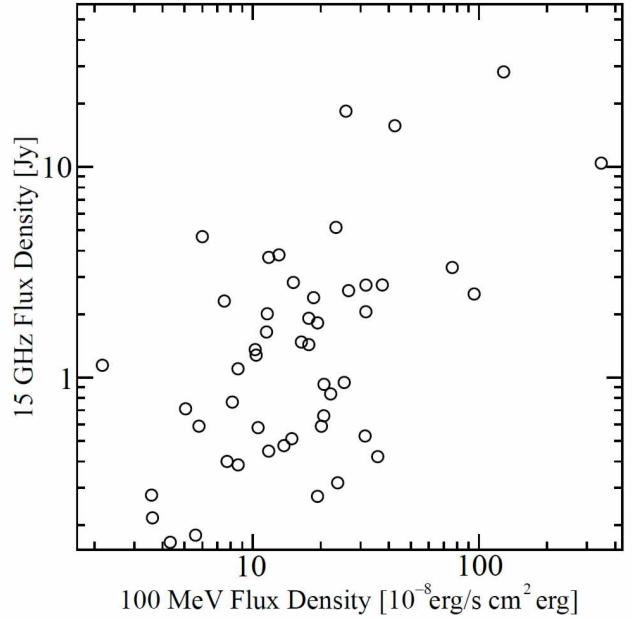
Fig. 1. Radio flux density at 15 GHz from OVRO 40-m Telescope and gamma-ray flux density at 100 MeV from *Fermi*-GST.
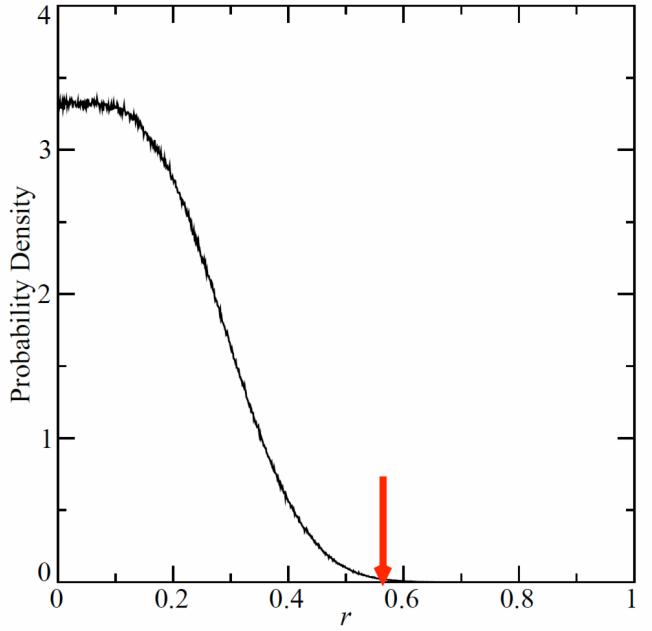
Fig. 2. Estimated probability density function for the correlation coefficient r obtained with the Monte Carlo simulations. The arrow indicates the value obtained for the data.

the observations, it is found that $\sim 75\%$ of the sources are variable at the 99.9% confidence level in both bands and only $\sim 6\%$ are not variable in either band. The rest of the sources ($\sim 19\%$) are variable in one of the two bands. The basic observation is that objects that vary at gamma-ray wavelengths are almost always also variable at radio wavelengths over the period of time spanned by our obser-

vations. The few exceptions are may be due to sampling, duty cycle or low level of variability effects.

The existence of time correlated variability can be investigated using the cross-correlation between the radio and gamma-ray light curves. This has been done using the method of Edelson and Krolik 1988, which is applicable to unevenly sampled time series. A related question is on the significance of these correlations and the possibility of detecting chance correlations for which the method doesn't provide any prescription. The interpretation of such correlations as real can lead to misleading conclusions and we address this by using simulated data sets to evaluate the significance, as described below.

The basic idea of our approach is to simulate a large number of radio/gamma-ray light curve pairs with similar properties and sampling as the data. The light curves are assumed to come from a noise process with a power-law power spectral density ($\propto 1/f^{\beta}$) and are identically sampled as the data. These simulated light curve pairs are treated in the same way as the data and the distribution of the resulting correlations for any given time lag is used to estimate the probability of a chance correlation. The results depend on the chosen power-law exponent and the particulars of the sampling. For the power-law exponent we use $\beta \sim 2-2.5$ for radio and $\beta \sim 1.5-2.0$ for gamma-rays. These values are consistent with what is found on the literature (Abdo et al. 2010a, Chatterjee et al. 2008).

We include some of our cross-correlation results as examples of the quality of the data in the two bands and the cross-correlations that we measure (Figs. 3, 5, 4 and 6). In view of the fact that the flares in these plots often last for a significant fraction of the duration of the observations, it is not surprising that high cross-correlations are seen. As shown by our significance analysis, this does not necessarily indicate that these events are related at the two frequencies. Given the short duration of the light curves, it is not yet possible to determine if the single observed gamma-ray flare is related to the observed radio flare, or to one occurring before/after and not included in the observations. As can be seen from these two examples (Figs. 4 and 6), the significance level is not high enough to make any claims yet, although the result that just reaches 3σ is interesting and should be watched carefully as more data are added.

Only 4 out of a total of 52 sources with data in radio and gamma-rays show correlations at the 3σ level. This indicates that longer duration observations are needed in order to make the associations definitive.

Since the significance of the correlations depends on the assumed noise properties of the radio and gamma-ray light curves, more work needs to be done to characterize the noise properties of our data set. However, it is clear that a significant fraction of the observed correlations could be due to statistical fluctuations and that they should be used cautiously so as not to over interpret that data. A complete discussion of these results will be presented in a publication we are preparing in collaboration with the *Fermi*-GST AGN science group.
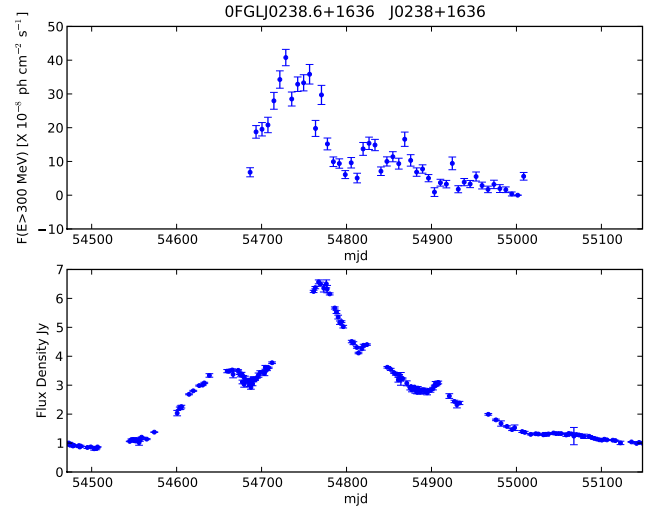
Fig. 3. Example radio and gamma-ray light curves for one of the sources in our study. Upper panel is gamma-ray flux and lower panel radio flux density.
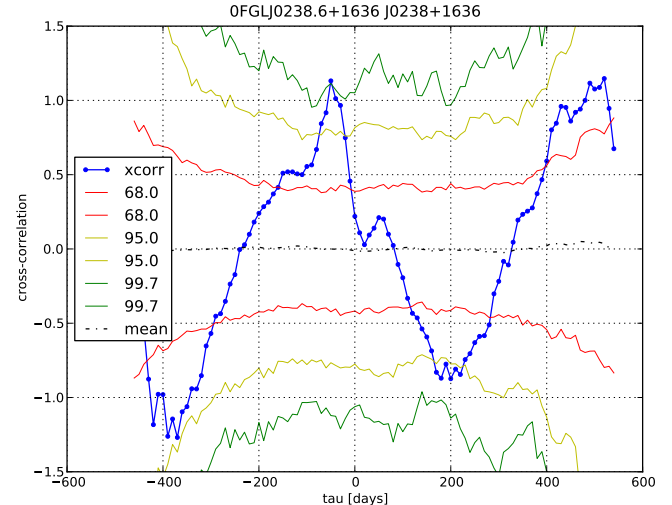
Fig. 4. Statistical significance of the cross-correlation for the source in Fig. 3. Solid blue curve is the cross-correlation and dotted colored contours show the significance levels.

5. Polarization Upgrade

Another important characteristic of blazars is the polarization of their low frequency emission. This polarization is naturally explained by synchrotron emission. Polarization monitoring can give us information about the magnetic field configuration and evolution of the emission region. This will allow direct comparison with optical observations, where large changes on the polarization degree and angle have been observed and used to argue in favor of a relation between the optical and gamma-ray emission regions (Abdo et al. 2010c).

This motivated our group to start the development of a new receiver with polarization capabilities. Besides being able to measure polarization, the new receiver will provide spectral measurements (the current instrument is
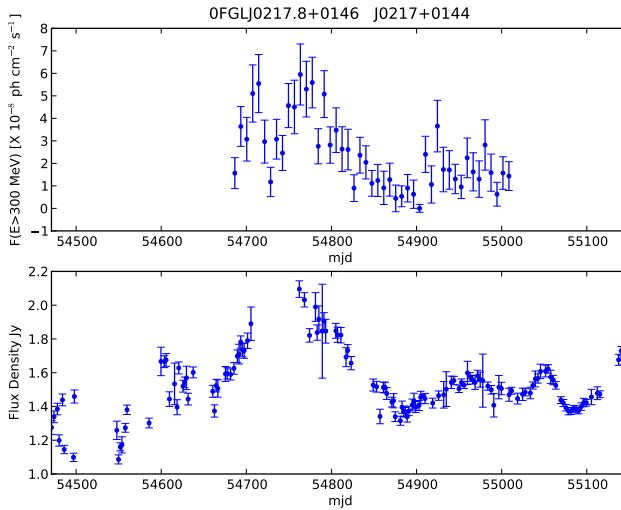
Fig. 5. Example radio and gamma-ray light curves for one of the sources in our study. Upper panel is gamma-ray flux and lower panel radio flux density.
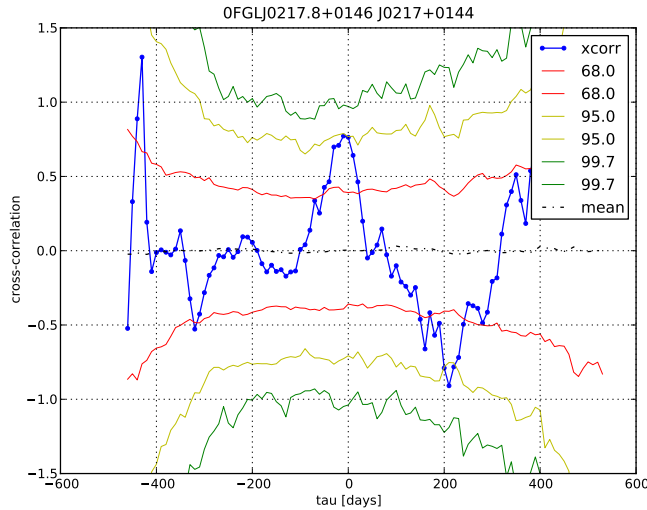

Fig. 6. Statistical significance of the cross-correlation for the source in Fig. 5. Solid blue curve is the cross-correlation and dotted colored contours show the significance levels.

a total power receiver) over a broader bandwidth and will have a lower system temperature. The spectral capabilities will allow for better radio frequency interference rejection improving the number of our flux measurements than can be used with confidence.

The receiver, made of a combination of commercial and custom designed radio frequency components and a reconfigurable digital backend based on Field Programmable Gate Array (FPGA) technology, is under construction and commissioning is planned by the end of this year.

6. Conclusions

We are monitoring a sample of ~ 1500 candidate gamma-ray sources at 15 GHz with a cadence of two observations per week. Most of the sources have been monitored since

mid-2007 and *Fermi* detected blazars have been added as data has been made public. Using data from the first 11 months of *Fermi*-GST operation, we find a correlation between mean radio and gamma-ray flux densities for the LBAS sources that are part of the OVRO 40-m Telescope sample. Using Monte Carlo simulations to study the effect of bias and sample selection it is shown that the correlation is statistically significant. On the time domain side it is seen that most of the sources are variable in radio and gamma-ray frequencies and their light curves show some degree of correlation. A significance analysis that makes use of simulated data sets is applied to the data and shows that only a few of the correlations are statistically significant. This confirms our original suspicion that it is too early in the program to associate radio and gamma-ray features and that longer time series or strong physical arguments are required to prove that the correlations are real.

References

Abdo, A. A., Ackermann, M., Ajello, M. et al. 2009, ApJ, 700, 597

Abdo, A. A. et al. 2010a, arXiv:1004.0348

Abdo A. A., Ackermann, M., Ajello, M. et al. 2010b, ApJ, 715, 429

Abdo A. A., Ackermann, M., Ajello, M. et al. 2010c, Nature, 463, 919

Chatterjee, R., Jorstad, S. G., Marscher, A. P. et al. 2008 ApJ, 689, 79

Edelson, R. A. & Krolik, J. H. 1988, ApJ, 333, 646

Healey, S. E., Romani, R. W., Cotter, G. at al. 2008, ApJS, 175, 97

Kovalev, Y. Y., Aller, H. D., Aller, M. F. et al. 2009, ApJ, 696, 17

Stecker, F. W., Salamon, M. H., Malkan, M. A. 1993, ApJ, 410, 71

The F-GAMMA program: multi-wavelength AGN studies in the Fermi-GST era

E. Angelakis[1], L. Fuhrmann[1], I. Nestoras[1], J. A. Zensus[1], N. Marchili[1], V. Pavlidou[2] and T. P. Krichbaum[1]

[1] Max-Planck-Institut f̈r Radioastronomie, Auf dem Ḧgel 69, Bonn 53121, Germany
[2] California Institute of Technology, 1200 East California Blvd., Pasadena CA 91125, USA

Abstract. The *F*-GAMMA program is a coordinated effort of several observing facilities to understand the AGN/blazar phenomenon via a multi-frequency monitoring approach, especially in the era of *Fermi*-GST. Some 60 prominent sources are monitored monthly with the Effelsberg 100-m telescope, the IRAM 30-m telescope and the APEX 12-m telescope, covering from 2.64 to 345 GHz. The program has been running since January 2007 and here some of its findings are summarized. (a) There are two major variability patterns that the spectra of sources follow, one spectral-evolution-dominated and one achromatic. (b) The FSRQs show higher brightness temperatures indicative of larger Doppler factors at play and (c) a statistically significant radio γ-ray correlation has been found with a method recently suggested by Pavlidou et al. (submitted).

1. Introduction

According to our current and rather complete understanding, in terms of system configuration, of the magnificent phenomenon of Active Galactic Nuclei (AGNs), the inconceivable amounts of energy radiated by these systems are generated by a super-massive black hole living in the nuclear region of the host galaxy. The even more extended variety of AGN phenomenologies are attributed to the same system seen at different viewing angles by the admittedly elegant unified model, reviewed by Urry & Padovani (1995). Blazars, as the most dramatic manifestation of the AGN phenomenon, display extreme observational characteristics due to their close to our line-of-sight orientation and the consequent boosting effects. Their double humped Spectral Energy Distribution (SED) is explained by means of two components. The low energy peaked one is explained as a synchrotron component whereas the high energy peaked one is assumed to be the result of inverse Compton processes either on external seed photons (from the disc or the broad line region) or synchrotron photons. What the exact mechanism is, is still unclear. Furthermore, what exactly causes the variability at vast timescale ranges is also unknown and so are numbers of fundamental questions.

Among the several incredible opportunities offered by *Fermi*-GST is the densely sampled γ-ray light curves it provides and which for the first time allow really simultaneous multi-energy studies. The *F*-GAMMA program is utilizing this approach for understanding some of these fundamental questions. In particular, roughly 60 sources have been monitored monthly since January 2010 with the Effelsberg 100-m telescope, the IRAM 30-m telescope and the APEX 12-m telescope covering vast frequency range. The observations at different telescopes are coordinated within 1 week. Here a few findings are discussed after a short introduction to the program.

2. The F-GAMMA program

It has been discussed elsewhere (Fuhrmann et al., 2007; Angelakis et al., 2009) that the *F*-GAMMA program is the coordinated effort for a multi-frequency study of AGN astrophysics in the light of *Fermi*-GST gathering data since January 2007. The pivotal facilities are the Effelsberg 100-m telescope covering the range between 2.64 and 43.00 GHz in 8 frequency steps, the IRAM 30-m telescope covering 86, 142, 220 GHz and the Apex 12-m telescope operating at 345 GHz. The monitoring is done monthly on a sample of 60 sources. The observations at these facilities are coordinated within roughly a week. Along with this effort there take place several other closely collaborating programs such as OVRO monitoring at 15 GHz, the IRAM 30-m polarization monitoring program (Thum et al. and Agudo et al. in prep.), and the Perugia AIT blazar monitoring (Tosti et al., 2002; Ciprini et al., 2008). Here we present Effelsberg data alone. The light curves produced and animated spectra are constantly updated at www.mpifr.de/div/vlbi/fgamma.

3. The sample

The main motivation for this work has been the multi-band approach to AGN and especially blazar astrophysics, in particular the investigation of correlations between the radio and γ-ray emission. For this reason the fist sample consisted of 61 blazars (32 FSRQs, 23 BL Lacs, 3 radio galaxies and 3 unclassified blazars) selected mostly on their likelihood of being *Fermi*-GST detectable (earlier EGRET detections). The release of the LAT Bright AGN Source list (LBAS, Abdo et al., 2009) showed that 29 of the 61 sources ($\sim 47\%$) were detected by LAT in the first three months of operation. In a major revision of the source sample LBAS as well as the *Fermi*-LAT First Source Catalog were consulted (Abdo et al., 2010)

in order to build up a new source sample with maximum *Fermi*-LAT detectability and reasonably fast and intense variability. Currently the observed sample includes a total of 66 sources from which 60 are observed monthly. From these, 36 are clarified as FSRQs, 17 as BL Lacs and 9 as unclassified blazars (classification by Massaro et al., 2005, 2008, 2009). Additionally, 1 source is classified as a Seyfert and 3 are radio galaxies.

From the above discussion it is very clear that the *F*-GAMMA sample suffers severely from biases and therefore it is statistically incomplete. Nevertheless, extracted generalizations may be tested by careful comparison with other statistically complete samples. In any case, any generalization must be stated with caution.

4. Spectral Variability

Blazar variability has been attributed to several factors and accordingly certain models have been developed to interprete and quantitatively describe it. One could distinguish between two model categories: (a) models which attribute the variability to mechanisms that impose spectral evolution on the observed events such as shock-in-jet models (Marscher & Gear, 1985) or colliding relativistic plasma shells (Guetta et al., 2004) and (b) models which explain the variability in terms of geometrical effects such as systematic changes in the beam orientation (lighthouse effect, Camenzind & Krockenberger, 1992) which could for instance cause a change in the Doppler factor and further induce achromatic changes in the observed radio spectrum. The expected bi-modality in the phenomenological behavior of the observed radio spectra is clearly seen in the *F*-GAMMA data.

Figure 1 shows the Effelsberg light curves and radio spectra for two representative cases that resemble what would be expected from the previous classification. In the case of 0235+164 the variability is dominated by spectral evolution (hereafter *type 1*), evidence of a three-stage evolutionary path (Compton, synchrotron and adiabatic losses, Marscher & Gear, 1985). The case of $0814+425$ on the other hand is representative of achromatic variability indicating some geometrical effect (hereafter *type 2*).

Interestingly, from the point of view of the variability pattern followed by the observed spectra, all the sources fall in only five classes which comprise modifications of these two basic behaviors.

The fact that there must be a fundamental difference in the mechanism causing the variability becomes evident also from the evolutionary paths followed by the turnover frequency and flux density at that point (S_m, ν_m). In figure 2 are shown the evolutionary tracks for three cases of *type 1* and three cases of *type 2* after the subtraction of mean quiescent spectra (with $S \propto \nu^\alpha$ and $\alpha = -0.5$). The former case seems to be described well by Marscher & Gear (1985) whereas *type 2*, needs a different interpretation. In a forthcoming publication (Angelakis et al. in prep.) we use this approach to estimate source parameters,
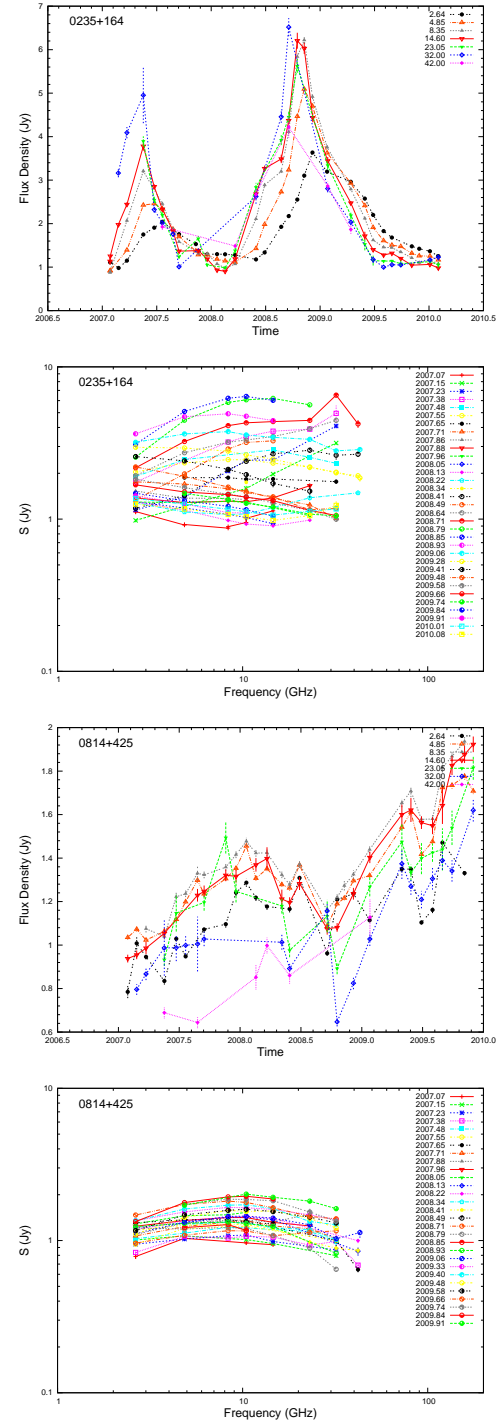
Fig. 1. Two prototype cases representing the two characteristic behaviors. In the case of $0235 + 164$ (1st and 2nd panels from the top) the variability is dominated spectral evolution. The case of $0814 + 425$ is representative of achromatic variability indicating some geometrical effect.

and investigate the presence of possible quasi-periodicities in *type 2* sources

From average spectra a low and high frequency spectral index can be calculated in order to examine whether there is a significant differentiation between BL Lacs and FSRQs. Figure 3 shows the spectral indices between 9 mm
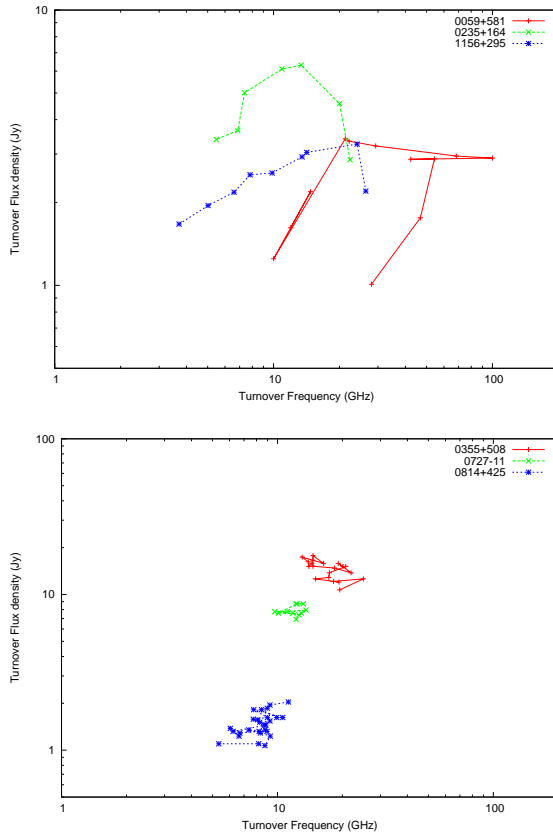
Fig. 2. The evolution of the peaks of convex spectra in the $S_m - \nu_m$ space for three members of each of the two characteristic classes *type 1* and *type 2*. In every case a quiescent spectrum of -0.5 is assumed ($S \propto \nu^\alpha$). Members of the same class follow qualitatively the same evolutionary paths.

observed with the Effelsberg telescope and 3 and 2 mm obtained with the IRAM 30-m telescope. What seems to be the case is a vague tendency of the BL Lacs to center around flatter high-frequency spectral indices as compared to FSRQs. This may for instance be due to the fact that the BL Lacs systematically peak at higher frequencies or, alternatively, their flares expand before reaching lower frequencies, maybe due to lower power. This requires further investigations.

5. Time series analysis

The level of variability present at all frequencies and in all sources becomes obvious as *excess variance* and has been quantified via a formal χ^2 test for which a significance reference level of 99.9 % has been adopted. For the first 2.5 years of observations (that is for the first target sample), χ^2 tests show that almost all the sources appear significantly variable at all wavelengths (91 % of the sources are significantly variable with the proportion of variable sources dropping at higher frequencies due to larger measurement uncertainties at these frequencies). Using the mean *rms* ($\langle\sigma\rangle$) averaged over all sources at each frequency as a measure of the variability amplitude, one can clearly
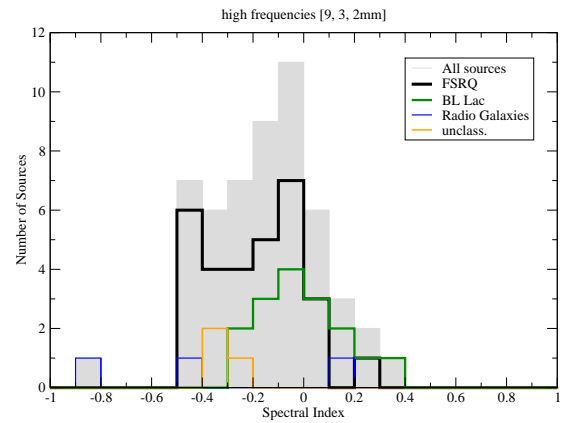
Fig. 3. The distribution of high-frequency spectral indices for BL Lacs and FSRQs with the former centering around flatter values than the latter.

see a monotonically rising trend as a function of frequency. That is expected from sources which are mostly spectral-evolution-dominated.

In order to investigate the presence of characteristic timescales in the acquired light curves, the first order *Structure Function* has been used (Rutman, 1978; Paltani et al., 1997; Simonetti et al., 1985). From the time series analysis applied to the first 2.5 years of data, the variability timescales are between 80 and 500 days. From the estimated timescales and on the basis of some fundamental assumptions (causality, a single emitting component), one can estimate the brightness temperatures $T_b = 4.5 \cdot 10^{10} \Delta S \left(\frac{\lambda D}{\tau(1+z)}\right)^2$, with T_b in K, ΔS the flux density variations in Jy, λ in cm, D the luminosity distance in Mpc, τ the characteristic timescale in days and z the redshift. Figure 4 shows the maximum brightness temperature distribution (calculated from the fastest time scales reliably detected) for FSRQs and BL Lacs. There is a clear and statistically significant separation between the two classes, with the FSRQs showing brightness temperatures systematically higher than the BL Lacs. A possible explanation for this could be that the former undergo stronger Doppler boosting.

6. Radio versus γ-ray fluxes

One of the remaining fundamental questions in AGN astrophysics is where and how high energy emission is produced. Searches for correlations between radio and γ-ray luminosities is meant as a means of investigating the connection between the mechanisms producing them and has been a rather debatable field. The situation becomes even more perplexing due to artifacts that may be introduced by selection biases, redshift dependencies, lack of simultaneity and so forth.

For a sample of 29 *F*-GAMMA sources from the first sample detected by *Fermi*-GST, simultaneous γ-ray and radio data have been used to investigate the presence of such a correlation. Figure 5 shows that there indeed exists a correlation. A new Monte-Carlo method has been
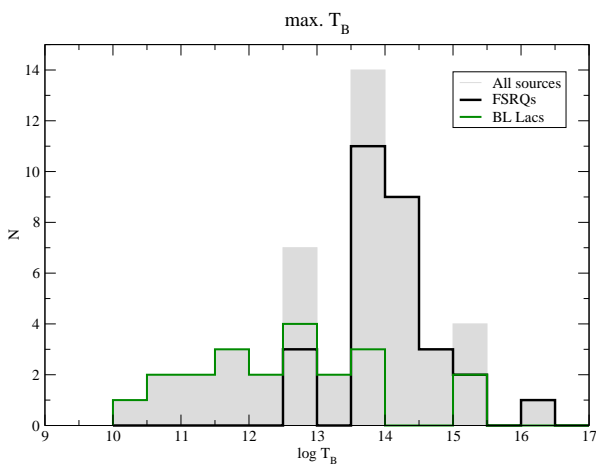
Fig. 4. The brightness temperature distribution for FSRQs and BL Lacs separately.

used to assess its significance and it shows that it is indeed intrinsic. The details of the newly applied method are describe by Pavlidou et al. (submitted).
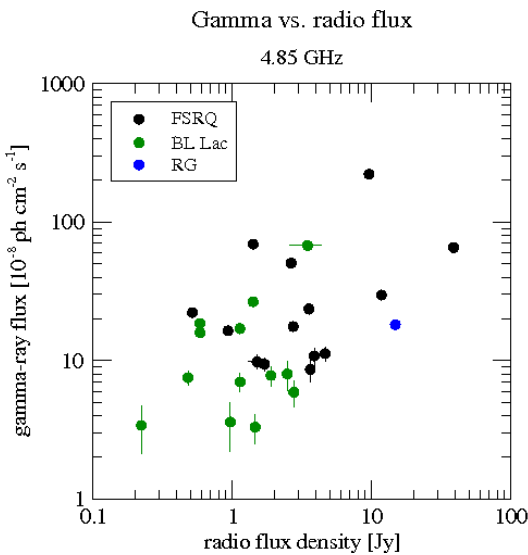
Fig. 5. Flux-flux correlation plots with three-month averaged radio data at 5 GHz.

7. Conclusions

After 3.5 years of observing the *F*-GAMMA program has produced a large volume of data which allows very detailed blazar studies. Some of them have been discussed here:

– The spectrum variability is not erratic but follows only two behaviors: (a) one dominated by spectral evolution and (b) one achromatic variability pattern resembling rather a geometrically induced variability. All the sources fall in these categories and their modifications.

Differences in the variability properties of sources from different classes must be sought .

– The high-frequency spectral indices imply a separation between FSRQs and BL Lacs, possibly due to the BL Lacs peaking at higher frequencies.
– A clear distinction in the brightness temperature distributions for BL Lacs and FSRQs may be due to higher Doppler factors at play in FSRQs.
– A newly suggested Monte-Carlo method assesses statistically significant radio and gamma-ray flux correlations.

References

Abdo, A. A., Ackermann, M., Ajello, M., et al. 2010, ApJS, 188, 405

Abdo, A. A., Ackermann, M., Ajello, M., et al. 2009, ApJ, 700, 597

Angelakis, E., Fuhrmann, L., Zensus, J. A., et al. 2009, in *Accretion and Ejection in AGN: A Global View*, ed. L. Maraschi, G. Ghisellini, R. Della Ceca, & F. Tavecchio, ASP Conf. Ser., in press (San Francisco: ASP) [arXiv:0910.0346]

Camenzind, M. & Krockenberger, M. 1992, A&A, 255, 59

Ciprini, S., Tosti, G., Nucciarelli, G., et al. 2008, in Blazar Variability across the Electromagnetic Spectrum

Fuhrmann, L., Zensus, J. A., Krichbaum, T. P., Angelakis, E., & Readhead, A. C. S. 2007, in *The First GLAST Symposium*, ed. S. Ritz, P. Michelson, & C. A. Meegan, Am. Inst. of Phys. Conf. Ser., Vol. 921, p. 249

Guetta, D., Ghisellini, G., Lazzati, D., & Celotti, A. 2004, A&A, 421, 877

Marscher, A. P. & Gear, W. K. 1985, ApJ, 298, 114

Massaro, E., Giommi, P., Leto, C., et al. 2009, VizieR Online Data Catalog, 349, 50691

Massaro, E., Sclavi, S., Giommi, P., Perri, M., & Piranomonte, S. 2005, *The Multi-Frequency Catalogue of Blazars*, http://www.asdc.asi.it/bzcat/

Massaro, E., Sclavi, S., Giommi, P., Perri, M., & Piranomonte, S. 2008, *The Multi-Frequency Catalogue of Blazars, 2nd Edition*, http://www.asdc.asi.it/bzcat/

Paltani, S., Courvoisier, T., Blecha, A., & Bratschi, P. 1997, A&A, 327, 539

Rutman, J. 1978, IEEE Proceedings, 66, 1048

Simonetti, J. H., Cordes, J. M., & Heeschen, D. S. 1985, ApJ, 296, 46

Tosti, G., Ciprini, S., & Nucciarelli, G. 2002, Memorie della Societa Astronomica Italiana, 73, 1024

Urry, C. M. & Padovani, P. 1995, PASP, 107, 803

Study of a complete sample of radio-bright AGNs: properties of gamma-ray bright and gamma-ray faint radio sources in the first year of Fermi operations

M. Tornikoski[1], E. Nieppola[1], E. Valtaoja[2], J. León-Tavares[1], and A. Lähteenmäki[1]

[1] Aalto University Metsähovi Radio Observatory, Metsähovintie 114, FI–02540 Kylmälä, Finland
[2] Tuorla Observatory, Department of Physics and Astronomy, University of Turku, FI–20014 Turku, Finland

Abstract. We have studied properties of a flux-limited complete sample of radio sources, ca. 2/3 of which were detected by *Fermi*/LAT. The non-detected sources have radio fluxes and historical variability comparable to those of the detected sources, but typically the *Fermi*/LAT-detected sources were flaring during the 1FGL observing period, whereas the non-detected ones were in a relatively uneventful state. The *Fermi*/LAT-detected sources also have higher Doppler boosting factors and higher synchrotron peak frequencies than the non-detected ones.

1. Introduction

Our team studied the connection between gamma-ray and radio emission in blazars already during the *Compton Gamma Ray Observatory* mission. We compared the gamma-ray detection information from EGRET with radio data from Metsähovi Radio Observatory, and found that gamma-ray emission is typically detected in the initial phases of high radio frequency outbursts (e.g., Valtaoja & Teräsranta 1995, 1996; Lähteenmäki & Valtaoja 2003). Using VLBI data, this was also independently found by Jorstad et al. (2001).

We also suggested that many sources that typically exhibited blazar-like behaviour in the radio domain were not detected by EGRET simply because they were in a quiescent state during the observations (Tornikoski & Lähteenmäki 2000). We now revisit the issue of gamma-ray detected versus non-detected radio sources, analysing the radio behaviour of a complete sample of Northern to equatorial sources, 66% of which were detected by *Fermi*/LAT in its first year of operations, and 34% of which were not detected.

2. Sample

For this study we used a sample of bright radio sources from our Metsähovi monitoring campaigns. The source sample is a complete flux-limited sample with the 37 GHz historical average fluxes $S(\text{radio})_{\text{ave,all}} > 1 \text{ Jy}$ and with the declination $\delta > -10$ degrees, altogether 104 sources. Most of them have been monitored in Metsähovi for 15–30 years, but a few of them were introduced to the source list relatively late (two as late as 2005). We wanted to use this flux-limited complete sample as a starting point to study the *Fermi*/LAT-detected vs. non-detected dichotomy, because from the radio-behaviour point of view this sample is as unbiased and homogenous as possible.

Table 1. Subclasses of the *Fermi*/LATdetected (*Fdet*) and non-detected (*Fnondet*) populations

Subclass	*Fdet*	*Fnondet*
BLO	17	3
GAL	5	5
HPQ	27	6
LPQ	10	10
QSO	8	11
ALL	67	35
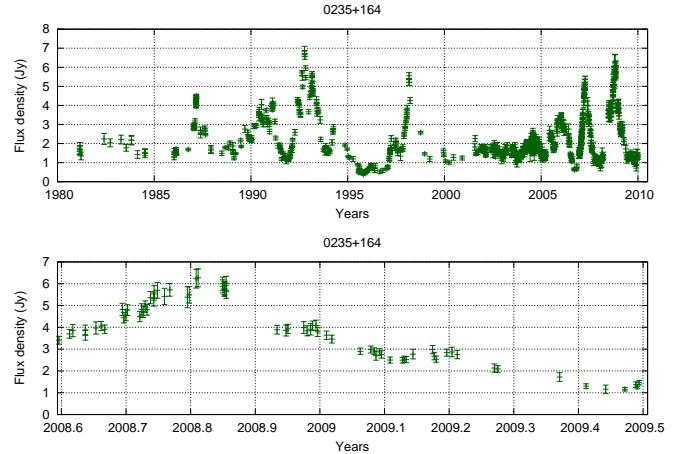
Fig. 1. Flux curves of the *Fermi*/LAT-detected source 0235+164. The upper panel shows the historical 37 GHz flux curve and the lower panel shows the 37 GHz flux curve during the F1 period. This source exhibits prominent variability in the past as well as during the period when *Fermi*/LAT was observing.

According to the *Fermi*/LAT First Source Catalog (Abdo et al. 2010, 1FGL), 67 of our sources, hereafter the *Fdet* subsample, were detected by *Fermi*/LAT and 35 sources, hereafter the *Fnondet* subsample, were not de-

tected. (Two sources from the initial sample were excluded from this study due to an ambiguous association with a *Fermi*/LAT source.) These can be divided into various subpopulations according to their spectral type (from the literature) as follows: BL Lacertae Objects (BLO), quasars with high optical polarization (HPQ), quasars with low optical polarization (LPQ), quasars with unknown optical polarization (QSO), and radio galaxies (GAL). The *Fdet* and *Fnondet* distributions according to this classification are shown in Table 1.

The HPQ subclass alone forms 40% of the *Fdet* population. This is not surprising if there is a tight connection between the radio and gamma-ray emission, because the high polarization seems to be an indication of a small viewing angle (Hovatta et al. 2009) and these sources would then have their jets with co-spatial radio and gamma-ray emitting regions pointing close to our line of sight.

3. Comparison of the Fermi/LAT-detected and non-detected sources

Our EGRET vs. radio studies suggested that a source is likely to show prominent gamma-ray activity when it is active also in the high-frequency radio domain. As indicated by Valtaoja & Teräsranta (1996) and Lähteenmäki & Valtaoja (2003), there are possible differences between classes, though: it is possible that at least in some source classes some other properties – instead of, or in addition to, the radio state – dictate whether a source is going to be bright in the gamma-ray domain.

Possible scenarios for explaining the *Fermi*/LAT-detected vs. non-detected dichotomy include the following:

1. Different physical properties. These can be properties like the jet speed, jet orientation, mass of the central black hole, properties of the surrounding medium, etc. Furthermore, different types of sources may have different (dominating) gamma-ray production mechanisms.
2. "Bad timing". If radio and gamma-ray emission are tightly connected, a source would not have been bright in gamma-rays during 1FGL if it was not active in the radio domain.
3. Combination of these and possible other factors.

3.1. Radio fluxes and variability (the "Bad Timing Scenario")

It is easiest to start by examining the "Bad Timing Scenario". This can first be done by the visual examination of radio flux curves, and in particular by the comparison of historical behaviour to the behaviour during the 1FGL observing period, hereafter *F1*. Also, we can directly compare radio flux density values (maxima & averages) and various radio variability indices calculated for the historical data sets and for the data taken during *F1* only.
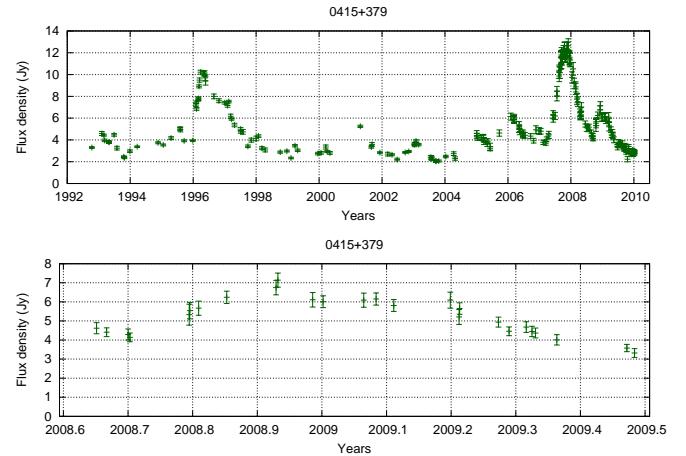
Fig. 2. As in Fig. 1, but for the source 0415+379.
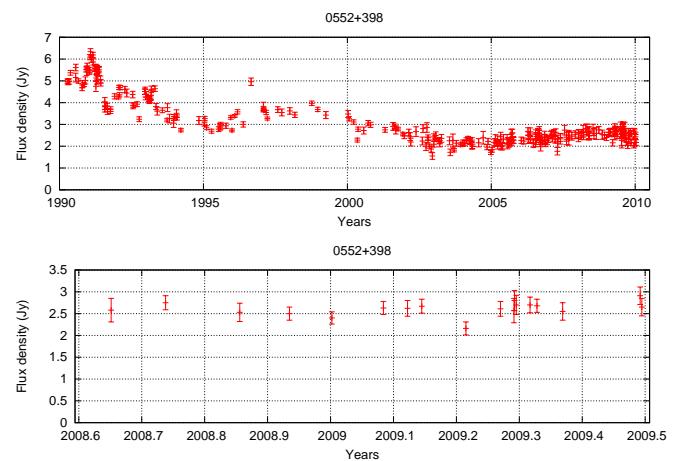
Fig. 3. Flux curves of the source 0552+398 that was not detected by *Fermi*/LAT. The upper panel shows the historical 37 GHz flux curve and the lower panel shows the 37 GHz flux curve during the F1 period. This source exhibits prominent variability in the past, but during the F1 period it was in an uneventful state.

Visual examination of flux curves shows that most of the detected sources were active in the radio domain also during *F1* (examples of two sources are given in Fig. 1 and Fig. 2). This is confirmed also by the more detailed studies of León-Tavares et al. and Nieppola et al. in these proceedings, p. 89 . Likewise, when we examine the flux curves of the sources that were not detected by *Fermi*/LAT, we can see that typical cases (examples in Fig. 3 and Fig. 4) show historical variability comparable to that of the *Fermi*/LAT-detected sources, but most of these sources were in a quiescent or at least relatively uneventful state during *F1*.

The *Fdet* sources have the very brightest historical and *F1* radio flux densities, but when we calculate the proportion of historical vs. *F1* fluxes

$$S(\text{radio})_{\text{prop}} = S(\text{radio})_{\text{all}}/S(\text{radio})_{F1} \qquad (1)$$
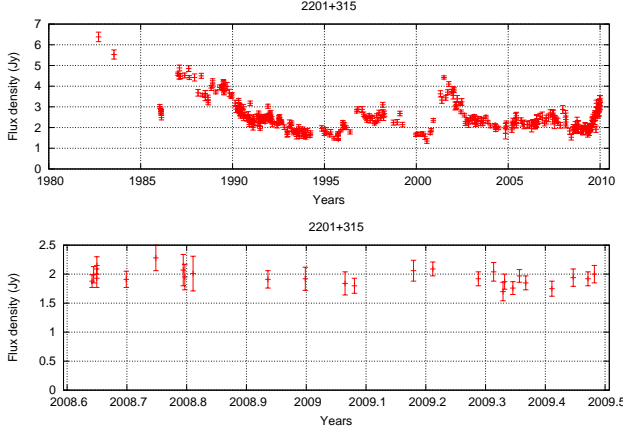
Fig. 4. As in Fig 3., but for the source 2201+315.
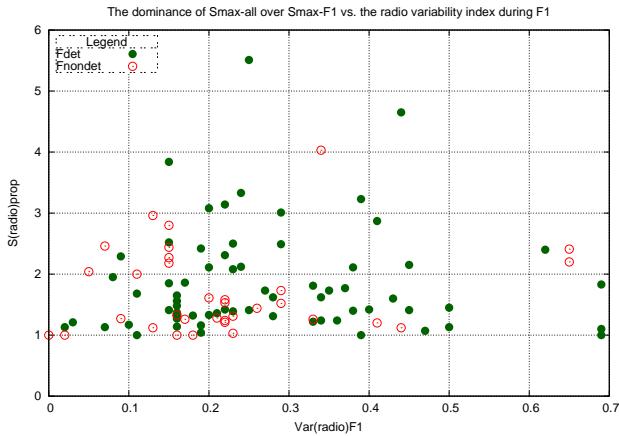
Fig. 5. The dominance of the historical radio flux over the radio flux in *F1* versus the radio variability index in F1. Open / red symbols show the *Fnondet* sources, filled / green symbols show the *Fdet* sources.

it turns out that the *Fdet* and *Fnondet* populations don't differ from each other[1].

From our visual examination we can also see that some of the *Fnondet* sources were relatively bright during *F1*, but on the other hand they lack prominent flares during that observing period. In order to compare variability indices during *F1* with historical values, we calculated a variability index

$$Var(\mathrm{radio}) = \frac{S(\mathrm{radio})_{\max} - S(\mathrm{radio})_{\min}}{S(\mathrm{radio})_{\max} + S(\mathrm{radio})_{\min}} \qquad (2)$$

for the all-time historical data as well as the *F1* period data.

The $S(\mathrm{radio})_{\mathrm{prop}}$ vs. $Var(\mathrm{radio})_{F1}$ distribution of the sources is plotted in Fig. 5.

When we compare the historical $Var(\mathrm{radio})$ values of both populations, they don't statistically differ from each other. On the other hand we can see (Fig. 6) that the

---

[1] All statistical tests where samples were compared for differences were done by running the Kruskall-Wallis One-Way ANOVA, method 95% t interval, in Unistat 5.6.01.
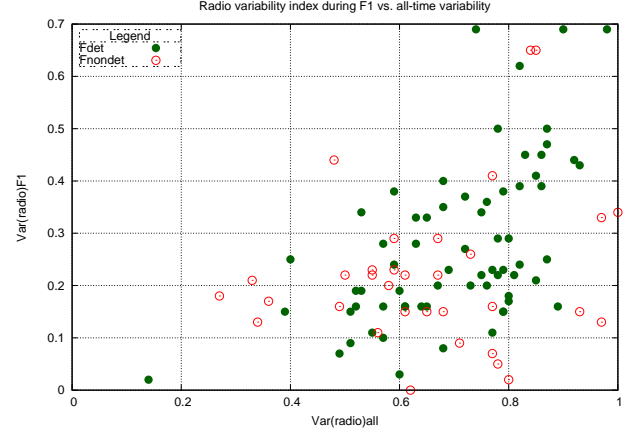
Fig. 6. Radio variability index in *F1* versus the historical variability index.

higher the historical variability, the higher the variability during *F1* for the *Fdet* sources. The *Fnondet* population does not show this trend, and in fact they preferably populate the space $Var(\mathrm{radio})_{F1} < 0.3$, $S(\mathrm{radio})_{\mathrm{prop}} < 2.8$ of Fig. 5. Using the $Var(\mathrm{radio})$ indices from *F1* only, the *Fdet* and *Fnodet* populations significantly differ from each other.

From both the visual examination of flux curves as well as from the statistical analysis of the flux and variability information, we can conclude that even though the historical radio behaviour of the *Fdet* and *Fnondet* sources does not statistically differ from each other, during *F1* the *Fdet* population sources were more variable than those of *Fnondet*. The *Fnondet* sources did not have to be in a quiescent radio state (i.e., close to their historical minima), but typically they were "non-active". **Most of the detected sources happened to be flaring during the time they were observed by *Fermi*/LAT, whereas the non-detected ones were in a relatively uneventful state during that time.**

3.2. Synchrotron peak frequencies and Doppler boosting factors

Even though the dichotomy in $Var(\mathrm{radio})_{F1}$ is significant, we can also see that there are some *Fdet* sources with relatively low $Var(\mathrm{radio})_{F1}$, and some *Fnondet* sources with as high $Var(\mathrm{radio})_{F1}$ index as that of the median *Fdet* population. Thus, as also found in our detailed study of the radio states of the *Fermi*/LAT-detected sources during the Fermi pointings (León-Tavares et al., these proceedings, p. 93), the radio state alone can not fully explain the gamma-ray detection probability.

We used the synchrotron peak (ν_{peak}) frequencies obtained by Nieppola et al. (2006) to study if there is a significant difference between the two populations. ν_{peak} values are available for 30 *Fnondet* sources and 64 *Fdet* sources. The *Fdet* sources have significantly higher ν_{peak} values than those of the *Fnondet* population. Also the *Fdet* BLO subpopulation alone, as well as the classical "blazars", a

merge between the BLO and HPQ subpopulations, have significantly higher ν_{peak} values than the *Fnondet* sources.

Doppler boosting is also suggested to play a significant role for the detection probability of strong gamma-ray emission in blazars (Lähteenmäki & Valtaoja 2003; Savolainen et al. 2010). We used the variability Doppler boosting factors D_{var} from Hovatta et al. (2009). They were available for 22 *Fnondet* sources and 52 *Fdet* sources. There is a statistically significant difference between *Fnondet* sources and the *Fdet* HPQ population as well as the *Fdet* "blazar" population (BLO + HPQ), with the HPQs or blazars having higher D_{var} values than the *Fnondet* sources. BLOs alone do not, however, differ from the *Fnondet* population.

In Fig. 7 we have plotted the D_{var} vs. ν_{peak} distribution for the 22 (62%) *Fnondet* and 55 (82%) *Fdet* sources for which we have these data. We can see, indeed, that the *Fdet* BLOs occupy the high end of the ν_{peak} distribution, whereas the *Fdet* HPQs preferably lie in the high D_{var}, low ν_{peak} end of the plot. When studying these "blazar" classes together, there is a significant negative correlation ($\rho = -0.373$, probability $p < 1\%$ for no correlation in the Spearman's rank correlation analysis). Interestingly, the BLO class alone only has a moderately significant ($p = 1.7\%$ for no correlation) negative correlation and for the HPQ class alone the correlation is absent. The detected BLOs and HPQs seem to form a continuum in the D_{var} vs. ν_{peak} space. It is worth noting here that most of the BLOs in our complete sample are bright and variable in the radio domain, and in fact not typical representatives of the BLO population as a whole (Nieppola et al. 2007, 2009). Furthermore, according to Nieppola et al. (2009), at least three of the sources can be classified as "sources exhibiting quasar-like radio behaviour".

4. Conclusions

We have studied the radio behaviour and other properties of a complete flux-limited sample of radio sources, ca. two thirds of which were included in 1FGL. The *Fermi*/LAT-detected sources have been bright and variable in the past as well as during the first year of Fermi operations.

The non-detected sources have radio fluxes and historical radio variability comparable to those of the detected sources. During the first year of *Fermi* operations some of them were relatively bright, but in general they did not exhibit strong variability during that period. In particular, they did not have prominent rising flares during the 1FGL observing period.

The *Fermi*/LAT-detected blazars have higher Doppler boosting factors and higher ν_{peak} values than the non-detected ones, and there is a significant negative correlation between their ν_{peak} and D_{var} values. The *Fdet* BLOs occupy the high end of the ν_{peak} distribution, and the HPQs lie in the high D_{var}, low ν_{peak} end of the distribution. This can either be an indication of the HPQ and BLO populations having at least partly different reasons for being gamma-ray active, or the two subpopulations
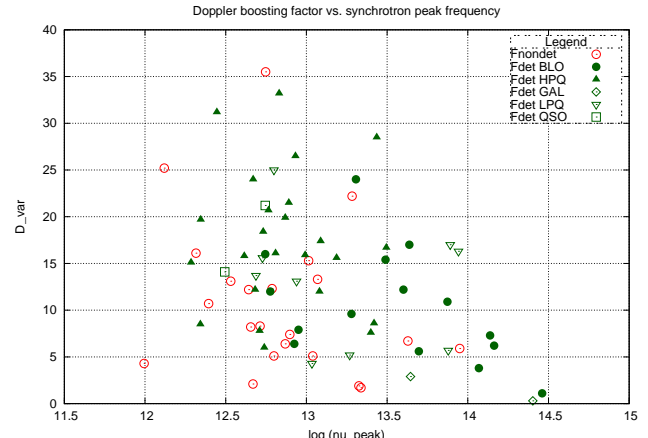
Fig. 7. Doppler boosting factor versus the synchrotron peak frequency for the sources for which we have these data. Open / red circles show the *Fnondet* sources, the other symbols show the various classes of the *Fdet* sources as explained by the legend.

being two extreme ends of a continuum of properties in the D_{var}, ν_{peak} -space. In either case, the BLOs from our sample do not necessarily represent "typical" objects of the BLO population, but rather a relatively extreme subclass of radio-bright, radio variable BLOs.

The first year results from the *Fermi* Large Area Telescope have confirmed the findings that we initially made from the EGRET data: the extragalactic radio sources to be detected in the gamma-rays are preferably sources that are bright and variable also in the radio-domain during the gamma-ray observations. Additionally, they tend to have high ν_{peak} values and/or high Doppler boosting factors. The fundamental reason for an AGN to be gamma-ray bright is probably a favourable combination of properties involving at least a developing radio shock, boosted radiation, and a high synchrotron peak frequency.

References

Abdo, A. A., Ackermann, M., Ajello, M. et al. 2010, ApJS, 188, 405
Hovatta, T., Valtaoja, E., Tornikoski, M., & Lähteenmäki, A. et al. 2009, A&A, 494, 527
Jorstad, S. G., Marscher, A. P., Mattox, J. R. et al. 2001, ApJ, 556, 738
Lähteenmäki, A. & Valtaoja, E. 2003, ApJ, 590, 95
Nieppola, E., Tornikoski, M., & Valtaoja, E. 2006, A&A, 445, 441
Nieppola, E., Tornikoski, M., Lähteenmäki, A. et al. 2007, AJ, 133, 1947
Nieppola, E., Hovatta, T., Tornikoski, M. et al 2009, AJ, 137, 5022
Savolainen, T., Homan, D. C., Hovatta, T., et al. 2010, A&A, 512, 24
Valtaoja, E. & Teräsranta, H. 1995, A&A, 297, L13
Valtaoja, E. & Teräsranta, H. 1996, A&A, 120, 491

Correlations between the Fermi/LATgamma-ray and 37 GHz radio properties of AGN averaged over 11 months

E. Nieppola[1], M. Tornikoski[1], E. Valtaoja[2], J. León-Tavares[1], T. Hovatta[3], A. Lähteenmäki[1], and J. Tammi[1]

[1] Aalto University Metsähovi Radio Observatory, Metsähovintie 114, FI–02540 Kylmälä, Finland
[2] Tuorla Observatory, Department of Physics and Astronomy, FI–20014 Turku, Finland
[3] Department of Physics, Purdue University, West Lafayette, Indiana, USA

Abstract. We have used 37 GHz radio observations obtained at Metsähovi Radio Observatory during the first year of *Fermi* to compare them with the results of *Fermi*/LAT. Our aim was to study the average radio and gamma-ray properties rather than individual pointings. We find that the gamma and radio fluxes, as well as luminosities, have a significant correlation. Using the average fluxes we derive the gamma dominance, S_γ/S_r, and test its dependence on luminosities and the frequency of the synchrotron peak of the spectral energy distribution.

1. Introduction

In the series of articles presented in these proceedings, our team revisits the results obtained in Lähteenmäki & Valtaoja (2003) about the connection between the gamma and radio variations in AGN during the Compton Gamma Ray Observatory era. In this part of the series, we complement the work on individual pointings (León-Tavares et al., these proceedings, p. 93) and detected populations (Tornikoski et al., these proceedings, p. 85) presenting the correlations of *Fermi* and 37 GHz luminosities and gamma dominance averaged over the first year of *Fermi* operation.

2. Sample and data

Our sample includes all AGN in the Metsähovi Radio Observatory source list which are detected by *Fermi*/LAT. All Metsähovi sources are northern ($\delta > -10°$) AGN. In total, the sample comprises 249 sources. 146 of them are BL Lacertae objects (BLOs), 26 high polarization quasars (HPQs), 10 are low polarization quasars (LPQs), 35 are quasars with no polarization data (QSOs) and 8 radio galaxies (GALs). 24 are unclassified radio sources. In this paper we use *Fermi* data from the 1-year catalogue (Abdo et al. 2010) and unpublished 37 GHz data from the Metsähovi Radio Observatory, averaged over the 1FGL *Fermi* period. We have 37 GHz data for 166 sources. The number of data points varies from 1 to a few hundred.

3. Flux and luminosity correlations

We did a simple comparison of gamma and radio fluxes and luminosities, shown in Fig. 1. The fluxes and luminosities were calculated with the formula from Ghisellini et al. (2009) using the energy fluxes. The flux plot has substantially more scatter, but there is a significant correlation in both when the whole sample is considered. We used only 37 GHz detections ($S/N \geq 4$) in these correla-
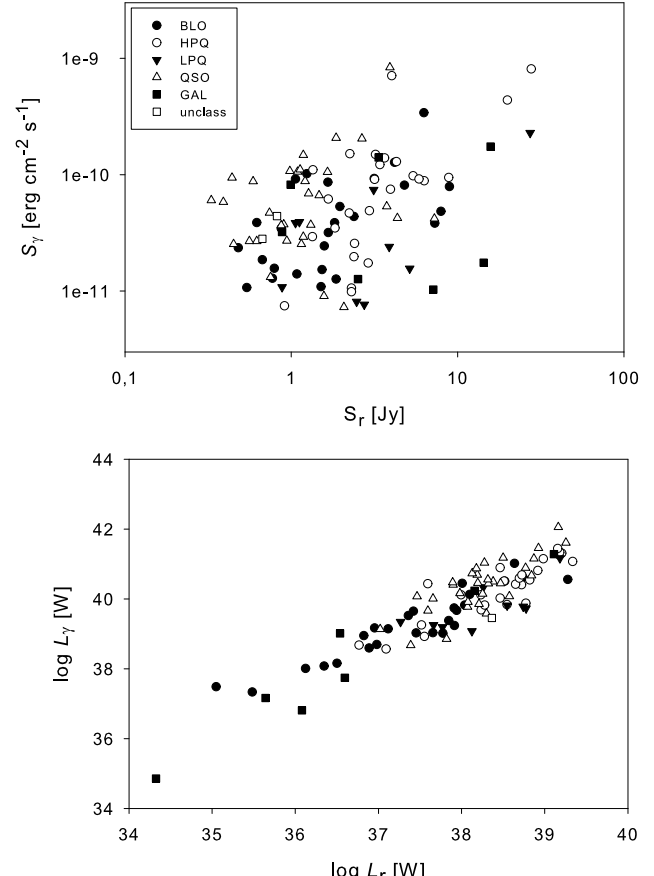

Fig. 1. The correlation between the *Fermi* and 37 GHz fluxes (top panel) and luminosities (bottom panel) averaged over the *Fermi* 1FGL period.

tions. For the flux plot the Spearman rank correlation test gives $\rho = 0.330$ and $P = 0.000$ for the whole sample combined. This value is very close to the correlation obtained
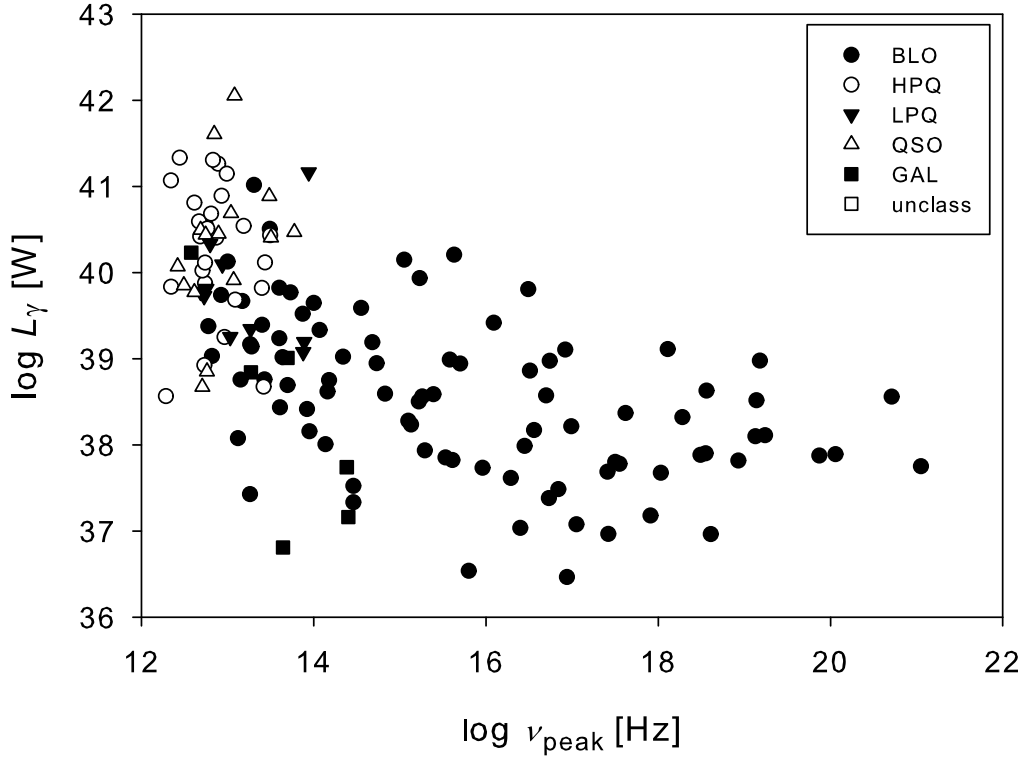
Fig. 2. The correlation between the *Fermi* luminosity and the synchrotron peak frequency.

by Giroletti et al. (2010) for *Fermi* fluxes and 8.4 GHz radio flux. The positive correlation is also significant for BLOs and HPQs, but not for the other subgroups. The luminosity correlation is very tight, the Spearman test gives $\rho = 0.417$ and $P = 0.000$ for the whole sample, with the effect of redshift removed. In both frequency bands, radio galaxies are weakest in luminosity, while HPQs and QSOs are brightest. The outlier radio galaxy with low luminosity in both bands is 3C 274 (M 87). The correlation between the gamma and radio bands indicates that the emission in these two bands has a similar origin.

Figure 2 shows the dependence of the *Fermi* luminosity on the peak frequency of the synchrotron component, ν_{peak}, of the spectral energy distribution. The synchrotron peak frequencies were taken from Nieppola et al. (2008), or, when not available, from Nieppola et al. (2006). They were available for 184 source in total. The figure indicates a negative correlation between the quantities, and one is also found with the Spearman test for the whole sample ($\rho = -0.696$ and $P = 0.000$). The negative correlation is also significant for BLOs and radio galaxies as subgroups. BLOs dominate the plot because they have a more extended distributions of peak frequencies, while the peaks of other subgroups are concentrated in the low-ν_{peak} end.

4. Gamma dominance

We calculated the gamma dominance for all available sources in our sample. In this context, we mean by gamma dominance the ratio of *Fermi* flux and 37 GHz flux in

the same units and averaged over the 1FGL period. For 114 sources in our sample we had only detections ($S/N \geq 4$) at 37 GHz, and 52 more had upper limit fluxes. In most analyses here we use only gamma dominances for the detected-only sources, and use gamma dominances calculated from upper limit fluxes only when clearly stated.

Figure 3 shows the distribution of the gamma dominance. The open distribution is for detections only, and the shaded one for gamma dominance calculated with upper limit 37 GHz fluxes. The distribution is very wide, starting from 3 and extending up to almost 2000 for the upper limit values. The peak of the distribution is around 100. According to the Kruskal-Wallis test, the AGN subgroup distributions are drawn from the same population, so there are no significant differences in the gamma dominance between BLOs, quasars and galaxies.

We also wanted to check the correlation between the gamma dominance and the peak frequency of the synchrotron component in the sources of our sample. The plot is shown in Fig. 4. In the upper panel we have included only the detected-only sample, divided to subgroups, while in the bottom panel we have included the gamma dominances calculated from upper limit fluxes. Even in the same ν_{peak}-bins the gamma dominance can vary by more than two magnitudes. The outlier data point in the top panel at $\log \nu_{peak}$=16.84 is Mark 501. With the detections-only values there is no significant correlation, except for QSOs separately there is a significant positive dependence ($\rho = 0.757$, $P = 0.001$). Also, for all subgroups combined
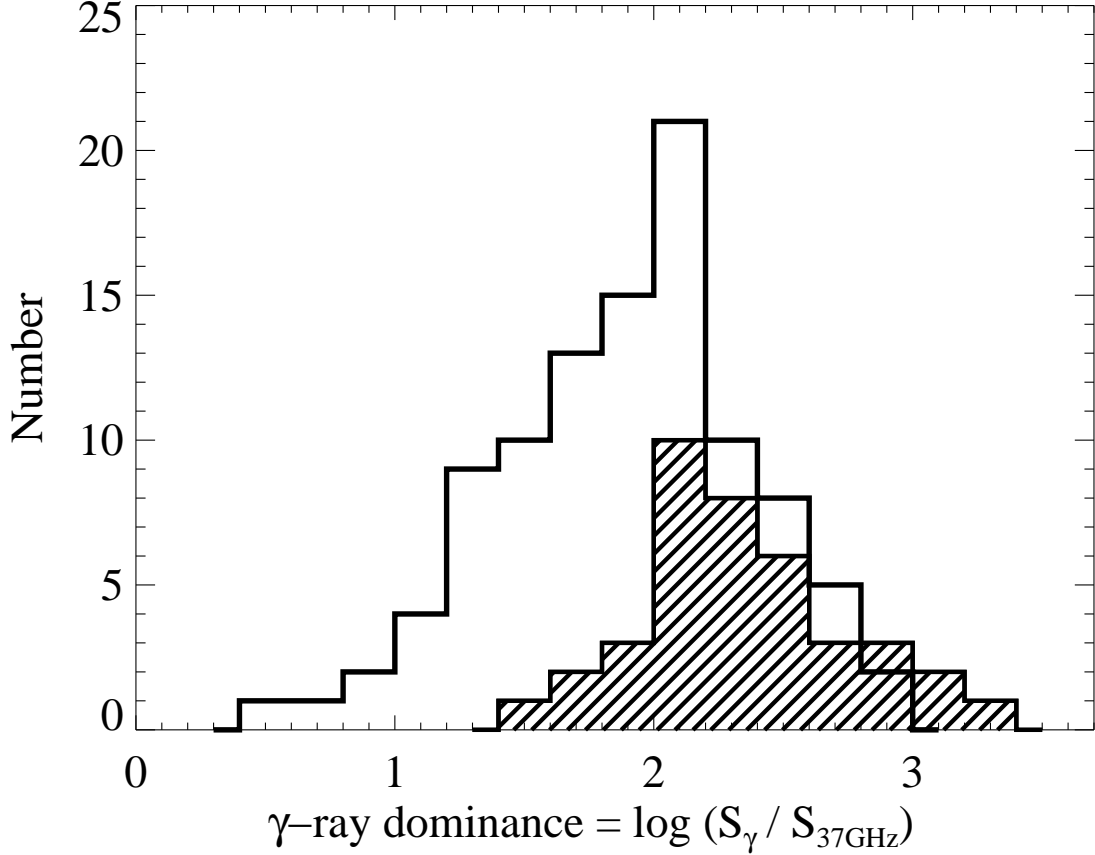
Fig. 3. Distribution of gamma dominance. The open distribution is for 37 GHz detections only, the shaded distribution is for the 37 GHz upper limit fluxes.

and using both detections-only and upper limit values, we get a positive correlation between gamma dominance and ν_{peak} ($\rho = 0.462$, $P = 0.000$). This is mostly because of the high-ν_{peak} BLOs from Nieppola et al. 2006 (the upper limit high-ν_{peak} data points in Fig. 4). At this point we have not considered the use of upper limit flux values in the calculation of the correlation coefficient. However, remembering that using upper limit radio fluxes means that the gamma dominances in the plot are really *lower* limits, we are quite confident that the correlation will hold even if the real flux levels would be considerably lower. Thus, there is some indication that, at least for BLOs at 37 GHz, the gamma dominance rises with increasing ν_{peak}.

In Fig. 5 we have plotted the gamma dominance versus the luminosities at 37 GHz and *Fermi* band. It is clear that the correlation of the gamma dominance with the gamma luminosity is stronger than with 37 GHz luminosity. In the gamma band, the positive correlation of the sample as a whole is significant ($\rho = 0.569$, $P = 0.000$), and for subgroups the correlation is significant for HPQs, QSOs and radio galaxies. In the case of the 37 GHz luminosity, there are no significant correlations. Comparing the two panels of the figure, it seems that the rise in gamma dominance is more due to the rise in gamma luminosity than in the decrease in radio brightness. However, the gamma correlation here does not include the upper limit gamma dominances. If they are added, the correlation becomes much weaker, but remains significant.

5. Conclusions

We have plotted some simple correlations using the *Fermi* and 37 GHz properties averaged over the 1FGL *Fermi* period. Our aim was to establish the long-term dependencies between these two bands, and see their possible differences between the AGN subgroups. It is important to note that our quantities are observational and have not been corrected for Doppler boosting. This we will do in a forthcoming paper.

We conclude that the *Fermi* and 37 GHz fluxes and luminosities correlate significantly, indicating a common origin of emission. The ratio of gamma to radio flux, the gamma dominance, has a wide distribution, peaking roughly at 100. Sources with high ν_{peak}, at least BLOs, seem to be more gamma dominated than low-ν_{peak} sources, but their gamma luminosities in *Fermi* band are lower than those of low-ν_{peak} sources. There is an indication that, among the low-ν_{peak} sources, the rise in gamma dominance is more due to the rise in gamma luminosity than a decrease in radio luminosity.

References

Abdo, A.A. et al. 2010, ApJS, arxiv:1002.2280

Ghisellini, G., Maraschi, L. and Tavecchio, F. 2009, MNRAS, 396, 105
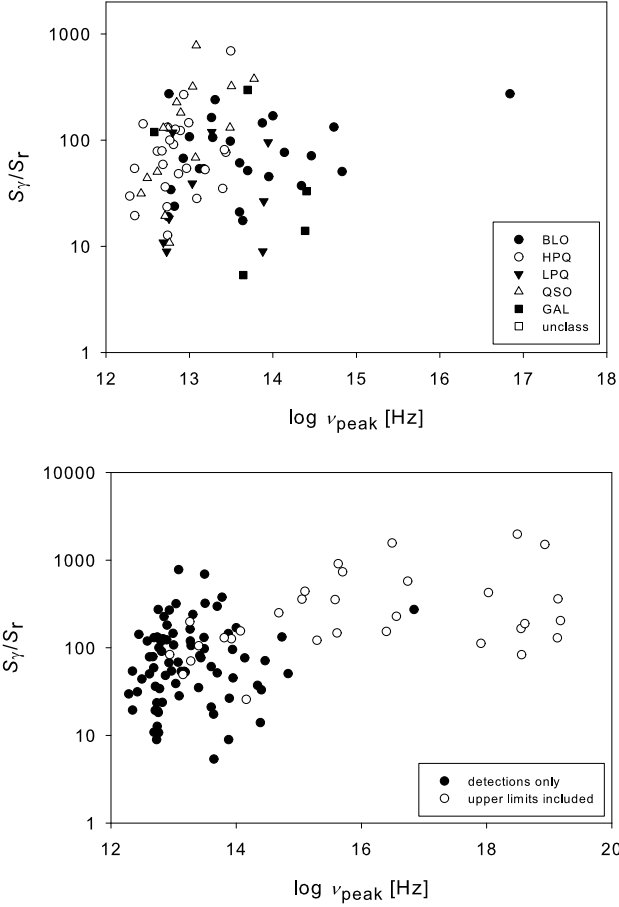
Fig. 4. Gamma dominance plotted against the peak frequency of the synchrotron component. The top panel includes only 37 GHz detections, the bottom panel shows also upper limits as stated in legend.
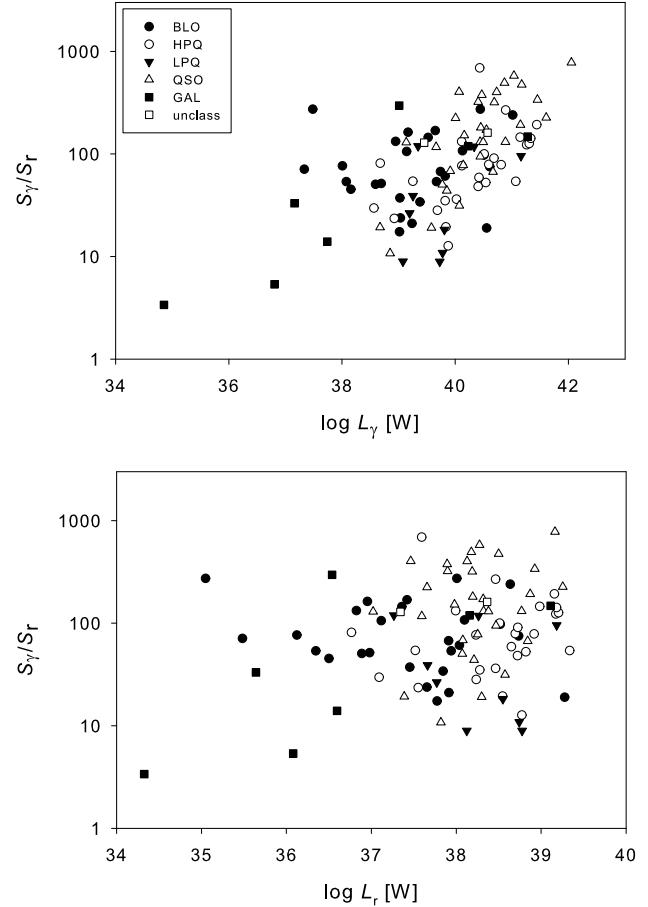
Fig. 5. Gamma dominance plotted against the *Fermi* luminosity (top panel) and 37 GHz luminosity (bottom panel).

Giroletti, M. et al. 2010, arxiv:1001.5123

Lähteenmäki, A. and Valtaoja, E. 2003, ApJ, 590, 95

Nieppola, E., Tornikoski, M. and Valtaoja, E. 2006, A&A, 445, 441

Nieppola, E., Valtaoja, E., Tornikoski, M. et al. 2008, A&A, 488, 867

The connection between γ-ray emission and radio flares in Fermi/LAT blazars

J. León-Tavares[1], E. Valtaoja[2], M. Tornikoski[1], A. Lähteenmäki[1], and E. Nieppola[1]

[1] Aalto University Metsähovi Radio Observatory, Metsähovintie 114, FIN-02540 Kylmälä, Finland
    e-mail: `leon@kurp.hut.fi`
[2] Tuorla Observatory, Department of Physics and Astronomy, University of Turku, 20100 Turku, Finland.

Abstract. We compare the gamma-ray photon flux variability of northern blazars contained in the *Fermi*/LAT First Source Catalog with 37 GHz radio flux curves from the Metsähovi quasar monitoring program. We find that the relationship between the millimeter (mm) and gamma-ray fluxes arises differently for each type of blazar. The flux relation between the two bands is positively correlated for quasars and absent for BL Lac type objects. Furthermore, we find that the levels of gamma-ray emission in high state depend on the phase of the high frequency radio flare, where the brightest gamma-ray events coincide with the initial stages of a mm flare.

1. Introduction

Blazars are the brightest and the dominant population of active galactic nuclei (AGN) detected at gamma-rays (e.g., Fitchel et al. 1994, Abdo et al. 2010). The continuum emission from the relativistic jets, occasionally dominates at all energies, swamping the emission originating in other regions. The origin of the gamma-ray emission in blazars is thought to be due to inverse Compton scattering of photons by the electrons of the relativistic jet. However, the origin of the low energy photons which are upscattered into gamma-rays is still an open issue.

Based on data from the EGRET instrument onboard the *Compton Gamma Ray Observatory*, Lähteenmäki & Valtaoja (2003) found that gamma-ray detected sources tend to have ongoing radio flares and the production of gamma-ray flares is connected to the shocks in the relativistic jets, several parsecs from the AGN core. This led them to conclude that strong gamma-ray emission in quasars is produced by synchrotron-self-Compton (SSC) mechanisms (e.g., Bloom & Marscher 1996 and references therein) in the same shocks in the relativistic jet that also produce the radio flares. The dramatically improved gamma-ray data by the Large Area Telescope (LAT) onboard the *Fermi Gamma-Ray Space Telescope*, allow us to test results obtained from the EGRET era and to provide details on the connection between the gamma-ray emission and radio flares to find out which mechanisms are likely to be responsible of the gamma-ray emission.

In this contribution we re-examine the connection between radio and gamma-rays regimes by comparing the Metsähovi radio monitoring data with the *Fermi*/LAT First Source Catalog (Abdo et al. 2010, 1FGL)

2. Comparison of Metsähovi and Fermi/LAT light curves

We aim to examine the dependence of gamma-ray flux on radio flare phase and amplitude based on the Metsähovi quasar monitoring at 37 GHz and the 1FGL catalogue. The Metsähovi quasar monitoring program currently observes about 250 AGN at 37 GHz. We have selected a sample of sources which fulfill the following criteria: (i) we had well-sampled light curves during the period 2007–2010, aiming to cover the 1FGL period, (ii) we have a firm association in the 1FGL catalogue and (iii) the gamma-ray monthly light curve during the 1FGL period is significantly different from a flat one.

Our final sample consists of 60 sources which have been classified according to their optical spectral type in high polarized quasars (HPQ, 22), low polarized quasars (LPQ, 5), quasars with absence of optical polarization data (QSO, 15), BL Lac type objects (BLO, 17) and radio galaxies (GAL, 1). For a description of the 1FGL gamma-ray detection and average properties associated with each type of source, see Tornikoski et al., these proceedings, p. 85   and Nieppola et al. in these proceedings. p. 89

In order to compare radio and gamma-ray fluxes, monthly binned radio light curves were created from the Metsähovi flux density curves at 37 GHz. The selected bins of time are the same as in the 11 months 1FGL flux history curves, allowing us to compare simultaneous gamma-ray and radio flux variations. With the aim to categorize the phase of the mm flares at the time of the gamma-ray maxima, we have decomposed the total flux density variations at 37 GHz into a small number of exponential flares as in previous works (e.g., Valtaoja et al. 1999, Savolainen et al. 2002, Lähteenmäki & Valtaoja 2003).

pointings from monthly averaged light curves
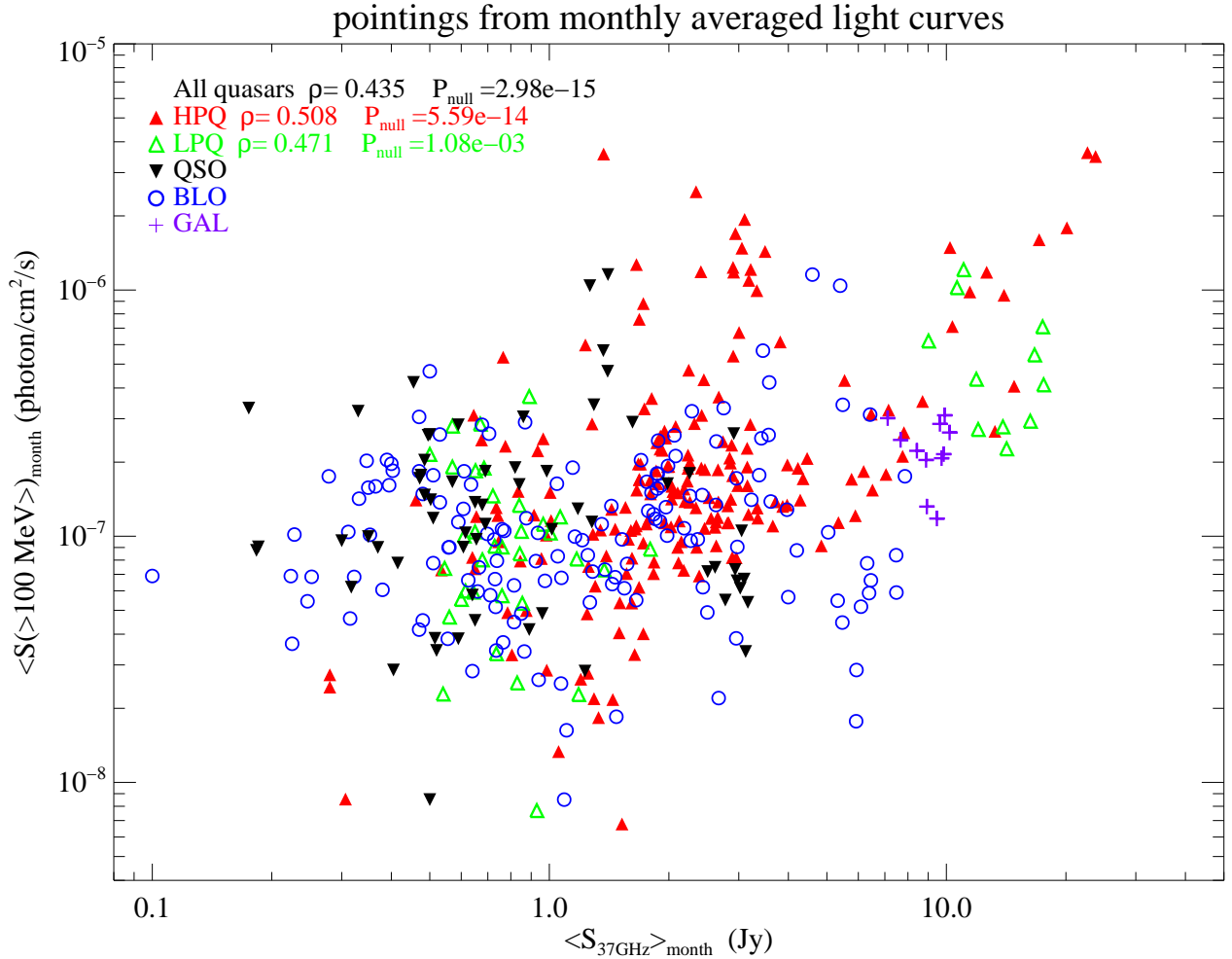
Fig. 1. Simultaneous flux-flux relation for the combined sample of 60 radio-loud AGN analyzed here. The different types of sources are symbol coded as shown in the legend, the correlation coefficients are shown only when the significance is ≥ 99.9 %

3. Results

For each of the 60 sources we could investigate the relation between the gamma-rays and 37 GHz flux during the 1FGL period. However, only for a subsample of 45 sources we had an adequate decomposition of the total flux density curves, allowing us to further categorize in detail the radio flare state in relation with the gamma-ray maxima during the 11 months of the 1FGL catalogue.

3.1. Simultaneous flux-flux relation

Using the densely covered light curves from the Metsähovi quasar monitoring program we compare simultaneous gamma-ray and 37 GHz fluxes. Figure 1 shows that simultaneous fluxes at two bands are apparently positive correlated. In detail, however we do find significant differences in quasars compared to BL Lacs, which we describe below. By applying the Spearman's rank correlation test, two very clear results emerge. First, there is a significant positive correlation between gamma-ray and 37 GHz fluxes for quasars, while fluxes associated to BL Lacs do not seem

to be correlated. Second, the strength and significance of the correlations is different for each type of quasar.

The flux-flux correlation among quasars is absent, significant ($\rho = 0.47, P_{null} = 99.9\%$) and very significant ($\rho = 0.50, P_{null} > 99.9\%$) for QSO, LPQ and HPQ, respectively. These apparent relation between the strength of correlation and optical polarization degree of the quasar, arises naturally if the latest traces the viewing angle of the jet, where sources with high optical polarization degree have their jets oriented closest to our line of sight (e.g., Hovatta et al. 2009). The dependence between flux-flux relation and optical polarization degree confirms previous results where it has been shown that the brightest gamma-ray emitters have preferentially smaller viewing angles (Valtaoja & Teräsranta. 1995, Lähteenmäki & Valtaoja 2003) and consequently higher Doppler boosting factors (Lister et al. 2009, Savolainen et al. 2010). Since gamma-ray and radio fluxes are significantly correlated for sources where the relativistic jet is pointing close to our line of sight, this suggests the existence of a strong coupling between the radio and gamma-ray emission mechanisms. The fact that the correlation is seen in monthly flux levels indicates a co-spatial origin.
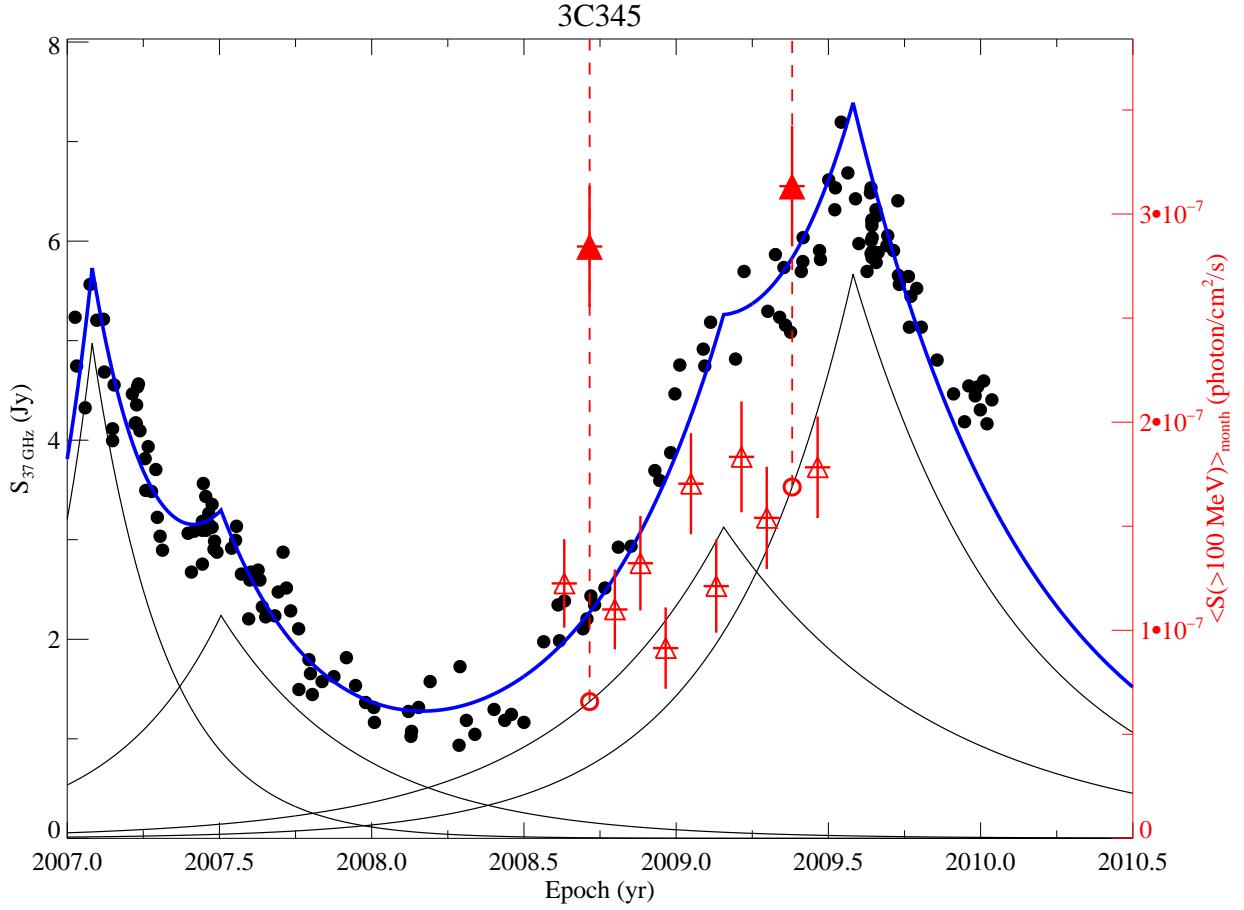
3C345

Fig. 2. Recent flux history at 37 GHz (filled circles) and gamma-rays (triangles) of 3C 345. The total flux density curve at 37 GHz has been decomposed using individual exponential flares following the method described in Valtaoja et al. (1999). The filled triangles represents the significant peaks in the gamma-ray flux during the 1FGL period. The two dashed vertical lines are drawn to highlight the relation between the strong gamma-ray events and rising stages of the radio flares.

3.2. Connections between ongoing flares and high states of gamma-ray emission

We have decomposed the 37 GHz light curves into individual exponential flares, each of which corresponds to a new shock created in the jet and is often detectable as a new VLBI component (Valtaoja et al. 1999, Savolainen et al. 2002). We compared the phase of the individual flares with the gamma-ray light curves obtained from the 1FGL catalogue in order to determine whether high states of gamma-ray emission are associated with shocks propagating downstream the jet.

To identify the maxima in the 1FGL variablity flux history, we calculate the derivative at each of the 11 months in the 1FGL period. In this work, a peak is a point in the 1FGL curve at which the derivative changes sign. We evaluate, for each peak, the number of points that have a positive derivative at its left plus the number of points with a negative derivative at its right. This is considered as the peak width. The sum of the absolute values of the derivatives for all the points inside the peak width constitutes the peak weight. The larger the weight the more significant is the peak. In order to avoid confusion with neighboring peaks not adequately sampled during the 1FGL period, or

with flickering, we focus our analysis on the peaks with the largest weight (the most significant) inside the 11 months of the 1FGL period. Hereafter, we refer to the peak with the largest weight as the gamma-ray peak.

Figure 2 shows the 37 GHz total flux density measurements (filled circles) and the 1FGL gamma-ray monthly flux curve (triangles) for 3C 345 as an example. We identify two well defined peaks in the gamma-ray light curve which have been highlighted by filled triangles, however, the peak around middle 2009 corresponds to the peak with the largest weight. The individual exponential flares and the total model fit to the flux curve are shown as thin and thick lines, respectively. The two vertical dashed lines are drawn to highlight that the two sharp gamma-ray flares in the 1FGL period occurred during the rising state of the individual radio flares, as previously found in Valtaoja & Teräsranta 1995 and Lähteenmäki & Valtaoja (2003) during the EGRET era.

The phase of the radio flare has been further categorized as : 0 - beginning of the flare, 1 - peak of the flare and 2 - end of the flare, consistent with previous works (Valtaoja & Teräsränta 1995, Lähteenmäki & Valtaoja 2003). We have determined the flare phases in 45 sources
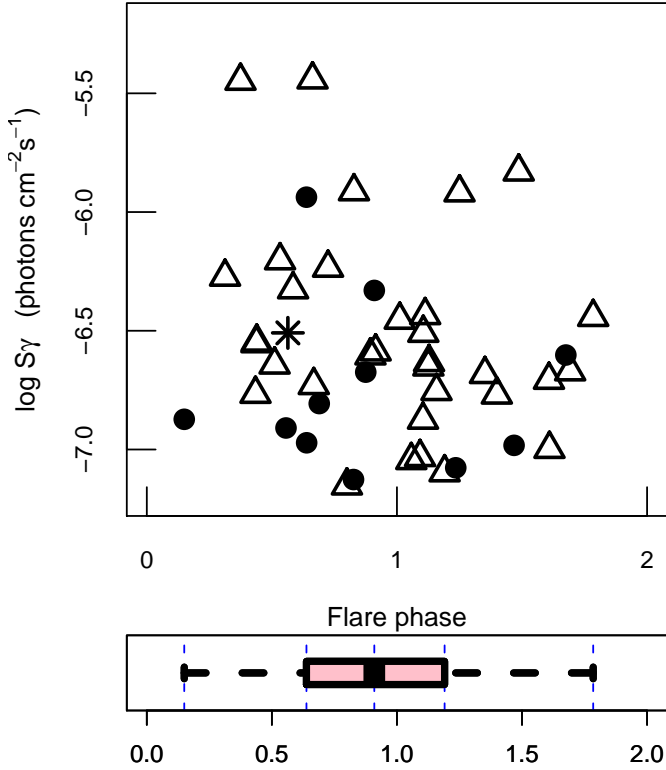
Fig. 3. Maximum gamma ray flux vs the radio flare phase (0, beginning; 1 peak; 2 end of the flare). The bottom panel shows the distribution of the flare phases in a box plot, with the median located at early stages of the flare. Quasars, BL Lacs and radio-galaxies are shown by triangles, circles and asterisks, respectively.

(33 quasars, 11 BL Lacs and 1 radio-galaxy) and compared them with the flux of the gamma-ray peak. The top panel in Figure 3 gives the distribution of flare phase versus the gamma-ray flux of the most significant peak during the 1FGL period. From the bottom panel of Figure 3, we can find that the majority of the radio-gamma-ray events occupy the region of early phases (0–1), which suggest that the gamma-ray flares tend to occur during the rising or peaking state of the radio flares. The relationship between the flare phase and the maxima in gamma-ray light curve is consistent with previous conclusions (Valtaoja & Teräsranta 1995, Lähteenmäki & Valtaoja 2003) drawn from the EGRET era.

4. Summary and Discussion

By comparing 1FGL and Metšahovi light curves in a sample of northern blazars, we have found (i) a significant correlation between simultaneous gamma-ray and 37 GHz fluxes in quasars, while for BL Lac type objects there is a lack of correlation between the two bands; (ii) we confirm previous results on the temporal coincidence of strong gamma-ray events with the rising states of a millimeter radio flare.

Although inverse Compton mechanism predicts a correlation between radio and gamma-ray emission strengths,

studies from the EGRET era did not find evidence of such correlation (e.g., Lähteenmäki & Valtaoja 2003). This apparent contradiction with results obtained here, is probably due to the limited EGRET sensitivity and to the sparse gamma-ray data available at that time. The absence of gamma-ray and radio flux correlation for BL Lacs is confirmed with *Fermi*/LAT data and might be an indication that gamma-ray emission mechanisms are different for quasars and BL Lacs.

On the other hand, the connection between high gamma-ray states and the rising or peaking phase of the mm flare found in this work confirms previous results from the EGRET era (Valtaoja & Teräsranta 1995, Lähteenmäki & Valtaoja 2003). This result supports the scenario where the gamma-ray emission in blazars originates from synchrotron-self-Compton mechanism in the same shocks that produce the radio outburst (Bloom et al. 1996). However, there is growing evidence of an outflow-related component of the broad-line region in radio galaxies (León-Tavares et al. 2010, Arshakian et al. 2010, Ilić et al. 2008). Thus, we could speculate on whether this outflowing broad-line region component could serve as a source of external seed photons to be upscattered to high energies by electrons in the jet, bringing back to the game the external Compton models (Sikora et al. 1994). As gamma-ray emission mechanism of blazars even at distances of parsecs down the jet.

References

Abdo, A.A., Ackermann, M., Ajello, M., et al. 2010, ApJS, in press arxiv:1002.2280

Arshakian, T.G., León-Tavares, J., Lobanov, A.P., et al. 2010, MNRAS, 401, 1231

Bloom, S.D. & Marscher A.P. 1996, ApJ, 461, 657

Fichtel C.E., Bertsch, D.L., Chiang, J., et al. 1994, ApJS, 94, 551

Ilić D., Popović, L.C., León-Tavares, J., Lobanov, A.P., Shapovalova, A.I., & Chavushyan, V.H. 2008, MmSAI, 79, 1105

Hovatta, T., Valtaoja, E., Tornikoski, M., & Lähteenmäki, A. 2009, A&A, 494, 527

Lähteenmäki, A. & Valtaoja, E. 2003, ApJ, 590, 95

León-Tavares, J., Lobanov, A.P., Chavushyan, V.H., et al. 2010 , ApJ, 715, 355

Lister M.L., Homan, D.C., Kadler, M., et al. 2009, ApJL, 696, 22

Savolainen, T., Wiik, K., Valtaoja, E., Jorstad, S.G., & Marscher, A.P. 2002, A&A, 394, 851

Savolainen, T., Homan, D.C., Hovatta, T., et al. 2010, A&A, 512, 24

Sikora, M., Begelman, M.C., & Rees, M.J. 1994, ApJ, 421, 153

Valtaoja, E. & Teräsranta, H. 1995, A&A, 297, L13

Valtaoja E., Lähteenmäki, A., Teräsranta, H., & Lainela, M. 1999, ApJS, 120,95

Shock-Shock Interaction in the Jet of CTA 102

C. M. Fromm[1]⋆, E. Ros[2,1], T. Savolainen[1], A. P. Lobanov[1], M. Perucho[2], J. A. Zensus[1], M. F. Aller[3], H. D. Aller[3], M. A. Gurwell[4] and A. Lähteenmäki[5]

[1] Max-Planck-Institut für Radioastronomie, Auf dem Hügel 69, D-53121 Bonn, Germany
[2] Departament d'Astronomia i Astrofísica, Universitat de València, E-46100, Burjassot, València, Spain
[3] University of Michigan, Ann Arbor, MI, 48109 USA
[4] Harvard-Smithsonian Center for Astrophysics, Cambridge, MA, 02138 USA
[5] Aalto University, Metsähovi Radio Observatory, FI-02540 Kylmälä, Finland

Abstract. The radio light curve and spectral evolution of the blazar CTA 102 during its 2006 outburst can be rather well explained by the standard shock-in-jet model. The results of a pixel-to-pixel spectral analysis of multi-frequency VLBI images, together with kinematics derived from the MOJAVE survey lead to the picture of an over-pressured jet with respect to the ambient medium. The interaction of a traveling shock wave with a standing one is a possible scenario which could explain the observed spectral behavior.

1. Introduction

The blazar CTA 102, (B2230+114), has a redshift of $z = 1.037$ (Hewitt & Burbidge 1989) and it is classified as a high polarization quasar (HPQ) with a linear optical polarization above 3% (Véron-Cetty & Véron 2003) with an optical magnitude of 17.33. The source was observed for the first time by Harris & Roberts (1960) and right from the beginning it was showing radio variability (e.g., Sholomitskii 1965) which led other scientists to suggest that the signal was coming from an extraterrestrial civilization (Kardashev 1964). Later observations identified CTA 102 as a quasar.

Since that time CTA 102 has been the target for numerous observations at different wavelengths. Besides the mentioned variation in the radio flux density, CTA 102 changes its optical behavior in a no less spectacular way. Pica et al. (1988) reported rapid variation up to 1.14 mag around an average value of 17.66 mag. An increase of 1.04 mag within 2 days in 1978 was so far the most significant outburst. The strongest radio flare since 1986 and a nearly simultaneous outburst in the optical regime took place around 1997 (Tornikoski et al. 1999). Even in the γ-ray regime the source has been detected by the telescopes EGRET on-board *CGRO* and *Fermi* with a luminosity, $L_\gamma = 5 \times 10^{47}$ erg/s (Nolan et al. 1993; Abdo et al. 2009).

Within the framework of the MOJAVE[1] program (Monitoring of Jets in Active galactic nuclei with VLBA Experiments) CTA 102 has been monitored since mid 1995 (see Lister et al. 2009, and Lister et al. (these proceedings, p. 159)). The results of these intensive observations deliver a detailed picture of the morphology and kinematics of this source. The results of the kinematic analysis show an apparent velocity of the features in the jet between 0.7 c

and 15.40 c (Lister et al. 2009). A multi-frequency VLBI study including data at 90 GHz, 43 GHz and 22 GHz was reported by Rantakyrö et al. (2003). The results from the multi-frequency VLBI observations were combined with the continuum monitoring performed at single dish observatories at 22 GHz, 37 GHz, 90 GHz, and 230 GHz. Within this multi-frequency data set (November 1992 until June 1998) CTA 102 showed a major flare around 1997. The authors could conclude that this flare was connected to the ejection of a new jet feature. The inferred apparent speed of 11 c, combined with the frequent and rapid flaring events throughout the electromagnetic spectrum, lead to the picture of a highly relativistic jet. This picture is supported by the conclusions of Jorstad et al. (2005) and Hovatta et al. (2009). They found Lorentz factors, Γ, of 17 and 15, and respectively, Doppler factors, δ, between 15 and 22.

In April 2006, CTA 102 underwent a major radio flux outburst and we will present the result of our analysis of this flaring event using single dish and multi-frequency VLBI observations. We found indications that this flaring event was created by the interaction between a re-collimation shock and a traveling shock wave.

2. Observations

2.1. Single-Dish Light Curves

In our analysis we concentrated on the radio flare around April 2006 and used single dish observations spanning from 4.8 GHz to 340 GHz (see Fig. 1). The flare is clearly visible at all the frequencies with increasing time delays towards smaller frequencies. The highest flux density of about 10 Jy is measured at 37 GHz.

A self-absorbed synchrotron spectrum is described by

$$S(\nu) = C \left(\frac{\nu}{\nu_1}\right)^{\alpha_t} \left\{ 1 - \exp\left[-\left(\frac{\nu}{\nu_1}\right)^{\alpha_0 - \alpha_t}\right] \right\}, \quad (1)$$

⋆ Member of the International Max Planck Research School for Astronomy and Astrophysics.
[1] http://www.physics.purdue.edu/MOJAVE
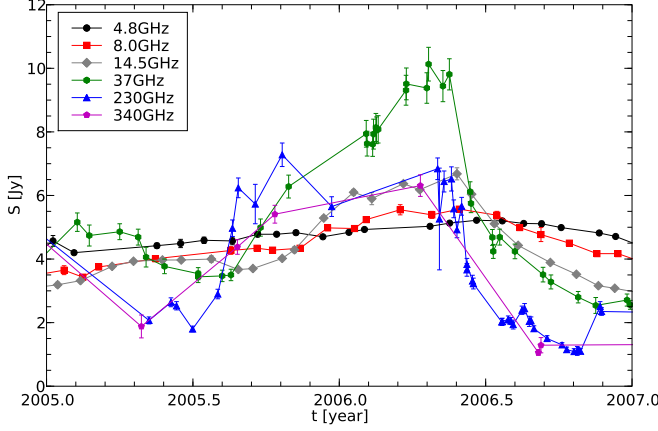
Fig. 1. Single dish light curves for CTA 102, centered around the 2006 radio flare. Used telescopes are 4.8–14.5 GHz UMRAO (M. F. Aller and H. D. Aller), 37.0 GHz Metsähovi (A. Lähteenmäki) and 230–340 GHz SMA (M. Gurwell)
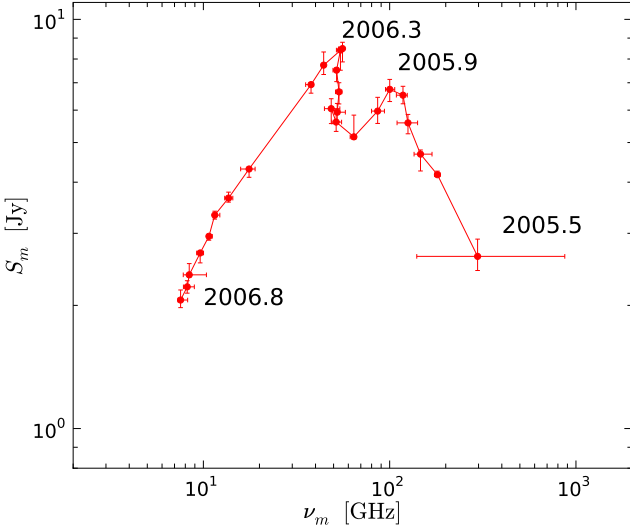
Fig. 2. The 2006 radio flare in the turnover frequency - turnover flux density plane. The numbers indicate the temporal evolution of the flare.

where $S(\nu)$ is the flux density, ν_1 is the frequency at which the opacity $\tau_s = 1$, and α_t and α_0 are the spectral indices for the optically thick and optically thin parts of the spectrum, respectively. The turnover frequency, ν_m, and the turnover flux density, S_m, can be calculated from the first and the second derivative of synchrotron spectrum and they can be regarded as the characteristics of the spectrum.

For the spectral analysis we interpolated the data to a time sampling of $\Delta t = 0.05$ yr and subtracted an underlying quiescent spectrum. This homogenous spectrum ($\nu_m = 1.70$ GHz, $S_m = 4.08$ Jy, $\alpha_0 = -0.35$ and $\alpha_t = 5/2$) was created from archival data. The spectral evolution of the 2006 radio flare in CTA 102 is presented in the turnover frequency - turnover flux density ($\nu_m - S_m$) plane (see Fig. 2).
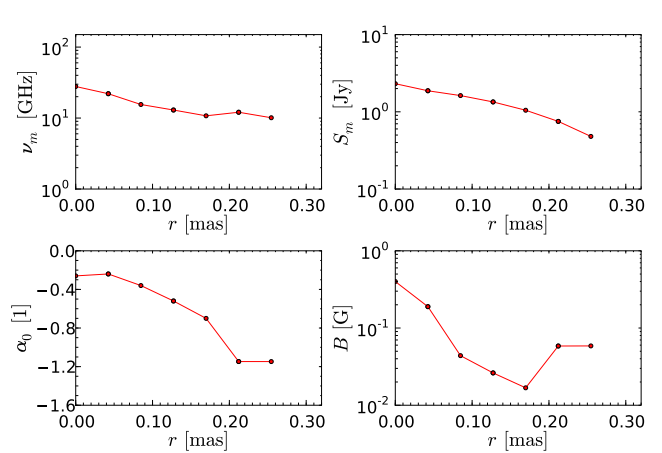
Fig. 3. Evolution of the spectral parameters along the jet axis derived from the 2005.39 multi-frequency observations of CTA 102. The estimate of the uncertainties are difficult due their dependence on the image alignment and the uneven uv-coverage between the different frequencies. Note that the individual pixels are not independent. An estimate for the errors, assuming correct alignment, on the turnover frequency and flux density is around 15% of the derived value (see Discussion).

The flare starts around 2005.6 at a high turnover frequency ($\nu_m \sim 300$ GHz) and low turnover flux density ($S_m \sim 3$ Jy). During the first 0.3 yr the turnover flux density, S_m, is increasing (to $S_m \sim 6.5$ Jy) while the turnover frequency, ν_m is decreasing (to $\nu_m \sim 120$ GHz). Following Marscher & Gear (1985) we could identify this stage as the Compton stage, where Compton losses are the dominant energy loss mechanism. The next stage in the shock-in-jet model should be the synchrotron one. This stage is characterized by a less prominent changes in the turnover flux density, S_m, while the turnover frequency, ν_m is still decreasing. One could consider the time between 2005.8 and 2005.9 as a possible candidate for this stage. During this time span of 0.1 yr the turnover flux density is slightly increasing (to $S_m \sim 7.0$ Jy) while the turnover frequency keeps on decreasing (to $\nu_m \sim 90$ GHz). In the final stage the energy losses are dominated by the adiabatic expansion of the jet and the relativistic shock, the adiabatic loss stage. During this stage the turnover flux density and and the turnover frequency are decreasing. The adiabatic losses start to dominate the spectral evolution between 2005.9 and 2006.0.

The increase of the turnover flux density starting from 2006.0 on and reaching a peak value of $S_m \sim 8.5$ Jy in 2006.3 can not be explained by the shock-in-jet model. After 2006.3 the turnover flux density decreases with decreasing turnover frequency. A detailed analysis of the single dish observations will be presented elsewhere.

2.2. Multi-Frequency VLBI Observations

Since single-dish observations do not provide structural information of the jet we used as well multi-frequency
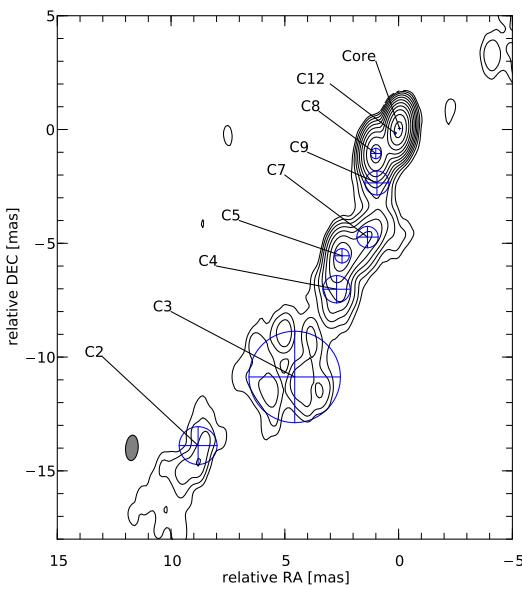
Fig. 4. 15 GHz VLBI image of CTA 102 observed on 6th of January 2007.

VLBI observations covering a frequency range from 2 to 86 GHz for accessing the neighborhood of the AGN central engine. CTA 102 was observed with the National Radio Astronomy Observatory's Very Long Baseline Array at three epochs (March 9th 2005, April 14th 2006 and 8th June 2006) using the all 10 antennas of the array. After calibration of the raw data, using the standard AIPS procedures and model fitting in DIFMAP, we performed a core-shift analysis ($\Delta r \propto \nu^{1/k_r}$) following Lobanov (1998) and a spectral analysis on the pixels along the jet axis using Equation 1. From the 2005.39 multi-frequency observations of CTA 102 we concluded from the core-shift results that the source is in equipartition (jet particle energy density equals magnetic field energy density). This circumstance is reflected by a value of $k_r = 0.98 \pm 0.03$ and leads to an absolute distance from the central object $r_{core,86\,GHz} = 3.29 \pm 1.12\,pc$ and to a magnetic field $B_{core,86\,GHz} = 0.40 \pm 0.14\,G$. From the derived spectral values (especially ν_m, S_m) we calculated the magnetic field $B \propto \nu_m^5 S_m^{-2}$.

Figure 3 presents the evolution of the physical parameters deduced by our analysis as a function of the distance from the core. The results show an increase in the turnover frequency, ν_m, (upper right panel), the optically thin spectral index, α_0, (lower right panel) and the magnetic field, B, at a distance of 0.2 mas away from the core. This behavior could be an indication for an re-collimation shock (standing shock wave) at this position.

2.3. MOJAVE Observations

To check the evidence for a re-collimation shock at a distance of 0.2 mas from the core we used the kinematic analysis of the 15 GHz VLBI monitoring of CTA 102 (Lister et al. 2009). A high resolution VLBI image of CTA 102
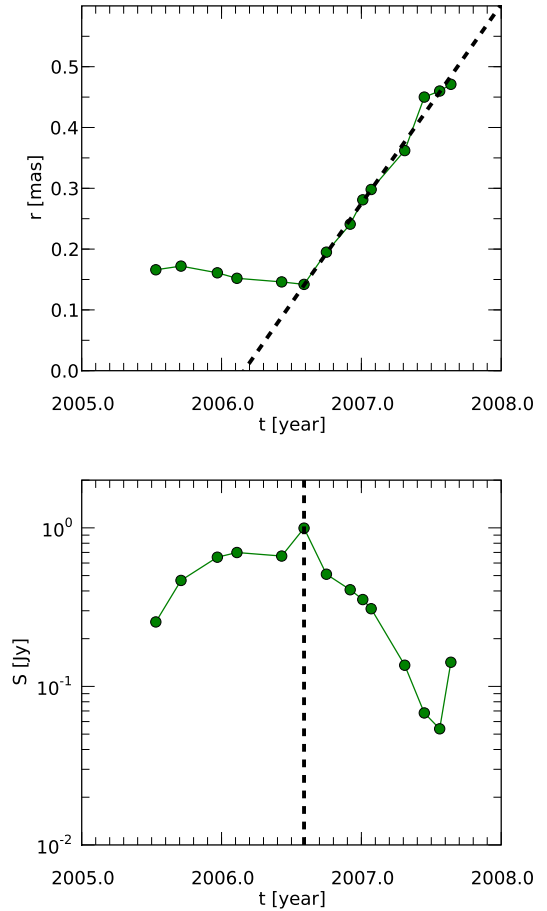
Fig. 5. Properties of the C12 component from the MOJAVE observations. Left: Separation from the core inclusive linear fit to the acceleration event (dashed line). Right: Evolution of the flux density and time of beginning of the acceleration event (dashed line, see text for explanation). The uncertainties for the flux densities are around 5% of the total intensities and the positional errors are of 1/5 of the restoring beam dimensions (typically around 0.01 mas)

observed at 15 GHz on January 2007, showing the location and size all fitted circular Gaussian components, is presented in Fig. 4. The kinematics and the evolution of the flux density of a fitted component labeled as C12 could be interpreted as the interaction of a moving shock wave with the re-collimation shock: the separation from the core ($r \sim 0.2$ mas) remains constant until mid 2006, when an acceleration event takes place together with a sharp drop in the flux density (see Fig. 5).

By fitting the acceleration part of the C12 trajectory and correcting for the core-shift we derived a value for the ejection time, $t_{ej} = 2005.83 \pm 0.05$ yr. This time corresponds to the first peak in the ν_m-S_m plane. The second peak is located slightly before the time of the beginning of the acceleration event (possible intersection of the moving shock wave with the re-collimation shock) $t_{intersec} \sim$ 2006.6 yr. Using a viewing angle of $\vartheta = 2.6 \pm 0.5°$ (Jorstad et al. 2005) we derived a velocity $\beta = v/c = 0.998 \pm 0.042$ and a bulk Lorentz factor $\Gamma = 17.7 \pm 0.7$.

3. Discussion

The evolution of the 2006 radio flare in the ν_m-S_m plane could be explained by the interaction of a moving shock wave with a re-collimation shock. Re-collimation shocks are stationary features in non-pressure matched jets and lead to local increase in pressure and change in the orientation and value of the magnetic field (Daly & Marscher 1988; Falle 1991; Perucho & Martí 2007). This behavior can be seen in the increase of the turnover frequency, ν_m and the increase in the magnetic field, B at a distance of 0.2 mas in the evolution of the spectral parameters derived from multi-frequency VLBI observations (see Fig. 3). The first peak in the ν_m-S_m plane corresponds to the ejection of the traveling shock wave around $t_{ej} \sim 2005.85$ yr. The trajectory of this new feature can not be observed at 15 GHz due to the limited resolution. The interaction of the moving shock wave with re-collimation shock takes place around mid 2006 which could lead to the second peak in the ν_m-S_m due to shock acceleration in a region of increased pressure and magnetic field. During the interaction of the two waves the re-collimation shock is pulled away by the moving one and should appear after some time again at the same position. One possible explanation why this reaction is not detected in the 15 GHz kinematics could be a rarefaction wave. This wave is traveling in the wake of the moving shock wave and decreases the pressure behind the shock front. Together with the limited dynamical range of the VLBI this could be the reason for the non-detection of the re-collimation shock after the collision with the traveling one.

4. Conclusions and Outlook

The combination of single-dish observations with multi-frequency, densely time-sampled VLBI monitoring is a powerful approach which can contribute towards a better understanding of flaring events. Using a high-quality set of observational data we presented a possible scenario which could explain the observed flare by a shock-shock interaction and derived estimates for the physical parameters of the jet and the traveling shock wave.

The spectral values presented have been derived from a spectral analysis applied on multi-frequency VLBI observations. This technique is sensitive to the correct image alignment and to effects of the uneven uv-coverage between the frequencies. The effect on the derived parameters due to small misalignments could lead to significant changes in the spectral values, especially in the magnetic field ($B \propto \nu_m^5 S_m^2$). Further analysis of the influence of the alignment is needed to provide adequate error bars for the derived values.

Besides quantifying the uncertainties on the observational parameters we started to test our assumption of the shock-shock interaction using 2D relativistic magneto-hydrodynamic simulations. These simulations will help us to understand the formation of re-collimation shocks in magnetized jets and their interactions with traveling shocks.

It is also of interest to investigate possible correlations between γ-ray flares and the collision of re-collimation shocks and traveling shock waves. These investigations could help to clarify the question where in the jet the high energy radiation is generated.

References

Abdo, A. A., Ackermann, M., Ajello, M., et al. 2009, ApJ, 700, 597

Daly, R. A. & Marscher, A. P. 1988, ApJ, 334, 539

Falle, S. A. E. G. 1991, MNRAS, 250, 581

Harris, D. E. & Roberts, J. A. 1960, PASP, 72, 237

Hewitt, A. & Burbidge, G. 1989, ApJS, 69, 1

Hovatta, T., Valtaoja, E., Tornikoski, M., & Lähteenmäki, A. 2009, A&A, 494, 527

Jorstad, S. G., Marscher, A. P., Lister, M. L., et al. 2005, AJ, 130, 1418

Kardashev, N. S. 1964, AZh, 41, 282

Lister, M. L., Aller, H. D., Aller, M. F., et al. 2009, ApJ, 137, 3718

Lobanov, A. P. 1998, A&A, 330, 79

Marscher, A. P. & Gear, W. K. 1985, ApJ, 298, 114

Nolan, P. L., Bertsch, D. L., Fichtel, C. E., et al. 1993, ApJ, 414, 82

Perucho, M. & Martí, J. M. 2007, MNRAS, 382, 526

Pica, A. J., Smith, A. G., Webb, J. R., et al. 1988, AJ, 96, 1215

Rantakyrö, F. T., Wiik, K., Tornikoski, M., Valtaoja, E., & Bååth, L. B. 2003, A&A, 405, 473

Sholomitskii, G. B. 1965, Soviet Ast., 9, 516

Tornikoski, M., Teräsranta, H., Balonek, T. J., & Beckerman, E. 1999, in ASP Conf. Ser., Vol. 159, BL Lac Phenomenon, ed. L. O. Takalo & A. Sillanpää, 307

Véron-Cetty, M.-P. & Véron, P. 2003, A&A, 412, 399

Cross-Analyzing Radio and γ-Ray Time Series Data: Fermi Marries Jansky

Jeffrey D. Scargle⋆

Space Science Division, NASA-Ames, Moffett Field, CA 94035, USA; *Fermi Gamma-Ray Space Telescope*

Abstract. A key goal of radio and $\gamma-$ray observations of active galactic nuclei is to characterize their time variability in order to elucidate physical processes responsible for the radiation. I describe algorithms for relevant time series analysis tools – correlation functions, Fourier and wavelet amplitude and phase spectra, structure functions, and time-frequency distributions, all for arbitrary data modes and sampling schemes. For example radio measurements can be cross-analyzed with data streams consisting of time-tagged gamma-ray photons. Underlying these methods is the Bayesian block scheme, useful in its own right to characterize local structure in the light curves, and also prepare raw data for input to the other analysis algorithms. One goal of this presentation is to stimulate discussion of these methods during the workshop.

1. Introduction

Active galactic nuclei (AGN) are highly variable at all wavelengths. A major fraction of their total luminosity fluctuates over time scales ranging from the shortest for which statistically significant signals can be obtained, to the longest time intervals over which data are available. Characterizing this variability has yielded growing insight into the physical processes powering the large AGN luminosities – a trend that will accelerate as observations, data analysis, and theory proliferate.

This paper outlines time series methods for analysis of the disparate data modes of radio, $\gamma-$ray, and other astronomical observations. The next section introduces a data structure that generalizes data modes traditionally used for time-sequential observations. This abstraction yields methods for estimating, from arbitrary time series data, including heterogeneous mixtures of data modes, all of the standard analysis functions:

- light curves
- autocorrelations
- Fourier power and phase spectra
- wavelet representations
- structure functions
- time-frequency distributions

As indicated in Table 1, for essentially arbitrary data modes these methods yield amplitude and phase information for single or multiple time series (auto- and cross-analysis, respectively) – if desired, conditional on auxiliary variables.

There are significant difficulties in the astrophysical interpretation of these quantities. The methods described

Table 1. Time Series Analysis for All Data Modes

	Auto	Cross	Amp	Phase	Condit.
Correlation	yes	yes	-	-	yes
Fourier	yes	yes	yes	yes	yes
Wavelet	yes	yes	yes	location	?
Struct Fcn	yes	yes	-	-	yes
Time-Freq	yes	yes	yes	yes	yes

here are of use in some of these, such as separation of observational errors from stochastic source variability (both of which, unfortunately, are often called *noise*). But I do not discuss other more difficult problems, which are probably beyond the scope of time series analysis methods, such as assessing the importance of *cosmic variance*, identifying causal or otherwise physically connected relationships in multi-wavelength time series data, *etc.*

Subsequent sections discuss each of the above-listed functions and give sample applications.

2. Abstract Data Cells

The time series algorithms to be described below can be applied to almost any type of time-sequential astronomical data. This generality is facilitated by identifying those features of the data modes that are necessary for analysis algorithms.

Each individual act of measurement may yield a large set of data values relevant to estimation of the signal amplitude, and its uncertainty, as a function of time. Of these, two pieces of information, related to the independent variable (time[1] of the measurement) and the dependent variable (amplitude of the signal at that time), are necessary

---
[1] In practice we always use a discrete time representation, such as a micro-second scale computer clock tick, or the finite time interval of signal averaging.

for any time series algorithm. In radio astronomy the typical example is the measurement of the flux of a source averaged over a short interval of time. In γ-ray astronomy the typical example is the detection of individual photons. The arrival time of the photon is obviously the timing quantity, but what about the signal? One scheme is to represent an individual photon with a delta-function in time. But more information can be extracted by incorporating the time intervals[2] between photons. Specifically, for each photon consider the interval starting half way back to the previous photon and ending half way forward to the subsequent photon. This interval, namely

$$\left[\frac{t_n - t_{n-1}}{2}, \frac{t_{n+1} - t_n}{2}\right], \tag{1}$$

is the set of times closer to t_n than to any other time,[3] and has length equal to the average of the two intervals connected by photon n, namely

$$\Delta t_n = \frac{t_{n+1} - t_{n-1}}{2} . \tag{2}$$

Then the reciprocal

$$x_n \equiv \frac{1}{\Delta t_n} \tag{3}$$

is taken as an estimate of the signal amplitude corresponding to observation n. When the photon rate is large, the corresponding intervals are small. Figure 1 demonstrates the data cell concept, including the simple modifications to account for variable exposure and for weighting by photon energy.

Consider gaps in the data. By this we mean that there are portions of the total observation interval during which the detection system is completely off (exposure zero). This situation is readily handled by defining the start of the data cell for the first photon detected after the gap at the end time of the gap. Correspondingly the data cell for the last photon before the gap is set at the start time of the gap. The statistical nature of independent events assures that this procedure rigorously estimates the true photon rate at the edge of the gap. Of course, no information is available about the signal during such a gap, and the various algorithms deal with gaps accordingly.

Now we consider data modes generally. Three common examples are: (a) measurements of a quasi-continuous physical variable (e.g., radio astronomy flux measurements) (b) the time of occurrence of discrete events (e.g., photons) and (c) counts of events in bins. The signal of interest is the time dependence of the measured quantity in case (a), or of the event rate in case (b). Case (c) is actually very similar to (b), but is often described as density estimation or determination of the event distribution

---

[2] A method for analyzing event data based solely on inter-event time intervals has been developed in (Prahl (1996)).

[3] These intervals form the *Voronoi tessellation* of the total observation interval. See (Okabe et al. (2000)) for a full discussion of this construct, highly useful in spatial domains of 2, 3, or higher dimension; see also (Scargle (2001a), Scargle (2001c)).
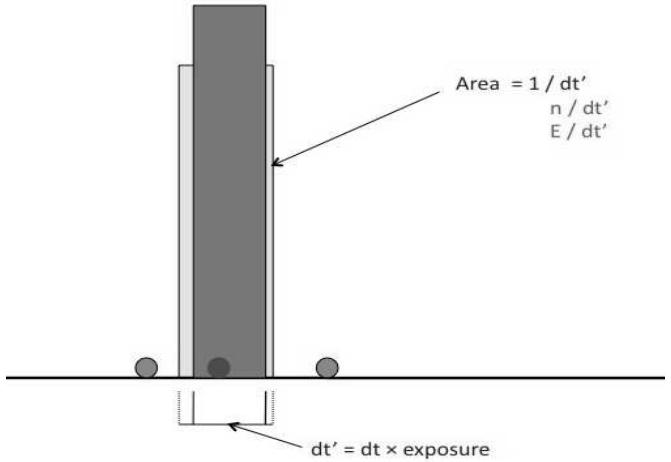
Fig. 1. Voronoi cell of a photon. Three successive photon detection times are circles on the time axis. The vertical dotted lines underneath delineate the time cell, and the light rectangle is the local estimate of the signal amplitude. If the exposure at this time is less than unity, the length of the data cell shrinks in proportion ($dt \rightarrow dt'$), yielding a larger estimate of the true event rate (darker rectangle). The height of the rectangle is n/dt', where n is the number of photons at exactly the same time (almost always 1), or by the photon energy for a flux estimate.

function. In all cases it is useful to introduce the concept of *cells* to represent the measurements. Letting $\mathbf{x_n}$ be the estimate of the signal amplitude for a cell at time t_n, a data set of N sequential observations is denoted

$$C_n \equiv \{\mathbf{x}_n, t_n\}, \quad n = 1, 2, \ldots, N. \tag{4}$$

The specific meaning of the quantities $\mathbf{x}_n$ depends on the type of data. For example, in the three cases mentioned above the array $\mathbf{x}$ contains (a) the sum or average over the measurement interval of an extensive or intensive quantity, respectively, plus one or more quantifiers of measurement uncertainty, (b) coordinates of events, such as photon arrival times, and (c) sizes and locations of the bins, and the count of events in them.

A major reason for constructing this abstract data representation is that it unifies all data modes into a common format that makes construction of universal algorithms easy. As we will see in the next sections, even mixtures of data types – either in the sense of cross-analyzing two very different data types, or mixing data within a single time series – can be handled.

3. Light Curve Analysis: Bayesian Blocks

The simplest and most direct way to study variability is to construct a representation of the intensity of the source as a function of time. More can be done than just plotting the intensity measurements as a function of the time of the measurement. Smoothing, interpolation, gap filling, etc. are all techniques meant to enhance one's understanding of the variability. Here we discuss a different
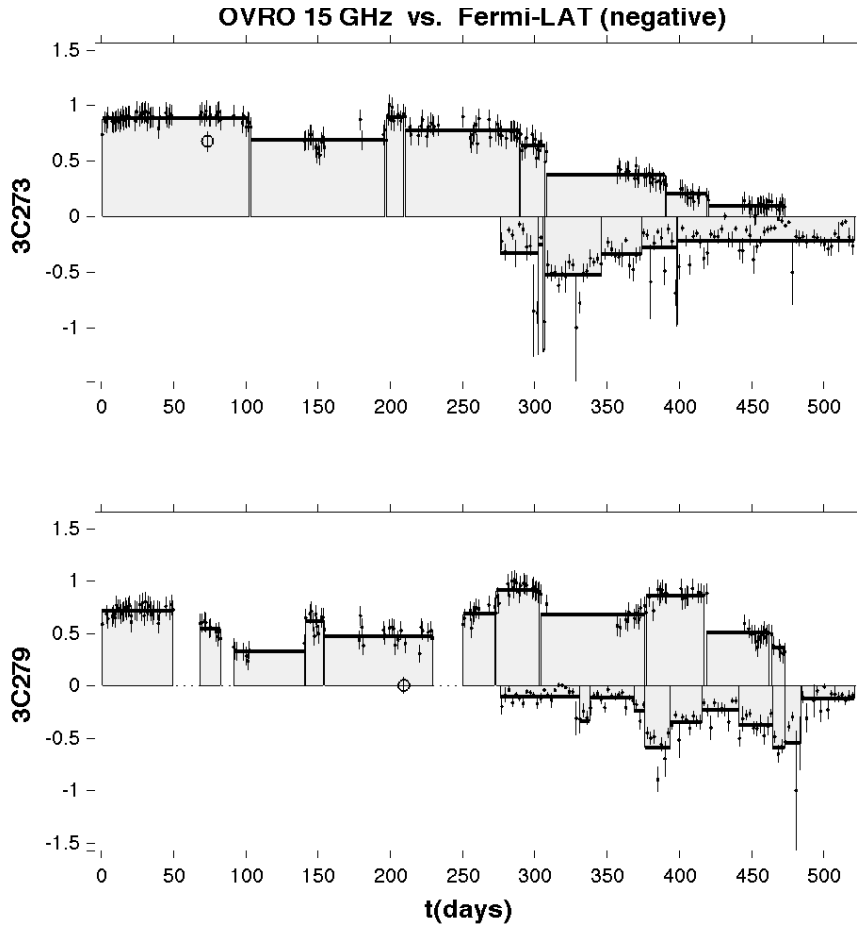
Fig. 2. Bayesian Block representations of the lightcurves of 3C 273 and 3C 279, two AGN in the OVRO/*Fermi* project. The co-aligned times are in days, relative to an arbitrary zero point; amplitudes are on a common relative scale. Binned LAT data is shown for comparison, but the BB representation is based on the photon data only.

procedure, namely construction of a simple, generic, non-parametric model of the data that as much as possible shows the actual variability of the source, and minimizes the effect of observation errors. The model adopted is the simplest possible non-parametric representation of time series data, namely a piece-wise constant model. Details of this approach are given in (Scargle et al. (2010)); the improved algorithm given there replaces the approximate one described in (Scargle (1998)).

The Bayesian Blocks algorithm finds the best partition of the observation interval into blocks, such that the source intensity is modeled as varying from block to block, but constant within each block. This is just a step-function representation of the data. The meaning of the "best" model is the one that maximizes a measure of goodness-of-fit function described in detail in (Scargle et al. (2010)). Another change since the earlier reference is the use of a very simple maximum likelihood fitness function, preferable to the Bayesian posterior previously used because it is invariant to a scale change in the time variable, thus eliminating a parameter from the analysis.

Figure 2 shows the Bayesian blocks analysis of two AGN in the OVRO/*Fermi* joint program. The data shown are from somewhat earlier in the program, where the overlap between the to instruments was not huge. Also these were just the first and third objects in the long list of

observed sources, and were not particularly selected for being highly variable cases.

4. Correlation Functions

A rather underutilized technique for studying correlated variability of two observables (such as time series for different wavelengths) is to construct a scatter plot of one against the other. If done carefully, this approach allows study of joint probability distributions for the two variables; these contain more statistical information than correlation functions or any of the other functions discussed here. The challenges of this approach include the difficulty of depicting the all-important time-sequence connecting the points in the scatter plot, and the need to consider plotting lagged versions of the variables, for a number of values of the lag. The understanding that comes from careful study of scatter plots most often makes it worthwhile to conquer these difficulties.

But probably the most used tool for studying statistical variability properties of a single time series is the auto-correlation function (ACF) or, for studying relations between the variability in two or more sets of simultaneous time series, the cross-correlation function (CCF). The meaning of the latter can be understood by modeling one
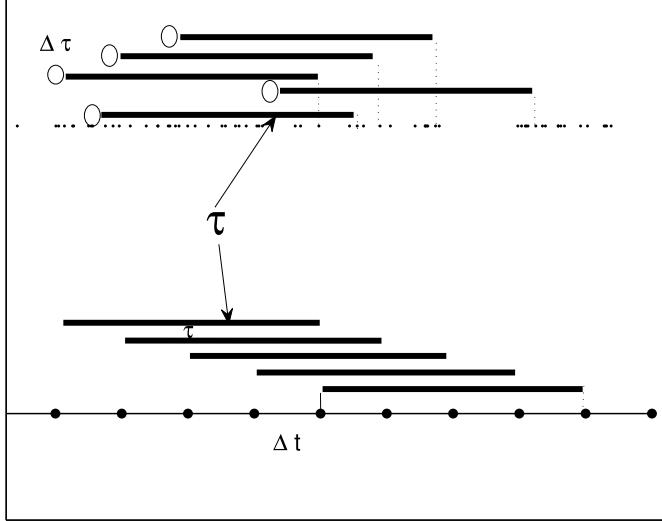
Fig. 3. Summation schemes for autocorrelation functions. The points represent data cells, derived from measured values (as in radio astronomy) or time-tagged events (as in *Fermi* photon data). **Top:** Summation over data with arbitrary spacing in the Edelson and Krolik algorithm. From each point average over all points within a bin $d\tau$ distant by τ; τ is binned, but t is not. **Bottom:** Standard lag summation over evenly spaced data. From each point (except near the ends) there is another point distant by exactly τ = an integer multiple of Δt.

time series as a lagged version of the other, and evaluating the posterior distribution of the lag τ, yielding

$$P(\tau) \sim e^{\frac{R_{X,Y}(\tau)}{K}} \ , \tag{5}$$

where K is a constant and $R_{X,Y}(\tau)$ is the cross-correlation function defined below (Scargle (2001b)).

Concentrating on the CCF, of which the ACF is really a special case, and following the notation and definitions of (Papoulis (1965), Papoulis (1977)), we have this definition of the *cross-correlation function* of two real processes $\mathbf{x}(t)$ and $\mathbf{y}(t)$

$$R_{xy}(t_1, t_2) = < \{ \ \mathbf{x}(t_1)\mathbf{y}(t_2) \ \} > \tag{6}$$

Assuming the processes are stationary, the time dependence is on only the difference $\tau \equiv t_2 - t_2$ and we have

$$R_{xy}(\tau) = < \{ \ \mathbf{x}(t)\mathbf{y}(t+\tau) \ \} > \tag{7}$$

The symbol $<>$ means the *expected value*, informally to be thought of as an average over realizations of the underlying random process X. In data analysis this theoretical quantity is typically not known, and must be therefore be estimated from the data at hand, *e.g.*

$$E[X(t)Y(t+\tau)] \equiv \frac{1}{N(\tau)} \sum_n x_n y_{n+\tau} \tag{8}$$

where x_n and y_n are the samples of the variable X, Y[4], and $N(\tau)$ is the number of terms for which the sum can be taken.

---

[4] **Caution:** It is common to center the processes about their means, to yield the *cross-covariance* and *auto-covariance* func-

Figure 3 is a cartoon of the lag relationships for correlation functions of evenly spaced data (bottom), as well as a solution to the difficulty posed by unevenly spaced time samples in general, and event data in particular. For a given sample or event at t_n there will in general not be a corresponding one at $t_n + \tau$, no matter what restriction is placed on τ.

For this problem an ingenious if straightforward algorithm (Edelson & Krolik (1988)) is in wide use. The basic idea is to pre-define a set of bins in the variable τ in order to construct a histogram of the corresponding time separations $\tau = t_m - t_n$, weighted by the corresponding $x_n y_m$ product. To be more specific, and modifying slightly Edelson and Krolik's formulas for our case (including not subtracting the process means), define for all measured pairs (x_n, y_m) the quantity

$$UDFC_{nm} = \frac{x_n y_m}{\sqrt{(\sigma_x^2 - e_x^2)(\sigma_y^2 - e_y^2)}} \ , \tag{9}$$

(for Un-binned Discrete Correlation Function) where σ_x is the standard deviation of the X-observations, e_x is the X-measurement error, and similarly for Y. The estimate of the correlation function is then

$$R_{xy}(\tau) = \frac{1}{N_\tau} \sum UDCF_{nm} \tag{10}$$

where the sum is over the pairs, N_τ in number, for which $t_m - t_n$ lies in the corresponding τ-bin.

There has been some confusion over the rationale for the denominator in Eq. (9) (" ... to preserve the proper normalization") and how to estimate it. The quantity $(\sigma_x^2 - e_x^2)$ is in principle the difference between the total observed variance and that ascribed to observational errors. How they are estimated from source and calibration data, and other instrumental considerations, no doubt varies from case to case. Edelson & Krolik discuss potential corruption by correlated observational errors. I recommend following their advice to exclude the terms $n = m$ from Eq. (10) only for autocorrelations, and then only if it is really necessary. These terms yield a spike in the auto-correlation function at $\tau = 0$, which can be a convenient visual assessment of the importance of the observational variance; it can be easily removed if needed. For CCFs it makes no sense to remove these terms, absent observational errors correlated between the two observables.

Auto- and cross-correlation involving photon event data is a simple matter of inserting the quantity in Eq. (3) into Eq. (9). Since essentially any time series data mode yields at least surrogates for t_n and x_n, the same is true in general. Figure 4 shows autocorrelation functions computed in this way, for the same AGNs shown in Figure 2

---

tions. Such mean-removal can have unfortunate consequences, such as distortion of the low-frequency power spectrum. In addition, the nomenclature is not completely standard. Various terms are used for the cases where the means of the processes have been subtracted off, and/or the resulting function normalized to unity at $\tau = 0$.
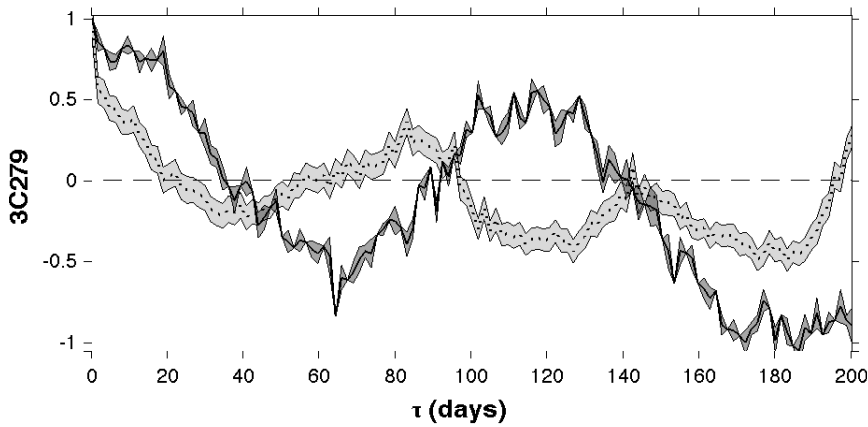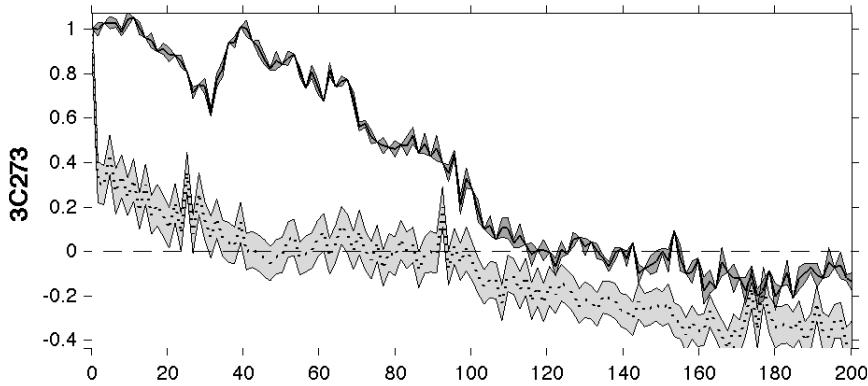
Fig. 4. Autocorrelation functions for the same two AGN as in Fig. 2 for radio and γ-ray data. Solid line with dark error band: OVRO 15 GHz; Dotted line with light error band: *Fermi*/LAT.
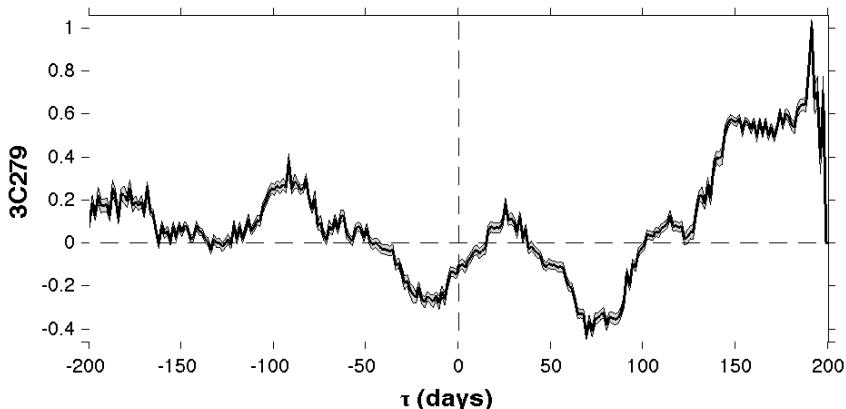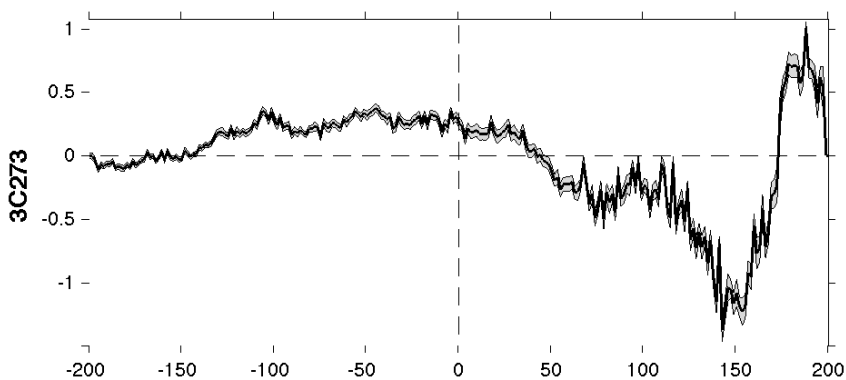

Fig. 5. Cross-correlation functions for the same two AGN as in Fig. 2, for radio and γ-ray data.

and Fig. 5 shows the corresponding cross-correlation functions.

5. Fourier Power and Phase Spectra

Perhaps the most used time series analysis technique in astronomy is estimation of the Fourier power spectrum, mainly with the goal of detecting and then characterizing periodic signals hidden in noisy data, but also for analyzing non-periodic signals such as quasi periodic oscillations and colored, or "$\frac{1}{f}$," noise. There are methods for direct estimation of Fourier power (Scargle (1982)) and phase (Scargle (1989)) spectra from time series data. However, it is often more convenient to make use of the well-known result that the power spectrum is the Fourier transform of the ACF computed as described above in §4. The sliding window power spectra depicted in §8 were computed in this way.

6. Wavelet Representations

It is relatively straightforward to compute the wavelet transform for any time series that can be put into the standard data cell representation. The wavelet shape (in this case the piecewise constant Haar wavelet) is integrated against the empirical signal amplitude assigned by the data cells. Figure 6 shows the scalegrams, or wavelet power spectra (Scargle et al. (1993)), for the same AGN data as in Fig. 4. There is not enough data to yield much detail in these spectral representations, but the rough power law characteristic of $\frac{1}{f}$ processes can be seen, as well as the noise floor for the LAT data.

7. Structure Functions

Another concept in wide usage is the structure function. For the most part its auto- and cross- versions are a repackaging of the same information contained in the corresponding correlations. This point has recently been emphasized by (Emmanoulopoulos et al. (2010)). In addition to summarizing some of the caveats and problems associated with structure functions, these authors give a formal proof of the exact relation between structure functions and the corresponding auto- and cross-correlation functions. In addition, the literature contains a number of claims for the superiority of the structure function that seem unwarranted, especially in view of the relation just mentioned. An example is the misconception that structure functions are somehow immune from sampling effects, including aliasing. Finally, some analysts believe that at short timescales the structure function always becomes flat; the actual generic behavior can be derived from Eq. (A10) of (Emmanoulopoulos et al. (2010)); the normalized structure function satisfies

$$NSF(\tau) = 2[1 - ACF(\tau)] \rightarrow C\tau^2 \qquad (11)$$

for $\tau \rightarrow 0$, since autocorrelation functions are even in τ. In practice this dependence may *seem* flat compared to
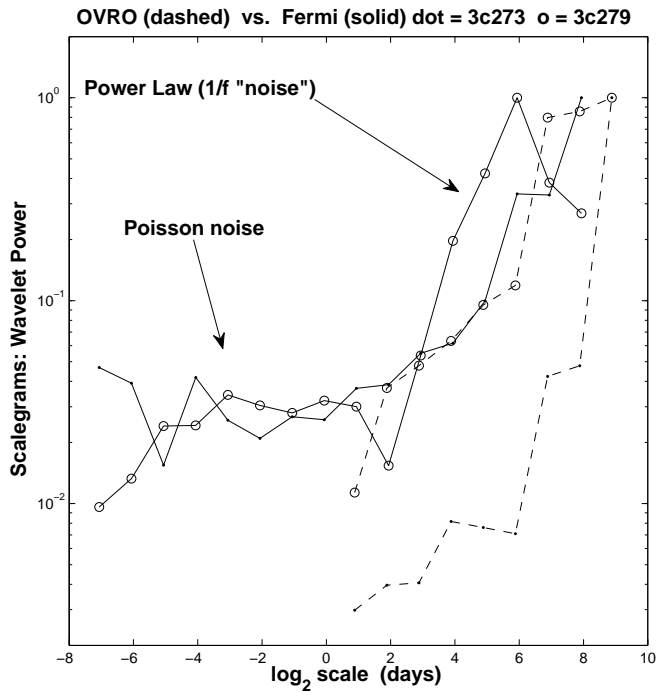
Fig. 6. Wavelet Power (scalegrams) for OVRO and LAT data on 3C 273 and 3C 279, with the Haar Wavelet. log_{10} of the power plotted against log_2 of time scale in days.

steeper behavior at intermediate time scales, transitioning to the typical asymptotic loss of correlation at large time scale expressed as $NSF(\tau) \rightarrow 2$, correctly assessed as flat.

A few other points perhaps favor the use of structure functions (beyond the fact that they have been widely used in the past, and therefore arguably should be computed if only for comparison with previous work). When the structure and correlation functions are estimated from actual data, this equivalence result quoted above does not hold exactly. There can in fact be significant departures from the theoretical relations in Appendix A of (Emmanoulopoulos et al. (2010)), due to end effects always present for finite data streams. In addition, when measuring slope of power-law relationships it can be slightly more convenient to fit polynomials to the typical shape of a structure function than to the corresponding correlation function or power spectrum.

8. Time-Frequency Distributions

The term *time-frequency distribution* refers to techniques for studying the time-evolution of the power spectrum of time series. This concept must deal with the fact that the spectrum is a property of the entire time interval, so that estimating it locally in time results in the need for trading off time resolution against frequency resolution. See (Flandrin (1999)) for a complete exposition of these issues.

There are many algorithms for computing time-frequency distributions, but little has been done for the case of event data, one exception being the approach de-
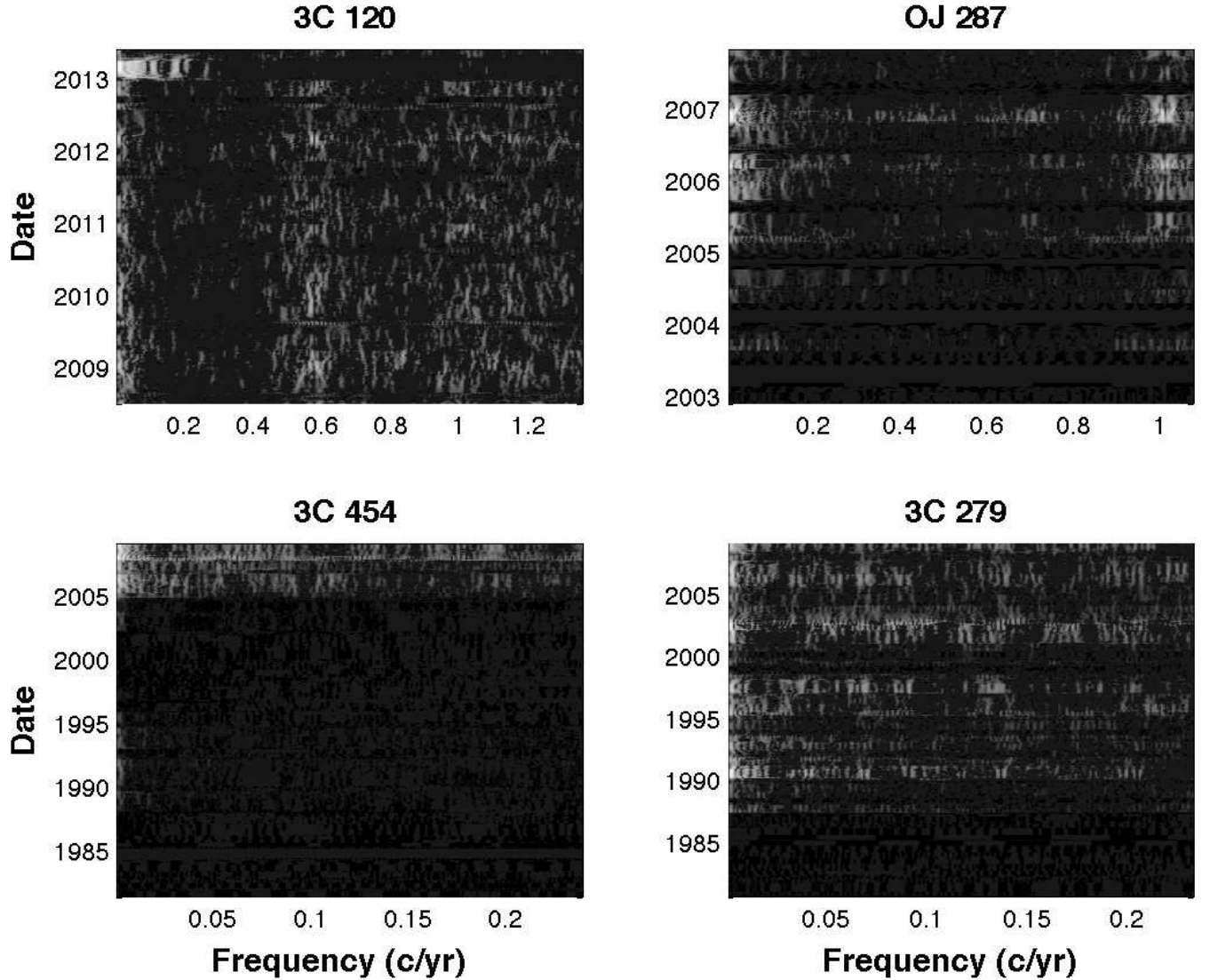
Fig. 7. Time-frequency distribution for 4 AGN data sets: 3C 120 x-ray data from Chatterjee et al. (2009) provided by Alan Marscher; optical, R magnitude data on OJ 278, by Villforth et al. (2010) provided by Iván Agudo, 37 GHz observations of 3C 454 and 3C 279 from the Metsähovi Radio Observatory, provided by Anne Lähteenmäki.

scribed in (Galleani et al. (2001)). Although there are advanced techniques based on the Wigner-Ville distribution, Cohen's class of distribution, and others, in many applications the sliding window power spectrum is of considerable use. The idea is simple: compute the power spectrum of a subsample of the data within a restricted time-interval, small compared to the total interval. Information on the time dependence results from the fact that the window is slid along the observation interval. Information on frequency dependence is contained in the power spectrum. The tradeoff of time- and frequency resolution is mediated by the length of the time window: a short window yields high time resolution and low spectral resolution, and *vice versa* for a long window. Implementation of this approach is straightforward through use of the techniques in §4 and 5.

Figure 7 shows sliding window power spectra computed, in this way, from time series data on four AGN provided by other authors at this workshop. These time-frequency distributions can show spectral details that are washed out in a power spectrum of the whole interval. In these cases there is little evidence for periodicities of any kind. Note that these are preliminary results, with no attempt being made to adjust the size of the window.

9. Conclusions

Rather than regurgitating the discussion above, I end with a few practical suggestions. They may seem obvious or trivial, but I have found them surprisingly useful in practice.

When addressing time series data in the form of Eq. (4), the first step should be to study the time intervals $t_{n+1} - t_n$; in particular compute, plot, and study the
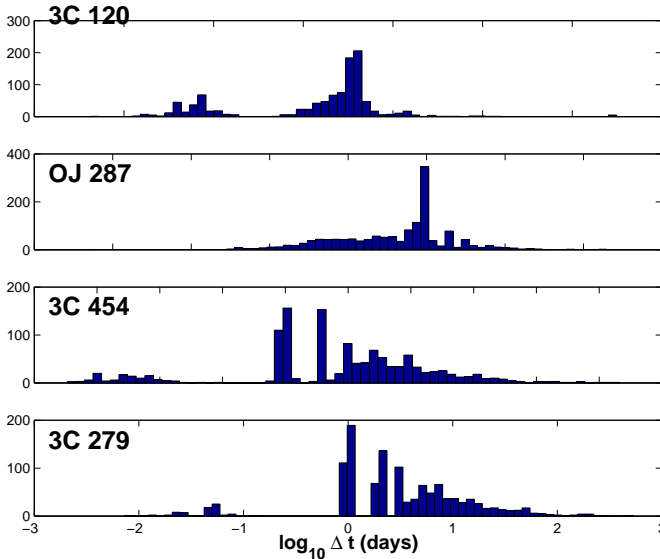
Fig. 8. Sampling histograms: the distributions of the time intervals between the samples for the data in Fig. 7.

their distribution with suitably constructed histograms. (Even if the provider of the data swears the times are evenly spaced, check it!) This often reveals many defects in the data, such as duplicate entries and observations out of order. The outliers of the distribution signal peculiarities, perhaps expected (such as known sampling irregularities, regularities, or semi-regularities) but often unexpected surprises. Figure 8 shows examples from the data for which time-frequency distributions were shown above. The reader is invited to see what conclusions can be deduced from these distributions.

Don't subtract the mean value! Or at least do so with attention to its effects. Too often time series data are detrended without careful consideration of the resulting effects on the estimated functions. Mean removal is a special case of detrending.

While there are some cases where the distinction between stationary and non-stationary processes is important, with limited data it is difficult or impossible to make this distinction in practice. For different reasons, the distinction between linearity and non-linearity is best left to the realm of physical models rather than data analysis. Linearity is a property of physical processes, and mathematical definitions (Priestly (1988), Tong (1990)) may or may not connect meaningfully to physical concepts.

Finally, in thinking about AGN variability in general it is useful to think in terms of the mathematical concept of doubly stochastic (or Cox) processes. Essentially, this is a picture in which there are two distinct random processes: the intrinsic variability of the source (truly random, periodic, quasi-periodic, etc.) and the observation process. The latter is random due to observational errors from photon counting, detector noise, background variability, etc. It is a major data analysis challenge to cleanly separate out the observational process to reveal the true variability of the astronomical source.

References

Chatterjee, R.B., Marscher, A.P., Jorstad, S.G., et al. 2009, ApJ 704, 1689

Edelson, R.A., & Krolik, J.H. 1988, ApJ 333, 646

Emmanoulopoulos, D., McHardy, I. M., and Uttley, P. 2010, MNRAS 404, 931

Flandrin, P. 1999, Time-Frequency/Time-Scale Analysis, Wavelet Analysis and Its Applications Vol. 10 (London: Academic Press)

Galleani, L., Cohen, L., Nelson, D., & Scargle, J. 2001, Proc. of the IEEE - EURASIP Workshop on Nonlinear Signal and Image Processing `arXiv:astro-ph/0100457`

Okabe, A., Boots, B., Sugihara, K., & Chiu, S.N. (2000), Spatial Tessellations: Concepts and Applications of Voronoi Diagrams, 2nd Editon (New York: John Wiley and Sons, Ltd.)

Papoulis, A. 1965, Probability, Random Variables, and Stochastic Processes (New York: McGraw-Hill)

Papoulis, A. 1977, Signal Analysis, (McGraw-Hill: New York)

Prahl, J. 1996, submitted to A&ASS `arXiv:astro-ph/9909399`

Priestly, M. 1988, Non-linear and non-stationary time series analysis, (London: Academic Press)

Scargle, J. 1982, ApJ 263, 835

Scargle, J. 1989, ApJ 343, 874

Scargle, J., Steiman-Cameron, T., Young, K., et al. 1993, ApJ 411, L91

Scargle, J. 1998, ApJ 504, 405

Scargle, J. 2001a, in Bayesian Inference and Maximum Entropy Methods in Science and Engineering, Rychert, J., Erickson, G., & Smith, R., AIP Conf. Proc., 567, p. 245

Scargle, J. 2001b, in Bayesian Inference and Maximum Entropy Methods in Science and Engineering (MAXENT 2001)

Scargle, J. 2001c, in Bayesian Inference and Maximum Entropy Methods in Science and Engineering (MAXENT 2001)

Scargle, J., Norris, J., Jackson, B., & Chiang, J. 2010, *Studies in Astronomical Time Series Analysis. VI. Bayesian Blocks, Triggers (and Histograms)*, in preparation.

Tong, H. 1990, Non Linear Time Series: A Dynamical System Approach, (Oxford University Press)

Villforth C., Nilsson K., Heidt J., et al., 2010, MNRAS 402, 2087,

Modeling AGN Spectral Energy Distributions with Leptonic Models

J. D. Finke⋆ for the *Fermi*-LAT Collaboration

U.S. Naval Research Laboratory, Code 7653, 4555 Overlook Ave SW, Washington, DC 20375-5352, USA

Abstract. Leptonic models have been the workhorse for modeling the spectral energy distributions (SEDs) of blazars, mainly due to their simplicity. In these models the lower energy bump in the SED is created by synchrotron emission and the high energy bump by Compton-scattering of a seed photon source such as disk radiation, a broad line region, or a dust torus. Due to recent detections of mis-aligned blazars, the SEDs of radio galaxies can also be modeled in this fashion. I review leptonic models for AGN, including some recent results, particularly for LAT-detected radio galaxies.

1. Introduction

Radiation from blazars is thought to originate from relativistic jet closely aligned with our line of sight, powered by supermassive black holes at the centers of active galaxies. Blazars are sub-divided into two sub-groups based on their optical spectra: BL Lacertae objects with weak or non-existent broad lines, and flat spectrum radio quasars (FSRQs) with strong broad lines (e.g., Marcha et al., 1996). The spectral energy distributions (SEDs) of these sources has a two-bump structure, with the lower "bump" almost certainly originating from non-thermal electron synchrotron radiation in the jet, and, in leptonic models, the higher bump is identified as being from Compton-scattering of one of several photon sources.

When modeling these sources, it is common to assume that all of the emission originates from a single, spherical region of optically thin non-thermal plasma in the jet (hereafter called a "blob"), where all of the parameters are the same throughout the region. This is justified in blazars to some extent where correlated variability between several energy band is observed. In the standard one-zone model discussed here, all parameters are assumed to be homogeneous in the zone (magnetic field, electron energy distribution, etc). The magnetic field B is assumed to be tangled and the electron distribution $N_e(\gamma)$ is assumed to be isotropic. The blob moves with a constant bulk Lorentz factor $\Gamma_j = (1 - \beta_j^2)^{-1/2}$ and an observer at angle $\theta_j = \arccos\mu$ will see a Doppler factor $\delta_D = [\Gamma_j(1 - \beta_j\mu)]^{-1}$. The blob is assumed to be spherical in its comoving frame, with radius R_b'. The observed variability time can constrain the blob size from the light travel time by $t_v \gtrsim t_{v,min} = (1 + z)R_b'/(\delta_D c)$.

In § 2 a review of the commonly-used synchrotron/SSC model is presented. In § 3 we discuss external Compton models and apply them to the FSRQ 3C 454.3. In § we apply the synchrotron/SSC model to several *Fermi*-LAT detected radio galaxies.

⋆ NRL/NRC Postdoctoral Research Associate

2. Synchrotron/SSC Model

2.1. Approximate Formulae

In the HSP BL Lacs, the high energy bump is thought to be dominated by Compton scattering of the synchrotron radiation by the same electrons which produce it, which is known as synchrotron self-Compton (SSC). This is the simplest possible model, and has a relatively small number of free parameters. The electron energy distribution can be constrained, since it should have a power law index p (where $N_e(\gamma) \propto \gamma^{-p}$) related to the synchrotron or Thomson-scattered spectral index α (where $F_\nu \propto \nu^{-\alpha}$) given by $p = 1 + 2\alpha$. Given this constraint and the constraint on the size scale mentioned in § 1, the model has only two free parameters: δ_D, and B. It is possible to estimate these free parameters by measuring the frequency, ν, and luminosity, L, of the νF_ν peaks of the synchrotron and SSC components by (Ghisellini et al., 1996; Tavecchio et al., 1998)

$$\delta_D \cong 5.3 \left(\frac{\nu_{SSC,25}}{t_d \nu_{syn,16}^2} \right)^{1/2} \left(\frac{A(\alpha_1, \alpha_2) \, L_{SSC,45}^2}{L_{syn,45}} \right)^{1/4} \quad (1)$$

$$B \cong 0.68 \, G \, (1+z) \frac{\nu_{syn,16}^3 t_d^{1/2}}{\nu_{SSC,25}^{3/2}} \left(\frac{L_{SSC,45}}{A(\alpha_1, \alpha_2) \, L_{syn,45}^2} \right)^{1/4} \quad (2)$$

where $A(\alpha_1, \alpha_2) = (\alpha_1 - 1)^{-1} + (1 - \alpha_2)^{-1}$, α_1 (α_2) is the spectral index of the synchrotron or SSC component above (below) the peak, t_d is the variability timescale in days, and $\nu_{syn} = \nu_{syn,16}10^{16}$ Hz is the peak synchrotron frequency and $\nu_{SSC} = \nu_{SSC,25}10^{25}$ Hz. This also requires that the redshift of the source is known so that its luminosity can be determined. It is clear that the location of the synchrotron peak is the largest source of error in these formulae. Also, they are in only valid for scattering in the Thomson regime, while for high-peaked BL Lacs, the Klein-Nishina (KN) effects do tend to be important. Nonetheless, they are a useful starting point for spectral modeling.

Fig. 1 The parameters $\delta_{\rm D}$ and B calculated for LAT HSPs and radio galaxies using eqns (1) and (2) assuming $t_d = 1$.

In Fig. 1 we calculate $\delta_{\rm D}$ and B for the high-synchrotron peaked (HSP) BL Lacs in the LAT Bright AGN Sample (Abdo et al., 2009a) with known redshifts using these approximate formulae. We have used the SEDs from Abdo et al. (2010e), where α_1 is taken to be the spectral index between 5 GHz and 5000 Å (6×10^{14} Hz) and α_2 between the 5000 Å optical and 1 keV, assuming $t_d=1$ for all sources. The results give parameters within reasonable agreement for what one would expect for these types of sources, and with what one gets from more detailed modeling. The FRI radio galaxies shown in this Fig. occupy an approximately different region of parameter space than the BL Lacs. This could be indicative of them being de-beamed BL Lacs, or another spectral component. The lack of variability on day or less timescales in these sources though, means this plot should not be taken too seriously. In particular, the high Doppler factor for NGC 1275 is unlikely to be physical. This unusual source is discusses further in § 4.3.

2.2. Photo-absorption

The synchrotron photons interact with the SSC γ-rays to absorb the γ-rays through e^+e^- pair production. The absorption optical depth for this process can be estimated from

$$\tau_{\gamma\gamma}(\epsilon_\gamma) \cong \frac{\sigma_{\rm T} D^2}{m_e c^2 t_{v,min} \delta_{\rm D}^4} \frac{f_{\bar{\epsilon}}^{\rm syn}}{\bar{\epsilon}} \qquad (3)$$

(Dondi & Ghisellini, 1995; Finke et al., 2008) where $\sigma_{\rm T}$ is the Thomson cross section, $f_{\bar{\epsilon}}^{\rm syn}$ is the νF_ν synchrotron spectrum, D is the (luminosity) distance, the dimensionless energy $\bar{\epsilon} = 2\delta_{\rm D}^2/[(1+z)^2 \epsilon_\gamma]$, and ϵ_γ is the dimensionless observed γ-ray energy. For a spherical geometry, $\gamma\gamma$ absorption will modify the observed high-energy spectrum by a factor

$$\frac{1}{2} + \frac{\exp(-\tau_{\gamma\gamma})}{\tau_{\gamma\gamma}} + \frac{1 - \exp(-\tau_{\gamma\gamma})}{\tau_{\gamma\gamma}^2} \ . \qquad (4)$$

The observations of high energy photons from a source suggests that $\tau_{\gamma\gamma} \leq 1$. This allows one to constrain the Doppler factor for the source, based on the highest energy photon observed, ϵ_γ, by

$$\delta_{\rm D} \geq \left[\frac{2^\alpha(1+z)^{2\alpha}\sigma_T D^2}{m_e c^4 t_{v,min}} \epsilon_\gamma f_{\epsilon_\gamma^{-1}}^{\rm syn} \right]^{\frac{1}{4+2\alpha}} \qquad (5)$$

where $\alpha = \alpha_1$ for

$$\epsilon_\gamma^{-1} < \frac{(1+z)^2 \epsilon_{\rm pk}^{\rm syn}}{2\delta_D}$$

and $\alpha = \alpha_2$ for

$$\epsilon_\gamma^{-1} > \frac{(1+z)^2 \epsilon_{\rm pk}^{\rm syn}}{2\delta_D}$$

where $\epsilon_{\rm pk}^{\rm syn}$ is the dimensionless energy of the synchrotron peak.

In the context of the one-zone synchrotron/SSC model, it is possible to eliminate $t_{v,min}$ in equation (5) by using equation (1), which leads to

$$\delta_D \geq 4.4 \left[2^{-\alpha}(1+z)^{2\alpha} \ \epsilon_{\gamma,7} \ D_{25} \ f_{\epsilon_\gamma^{-1},-10}^{\rm syn} \right. \qquad (6)$$

$$\left. \times \frac{\epsilon_{\rm pk,-7}^{\rm syn}}{\epsilon_{\rm pk}^{\rm SSC}} \ \frac{\sqrt{f_{\rm pk,-10}^{\rm syn}}}{f_{\rm pk,-10}^{\rm SSC}} \ \frac{1}{\sqrt{A(\alpha_1,\alpha_2)}} \right]^{1/4}$$

where $D = 10^{25} D_{25}$ cm, $f_{\rm pk}^{\rm syn} = 10^{-10} f_{\rm pk,-10}^{\rm syn}$ erg s^{-1} cm^{-2} is the νF_ν synchrotron peak, and $f_{\rm pk}^{\rm SSC} = 10^{-10} f_{\rm pk,-10}^{\rm SSC}$ erg s^{-1} cm^{-2} is the νF_ν SSC peak (Abdo et al., 2010b).

Photo-absorption by the Extragalactic Background Light (EBL) can also be important at high γ-ray energies (e.g., Finke et al., 2010), and must be taken into account in detailed modeling for sources at high z. However, this is beyond the scope of this proceeding.

2.3. Energetics

The synchrotron emission implies a minimum total (particle and field) jet power, for a given Doppler factor, variability timescale, and magnetic field. The magnetic field which minimizes this jet power will be called $B_{\rm min}$. Modeling the SSC component implies the departure of the magnetic field and jet power from these values.

Due to the lack of Bulk Comptonization signatures in the spectra of blazars, it seems likely there is some hadronic content in their jets.

$$P_j = 2\pi \ R_b'^2 \ \beta \ \Gamma^2 \ c \ u_{\rm tot}' \qquad (7)$$

(Celotti & Fabian, 1993; Celotti et al., 2007), where $u_{\rm tot}' = u_{\rm par}' + u_B'$, and the factor of 2 is due to the assumption that the black hole powers a two-sided jet. The magnetic energy density is given by

$$u_B' = \frac{B^2}{8\pi} \qquad (8)$$

and the electron energy density by

$$u_e' = m_e c^2 \int_{\gamma_{min}'}^{\gamma_{max}'} d\gamma_s' \ \gamma_s' \ n_e'(\gamma_s') \ . \qquad (9)$$

A lack of Bulk Comptonization features in the SEDs of blazars indicates that protons make a significant component of the jet (e.g., Sikora et al., 1997). In a shock scenario, it is expected that the jet power in protons will dominate over electrons, and that their will be approximately ten times as much power in protons as in electrons.

3. External Compton Models and FSRQs

For FSRQs and often for low synchrotron-peaked BL Lacs, the synchrotron/SSC model is not sufficient to explain the SED. Several other sources of seed photons have been suggested, such as the accretion disk (Dermer & Schlickeiser, 1993, 2002), the broad-line region (Sikora et al., 1994; Donea & Protheroe, 2003), or the dust torus (Kataoka et al., 1999). The calculation of the Compton-scattering of the full Shakura-Sunyaev (Shakura & Sunyaev, 1973) accretion disk and the BLR radiation using the full Compton cross section was done by Dermer et al. (2009).

3.1. Application to 3C 454.3

The FSRQ 3C 454.3 was one of the brightest objects to be observed by the LAT in the first few months of *Fermi* operation, where it was found to have a break in its γ-ray spectrum (Abdo et al., 2009b). The SED during this time period can be seen in Fig. 2. The SSC model can give an adequate fit to the broadband data (dotted curve) but a poor fit to the LAT spectrum. It also requires a magnetic field that is far below equipartition. Therefore this model is disfavored for this source.

A single External-Compton scattering component would be difficult to explain the γ-ray spectrum of this source, which is constrained by the optical and X-ray data (Finke & Dermer, 2010). However, a combination of two Compton-scattering components can explain this, including the spectral break (orange curve in Fig. 2). In order for the energy density of the seed photons from the BLR and disk to be approximately equal, which is needed for them to explain this break, it requires that the BLR electron number density $n_{BLR}(R) \propto R^{-2}$ where R is the distance from the black hole. As seen in Fig. 2, this model reproduces the LAT spectrum better and results in a magnetic field closer to equipartition ($B/B_{eq} = 0.6$).

During this time period, the X-ray light curve of 3C 454.3 shows little variability and is not correlated with the optical or γ-rays, although the optical and γ-rays are well-correlated with each other (Bonning et al., 2009). This can be explained by the longer cooling timescale for these lower-energy electrons, as shown in Fig. 3. These timescale calculations use monochromatic approximations for the Compton-scattered disk and BLR components, but the full Compton cross section for all components. The
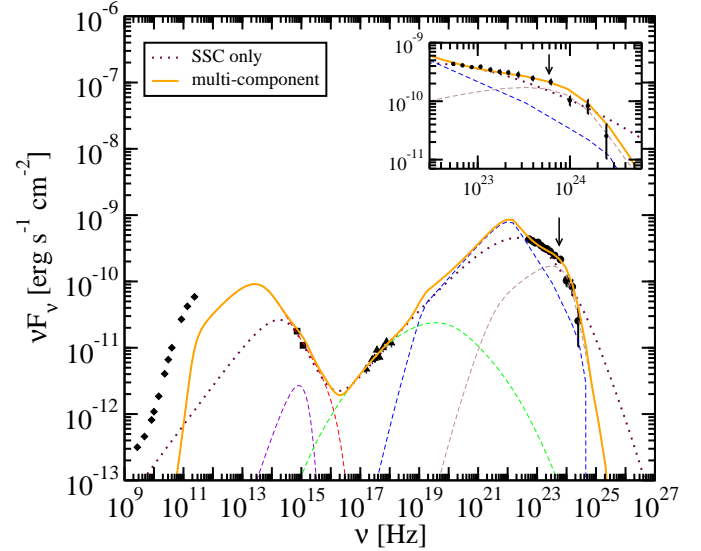
Fig. 2 The SED of 3C 454.3. The data (black symbols) are from Abdo et al. (2009b). The model components for the multi-component model are shown as dashed curves, where the purple dashed curve is the Shakura-Sunyaev disk, the red is the synchrotron, the green is the SSC, the blue is the Compton-scattered disk, and the brown is the Compton-scattered BLR component assuming $\tau_{BLR} = 0.01$. The thick dotted curve gives the SSC fit, and the thick solid curve shows the multi-component model. The inset shows the *Fermi*-LAT spectrum in more detail. See Finke & Dermer (2010) for more details on the modeling. The arrows indicate the frequency of the spectral break. Figure is from Finke & Dermer (2010).
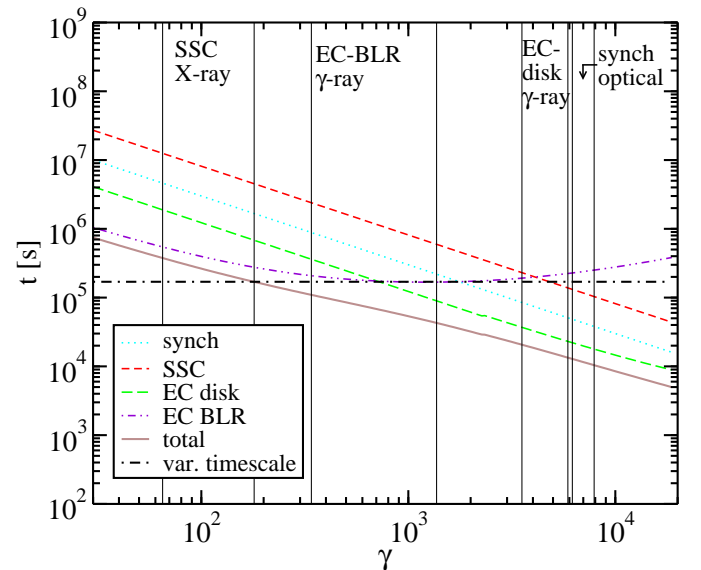
Fig. 3 Cooling timescales in the observer's frame. The electrons with γ which produce the majority of the radiation in certain wavebands are marked. The electrons which produce X-rays from SSC emission have total cooling timescales longer than the variability timescale, explaining the lack of X-ray variability. The optical synchrotron radiation is made by electrons with $\gamma \approx (6-8) \times 10^3$ which would therefore correlate with the γ-rays formed by Compton-scattered disk radiation. Figure is from Finke & Dermer (2010).

electrons which make the X-rays by SSC have lower energies than those that make the optical and γ-rays, and thus cool more slowly than the observed variability timescale.

The lack of correlated variability between X-rays and optical and γ-rays might indicate that the X-rays originate from another part of the jet than the LAT γ-rays. However, in this case, the emission would still likely be in the fast cooling regime, since the γ-ray flux is significantly greater than the optical and radio fluxes, and as long as one is in the fast cooling regime, Compton scattering of a single component cannot explain the LAT spectrum. Furthermore, during the 2007 November flares of 3C 454.3, detected by *Swift* UVOT, XRT and BAT, *INTEGRAL*, and *AGILE*, the X-rays were weakly variable, compared with other wavebands, but did seem to show correlated variability (Vercellone et al., 2009), which indicates they originate from the same emission region.

4. Radio Galaxies

Radio galaxies are thought to be blazars observed at large angles to the lines of sight, where Fanaroff-Riley (FR) type Is (Fanaroff & Riley, 1974) are thought to misaligned BL Lacs, and FRIIs are thought to be misaligned FSRQs (Urry & Padovani, 1995).

The jet's inclination angle puts constraints on the Doppler factor. For a jet inclined at an angle θ_j with respect to the line of sight, the Doppler factor must be

$$\delta_D \leq \csc \theta_j \qquad (10)$$

(Urry & Padovani, 1995; Abdo et al., 2010b). Thus radio galaxies with large θ_j, must have a small amount of Doppler beaming compared to blazars. The fact that radio galaxies appear brighter than what one would expect for de-beamed blazars has led to the suggestion that the emission from radio galaxies is from a different, slower region of the jet than the emission from blazars (Chiaberge et al., 2000).

In the following sections, the modeling of three LAT-detected radio galaxies is discussed.

4.1. Centaurus A

The FRI Cen A is the nearest radio galaxy to the Earth, at a distance of 3.7 Mpc (Ferrarese et al., 2007). Its giant lobes have been seen in γ-rays by the *Fermi*-LAT. This emission is thought to be the result of Compton-scattering of the CMB and EBL (Abdo et al., 2010a, Cheung et al., this workshop). The core of the source is also γ-ray bright, an indication of possible blazar-like emission (Abdo et al., 2010b). Cen A has also been seen with the VHE atmospheric Cherenkov telescope HESS (Aharonian et al., 2009). The LAT spectrum, extrapolated to higher energies as a straightforward power-law, does not seem to be able to explain the HESS emission. However, if the HESS spectrum is scaled down by its normalization uncertainty, it seems to be just barely consistent with the LAT spectrum, when the LAT statistical and systematic errors are
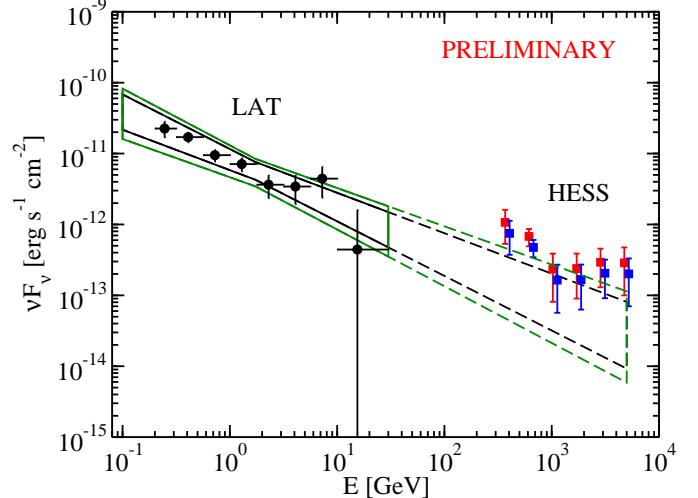
Fig. 4 Spectrum of the Cen A core from differential fluxes derived for successive energy ranges (black circles). The black bow-tie indicates the best fit $0.1 - 30$ GeV LAT flux and Γ with statistical errors only, while the green bow-tie indicates this with systematic errors as well. The LAT spectrum is extrapolated into the HESS energy range (dashed lines). The HESS data from Aharonian et al. (2009) are shown (red squares) and the HESS data shifted to lower flux by their statistical and systematic normalization error (blue squares). The latter are also shifted in energy by 10% for clarity. Figure is from Abdo et al. (2010b).

included (see Fig. 4). It should also be pointed out that these HESS data are from 2004–2008, and are not contemporaneous with the LAT observations. However, neither the HESS nor the LAT light curves showed any significant variability, so it is plausible they have not changed during the different epochs.

Since FRIs are thought to be misaligned BL Lac objects, and the one-zone synchrotron/SSC model is successful in explaining emission from BL Lacs, it makes sense to see if this model can explain the emission from Cen A. A synchrotron/SSC model fit to archival and contemporaneous data can be seen in Fig. 5. Internal $\gamma\gamma$ absorption and the high inclination angle ($\theta_j \geq 15$ deg; Hardcastle et al., 2003), constrain the Doppler factor of the source, equations (5) and (10), respectively. From these it can be shown (Abdo et al., 2010b) that the same Compton-scattering component cannot explain the LAT and HESS emission. Note that this result does not depend on the adopted size of the emitting region. Parameters of the model fit shown in Fig. 5 can be seen in Table 1.

4.2. M 87

Another of the nearest γ-ray loud radio galaxies is the FRI M 87, at 16 Mpc (Tonry, 1991). M 87 has been regularly detected by TeV telescopes (Aharonian et al., 2006; Albert et al., 2008; Acciari et al., 2008, 2009) and was recently reported as being detected by the *Fermi*-LAT (Abdo et al., 2009d). The angle to the line of sight of the M 87 jet is
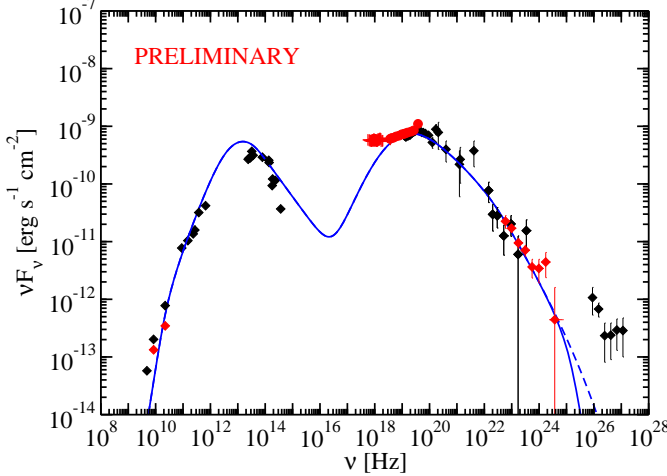
Fig. 5 The SED of the Cen A core with one-zone synchrotron/SSC model fit (blue curve). Red symbols are observations contemporaneous with the LAT observations. The dashed curve shows this model without $\gamma\gamma$ attenuation. See Table 1 for the parameters of the model curve. This figure in a slightly modified form, and the details on the data, can be found in Abdo et al. (2010b).

Fig. 6 The SED of M 87 with a one-zone synchrotron/SSC model fit (blue curve). Red symbols are contemporaneous with the LAT data while other symbols are archival. See Table 1 for parameters of the model curve. This figure and a description of the data can be found in Abdo et al. (2009d).

Table 1 Radio galaxy synchrotron/SSC model parameters.

| Parameter	Symbol	Cen A	M 87	NGC 1275
Bulk Lorentz Factor	Γ_j	1.0/7.0	2.3	1.8
Doppler Factor	δ_D	1.0	3.9	2.3
Jet Angle	θ_j	30°	10°	25°
Magnetic Field [G]	B	6.2	0.055	0.05
Variability Timescale [sec]	t_v	1.0×10^5	1.2×10^5	3.0×10^7
Comoving blob size scale [cm]	R'_b	3.0×10^{15}	1.4×10^{16}	2.0×10^{18}
Low-Energy Electron Spectral Index	p_1	1.8	1.6	2.1
High-Energy Electron Spectral Index	p_2	4.3	3.6	3.1
Minimum Electron Lorentz Factor	$\gamma_{\min}$	3×10^2	1.0	8.0×10^2
Maximum Electron Lorentz Factor	$\gamma_{\max}$	1×10^8	1.0×10^7	4.0×10^5
Break Electron Lorentz Factor	γ_{brk}	8×10^2	4×10^3	9.6×10^2
Jet Power in Magnetic Field [erg s^{-1}]	$P_{j,B}$	$0/6.5 \times 10^{43}$	2.0×10^{40}	2.3×10^{44}
Jet Power in Electrons [erg s^{-1}]	$P_{j,e}$	$0/3.1 \times 10^{43}$	7.0×10^{42}	2.3×10^{43}
Jet Power in protons ($10 \times P_{j,e}$) [erg s^{-1}]	$P_{j,p}$	$0/3.1 \times 10^{44}$	7.0×10^{43}	2.3×10^{44}

constrained to be $\leq 19°$ by superluminal VLBA observations (Biretta et al., 1999). We adopt in our modeling $\theta_j = 10°$, consistent with this. This means equation 10 gives $\delta_D \leq 5.8$, and allows a fit the entire SED, including TeV γ-rays. The result does depend strongly on the angle to the line of sight, however. Larger angles would make it difficult to find a Doppler factor large enough to avoid $\gamma\gamma$ attenuation, and thus allow the model to explain the emission from the TeV γ-rays.

The TeV emission from M 87 shown in Fig. 6 is not strictly contemporaneous the *Fermi* and the other observations, however, the TeV emission is the lowest yet found from the source (Aharonian et al., 2006). It does seem unlikely that the TeV emission would be below this level.

In the future, if simultaneous Cherenkov-LAT observations reveal a correlated light curve, it would be strong

evidence that the radiation comes from the same region. Modeling and the necessity to avoid $\gamma\gamma$ attenuation could provide strong constraints on θ_j.

4.3. NGC 1275

The radio galaxy at the center of the Perseus Cluster, NGC 1275 (Per A, 3C 84) has been detected with the *Fermi*-LAT (Abdo et al., 2009c). In the initial data set (4 months) it was unclear whether the γ-ray emission was from the RG or the cluster itself, and their was no evidence for variability in the LAT light curve. However, the source must have been variable on at most decade timescales, since the LAT detection was above the EGRET lower limit for the source (Reimer et al., 2003). An additional 8 months of LAT data have confirmed that it is indeed from the radio source and detected γ-ray variability on month timescales (Kataoka et al., 2010). NGC 1275 has a luminosity distance of 75 Mpc given its redshift of $z = 0.0179$, using cosmological parameters (h, Ω_m, Ω_Λ)=(0.71, 0.27, 0.73).

VLBA observations (Walker et al., 1994) constrain the jet angle in NGC 1275 to be $30° \lesssim \theta_j \lesssim 55°$. Using equation (10) this implies $\delta_D \leq 2.0$. If the angle is a bit smaller, $\theta_j = 25°$, then $\delta_D \leq 2.4$. This is the angle used by Abdo et al. (2009c) when modeling this source with the one-zone synchrotron/SSC model. Those results are presented in Fig. 7 and Table 1.

These modeling results assume a rather large variability timescale, consistent with the original LAT observations (Abdo et al., 2009c). However, with the a variability timescale of 1 month (Kataoka et al., 2010), equation (1) gives $\delta_D = 8.6$ which means $\theta_j \leq 6.6°$ by equation (10) to be consistent with this constraint (note that the $\gamma\gamma$ constraint from equation [6] implies $\delta_D \geq 0.9$ which is easily compatible with the jet angle from the VLBA observa-
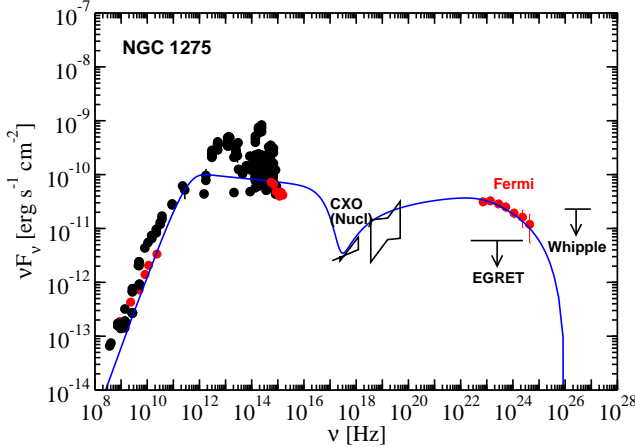
Fig. 7 The SED of NGC 1275 with a one-zone synchrotron/SSC model fit. The red symbols are contemporaneous. This figure in a slightly modified form and a description of the data can be found in Abdo et al. (2009c).

tions). In many ways, the γ-ray emission from NGC 1275 resembles that of a blazar. Its SED requires a high Doppler factor for an adequate fit, and in the γ-ray luminosity - γ-ray spectral index plane it covers an area of phase space with other blazars, rather than radio galaxies (Abdo et al., 2010c). However, its radio morphology is clearly that of a radio galaxy (Walker et al., 1994), which is a bit of a mystery.

5. Summary

We have discussed leptonic models for blazars and radio galaxies related to their detection by the *Fermi*-LAT. Many mysteries remain, such as the cause of the spectral break in 3C 454.3 and the nature of NGC 1275, which future multi-wavelength campaigns and modeling will hopefully resolve.

References

Abdo, A. A., Ackermann, M., Ajello, M., et al. 2009a, ApJ, 700, 597

Abdo, A. A., Ackermann, M., Ajello, M., et al. 2009b, ApJ, 699, 817

Abdo, A. A., Ackermann, M., Ajello, M., et al. 2009c, ApJ, 699, 31

Abdo, A. A., Ackermann, M., Ajello, M., et al. 2009d, ApJ, 707, 55

Abdo, A. A., Ackermann, M., Ajello, M., et al. 2010a, Science, 328, 725

Abdo, A. A., Ackermann, M., Ajello, M., et al. 2010b, ApJ, submitted

Abdo, A. A., Ackermann, M., Ajello, M., et al. 2010c, ApJ, 715, 429

Abdo, A. A., Ackermann, M., Ajello, M., et al. 2010d, ApJ, 716, 30

Acciari, V. A., Beilicke, M., Blaylock, G., et al. 2008, ApJ, 679, 397

Acciari, V. A., Aliu, E., Arlen, T. et al. 2009, Science, 325, 444

Aharonian, F., Akhperjanian, A. G., Bazer-Bachi, A. R., et al. 2006, Science, 314, 1424

Aharonian, F., Akhperjanian, A. G., Anton, G., et al. 2009, ApJ, 695, L40

Albert, J., Aliu, E., Anderhub, H., et al. 2008, ApJ, 685, L23

Biretta, J. A., Sparks, W. B., & Macchetto, F. 1999, ApJ, 520, 621

Bonning, E. W., Bailyn, C., Urry, C. M., et al. 2009, ApJ, 697, L81

Celotti, A., & Fabian, A. C. 1993, MNRAS, 264, 228

Celotti, A., Ghisellini, G., & Fabian, A. C. 2007, MNRAS, 375, 417

Chiaberge, M., Celotti, A., Capetti, A., & Ghisellini, G. 2000, A&A, 358, 104

Dermer, C. D., Finke, J. D., Krug, H., & Böttcher, M. 2009, ApJ, 692, 32

Dermer, C. D., & Schlickeiser, R. 1993, ApJ, 416, 458

Dermer, C. D., & Schlickeiser, R. 2002, ApJ, 575, 667

Dondi, L., & Ghisellini, G. 1995, MNRAS, 273, 583

Donea, A., & Protheroe, R. J. 2003, Astroparticle Physics, 18, 377

Fanaroff, B. L., & Riley, J. M. 1974, MNRAS, 167, 31P

Ferrarese, L., Mould, J. R., Stetson, P. B., et al., 2007, ApJ, 654, 186

Finke, J. D., & Dermer, C. D. 2010, ApJ, 714, L303

Finke, J. D., Dermer, C. D., & Böttcher, M. 2008, ApJ, 686, 181

Finke, J. D., Razzaque, S., & Dermer, C. D. 2010, ApJ, 712, 238

Ghisellini, G., Maraschi, L., & Dondi, L. 1996, A&AS, 120, C503

Hardcastle, M. J., Worrall, D. M., Kraft, R. P., et al. 2003, ApJ, 593, 169

Kataoka, J., Stawarz, Ł., Cheung, C. C., et al. 2010, ApJ, 715, 554

Kataoka, J., et al. 1999, ApJ, 514, 138

Marcha, M. J. M., Browne, I. W. A., Impey, C. D., & Smith, P. S. 1996, MNRAS, 281, 425

Reimer, O., Pohl, M., Sreekumar, P., & Mattox, J. R. 2003, ApJ, 588, 155

Shakura, N. I., & Sunyaev, R. A. 1973, A&A, 24, 337

Sikora, M., Begelman, M. C., & Rees, M. J. 1994, ApJ, 421, 153

Sikora, M., Madejski, G., Moderski, R., & Poutanen, J. 1997, ApJ, 484, 108

Tavecchio, F., Maraschi, L., & Ghisellini, G. 1998, ApJ, 509, 608

Tonry, J. L. 1991, ApJ, 373, L1

Urry, C. M., & Padovani, P. 1995, PASP, 107, 803

Vercellone, S., et al. 2009, ApJ, 690, 1018

Walker, R. C., Romney, J. D., & Benson, J. M. 1994, ApJ, 430, L45

Localization of the gamma-ray emission site using multi-waveband data and mm-VLBI

S. G. Jorstad[1,2], A. P. Marscher[1], P. S. Smith[3], V. M. Larionov[2,4],, and I. Agudo[1]

[1] Boston University, 725 Commonwealth Avenue, Boston, MA 02215, USA
[2] St. Petersburg State University, Universitetskij Pr. 28, Petrodvorets, 198504 St. Petersburg, Russia
[3] Steward Observatory, University of Arizona, Tucson, AZ 85721-0065, USA
[4] Isaac Newton Institute of Chile, St. Petersburg Branch, St. Petersburg, Russia

Abstract. We perform monthly monitoring of a sample of γ-ray blazars with the VLBA at 43 GHz along with optical photometric and polarimetric observations and 2-week campaigns (once per year) with 3 epochs during each campaign. We demonstrate that the γ-ray variability is tightly connected with the variability in the mm-wave core, especially in quasars. We show that, for all sources in our sample for which a high γ-ray state was observed, the high energy events are simultaneous with an increase of the flux in the mm-wave core. We resolve features of enhanced brightness on our VLBA images that appear be responsible for the mm-wave flux increase. We also find a strong correlation between optical and γ-ray light curves, with a delay of γ-ray variations within 1-3 days, as well as a strong correlation between optical flux and degree of polarization during a high γ-ray state. We observe new examples of marked rotation of the optical polarization angle that accompanies a γ/optical flare. In 1633+382 the position angle of polarization in the core agrees with the optical PA during the rotation period. These are strong arguments in support of the conclusion that a high γ-ray state in blazars is connected with processes originating near the mm-VLBI core.

1. Introduction

Blazars were the largest class of identified γ-ray sources detected by EGRET on board the *Compton Gamma Ray Observatory* (Hartman et al. 1999). Although the main questions - the mechanism(s) of γ-ray production and the site(s) of γ-ray emission - were not answered, it became clear that γ-ray emission arises in highly relativistic jets (Jorstad et al. 2001a, Kellermann et al. 2004). A positive correlation between VLBI core flux at 22/43 GHz and γ-ray flux (Jorstad et al. 2001a) suggested that the production of the γ-ray emission takes place in the most compact region of the relativistic jet, close to the VLBI core. Moreover, examination of the coincidence of times of high γ-ray flux and ejections of superluminal knots showed that the two events are associated (Jorstad et al. 2001b). This result implied that the γ-ray flares are caused by inverse Compton scattering by relativistic electrons in the parsec-scale regions of the jet rather than closer to the central engine. This was supported by the analysis of radio light curves of γ-ray blazars indicating that the highest levels of γ-ray emission are observed during the initial (or peak) stages of high-frequency radio flares (Lähteenmäki & Valtaoja 2003). These results imply that the bulk of γ-rays are generated parsecs from the black hole (BH), near where the radio core of the jet is located (Marscher 2006). However, the opposite point of view finds support in the short timescales of γ-ray variability: that the γ-ray emission is produced closer to the black hole (BH) through inverse Compton scattering of photons from the accretion disk (Dermer & Schlickeiser 1994) or broad line regions (Sikora, Begelman, & Rees 1994).

The dramatically improved γ-ray sensitivity of the *Fermi* Large Area Telescope (LAT) has provided detailed light curves of a number of blazars. This has rekindled debates about mechanisms and sites of γ-ray production in blazars. According to Finke & Dermer (2010), a sharp break found in the γ-ray spectrum of the quasar 3C 454.3 is inconsistent with a cooling distribution and poorly fit with a synchrotron self-Compton model (SSC), but can be explained by the combination of Compton-scattered disk emission and BLR radiation. Poutanen & Stern (2010) interpret the γ-ray break as the result of opacity from photon-photon pair production on He II Lyman recombination continuum and lines, which implies that the site of γ-ray emission lies within a light-year of the BH. However, the correlation between γ-ray and radio flux has received strong confirmation from the extensive MOJAVE survey (Kovalev et al. 2009) which leads to the conclusion that γ-ray emission is tightly connected with highly relativistic radio jets (Lister et al. 2009). Multi-band observations suggest that γ-ray emission is produced as a superluminal knot moves from the BH to the mm-wave core. As it does, it encounters different sources of seed photons for inverse Compton scattering from both within and outside the jet, including the sheath of the jet (Marscher et al. 2010). Using the most recent γ-ray and mm-wave VLBA data, as well as optical photometric and polarimetric light curves, we demonstrate a close connection between high states of γ-ray emission and activity in the VLBI mm-wave core region in blazars.

2. Observations and Data Reduction

We monitor monthly a sample of bright γ-ray blazars with the VLBA at 43 GHz (7 mm). The calibrated uv-FITS files and images can be found at our website[1]. We also carried out 2-week campaigns in October 2008, October 2009, and April 2010 with 3 VLBA epochs within each campaign. We have performed the data reduction, electric vector position angle (EVPA) calibration, and brightness distribution modelling in the manner of Jorstad et al. (2005) and used their method, as well as the same cosmological parameters ($\Omega_m = 0.3$, $\Omega_\Lambda = 0.7$, and $H_\circ$=70 km s^{-1} Mpc^{-1}) to calculate the proper motions, apparent speeds, and times of ejection from the 43 GHz core of moving features.

We carry out optical photometric and polarimetric monitoring of the blazars using i) the Perkins telescope of Lowell Observatory (Flagstaff, AZ, USA), with the PRISM camera[2]; ii) the 70 cm telescope of the Crimean Astrophysical Observatory (Ukraine (Ukraine) with a photometer-polarimeter; iii) the 40 cm telescope of St. Petersburg State University (Russia) with a photometer-polarimeter; iv) the 2.2 m Telescope at the Calar Alto Observatory (Almería, Spain)[3]; and v) the 1.54 m Kuiper and the 2.3 m Bok telescopes at Steward Observatory[4] (AZ, USA). More detailed descriptions of optical observations can be found in Jorstad et al. (2010). We also use the 2 m Liverpool telescope at La Palma (Canary Islands, Spain) and the 1.1 m telescope of the Main (Pulkovo) Astronomical Observatory of the Russian Academy of Sciences at Campo Imperatore, Italy to obtain near-IR photometric measurements.

We have calculated γ-ray light curves for all sources in the sample at 0.1–200 GeV with weekly binning using the software and following the Analysis Threads provided by the *Fermi* Science Support Center (FSSC). We used the response function generated by the FSSC, and created a model file that consisted of a power-law model (prefactor and index) for each source. The model file included all bright γ-ray sources within 15° of the source. We used spectral indices listed in the 11-month Fermi LAT Catalog (Abdo et al. 2010) for all sources. However, for sources in a high γ-ray state we have calculated daily γ-ray light curves with both prefactor and spectral index left as free parameters.

3. Connection between Gamma-Ray and mm-Wave Core Variability

We have calculated variability indices of the γ-ray emission, V_g, and of the flux in the core of jets, V_r, for all sources in our sample using formalism developed by Aller, Aller, & Hughes (2003), adjusted for γ-ray light curves that contain both measurements and upper limits. The radio variability index, V_r, and γ-ray variability index V_g
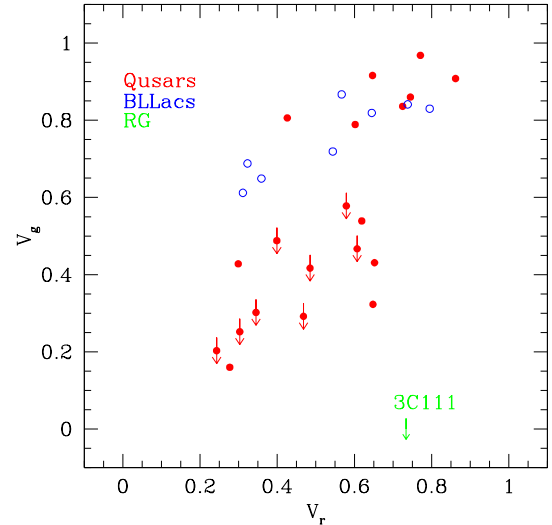
Fig. 1. Dependence between γ-ray and mm-wave core variability indices for quasars (filled circles) and BL Lac objects (open circles).

were determined as follows:

$$V_r = \frac{(S_r^{\max} - \sigma_{\max}) - (S_r^{\min} + \sigma_{\min})}{(S_r^{\max} - \sigma_{\max}) + (S_r^{\min} + \sigma_{\min})}$$

$$V_g = \frac{(S_\gamma^{\max} - \sigma_{\max}) - 2S_\gamma^{\min\downarrow}}{(S_\gamma^{\max} - \sigma_{\max}) + 2S_\gamma^{\min\downarrow}}$$

$$V_g^\downarrow = \frac{S_\gamma^{\max\downarrow} - S_\gamma^{\min\downarrow}}{S_\gamma^{\max\downarrow} + S_\gamma^{\min\downarrow}},$$

where $S_r^{\max}$ and $S_r^{\min}$ are the maximum and minimum observed fluxes in the 43 GHz core, respecively, $\sigma_{\max}$ and $\sigma_{\min}$ are their uncertainties, $S_\gamma^{\max} \pm \sigma_{\max}$ is the maximum detected γ-ray flux at 0.1–200 GeV, $S_\gamma^{\max\downarrow}$ and $S_\gamma^{\min\downarrow}$ are the maximum and minimum upper limits of γ-ray flux at 0.1–200 GeV, respectively. Figure 1 shows a good correlation between V_g and V_r for both quasars and BL Lac objects. All quasars undetected by the LAT with weekly binning have a low variability index in the mm-wave core, $V_r \leq 0.6$, which implies that γ-ray detection of quasars strongly depends on variability of the mm-wave core. The BL Lac objects have a similar range of V_r as the quasars but a weaker dependence between variability indices. This suggests an additional mechanism for the γ-ray production in BL Lac objects, different from quasars and located outside the mm-wave radio core. Lähteenmäki & Valtaoja (2003) noted previously that BL Lac objects do not possess a clear connection between radio and γ-ray variations.

4. Analysis of Multi-waveband data for Individual Sources

Figure 2 shows the γ-ray and 43 GHz core light curves for sources in our sample that exhibited strong γ-ray activity during 2008 Summer–2010 Spring. Visual examination of the light curves reveals that a high γ-ray state is characterized by strong variability that lasts several months.

---

[1] http://www.bu.edu/blazars/VLBAproject.html
[2] http://www.bu.edu/prism/
[3] http://www.iaa.es/~iagudo/research/MAPCAT/
[4] http://james.as.arizona.edu/~psmith/Fermi
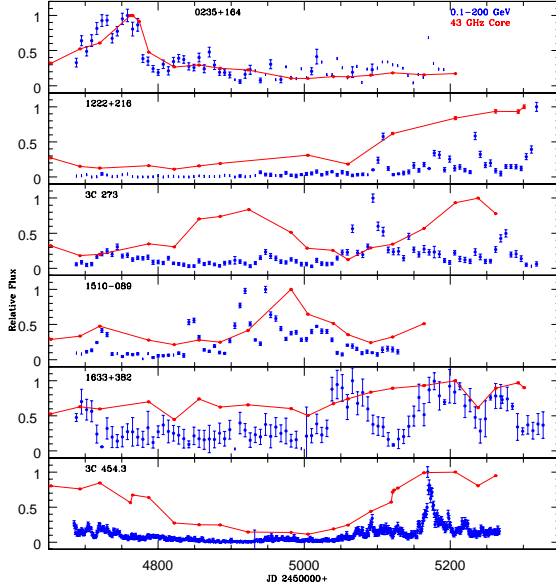
Fig. 2. Gamma-Ray and 43 GHz VLBI core (solid lines) light curves of sources from our sample exhibiting high γ-ray states.

Table 1. Results of Gamma-Ray/43 GHz Core Correlation Analysis

Source	Max. Coeff.	Delay (days)
0235+164	0.89±0.03	−7±7
1222+216	0.64±0.04	0±7
3C 273	0.40±0.05	−119±7
1510−089	0.66±0.05	−28±7
1633+382	0.55±0.04	−7±7
3C 454.3	0.54±0.02	0±7

Remarkably, these prolonged periods coincide with a successive increase of flux in the mm-VLBI core region for all sources except 3C 273. We have performed a correlation analysis between the γ-ray and core light curves using weekly binned γ-ray light curves and a cubic spline approximation for core light curves. We used the latter to obtain an estimate of the core flux for each γ-ray measurement. We have calculated the correlation function between the light curves with delays running from −140 to 140 days (a negative delay indicates that the γ-ray variations lead those in the core). The correlation analysis shows statistically significant correlation between the γ-ray and mm-wave core light curves for all sources. The results are listed in Table 1. In four cases the delay between the light curves is within the uncertainties of the value, in 1510−089 the γ-ray variations precede the activity in the core by ∼30 days, and in 3C 273 the γ-ray activity leads variations in the core by ∼4 months.

4.1. Quasar 1222+216 (4C +21.35)

The quasar 1222+216 ($z=0.435$) was in a quiescent state from 2008 August to 2009 September (see Fig. 3): i) the γ-ray flux was below the detection level; ii) the optical
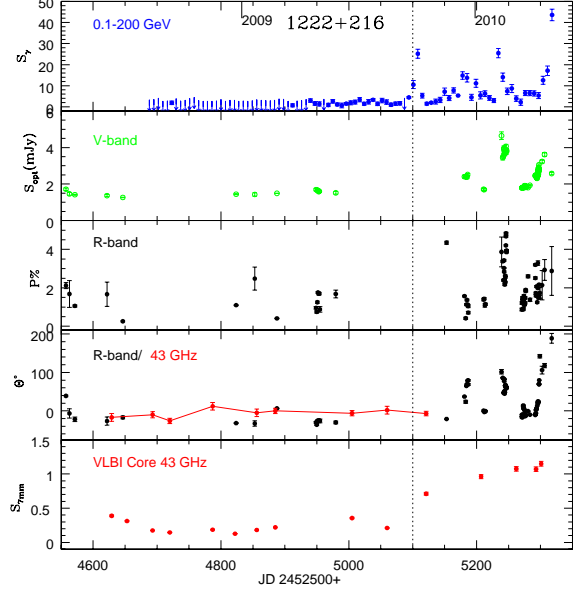
Fig. 3. Light curves in γ-ray, optical (photometric and polarimetric), and 43 GHz VLBI core of the quasar 1222+216; the fourth panel shows optical and 43 GHz core EVPAs (points connected by lines); dotted line denotes beginning of the γ-ray activity.

magnitude was faint, V∼16^m; iii) the degree of optical polarization was ≤2%; iv) the position angle of polarization was stable, close to the jet direction, $\Theta_{opt} \sim -20°$, and close to the EVPA in the core; v) the jet had a stable structure observed at many epochs, consisting of a weak core (∼0.25 Jy) and a stationary feature, St, located ∼0.3 mas from the core (Fig. 4). The situation dramatically changed around 25 September 2009 (vertical dotted line in Fig. 3), when the γ-ray flux increased by a factor of ∼10. This epoch coincided with an increase of the flux in the mm-wave core. The high γ-ray activity as well as brightening of the VLBI core of the quasar have been in progress for 9 months. The optical emission has shown strong variability and an increase in brightness by more than a magnitude. This was accompanied by strong variability of the degree and position angle of polarization, with an increase of p up to 6% and rotation of the optical EVPA by ∼200°. The rotation of Θ_{opt} coincided with the largest γ-ray outburst and an optical flare. Such behavior is reminiscent of that seen in BL Lac and 1510−089 (Marscher et al. 2008, 2010). Moreover, although we cannot yet make a robust conclusion that a new superluminal component was ejected from the core during the last γ-ray outburst, some indication of the appearance of a new feature in the jet is seen on the most recent image of the quasar, taken on 2010 April 16 (Fig. 5). The γ-ray and optical light curves during RJD: 5180–5318 (RJD = JD−2450000.0) are well-correlated (coefficient of correlation $\rho = 0.69 \pm 0.03$) with γ-ray variations delayed by 1±1 day, i.e., variations at both wavebands are possibly simultaneous. The variability of the degree of optical polarization strongly correlates with the optical flux behavior ($\rho = 0.60 \pm 0.04$) and leads
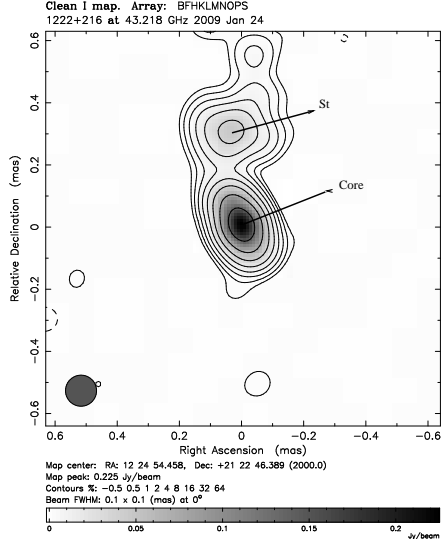
Fig. 4. Total intensity image of the quasar 1222+216 at 43 GHz during a quiescent state.
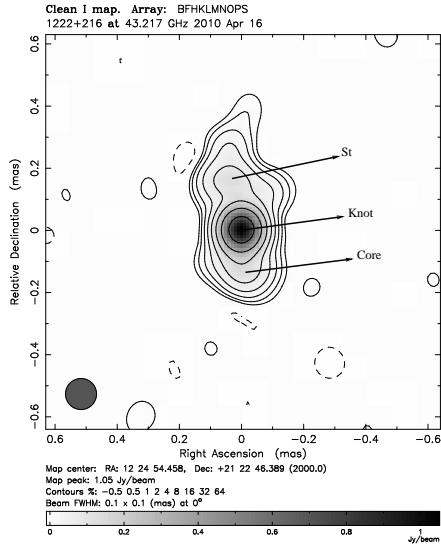
Fig. 5. Total intensity image of the quasar 1222+216 at 43 GHz during a high γ-ray state.

the latter by 2 ± 1 day. A possible scenario is as follows: propagation of a disturbance (possibly a shock) through the mm-wave core causes an increase in ordering of the magnetic field, followed by a rise in the density of relativistic electrons radiating at optical wavelengths and generation of γ-rays via inverse Compton scattering of UV/optical/IR photons from both inside and outside the jet.

4.2. Quasar 3C 273 (1226+023)

The quasar 3C 273 is one of the nearest blazars (z=0.158), which allows us to study the core region of the quasar in some detail. Figure 6 shows that the correlation between γ-ray and near-IR (H-band) light curves is very poor, although IR variations are stronger than the optical varia-

Table 2. Parameters of Superluminal Knots in 3C 273

Knot	$\beta_{\rm app}$	$S_{\rm max}$	Γ	$\Theta_\circ$	δ
K2	7.6±1.5	0.83±0.15	9	3.6	14
K3	8.3±0.3	8.5±0.3	9	4.6	12
K4	10.7±1.4	2.8±0.2	12	3.3	16
K5	6.6±3.0	9.7±0.3	10	2.2	17

Notes: $\beta_{\rm app}$ - apparent speed in units of c; $S_{\rm max}$ - maximum flux in Jy; Γ - bulk Lorentz factor; $\Theta_\circ$ - angle between the centroid of knot and line of sight in degrees; δ - Doppler factor.

tions, which are suppressed by contamination by the big blue bump (Impey et al. 1989). A significant contribution from the BBB decreases the degree of optical polarization, which is usually under 0.5%. The increase of the optical polarization to 1.5±0.02% in 2010 Spring is therefore very significant and coincides with a γ-ray flare. We have performed a correlation analysis between the daily binned γ-ray light curve and degree of optical polarization over the period from RJD:5150 to RJD:5300 that gives a strong correlation ($\rho = 0.67\pm0.03$), with γ-ray variations delayed with respect to variations of degree of optical polarization by 3±1 days. This indicates that γ-ray production is strongly related to an increase in the optical synchrotron flux, probably as the result of an increase in the number of relativistic electrons that produce both optical/IR synchrotron and, through scattering, γ-ray photons. The position angle of optical polarization does not change significantly, and aligns with the jet direction during the outburst. The 43 GHz core has very low polarization and is subject to the effects of Faraday rotation (Jorstad et al. 2007). However, during an outburst some part of the core is often polarized with EVPA aligned with the jet direction, while knots downstream have EVPAs perpendicular to the jet axis (see Fig. 7). The significant delay of variations in the 43 GHz core with respect to γ-ray variations (Table 1) can be explained by the difference in time when the maximum number of relativistic electrons radiating at optical vs. mm-waves has been achieved. There are two superluminal knots ejected during a high state of γ-ray emission, $K4$ and $K5$. However, ejection of a knot also occurs during a relatively low γ-ray state in 2008 ($K3$). This raises the question about differences in properties of superluminal features associated with high γ-ray states with respect to those which are "γ-ray quiet". Table 2 lists parameters of knots determined as in Jorstad et al. (2005) showing that $K3$ is among the brightest features and decays slowly (the parameters of $K5$ are not well determined yet).

4.3. Quasar 1633+382 (4C +38.41)

The high-redshift (z=1.814) quasar 1633+382 displays i) modest γ-ray activity in 2008 August, which is accompanied by a minor optical flare and a small increase in optical polarization; ii) a relatively quiet period at all wavelengths
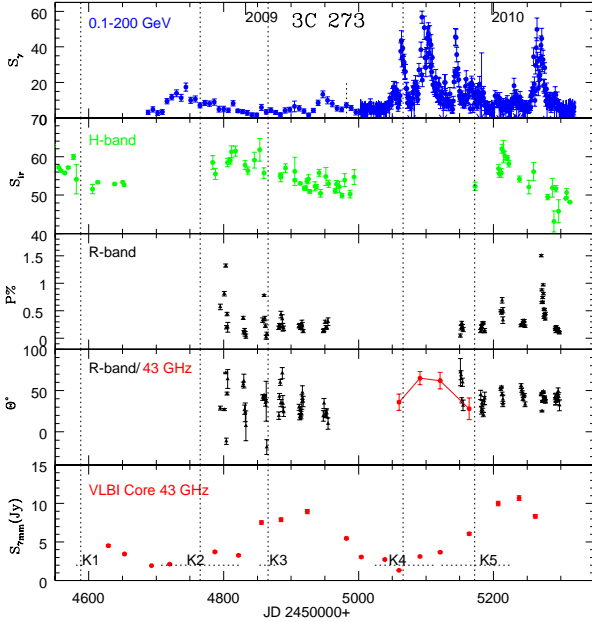
Fig. 6. Gamma-ray, H-band photometric, R-band polarimetric, and 43 GHz VLBI core light curves of the quasar 3C 273; the fourth panel shows optical and 43 GHz core EVPAs (points connected by lines); optical polarization is corrected for interstellar polarization according to Impey et al. (1989); dotted lines show the time of ejection of superluminal knots.

Fig. 7. Total and polarized intensity image of the quasar 3C 273 at 43 GHz during the beginning of high γ-ray activity in 2009 August, the line segments show direction of polarization.

from 2008 Autumn to 2009 August, during which the optical polarization drops to 1%; and iii) a dramatic increase of the γ-ray (by a factor of $\sim$10), optical (factor of $\sim$5), and 43 GHz VLBI core (factor of 2) emission starting in September 2009. During the high state the optical polarization reaches 20%. A rotation of the optical EVPA from 100° to $-100°$ is observed, coinciding with the peak of the γ/optical flare and the maximum degree of optical polarization. The EVPA in the 43 GHz core behaves in a similar way, which implies that the polarized optical emission comes from the region close to the VLBI core, as suggested previously (Jorstad et al. 2007). Correlation between the γ-ray and optical light curves is moderately high (ρ=0.56±0.04), with a delay of +1±1 day; the same holds for the degree of polarization (ρ=0.55±0.05), with a delay of 0 ± 1 day.

The VLBA images (Fig. 9) reveal the appearance of a bright superluminal knot, K1, on 2009 September 14 (±43 days), moving with an apparent speed 7.8±2.2 c (Fig. 10). The knot is very bright and compact, reaching 1.4 Jy on 2010 January 10. The time of the ejection of K1, despite an uncertainty of $\sim$1 month, agrees with the pronounced γ/optical flare.

Fig. 8. Light curves in γ-ray, optical (photometric and polarimetric), and 43 GHz VLBI core of the quasar 1633+382; the fourth panel shows optical and 43 GHz core EVPAs (points connected by lines); dotted line shows the time of ejection of superluminal knot.

5. Conclusions

Our multi-frequency data reveal a strong correlation between optical synchrotron and γ-ray emission in blazars. Analysis of optical and 43 GHz VLBA polarization and the timing of passages of superluminal knots through the core suggest that optical synchrotron emission originates in the vicinity of the mm-wave core, most likely through shocks, and that enhanced γ-ray emission is associated with this process. This implies that γ-ray flares originate near the mm-wave VLBI core.
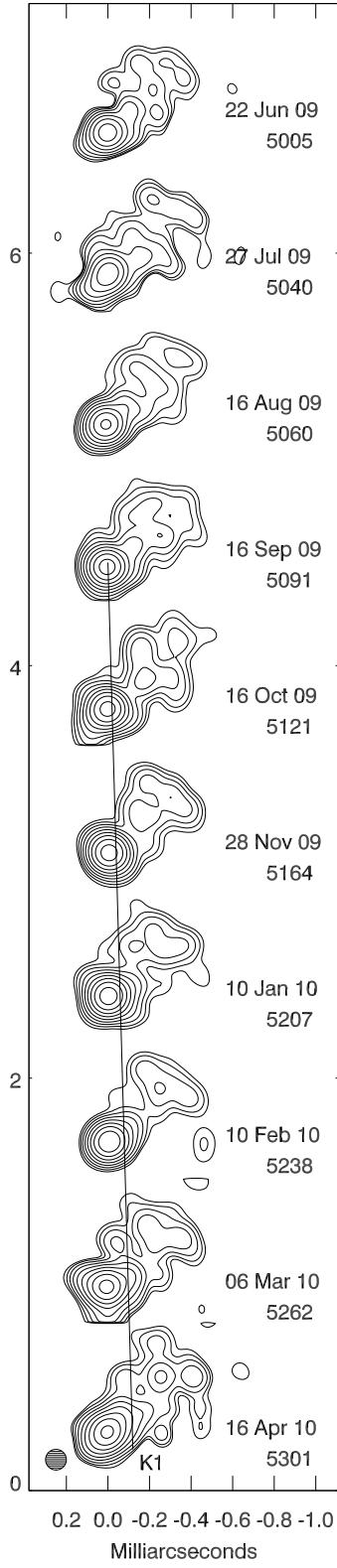
Fig. 9. VLBA images at 43 GHz of the quasar 1633+382 with convolving beam 0.1×0.1 mas, $S_{\rm peak}$=2.45 Jy/Beam, and contours representing 0.25,0.5,...,64% of the peak.
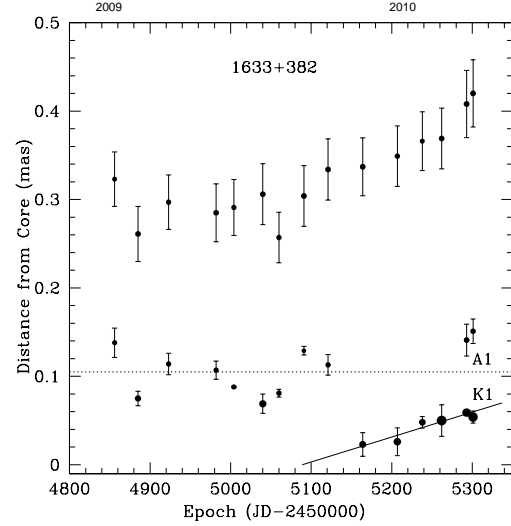
Fig. 10. Separation of knot K1 from the core.

References

Abdo, A. A., Ackermann, M., Ajello, M., et al. 2010, ApJ, 715, 429

Aller, M. F., Aller, H. D, & Hughes, P. A. 2003, ApJ, 586, 33

Dermer, C. D., & Schlickeiser, R. 1994, ApJS, 90, 945

Finke, J. D., & Dermer, C. D. 2010, ApJ, 714, L303

Hartman, R. C., Bertsch, D. L., Bloom, S. D., et al. 1999, ApJS, 123, 79

Impey, C. D., Malkan, M. A., & Tapia, S. 1989, ApJ, 347, 96

Jorstad, S. G., Marscher, A. P., Mattox, J. R., et al. 2001a, ApJS, 134, 181

Jorstad, S. G., Marscher, A. P., Mattox, J. R., et al. 2001b, ApJ, 556, 738

Jorstad, S. G., Marscher, A. P., Lister, M. L., et al. 2005, AJ, 130, 1418

Jorstad, S. G., Marscher, A. P., Stevens, J. A., et al. 2007, AJ, 134, 799

Jorstad, S. G., Marscher, A. P., Larionov, V. M., et al. 2010, ApJ, 715, 362

Kellermann, K. I., Lister, M. L., Homan, D. C., et al. 2004, ApJ, 609, 539

Kovalev, Y. Y., Aller, H. D., Aller, M. F., et al. 2009, ApJ, 696, L17

Lähteenmäki, A. & Valtaoja, E. 2003, ApJ, 590, 95

Lister, M. L., Homan, D. C., Kadler, M., et al. 2009, ApJ, 696, 22

Marscher, A. 2006, in The Common Physics of AGNs, Microquasars, and Gamma-Ray Bursts, eds. P.A. Hughes & J.N. Bregman, AIP Conf. Proc. 856, 1

Marscher, A. P., Jorstad, S. G., D'Arcangelo, F. D., et al. 2008, Nature, 452, 966

Marscher, A. P., Jorstad, S. G., Larionov, V. M., et al. 2010, ApJ, 710, L126

Poutanen, Y., & Stern, B. 2010, submited to ApJ, arXiv:1005.3792

Sikora, M., Begelman, M.C., & Rees, M. 1994, ApJ, 421, 153

Recent multi-wavelength campaigns in the Fermi-GST era

Lars Fuhrmann[1] on behalf of the *Fermi*/LAT and many MW collaborators[⋆]

Max-Planck-Institut für Radioastronomie, Auf dem Hügel 69, 53121 Bonn, Germany

Abstract. Since 2008 the *Fermi*/LAT instrument has delivered highly time-resolved γ-ray spectra and detailed variability curves for a steadily increasing number of AGN. For detailed AGN studies the *Fermi*/LAT data have to be combined with, and accompanied by, dedicated ground- and space-based multi-frequency observations. In this framework, the *Fermi* AGN team has realized a detailed plan for multi-wavelength campaigns including a large suite of cm/mm/sub-mm band instruments. Many of those campaigns have been triggered, often for sources detected in flaring states. We review here a few interesting results recently obtained during three such campaigns, namely for the flat-spectrum radio quasar 3C 279, the Narrow Line Seyfert 1 PMN J0948+0022 and quasar 3C 454.3.

1. Introduction

The successful launch in 2008 and subsequent smooth operation of the *Fermi* Gamma-ray Space Telescope (*Fermi*-GST) has brought the community a powerful instrument which is monitoring the entire γ-ray sky about every 3 hours. Thus, as an "all-sky-monitor", *Fermi*/LAT delivers highly time-resolved γ-ray spectra and detailed variability curves for a steadily increasing number of AGN. For the first time, detailed studies of AGN properties at γ-ray energies become possible and already many interesting results have been obtained (e.g., Abdo et al. 2009c, Abdo et al. 2010a, Abdo et al. 2010c). However, only when combined with, and accompanied by, dedicated ground- and space-based multi-frequency observations, can the *Fermi*/LAT unfold its full capability of providing a tremendous opportunity for systematic and detailed studies of the physical processes at work in AGN. Consequently, a large suite of different multi-wavelength (MW) monitoring data and projects ("single-dish", VLBI, polarization, spectra) across the whole electromagnetic spectrum (cm/mm/sub-mm, IR/optical/UV, X-ray, TeV) are essential to complement the *Fermi* γ-ray observations. Together, important fundamental questions about e.g., γ-ray production, overall emission and variability processes as well as the location of the γ-ray emission region can be effectively addressed.

In this framework, the *Fermi* AGN group has realized a detailed plan for ad-hoc as well as intensive long-term campaigns. Many of these have been triggered, often for sources detected in flaring states. Here, the 15 GHz OVRO 40-m and F-GAMMA cm to sub-mm (Effelsberg 100-m, IRAM 30-m, APEX 12-m) monitoring programs, the GASP (radio/IR/optical) collaboration

including many IR/optical telescopes (radio: UMRAO, Metsähovi, SMA, Medicina, Noto), RATAN-600, ATCA, Kanata, ATOM, SMARTS, Stewart observatory, MDM, WIRO, KVA, INAOEP, VLT/VISIR as well as VLBI: MOJAVE, TANAMI, the Boston 43 GHz program, a VLBA multi-frequency ToO program and the EVN/LBA have been participating in one or more of the various campaigns.

In addition the X-ray bands have often been covered by the space-based X-ray observatories *Swift*, *Suzaku*, and RXTE. In particular, *Swift* has proven to be extremely valuable in quickly providing detailed and simultaneous observations at optical/UV and X-ray bands for many sources. Furthermore, *Spitzer* has participated in the case of 3C 454.3 with important near-IR data. Finally, first combined *Fermi*/LAT and TeV campaigns led to joint studies with the Cherenkov telescopes HESS and VERITAS as e.g., in the case of PKS 2155-304 (Aharonian et al. 2009) and 3C 66A (Abdo et al. in prep.).

Since the launch of *Fermi*-GST in 2008, many sources have been target of detailed MW campaigns triggered by the *Fermi* AGN group. Table 1 provides a short summary of those which have been published so far. Many other MW campaign publications are accepted, have been submitted or are in progress, e.g., for the galactic plane source J 0109+6134, PKS 1510-089, Mrk 501, Mrk 421 and 3C 454.3.

As examples, we review here a few interesting results from three selected MW campaigns recently conducted (2008–2009) by the *Fermi* AGN group together with many MW collaborators.

2. The γ-ray/optical polarization angle event in 3C 279

After about 100 days of *Fermi*/LAT routine operations, the quiescent phase of flat-spectrum radio quasar (FSRQ) 3C 279 turned into a phase of strong γ-ray activity and a MW campaign was triggered including a large number of instruments (see Fig. 1, Abdo et al. 2010b).

[⋆] The work reviewed here was possible only due to the large efforts and great work of many multi-wavelength (MW) projects/collaborators, it is impossible to mention all in detail here. Representatively, we give the names of the corresponding projects in the text. The collaborators are part of the referenced publications for each campaign.

Table 1. Publication summary of sources studied by the *Fermi* AGN group including (quasi-) simultaneous MW data. Joint GeV/TeV projects are also included.

Source	Reference
RGB J0710+591	Acciari, V. A., et al. 2010, ApJ, 715, L49
5 FSRQs	Abdo, A. A., et al. 2010, [arXiv:1004.2857]
PKS 1424+240	Acciari, V. A., et al. 2010, ApJ, 708, L100
3C 279	Abdo, A. A., et al. 2010, Nature, 463, 919
PKS 1502+106	Abdo, A. A., et al. 2010, ApJ, 710, 810
NGC 1275	Acciari, V. A., et al. 2009, ApJ, 706, L275,
	Abdo, A. A., et al. 2009, ApJ, 699, 31
3C 454.3	Abdo, A. A., et al. 2009, ApJ, 699, 817
PKS 2155-304	Aharonian, F., et al. 2009, ApJ, 696, L150
PMN J0948+0022	Abdo, A. A., et al. 2009, ApJ, 707, 727,
	Abdo, A. A., et al. 2009, ApJ, 699, 976
PKS 1454-354	Abdo, A. A., et al. 2009, ApJ, 697, 934

As seen from Fig. 1, 3C 279 went into a high γ-ray state at around MJD 54780 lasting for about 120 days and characterized by a double-peak structure with overall variations of the flux by a factor ~ 10. The observed γ-ray luminosity of $\sim 10^{48}\,\mathrm{erg\,s^{-1}}$ dominates the power emitted across the whole electromagnetic spectrum (see Fig. 2).

The most striking event occured during the rapid, second γ-ray flare (around MJD 54880, doubling time scale of about one day). Here, a highly correlated behavior of the γ-ray and optical bands is evident between MJD 54800 and 54830, with the γ-ray flare coincident with a significant drop of the level of optical polarization, from about 30 % down to a few percent lasting for about 20 days. In particular, this event is associated with a dramatic change of the electric vector position angle (EVPA) by 208° (12°/day), in contrast to being relatively constant earlier, at about 50°, which corresponds to the jet direction of 3C 279 as observed by VLBI. The close association of the γ-ray flare with the optical polarization angle event clearly suggests that the γ-ray emission was produced in a single, coherent event and happened co-spatial with the optical. It furthermore suggests highly ordered magnetic fields in the γ-ray emission region.

Compared to the higher energy emission, the radio cm/mm bands showed less strong variability and no obvious "correlated event" is evident from the light curves shown in Fig. 1. Still, the source appears to be at higher radio flux levels (factor ~ 2) during the period of the overall γ-ray high state as seen from the 230 GHz SMA data. However, assuming the source was still optically thick at these bands, synchrotron self-absorption arguments constrain the transverse size of the emission region to $< 5 \times 10^{16}$ cm, in good agreement with the values obtained from the shortest γ-ray variability.

The gradual rotation of the optical polarization angle requires a non-axisymmetric trajectory of the emission pattern, since in a uniform, axially-symmetric case, any e.g., compression due to a shock moving along the jet would result in a change of polarization degree, but
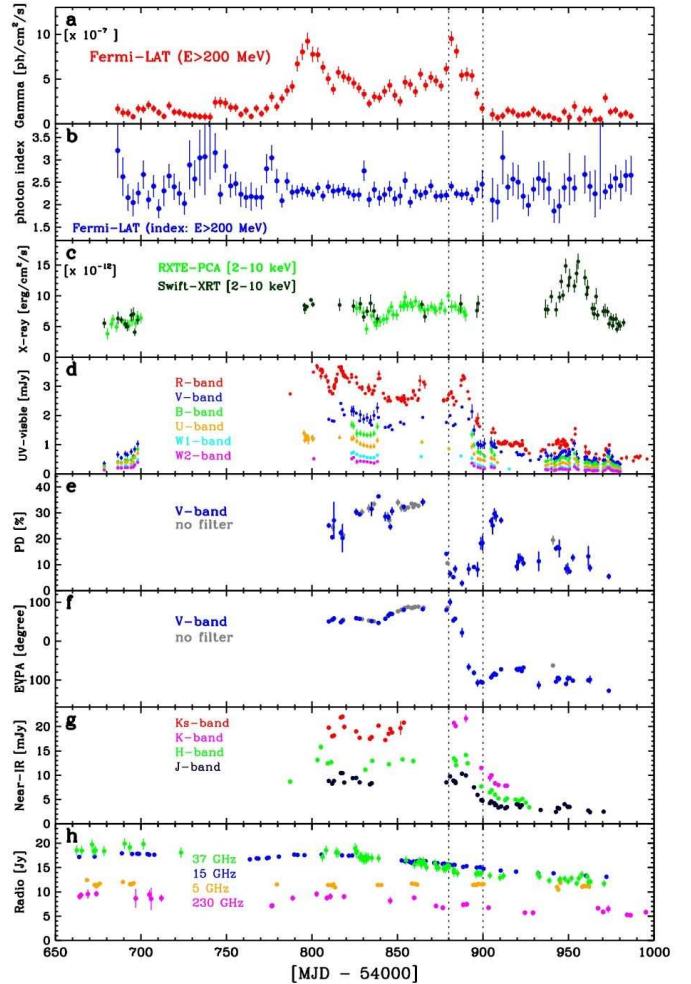
Fig. 1. Multi-frequency light curves of 3C 279 obtained during the large MW campaign between July 2008 and June 2009 (see Abdo et al. 2010b for details). Many MW facilities participated such as *Swift*-XRT and RXTE at X-ray bands; many telescopes of the GASP collaboration, Kanata, *Swift* UVOT and KVA at IR/optical/UV bands, as well as SMA, UMRAO, OVRO, Metsähovi, Medicina, Noto and Effelsberg at radio bands. Note the smooth optical polarization angle swing during the period of the second, rapid γ-ray flare (dotted lines).

not in a gradual change of the EVPA. Consequently, two models have been discussed to explain the observed behavior in a non-axisymmetric/curved geometry: the emission region/knot propagating outwards along (i) helical magnetic field lines (similar to the optical polarization event observed in BL Lacertae, Marscher et al. 2008) and (ii) along the curved trajectory of a bent jet.

In both scenarios the distance of the dissipation region from the central engine can be constrained from the ~ 20 day time-scale of the event. The distance obtained is about 5 orders of magnitude larger than the gravitational radius of the black hole in 3C 279 and implies a jet opening angle of $< 0.2°$, smaller than typically observed with VLBI. Although less likely, models resulting in a much smaller distance (sub-parsec) can not be completely ruled out. At the large distances implied by the two models (par-
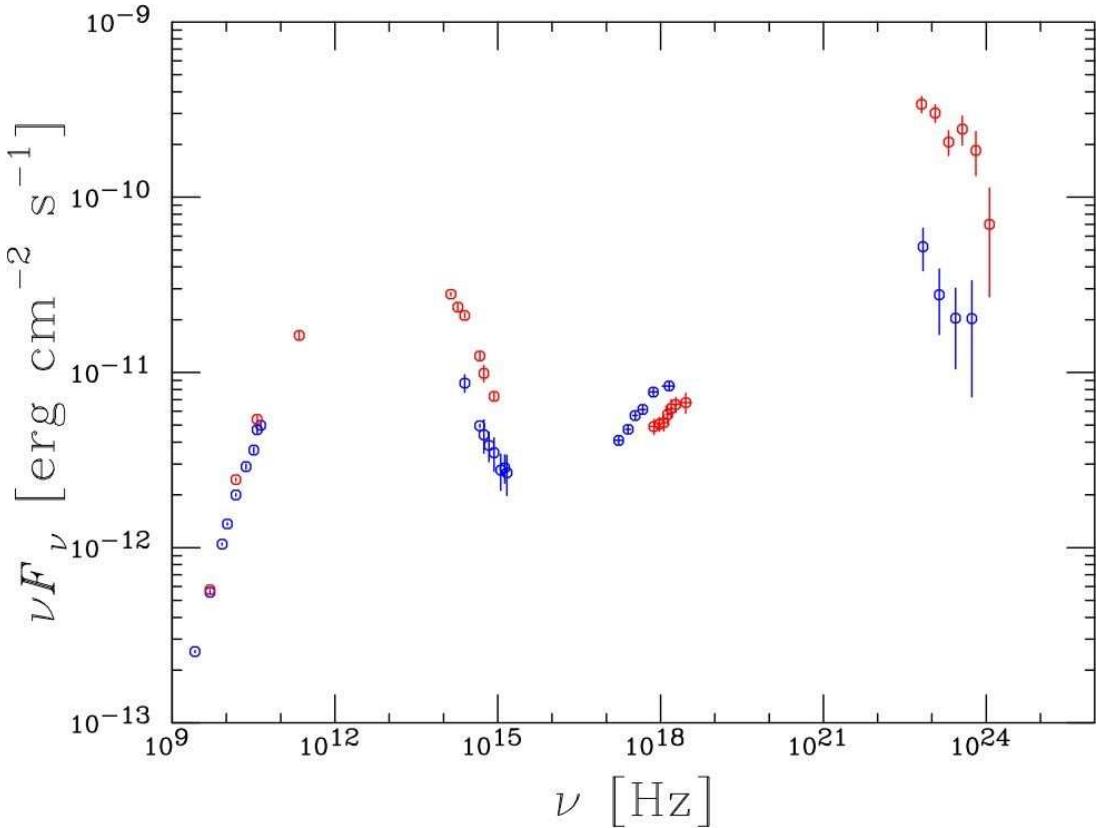
Fig. 2. Broad band SED of 3C 279 obtained during the MW campaign of 2008/2009. The red data points denote the period of the γ-ray/optical event. The blue data points have been taken during the period of the isolated X-ray flare.

secs), the seed photons for the IC emission should then mostly be provided by the torus IR and jet synchrotron emission rather than BLR or accretion disk emission.

Another interesting feature is the isolated X-ray flare at MJD 54950, about 60 days after the second γ-ray flare. The hard X-ray spectrum during this period and the similarity of its shape and time-scale to the γ-ray flare argue in favor of an isolated event which is difficult to reconcile with simple one-zone models.

3. PMN J0948+0022 and Narrow-line Seyfert 1 galaxies

Before the launch of *Fermi*-GST the known types of γ-ray emitting AGN were blazars and radio galaxies. Indeed, the early *Fermi*/LAT three month results (Abdo et al. 2009c) confirmed that the extragalactic γ-ray sky is dominated by radio-loud AGN, being mostly blazars and a few radio galaxies. However, an important and impressive early discovery of *Fermi*-GST is the detection of γ-rays from a different class of AGN: Narrow Line Seyfert 1 galaxies (NLS1). These types of objects are believed to be active nuclei similar to those of Seyferts with optical spectra showing permitted lines from the broad-line region, although much narrower than typically seen in Seyfert 1s or blazars (FWHM(Hβ) $< 2000\,\mathrm{km\,s^{-1}}$). This and other characteristics make them a unique class of AGN, whereas a large fraction is radio-quiet, and only less than 7 % (Komossa et al. 2006) are found to be radio-loud. The first *Fermi*/LAT detection of γ-rays from a NLS1, namely

in PMN J0948+0022 (Abdo et al. 2009b), certainly once more raised the question whether relativistic jets exist in this type of object, as indicated by previous studies in particular for the most radio-loud NLS1 (e.g., Foschini et al. 2009).

In summary, the *Fermi*/LAT and MW observations of PMN J0948+0022 clearly demonstrate for the first time the existence of a γ-ray emitting NLS1 hosting a relativistic jet similar to blazars even though the environment in the vicinity of the central engine is most likely pretty different. However, this strongly challenges our view that jets can only develop in elliptical galaxies. Follow-up *Fermi*/LAT and MW observations of PMN J0948+0022 and the three other NLS1 detected by *Fermi*/LAT (Abdo et al. 2009) will certainly shed further light on this interesting new type of γ-ray emitting AGN.

The answer came promptly. MW follow-up observations of PMN J0948+0022 performed right after its γ-ray detection (Abdo et al. 2009b) as well as through a triggered MW campaign during March–July 2009 (Abdo et al. 2009d) demonstrated the efficiency of MW observations/campaigns in conjunction with *Fermi*/LAT: these MW studies have demonstrated that PMN J0948+0022 hosts a relativistic jet. Here, early SED studies using non-simultaneous plus simultaneously acquired MW data (Effelsberg 100-m, OVRO 40-m, *Swift*) satellite) revealed an SED similar to that of powerful FSRQs with the typical double-humped appearance peaking in the far-IR and in the 40–400 MeV range (see Fig. 3). Signs of the accretion disk peaking in the *Swift* UV frequency range are clearly
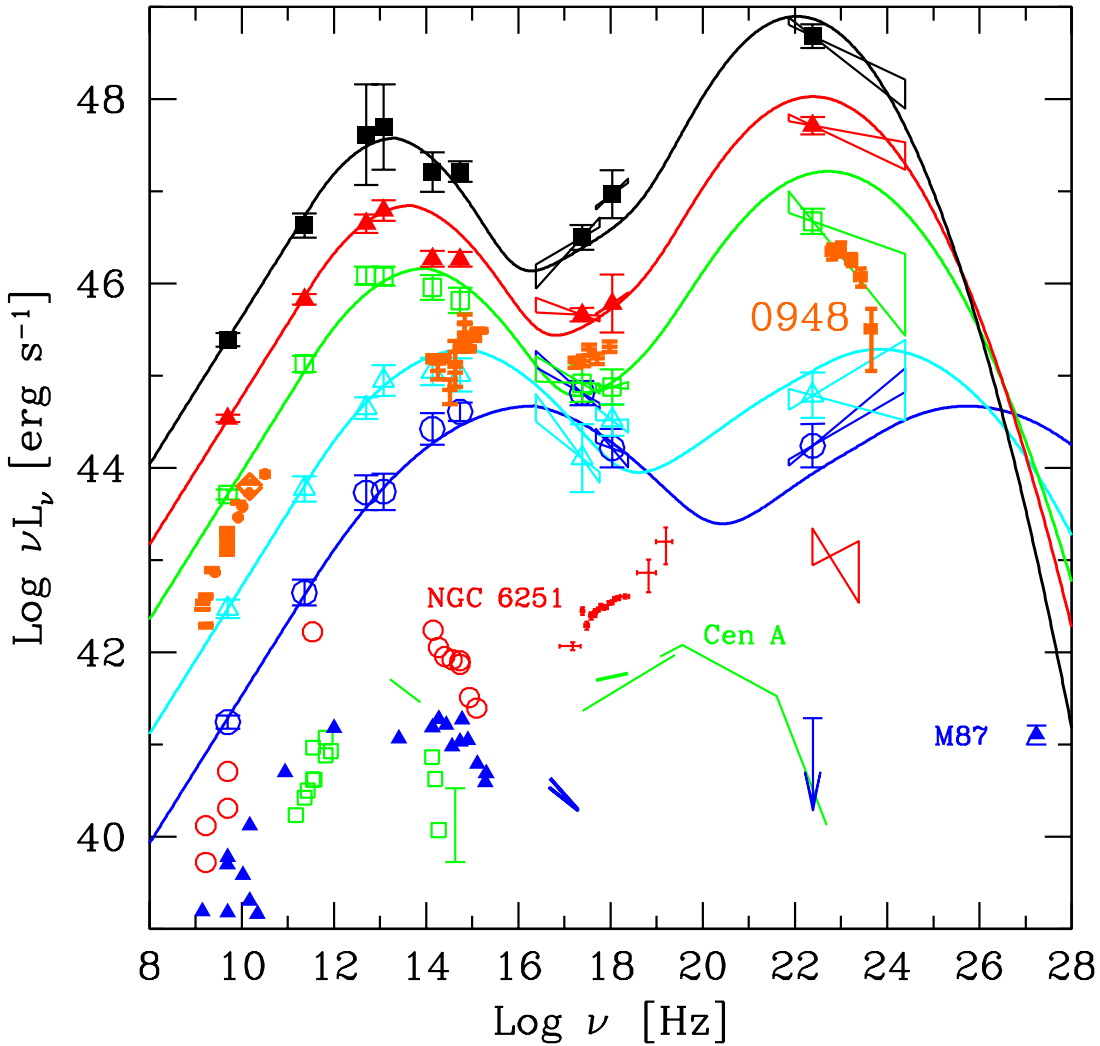
Fig. 3. The SED of PMN J0948+0022 as obtained during the MW campaign, here shown in comparison to other γ-ray emitting FSRQs, BL Lacs and radio galaxies (see also Abdo et al. 2009b, Abdo et al. 2009d and Foschini et al. 2009)

seen, which yields a lower limit to the black hole mass of $1.5 \times 10^8 \, M_\odot$. The time-resolved SEDs have been fitted using the one-zone synchrotron/IC model of Ghisellini & Tavecchio (2009) resulting in synchrotron/SSC components (dominating the radio to X-ray frequencies) and an EC component producing the γ-ray emission. The physical parameters are similar to those of blazars, however, with lower power compared to FSRQs but higher values than typically seen for BL Lacs (see Fig. 3).

From the radio perspective alone, the presence of a relativistic jet in PMN J0948+0022 appears obvious due to several findings, such as (i) flux density as well as spectral variability/flare over the duration of the campaign with flat ($\alpha_{5-15\,\mathrm{GHz}} \sim 0$) to highly inverted (max.: $\alpha_{5-15\,GHz} = 0.98\pm0.05$) Effelsberg/RATAN radio spectra, (ii) equipartition Doppler factors of up to ~ 7, (iii) a highly compact, unresolved core on pc-scales (MOJAVE VLBA and EVN/LBA) with a 15 GHz core size of $< 60\,\mu$as and corresponding core brightness temperature of 1.0×10^{12} K and finally, (iv) VLBI core fractional linear polarization of 0.7%. This is the signature of a relativistic radio jet similar to those seen in powerful blazar type objects. The radio flare seen in the OVRO/Metsähovi light curves as

well as Effelsberg/RATAN radio spectra appears to be delayed with respect to the γ-ray peak by 1.5–2 months.

4. The early γ-ray flare of 3C 454.3 during 2008

During the early check-out phase of *Fermi*/LAT and the subsequent early operation in survey mode (July-October 2008), strong and highly variable γ-ray emission from the quasar 3C 454.3 was detected (Abdo et al. 2009a) showing a large outburst in July 2008 and subsequently, distinct symmetrically shaped sub-flares on time scales of days (see Fig. 4).

Such rapid γ-ray variability indicates a highly compact emission region and relativistic beaming with a Doppler factor of $\delta > 8$ in order to be optically thin to pair production. The observed γ-ray spectrum obtained from the early *Fermi*/LAT data has demonstrated for the first time the existence of a spectral break for a high-luminosity blazar above 100 MeV, which may be regarded as evidence for an intrinsic break in the energy distribution of the radiating particles. Alternatively, the spectral softening above 2 GeV could be due to γ-ray absorption via photon-photon pair production on the soft X-ray photon field of the host active galactic nucleus or due to the superposition of two
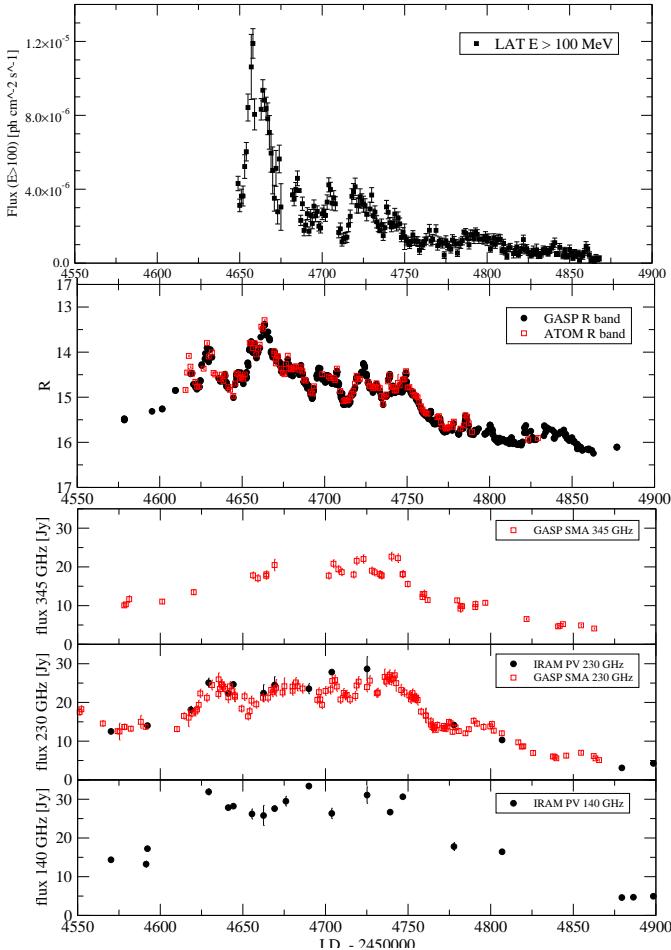
Fig. 4. Selection of multi-band light curves for 3C 454.3 obtained at γ-rays, optical R band (GASP and ATOM telescopes) and mm/sub-mm bands (SMA, IRAM 30-m). Note the similar variability pattern.

different spectral components at high energies (Abdo et al. 2009a, see also Finke & Dermer 2010 for a more detailed study of the spectral break).

The large multi-wavelength campaign (Abdo et al. in prep.) triggered by the Fermi AGN team shortly after the detection of the high γ-ray state of the source in July/August 2008, resulted in a so far unprecedented frequency coverage from cm/mm/sub-mm bands, IR/optical/UV, X-ray to the GeV range. These data sets demonstrate an active phase of 3C 454.3 across the whole electromagnetic spectrum. Figure 4 shows a selection of MW light curves including the γ-ray, optical (R) and short-mm bands. Interestingly, a similar variability pattern is seen at all bands, even down to the short-mm bands - up to frequencies higher than or close to the radio synchrotron turn-over at around 100 GHz. A detailed time series and cross-band analysis of the best sampled light curves reveals (i) strong correlations between γ-ray/optical and optical/mm-bands (ii) a quasi-periodic modulation of the variability with a fast (about 20 days) and slow (about 60 days) component seen at all bands, with similar start and stop times. The optical polarization

angle data, however, shows no obvious strong pattern, in contrast to the case of 3C 279.

Doppler factors in the range of 3–9 derived from the radio variability (Fig. 4) are in good agreement with those obtained from synchrotron self-absorption and γ-pair production arguments. Three epochs of multi-frequency VLBA ToO observations clearly show that the total single-dish variability originates from the core region while the core spectrum nicely resembles the (inverted) total single-dish spectrum.

The evolution of the synchrotron turnover frequency as obtained from the detailed radio light curves shown in Fig. 4 is in good agreement with the shock-in-jet model of Marscher & Gear (1985) (as are the increasing time lags towards longer radio wavelengths), at least in the synchrotron and adiabatic phases. However, departures from the Compton phase indicate additional processes at work as indicated already by the cross-band analysis. Detailed modeling with geometrical (e.g., helical jet) as well as SSC/EC models are in progress in order to explain the complex behavior of the source in a consistent manner.

5. Conclusions

As a powerful "all-sky-monitor" the *Fermi*/LAT instrument provides a unique opportunity to explore the high energy γ-ray sky and the γ-ray characteristics of the AGN population. In particular, when combined with ground- and space-based multi-frequency observations, *Fermi*/LAT unfolds its full capability in addressing fundamental questions about energy production in AGN. This becomes possible due to the large efforts of the MW community in providing detailed, (quasi-) simultaneous broad-band data for a large number of *Fermi*-detected AGN. Since 2008 the *Fermi* team has triggered a large number of MW campaigns. The success of such campaigns, although challenging for both observers and theoreticians—as demonstrated by the examples presented here—increasingly provides deeper insight into the physical processes involved.

References

Abdo, A. A., et al. 2010c, ApJ, 715, 429
Abdo, A. A., et al. 2010b, Nature, 463, 919
Abdo, A. A., et al. 2010a, ApJ, 710, 1271
Abdo, A. A., et al. 2009d, ApJ, 707, 727
Abdo, A. A., et al. 2009c, ApJ, 700, 597
Abdo, A. A., et al. 2009b, ApJ, 699, 976
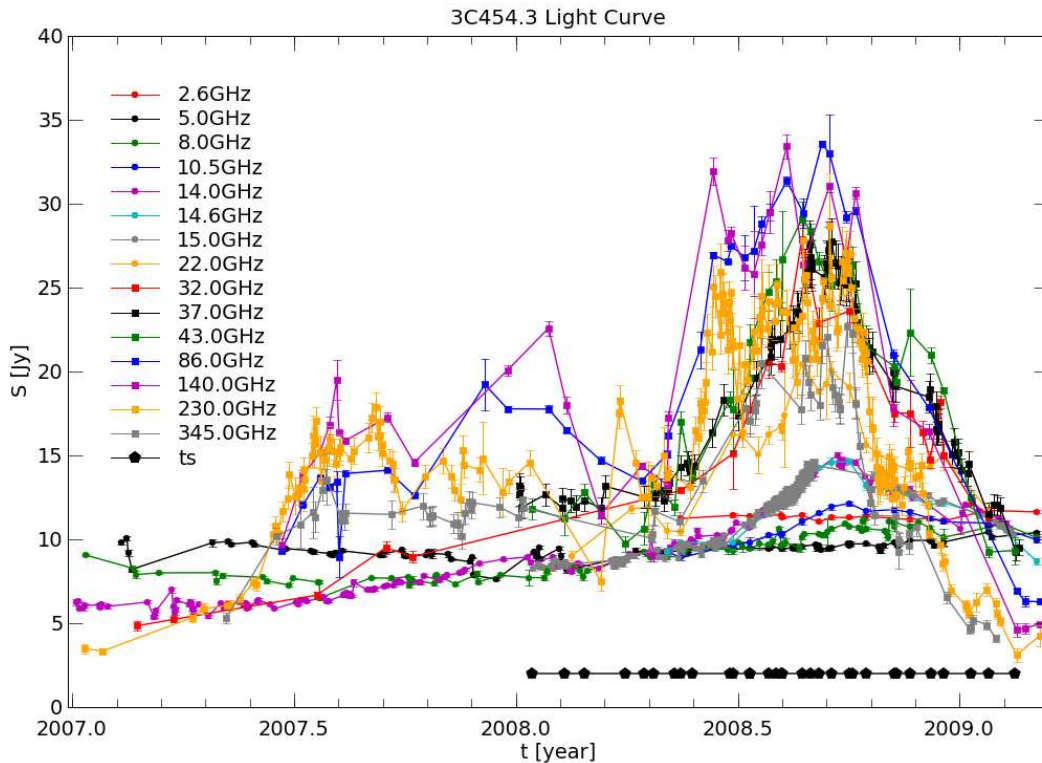
Fig. 5. The full collection of multi-frequency radio cm/mm/sub-mm light curves of 3C 454.3 obtained during the MW campaign. Many radio telescopes were involved: UMRAO, Medicina, Noto, Effelsberg, OVRO, Metsähovi, IRAM 30-m, SMA. The great frequency coverage has been used to study detailed spectral evolution.

Abdo, A. A., et al. 2009a, ApJ, 699, 817

Aharonian, F., et al. 2009, ApJ, 696, L150

Finke, J. D., & Dermer, C. D. 2010, ApJ, 714, L303

Foschini, L., for the Fermi/LAT Collaboration, Ghisellini, G., Maraschi, L., Tavecchio, F., & Angelakis, E. 2009, arXiv:0908.3313

Ghisellini, G., & Tavecchio, F. 2009, MNRAS, 397, 985

Komossa, S., Voges, W., Xu, D., Mathur, S., Adorf, H.-M., Lemson, G., Duschl, W. J., & Grupe, D. 2006, AJ, 132, 531

Marscher, A. P., et al. 2008, Nature, 452, 966

Marscher, A. P., & Gear, W. K. 1985, ApJ, 298, 114

Monitoring of γ-ray blazars with AGILE

F. D'Ammando on behalf of the *AGILE* Team

INAF–IASF Palermo, Via Ugo La Malfa 153, I-90146 Palermo, Italy

Abstract. Thanks to the wide field of view of its γ-ray imager, the *AGILE* satellite obtained a long term monitoring of the brightest blazars in the sky and during the first 3 years of operation detected several blazars in a high γ-ray state: 3C 279, 3C 454.3, PKS 1510−089, S5 0716+714, 3C 273, W Comae, and Mrk 421. Through the rapid dissemination of our alerts we were able to obtain also multi-wavelength data from many observatories such as *Spitzer*, *Swift*, RXTE, *Suzaku*, XMM-*Newton*, INTEGRAL, MAGIC, VERITAS, and ARGO as well as radio-to-optical coverage by means of the MOJAVE project, the GASP project of the WEBT and the REM Telescope. This large coverage over the whole electromagnetic spectrum gave us the opportunity to study the variability correlations between the emission at different frequencies and to build truly simultaneous spectral energy distributions of these sources from radio to γ-rays, investigating in detail the emission mechanisms of blazars and uncovering in some cases a more complex behaviour with respect to the standard models. We present an overview of the most interesting *AGILE* results on these γ-ray blazars and the relative multi-wavelength data.

1. Introduction

Blazars constitute the most enigmatic subclass of Active Galactic Nuclei (AGNs), characterized by the emission of strong non-thermal radiation across the entire electromagnetic spectrum and in particular intense and variable γ-ray emission above 100 MeV (Hartman et al. 1999). The typical observational properties of blazars include irregular, rapid and often very large variability, apparent super-luminal motion, flat radio spectrum, high and variable polarization at radio and optical frequencies. These features are interpreted as the result of the emission of electromagnetic radiation from a relativistic jet that is viewed closely aligned to the line of sight (Blandford & Rees 1978; Urry & Padovani 1995).

Blazars emit across several decades of energy, from radio to TeV energy bands, and thus they are the perfect candidates for simultaneous observations at different wavelengths. Multi-wavelength studies of variable γ-ray blazars have been carried out since the beginning of the 1990s, thanks to the EGRET instrument onboard *Compton Gamma-Ray Observatory* (*CGRO*), providing the first evidence that the Spectral Energy Distributions (SEDs) of the blazars are typically double humped with the first peak occurring in the IR/optical band in the so-called *red blazars* (including Flat Spectrum Radio Quasars, FSRQs, and Low-energy peaked BL Lacs, LBLs) and in UV/X-rays in the so-called *blue blazars* (including High-energy peaked BL Lacs, HBLs).

The first peak is interpreted as synchrotron radiation from high-energy electrons in a relativistic jet. The SED second component, peaking at MeV–GeV energies in *red blazars* and at TeV energies in *blue blazars*, is commonly interpreted as inverse Compton (IC) scattering of seed photons, internal or external to the jet, by highly relativistic electrons (Ulrich et al. 1997), although other mod-

els involving hadronic processes have been proposed (see e.g. M. Böttcher 2007 for a recent review).

With the detection of several blazars in γ-rays by EGRET (Hartman et al. 1999) the study of this class of object has made significant progress. In fact, considering that the large fraction of the total power of blazars is emitted in the γ-rays, information in this energy band is crucial to study the different radiation models. 3C 279 is the best example of multi-epoch studies at different frequencies performed by EGRET during the period 1991–2000 (Hartman et al. 2001). Nevertheless, only a few objects were detected in the EGRET *era* on a time scale of few weeks in the γ-rays and simultaneously monitored at different energies to obtain a wide multi-frequency coverage.

The interest in blazars is now even more renewed thanks to the simultaneous presence of two γ-ray satellites, *AGILE* and *Fermi*, and the possibility to obtain γ-ray observations over long timescales simultaneously with data collected from radio to TeV energies allowing us to reach a deeper insight on the jet structure and the emission mechanisms at work in blazars.

2. Blazars and AGILE

The γ-ray observations of blazars are a key scientific project of the *AGILE* (*Astrorivelatore Gamma ad Immagini LEggero*) satellite (Tavani et al. 2009). Thanks to the wide field of view of its γ-ray imager ($\sim$ 2.5 sr), *AGILE* monitored tens of potentially γ-ray emitting AGNs during each pointing and after November 2009 in the new spinning mode the number of γ-ray sources simultaneously monitored by the satellite is still increased.

In the first 3 years of operation, *AGILE* detected several blazars during high γ-ray activity and extensive multi-wavelength campaign were organized for many of them, providing the possibility to monitoring on

3C 454.3   Jul. 2007 – Jan. 2009
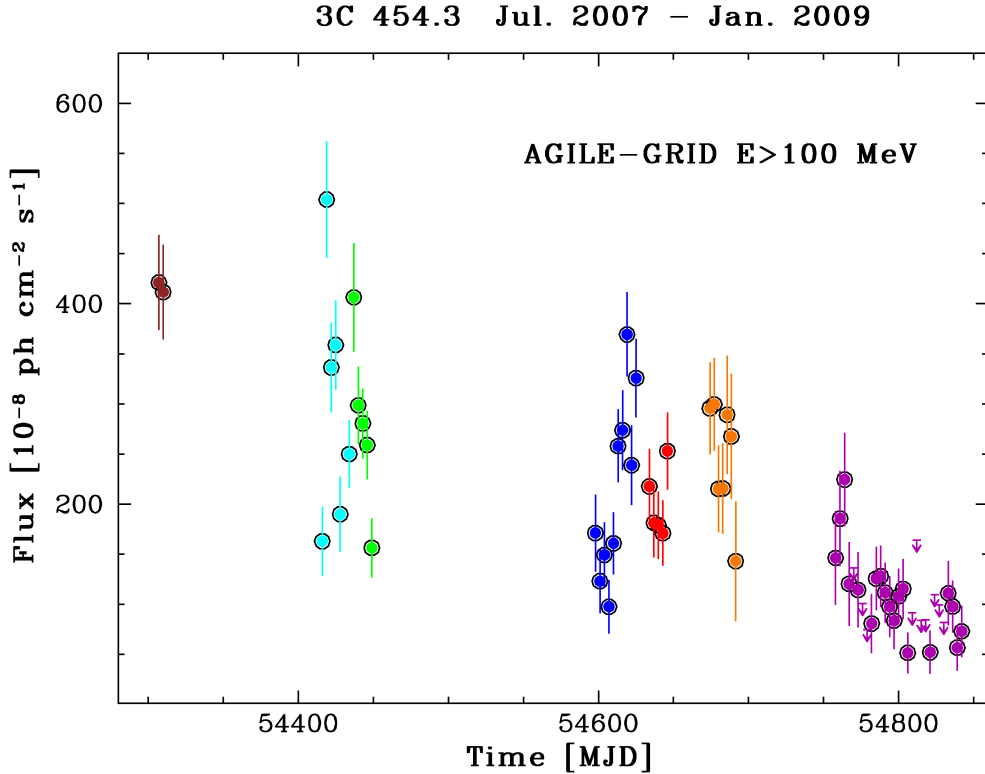
Fig. 1. *AGILE* GRID light curve of 3C 454.3 collected between July 2007 and January 2009 at ~3 day resolution in units of 10^{-8} ph cm^{-2} s^{-1}. [Adapted from Vercellone et al. 2010].

long timescales the brightest objects. The γ-ray activity timescales of these blazars goes from a few days (e.g. S5 0716+714 and 3C 273) to several weeks (e.g., 3C 454.3 and PKS 1510−089) and the flux variability observed has been negligible (e.g., 3C 279), very rapid (e.g., PKS 1510−089) or extremely high (e.g., 3C 454.3 and PKS 1510−089). However, we note that only a few objects were detected more than once in flaring state by *AGILE* and mostly already known γ-ray emitting sources showed intense flaring activity. This evidence, together with the results of *Fermi*/LAT obtained during the first 11 months of operation (Abdo et al. 2010), suggest possible constraint on the properties of the most intense γ-ray emitters. In the following we will present the most interesting results on the studies of the individual sources detected by *AGILE* .

3. Individual Sources

3.1. 3C 454.3

Among the FSRQs 3C 454.3 is one of the brightest object and also the source that exhibited the most variable activity in the last years. In particular during May 2005, 3C 454.3 was reported to undergo a very strong optical flare (Villata et al. 2006). This exceptionally high state triggered observations by high-energy satellites (RXTE: Remillard 2005; *Chandra*: Villata et al. 2006; INTEGRAL: Pian et al. 2006; *Swift*: Giommi et al. 2006) which confirm an exceptionally high flux also in X-ray band. Unfortunately, no γ-ray satellite was operative at that time.

In mid-July 2007, 3C 454.3 underwent a new optical brightening that triggered observations at all frequencies, including a Target of Opportunity (ToO) by the *AGILE* γ-ray satellite (Vercellone et al. 2008). That was the beginning of an extraordinary long-term γ-ray activity of the source until the huge γ-ray flare observed in early December 2009 (Striani et al. 2010). In the period July 2007–January 2009 the *AGILE* satellite monitored intensively 3C 454.3 together with *Spitzer*, GASP-WEBT, REM, MITSuME, *Swift*, RXTE, *Suzaku* and INTEGRAL observatories, with two dedicated campaigns organized during November 2007 and December 2007, as reported respectively in Vercellone et al. (2009) and Donnarumma et al. (2009), and yielding the longest multi-wavelength coverage of this γ-ray quasar so far (Vercellone et al. 2010).

The source underwent an unprecedented long period of high γ-ray activity, showing flux levels variable on short timescales of 24–48 hours and reaching on daily timescale a γ-ray flux higher than 500×10^{-8} ph cm^{-2} s^{-1} (Fig. 1 and Fig. 2, bottom panel). A diminishing trend of the γ-ray flux from July 2007 and January 2009 was observed with a hint of "harder-when-brighter" behaviour, previously observed in γ-rays only for 3C 279 in the EGRET *era* (Hartman et al. 2001). Also the optical flux appears extremely variable with a brightening of several tenths of magnitude in a few hours. Emission in optical range appears to be correlated with that at γ-rays, with a lag of the γ-ray flux with respect to the optical one less than 1 day during bright states. However, over-imposed to the overall trend some sub-structures on shorter timescales with different variability could be present in optical and γ-rays.
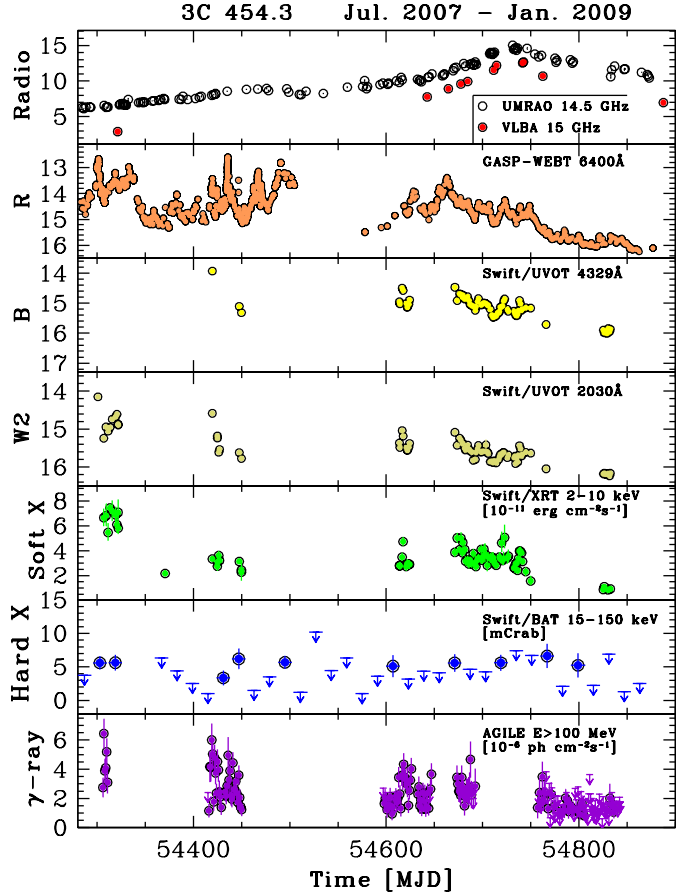
Fig. 2. 3C 454.3 light curves between July 2007 and January 2009 at increasing energies from top to bottom. Data were collected by *AGILE* , *Swift* (BAT, XRT and UVOT), GASP-WEBT, and VLBA. [Adapted from Vercellone et al. 2010.]

From the comparison of the light curves from radio to γ-rays shown in Fig. 2 it is noticeable that, while at almost all the frequencies the flux shows a diminishing trend with time during the period July 2007–January 2009, the 15 GHz radio core flux increases, although no new jet component seems to be detected in the high resolution VLBA images. The different behaviour observed in radio, optical and γ-rays from the end of 2007 could be interpreted in the framework of a helical jet model as a change in the jet geometry between 2007 and 2008.

The dominant emission mechanism above 100 MeV in 3C 454.3 seems to be the IC scattering of relativistic electrons in the jet on the external photons from the Broad Line Region (BLR), even if in some cases also the contribution of external Compton (EC) of seed photons from a hot corona could be not negligible (Donnarumma et al. 2009).

During December 2009, 3C 454.3 became the brightest γ-ray source in the sky, reaching a peak flux of about 2000 $\times 10^{-8}$ ph cm^{-2} s^{-1} on 2–3 December 2009. Intensive multi-frequency observations showed an overall correlation at all wavelengths for both long and short timescales. However, the unusual γ-ray super-flaring activity is not accompanied by strong emission of similar intensity in the optical or even in the soft X-ray bands. The pre- and post-flare broad band behaviour can be adequately represented by a simple one-zone synchrotron self Compton (SSC) model plus EC in which the accretion disk and the BLR provide the necessary soft radiation field for the IC components. Instead, the spectrum of the 2-3 December 2009 super-flare would require with respect to the pre-flare an increase of the electron energy and density and a slight reduction of the comoving magnetic field for the whole electron population of the blob (see also Bonnoli et al. 2010). We use a different approach, assuming a long-term rise and fall of the accretion rate onto the central black hole that causes an overall increase of the synchrotron emission and of the soft photon background scattered. An additional population of electrons, due to an additional particle acceleration and/or plasmoid ejection near the jet basis, could be present during the super-flare (Fig. 3; Pacciani et al. 2010).

3.2. PKS 1510−089

PKS 1510−089 is another blazar that in the last three years showed high variability over all the electromagnetic spectrum, in particular high γ-ray activity was observed by *AGILE* and *Fermi*. *AGILE* detected intense flaring episodes in August 2007 (Pucella et al. 2008) and March 2008 (D'Ammando et al. 2009) and an extraordinary activity during March 2009 (D'Ammando et al. 2010).

During the period 1–16 March 2008, *AGILE* detected an average flux from PKS 1510−089 of $(84 \pm 17) \times 10^{-8}$ ph cm^{-2} s^{-1} for E > 100 MeV. The flux measured between 17 and 21 March was a factor of 2 higher, with a peak level of $(281 \pm 68) \times 10^{-8}$ ph cm^{-2} s^{-1} on 19 March 2008. Moreover, between January and April 2008 the source showed an intense and variable optical activity with several flaring episodes of fast variability. A significant increase of the flux was observed also at millimetric frequencies in mid April, suggesting that the mechanisms producing the flaring events in the optical and γ-ray bands also interested the millimetric zone, with a delay.

The γ-ray flare triggered 3 *Swift* ToO observations in three consecutive days between 20 and 22 March 2008. The first XRT observation showed a very hard X-ray photon index ($\Gamma = 1.16 \pm 0.16$) with a flux in the 0.3–10 keV band of $(1.22 \pm 0.17) \times 10^{-11}$ erg cm^{-2} s^{-1} and a decrease of the flux of about 30% between 20 and 21 March. The *Swift*/XRT observations show a harder-when-brighter behaviour of the spectrum in the X-ray band, confirming a behaviour already observed in this source by Kataoka et al. (2008), a trend usually observed in HBL but quite rare in FSRQs such as PKS 1510−089.

This harder-when-brighter behaviour is likely due to the different variability of the SSC and EC components, therefore to the change of the relative contribution of each component. Thus, the X-ray photon index observed on 20 March could be due to the combination of SSC and EC emission and therefore to the mismatch of the spectral slopes of these two components. The SED for the
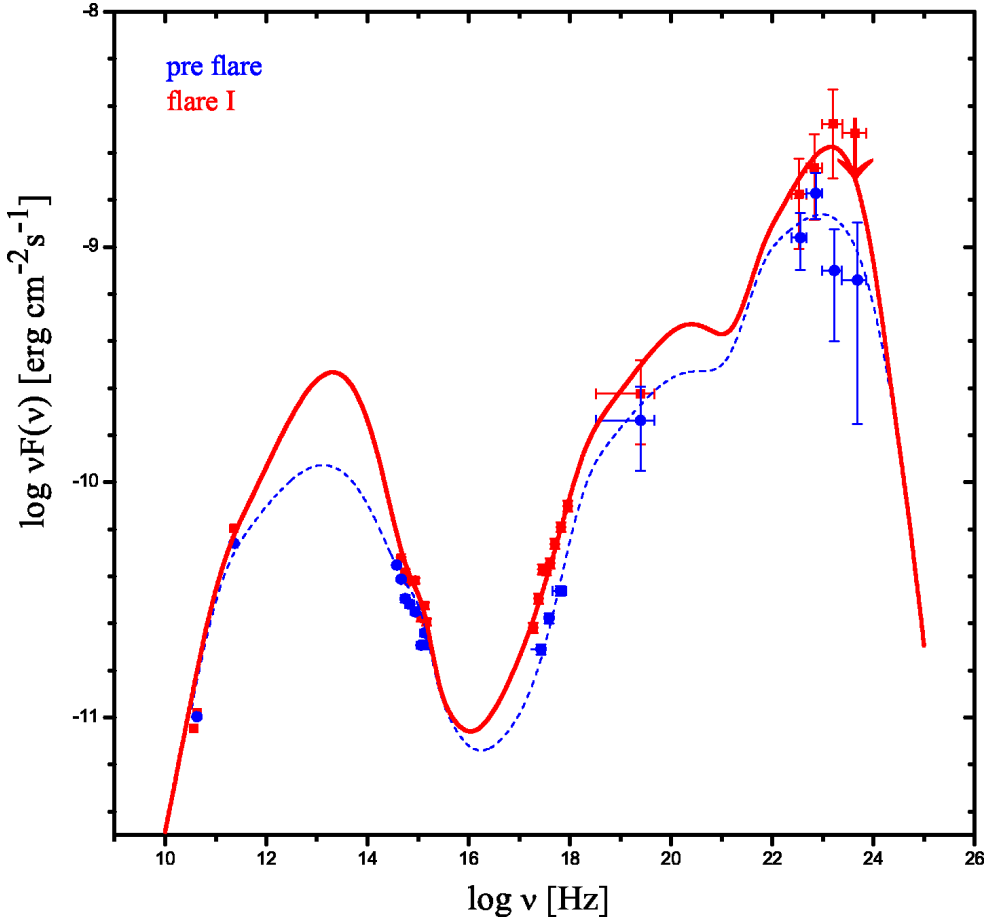
Fig. 3. Spectral energy distribution of 3C 454.3 in the pre-flare and super-flare periods during December 2009. In the modeling of the SED relative to the super-flare an additional component is added. [Adapted from Pacciani et al. 2010].

AGILE observation of 17–21 March 2008 together with the simultaneous data collected from radio-to-X-rays by GASP-WEBT and *Swift* is modelled with thermal emission of the disc, SSC model plus the contribution by EC scattering of direct disc radiation and of photons reprocessed by the BLR (see Fig. 4). Some features in the optical/UV spectrum indicate the presence of Seyfert-like components, such as the little and big blue bumps.

PKS 1510−089 showed an extraordinary γ-ray activity during March 2009, with several flaring episodes and a flux that reached 600×10^{-8} ph cm^{-2} s^{-1} (Fig. 5). During February–March 2009 the source also showed an increasing activity in optical and near-IR, with a flaring episode on 26–27 March 2009 observed by GASP-WEBT and REM. Instead the *Swift*/XRT observations show no clear correlation of the X-ray emission with the optical and γ-ray ones. In Fig. 6 we compare the SED from radio-to-UV for 25-26 March 2009 with those collected on 20–22 March 2008 and 18 March 2009. The SED collected on 18 March 2009 confirmed the evidence of thermal signatures in the optical/UV spectrum of PKS 1510−089 also during high γ-ray states. On the other hand, taking into account that the dip at W1 could be systematic, the broad band spectrum from radio-to-UV during 25–26 March 2009 show a flat spectrum in the optical/UV energy band, suggesting an important contribution of the synchrotron emission in this part of the spectrum during the larger γ-ray flare and

therefore a significative shift of the synchrotron peak, usually observed in this source in the infrared. The increase of the synchrotron emission leads to the decrease of the evidence of the thermal features observed in the other SEDs.

3.3. S5 0716+714

The intermediate BL Lac (IBL) object S5 0716+714 was observed by *AGILE* during two different periods: 4–23 September and 23 October–1 November 2007, as discussed in Chen et al. (2008). In particular, between 7 and 12 September 2007 the source showed a high γ-ray activity with an average flux of $F_{E > 100\,MeV} = (97 \pm 15) \times 10^{-8}$ ph cm^{-2} s^{-1} and a peak level of $F_{E > 100\,MeV} = (193 \pm 42) \times 10^{-8}$ ph cm^{-2} s^{-1}, with an increase of flux by a factor of four in three days. The flux detected by *AGILE* is the highest ever detected from this object and one of the most high flux observed from a BL Lac object. A simultaneous GASP-WEBT optical campaign was performed and the resulting SED is well consistent with a two-components SSC model (see Fig. 7). Another very intense γ-ray flare, with a flux of the order of 200×10^{-8} ph cm^{-2} s^{-1}, was detected by *AGILE* on 22-23 September 2007.

Recently, Nilsson et al. (2008) estimated the redshift of the source ($z = 0.31 \pm 0.08$) and this allowed us to calculate the total power transported in the jet, which results extremely high for the two flaring episodes, approaching
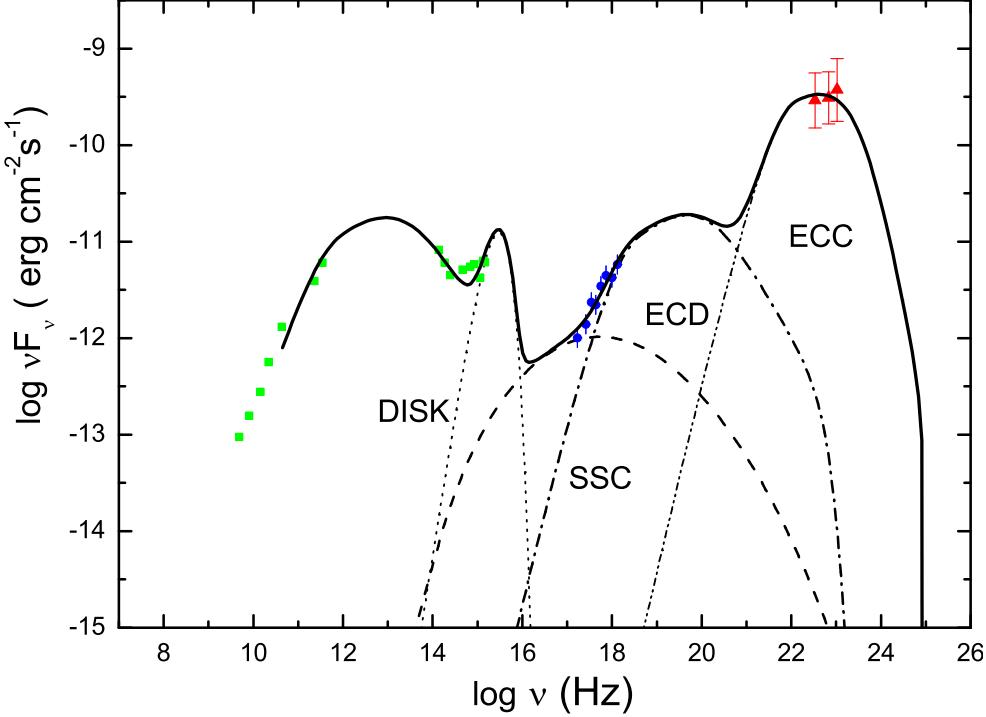
Fig. 4. SED of PKS 1510−089 on mid-March 2008 with *AGILE*, *Swift* and GASP-WEBT data. The dotted, dashed, dot-dashed, and double dot-dashed lines represent the accretion disk emission, the SSC, the external Compton on the disk radiation (ECD) and on the BLR radiation (ECC), respectively. [Adapted from D'Ammando et al. 2009.]
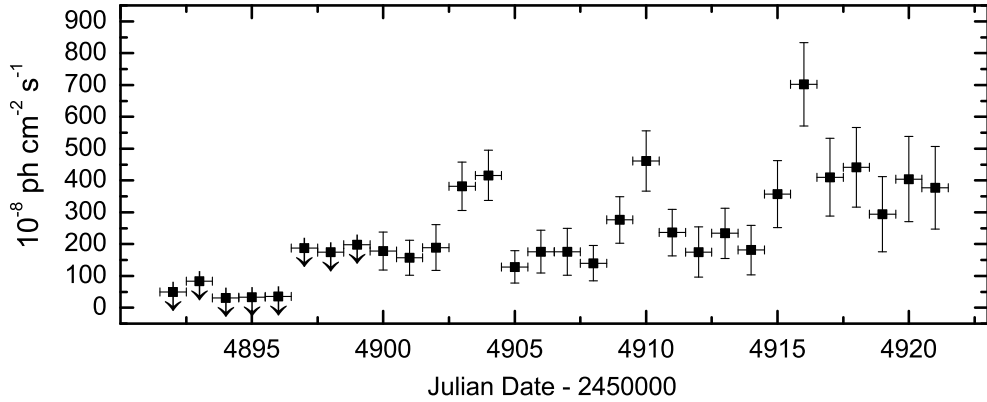
Fig. 5. *AGILE* light curve of PKS 1510−089 between 1 and 30 March 2009 for E > 100 MeV. The downward arrows represent 2-σ upper limits. [Adapted from D'Ammando et al. 2010.]

or slightly exceeding the maximum power generated by a spinning BH of 10^9 M$_\odot$ through the pure Blandford and Znajek mechanism (see Vittorini et al. (2009)). If confirmed, this violation could be explained in terms of the alternative Blandford-Payne mechanism (Blandford & Payne 1982) that, however, requires an ongoing accretion not supported by the observations of S5 0716+714. Alternatively, a so high power could be due to a less conservative value of the magnetic field related to particle orbits plunging from the disk toward the BH horizon (Meier 2002) into a region fully related by strong gravity effects.

During October 2007, *AGILE* detected the source at a flux about a factor of 2 lower than the September one with no significant variability. Simultaneously, *Swift* observed strong variability (up to a factor ∼ 4) in soft X-rays, moderate variability at optical/UV (less than a factor 2) and approximately constant hard X-ray flux. Also the different variability observed in optical/UV, soft and hard X-rays suggests the presence of 2 SSC components in the SED of this object (Giommi et al. (2008)).

3.4. The Virgo Region: 3C 279 and 3C 273

Past observations of the Virgo region by the *CGRO* revealed the presence of two bright and variable γ-ray blazars: 3C 273 and 3C 279; therefore, the *AGILE* satellite performed dedicated pointings of the Virgo region for investigating the properties of these two blazars.

3C 279 is the first extragalactic source detected by *AGILE* in mid July 2007, as reported in Giuliani et al. (2009). The average γ-ray flux over 4 days of observation is $F_{E>100\,MeV} = (210 \pm 38) \times 10^{-8}$ ph cm^{-2} s^{-1}, a flux level similar to the highest observed by EGRET and *Fermi*/LAT. The spectrum observed during the flaring episode by *AGILE* is soft with respect to the previous EGRET observations and this could be an indication of a low accretion state of the disk occurred some months before the γ-ray observations, suggesting a dominant contribution of the external Compton scattering of direct disk (ECD) radiation compared to the external Compton scattering of the Broad Line Region
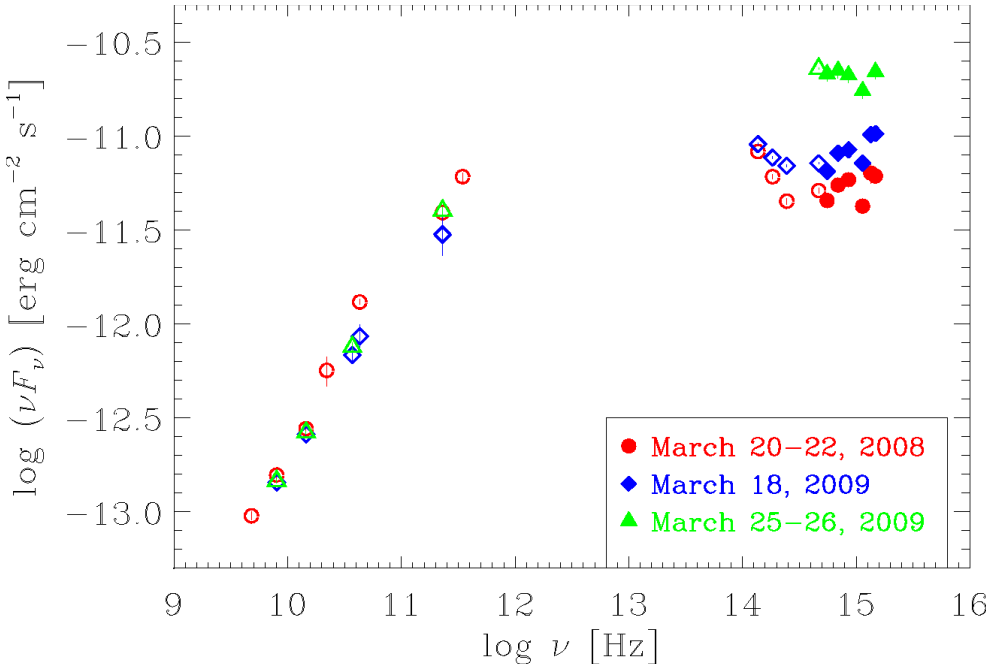
Fig. 6. SED of the low-energy part of the spectrum of PKS 1510−089 constructed with data collected by GASP-WEBT and *Swift*/UVOT during March 2008 and March 2009. [Adapted from D'Ammando et al. 2010.]
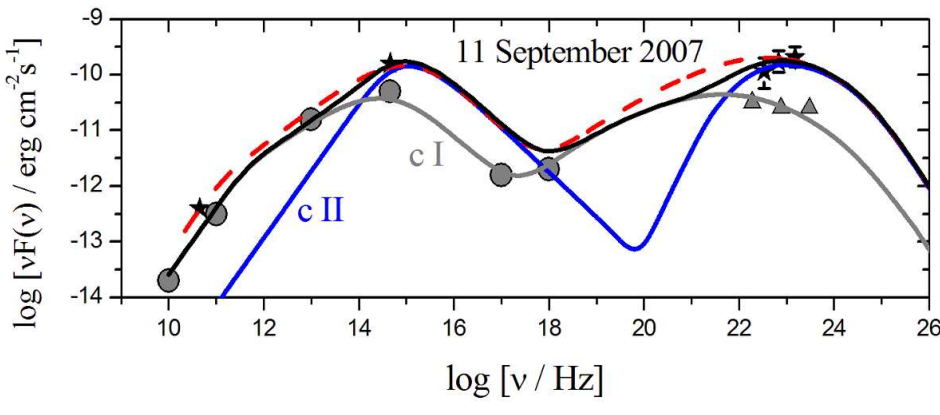
Fig. 7. SED of S5 0716+714 in mid-September 2007 including optical GASP-WEBT and γ-ray *AGILE* data (black stars). Historical data relative to a ground state and EGRET data are represented with grey dots. Curves "c I" and "c II" represent the two separate components. The solid black line and the dashed red lines represent the two-components and one-component model, respectively. [Adapted from Vittorini et al. (2009)].

clouds (ECC). As a matter of fact, a strong minimum in the optical band was detected by REM two months before the *AGILE* observations and the reduction of the activity of the disk should cause the decrease of the photon seed population produced by the disk and then a deficit of the ECC component with respect to the ECD, an effect delayed by the light travel time required to the photons to go from the inner disk to the BLR.

On the other hand, 3C 273 is a very peculiar AGN that shows properties characteristic of a blazar, like strong radio emission, apparent superluminal jet motion, large flux variations and SED with the two humps (see Courvoisier 1998 for a review), but also other features typical of Seyfert galaxies appear as well as the broad emission lines, the soft X-ray excess and the big blue bump. Surprisingly, 3C 273 was discovered to emit in γ-rays by COS-B in 1976 (Swanenburg et al. 1978). EGRET pointed this FSRQ several times, not always detecting it, with an average flux of $(15.4 \pm 1.8) \times 10^{-8}$ ph cm^{-2} s^{-1} (E > 100 MeV) and only recently *Fermi*/LAT detected two exceptional γ-ray

outbursts by 3C 273 with peak flux of $\sim 1000 \times 10^{-8}$ ph cm^{-2} s^{-1} (Abdo et al. 2010).

We organized a 3-week multi-frequency campaign between mid-December 2007 and January 2008 on 3C 273 involving REM, RXTE, INTEGRAL, *Swift* and *AGILE* , with the aim of studying the correlated variability in the different energy ranges and time-resolved energy density distribution for each of the 3-weeks from near-IR to γ-rays. During this campaign, whose results are reported in Pacciani et al. (2009), the source was detected in a high state in X-rays, with a 5–100 keV flux a factor of ~ 3 higher than the typical value in historical observations (Courvoisier et al. 2003), whereas the source was detected in γ-rays only in the second week, with an average flux of $F_{E>100\,MeV} = (33 \pm 11) \times 10^{-8}$ ph cm^{-2} s^{-1}. The simultaneous light curves from near-IR to γ-rays do not show any strong correlation, except for an indication of anti-correlated variability between X-rays and γ-rays. The SED is well modelled by a leptonic model where the soft X-ray emission is produced by the combination of SSC
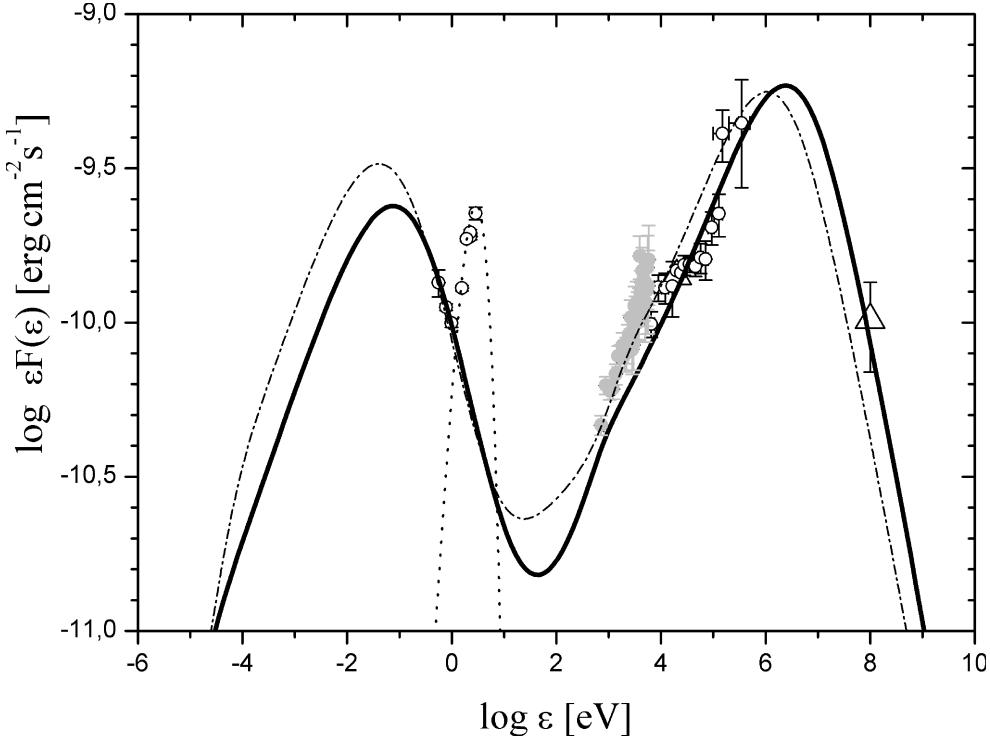
Fig. 8. SED of 3C 273 for the first (dot-dashed line) and second (solid line) week. Triangle is for the *AGILE* data. The light grey data refers to XRT observations, performed in the third week. [Adapted from Pacciani et al. (2009)].

and EC models, while the hard X-ray and γ-ray emission is due to ECD (Fig. 8). The spectral variability between the first and the second week is consistent with the acceleration episode of the electron population responsible for the synchrotron emission. A possible shift of the IC peak were proposed comparing the June 1991 campaign with the OSSE observation in September 1994 (McNaron-Brown et al. 1997). Our multi-frequency observation suggests that this behaviour could be a more general feature of this source, happening on shorter timescales.

3.5. TeV blazars: Mrk 421 and W Comae

With the advent of the latest generation of Imaging Atmospheric Cherenkov Telescopes (IACTs) the number of sources detected in the TeV energy regime has significantly increased. The majority of TeV sources are galactic, however 28 AGNs are detected until now, but only 8 of the 28 AGN TeV-emitters were detected by EGRET (Hartman et al. 1999) and most of these sources were discovered at TeV energies only by the new generation of IACTs, therefore the number of TeV blazars detected contemporaneous at MeV–GeV and TeV energy bands is very low. With the launch of two new γ-ray satellites, *AGILE* and *Fermi*, the gap in the MeV–GeV domain have been closed giving the possibility to remove the degeneracies in the modelling of the SEDs of these objects. Multi-wavelength campaigns involving γ-ray *AGILE* observations, together with MAGIC and VERITAS TeV observations of Mrk 421 and W Comae were performed in June 2008.

On 8 June 2008, VERITAS announced the detection of a TeV flare from the IBL object W Comae (Swordy 2008),

with a three times higher flux with respect to the flare observed in March 2008 (Acciari et al. 2008). About 24 hours later, *AGILE* re-pointed towards the source and detected it with a flux for E > 100 MeV of $(90 \pm 32) \times 10^{-8}$ ph cm^{-2} s^{-1}, roughly a factor of 1.5 larger than the highest flux observed by EGRET (see Verrecchia et al. 2008). The VERITAS observations triggered a multi-wavelength campaign including also *Swift*, XMM-*Newton* and GASP observations, covering the entire electromagnetic spectrum from radio to TeV. The SED of W Comae during the VHE γ-ray flare can be modelled by a simple leptonic SSC model, but the wide separation of the two peaks in the SED requires low ratio of the magnetic field to electron energy density ($\epsilon_B = 2.3 \times 10^{-3}$), far from the equipartition. The SSC+EC model returns magnetic field parameters closer to equipartition, providing a satisfactory description of the broadband SED (Acciari et al. 2009).

During the ToO towards W Comae, *AGILE* detected also the HBL object Mrk 421, in hard X-rays and γ-rays. SuperAGILE detected a fast increase of flux from Mrk 421 up to 40 mCrab in the 15–50 energy band, about a factor of 10 higher than its typical flux in quiescence (Costa et al. 2008), reaching about 55 mCrab on 2008 June 13. This observation was followed by the detection in γ-ray by GRID with a flux, $F_{E>100\,MeV} = (42 \pm 13) \times 10^{-8}$ ph cm^{-2} s^{-1}, about a factor 3 higher than the average EGRET value, even if consistent with its maximum. An extensive multi-wavelength campaign from optical to TeV energy bands was organized with the participation of WEBT, *Swift*, RXTE, *AGILE*, MAGIC and VERITAS, as reported in detail in Donnarumma et al. (2009). SuperAGILE, RXTE/ASM and *Swift*/BAT show a clear correlated flaring structure between soft and hard
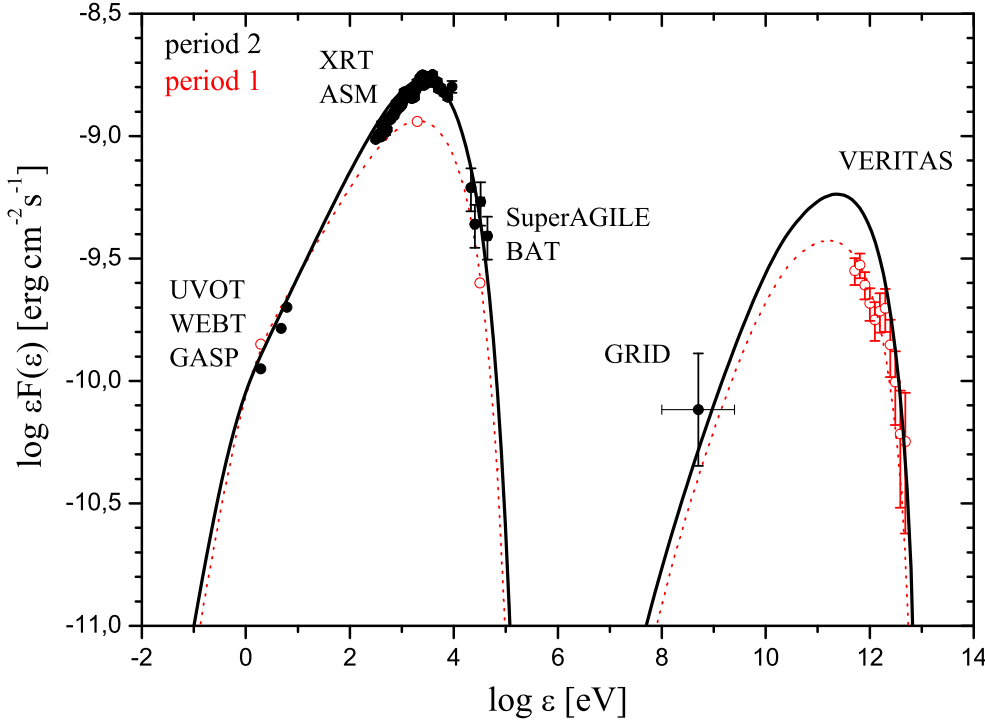
Fig. 9. SEDs of Mrk 421 obtained by combining GASP-WEBT, *Swift* (UVOT, XRT, BAT), RXTE/ASM, SuperAGILE, GRID and VERITAS data in the period 1 (2008 June 6; empty circles) and period 2 (2008 June 9–15; filled circles). Both are one-zone SSC models. [Adapted from Donnarumma et al. (2009)]

X-rays with a high flux/amplitude variability in hard X-rays. Hints of the same flaring behaviour is also detected in optical band by GASP-WEBT. Moreover, *Swift*/XRT observed the source at the highest 2–10 keV flux ever observed, with a peak of the synchrotron at ∼ 3 keV, showing a shift with respect to the typical values of 0.5–1 keV. VERITAS and MAGIC observed the source on 2008 June 6–8 in a bright state at TeV energies, well correlated with the simultaneous peak in X-rays. The SED can be interpreted within the framework of the SSC model in terms of a rapid acceleration of leptons in the jet (Fig. 9). An alternative more complex scenario, in the context of the helical jet models, is that optical and X-ray emissions come from different regions of the jet, with the inner jet region that produces X-rays and is partially transparent to the optical radiation, whereas the outer region produces only the lower-frequency emission.

References

Abdo, A. A., et al. 2010, ApJ, 714, L73
Acciari, V. A., et al. 2008, ApJ, 684, L73
Acciari, V. A., et al. 2009, ApJ, 707, 612
Blandford, R. D., & Payne, D. G. 1982, MNRAS, 199, 883
Blandford, R. D., & Rees, M. 1978, in BL Lac Objects, ed. A. M. Wolfe, Pittsburgh Press
Bonnoli, G., et al. 2010, MNRAS accepted, [arXiv:1003.3476]
Böttcher, M. 2007, Ap&SS, 309, 95
Chen, A. W., D'Ammando, F., et al. 2008, A&A, 489, L37
Costa, E., et al. 2008, Astronomer's Telegram, 1574
Courvoisier, T. J. L. 1998, A&AR, 9, 1
Courvoisier, T. J. L., et al. 2003, A&A, 411, L343
D'Ammando, F., et al. 2009, A&A, 508, 181
D'Ammando, F., et al. 2010, to be submitted to A&A
Donnarumma, I., et al. 2009, ApJ, 707, 1115
Donnarumma, I., et al. 2009, ApJ, 691, L13
Giommi, P. et al. 2006, A&A, 456, 911
Giommi, P., et al. 2008, A&A, 487, L49
Giuliani, A., D'Ammando, F., et al. 2009, A&A, 494, 509
Hartman, R. C., et al. 1999, ApJS, 123, 79
Hartman, R. C., et al. 2001, ApJ, 553, 683
Kataoka, J., et al. 2008, ApJ, 672, 787
McNaron-Brown, K., et al. 1997, ApJ, 474, L85
Meier, D. L. 2002, NewAR, 46, 247
Nilsson, K., et al. 2008, A&A, 487, L29
Pacciani, et al. 2009, A&A, 494, 49
Pacciani, L., et al. 2010, ApJ accepted, [arXiv:1005.3263]
Pian, E., et al. 2006, A&A, 449, L21
Pucella, G., et al. 2008, A&A, 491, L21
Remillard, R. 2005, Astronomer's Telegram, 484
Striani, E., et al. 2010, ApJ accepted, [arXiv:1005.4891]
Swanenburg, B. N., et al. 1978, Nature, 275, 298
Swordy, S. 2008, Astronomer's Telegram, 1565
Tavani, M., et al. 2009, A&A, 502, 995
Ulrich, M., et al. 1997, ARA&A, 35, 445
Urry, C. M., & Padovani, P. 1995, PASP, 107, 803
Vercellone, S., et al. 2008, ApJ, 676, L13
Vercellone, S., et al. 2009, ApJ, 690, 1018
Vercellone, S., D'Ammando, F., et al. 2010, ApJ, 712, 405
Verrecchia, F., et al. 2008, Astronomer's Telegram, 1582
Villata, M., Raiteri, C. M., et al. 2006, A&A, 453, 817
Vittorini, V., et al. 2009, ApJ, 706, L1433

Long-term Multi-Wavelength Monitoring of the Blazar 3C 454.3

S. Vercellone on behalf of the *AGILE* AGN Working Group

INAF/IASF Palermo, Via U. La Malfa 153, 90146 Palermo, Italy

Abstract. The *AGILE* gamma-ray satellite and several more space and ground based observatories monitored the activity of the flat-spectrum radio quasar 3C 454.3 during the period July 2007 - January 2009, yielding the longest multi-wavelength coverage of this gamma-ray quasar so far. The source underwent an unprecedented period of very high activity above 100 MeV, reaching gamma-ray flux levels on a 1-day timescale higher than $F = 500 \times 10^{-8}$ photons cm^{-2} s^{-1}, simultaneously with an extremely variable behavior in the optical R-band of the order of several tenths of a magnitude in a few hours. We present the results of this long term multi-wavelength monitoring campaign, with particular emphasis on the study of possible lags among the different wavebands, the interplay between the radio and gamma-ray energy bands, and the results of the modeling of simultaneous spectral energy distributions at different levels of activity.

1. Introduction

The FSRQ 3C 454.3 (PKS 2251+158; $z = 0.859$) is certainly one of the most active extragalactic sources at high energy. In the *EGRET* era it was detected in 1992 during an intense γ-ray flaring episode (Hartman et al., 1992, 1993) when its flux $F_{\mathrm{E>100\,MeV}}$ was observed to vary within the range $(0.4-1.4) \times 10^{-6}$ photons cm^{-2} s^{-1}. In 1995 a 2-week campaign detected a γ-ray flux $< 1/5$ of its historical maximum (Aller et al., 1997). Since the detection of the exceptional 2005 outburst (see Giommi et al., 2006; Fuhrmann et al., 2006; Pian et al., 2006), several monitoring campaigns were carried out to follow the source multi-frequency behavior: Villata et al. (2006, 2007); Raiteri et al. (2007, 2008a, 2008b).

Since the launch of the *AGILE* satellite in April 2007 (Tavani et al., 2009), 3C 454.3 became one of the most active sources in the γ-ray sky (see Vercellone et al., 2008, 2009; Donnarumma et al., 2009). Its very high γ-ray flux (well above 100×10^{-8} photons cm^{-2} s^{-1} for $E > 100$ MeV), its flux variability (on a timescale of 1 to 2 days), with long-lasting activity on a time-scale longer than any other γ-ray blazar (as discussed in Vercellone et al. 2010, V2010 hereafter) earned it the nickname of *Crazy Diamond*. Thus, 3C 454.3 is the best candidate to explore long-term behavior at several frequencies and to study the jet properties at different emission levels.

2. The 2007–2009 γ-ray data

Figure 1 shows the *AGILE*/GRID light curve at $\approx$ 3-day resolution for E>100 MeV in units of 10^{-8} photons cm^{-2} s^{-1} covering the period 2007-07-24–2009-01-12. The light curve shows several γ-ray flares, with a dynamic range of a factor of 3–4 on a time scale of about ten days. Moreover, a clear dimming trend in the long-term light curve is present. The correlation between the flux level and the spectral slope in the γ-ray energy band was extensively studied by means of analy-
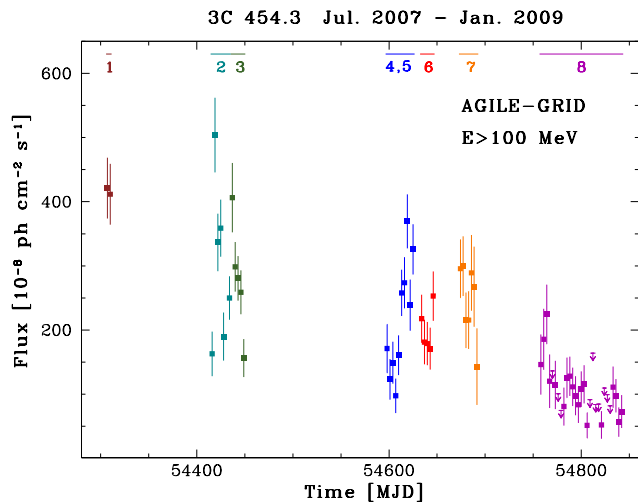
Fig. 1. *AGILE*/GRID light curve at $\approx$ 3 day resolution for E>100 MeV in units of 10^{-8} photons cm^{-2} s^{-1}. Different colors correspond to different observing campaigns. Adapted from V2010.

sis of *EGRET* data, and Nandikotkur et al. (2007) found that the behavior of *EGRET* blazars is inhomogeneous. Figure 2 shows the *AGILE*/GRID photon index as a function of the γ-ray flux at different epochs. A "harder-when-brighter" trend seems to be present in the long time scale *AGILE* data.

3. The long-term multi-wavelength data

During the γ-ray monitoring period, we collected data at different wavelengths by means of pre-approved GI programs, as well as dedicated target of opportunity (ToO) observations. In particular, we obtained a detailed and almost continuous monitoring in the radio-to-optical bands by the *GLAST-AGILE* Support Program within the Whole Earth Blazar Observatory (GASP–WEBT[1]),

---

[1] `http://www.oato.inaf.it/blazar/webt`
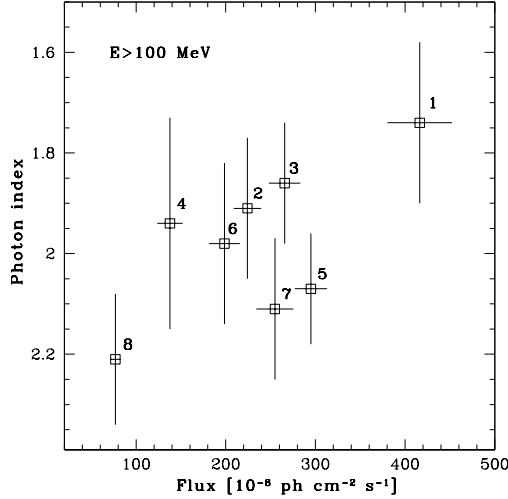
Fig. 2. *AGILE*/GRID photon index as a function of the γ-ray flux above 100 MeV. Numbers beside each points represent the epochs shown in Figure 1. Adapted from V2010.
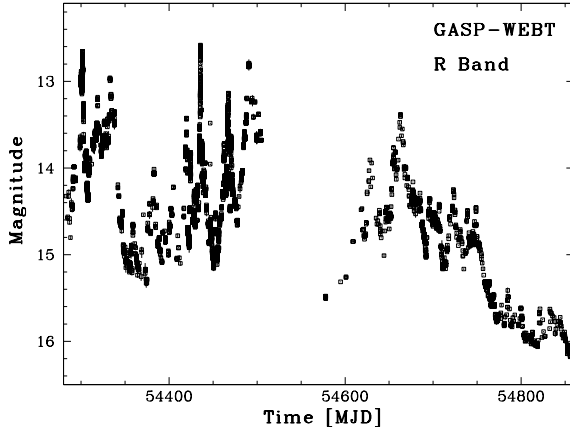
Fig. 3. GASP-WEBT light curve in the R optical band in the 2007–2008 and 2008–2009 observing seasons. Adapted from V2010.

in the optical-UV up to soft and hard X-ray by *Swift* and in the radio by UMRAO and VLBI.

The GASP–WEBT optical *R*-band data show several intense flares with a dynamic range of $\sim$ 2.4 mag in about 14 days, as shown in Figure 3. While the hard X-ray *Swift*/BAT 15–150 keV light curve shows no particular variability over the whole period, the soft X-ray *Swift*/XRT 2–10 keV energy band shows both flux and spectral variations among observations taken in different periods. Figure 4 clearly shows a "harder-when-brighter" trend also in this energy band. At lower energies, we collected VLBI radio data at 15 and 43 GHz. In Figure 5 we show the 3C 454.3 VLBI radio core flux (panel (a)) at 15 and 43 GHz, the radio component flux densities at 15 GHz (panel (b)), and the distance of radio components from the core (panel (c)) as a function of time. The flux shows a constant increase from 2006 June 15 (MJD 53901) until 2008 October 3 (MJD 54742), followed by a fast decrease towards the last epoch available, 2009 June 25 (MJD 55007). Jet components show a well defined flux density decrease
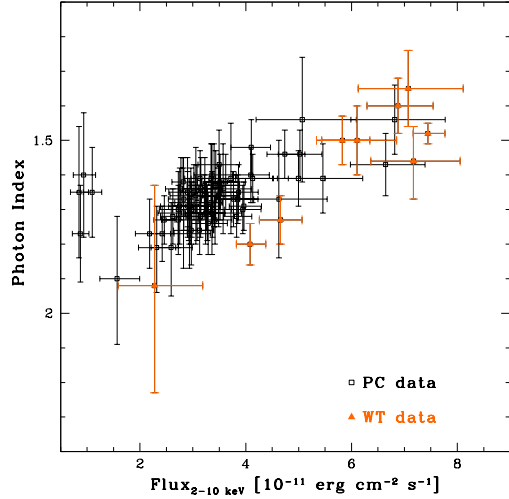
Fig. 4. *Swift*/XRT photon index as a function of the 2–10 keV flux. Orange triangles and black squares mark the *Swift*/XRT windowed timing (WT) and photon counting (PC) data, respectively. Adapted from V2010.
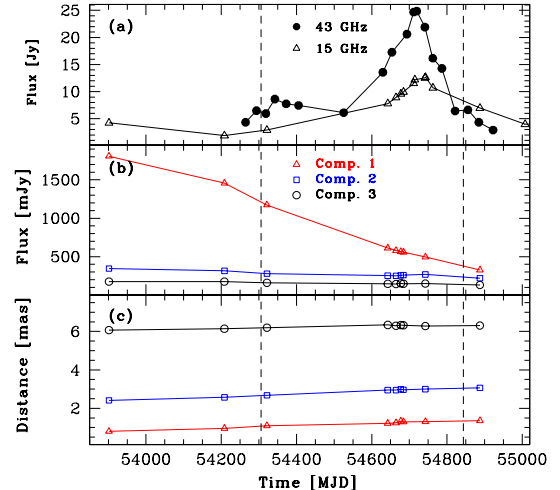
Fig. 5. Panel (a): radio core flux density at 15 GHz (open triangles) and at 43 GHz (filled circles), respectively. Panel(b): radio components flux density at 15 GHz. Panel (c): radio components motion at 15 GHz. The vertical dashed lines represent the start (2007 July 24) and the stop (2009 January 12) of all *AGILE* observations, respectively. Adapted from V2010.

(component 1) or a slower flux density decrease which becomes almost constant in the last epochs. Proper motion is evident, but slowing in time for components 1 and 2; it is almost absent for component 3. All data are in agreement with a strong core flux density variability possibly connected to the γ-ray activity, while jet components are moving away and slowly decreasing in flux density, and are not affected by the recent core activity.

4. Discussion

4.1. Optical vs γ-ray data correlation

We investigated the correlation between the γ-ray flux and the optical flux density in the *R* band by means of the dis-
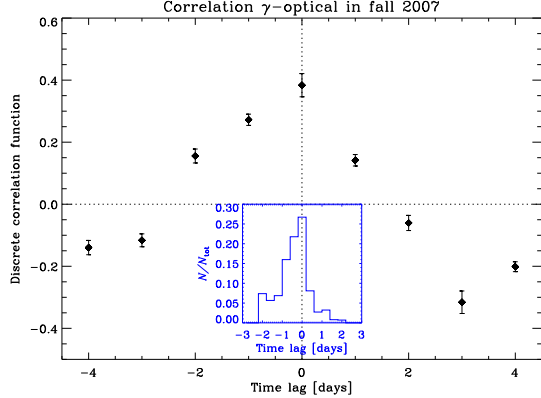
Fig. 6. Discrete correlation function between the γ-ray and optical fluxes during the "fall 2007" period. The inset shows the resulting centroid distribution. Adapted from V2010.

crete correlation function (DCF). Because of the sampling gaps in the light curves, especially at γ-rays, we calculated the DCF in four distinct periods: July 2007 (mid 2007), November–December 2007 (Fall 2007), May–August 2008 (mid 2008), and October 2007 - January 2009 (Fall 2008). The period "fall 2007" offers a good opportunity to test the correlation, since the γ-ray flux, and even more the optical flux, exhibited strong variability. Moreover, the period of common monitoring lasted for more than a month. The corresponding DCF (see Figure 6) shows a maximum DCF ~ 0.38 for a null time lag. However, the shape of the peak is asymmetric, and if we calculate the centroid, we find that the time lag is $\tau = -0.4^{+0.6}_{-0.8}$ day, the uncertainty corresponding to a 1σ error for a normal distribution.

4.2. Radio VLBI vs γ-ray data correlation

Figure 5 clearly shows a strong enhancement of the radio core flux starting on about MJD 54500. The highest flux density is on MJD 54742 at 15 GHz and on MJD 54719 at 43 GHz. This variability is not well correlated with the variability at higher frequencies: optical and γ-ray data show more different flares in the period MJD 54400–54800. Moreover, the radio flux density increase is smooth and longer in time, while γ-ray and optical flares are evolving faster.

This poses an interesting question as to the nature of such an increase of the core radio flux. As reported in Ghisellini et al. (2007) it is likely that the emitting region is more compact and has a smaller bulk Lorentz factor closer to the super-massive black hole. We can assume that in the region active at 43 GHz, in the quiescent state, the jet Lorentz factor is $\Gamma \sim 10$ (Giovannini et al., 2001). To obtain the flux density increase of the core at 43 GHz (from ~ 5 Jy up to 25 Jy) the Doppler factor has to increase up to $\delta \sim 30$. Such an increase requires that the source is oriented at a small angle θ with respect to the line of sight, since a large change in the jet velocity will produce a small increase in the Doppler factor. A Doppler factor $\delta = 30$ can be obtained if $\theta = 1.5°$ and $\Gamma = 20$, corresponding

to a bulk velocity increase from 0.9950 to 0.9987 (note that a larger orientation angle, e.g. $\theta = 3°$ with the same increase in the jet velocity, will produce a small change in the Doppler factor δ, from 16 to 19).

The presence of one or more new jet components is not revealed in high resolution VLBA images. Because of their different properties (multiple bursts at high frequencies, a single peak in the radio band) it is not possible to correlate the radio peak with a single γ-ray or optical burst. We can speculate that a multiple source activity in the optical and γ-ray bands is integrated in the radio emitting region in a single event. This event has a clear flux density peak on MJD ~ 54720 and we can assume that 43 GHz is the self-absorption frequency at that epoch.

4.3. SED modeling

Different emission mechanisms can be invoked to explain the γ-ray emission. In the leptonic scenario, the low–frequency peak in the blazar SED is interpreted as synchrotron radiation from high–energy electrons in the relativistic jet, while the high–energy peak can be produced by IC on different kinds of seed photons (see Ghisellini & Tavecchio 2009 for a detailed review). In the synchrotron self–Compton (SSC) model the seed photons come from the jet itself. Alternatively, the seed photons can be those of the accretion disk (external Compton scattering of direct disk radiation, ECD) or those of the broad–line region (BLR) clouds (external Compton scattering from clouds, ECC). The target seed photons can also be those produced by the dust torus surrounding the nucleus (external Compton scattering from IR-emitting dust, ERC(IR)).

We fit the SEDs for the different observing periods by means of a one-zone leptonic model, considering the contributions from SSC and from external seed photons originating both from the accretion disk and from the BLR (a detailed description of this model is given in Vittorini et al. 2009). Indeed, emission from both of them were detected during faint states of the source, as shown in Raiteri et al. (2007). Figure 7 shows the SED during the period MJD 54800–54845, when the source flux was at the minimum level (about 70×10^{-8} photons cm^{-2} s^{-1}). The insert shows the portion of the SED dominated by the contribution of the disk blackbody radiation, which clearly emerges since the source is in a relatively low state. The emission along the jet is assumed to be produced in a spherical blob with co-moving radius R by accelerated electrons characterized by a co-moving broken power law energy density distribution. As discussed in Vercellone et al. (2010), by assuming typical values for the model fit parameters, we obtain a measure of the total power carried in the jet, $P_{\rm jet}$, of the order of 2.5×10^{46} erg s^{-1}.

4.4. Jet geometry

An important piece of evidence related to jet physics comes from the possible relation between the light curves,
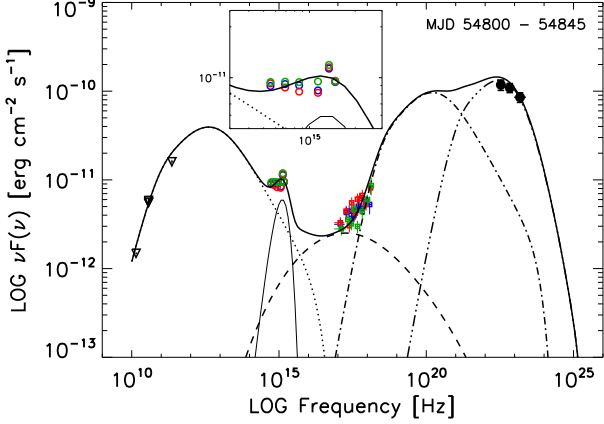
Fig. 7. 3C 454.3 SED during the period MJD 54800–54845. Black upside down triangles, multicolor circles and squares, and black circles represent radio, *Swift*/UVOT, *Swift*/XRT, and *AGILE*/GRID data, respectively. UV and X-ray data are de-reddened and corrected for Galactic extinction. The thin solid, dotted, dashed, dot-dashed, and the triple-dot-dashed lines, represent the accretion disk blackbody, the synchrotron, the SSC, the external Compton on the disk, and the external Compton on the BLR radiation, respectively. The thick solid line represents the sum of all the individual components. The insert shows the portion of the SED dominated by the contribution of the disk blackbody radiation. Adapted from V2010.
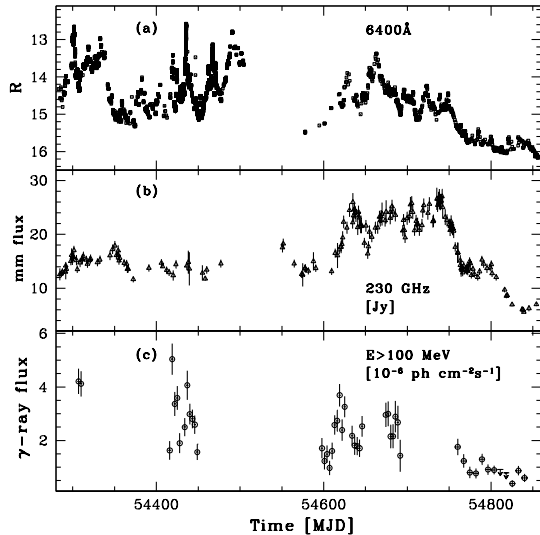
Fig. 8. Comparison between the light curves in different bands. Panel (a), (b), and (c) show the light curves in the optical, millimeter, and γ-ray energy bands, respectively. Adapted from V2010.

and hence between their emitting zones, in the R, in the millimetre and in the γ-ray energy bands, respectively. Figure 8 shows the light curves in the R band, at 1.3 mm (230 GHz), and above 100 MeV. The light curves show a different behavior starting from the end of 2007 among the different energy bands.

As shown in 2009, a possible interpretation arises in the framework of a change in orientation of a curved jet,

yielding different alignment configurations within the jet itself.

During 2007 the more pronounced fluxes and variability of the optical and γ-ray bands seem to favor the inner portion of the jet as the more beamed one. On the other hand, the dimming trend in the optical and in the γ-ray bands, the higher mm-flux emission and its enhanced variability during 2008, seem to indicate that the more extended region of the jet became more aligned with respect to the observer line of sight.

5. Conclusions

The *AGILE* high-energy long-term monitoring of the blazar 3C 454.3 allowed us to organize a few multi-wavelength campaigns over a time period of about eighteen months. In particular, our results support the idea that the dominant emission mechanism in the γ-ray energy band is inverse Compton scattering of external photons from the BLR clouds scattering off the relativistic electrons in the jet, and the different behavior of the light curves at different wavelengths could be interpreted by a changing of the jet geometry between 2007 and 2008.

References

Aller, M. F., et al. 1997, in Proc. of the Fourth Compton Symposium, ed. C.D. Dermer, M.S. Strickman, & J.D. Kurfess, AIPC, 410, 1423
Donnarumma, I., et al. 2009, ApJ, 707, 1115
Fuhrmann, L., et al. 2006, A&A, 445, L1
Ghisellini, G., et al. 2007 MNRAS, 382, L82
Ghisellini, G., & Tavecchio, F. 2009 MNRAS, 397, 985
Giommi, P., et al. 2006, A&A, 456, 911
Giovannini, G., et al. 2001 ApJ, 552, 508
Hartman, R. C., et al. 1992, IAU Circ., 5477, 2
Hartman, R. C., et al. 1993, ApJ, 407, L41
Nandikotkur, G., et al. 2007 ApJ, 657, 706
Pian, E., et al. 2006, A&A, 449, L21
Raiteri, C. M., et al. 2007, A&A, 473, 819
Raiteri, C. M., et al. 2008a, A&A, 485, L17
Raiteri, C. M., et al. 2008b, A&A, 491, 755
Tavani, M., et al. 2009, A&A, 502, 995
Vercellone, S., et al. 2008, ApJ, 676, 13
Vercellone, S., et al. 2009, ApJ, 690, 1018
Vercellone, S., et al. 2010, ApJ, 712, 405
Villata, M., et al. 2006, A&A, 453, 817
Villata, M., et al. 2007, A&A, 464, L5
Villata, M., et al. 2009, A&A, 504, L9
Vittorini, V., et al. 2009, ApJ, 706, 1433

The Broadband Spectral Energy Distribution of the MOJAVE Sample

C. S. Chang[1], E. Ros[2,1], M. Kadler[3,4,5], M. F. Aller[6], H. D. Aller[6], E. Angelakis[1], L. Fuhrmann[1], I. Nestoras[1], and H. Ungerechts[7]

[1] Max-Planck-Institut für Radioastronomie, Auf dem Hügel 69, D-53121 Bonn, Germany
[2] Departament d'Astronomia i Astrofísica, Universitat de València, E-46100 Burjassot, Spain
[3] Dr. Remeis-Sternwarte & ECAP, Sternwartstr. 7, D-96049 Bamberg, Germany
[4] CRESST/NASA Goddard Space Flight Center, Greenbelt, MD 20771, USA
[5] USRA, 10211 Wincopin Circle, Suite 500 Columbia, MD 21044, USA
[6] Astronomy Department, University of Michigan, Ann Arbor, MI 48109-1042, USA
[7] Institut de Radio Astronomie Millimétrique, Avenida Divina Pastora 7, Local 20, 18012 Granada, Spain

Abstract. We are constructing the broadband SED catalog of the MOJAVE sample from the radio to the γ-ray band using MOJAVE, *Swift* UVOT/XRT/BAT, and *Fermi*/LAT data, in order to understand the emission mechanism of extragalactic outflows and to investigate the site of high-energy emission in AGN. Since the launch of *Fermi* γ-ray Space Telescope in August 2008, two thirds of the MOJAVE sources have been detected by *Fermi*/LAT. Combining the results of high-resolution VLBI, X-ray, and γ-ray observations of the jet-dominated AGN sample, we want to pin down the origin of high-energy emission in relativistic jets. Here we present our overall project and preliminary results for 6 selected sources.

1. Introduction

Blazars are extremely powerful objects which only represent a small subset of active galactic nuclei (AGN), yet they dominate the extragalactic radio and high-energy sky. Blazars are those AGN whose jet is pointing towards us, which results in strong Doppler-boosting of the emitted radiation. The small viewing angle is also responsible for the superluminal jet motions observed in their jets. Since August 2008, the *Fermi* Large Area Telescope (LAT) is performing a continuous all-sky survey in γ-rays. After one year of operation, *Fermi*/LAT has detected 709 AGNs, of which 85% are blazars (Abdo et al. 2010b). The Monitoring Of Jets in Active galactic nuclei with VLBA Experiments (MOJAVE) program has monitored a radio-selected sample of 135 AGNs since the mid-1990s (J2000.0 declination $\leq -20°$; galactic latitude $|b| \leq 2.5°$; 15 GHz VLBA flux density ≤ 1.5 Jy), and most of the MOJAVE sources are blazars due to the selection criteria (see details in Lister et al. 2009a; Lister 2010). In the one-year AGN catalog of *Fermi*, two-thirds of the MOJAVE sources are detected (Boeck 2010). Based on theoretical models, it is suggested that the γ-ray and radio emission in blazars are closely connected (Dermer & Schlickeiser 1993; Sikora et al. 1994). Dermer & Schlickeiser (1994) proposed that the γ-ray emission from highly-beamed relativistic AGN outflows originates near the base of the jet. The high-resolution capability of very-long-baseline interferometry (VLBI) enables us to pin down the structure of extragalactic outflows up to the scale of sub-parsecs, and to trace component ejections and evolution along jets.

To understand the physical mechanisms ongoing in blazar jets, one of the best approaches is to study the broadband spectral energy distribution (SED). By using the multi-frequency data and investigating the correlations, one can apply theoretical models to the broadband emission to constrain further the parameters in the local frame of AGN jets.

2. The SED catalog of MOJAVE sources

We want to investigate the broadband SED properties of the complete radio-selected MOJAVE sample. All of the MOJAVE sources are X-ray emitters (Kadler 2005), and recent results also show that the γ-ray brightness of AGN is correlated with VLBI jet properties (Kovalev et al. 2009; Pushkarev et al. 2009; Savolainen et al. 2010; Lister et al. 2009c; Ojha et al. 2010). A *Swift* fill-in survey has been conducted since 2007 for the MOJAVE sample (P.I.: M. Kadler), providing optical, UV, and X-ray observations. As bright, well-studied radio sources, the MOJAVE sources have very good flux-density sampling in the radio band. Combining the *Fermi*/LAT results, we are constructing the broadband SED catalog from the radio to the γ-ray band of the 135 MOJAVE sources of the statistical complete sample. Our goal is to study their characteristics, and to determine the correlations of the emission properties between different bands. In the MOJAVE sample, there are 101 flat-spectrum radio quasars, 22 BL Lac objects, 8 radio galaxies, and 4 unidentified AGNs. In the following sections, the broadband SED data acquisition will be introduced. We will show preliminary results of 6 selected sources which have good broadband SED data

Table 1. Multi-wavelength facilities from the radio to the γ-ray bands that are used to construct the MOJAVE SED catalog.

Facility	Band	Frequency (Hz)
VLBA[a]	Radio	1.5×10^{10}
UMRAO	Radio	$(4.8, 8, 14.5) \times 10^9$
Effelsberg[b]	Radio	$(2.6, 4.9, 8.4, 10.5,\ 14.6, 23, 32) \times 10^9$
IRAM[b]	Millimeter	$(8.6, 14.2, 22.8) \times 10^{10}$
Swift/UVOT	UV-Optical	$(5.5, 6.9, 8.6, 11.3, 13.4,\ 14.8) \times 10^{14}$
Swift/XRT	X-ray	$(7.25\text{-}242) \times 10^{16}$
Swift/BAT	X-ray	$(3.6\text{-}36) \times 10^{18}$
Fermi/LAT	γ-ray	4.8×10^{21} to $> 7.3 \times 10^{24}$

[a] MOJAVE program.
[b] F-GAMMA project.

coverage. All sources are in the *Fermi* first-year catalog, and were not included in the SED study of *Fermi* LBAS sample (Abdo et al. 2010a). We will discuss the preliminary results.

3. Data acquisition and analysis

Here we introduce the instruments and characteristics of the data included in the MOJAVE SED catalog. In the γ-ray band, we included the result of the 11-month *Fermi*/LAT catalog (Abdo et al. 2010b). We used the X-ray telescope (XRT) and burst alert telescope (BAT) on-board *Swift* to cover the X-ray band, and we used the *Swift* UV-optical telescope (UVOT) for UV and optical band data. For each of the MOJAVE sources, we reduced one epoch of *Swift* XRT/UVOT data observed after August 2008 with the longest XRT integration time. Many of the MOJAVE sources are weak in X-rays, and typically we used epochs with XRT integration time around 5–10 ksec. For the sources with no recent data, we submitted *Swift* Target-of-Opportunity (ToO) observing requests. As of May 2010, only 5% of the MOJAVE sources have no *Swift* data after August 2008, and are waiting observation. Table 2 summarizes our results of *Swift*/XRT data analysis, together with other relevant parameters of the 6 sources.

The 26-meter radio telescope in the University of Michigan Radio Astronomy Observatory (UMRAO) has monitored a large number of AGN for the past four decades (Aller et al. 1985, 2003), including all MOJAVE sources. Here we included the UMRAO data closest in time to the *Swift* observation used. We also included the Effelsberg 100 m telescope and the IRAM 30 m telescope observations in the framework of the *Fermi*-GST AGN Multi-frequency Monitoring Alliance[1] (F-GAMMA; Fuhrmann 2010; Angelakis 2010). Also, we included the broadband historical data from the NASA/IPAC Extragalactic Database[2] (NED). Table 1 lists the facilities and wavebands covered in our study.

4. Results

We selected 6 of the MOJAVE sources with good data coverage, and present the preliminary SED here (see Fig. 1). The presented sources are three flat-spectrum-radio quasars, two BL Lac objects, and one radio galaxy (see Table 2). All of them are in the *Fermi* first-year catalog, but were not included in the broadband SED study of *Fermi* LBAS sample (Abdo et al. 2010a).

The SEDs of the 6 MOJAVE sources show a classical double-peak blazar shape (Dermer & Schlickeiser 1993). Current models suggest that the major part of emission from blazars are non-thermal, and the low-energy peak ($10^7 - 10^{16}$ Hz in Fig. 1) is due to synchrotron emission from the radio jet, and the high-energy peak ($10^{17} - 10^{27}$ Hz in Fig. 1) can be interpreted as inverse Compton emission of various radiation sources, e.g., synchrotron self-Compton (SSC; Jones et al. 1974; Ghisellini & Maraschi 1989) and external radiation Compton (Sikora et al. 1994; Dermer & Schlickeiser 2002). The physical processes involved in the SED study are complex, and the fact that we cannot distinguish different emission regions from a target source makes broadband SED modeling challenging. For example, the SED study of 48 *Fermi* bright blazars (Abdo et al. 2010a) shows that a homogeneous one-zone model with SSC mechanism cannot explain most of their results, and more complex models involving external Compton radiation or multiple SSC components are needed to model the blazar SEDs. In Fig. 1, we present the SED of the 6 sources in ν-νF_ν plots. We performed a mathematical polynomial fit of 2nd to 4th order to the two humps, providing numerical values of the peak positions of the synchrotron and inverse-Compton components. Also, the total energy output of the low- and high- energy humps could be estimated from the polynomial fit. From Fig. 1, one can see that in each source, the total energy output of the low- and high- energy components differs. The high-energy hump of B0754+100 is significantly lower than the low-energy one, whereas the other sources have comparable height of the two humps. We discuss the 6 individual sources below.

B0300+470 4C +47.08 is a BL Lac object, which shows a compact asymmetric morphology in VLBI observations (Lister et al. 2009a). It displays a one-sided halo at kiloparsec scale. This source is variable on a monthly timescale at centimeter wavelengths (Aller et al. 1985) in total flux and linear polarization, and the source is core-dominated (Nan et al. 1999). We analyzed one epoch of *Swift* observations of this source obtained in September 2008 (ID 00036235005) with an integration time of 7 ks.

B0415+379 3C 111 is a well-studied broad-line radio galaxy which shows a classical Fanaroff and Riley Class II morphology on kiloparsec scales (Linfield & Perley 1984). It hosts a highly collimated one-sided jet emitting from the central core to the northeastern lobe (see e.g., Kadler

Table 2. Summary of our X-ray and the γ-ray measurements of Abdo et al. (2010b) of the 6 sources in this study.

IAU Name	1LAC 1FGL	Source type	z	β_{app}	F_X [10^{-13} erg cm^{-2} s^{-1}]	F_γ [10^{-13} photon MeV^{-1} cm^{-2} s^{-1}]	α_X	α_γ
(1)	(2)	(3)	(4)	(5)	(6)	(7)	(8)	(9)
B0300+470*	J0303.1+4711	B	-	-	7.38	49.9±7.9	1.38±0.41	2.56±0.13
B0415+379	J0419.0+3811	G	0.049	5.9±0.1	454	76.3±15.8	1.73±0.01	2.61±0.16
B0754+100	J0757.2+0956	B	0.266	14.4±1.2	29.8	75.2±6.7	1.81±0.08	2.39±0.08
B0836+710	J0842.2+7054	Q	2.218	25.4±1.0	122	366±32	1.43±0.02	2.98±0.12
B1730−130	J1733.0−1308	Q	0.902	35.7±2.1	12.1	85.4±7.6	1.98±0.33	2.34±0.07
B2209+236	J2212.1+2358	Q	1.125	3.4±0.5	4.80	3.3± 0.7	1.43±0.60	2.13±0.19

(1) Source Name; (2) The first LAT AGN catalog name (Abdo et al. 2010b); (3) Optical class (B: BL Lac, G: radio galaxy, Q: quasar);
(4) Redshift; (5) The maximum apparent projected speed measured by the MOJAVE team (Lister et al. 2009b); (6) X-ray flux measured by *Swift*/XRT (0.2-10 keV); (7) γ-ray flux measured by *Fermi*/LAT using 11-month data (Abdo et al. 2010b);
(8) X-ray photon index; (9) γ-ray photon index.
* Luminosity distance unknown, measured maximum apparent speed 287±23 μas yr^{-1}.

et al. 2008). 3C 111 is associated with the EGRET source 3EG J0416+3650, and the broadband SED study of the historical data suggests that the SED profile is similar to EGRET flat spectrum radio quasars (Hartman et al. 2008). Here we analyzed *Swift* data observed in January 2010 (obsid 00036367005) with an integration time of 9 ks.

B0754+100 B0754+100 is cataloged as a low-frequency peaked BL Lac (LBL) by Fiorucci et al. (2004). By the blazar classification of Abdo et al. (2010a), B0754+100 is a low synchrotron peaked blazar ($\nu_{peak} \leq 10^{14}$ Hz) based on our fitting result. VLA observations showed that there is a diffuse halo around the core at 1.5 and 5 GHz up to scales of >120 kpc (Antonucci & Ulvestad 1985; Kollgaard et al. 1992). Recently, B0754+100 was reported to be flaring in the near-infrared band (Carrasco et al. 2010). We requested *Swift* ToO request for this source, which was observed in February 2010 (obsid 00036195002) with an integration time of 9 ks.

B0836+710 4C +71.07 is a luminous quasar which hosts a radio jet extending up to kiloparsec scales. Broadband variability was observed in this source (Otterbein et al. 1998), and space VLBI observations have revealed detailed jet structures (Lobanov et al. 1998; Perucho & Lobanov 2007). Here we included the *Swift* data of B0836+710 observed in February 2009 with an integration time of 9 ks (obsid 00036376005).

B1730−130 NRAO 530 is a high-polarized radio quasar which hosts a double-sided kilo-parsec scale jet. This source is actively variable in the radio (Marscher & Broderick 1981; Feng et al. 2006), optical (Pollock et al. 1979), X-ray (Foschini et al. 2006), and γ-ray (Hartman et al. 1999) wavebands. We used the *Swift* data of NRAO 530 observed in June 2009 with an integration time of 5 ks (obsid 00035387012).

B2209+236 B2209+236 is a core-dominated flat-spectrum radio quasar. The radio turn-over frequency of this source is above 5 GHz (Dallacasa et al. 2000), which indicates that the source is very compact and is possibly young. Here we used the *Swift* observation obtained in April 2009 with an integration time of 9 ks in the SED study (obsid 00036359002).

5. Outlook

As of May 2010, we completed the data collection and construction of quasi-simultaneous SEDs during the time between August 2008 to July 2009. Almost all sources have nearly simultaneous observations from radio to X-ray with good data coverage. We are compiling the statistical properties of the 135 sources (e.g., correlation study between VLBI properties, X-ray and γ-ray parameters, and broadband SED characteristics), and the results will be presented elsewhere (Chang et al., in preparation). Physical SED models will be applied to the whole sample, to shed light on the mechanisms of general AGN picture.

References

Abdo, A. A., Ackermann, M., Agudo, I., et al. 2010a, ApJ, 716, 30

Abdo, A. A., Ackermann, M., Ajello, M., et al. 2010b, ApJ, 715, 429

Fig. 1. The broadband spectral energy distribution of 6 selected MOJAVE sources. Polynomial fitting results are shown as solid lines.

Aller, H. D., Aller, M. F., Latimer, G. E., & Hodge, P. E. 1985, ApJS, 59, 513

Aller, M. F., Aller, H. D., & Hughes, P. A. 2003, ApJ, 586, 33

Angelakis, E. 2010, these proceedings

Antonucci, R. R. J. & Ulvestad, J. S. 1985, ApJ, 294, 158

Boeck, M. 2010, these proceedings

Carrasco, L., Mayya, D. Y., Carramiñana, A., Recillas, E., & Porras, A. 2010, The Astronomer's Telegram, 2516, 1

Dallacasa, D., Stanghellini, C., Centonza, M., & Fanti, R. 2000, A&A, 363, 887

Dermer, C. D. & Schlickeiser, R. 1993, ApJ, 416, 458

Dermer, C. D. & Schlickeiser, R. 1994, ApJS, 90, 945

Dermer, C. D. & Schlickeiser, R. 2002, ApJ, 575, 667

Feng, S., Shen, Z., Cai, H., et al. 2006, A&A, 456, 97

Fiorucci, M., Ciprini, S., & Tosti, G. 2004, A&A, 419, 25

Foschini, L., Pian, E., Maraschi, L., et al. 2006, A&A, 450, 77

Fuhrmann, L. 2010, these proceedings

Ghisellini, G. & Maraschi, L. 1989, ApJ, 340, 181

Hartman, R. C., Bertsch, D. L., Bloom, S. D., et al. 1999, ApJS, 123, 79

Hartman, R. C., Kadler, M., & Tueller, J. 2008, ApJ, 688, 852

Jones, T. W., O'Dell, S. L., & Stein, W. A. 1974, ApJ, 188, 353

Kadler, M. 2005, PhD Thesis, Rheinische Friedrich-Wilhelms-Universität Bonn

Kadler, M., Ros, E., Perucho, M., et al. 2008, ApJ, 680, 867

Kollgaard, R. I., Wardle, J. F. C., Roberts, D. H., & Gabuzda, D. C. 1992, ApJ, 104, 1687

Kovalev, Y. Y., Aller, H. D., Aller, M. F., et al. 2009, ApJ, 696, L17

Linfield, R. & Perley, R. 1984, ApJ, 279, 60

Lister, M. L. 2010, these proceedings

Lister, M. L., Aller, H. D., Aller, M. F., et al. 2009a, ApJ, 137, 3718

Lister, M. L., Cohen, M. H., Homan, D. C., et al. 2009b, ApJ, 138, 1874

Lister, M. L., Homan, D. C., Kadler, M., et al. 2009c, ApJ, 696, L22

Lobanov, A. P., Krichbaum, T. P., Witzel, A., et al. 1998, A&A, 340, L60

Marscher, A. P. & Broderick, J. J. 1981, ApJ, 249, 406

Nan, R. D., Zhang, H. Y., Gabuzda, D. C., & Inoue, M. 1999, PASJ, 51, 955

Ojha, R., Kadler, M., Böck, M., et al. 2010, A&A in press [arXiv:1005.4432]

Otterbein, K., Krichbaum, T. P., Kraus, A., et al. 1998, A&A, 334, 489

Perucho, M. & Lobanov, A. P. 2007, A&A, 469, L23

Pollock, J. T., Pica, A. J., Smith, A. G., et al. 1979, ApJ, 84, 1658

Pushkarev, A. B., Kovalev, Y. Y., Lister, M. L., & Savolainen, T. 2009, A&A, 507, L33

Savolainen, T., Homan, D. C., Hovatta, T., et al. 2010, A&A, 512, A24

Sikora, M., Begelman, M. C., & Rees, M. J. 1994, ApJ, 421, 153

The multi-spectral-range behavior of OJ 287 in 2005–2010

I. Agudo[1], S. G. Jorstad[1], A. P. Marscher[1], V. M. Larionov[2,3], J. L. Gómez[4], H. Wiesemeyer[5], C. Thum[6], M. Gurwell[7], J. Heidt[8], and F. D. D'Arcangelo[1,9]

[1] Institute for Astrophysical Research, Boston University, 725 Commonwealth Avenue, Boston, MA 02215, USA

[2] Astronomical Institute, St. Petersburg State University, Universitetskij Pr. 28, Petrodvorets, 198504 St. Petersburg, Russia

[3] Isaac Newton Institute of Chile, St. Petersburg Branch, St. Petersburg, Russia

[4] Instituto de Astrofísica de Andalucía, CSIC, Apartado 3004, 18080, Granada, Spain

[5] Instituto de Radio Astronomía Milimétrica, Avenida Divina Pastora, 7, Local 20, E-18012 Granada, Spain

[6] Institut de Radio Astronomie Millimétrique, 300 Rue de la Piscine, 38406 St. Martin d'Hères, France

[7] Harvard-Smithsonian Center for Astrophysics, 60 Garden St., Cambridge, MA 02138, USA

[8] ZAH, Landessternwarte Heidelberg, Königstuhl, 69117 Heidelberg, Germany

[9] MIT Lincoln Laboratory, 244 Wood Street, Lexington, MA 02421, USA

Abstract. The BL Lac object OJ 287 is well known to exhibit quasi-periodic optical double outbursts every ~12 years, the latest reported between 2005 and 2008. We have been monitoring the source monthly at 43 GHz (VLBA imaging), 86 GHz (IRAM 30m), and optical frequencies, including polarimetry, since 2006. This program is supported by parallel monitoring observations at several other spectral ranges, and by publicly available X-ray and γ-ray data. Analysis of the VLBA images since 2005 shows an unexpected bright feature propagating at a sub-luminal speed southward from the core. This new projected direction of ejection of the jet does not support a binary black hole system with a ~12 years period as the origin of the previously known jet wobbling in the source. We propose a jet perturbation (i.e., a Kelvin-Helmholtz instability) as the origin of the dramatic change of structure of the jet in OJ 287. We also report on the time coincidence of two γ-ray flares with two mm and sub-mm flares produced in the 43 GHz VLBI core, and two sharp increases of linear polarization degree in the core region. In contrast, we do not find any obvious relation between the R-band total flux light curve of OJ 287 and those at the other spectral ranges.

1. Introduction

During the past ~ 40 yr, OJ 287 has shown quasi-periodic double-peaked optical outbursts (separated by 400 to 700 days) every ~ 12 yr, the last of which occurred between 2005 and 2007 (e.g., Villforth et al. 2010). This quasi-periodicity has been used as the main argument supporting binary black-hole (BH) models, or other, less exotic, scenarios such as instabilities in the accretion disk of the AGN or in its corresponding jet (see Villforth et al. 2010, for a discussion about these different scenarios). Consistent with the latter scenario, Tateyama & Kingham (2004) reported a jet wobbling behavior from their long-term 8 GHz VLBI study, which they explain with a ballistic jet precession model, also with a periodicity of ~ 12 yr.

Here we present a new observational approach on OJ 287 from 2005 to 2010 that aims at investigating the overall multi-spectral-range (and mm and optical polarimetric) properties of this blazar and their relation to its double flaring state during the 2005–2010 time range.

2. The observations

We have monitored OJ 287 with a time sampling of one month or better with 43 GHz VLBA polarimetry (Fig. 1), 86 GHz IRAM 30 m polarimetry, and optical (Calar Alto, Lowell, Crimean Astrophysical, and St. Petersburg State University Observatories) polarimetry (Figs. 2 and 3) since the beginning of 2006. These programs are also supported by several other independent 43 GHz VLBA observations dating back to 1995

(with a gap in 2002–2004), by total flux monitoring SMA observations at 230 and 350 GHz since late 2002, and by publicly available X-ray (*Swift*-XRT) and γ-ray (*Fermi*-LAT) data starting in mid-2005 and mid-2008, respectively (see Fig. 2). Moreover, most of the comprehensive set of photo-polarimetric R-band optical data presented in Fig. 3 was taken from Villforth et al. (2010), to which we refer the reader for details on the data acquisition and reduction.

The reduction of VLBA, optical polarimetric, *Swift*-XRT, and *Fermi*-LAT data was performed following Marscher et al. (2010) and Jorstad et al. (2010), whereas the IRAM data was reduced following Agudo et al. (2010). The SMA data reduction was performed according to Gurwell et al. (2007).

3. Total flux results

3.1. The innermost jet as seen by the VLBA at 43 GHz

Figure 1 (left) shows a clear clockwise wobbling behavior of the jet in OJ 287 consistent with the one reported by (Tateyama & Kingham 2004). However, their periodic precession model predicted a jet structural position angle ~ −95° in 2009, whereas we measure a drastically different and persistent inner jet position angle of ~ 160°. Clearly, the present jet structure shown in Fig. 1 does not follow Tateyama & Kingham's regular 12 yr periodic precession model. This result argues against the idea that the jet wobbling in OJ 287 is directly induced by precession in a binary BH system with a 12 yr period.
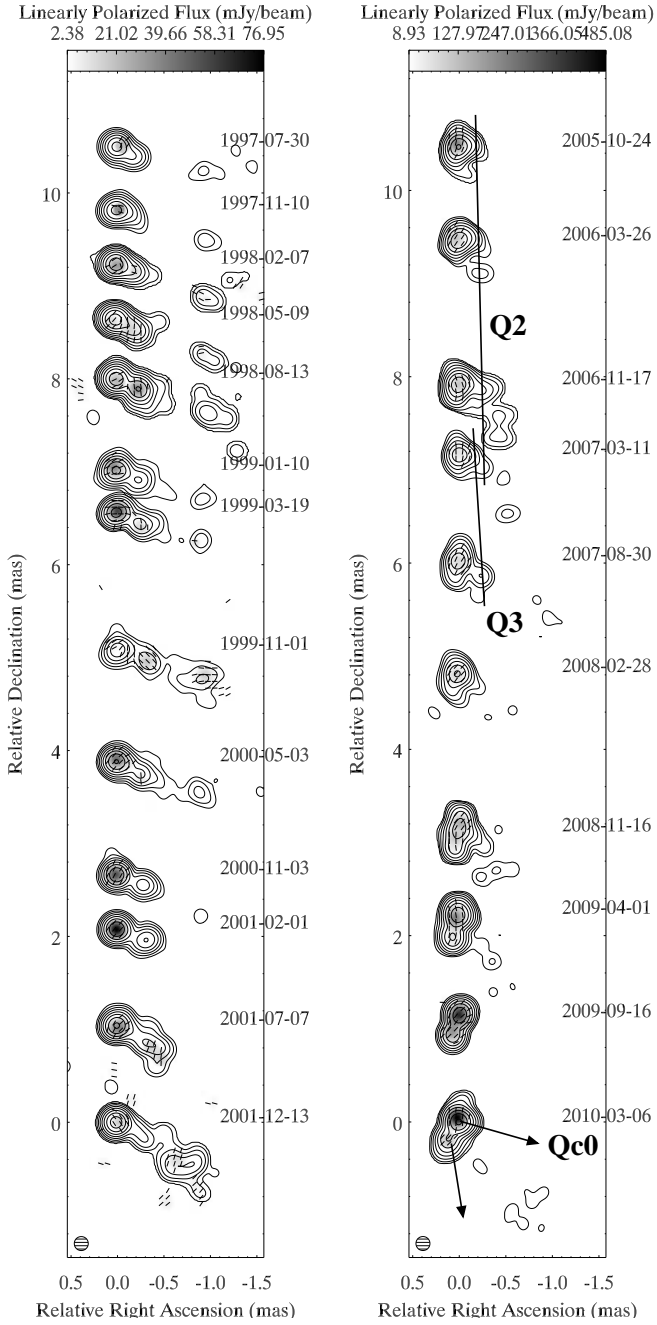
Fig. 1. Sequence of 43 GHz VLBA images of OJ 287 taken from mid-1997 to the end of 2001 (left) and from the end of 2005 to the beginning of 2010 (right). All images were convolved with a circular Gaussian beam with FWHM = 0.15 mas. Contours represent the observed total intensity, the color scale indicates the linearly polarized intensity, whereas the superimposed sticks show the orientation of the polarization electric vector position angle.

For the time range from 2005, we modeled the inner jet region containing a completely new ejection angle to the south with two circular Gaussian components labelled Qc0 (the northern one, which we identify with the core) and Qc1 (the southern one). These two features have generally contained $\gtrsim 90\%$ of the 43 GHz VLBA integrated emission of the entire source during the time range since Qc1 first appeared (in

2005), and hence currently govern the total flux evolution of OJ 287 at mm-wavelengths.

Qc1 separates from the core at an essentially ballistic trajectory with sub-luminal speed $\sim 0.6c$ and estimated ejection time of 2005.48 ± 0.27. In contrast, jet features seen in our maps propagating along trajectories typical before 2002, i.e. to the west or southwest (e.g., Fig. 1-left), exhibit considerably faster, superluminal speeds and much lower fluxes. This is the case for Q2, another jet feature close to the core (see Fig. 1 (right)), which we estimate to have been ejected contemporaneously with Qc1 (in 2005.50 ± 0.28), but along a position angle typical of the range of position angles of the jet before 2002 (i.e., at $-105°$). Q2 propagates at a superluminal speed of $\sim 1.6c$ and displays much lower flux density than Qc1 ($\bar{S} \approx 0.2$ mJy). Q3 follows a similar evolution as Q2, separating from the core along position angle $\sim -112°$ with a low mean flux, $\bar{S} \approx 0.2$ mJy, and an even larger mean superluminal speed of $\sim 6.9c$.

3.2. Light curves from mm wavelengths to γ-rays

The 230 and 350 GHz light curves from the SMA (see Fig. 2) reveal a relatively quiescent state (at ~ 2 Jy) of sub-mm and mm emission between 2005 and 2008.5, whereas the $[2008.5, 2010.4]$ time range is characterized by two of the largest (sub-)mm-wave flares detected thus far in OJ 287. These two emission peaks had fluxes of 8.28 ± 0.43 Jy and 7.02 ± 0.45 Jy on RJD=54873.1 (2009-02-10) and RJD=55202.9 (2010-01-06), respectively. Our 43 GHz VLBA model fits allow us to identify the two mm flares displayed by the SMA light curves with flux enhancements of the core (i.e., Qc0) in the 43 GHz images. No new jet features related to these two prominent flares have yet been detected separating from the core.

The optical R-band light-curve (Figs. 2 and 3) includes the two optical flares in 2005 and 2007 recently discussed by Villforth et al. (2010, see also references therein).

The 0.3–10 keV flux evolution curve from XRT presented in Fig. 2 shows an overall higher flux level ($[4, 13] \times 10^{-12}$ erg/cm^2/s) in the time range from mid 2008 to the beginning of 2010. This contrasts with the low X-ray levels displayed by the source in the time range from the beginning of 2005 to mid 2008 ($\lesssim 4 \times 10^{-12}$ erg/cm^2/s). This behavior is consistent with that shown by OJ 287 in the mm range (Fig. 2), suggestive of a connection between the X-ray and the mm emitting regions. In contrast, the optical light curve shows radically different long-term variability behavior than that at X-ray and (sub-)mm wavelengths.

The *Fermi*-LAT γ-ray light-curve of OJ 287 shows a prominent flare peaking on RJD~55129.0 (2009-10-24). This peak has a 0.1–300 GeV photon flux of $(4.91 \pm 0.66) \times 10^{-7}$ phot/cm^2/s, which is a factor ~ 5 larger than the quiescent γ-ray level of the source ($\sim 1 \times 10^{-7}$ phot/cm^2/s). Fig. 2 also shows another, much less pronounced, γ-ray flare one year before, on RJD~54744.0 (2009-10-04), with photon flux $= (2.19 \pm 0.46) \times 10^{-7}$ phot/cm^2/s.
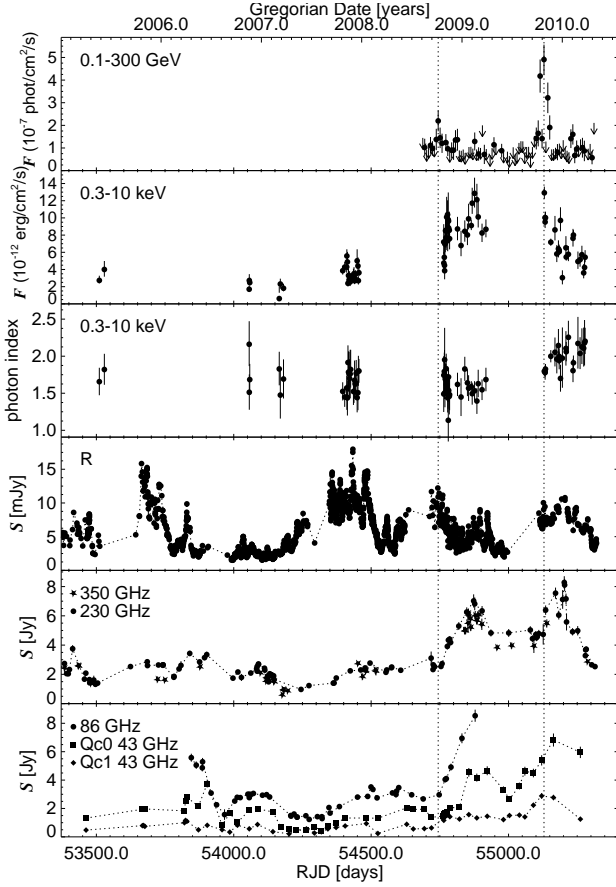
Fig. 2. OJ 287 evolution curves from the γ-ray to the mm spectral ranges. The γ-ray and X-ray data (in the 0.1–300 GeV and 0.3–10 keV energy ranges) were acquired by *Fermi*-LAT and *Swift*-XRT, respectively. The optical R-band data are those also presented in Fig. 3, whereas the 230, 86, and 43 GHz measurements were obtained by the SMA, the IRAM 30 m Telescope and the VLBA, respectively. The vertical lines symbolize the peak times of the two γ-ray flares discussed in the text. RJD = Julian Date - 2400000.

We cannot draw a firm conclusion about the possible relation between the two γ-ray flares and any peak in the optical light curve. This is because of the lack of sharp optical flares in the time range of the *Fermi*-LAT observations—as those in PKS 1510−089 (Marscher et al. 2010) or 3C 454.3 (Jorstad et al. 2010). Moreover, the fast and frequent optical variability of OJ 287 would allow us to associate a variety of different such optical peaks with the γ-ray flares. Longer-term monitoring of the source is needed to clarify the possible optical to γ-ray connection in OJ 287.

In contrast, the connection between γ-ray flares and (sub-)mm flares appears clearer in view of Fig. 2. The two γ-ray flares reported above happened just before the two (sub-)mm flares of OJ 287 at the beginning of 2009 and 2010, which we locate in the 43 GHz core. Moreover, the two γ-ray flares, which are much sharper than those at mm wavelengths (i.e., with time duration $\lesssim 50$ days) occur at about the time when the mm flares (with longer durations $\lesssim 240$ days) start to rise, i.e., when the mm-VLBI core starts to increase in flux.

4. Linear polarization results

During 2005–2010, it was very unusual to detect linear polarization in OJ 287 in our 43 GHz images at more than a few tenths of mas from the core (see Fig. 1). Indeed, only Qc0 and Qc1 show linear polarization at essentially all observing epochs when they were detected. Fig. 3 shows that these two features govern not only the total mm flux light curve of OJ 287 but also the evolution of the VLBA integrated linear polarization degree (m, with mean $\bar{m} = (6 \pm 2)$ % in 2005–2010) and electric vector position angle (χ, with mean $\bar{\chi} = (170 \pm 15)°$). The 86 GHz and 43 GHz linear polarization evolution curves correspond to each other rather well. Although there is some χ variability, the polarization angle of OJ 287 at 43 GHz during this time span is surprisingly stable in the direction of propagation of Qc1, except for two large turns of $\sim 90°$ from mid 2006 to beginning of 2007 when the linear polarization was very low. No clear emergence of a new, orthogonally polarized component appears to have occurred to explain this decrease of m. Despite the similarities of the polarization properties between Qc0 and Qc1, they differ in their m behavior, which exhibits two sharp peaks of 13.76 % and 22.43 % for Qc0 in 2008-11-04 and 2009-10-16, respectively. The fact that these dates are close to those of the reported γ-ray flares makes these sharp increases in polarization of special interest.

One of the most salient results regarding optical polarization in OJ 287—already pointed out by Villforth et al. (2010)—is the large level of polarization angle stability at mean polarization angle $\bar{\chi} = (169 \pm 55)°$. This stability is only greatly altered by sporadic short-term (10–20 days long) rotations of χ by up to 180° (see Villforth et al. (2010)), consistent with turbulent plasma behavior (D'Arcangelo (2009)). The mean optical linear polarization angle is essentially the same as that observed in the mm range, which suggests that both the optical and mm emitting regions posses the same overall magnetic field configuration in OJ 287.

Both the mean level of optical polarization degree ($\bar{m}_{opt} = 17 \pm 8$ %), and its variability amplitude are considerably larger than at mm wavelengths. This, along with the similar magnetic field directions at the two wavebands, can be explained by the model proposed by Marscher & Jorstad (these proceedings), according to which the optical emission occurs only in a limited number of cells inside the overall region emitting at mm wavelengths.

There is an interesting linear polarization event in our optical polarization evolution curves. About 50 days after the larger γ-ray peak, there is a systematic and dramatic m decrease from ~ 30 % to ~ 5 %. This is accompanied by a linear polarization angle rotation of $\sim 80°$. This phenomenon is expected if, in the presence of a stationary linearly polarized jet feature with $\bar{\chi} \sim 170°$, another component with orthogonal polarization angle appears in the jet. If this is the actual case in OJ 287, and if the portion of the jet between the optical emitting region and the farther downstream mm core is straight, we can predict a $\sim 90°$ swing of χ at mm wavelengths in the near future. Within this scenario, the new moving feature is a plane perpendicular shock, and it should propagate to the west-southwest direction in order for $\chi \sim -100°$ to occur.
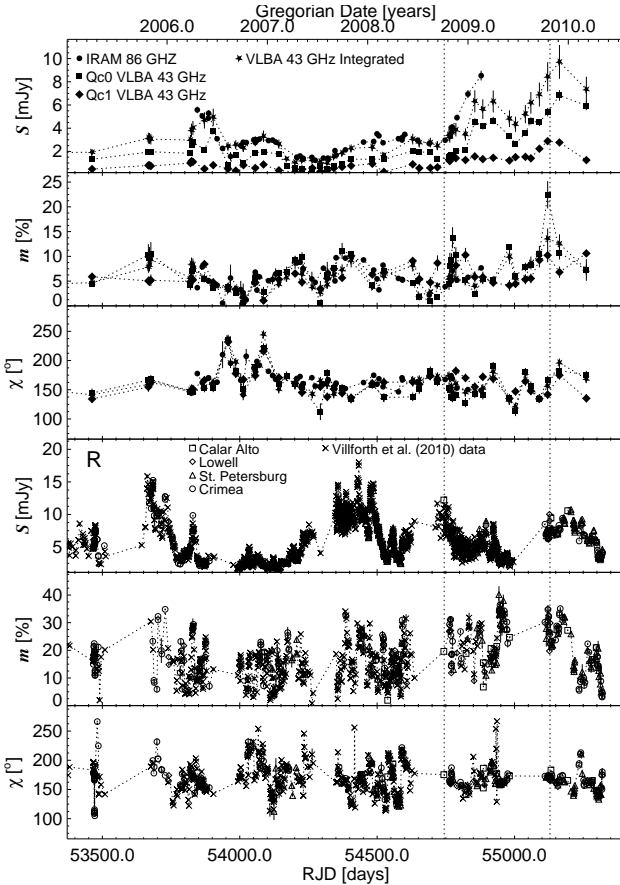
Fig. 3. Total flux (S) and linear polarization (m, and χ) evolution curves of OJ 287 at mm wavelengths (three first plots) and in the optical R band (last three plots). The vertical lines symbolize the times at which the γ-ray light curve had its two strongest peaks (see Fig. 2).

5. Discussion

The match between the estimated ejection times of Qc1 and Q2 tempts us to relate both moving jet regions with the same physical feature propagating down the jet. We can explain this if we allow the innermost jet regions to point almost at $0°$ to the line of sight, and the jet to contain a moving kink that does not disrupt the flow (i.e., Kelvin-Helmholtz or current driven instability). Within this scenario, the unexpected direction of propagation of Qc1 may be explained as the result of the outward propagation of such a kink at a tiny angle to the line of sight (hence the large flux and small sub-luminal speed of Qc1) after crossing the line of sight from the typical projected jet direction (to the southwest) to a new direction (almost to the south). In this case, Q2 (as well as Q3) would be a bent jet region at the opposite side of the line of sight and at a larger angle to the line of sight (hence displaying lower flux, but faster apparent speeds). Such a phenomenon does not require strong intrinsic curvature in the jet, only a nearly zero mean angle to the line of sight.

Together with the contemporaneous time of ejection of both Qc1 and Q2, our observations contain a number of relevant coincidences in the multi-spectral range behavior of OJ 287 that will be the subject of further interpretation and modeling else-

where. This includes: *i)* the two γ-ray flares, *ii)* the two mm and sub-mm flares associated with the flux increase in the 43 GHz core, *iii)* the sharp increase of linear polarization degree in the mm core at times close to the γ-ray flares, and *iv)* a plausible connection of the X-ray with the mm-wavelength emission.

We do not find an obvious relation between the R-band total flux light curve of OJ 287 and those at the other spectral ranges studied here. This contrasts with the behavior of other blazars for which their optical emission has been reported to be correlated with flares at γ-ray energies, among other spectral regions (see, Jorstad et al. 2010; Marscher et al. 2010; Abdo et al. 2010, for the cases of 3C 454.3, PKS 1510−089, and 3C 279, respectively).

Even the large optical flares in 2005 and 2007, related to the proposed ~ 12 yr quasi-periodicity of OJ 287, do not show a clear correspondence at other spectral ranges in our data, which suggests that either their corresponding emitting regions or their emission mechanisms (or a mix of both) are driven by different conditions. Perhaps an explanation may come from the idea that such major optical flares, and part of the optical emission in OJ 287 in non flaring states, comes from the accretion disk (either in a binary black hole scenario or not). In this case, no direct correlation with the jet emission at other spectral ranges would be required. This issue, which lies beyond the scope of this paper, is not easy to quantify, since it is known that some connection between the accretion disk and the jet may exist in radio loud AGN (e.g., Marscher et al. 2002).

Our new 43 GHz VLBA images have revealed that the time scale of the long term jet wobbling of OJ 287 ($>> 15$ yr)— which we cannot assure that it is periodic, i.e., precession like—is much longer than that suggested by the optical variability. The large difference between these time scales is against the explanation of such jet wobbling as the result of tidally induced disk precession in a binary BH system with an orbital period of ~ 12 yr.

References

Abdo, A. A., Ackermann, M., Ajello, M., et al., 2010, Nature, 463, 919

Agudo I., Thum C., Wiesemeyer H., Krichbaum T. P., 2010, ApJS, in press (arXiv:0911.5523)

D'Arcangelo, F. D., 2009, PhD Thesis (Boston U.)

Gurwell M. A., Peck A. B., Hostler S. R., Darrah M. R., Katz C. A., 2007, From Z-Machines to ALMA: (Sub)Millimeter Spectroscopy of Galaxies ASP Conference Series, 375, 234

Jorstad S. G., Marscher A. P., Larionov V. M., et al., 2010, ApJ, 715, 362

Marscher A. P., Jorstad S. G., Gómez J. L., et al., 2002, Nature, 417, 625

Marscher A. P., Jorstad S. G., Larionov V. M., et al., 2010, ApJ, 710, L126

Tateyama C. E., Kingham K. A., 2004, ApJ, 608, 149

Villforth C., Nilsson K., Heidt J., et al., 2010, MNRAS, 402, 2087

The Unusual Radio & Gamma-Ray Properties of the Quasar 4C +55.17

W. McConville[1,2], L. Stawarz[3,4], L. Ostorero[5,6], R. Moderski[7], and C. C. Cheung[1,8]

[1] NASA Goddard Space Flight Center, Astrophysics Science Division, Greenbelt, MD 20771, USA

[2] University of Maryland, Department of Physics, College Park, MD, 20742 USA

[3] Institute of Space and Astronautical Science, JAXA, 3-1-1 Yoshinodai, Sagamihara, Kanagawa 229-8510, Japan

[4] Astronomical Observatory, Jagiellonian University, ul. Orla 171, 30-244 Kraków, Poland

[5] Dipartimento di Fisica Generale "Amedeo Avogadro", Università degli Studi di Torino, Via P. Giuria 1, 10125 Torino, Italy

[6] Istituto Nazionale di Fisica Nucleare (INFN), Via P. Giuria 1, 10125 Torino, Italy

[7] Nicolaus Copernicus Astronomical Center, Bartycka 18, 00-716 Warsaw, Poland

[8] Naval Research Laboratory, Space Science Division, Washington, DC 20375, USA

Abstract. We present the detailed radio and gamma-ray properties of the high redshift (z=0.896) quasar 4C +55.17. During the EGRET era, the gamma-ray source 3EG J0952+5501 was associated with 4C +55.17. The association remained tentative at the time, however, due to the limited angular resolution and sensitivity of the EGRET instrument. In addition, the unusual radio properties of the source were difficult to reconcile among the EGRET blazars. The Fermi Large Area Telescope (LAT) features an improved sensitivity, angular resolution, and energy range over the EGRET instrument. Since its launch in June 2008, it has confirmed the association with 4C +55.17 to an order-of-magnitude improvement in the localization. Furthermore, the LAT has revealed 4C +55.17 to be a unique source not only in the radio, but among the gamma-ray emitting AGN as well. Here we discuss the constraints on the source physics, focusing particularly on both blazar and possible young radio source scenarios.

1. Introduction

The radio-loud quasar 4C +55.17 (0954+556), classified as such from its broad optical emission lines, was associated as a gamma-ray source during the EGRET era, initially as 2EG J0957+5515, and later confirmed as 3EG J0952+5501 (Hartman et al. 1999; Mattox et al. 2001) and EGR J0957+5513 (Casandjian & Grenier 2008). The best localization obtained for the source (95% confidence radius $= 28.2'$) left the association with 4C +55.17 tentative at that time, however. Later deemed spurious by Marscher et al. (2002), the VLBI morphology of 4C +55.17 also appeared entirely inconsistent with the other bright gamma-ray blazars, which are characterized by the presence of a central compact radio core exhibiting variable flat-spectrum continuum, high brightness temperatures ($T_b = 10^{10} - 10^{14}$ K; Marscher et al. 2002; Kovalev et al. 2009), as well as a complex and variable polarization pattern (Urry & Padovani 1995). On the other hand, 4C +55.17 has been found to be non-variable across all wavelengths, and exhibits a radio morphology extended over ~ 400 pc (projected), with the brightest feature reaching a brightness temperature of only $T_b < 2 \times 10^8$.

As pointed out by Rosetti et al. (2005), the radio morphology of 4C +55.17 is in fact suggestive of another type of radio source, namely the "compact/medium symmetric objects" (CSOs/MSOs). These young radio sources are largely non-variable, and are characterized by symmetric double radio structures indicative of "classical doubles", but smaller in size (Odea 1998). In classifying such objects, one must be careful, as similar morphologies can occasionally be seen in blazars (see Tremblay et al. (2010) for a recent example). Thus a close look at the variability and polarization of such sources, in addition to a careful study of the broadband emission, are often necessary for determining the true nature of these more enigmatic cases.

Here we present a detailed analysis of 4C +55.17 using 19 months of LAT data and investigate the origin of the gamma-ray emission in both the blazar and young radio source scenarios. In the following, we assume modern cosmology with $H_0 = 71$ km s^{-1} Mpc^{-1}, $\Omega_M = 0.27$ and $\Omega_\Lambda = 0.73$. At redshift z=0.896, obtained from HST-FOS (Wills et al. 1995) and SDSS (Schneider et al. 2007) spectra, the luminosity distance $d_L = 5785$ Mpc, and the conversion scale 1 mas $= 7.8$ pc. The linear size of the discussed radio structure is then 53 mas $= 413$ pc.

2. Fermi/LAT Observations

Following the launch of *Fermi*, 4C +55.17 has appeared with high significance in the LAT 3 month bright source list as 0FGL J0957.6+5522 (Abdo et al. 2009a), and now in the *Fermi* first year catalog as 1FGL J0957.7+5523 (Abdo et al. 2010a). It is also included in the *Fermi* first year AGN catalog (1LAC; Abdo et al. 2010b), where it was found to be the hardest FSRQ in the flux-limited sample (> 100 MeV flux larger than 3×10^{-8} ph cm^{-2} s^{-1}). The source was also found to be extremely stable over the 11-month viewing period, with no indication of variability
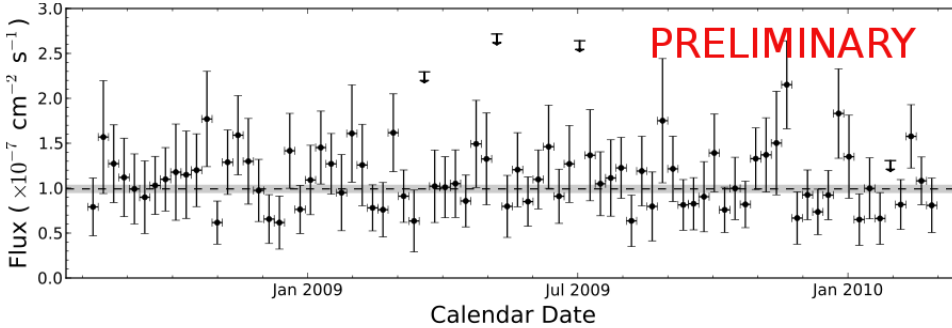
**Fig. 1.** 5σ weekly light curve of 4C +55.17 over the 19 month viewing period. The horizontal dashed line and gray span represent the weighted average and respective error of all $> 5\sigma$ detections.

Table 1. De-absorbed γ-ray spectral results using several models of EBL

EBL model	Γ_1	Γ_2	Flux*	$-\log(\text{likelihood})$
(1)	1.803±0.047	2.174±0.057	9.26±0.46	595981.796
(2)	1.802±0.046	2.180±0.057	9.26±0.46	595981.761
(3)	1.802±0.046	2.179±0.057	9.26±0.46	595981.702
(4)	1.806±0.046	2.162±0.058	9.28±0.46	595981.586
(5) best fit	1.807±0.046	2.158±0.058	9.28±0.46	595982.057
(5) high UV	1.816±0.046	2.109±0.059	9.34±0.46	595982.419
(6) baseline	1.824±0.046	2.080±0.062	9.38±0.46	595988.540
(6) fast evolution	1.825±0.046	2.071±0.063	9.39±0.46	595990.068
(7)	1.815±0.046	2.122±0.060	9.33±0.46	595983.647

Refs.: 1: Finke et al. (2010); 2: Franceschini et al. (2008); 3: Gilmore et al. (2009); 4: Primack et al. (2005); 5: Kneiske (2004); 6: Stecker (2006); 7: Salamon & Stecker (1998).
Notes: Γ_1 and Γ_2 represent the intrinsic low and high spectral indices of the broken power law fit. Lower values in $-\log(\text{likelihood})$ represent an improvement in the fit over higher values, as outlined in Mattox et al. (1996).
* Flux above 100 MeV in units of $10^{-8}\,\text{cm}^{-2}\,\text{s}^{-1}$

both over the LAT observations, as well as with the previous EGRET measured flux.

In the present analysis, we extend the LAT observing period of 4C +55.17 to 19 months of *Fermi*/LAT all-sky survey data, using science tools version `v9r16p0` and the latest `P6_V8_DIFFUSE` irfs, which utilize the on-orbit calibrated LAT point-spread function (psf) at energies > 1.8 GeV. Further details regarding the analysis procedures will be outlined in an upcoming paper (McConville et al. 2010).

A detailed spectral analysis of 4C +55.17 was performed by running a model-independent fit over 9 equal logarithmic energy bins spanning the observed energy range of the source from 100 MeV to 145 GeV. The full spectrum was fit to a broken power law ($E_{br} = 1.562$ GeV, consistent with the highest spectral point) with attenuation from the extragalactic background light as predicted from eight different models. These results are illustrated in Table 1.

To test the gamma-ray variability, we made light curves in time bins of 7 and 28 days. The source was fit to a simple power law with index and prefactor parameters left free. Figure 1 illustrates the weekly light curve of 4C +55.17, together with the weighted mean of all $> 5\sigma$ detections over the 19 month observing period. The weighted mean was found to be $9.9 \pm 0.4 \times 10^{-8}\,\text{ph}\,\text{cm}^{-2}\,\text{s}^{-1}$, consistent with the average EGRET flux of $9.28 \pm 0.82 \times 10^{-8}\,\text{ph}\,\text{cm}^{-2}\,\text{s}^{-1}$ (Hartman et al.

1999). We thus find the γ-ray flux to be stable over decade timescales. In addition, a chi-squared analysis of the 7 and 28 day light curves against their respective weighted means yielded probabilities 0.97 and 0.84 respectively, indicating stability over the entire LAT observing period.

3. Multi-wavelength Observations

All *Swift* (Gehrels et al. 2004) data of the source that were simultaneous with the LAT observations were analyzed. Three *Swift* X-Ray Telescope (XRT; Burrows et al. 2005) snapshots (1.6–4.5 ks) were obtained in order to check the X-ray state of the source and to search for variability. Adding the exposures and performing a spectral fit over the energy range 2–10 keV, we obtained the photon index $\Gamma = 1.84 \pm 0.19$, with an absorbed flux of $(4.5^{+1.2}_{-0.9}) \times 10^{-13}\,\text{erg}\,\text{cm}^{-2}\,\text{s}^{-1}$ (minimal change in the intrinsic flux was seen). Comparing between each of the XRT observations, no X-ray variability was found. In addition, we compared these results to previous X-ray detections by Comastri et al. (1997) and Tavecchio et al. (2007) and found the source again to be non-variable.

Short (1.6–4.5 ks) exposures were also obtained with the *Swift* Ultra-Violet/Optical Telescope (UVOT; Roming et al. 2005). Data from all 6 filters were obtained in the first two epochs, and the last epoch with only the W2 filter. These results are illustrated in table 2. We find the results to be consistent with non-variability across the three epochs. These data were also compared with archival SDSS data from Feb 2, 2002 (Adelman-McCarthy et al. 2008), where an increase in the U band from 0.19 mJy in the SDSS data to 0.25 mJy was found, indicating a $\sim 30\%$ increase over 7 years. The SDSS g band, which falls between the UVOT V and B bands, also shows an $\sim 25\%$ increase from the 0.25 mJy in the SDSS data to 0.3 mJy in the UVOT measurements.

To model the SED, we analyzed available *Swift* BAT data (Ajello et al. 2008, 2009), obtaining a faint detection of the 15–150 keV flux of $6.75^{+0.38}_{-5.21} \times 10^{-12}\,\text{erg}\,\text{cm}^2\,\text{s}^{-1}$. In the near-infrared, we include historical data from the 2MASS All-Sky Point Source Catalog (PSC; Cutri et al. 2003). Also included are contemporaneous WMAP measurements (Wright et al. 2009), along with radio data from Altschuler & Wardle (1976), Owen et al. (1980), Kühr et al. (1981), Wardle et al. (1981), and Seielstad et al. (1983),

Table 2. *Swift* UVOT Observations from 2009

Band	λ [A]	FWHM	F_{ep1} [mJy]	F_{ep2} [mJy]	F_{ep3} [mJy]
V	5402	769	0.331 ± 0.061	0.337 ± 0.029	
B	4329	975	0.262 ± 0.015	0.286 ± 0.015	
U	3501	785	0.249 ± 0.010	0.251 ± 0.011	
UVW1	2634	693	0.175 ± 0.007	0.174 ± 0.007	
UVM2	2231	498	0.142 ± 0.029	0.167 ± 0.007	
UVW2	2030	657	0.125 ± 0.009	0.127 ± 0.005	0.130 ± 0.005

where we note the radio measurements to be consistent with non-variability.

4. Discussion

The non-variability of 4C +55.17 over all observed timescales in the radio, X-ray, and γ-ray bands, coupled with the extended VLBA morphology of the source, give sufficient reason to question the blazar nature of 4C +55.17, and instead to consider that it may be a member of the CSO-type radio sources, with young and symmetric inner radio structure. In order to test this hypothesis, we apply the dynamical model for the broad-band emission of CSO's proposed by Stawarz et al. (2008) and successfully tested against a sample of all X-ray-detected CSO type young radio galaxies by Ostorero et al. (2010). We compare this against a model of the alternative hypothesis — namely the "blazar" scenario, in which the non-thermal emission of the source is expected to originate from highly Doppler boosted emission from the inner regions of an aligned relativistic jet (e.g. Sikora et al. 1994). For this we use the model of Moderski et al. (2003), updated for the correct treatment of the Klein-Nishina regime (Moderski et al. 2005), and successfully tested against several multi-wavelength datasets (e.g. Sikora et al. 2008; Kataoka et al. 2008).

Figure 2 illustrates the "young radio source" model fit of the broad-band data set, from which we obtain the following model free parameters: $L_j \simeq 8 \times 10^{45}\,\mathrm{erg\,s^{-1}}$, $L_{\mathrm{disk}} \simeq 2 \times 10^{46}\,\mathrm{erg\,s^{-1}}$, $L_{\mathrm{star}} \simeq 10^{45}\,\mathrm{erg\,s^{-1}}$, $L_{\mathrm{dust}} \simeq 1 \times 10^{45}\,\mathrm{erg\,s^{-1}}$, $U_e/U_B \simeq 30$, and $n_{\mathrm{ext}} \simeq 0.01\,\mathrm{cm^{-3}}$. In the proposed model, L_j represents the total kinetic power of the jet, which propagates in the interstellar medium of density n_{ext}. The relevant photon fields for the inverse-Compton scattering of the electrons injected through the termination shock are the UV emission of the accretion disk (mean photon energy $\varepsilon_{\mathrm{disk}} = 10\,\mathrm{eV}$, disk luminosity L_{UV}), starlight ($\varepsilon_{\mathrm{star}} = 1\,\mathrm{eV}$, host luminosity L_{star}), and the infrared emission of the obscuring nuclear torus ($\varepsilon_{\mathrm{dust}} = 0.025\,\mathrm{eV}$, dust luminosity L_{dust}). The magnetic field intensity is expressed in terms of the ratio of energy densities stored in the radiating electrons and the magnetic field, U_e/U_B (for further details, see Stawarz et al. (2008)).

We find that the proposed "young radio source" model fits well with the observed multi-wavelength data. We also note that in the proposed framework the optical/UV
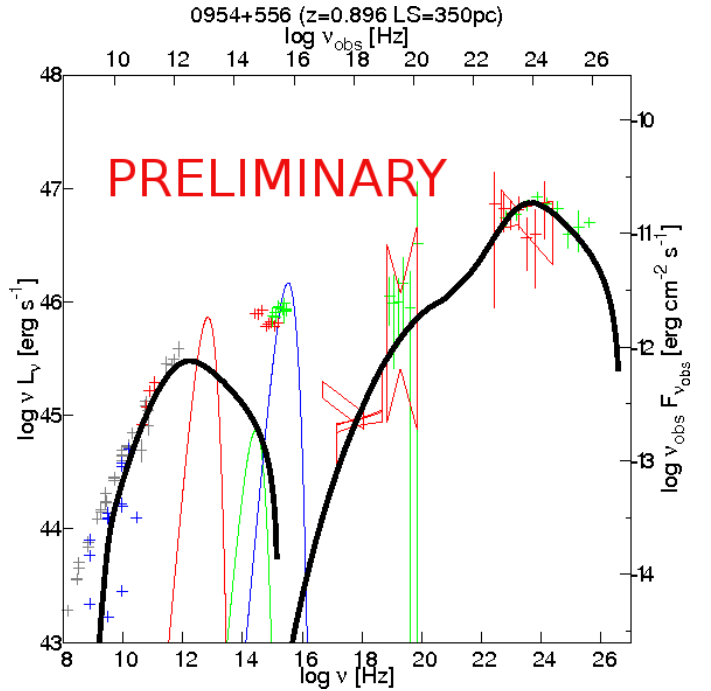
Fig. 2. Model of CSO/MSO versus multi-wavelength data including the new LAT spectrum along with contemporaneous data with *Swift* XRT/UVOT, & WMAP. Archival detections with EGRET (Hartman et al. 1999), SDSS, 2MASS point-source catalog, and historic radio data are also included (see §3). Thick black curves indicate non-thermal emission of the lobes. Thinner blackbody-type peaks correspond to the dusty torus, starlight, and the UV disk emission components, respectively, as required by the model.

emission is dominated by the UV disk, which in principle can vary over longer timescales, and is thus still consistent with the observed UVOT and SDSS results. Comparing the physical parameters obtained with the other known young radio galaxies analyzed by the same model (Ostorero et al. 2010), we find the only significant differences to be in the kinetic luminosity of the jet L_j, the UV luminosity of the accretion disk L_{disk}, and the ambient medium number density n_{ext}. In particular, we find the jet and disk luminosities to be higher by approximately an order of magnitude, while the gas number density was found to be an order of magnitude lower. These results could be expected in the case where the lobes are propagating through a particularly low density medium, whereby the IC cooling is expected to dominate over the synchrotron cooling due to the decreased internal pressure of the lobes. In the case of 4C +55.17, this would naturally explain the exceptionally high IC peak found at γ-ray energies, yielding an overall consistent result with the observed LAT spectrum.

In the alternative "blazar" hypothesis, we consider the production of the non-thermal emission originating from thin shells of plasma propagating along a conical relativistic jet, with bulk Lorentz factor $\Gamma_j \gg 1$ and jet opening angle $\theta_j \sim \Gamma_j$. Ultra-relativistic electrons, which carry a fraction of the jet kinetic power L_e, are injected into

an emission region of size R and magnetic field intensity B, starting from an initial distance r_0 from the jet base, where the synchrotron and IC components supply the non-thermal emission at $r \simeq R/\theta_j \gtrsim r_0$. In fitting this model to the broad-band spectrum of 4C +55.17, we obtain the following model free parameters: $L_j \gtrsim L_e \simeq 2 \times 10^{44}\,\mathrm{erg\,s^{-1}}$, $L_{\mathrm{disk}} \simeq 2 \times 10^{46}\,\mathrm{erg\,s^{-1}}$, $L_{\mathrm{dust}} \simeq 10^{45}\,\mathrm{erg\,s^{-1}}$, $r_0 \simeq 4 \times 10^{18}$ cm, $r \simeq 9 \times 10^{18}$ cm, $\Gamma_j \simeq 12$, and $B \simeq 0.2$ G. The injection electron energy distribution is characterized by the minimum, break, and the maximum Lorentz factors $\gamma_{min} \simeq 1$, $\gamma_{br} \simeq 10^3$, and $\gamma_{\max} \simeq 10^6$, respectively, as well as by the low- and high-energy spectral indices $s_1 \simeq 0.5$ and $s_2 \simeq 2.8$.

The model parameters obtained from the "blazar" fit can be considered plausible. Notable differences from the "young radio source" scenario can be found, however. In particular, the blazar model fit does not account for the bulk of the emission at radio and sub-mm wavelengths, which must instead be produced farther from the parsec-scale emission zone in order to properly take into account the extended (~ 100 pc) VLBI morphology. As such, the IC component of the blazar emission falls short of the observed hard X-ray excess, requiring an additional spectral component.

5. Conclusions

We have found that both the "young radio source" and "blazar" fits offer physical parameters that fall reasonably within their respective models. In the case of the "young radio source" hypothesis, we find the observations to be consistent with a newly born radio structure passing through the vicinity of an exceptionally small amount of cold molecular gas, resulting in the dominance of IC cooling over synchrotron cooling which well reproduces the observed high energy spectrum. In the blazar scenario, we find the obtained model parameters to fall within reasonable physical limits. However, we would consider these results to challenge the standard core-jet models of highly variable Doppler boosted emission in a compact ($\lesssim 1$ pc) emission region. While this hypothesis cannot be ruled out, it serves to place doubt in the blazar nature of 4C +55.17.

References

Abdo, A., et al. 2009a, ApJS, 183, 46
Abdo, A., et al. 2010a, submitted
Abdo, A., et al. 2010b, submitted
Adelman-McCarthy, J. K., et al. 2008, ApJS, 175, 297A
Ajello, M., et al. 2008, ApJ, 673, 96
Ajello, M., et al. 2009, ApJ, 699, 603
Altschuler, D. R., & Wardle, J. F. C. 1976, MmRAS, 82, 1
Burrows, D. N., et al. 2005, Space Science Reviews, 120, 165
Casandjian, J. M., & Grenier, I. A. 2008, A&A, 489, 849
Comastri, A., Fossati, G., Ghisellini, G., & Molendi, S. 1997, ApJ, 480, 534
Cutri, R. M., et al. 2003, The IRSA 2MASS All-Sky Point Source Catalog, NASA/IPAC Infrared Science Archive. http://irsa.ipac.caltech.edu/applications/Gator/,
Gehrels, N., et al. 2004, ApJ, 611, 1005
Hartman, R. C., et al. 1999, ApJS, 123, 79
Kataoka, J., et al. 2008, ApJ, 672, 787
Kovalev, Y. Y., et al. 2009, ApJ, 696, 17
Kühr, H., Witzel, A., Pauliny-Toth, I. I. K., & Nauber, U. 1981, A&AS, 45, 367
Mattox, J. R., Hartman, R. C., & Reimer, O. 2001, ApJS, 135, 155
Marscher, A. P., Jorstad, S. G., Mattox, J. R., & Wehrle, A. E. 2002, ApJ, 577, 85
Mattox, J. R., et al. 1996, ApJ, 461, 396
McConville, W., et al. for the *Fermi*/LAT collaboration 2010, *in prep*
Moderski, R., Sikora, M., & Błażejowski, M. 2003, A&A, 406, 855
Moderski, R., Sikora, M., Coppi, P. S., & Aharonian, F. 2005, MNRAS, 363, 954
Odea, C. P. 1998, PASP, 110, 493
Ostorero, L., et al. 2010, ApJ, 715, 1071
Owen, F. N., Spanger, S. R., & Cotton, W. D. 1980, AJ, 85, 351
Roming, P. W. A., et al. 2005, Space Science Reviews, 120, 95
Rossetti, A., Mantovani, F., Dallacasa, D., Fanti, C., & Fanti, R. 2005, A&A, 434, 449
Schneider, D. P., et al. 2007, AJ, 134, 102
Seielstad, G. A., Pearson, T. J., & Readhead, A. C. S. 1983, PASP, 95, 842
Sikora, M., Begelman, M. C., & Rees, M. J. 1994, ApJ, 421, 153
Sikora, M., Moderski, R., & Madejski, G. M. 2008, ApJ, 675, 71
Stawarz, Ł., Ostorero, L., Begelman, M. C., Moderski, R., Kataoka, J., & Wagner, S. 2008, ApJ, 680, 911
Tavecchio, F., Maraschi, L., Wolter, A., et al. 2007, ApJ, 662, 900
Tremblay, S. E. et al. 2010, ApJ, 712, 159T
Urry, M. C., & Padovani, P. 1995, PASP, 107, 803
Wardle, J. F. C., Bridle, A. H., & Kesteven, M. J. L. 1981, AJ, 86, 848
Wright, E. L., et al. 2009, ApJS, 180, 283
Wills, B. J., et al. 1995, ApJ, 447, 139

Physical properties of blazar jets from VLBI observations

Andrei Lobanov

Max-Planck-Institut für Radioastronomie, Auf dem Hügel 69, 53121 Bonn, Germany

Abstract. Relativistic jets, formed in the vicinity of central supermassive black holes in AGN, show ample evidence connecting them to physical conditions in the accretion disc and broad-line region. The jets are responsible for a large fraction of non-thermal continuum emission (particularly during powerful flares), which makes understanding their physics an important aspect of studies of blazars characterised by profound flaring activity arising from extremely compact regions. Imaging and polarimetry of radio emission on milliarcsecond scales provided by very long baseline interferometry (VLBI) offers a range of possibilities for studying ultra-compact regions in relativistic jets and relating them to main manifestations of the blazar activity in AGN. Simultaneous monitoring of optical/high energy variability and evolution of parsec-scale radio structures yields arguably the most detailed picture of the relation between acceleration and propagation of relativistic flows and non-thermal continuum generation in blazars. Opacity effects provide a measure of magnetic field strength on scales down to ~ 1000 gravitational radii and trace the distribution of broad-line emitting material. Correlations observed between parsec-scale radio emission and optical and gamma-ray continuum indicate that a significant fraction of non-thermal continuum may be produced (particularly during flares) in extended regions of relativistic jet at distances up to 10 parsecs from the central engine. Combined with studies of jet component ejections and X-ray variability, these correlations also suggest that time delays, nuclear opacity, and jet acceleration may have a pronounced effect on the observed broad-band variability and instantaneous spectral energy distribution (SED). These effects will be reviewed below and discussed in the context of deriving accurate and self-consistent models for central regions of blazars.

1. Introduction

In the current astrophysical paradigm for active galactic nuclei (AGN), each constituent of an AGN contributes to a specific domain in the broad-band spectral energy distribution (Ghisellini & Tavecchio 2009). Variability of continuum flux in AGN, signalling the activity of the central engine, is detected throughout the entire electromagnetic spectrum, on time-scales from days to years. Substantial progress achieved during the past decade in studies of active galactic nuclei (see Lobanov & Zensus 2006 for a review of recent results) has brought an increasingly wider recognition of the ubiquity of relativistic outflows (jets) in AGN (Falcke 2001; Zensus 1997) and in blazars in particular.

Understanding the physics of blazars jets has acquired a particular importance after the launch of *Fermi Gamma-Ray Space Telescope*, as the compact, relativistic flows contribute strongly to the broad-band continuum – a fact that is still somewhat overlooked in physical models describing high-energy emission from AGN.

Emission properties, dynamics, and evolution of an extragalactic jet are intimately connected to the characteristics of the supermassive black hole, accretion disk and broad-line region in the nucleus of the host galaxy (Lobanov 2008). The jet continuum emission is dominated by non-thermal synchrotron and inverse-Compton radiation (Unwin et al. 1997). The synchrotron mechanism plays a more prominent role in the radio domain, and the properties of the emitting material can be assessed using the turnover point in the synchrotron spectrum

(Lobanov 1998b; Lobanov & Zensus 1999), synchrotron self-absorption (Lobanov 1998a), and free-free absorption in the ambient plasma (Walker et al. 2000; Kadler et al. 2004).

There is growing evidence for relativistic flows contributing substantially to generation of non-thermal continuum in the optical (Arshakian et al. 2010; León-Tavares et al. 2010; Jorstad et al. 2010), X-ray (Unwin et al. 1997; D'Arcangelo et al. 2007; Marscher et al. 2008); Soldi et al. 2008; Chatterjee et al. 2009), γ-ray (Otterbein et al. 1998; Jorstad et al. 2010; Marscher et al. 2010; Savolainen et al. 2010; Schinzel et al. 2010) and TeV (Piner & Edwards 2004; Charlot et al. 2006; Acciari et al. 2009) domains. Accurate spatial localisation of production sites of variable non-thermal continuum emission in AGN is therefore instrumental for understanding the mechanism for release and transport of energy in active galaxies.

In the radio regime, very long baseline interferometry (VLBI) enables direct imaging of spatial scales comparable the gravitational radius, $R_{\mathrm{g}} = G\,M_{\mathrm{bh}}/c^2$, of the central black hole in AGN using ground VLBI observations at 86 GHz and higher (cf., GMVA[1] observations; Krichbaum et al. 2008) and space VLBI observations at centimetre wavelengths (Takahashi et al. 2004). Such high-resolution radio observations also access directly the regions where the jets are formed (Junor et al. 1999), and trace their evolution and interaction with the nuclear environment (Lobanov 2007, 2008 and Middelberg & Bach

---

[1] Global Millimeter VLBI Array; http://www.mpifr-bonn.mpg.de/div/vlbi/globalmm

2008). Evolution of compact radio emission from several hundreds of extragalactic relativistic jets is now systematically studied with dedicated monitoring programs and large surveys using very long baseline interferometry (such as the 15 GHz VLBA[2] survey (Kellermann et al. 2004) the MOJAVE[3] survey (Lister & Homan 2005) and a dedicated 22/43/86 GHz VLBA gamma-ray blazar monitoring program at the Boston University[4] (Jorstad et al. 2001). These studies, combined with optical and X-ray studies, yield arguably the most detailed picture of the vicinity of supermassive black holes in AGN (Marscher 2005).

Presented below is a brief (and certainly incomplete) summary of recent results from VLBI studies of compact extragalactic radio sources, outlining the physical properties of relativistic parsec-scale jets and their relation to supermassive black holes, accretion disks and broad-line regions in prominent blazars.

2. Physics of compact jets

Jets in active galaxies are formed in the immediate vicinity of the central black hole (Camenzind 2005), at distances of 10–$10^2\,R_{\mathrm{g}}$ (Meier 2009). The jets carry away a fraction of the angular momentum and energy stored in the accretion flow (Blandford & Payne 1982; Hujeirat et al. 2003 or corona (in low luminosity AGN; Merloni & Fabian 2002) and in the rotation of the central black hole (Blandford & Znajek 1977, Koide et al. 2002; Komissarov 2005; Semenov et al. 2004).

The production of highly-relativistic outflows requires a large fraction of the energy to be converted to Poynting flux in the very central region (Sikora et al. 2005). The efficiency of this process may depend on the spin of the central black hole (Meier 1999). The collimation of such a jet requires either a large scale poloidal magnetic field threading the disk (Spruit et al. 1997) or a slower and more massive MHD outflow launched at larger disk radii by centrifugal forces (Bogovalov & Tsinganos 2005). The flowing plasma is likely to be dominated by electron-positron pairs (Wardle et al. 1998; Hirotani 2005) although a dynamically significant proton component cannot be completely ruled out at the moment (Celotti & Fabian 1993).

Acceleration or collimation of the flow may be complete within about $10^3\,R_{\mathrm{g}}$ (Meier et al. 2009) or continue all the way to scales of a few parsecs (Vlahakis & Königl 2004). At distances of $\sim 10^3\,R_{\mathrm{g}}$, the jets become visible in the radio regime. Recent studies indicate that at 10^3–$10^5\,R_{\mathrm{g}}$ ($\leq 1\,\mathrm{pc}$) the jets are likely to be dominated by pure electromagnetic processes such as Poynting flux (Sikora et al. 2005) or have both MHD (kinetic flux) and electrodynamic components (Meier 2003). At larger scales, the jets are believed to be kinetic flux-dominated. The magnetic field is believed to play an important role in accel-

erating and collimating extragalactic jets on parsec scales (Vlahakis & Königl 2004). Three distinct regions with different physical mechanisms dominating the observed properties of the jets can be considered: 1) ultra-compact jets (on scales of up to $\sim 1\,\mathrm{pc}$) where collimation and acceleration of the flow occurs; 2) parsec-scale flows ($\sim 10\,\mathrm{pc}$ scales) dominated by relativistic shocks and 3) larger-scale jets ($\sim 100\,\mathrm{pc}$) where plasma instability gradually becomes dominant. This picture may be further complicated by transverse stratification of the flow, with the jet velocity, particle density and magnetic field changing substantially from the jet axis to its outer layers. As a practical result of this stratification, shocks and instabilities may in fact co-exist on all scales in the jets, with instabilities simply remaining undetected in compact flows, owing to limited resolution and dynamic range of VLBI observations.

2.1. Ultra-compact jets

Blazar jets usually feature a bright, compact (often unresolved) "core" and a weaker, extended jet (often also transversely unresolved), with several regions of enhanced emission (traditionally branded "jet components") embedded in the flow and separating from the core at apparently superluminal speeds. The radio core is offset from the true base of the jet, and this "invisible" flow is probably Poynting flux-dominated (Meier 1999, 2003; Sikora et al. 2005).

The radio core has a flat spectrum, expected to result from synchrotron self-absorption in a conically expanding ultra-compact flow (Königl 1981). As a result, the observed position, r_{c}, of the core depends on the frequency of observation, ν, so that $r_{\mathrm{c}} \propto \nu^{-1/k_{\mathrm{r}}}$ (this is so called "core shift" effect). If the core is self-absorbed and in equipartition, the power index $k_{\mathrm{r}} = 1$ (Blandford & Königl 1979). Recent measurements (Kovalev et al. 2008) have also shown that the frequency dependent core shift increases during flares as expected from the synchrotron self-absorption.

The core shift can be used for determining basic physical properties of the ultra-compact flow and the surrounding absorbing material (Lobanov 1998a). Changes of the core position measured between three or more frequencies can be used for determining the value of k_{r} and estimating the strength of the magnetic field, B_{core}, in the nuclear region and the offset, R_{core}, of the observed core positions from the true base of the jet. The combination of B_{core} and R_{core} gives an estimate for the mass of the central black hole $M_{\mathrm{bh}} \approx 7 \times 10^9\,M_{\odot}\,(B_{\mathrm{core}}/\mathrm{G})^{1/2}(R_{\mathrm{core}}/\mathrm{pc})^{3/2}$.

Core shift measurements provide estimates of the total (kinetic + magnetic field) power, the synchrotron luminosity, and the maximum brightness temperature, $T_{\mathrm{b,max}}$ in the jets can be made. The ratio of particle energy to magnetic field energy can also be estimated, from the derived $T_{\mathrm{b,max}}$. This enables testing the original Königl model and several of its later modifications (e.g., Hutter & Mufson 1986; Bloom & Marscher 1996). The known distance from

---

the nucleus to the jet origin can also enable constraining the self-similar jet model (Marscher 1995) and the particle-cascade model (Blandford & Levinson 1995).

Studies of free-free absorption in AGN indicate the presence of dense, ionised circumnuclear material with $T_e \approx 10^4$ K distributed within a fraction of a parsec of the central nucleus (Lobanov 1998a; Walker et al. 2000). Properties of the circumnuclear material can also be studied using the variability of the power index k_r with frequency. This variability results from pressure and density gradients or absorption in the surrounding medium most likely associated with the broad-line region (BLR). Changes of k_r with frequency, if measured with required precision, can be used to estimate the size, particle density and temperature of the absorbing material surrounding the jets. Estimates of the black hole mass and size of the BLR obtained from the core shift measurements can be compared with the respective estimates obtained from the reverberation mapping and applications of the M_{bh}–$\sigma_\star$ relation.

The non-thermal continuum radio emission from the jet core does not appear to have strong shocks (Lobanov 1998b), and its evolution and variability can be explained by smooth changes in particle density of the flowing plasma, associated with the nuclear flares in the central engine (Lobanov & Zensus 1999). Compelling evidence exists for acceleration (Vlahakis & Königl 2004; Bach et al. 2005; Lee et al. 2008) and collimation (Junor et al. 1999; Krichbaum et al. 2008) in the ultra-compact flows.

The brightness temperature of the radio emission from the cores reaches the inverse-Compton limit of $\approx 10^{12}$ K (Unwin et al. 1997; Lobanov et al. 2000; Kovalev et al. 2005), while it drops rapidly to the equipartition limit of $\approx 5 \times 10^{10}$ K in the jet components moving downstream from the core (Lähteenmäki et al. 1999; Lobanov et al. 2000; Homan et al. 2006). This supports earlier conclusions that ultra-compact jets are particle-dominated, while the plasma in moving jet components is likely to be close to the equipartition (Unwin et al. 1997; Lobanov 1998a; Hirotani 2000). Combining these calculations with estimates of the jet kinetic power provides strong indications that the relativistic fraction of the outflowing material is most likely represented by the electron-positron plasma (Reynolds et al. 1996; Hirotani et al. 2000; Hirotani 2005).

2.2. Parsec-scale flows: shocks and instabilities

Parsec-scale outflows are characterised by pronounced curvature of trajectories of superluminal components (Kellermann 2004; Lobanov & Zensus 1999), rapid changes of velocity and flux density (Lister et al. 2009) and predominantly transverse magnetic field 2005. Statistical studies of speed and brightness temperature distributions observed in the superluminal features propagating on parsec scales indicate that the jet population has an envelope

Lorentz factor of ≈ 30 and an un-beamed luminosity of $\sim 1 \times 10^{25}$ W Hz^{-1} (Cohen et al. 2007).

Physical conditions of the jet plasma can be assessed effectively by studying the spectral peak (turnover point) of the synchrotron emission. Mapping the turnover frequency distribution provides a sensitive diagnostic of the plasma (Lobanov 1998b). Obviously, the observed morphology and velocity of these flows are affected substantially by Doppler boosting, aberration, and time delays, which makes uncovering true physical properties a nontrivial task (Gómez et al. 1994; Cohen et al. 2007). As a result, it becomes difficult to distinguish between apparent and true physical accelerations of the moving features (Lister et al. 2009) and making such a distinction often requires a detailed physical modelling of a given jet component (Lobanov & Zensus 1999; Homan et al. 2003). Similarly to stellar jets, rotation of the flow is expected to be important for extragalactic jets (Fendt 1997), but observational evidence remains very limited on this issue.

VLBI studies have demonstrated that relativistic shocks are prominent in jets on parsec scales, which is manifested by strong polarization (Ros et al. 2000) and rapid evolution of the turnover frequency of synchrotron emission (Lobanov et al. 1997; Lobanov & Zensus 1999). Evidence is growing for the presence of stationary features in parsec-scale flows, typically separated by ~ 1 pc distance from the jet core (Kellermann et al. 2004; Savolainen et al. 2006; Lister et al. 2009; Arshakian et al. 2010; León-Tavares et al. 2010).

Specific geometric conditions and extremely small viewing angles could lead to formation of stationary features in relativistic flows (Alberdi et al. 2000). However, a more general and physically plausible explanation is offered by standing shocks (for instance, recollimation shocks in an initially over-pressurised outflow; Daly & Marscher 1988; Gómez et al. 1995; Perucho & Martí 2007). Such standing shocks may play a major role in accelerating particles near the base of the jet (Mandal & Chakrabarti 2008; Becker et al. 2008), and could be responsible for the persistent high levels of polarization in blazars (D'Arcangelo et al. 2007; Marscher et al. 2008)). More speculatively, the stationary features in jets could also be the sites of continuum emission release due to conversion from Poynting flux-dominated to kinetic flux-dominated flow.

Complex evolution of the moving shocked regions is revealed in observations (Gómez et al. 2001; Jorstad et al. 2005; Lobanov & Zensus 1999) and numerical simulations (Agudo et al. 2001) of parsec-scale outflows. However, the shocks are shown to dissipate rapidly (Lobanov & Zensus 1999), and shock dominated regions are not likely to extend beyond ~ 100 pc. Starting from these scales, instabilities (most importantly, Kelvin-Helmholtz instability, cf., Hardee 2000) determine at large the observed structure and dynamics of extragalactic jets (Lobanov et al. 1998; Walker et al. 2001; Lobanov & Zensus 2001; Lobanov et al. 2003; Hardee et al. 2005; Perucho et al. 2006).

The elliptical mode of the instability is responsible for appearance of thread-like features in the jet interior , while overall oscillations of the jet ridge line are caused by the helical surface mode (Lobanov & Zensus 2001). Successful attempts have been made to represent the observed brightness distribution of radio emission on these scales, using linear perturbation theory of Kelvin-Helmholtz instability (Lobanov & Zensus 2001; Lobanov et al. 2003; Hardee et al. 2005) and a spine-sheath (analogous to the two-fluid) description of relativistic flows (Canvin et al. 2005; Laing & Bridle 2004). Non-linear evolution of the instability (Perucho et al. 2004a, 2004b), stratification of the flow (Perucho et al. 2005), and stabilisation of the flow via magnetic field (Hardee 2007) are important for reproducing the observed properties of jets. At larger scales, the helical surface mode of Kelvin-Helmholtz instability is likely to be one of the most important factor for disrupting and destroying the outflows (Lobanov et al. 2003, 2006; Perucho & Lobanov 2007).

2.3. Structure of the magnetic field

The structure of magnetic field in blazar jets can be assessed with VLBI via linear (e.g., Lister & Homan 2005) and circular polarisation (Homan & Lister 2006) measurements. The ultra-compact jets (VLBI cores) are shown to be typically less than 5 % linearly polarised, with the polarisation angle in BL Lac objects showing a stronger tendency to be aligned with the inner jet direction (Lister & Homan 2005). The low degree of polarisation in the VLBI cores can be caused by a disordered magnetic field (Hughes 2005) or strong Faraday de-polarisation (Zavala & Taylor 2004), or result from the "beam de-polarisation" if the magnetic field in the cores is structured on scales much smaller than the resolution of the VLBI experiments.

The fractional linear polarisation in moving jet components grows with increasing distance from the core (Lister & Homan 2005), and the position angle of the polarisation vector is again better aligned with the jet direction in the BL Lac objects. At the same time, the linearly polarised emission in transversely resolved flows displays both strong rotation of the polarisation angle near the core and remarkable edge brightening (e.g., Ros et al. 2000), with the polarisation vectors tending to be perpendicular to the jet direction. This indicates overall complexity and likely stratification of the magnetic field in the jets, with the internal part ("spine") of the flow being dominated by a helical magnetic field further compressed by relativistic shocks, while the external, slower moving layers ("sheath") of the flow could be dominated by a longitudinal magnetic field. This conclusion is in a good agreement with the turnover frequency distribution (Lobanov et al. 1997), internal structure (Lobanov & Zensus 2001), and transverse velocity stratification in the jets (Perucho et al. 2006). Here again, the effect that the flow, and magnetic field, rotation (due to residual angular momentum inherited from the initial disk-to-jet coupling) remains difficult to assess. Presence of a strong toroidal or helical magnetic field either in the spine or in the sheath has also been suggested from observations of Faraday rotation gradients across the flow (Asada et al. 2002; Zavala & Taylor 2005; Attridge et al. 2005; Gómez et al. 2008).

Circular polarisation has been detected in a number of AGN jets (Homan & Lister 2006), with a typical level of polarisation of ≤0.5 %. The circular polarisation can be either intrinsic to the synchrotron emission (Legg & Westfold 1968; implying the presence of a strong relativistic proton component) or result from scintillations (Macquart & Melrose 2000), relativistic effects in dispersive plasma (Broderick & Blandford 2002) or Faraday conversion of linearly polarised synchrotron emission from electron-positron plasma (Jones & O'Dell 1977). The observed properties of circularly polarised emission in blazar jets support the last mechanism for its formation (Wardle et al. 1998; Homan & Lister 2006; Homan et al. 2009).

The strength of the magnetic field in blazar jets is typically assessed by combining multi-band measurements (Unwin et al. 1997), by deriving information about the peak in the synchrotron spectrum (Marscher 1983; Lobanov et al. 1997; Lobanov 1998b; Savolainen et al. 2008; Sokolovsky et al. 2010), or by using the opacity due to synchrotron self-absorption (Lobanov 1998a). In most objects, values around 1 G are obtained for the VLBI cores and lower magnetic field is measured in the jets, all falling well in agreement with magnetic field generation being ultimately processes in the magnetised accretion disk (Field & Rogers 1993).

2.4. Periodic changes of the structure

Structural changes are abound on milliarcsecond scales in the blazar jets, enhanced and magnified by small viewing angles and relativistic effects. In addition to extreme curvature observed in the jet ridge line of some objects (e.g., Polatidis et al. 1995), the position angle of the inner jet (as traced by jet components nearest to the core) changes substantially both as a function of observing frequency (Savolainen et al. 2006; Agudo et al. 2007) and in time (Mutel & Denn 2005; Lobanov & Roland 2005).

The frequency dependent changes are most likely caused by the opacity and spectral index gradients in the flow. The temporal variations of the position angle can result from precession and rotation of the flow (Camenzind et al. 1992) as well as from the pattern motion of Kelvin-Helmholtz instability (Hardee 2003; Hardee et al. 2005), in which case the motion should also be evident in long-term evolution of the ridge line of a flow (e.g., Krichbaum et al. 2001).

Variations of the jet position angle, as well as the observed morphology of parsec-scale jets and trajectories of superluminal features propagating in the jets, are often described in terms of a helical geometry (Steffen et al. 1995), with helicity supposed to be arising from some periodic process in the nucleus. Jet precession, both in sin-

gle and binary black hole systems, have been commonly sought to be responsible for the observed helicity on parsec scales. However, as the observed periods of the position angle changes (and, similarly, periods inferred from the component trajectories and oscillations of the jet ridge lines) are typically within a range of a few years, the precession-based models face severe difficulties (Lobanov & Roland 2005) as they require either allowing for extremely small ($\leq 10^4 R_{\mathrm{g}}$) orbital separations in supermassive binary black holes or adopting an assumption that the jet direction responds exclusively to changes in the innermost parts of the accretion disk and it is decoupled from the spin of the central black hole. In view of these difficulties, rotation of the flow and pattern motion of the instability seem to be more viable alternatives. The precession of the flows, evident on kiloparsec-scales (Gower et al. 1982; Hardee et al. 1994) acts on much longer timescales (typically $\geq 10^4$ yr), typically of several hundred years and longer, and thus should only be visible in long-term changes of the position angle of the entire milliarcsecond-scale jet (Lobanov & Roland 2005).

3. Emission from blazar jets

VLBI observations enable tracing both temporal and spatial changes in radio emission from blazar jets, offering a unique opportunity for connecting these changes to properties of the blazar emission observed in other wavelength domains and even localising spatially the dominant components in the broad-band emission. Emission from jets may also contribute substantially to the broad-band SED (Yuan et al. 2002), alongside with the canonical contributions from the accretion disk and hot material in the vicinity of the central black hole. VLBI observations help here enormously by providing an accurate measure of radio emission produced in these regions and excluding contributions from kiloparsec-scale jets and lobes of radio sources.

3.1. Parsec-scale radio emission

Parsec-scale radio emission is variable on timescales from decades (e.g., O'Dea et al. 1984; Asada et al. 2006) to hours (Savolainen & Kovalev 2008), with the longest timescales most likely related to large-scale changes in the nuclear region feeding the black hole, and the shortest timescales resulting from interstellar scintillations. The variability on hour-to-day timescales may also be related to "quasar QPO" type of variations recently observed in the soft X-ray band (Gierliński et al. 2008), remembering that if variability periods scale with the black hole mass, this would correspond to canonical QPO seen in X-ray binaries at frequencies around 100 Hz.

On intermediate timescales (months-to-years), most of variable radio emission is believed to be associated with flares in the VLBI cores (Lobanov & Zensus 1999) and shock evolution of plasma propagating downstream (Hughes et al. 1985; Marscher & Gear 1985; Marscher

1990). The radio flares last, on average, for 2.5 years (at a wavelength of about 1 cm; Hovatta et al. 2008), and in many objects they are repeated quasi-periodically (Hovatta et al. 2007). The flares are firmly associated with ejections of new jet components (Valtaoja et al. 1999; Lobanov & Zensus 1999; Marscher et al. 2002; Chatterjee et al. 2009), but the release of non-thermal continuum emission may not necessarily be restricted to the vicinity of the black hole or even the radio core (Arshakian et al. 2010; León-Tavares et al. 2010; Schinzel et al. 2010). Detailed evolution of a flaring emission is best determined through variations of its turnover peak (Otterbein et al. 1998; Fromm et al. 2010) and can be further constrained using observed kinematic properties of an emitting region (Lobanov & Zensus 1999).

Quasi-periodic variability of the radio emission from the ultra-compact jets is most likely related to instabilities and non-stationary processes in the accretion disks around central black holes in AGN (Igumenschev & Abramowicz 1999; Lobanov & Roland 2005). Alternative explanations involve binary black hole systems in which flares are caused by passages of the secondary through the accretion disk around the primary (Ivanov et al. 1998; Lehto & Valtonen 1996). Similarly to the attempts of using binary black holes to explain short-term morphological changes, these models require very tight binary systems, with orbits of the secondary lying well within $10^4 R_{\mathrm{g}}$ of the primary, which poses inevitable problems for maintaining an accretion disk around the primary (for massive secondaries; Lobanov 2008) or rapid alignment of the secondary with the plane of the accretion disk (for small secondaries; Ivanov et al. 1999).

3.2. Blazar jets and broad-band continuum

Relativistic flows are prominent emitters in all bands of the electromagnetic spectrum, generating optical and X-ray emission even on kiloparsec scales (Schwartz et al. 2000; Marshall et al. 2002; Siemiginovska et al. 2002; Sambruna et al. 2008) and at TeV energies (Acciari et al. 2010). The jet plasma is believed to emit via synchrotron emission in the radio to soft X-ray range and via inverse Compton emission in the hard X-ray to TeV range (Acciari et al. 2010; Marscher et al. 2010). Contested is, however, the primary source of the seed photons for the inverse Compton part of the radiation. These could be the synchrotron photons themselves (synchrotron self Compton mechanism, SSC) or photons from an external radiation field located, for instance, in the accretion disc emission, X-ray corona, the broad-line region, the infrared emitting torus and the cosmic background radiation (Ghisellini & Tavecchio 2009).

Results from the first year of the *Fermi*/LAT operations have enabled most detailed studies of the connection between relativistic flows and γ-ray production in blazars. Early statistical comparisons of the properties of γ-ray emission and compact radio jets in blazars indicate un-

equivocally that they are closely related (Pushkarev et al. 2009; Savolainen et al. 2010). Several of the γ-ray flares detected with *Fermi*/LAT can be associated with emission from accelerated plasma cloud embedded in the jets (Marscher et al 2010; Schinzel et al. 2010), although detailed localisation of the γ-ray emitting sites remain elusive, clearly calling for continuation of extensive, co-ordinated *Fermi*/LAT and VLBI campaigns.

There is now growing evidence for the broad-band continuum (and its flaring components in particular) to be produced at multiple locations in AGN (Arshakian et al. 2010), with the emission in different bands dominated by contributions from spatially different regions (León-Tavares 2010). These findings put an additional strain on single-zone models commonly used for fitting the broad-band SED in AGN. The situation with the quiescent (and slowly variable) component of the γ-ray emission is also puzzling, with indications that it may be produced in the region of the jet extending up to ∼10 pc (Schinzel et al. 2010).

These results give a compelling indication that formation of jet components may correspond to the strongest nuclear events, while some of them may not survive a passage through a standing shock (León-Tavares et al. 2010). The source of the continuum emission is localised not only in the accretion disk (at the extreme vicinity of the black hole) but also in the entire acceleration zone of the jet, with strong flares happening both near the central black hole and at a standing shock in the jet. Clearly, a more general and systematic study of relation between the radio, optical and X-ray emission in blazars is strongly justified, and co-ordinated VLBI–*Fermi*/LAT campaigns would one of the prime methods for such studies.

4. Outlook

More than thirty years after their appearance on the scientific scene, blazars remain one of the focal points of extragalactic astrophysics. High-resolution radio observations of blazars provide essential information about structure, kinematics and emission of relativistic flows in these objects on scales inaccessible to direct imaging in other bands. This information turns out to be arguably an indispensable tool for constructing viable physical models capable of explaining the blazar phenomenon and its spectacular observational manifestations.

There are still a number of unanswered questions about the jets themselves and their relations to the broad-band emission produced in blazars. Extragalactic jets are an excellent laboratory for studying physics of relativistic outflows and probing conditions in the central regions of active galaxies. Recent studies of extragalactic jets show that they are formed in the immediate vicinity of central black holes in galaxies and carry away a substantial fraction of the angular momentum and energy stored in the accretion flow and rotation of the black hole. The jets are most likely collimated and accelerated by electromagnetic fields. Relativistic shocks are present in the flows on small scales, but dissipate on scales of decaparsecs. Plasma instabilities dominate the flows on larger scales. Convincing observational evidence exists, connecting ejections of material into the flow with instabilities in the inner accretion disks.

In the coming years, new breakthroughs should be coming in studies of relativistic jets and blazars, enriched by *Fermi*/LAT results and by an effective use of the VLBI potential for studies of blazars. There are several potential focal points for these studies.

In particular, the jet composition remains an open issue, in particular with regard to the role of relativistic protons in high-energy emission production in extreme vicinity of the central black holes (while it seems that pair plasma is chiefly responsible for the emission from parsec-scale jets).

Accurate spatial localisation of the sites of high-energy continuum production will play a crucial role for modelling the broad-band SED of blazars and understanding their physical nature in general. To this end, variability of the high-energy continuum emission is best related to structural and radiative changes in parsec-scale radio emission resolved by VLBI observations.

Last but not least, the continued observational quest for reaching ever closer to the regions where the relativistic flows are formed will bring new answers not only about the physical nature of relativistic flows, but also about the physical properties of black holes and their connection to major manifestations of nuclear activity in galaxies. This would be particular important for studies of the γ-ray and TeV emission from blazars, as this emission has all chances to come from the immediate vicinity of the central black holes in galaxies. Combination of high-energy observations with VLBI extensive monitoring at centimetre wavelengths and focused, specific VLBI programs at millimetre wavelengths certainly has a quality of the tool of choice for such studies.

References

Acciari, V.A., Aliu, E., Arlen, T., et al. 2009, Science, 325, 444
Acciari, V.A., Aliu, E., Arlen, T., et al. 2010, ApJ, 716, 819
Agudo, I., Gómez, J.L., Martí, J.-M., et al., 2001, ApJ, 549, 183
Agudo, I., Bach, U., Krichbaum, T.P., et al. 2007, A&A, 476, L17
Alberdi, A., Gómez, J.L., Marcaide, J.M., Marscher, A.P., Pérez-Torres, M.A. 2000, A&A, 361, 529
Arshakian, T.G., León-Tavares, J., Lobanov, A.P., et al. 2010, MNRAS, 401, 1231
Asada, K., Inoue, M., Kameno, S., Nagai, H. 2008, ApJ, 675, 79
Asada, K., Kameno, S., Shen, Z.-Q., et al. 2006, PASJ, 58, 261
Attridge, J.M., Wardle, J.F.C., Homan, D.C. 2005, ApJ, 633, L85
Bach, U., Kadler, M., Krichbaum, T.P., et al., in *Future Directions in High Resolution Astronomy: The 10th Anniversary of the VLBA*, J. Romney, M. Reed (eds.), ASP Conf. Ser., v. 340, p. 30
Becker, P.A., Das, S., Le, T. 2008, ApJ, 677, L93

Blandford, R.D., Königl, A. 1979, ApJ, 232, 34

Blandford, R.D., Levinson, A. 1995, ApJ, 441, 79

Blandford, R.D., Payne, D.G. 1982, MNRAS 199, 883

Blandford, R.D., Znajek, R.L. 1977, MNRAS, 179, 433

Bloom, S.D., Marscher, A.P. 1996, ApJ, 461, 657

Bogovalov, S.V., Tsinganos, V. 2005, MNRAS 357, 918

Broderick, A., Blandford, R. 2002,Ap&SS, 288, 161

Camenzind, M. 2005, MemSAIt, 76, 98

Camenzind, M., Krockenberger, M. 1992, A&A, 255, 59

Canvin, J.R., Laing, R.A., Bridle, A.H., Cotton, W.D. 2005, MNRAS, 363, 1223

Celotti, A., Fabian, A.C. 1993, MNRAS 264, 228

Charlot, P., Gabuzda, D.C., Sol, H., Degrange, B., Piron, F. 2006, A&A, 457, 455

Chatterjee, R., Marscher, A.P., Jorstad, S.G., et al. 2009, ApJ, 704, 1689

Cohen, M.H., Lister, M.L., Homan, D.L., et al. 2007, ApJ, 658, 232

Daly, R.A., Marscher, A.P. 1988, ApJ, 334, 539

D'Arcangelo, F.D., Marscher, A.P., Jorstad, S.G., et al. 2007, ApJ, 659, L10

Falcke, H. 2001, Rev. Mod. Astron., 14, 15

Fendt, C., 1997, A&A, 323, 999

Field, G.B., Rogers, R.D. 1993, ApJ, 403, 94

Fromm, C.M., Ros, E., Savolainen, T., et al. 2010, *(these proceedings, p. 97)*

Ghisellini, G., Tavecchio, F. 2009, MNRAS, 397, 985

Gierlínski, M., Middleton, M., Ward, M., Done, C. 2008, Nature, 455, 369

Gómez, J.L., Alberdi, A., Marcaide, J.M., Marscher, A.P., Travis, J.P. 1994, A&A, 292, 33

Gómez, J.L., Marti, J.M., Marscher, A.P., Ibanez, J.M., Marcaide, J.M. 1995, ApJ, 449, L19

Gómez, J.L., Marscher, A.P., Alberdi, A., et al. 2001, ApJ, 561, 161

Gómez, J.L., Marscher, A.P., Jorstad, S.G., Agudo, I., Roca-Sogorb, M. 2008, ApJ, 681, L69

Gower, A.C., Gregory, P.C., Unruh, W.G., Hutchings, J.B. 1982, ApJ, 262, 478

Hardee, P.E. 2000, ApJ, 533, 176

Hardee, P.E. 2003, ApJ, 597, 798

Hardee, P.E. 2007, ApJ, 664, 26

Hardee, P.E., Cooper, M.A., Clark, D.A. 1994, ApJ, 424, 126

Hardee, P.E., Walker, R.C., Gómez, J.L. 2005, ApJ, 620, 646

Hirotani, K. 2005, 619, 73

Hirotani, K., Iguchi, S., Kimura, M, Wajima, K. 2000, ApJ, 545, 100

Homan, D.C., Lister, M.L. 2006, AJ, 131, 1262

Homan, D.C., Lister, M.L., Kellermann, K.I., et al. 2003, ApJL, 589, L9

Homan, D.C., Kovalev, Y.Y., Lister, M.L., et al. 2006, ApJ, 642, 115

Homan, D.C., Lister, M.L., Aller, H.D., Aller, M.F., Wardle, J.F.C. 2009, ApJ, 696, 328

Hovatta, T., Tornikoski, M., Lainela, M., et al. 2007, A&A, 469, 899

Hovatta, T., Nieppola, E., Tornikoski, M., et al. 2008, A&A, 485, 51

Hughes, P.A. 2005, ApJ, 621, 635

Hughes, P.A., Aller, H.D., Aller, M.F. 1985, ApJ, 298, 301

Hujeirat, M. Livio, M. Camenzind,M., et al. 2003, A&A 408, 415

Hutter, D.J., Mufson, S.L. 1986, ApJ, 301, 50

Ivanov, P.B., Igumenschev, I.V., Novikov, I.D. 1998, ApJ 507 131

Ivanov, P.B., Papaloizou, J.C.B., Polnarev, A.G. 1999, MNRAS 307, 79

Igumenschev, I.V., Abramowicz, M.A. 1999, MNRAS 303, 309

Jones, T.W., O'Dell, S.I. 1977, ApJ, 214, 522

Jorstad, S.G., Marscher, A.P., Mattox, J.R., et al. 2001, ApJS, 134, 181

Jorstad, S.G., Marscher, A.P., Lister, M.L., et al. 2005, AJ, 130, 1418

Jorstad, S.G., Marscher, A.P., Larionov, V.M., et al. 2010, ApJ, 715, 362

Junor, W., Biretta, J.A., Livio, M. 1999, Nature 401, 891

Kadler, M., Ros. E., Lobanov, A.P., et al. 2004, A&A, 426, 481

Kellermman, K.I., Lister, M.L., Homan, D.C., et al. 2004, AJ, 609, 539

Königl, A. 1981, ApJ 243, 700

Koide, S., Shibata, K., Kudoh, T., et al., 2002, Science 295, 1688

Komissarov, S.S. 2005, MNRAS 359, 801

Kovalev, Y.Y., Kellermann, K.I., Lister, M.L., et al. 2005, AJ, 130, 2473

Kovalev, Y.Y., Lobanov, A.P., Pushkarev, A.B., Zensus, J.A. 2008, A&A, 384, 759

Krichbaum, T.P., Graham, D.A., Witzel, A., et al. 2001, in *Particles and Fields in Radio Galaxies*, R.A. Laingm K.M. Blundell (eds.), ASP Conf. Ser., v. 250, p. 184

Krichbaum, T.P., Lee, S.S., Lobanov, A.P., Marscher, A.P., Gurwell, M.A. 2008, in *Extragalactic Jets: Theory and Observation from Radio to Gamma Ray*, T.A. Rector, D.S. De Young (eds)., ASP Conf. Ser., v. 386, p. 186

Laing, R.A., Bridle, A.H. 2004, MNRAS, 348, 1459

Lähteenmäki, A., Valtaoja, E., Wiik, K. 1999, ApJ, 511, 112

Lee, S.-S., Lobanov, A.P., Krichbaum, T.P., et al. 2008, AJ, 136, 159

Legg, M.P.C., Westfold, K.C., 1968, ApJ, 154, 499

Lehto, H.J., Valtonen, M.J. 1996, ApJ 460, 207

León-Tavares, J., Lobanov, A.P., Chavushyan V.H., et al. 2010, ApJ, 715, 355

Lister, M.L., Homan, D.C. 2005, AJ, 130, 1389

Lister, M.L., Cohen, M.H., Homan, D.C., et al. 2009, AJ, 138, 1874

Lobanov, A.P. 1998, A&A 390, 79

Lobanov, A.P. 1998, A&AS 132, 261

Lobanov, A.P. 2007, Ap&SS, 311, 263

Lobanov, A.P. 2008, Mem.S.A.It. 79, 1062

Lobanov, A.P., Roland, J. 2005, A&A 431, 831

Lobanov, A.P., Zensus, J.A. 1999, ApJ, 521, 590

Lobanov, A.P., Zensus, J.A. 2006, in *Exploring the Cosmic Frontier: Astrophysical Instruments for the 21*[st] *Century*, ESO Astrophysical Symp. Series, ed. by A.P. Lobanov, J.A. Zensus, C. Cesarsky, P.J. Diamond (Springer, Heidelberg) p. 147

Lobanov, A.P., Zensus, J.A. 2001, Science, 294, 128

Lobanov, A.P., Carrara, E., Zensus, J.A. 1997, VA, 41, 253

Lobanov, A.P., Hardee, P.E., Eilek, J.A. 2003, NewAR, 47, 629

Lobanov, A.P., Krichbaum, T.P., Witzel, A., et al. 1998, A&A, 340, 60

Lobanov, A.P., Krichbaum, T.P., Graham, D.A., et al. 2000, A&A, 364, 39

Lobanov, A.P., Krichbaum, T.P., Witzel, A., Zensus, J.A. 2006, PASJ, 58, 253

Mandal, S., Chakrabarti, S.K. 2008, ApJ, 689, L17

Marscher, A.P. 1990, in *Parscec-scale radio jets*, J.A. Zensus, T.J. Pearson (eds.), (Cambridge: CUP), p. 236

Marscher, A.P., PNAS, 92, 11439

Marscher, A.P. 2005, Mem.S.A.It. 76, 13

Marscher, A.P. 1983, ApJ, 264, 296

Marscher, A.P., Gear, W.K. 1985, ApJ, 298, 114

Marscher, A.P., Jorstad, S.G., Gómez, J.L., et al. 2002, Nature 417, 625

Marscher, A.P., Jorstad, S.G., D'Arcangelo, F.D., et al. 2008, Nature, 452, 966

Marscher, A.P., Jorstad, S.G., Larionov, V.M., et al. 2010, ApJ, 710, 126

Marshall, H.L., Miller, B.P., Davis, D.S., et al. 2002, ApJ, 564, 683

Macquart, J.-P., Melrose, D.B. 2000, ApJ, 545, 842

Meier, D.L. 1999, ApJ, 522, 753

Meier, D.L. 2003, New Astron. Rev., 47, 667

Meier, D.L. 2009, in *Approaching Micro-Arcsecond Resolution with VSOP-2: Astrophysics and Technologies*, Y. Hagiwara, E. Fomalont, M. Tsuboi, Y. Murata (eds.), ASP Conf. Ser., v. 402, p. 342

Merloni, A., Fabian, A.C. 2002, MNRAS 332, 165

Middelberg, E., Bach, U. 2008, Reports on Progress in Physics, v. 71, p. 066901.

Mutel, R.L., Denn, G.L. 2005, ApJ, 623, 79

O'Dea, C.P., Dent, W.A., Balonek, T.J. 1984, ApJ, 278, 89

Otterbein, K., Krichbaum, T.P., Kraus, A., et al. 1998, A&A, 334, 489

Perucho, M., Lobanov, A.P. 2007, A&A 469, 23

Perucho, M., Martí, J.M. 2007, MNRAS, 382, 526

Perucho, M., Hanasz, M., Martí, J.-M., et al. 2004, A&A, 427, 415

Perucho, M., Martí, J.-M. Hanasz, M., 2004, A&A, 427, 431

Perucho, M., Martí, J.-M., Hanasz, M., 2005, A&A, 443, 863

Perucho, M., Lobanov, A.P., Martí, J.-M., Hardee, P.E. 2006, A&A, 456, 493

Piner, B.G., Edwards, P.G. 2004, ApJ, 600, 115

Polatidis, A.G., Wilkinson, P.N., Xu, W., et al. 1995, ApJS, 98, 1

Pushkarev, A.B., Kovalev, Y.Y., Lister, M.L., Savolainen, T. 2009, A&A, 507, L33

Reynolds, C.S., Fabian, A.C., Celotti, A., Rees, M.J. 1996, MNRAS, 283, 873

Ros, E., Zensus, J.A., Lobanov, A.P., 2000, A&A, 354, 55

Sambruna, R.M., Donato, D., Cheung, C.C., Tavecchio, F., Maraschi, L. 2008, ApJ, 684, 862

Savolainen, T., Kovalev, Y.Y. 2008, A&A, 489, L33

Savolainen, T., Wiik, K., Valtaoja, E., et al. 2006, ApJ, 647, 172

Savolainen, T., Wiik, K., Valtaoja, E., Tornikoski, M. 2008, in *Extragalactic Jets: Theory and Observation from Radio to Gamma Ray*, T.A. Rector, D.S. De Young (eds.), ASP Conf. Ser., v. 386, p. 451

Savolainen, T., Homan, D.C., Hovatta, T., et al. 2010, A&A, 512, A24

Schinzel, F.K., Lobanov, A.P., Taylor, G.B., et al. 2010, *(these proceedings, p. 175)*

Schwartz, D.A., Marshall, H.L., Lovell, J.E.J., et al. 2000, ApJ, 540, 69

Semenov, V., Dyadechkin, S., Punsly, B. 2004, Science, 305, 978

Siemiginowska, A., Bechtold, J., Aldcroft, T.L., et al. 2002, ApJ, 570, 543

Sikora, M., Begelman, M.C., Madejski, G.M., et al., 2005, ApJ 625, 72

Sokolovsky, K.V., Kovalev, Y.Y., Lobanov, A.P., et al. 2010, *(these proceedings, p. 167)*

Soldi, S., Türler, M., Paltani, S., et al. 2008, A&A, 486, 41

Spruit, H.C., Foglizzo, T., Stehle, R. 1997, MNRAS 288, 333

Steffen, W., Zensus, J.A., Krichbaum, T.P., et al. 1995, A&A, 302, 335

Takahashi, R. 2009, in *Approaching Micro-Arcsecond Resolution with VSOP-2: Astrophysics and Technologies*, Y. Hagiwara, E. Fomalont, M. Tsuboi, Y. Murata (eds.), ASP Conf. Ser., v. 402, p. 321

Unwin, S.C., Wehrle, A.E., Lobanov, A.P., et al. 1997, ApJ, 480, 596

Valtaoja, E., Lähteenmäki, A., Teräsranta, H., Lainela, M. 1999, ApJS, 120, 95

Vlahakis, N., Königl, A. 2004, ApJ, 605, 656

Walker, R.C., Dhawan, V., Romney, J.D., et al., 2000, ApJ 530, 233

Walker, R.C., Benson, J.M., Unwin, S.C., et al. 2001, ApJ, 556, 756

Wardle J.F.C., Homan, D.C., Ojha, R., Roberts, D.H. 1998, Nature, 395, 457

Yuan, F., Markoff, S., Falcke, H. 2002, A&A, 383, 854

Zavala, R.T., Taylor, G.B. 2004, ApJ, 612, 749

Zavala, R.T., Taylor, G.B. 2005, ApJ, 626, L73

Zensus, J.A. 1997, Ann. Rev. Astron. Astrophys., 35, 607

Parsec-scale jet properties of Fermi-detected AGN

M. L. Lister

Purdue University, 525 Northwestern Ave., West Lafayette IN, 47907 USA

Abstract. The continuous, all-sky coverage of the gamma-ray sky provided by the Fermi mission has been of remarkable benefit to the study of blazars, not only because of its rich public data stream, but also by providing a rallying point for numerous supporting multi-wavelength surveys. One of the most impressive examples thus far has been the combination of Fermi and VLBI radio data, which holds great promise for ultimately determining the nature and locations of gamma-ray emission regions in AGN. This has already been demonstrated via the large degree of overlap seen between the Fermi 1FGL catalog and statistically complete VLBI surveys such as the VLBA Calibrator Survey, MOJAVE and TANAMI. In this review I will discuss our current understanding of the factors that go into making a particular AGN gamma-ray loud, which include relativistic beaming, intrinsic jet power, duty cycle and flaring state. Special attention will be paid to the role of selection effects in both radio and gamma-ray blazar surveys, and how they can influence and create trends in flux-limited samples. Finally, I will mention several recent observational results that have found a good connection in blazars between the parsec-scale radio jet (e.g., superluminal speed, compactness, and morphology) and the high energy gamma-ray emission.

1. Introduction

One of the most impressive initial findings of the *Fermi* observatory has been a remarkable correspondence between the extragalactic sky at gamma-ray and radio wavelengths. The prevalence of 1st Fermi catalog sources (1FGL; Abdo et al. 2010c) that are associated with compact, flat-spectrum radio sources has provided a strong confirmation of the relativistic beaming model for AGN. The effects of Doppler boosting on the observed synchrotron and inverse-Compton flux from AGN jets strongly biases the distribution of the brightest extragalactic gamma-ray and high frequency radio sources towards fast jets aligned closely with our line of sight (blazars). Here I discuss results from an ongoing monitoring program (MOJAVE; Monitoring of Jets in Active Galactic Nuclei with VLBA Experiments) that aims to investigate beaming effects in both these energy regimes via regular Very Long Baseline Array (VLBA) observations of parsec-scale radio jets in two large flux-limited blazar samples.

2. Variability and Blazar Samples

The highly variable nature of blazars has made them compelling objects for detailed study, since changes in the time domain can provide strong constraints on physical models for their emission and underlying structure. At the same time, blazar variability creates problems for statistical population studies, as changes in their spectral energy distribution and activity state can frequently move many blazars in and out of survey sensitivity limits. The notion of a 'complete' blazar sample thus becomes fuzzy, and the presence of variability-induced biases can complicate statistical analyses of blazar properties. During the EGRET era these were especially problematic, given

the telescope's unequal temporal and sensitivity coverage for different regions of the sky. The small number of blazars that were discovered, however, provided a tantalizing glimpse of the wealth of information on blazar demographics that could be obtained with a more sensitive detector with all-sky monitoring capabilities. EGRET also revealed a strong connection between gamma-ray flux and highly-beamed jet emission in some blazars, which suggested that at fainter emission levels, the extragalactic sky would be dominated by flat-spectrum, compact radio sources.

3. The MOJAVE Program

In anticipation of the *Fermi* mission, we undertook a program (MOJAVE: Lister & Homan 2005, Lister et al. 2009b) to assemble the most complete sample possible of AGN that could be observed relatively easily on a regular basis with the VLBA. This meant choosing radio sources located at sufficiently high declinations that were bright enough for direct fringe detection on short integration times. Because of its long interferometric baselines, the VLBA effectively filters out diffuse radio emission, guaranteeing that this sample would be dominated by compact radio sources. As a further discriminator against steep-spectrum diffuse emission, we carried out the selection at a relatively high radio frequency (15 GHz).

Unlike blazar surveys in the optical or soft X-ray regimes, the radio emission from the brightest radio-loud blazars is not substantially obscured by or blended with emission from the host galaxy. Our VLBA-selected sample thus provides a relatively 'clean' blazar sample, namely, one selected on the basis of beamed synchrotron jet emission. The sole exceptions are the inclusion of one or two young, GHz-peaked spectrum (GPS) AGN. These sources have highly luminous 'mini-lobes' on parsec-scales that
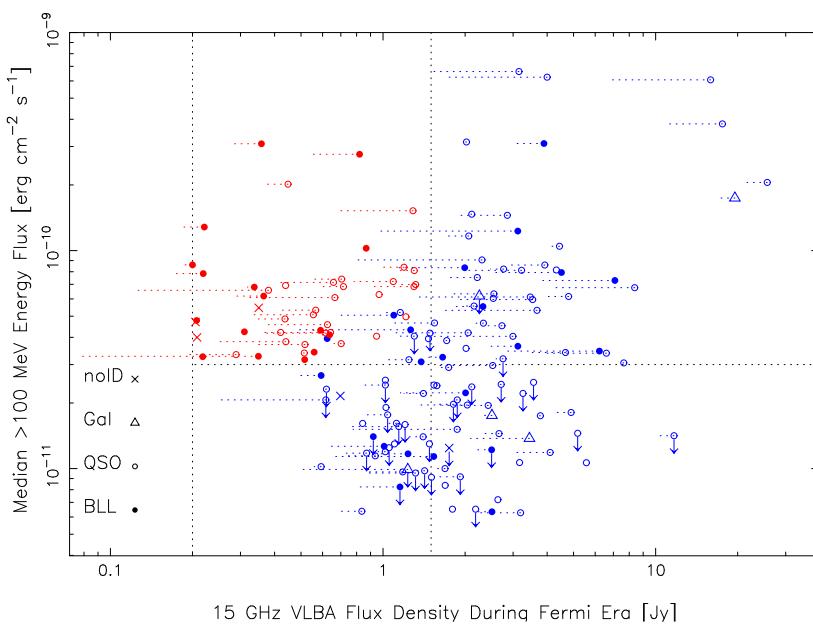
Fig. 1. Median 11 month LAT energy flux above $100\,\mathrm{MeV}$ versus $15\,\mathrm{GHz}$ VLBA flux density for sources in the MOJAVE (blue symbols) and 1FM samples. Sources above the horizontal dashed line are in the gamma-ray limited 1FM sample. The red symbols (upper left quadrant) are 1FM sources that are not members of the MOJAVE flux-limited sample. The symbol shapes correspond to optical classifications, where triangle = radio galaxy, open circle = quasar, closed circle = BL Lac, cross = unidentified. The symbols are plotted at the locations of maximum measured VLBA flux density since Fermi launch, and the dotted lines extend to the minimum flux density. No dotted lines are plotted for sources with only one VLBA epoch. Gamma-ray upper limits are from Kadler et al. (in preparation). There are 11 MOJAVE sources that are not plotted since they did not have upper limit determinations.

aren't strongly beamed, but instead are bright because they are interacting with dense gas in their inner host galaxy regions (O'Dea 1998).

In order to ensure a high overlap with *Fermi* and other blazar samples, we wished to include in MOJAVE all blazars down to a specified radio flux density limit. The use of a lower flux-density cutoff in astronomical surveys is often dictated by practical concerns such as detector sensitivity or available observing time, but it also plays an important role in luminosity function studies and source population simulations. A well-recognized downside is its introduction of a luminosity (Malmquist) bias, in which the average luminosity of sources increases with redshift, but well-defined flux limits are essential in blazar population studies, where the same objects are sampled in a variety of surveys at different wavelengths. With blazars also comes the difficulty of substantial flux variability. How does one compare data from different wavelength surveys that are not co-temporaneous, let alone account for the presence/absence of objects in high or low states in a single wavelength survey?

One method of dealing with variable flux populations is to consider a wide time window during which any source that exceeds the flux limit is included in the sample. Although this can potentially introduce a different kind of bias towards highly flaring sources, it has been effectively used in the 1FGL catalog (Abdo et al. 2010c) and in past radio blazar surveys (e.g., VSS: Wehrle et al. 1992 and 2 Jy Metsähovi: Valtaoja et al. 1992). It generally requires a large set of well-sampled flux density monitoring data. Fortunately we had a large archive of VLBA and single-dish (UMRAO and RATAN) radio flux density measurements of bright AGN ranging from 1994.0 to 2004.0 from which we could formulate the final MOJAVE sample. Any AGN with declination above $-20°$ with measured or inferred $15\,\mathrm{GHz}$ VLBA density that exceeded 1.5 Jy (2 Jy for declinations $< 0°$) during this period was included. In order to obtain an even larger overlap with *Fermi* we are currently extending the sample down to 1.5 Jy above declination $-30°$ for all epochs from 1994.0 to the present.

4. Connections with Fermi

The *Fermi*/LAT instrument has proved to be a remarkable tool for blazar studies by providing continuous high-energy monitoring of the entire sky. This has not only provided an indispensable rallying point for multi-wavelength observing campaigns, but has made it possible to construct large and reasonably complete gamma-ray blazar samples. There are still some issues related to source confusion and varying detector response across the energy bands (see, e.g., Abdo et al. 2010b), but in general the 1st LAT AGN catalog (1FGL) represents a significant leap forward in the study of blazar demographics.

The 1FM sample We have used the 1FGL to construct a gamma-ray flux-limited blazar sample in much the same fashion as MOJAVE. We began by eliminating all the 1FGL sources known to be associated with non-extragalactic objects, as well as one gravitationally lensed AGN (0218+357 = 1FGL J0221.0+3555). We excluded all sources below declination $-30°$ and within $10°$ of the galactic plane, and kept all that had a median 11 month $> 100\,\mathrm{MeV}$ energy flux above $3 \times 10^{-11}\,\mathrm{MeV\,cm^{-2}\,s^{-1}}$. This level was chosen to provide a sample similar in size to MOJAVE. At this point there were 123 candidate AGN. However, to ensure direct fringe detection with the VLBA it was necessary to impose a VLBA radio flux density criterion of $S_{15\,\mathrm{GHz}} > 0.2\,\mathrm{Jy}$, met at any epoch between the start of LAT science observations (2008 Aug 10) to 2009 Dec 31. This left 98 1FGL sources with known ra-

dio AGN associations in the final sample, which we have called the first Fermi-MOJAVE (1FM) sample (Lister et al., in prep.).

In Fig. 1 we plot the 11 month median Fermi energy flux against VLBA 15 GHz flux density for the 1FM and MOJAVE sample AGNs located outside the $\pm 10°$ galactic plane region. The horizontal and vertical dashed lines denote the flux limits of the samples. The VLBA flux density sampling is much less dense than the Fermi sampling, with typically fewer than 5 epochs per source, thus the former data are represented by high-low bars rather than median values. It is for this reason that the radio-gamma-ray correlation appears much poorer here than those reported in other papers (e.g., Kovalev et al. 2009, Abdo et al. 2010a, Pushkarev et al., these proceedings, p. 163). In this sky region, two-thirds of the MOJAVE sample are either in the 1FGL or have been detected by the LAT at slightly lower confidence level (Kadler et al., in prep.), and one third (42 AGN) are members of the 1FM. Given the previous findings of strong correlations between relativistically beamed jet emission and gamma-ray flux density in blazars, these fractions might appear lower than expected. We discuss possible reasons for this below.

Radio-weak gamma-ray blazars Slightly more than half of the gamma-ray-limited 1FM sample consists of AGN that are not in the flux-limited MOJAVE sample (red symbols in the upper left quadrant of Fig. 1), implying that they have lower than average radio-to-gamma-ray flux ratios. All of them lie below the MOJAVE limit (1.5 Jy), which rules out the possibility that some were radio weak in 1994–2004 but have recently brightened. A well-represented blazar class in the 1FGL discussed by Abdo et al. (2010b) are the high-spectral peaked (HSP) objects, whose synchrotron and inverse-Compton peaks in a $\nu\,F_\nu$ vs. ν plot are shifted to higher frequencies, thus lowering their radio-to-GeV flux ratios. According to the SED classifications of Abdo et al. (2010b), only 10 of the 56 AGN in the upper left quadrant of Fig. 1 are known to be HSP or ISP, however. This reflects an overall trend seen in the 1FGL that the fraction of HSP drops as one goes to higher gamma-ray fluxes.

What could therefore be responsible for the low radio-to-GeV flux ratios in the low-spectral energy peaked non-MOJAVE-1FM sources as compared to the MOJAVE-1FM sources? There are no major differences in their redshift distributions, according to a Kolmogorov-Smirnov test. One possibility is that the gamma-ray emission from blazars is boosted by a higher power of the Doppler factor than their radio emission, as in the case of the external Compton model of Dermer et al. (1995). This would then imply a lower radio-to-GeV for higher Doppler factor blazars. We are investigating this scenario by gathering VLBA epochs on the non-MOJAVE 1FM sources to determine their superluminal speeds. High-frequency radio monitoring on these sources will also be useful for obtaining their variability Doppler factors (e.g., Hovatta et

al. 2009). An alternative explanation that can be checked with longer Fermi time baselines and simultaneous VLBA flux density data is that the median gamma-ray fluxes of these sources are elevated due to short-duration flares that don't propagate down to the radio regime.

Gamma-ray weak radio blazars Although the *Fermi*/LAT-detected fraction of the flux-limited MOJAVE sample increased substantially between the 3-month list (Abdo et al. 2009 and 1FGL catalogs, fully one-third of these radio-bright MOJAVE AGN have not yet been detected by *Fermi* . These are indicated by upper limit arrows in Fig. 1 (11 non-detected MOJAVE sources are omitted from the plot since they do not yet have *Fermi* upper limit values). In only a small fraction of the cases (less than $\sim 15\%$) the non-detection may be attributed to crowding/source confusion (Kadler et al., in prep.). The remainder appear to have genuinely high radio-to-GeV flux ratios.

An obvious question to ask is whether these sources are the lower-Doppler factor counterparts to the sources discussed in § 4. A useful diagnostic is to plot the jets in the apparent-speed versus apparent radio luminosity plane (Fig. 2). The upper envelope in the distribution is likely a consequence of relativistic beaming and an intrinsic correlation between the speed and radio luminosity of blazar jets (Cohen et al. 2007, Lister et al. 2009b). Plotted on the diagram are two parametric curves that show the positions of a single jet as it is varied in viewing angle from 0 to 25 degrees. The outer curve is for Lorentz factor 40 and an unbeamed luminosity of 10^{25} W Hz^{-1}, while the inner curve is drawn for a jet with Lorentz factor 20 and an unbeamed luminosity of 3×10^{25} W Hz^{-1}. These curves are not fits to the data, but serve only to illustrate the effects of viewing angle and relativistic beaming.

Although there are some individual exceptions, there is a general trend that the sources closest to the outer curve are in the 1FM (filled circles), i.e., they are among the brightest *Fermi* AGN. *Fermi* has so far detected every single jet in the MOJAVE sample with superluminal speed above 20c. Another apparent trend is that the non-detections are clustered in the center of the plot, below the $\Gamma = 20$ curve. The main exceptions are the GPS source 0642+449 at 10^{29} W Hz^{-1}, the two-sided radio galaxy NGC 1052 at $10^{22.7}$ W Hz^{-1}, and the unusual radio galaxy III Zw 2 at $10^{25.3}$ W Hz^{-1}. The parsec-scale properties of these outlier sources are known to be consistent with their jets being aligned close to the plane of the sky (Lister et al. 2009a, 2009b).

By examining the kiloparsec-scale structure of the MOJAVE sample with deep VLA images, Cooper (2010) has found a positive correlation between kiloparsec-scale radio flux density and gamma-ray flux. Since the former has been shown to be a good indicator of intrinsic jet power (e.g., Giovannini et al. 1988), this suggests that there may be a minimum jet power that is required to produce a bright gamma-ray blazar. Some of the Fermi non-detections in MOJAVE may therefore have high Doppler
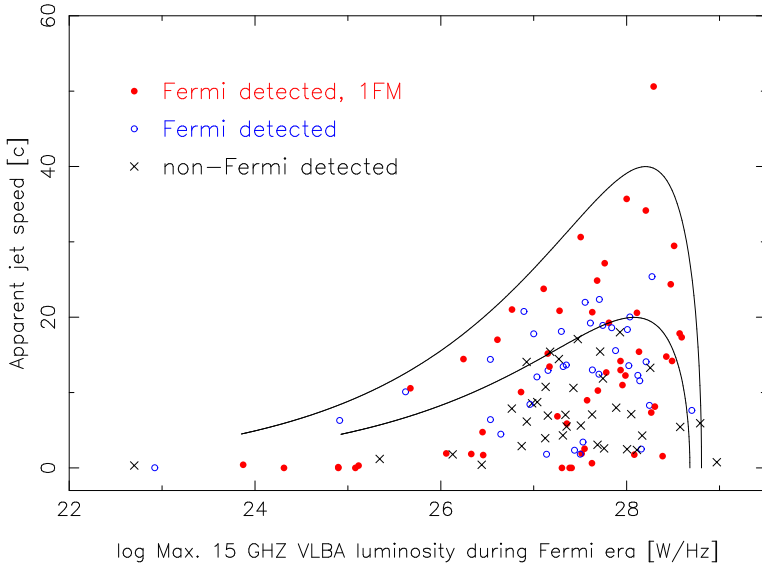
Fig. 2. Maximum measured jet speed versus maximum 15 GHz VLBA luminosity during the Fermi era for the flux-limited MOJAVE sample. The red filled circles indicate 1FM sources, the open circles LAT-detected non-1FM sources, and the crosses Fermi non-detections. The outermost solid curve shows the locus of points for a jet with Lorentz factor 40 and an unbeamed luminosity of 10^{25} W Hz^{-1} as it is varied in angle from 0 to 25 degrees from the line of sight. The inner curve is drawn for a jet with Lorentz factor 20 and an unbeamed luminosity of 3×10^{25} W Hz^{-1}. The luminosity is boosted by the Doppler factor squared in both cases.

factors, but low intrinsic jet power. Another piece of the puzzle may come from the recent findings of Savolainen et al. (2010), who found a deficiency in the expected number of *Fermi* sources oriented a very small angles to the line of sight. In a flux-limited radio blazar sample, these small-angle, high Doppler-boosted sources have lower-than-average intrinsic radio luminosities (Lister & Marscher 1997), and thus may not be expected to be as gamma-ray bright. With continued *Fermi* observations, it should be possible to determine which sources fall into this category, and which may simply be in a temporary low-gamma-ray state for their given radio luminosity level.

5. Summary

The *Fermi* observatory has opened up many new avenues for exploring the statistical properties of blazars by providing excellent temporal and spatial coverage of the gamma-ray sky. Numerous challenges remain however, in unraveling the effects of beaming and Doppler bias in flux-limited blazar samples constructed in different energy regimes. As new improved determinations of superluminal speeds and Doppler factors from VLBI (e.g., Lister et al. 2009a; Ojha et al. 2010; Jorstad et al. 2007) and single-dish monitoring programs (e.g., Aller et al., these proceedings, p. 65 ; Richards et al. 2009; Angelakis et al. 2009; Kovalev et al. 2006) are being obtained, we can look forward to continued insight into the connection between parsec-scale radio and gamma-ray emission in blazars.

References

Abdo, A. A., Ackermann, M., Ajello, M., et al. 2009, ApJS, 183, 46

Abdo, A. A., Ackermann, M., Ajello, M., et al. 2010, ApJ, 715, 429

Abdo, A. A., Ackermann, M., Agudo, I., et al. 2010, ApJ, 716, 30

Abdo, A. A., Ackermann, M., Ajello, M., et al. 2010, ApJS, 188, 405

Angelakis, E., Fuhrmann, L., Zensus, J. A., et al. 2009, in *Accretion and Ejection in AGN: A Global View*, eds. L. Maraschi, G. Ghisellini, R. Della Ceca, & F. Tavecchio, ASP Conf. Ser., in press, (San Francisco: ASP) [arXiv:0910.0643]

Cooper, N. 2010, Ph.D. thesis, Purdue University

Cohen, M. H., Lister, M. L., Homan, D. C., et al. 2007, ApJ, 658, 232

Dermer, C. D. 1995, ApJ, 446, L63

Giovannini, G., Feretti, L., Gregorini, L., & Parma, P. 1988, A&A, 199, 73

Hovatta, T., Valtaoja, E., Tornikoski, M., Lähteenmäki, A. 2009, A&A, 494, 527

Jorstad, S. G., Marscher, A. P., Stevenson, J. A., et al. 2007, AJ, 134, 799

Kovalev, Y. A., & Kovalev, Y. Y. 2006, ASP Conf. Ser., 360, 137

Kovalev, Y. Y., Aller, H. D., Aller, M. F., et al. 2009, ApJ, 696, L17

Lister, M. L. & Homan, D. C. 2005, AJ, 130, 1389

Lister, M. L. & Marscher, A. P. 1997, ApJ, 476, 572

Lister, M. L., Aller, H. D., Aller, M. F., et al. 2009, AJ, 137, 3718

Lister, M. L., Cohen, M. H., Homan, D. .C., et al. 2009, AJ, 138, 1874

O'Dea, C. P. 1998, PASP, 110, 493

Ojha, R., Kadler, M., Böck, M., et al. 2010, A&A, in press [arXiv:1005.4432]

Richards, J. L., Max-Moerbeck, W., Pavlidou, V., et al. 2009, in *2009 Fermi Symposium*, eConf Proceedings C091122 [arXiv:0912.3780]

Savolainen, T., Homan, D. C, Hovatta, T., et al. 2010, A&A, 512, A24

Valtaoja, E., Lähteenmäki, A., & Teräsranta, H. 1992, A&AS, 95, 73

Wehrle, A. E., Cohen, M. H., Unwin, S. C., Aller, H. D., Aller, M. F., & Nicolson, G. 1992, ApJ, 391, 589

Radio/gamma-ray time delay in the cores of AGN

A. B. Pushkarev[1,2,3], Y. Y. Kovalev[4,1], and M. L. Lister[5]

[1] Max-Planck-Institut für Radioastronomie, Auf dem Hügel 69, 53121 Bonn, Germany
[2] Pulkovo Observatory, Pulkovskoe Chaussee 65/1, 196140 St. Petersburg, Russia
[3] Crimean Astrophysical Observatory, 98409 Nauchny, Crimea, Ukraine
[4] Astro Space Center of Lebedev Physical Institute, Profsoyuznaya 84/32, 117997 Moscow, Russia
[5] Department of Physics, Purdue University, 525 Northwestern Avenue, West Lafayette, IN 47907, USA

Abstract. We report on detecting a non-zero time delay between radio emission measured by the VLBA at 15.4 GHz and γ-ray radiation (γ-ray leads radio) registered by the Large Area Telescope (LAT) on board the Fermi Space Observatory for a sample of 183 radio and γ-ray bright active galactic nuclei (AGNs). For the correlation analysis we used 100 MeV–100 GeV γ-ray photon fluxes, taken from the monthly binned measurements from the first Fermi-LAT catalog, and flux densities of the compact core. The correlation is most pronounced if the parsec-scale core flux density is used, strongly indicating that γ-ray emission is generated within a compact region of the 15 GHz VLBA core. Determining the Pearson's r and Kendall's τ correlation coefficients for different time lags, we found that for the majority of sources the radio/γ-ray delay ranges from 1 to 8 months and peaks at 2.5 months in the observer's frame and at about 1.2 months in the source's frame.

1. Introduction

Long-term systematic observations of active galactic nuclei (AGN) resulted in accumulation of data over decades making the obtained light curves to be a powerful tool for investigating the nature of this type of objects. AGNs show variability across the full electromagnetic spectrum and monitoring programs carried out at different wavelengths help to establish connections of flux variation at different energy bands, which is important not only for constructing the models but also for planning multi-wavelengths campaigns.

The first comparison between long-term records of radio (10.7 GHz) and optical fluxes for a sample of 24 variable extragalactic sources (Pomphrey et al. 1976) analysis showed that the correlation was found only for 13 sources with the optical events preceeding radio by intervals ranging from 0 to 14 months. Later analysis of internally consistent light curves for 18 AGNs taken in optical and radio (4.6–14.5 GHz) domains (Clements et al. 1995) demonstrated similar statistics: nine sources manifested positive radio-optical correlations, with the the time lag ranging from 0 to 14 months. Tornikoski et al. (1994) reported on a correlation in 10 out 22 sources comparing optical and radio (22–230 GHz) observations. Remarkably, in 6 sources the optical and high-frequency radio variability was simultaneous. More recent statistical study of the time delay between individual millimeter- and centimeter-wave flare peaks made by Hovatta et al. (2008) for a sample of 55 sources showed a large scatter of the time lags that ranges up to several hundreds of days between 4.8 and 230 GHz and tends to increase with decreasing of frequency. Jorstad et al. (2010) investigated flaring behavior of the quasar 3C 454.3 and showed that optical outbursts are ahead of the 230 GHz flares by 15–50 days, confirm-

ing earlier results by Raiteri et al. (2008) of the millimeter flux changes lagging behind the optical ones on a time scale of about 60 days. A longer delay of about ten months in this source was detected between optical and 37 GHz radio flux variations (Volvach et al. 2008).

The *Fermi Gamma-Ray Space Telescope* successfully launched in June 2008 has opened a new era in the γ-ray astronomy. A number of AGN radio/γ-ray connections have been recently established on a basis of first three months of the *Fermi* science operations and quasi-simultaneous VLBI observations: γ-ray photon flux correlates with the parsec scale radio flux density (Kovalev et al. 2009), the jets of the LAT-detected blazars have higher-than-average apparent speed with a median of $15\,c$ (Lister et al. 2009a), larger apparent opening angles with a median of $20°$ (Pushkarev et al. 2009), and higher variability Doppler factors with a mean of 20 (Savolainen et al. 2010). In addition, AGN jets tend to be found in a more active radio state within several months from LAT-detection of their strong γ-ray emission (Kovalev et al. 2009). A significant correlation was detected even between non-simultaneous measurements of $0.1 - 100$ GeV photon flux and 8 GHz VLBA flux density (Kovalev 2009). Nonetheless, there are several key questions to address by future studies that include: (i) the dominant production mechanisms of γ-ray photons, (ii) the exact site location of high-energy emission, (iii) AGN γ-ray duty cycle. Here we investigate the radio/γ-ray time delays for parsec-scale jets and put constrains on the localization of the region where most of the γ-ray photons are produced in AGNs.

2. The radio data and source sample

The MOJAVE program (Lister et al. 2009b) is a long-term VLBA project to study the total intensity structure changes and polarization evolution of extragalactic relativistic radio jets in the northern sky. The observed sources include a statistically complete, flux-density limited sample of 135 AGNs (MOJAVE-1). All the MOJAVE-1 sources have J2000 declination $\delta > -20°$ and a 15 GHz VLBA correlated flux density $S_{corr} > 1.5$ Jy (2 Jy for $\delta < 0°$) at any epoch between 1994.0 and 2004.0. The weaker radio blazars ($S_{corr} > 0.2$ Jy) detected by *Fermi* extend the complete MOJAVE-1 sample to MOJAVE-2. The full monitoring list currently consists of 292 sources, 187 of which are the members of the First *Fermi* LAT catalog (1FGL, Abdo et al. 2010) positionally associated with AGNs.

We note that the 187 sources do not represent a complete sample selected on either parsec-scale radio flux density or γ-ray photon flux. Other connection based on γ-ray/radio complete samples will be discussed in our future publications.

3. Results

3.1. Radio/γ-ray delay in VLBI cores

Apart from the median γ-ray photon and energy fluxes, the 1FGL catalog provides flux history data, representing the monthly binned integrated from 100 MeV to 100 GeV photon flux measurements during the first 11 months of the *Fermi* scientific operations, which started on 2008 August 4. The time sampling of our radio observations is source-dependent: objects with faster structure changes (faster apparent speeds) are observed more frequently and vice versa. There are only five sources (3C 111, 3C 120, 0716+714, 1510−089, and BL Lac), which are monitored with a cadence of less then two months. Starting from the early 2009, fifty five bright γ-ray detections ($> 10\sigma$) from the *Fermi* LAT 3-month list positionally associated with bright radio-loud blazars (Abdo et al. 2009c, Abdo et al. 2009a, Kovalev 2009) have been continuously added to the MOJAVE program. More than half of the LAT-detected sources have less than three epochs of radio observations during the *Fermi* era, which precludes the correlation analysis of individual light curves. Therefore, our study is based on a statistical approach.

Overall, we obtained 564 VLBA images and corresponding model-fits for 183 bright γ-ray sources within a period from June 2008 through March 2010. Four LAT-detected sources did not have radio epochs within the specified period of time. The parsec-scale structure, typically represented by a one-sided core-jet morphology, was fitted with the procedure *modelfit* in the Difmap package (Shepherd 1997) using a limited number of primarily circular Gaussian components.

We analyzed the correlation between the γ-ray photon fluxes and 15 GHz VLBA core flux densities in the following way: (i) select the measurements with radio mi-
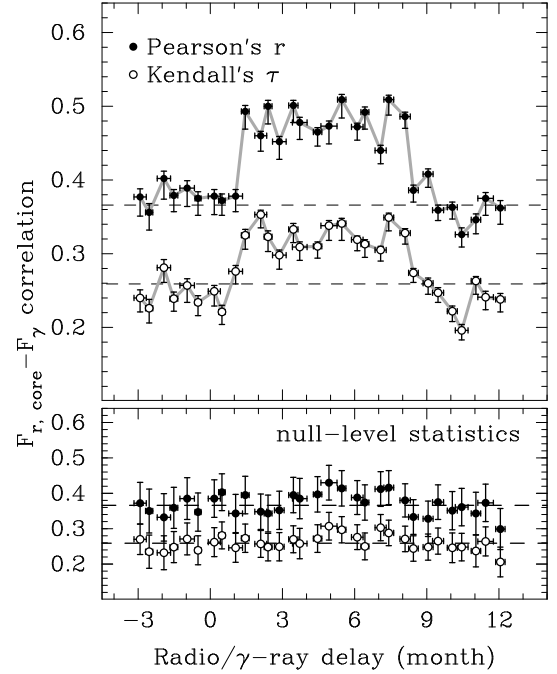

Fig. 1. Upper panel: flux-flux correlation as a function of the time interval between integrated $0.1 - 100$ GeV photon flux and radio core flux densities in the observer's frame. Filled circles represent the Pearson's r, open circles denote the Kendall's τ. The errors are shown at a 68% level. Dashed lines show the null-basis level of the correlation due to the overall γ-ray photon flux versus radio flux density correlation. Lower panel: estimation of the null level correlation by shuffling γ-ray photon fluxes for every source and keeping radio flux densities the same.

nus γ-ray epoch within a limited time interval, for instance, $[-0.5, +0.5]$ month, (ii) if more than one pair of fluxes are available for a source, select the one with the epoch difference closest to the mean of the time interval. The procedure is repeated by shifting the time interval by 0.5 month. We used a cutoff of SNR > 3 for the γ-ray photon flux measurements for two reasons: (i) not to be biased by the lack of sources both weak in radio and γ-rays, (ii) to exclude the influence of data points of low fidelity. For each data set we calculate the Pearson's r and non-parametric Kendall's τ correlation coefficients together with a corresponding probability of a chance correlation. A non-zero radio/γ-ray time lag, clearly seen as a bump on the correlation-delay curves (Fig. 1, top panel), ranges from 1 to 8 months.

To show that the result is robust, we estimated uncertainties of the correlation coefficients. Since the radio flux densities as well as γ-ray photon fluxes are far from being normally distributed, direct methods like the Fisher transformation or Student's t-distribution cannot be used for this purpose. Thus, we applied randomization techniques based on permutation tests to construct confidence intervals on correlation coefficients. For each data set the randomization was done in the following way: (i) randomly swap the radio measurements for one source with another source, keeping the γ-ray fluxes the same; (ii) calculate
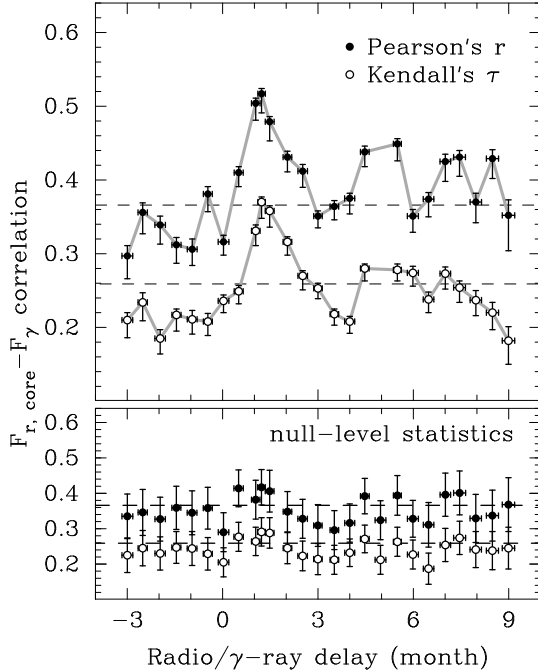
Fig. 2. Same as in Fig. 1 but in the source's frame. A sharp peak at a delay of ~ 1.2 months is detected.

correlation coefficients r and τ from the randomized data; (iii) repeat steps (i) and (ii) 2000 times. A 68% confidence interval for the correlation coefficients was defined as the interval spanning from the 16-th to the 74-th percentile of the re sampled r and τ values. To estimate the null-basis level of the flux-flux correlation, existed due to an overall radio/γ-ray correlation, we shuffled the γ-ray photon fluxes among 11 measurements available for every source, keeping epochs and radio flux densities the same. The obtained values are $r_0 = 0.37$ and $\tau_0 = 0.26$ (Fig. 1, bottom panel). We have also performed a test randomly selecting 90% (and 80%) of the sample to show that correlations hold and, therefore, are not driven by outliers, confirming that our conclusions are robust.

The wide range of the observed delays (Fig. 1) is presumably a result of a number of parameters determining the conditions in the nucleus (black hole mass, its spin and accretion rate), and in nearby interstellar medium. The delay is also affected by geometry including angle to the line of sight and by a variety of redshifts that sources have. The redshifts are known for more than 90% of the sources (166 out of 183). To reduce the problem to conditions in the distant object, we did the analysis in the source's frame first dividing a radio/γ-ray epoch difference for each source by a factor of $(1+z)$. This eliminated the smearing and allowed to assess a typical time delay of ~ 1.2 months in the source's frame (Fig. 2), which corresponds to ~ 2.5 months (for $z \sim 1$) in the observer's frame. The other sub-peaks are not significantly different from the null level of correlation, though they may indicate longer delay for smaller number of sources.

On Fig. 3 we plot the data set of the integrated $0.1-100$ GeV γ-ray photon flux against the 15 GHz VLBA
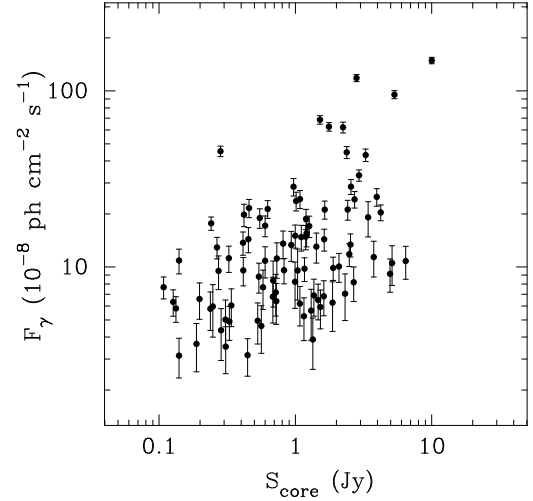

Fig. 3. Integrated 100 MeV–100 GeV *Fermi* LAT photon flux versus 15 GHz VLBA core flux density with an observed radio/γ-ray time lag of 2.5 months.

core flux density, when the γ-ray radiation is leading radio emission of about 2.5 months. Note that, if we drop the three extreme points in the upper right corner, the correlation is still present at a very high level of significance. Notable is also the span over one order of magnitude in the γ-ray fluxes on a given radio flux density. Several factors can contribute into this scatter: a shape of the γ-ray spectrum, effect of K-correction, different seed photons, different Doppler boosting at γ-ray and radio domains (Lister 2007).

3.2. Localization of the γ-ray emission region

Typical parsec-scale morphology of the sources in our sample is represented by a one-sided core-jet structure (Lister et al. 2009b) implying strong selection effects and Doppler boosting of the jet emission. In which part of the radio structure the γ-ray photons detected by the LAT are generated? Localization of the γ-ray emission region in AGN together with the mechanism responsible for γ-ray production is still one of the actively debated questions. There are three possible scenarios to be tested for the site where the high-energy emission is produced: (a) only within the unresolved radio core, (b) only in the resolved jet, (c) both in the core and jet.

Repeating the same analysis as in § 3.1 for the total VLBA flux density, we found that the corresponding correlation coefficients agree within the 95% errors with those taken for the core fluxes. Thus, any conclusion can be drawn out of this comparison. Indeed, the sources in our sample are highly core dominated with the median value of $S_{core}/S_{VLBA} = 0.71$, where S_{core} and S_{VLBA} are the core and total VLBA flux density, respectively. On the contrary, when the jet flux densities $(S_{VLBA} - S_{core})$ are used, the correlation coefficients are significantly lower, instantly grading the scenario (b) as least probable. Nevertheless, the correlation between the

jet flux densities measured quasi-simultaneously with γ-ray photon flux is still significant. Indeed, both the radio emission and γ-ray flux are boosted by the same Doppler factor (Lister et al. 2009a, Kovalev et al. 2009, Savolainen et al. 2010). Assuming the same Doppler factor for the jet and the core (jet base), it results in the weak but significant correlation between the jet flux density and integral γ-ray emission. Alternatively, it is possible that at least in some cases the γ-ray emission can also be produced out of the radio core, as it could be the case in 3C 84 (Abdo et al. 2009b), where radio flare accompanying the γ-ray activity was detected in the innermost jet region.

We have also tested the correlations between non-simultaneous measurements: median of the integrated $0.1 - 100$ GeV LAT photon flux during its first 11 months of scientific operations and median radio core flux density over a period of $1999.0 - 2008.0$. As expected, the correlation is found to be weaker than for quasi-simultaneous measurements, but still significant. The latter suggests that the Doppler factors in the outflows are not substantially changing in time. The correlation between the *Fermi*/LAT $0.1 - 100$ GeV photon flux from the three-month integration and 8 GHz radio flux density non-simultaneously measured by the VLBA was also reported by Kovalev (2009).

Out of all the performed analysis we conclude that the γ-ray emission is most probably generated within the compact radio core.

4. Conclusions

We have investigated the dependence between the integrated $0.1 - 100$ GeV γ-ray photon flux and 15 GHz radio flux densities for a large sample of 183 LAT-detected AGNs observed with the MOJAVE program and conclude the following.

1. The correlation between γ-ray photon flux and radio flux density is found to be highly significant. The correlation analysis results for the core and total VLBA flux are indistinguishable. Correlation is systematically weaker if the jet flux is used, providing a further support for the localization of the γ-ray emission around the core region as well as a connection of the inverse-Compton gamma with synchrotron radio from the jet.

2. We found a non-zero radio/γ-ray delay (γ-ray photon flux is ahead of radio emission) that ranges from 1 to 8 months in the observer's frame and peaks at ~ 1.2 months in the source's frame. The delay is most probably connected to the synchrotron opacity, although other mechanisms may play a role.

3. The region, where most of γ-ray photons are produced, is found to be located within the 15 GHz VLBA core.

These results being consistent with earlier findings reported by Kovalev et al. (2009) put further constraints on the localization of the γ-ray production zone in parsec-scale jets. We continue monitoring the LAT-detected AGNs with the MOJAVE program for future more comprehensive study when the history photon fluxes are available from the next *Fermi* data release.

References

Abdo, A. A., Ackermann, M., Ajello, M., et al. 2009a, ApJ, 700, 597
Abdo, A. A., Ackermann, M., Ajello, M., et al. 2009b, ApJ, 699, 31
Abdo, A. A., Ackermann, M., Ajello, M., et al. 2009c, ApJ, 183, 46
Abdo, A. A., Ackermann, M., Ajello, M., et al. 2010, ApJ, 708, 1254
Abdo, A. A., Ackermann, M., Ajello, M., et al. 2010a, ApJ, submitted
Abdo, A. A., Ackermann, M., Ajello, M., et al. 2010, ApJS, accepted, `arXiv:1002.2280`
Blandford, R. D., & Königl, A. 1979, ApJ, 232, 34
Clements, S. D., Smith, A. G., Aller, H. D., & Aller, M. F. 1995, AJ, 110, 529
Hovatta, T., Nieppola, E., Tornikoski, M., et al. 2008, A&A, 485, 51
Jorstad, S. G., Marscher, A. P., Larionov, V. M., et al. 2010, ApJ, 715, 362
Kovalev, Y. Y. 2009, ApJ, 707, L56
Kovalev, Y. Y., Aller, H. D., Aller, M. F., et al. 2009, ApJ, 696, L17
Lister, M. L. 2007, in American Institute of Physics Conference Series, Vol. 921, The First GLAST Symposium, ed. S. Ritz, P. Michelson, & C. A. Meegan, 345–346
Lister, M. L., Homan, D. C., Kadler, M., et al. 2009a, ApJ, 696, L22
Lister, M. L., Aller, H. D., Aller, M. F., et al. 2009b, AJ, 137, 3718
Pomphrey, R. B., Smith, A. G., Leacock, R. J., et al. 1976, AJ, 81, 489
Pushkarev, A. B., Kovalev, Y. Y., Lister, M. L., & Savolainen, T. 2009, A&A, 507, L33
Raiteri, C. M., Villata, M., Larionov, V. M., et al. 2008, A&A, 491, 755
Savolainen, T., Homan, D. C., Hovatta, T., et al. 2010, A&A, 512, 24
Shepherd, M. C. 1997, in ASP Conf. Ser., Vol. 125, Astronomical Data Analysis Software and Systems VI, ed. G. Hunt & H. E. Payne (San Francisco: ASP), 77
Tornikoski, M., Valtaoja, E., Terasranta, H., et al. 1994, A&A, 289, 673
Volvach, A. E., Volvach, L. N., Larionov, M. G., et al. 2008, Astronomy Reports, 52, 867

Constraints on the gamma-ray emitting region in blazars from multi-frequency VLBI measurements

K. V. Sokolovsky[1,2][*], Y. Y. Kovalev[2,1], A. P. Lobanov[1], J. D. Finke[3][**], T. Savolainen[1],
A. B. Pushkarev[1,4,5], M. Kadler[6,7,8], F. K. Schinzel[1], V. H. Chavushyan[9], L. Carrasco[9], A. Carramiñana[9],
and M. A. Gurwell[10]

[1] Max–Planck–Institut für Radioastronomie, Auf dem Hügel 69, 53121 Bonn, Germany
[2] Astro Space Center of Lebedev Physical Institute, Profsoyuznaya Str. 84/32, 117997 Moscow, Russia
[3] U.S. Naval Research Laboratory, Code 7653, 4555 Overlook Ave. SW, Washington DC, 20375 USA
[4] Pulkovo Astronomical Observatory, Pulkovskoe Chaussee 65/1 196140 St. Petersburg, Russia
[5] Crimean Astrophysical Observatory 98688 Nauchny, Crimea, Ukraine
[6] Dr. Karl Remeis-Observatory & ECAP, Friedrich-Alexander University Erlangen-Nuremberg, Sternwartstr. 7, 96049 Bamberg, Germany
[7] CRESST/NASA Goddard Space Flight Center, Greenbelt, MD 20771, USA
[8] Universities Space Research Association, 10211 Wincopin Circle, Suite 500 Columbia, MD 21044, USA
[9] Instituto Nacional de Astrofísica, Óptica y Electrnica, Apdo. Postal 51 y 216, 72000 Puebla, Pue., México
[10] Harvard-Smithsonian Center for Astrophysics, Cambridge, MA 02138, USA

Abstract. Single-zone synchrotron self-Compton and external Compton models are widely used to explain broadband Spectral Energy Distributions (SEDs) of blazars from infrared to gamma-rays. These models bear obvious similarities to the homogeneous synchrotron cloud model which is often applied to explain radio emission from individual components of parsec-scale radio jets. The parsec-scale core, typically the brightest and most compact feature of blazar radio jet, could be the source of high-energy emission. We report on ongoing work to test this hypothesis by deriving the physical properties of parsec-scale radio emitting regions of twenty bright Fermi blazars using dedicated 5–43 GHz VLBA observations and comparing these parameters to results of SED modeling.

1. Introduction

Blazar jets are known to radiate across the entire electromagnetic spectrum (e.g. Marscher 2006, 2010). Their radio to UV (sometimes – X-ray) emission is believed to be dominated by synchrotron radiation of relativistic electrons while radiation at higher energies could be due to the inverse Compton scattering of synchrotron photons emitted by the electrons themselves (the synchrotron self-Compton process, SSC, Jones et al. 1974, Ghisellini & Maraschi 1989) and photons from external sources (External Compton, EC, Sikora et al. 1994, Dermer & Schlickeiser 2002). The sources of the external seed photons for the EC process include the accretion disc, broad line region (BLR) clouds, warm dust and the cosmic microwave background (CMB), with their relative contribution vary for different blazars.

Despite the wide acceptance of the picture outlined above, the exact location, geometry and physical properties of the regions responsible for blazar emission at different bands remain largely unknown. Considerable success was achieved by single-zone models (assuming a single spherical relativistically moving blob of magnetized plasma which emits synchrotron radiation and interacts with an ambient photon field) in explaining blazar emission from IR to γ-ray energies (among the many recent examples: Abdo et al. 2010, Finke & Dermer 2010 and the references in Table 1). A significant fraction of blazar radio emission is known to originate at the extended parsec-scale jet and cannot be accounted for in the framework of a single-zone model. However, emission from individual jet components resolved with the Very Long Baseline Interferometry (VLBI) can usually be well described by a single uniform synchrotron source model (Pacholczyk 1970). It is tempting to identify one of the jet components resolved by VLBI with the zone responsible for the emission at higher frequencies.

In this contribution we describe a program of coordinated multi-frequency (4.6–43.2 GHz) Very Long Baseline Array (VLBA), *Swift* and *Fermi* observations of selected γ-ray bright blazars with the aim to identify the possible source of high-energy radiation within the parsec-scale jet and put constraints on physical properties based on radio spectra.

2. Observations and analysis

We have used the VLBA (Napier 1994) to observe twenty blazars that were expected to be bright γ-ray emitters, prior to the launch of *Fermi*-GST. The observations were conducted simultaneously at seven frequencies (4.6–43.2 GHz) utilizing the array's unique capability of fast

---

[*] e-mail: `ksokolov@mpifr-bonn.mpg.de`

[**] NRL/NRC Research Associate

Table 1: Comparison of the emission region parameters estimated from the VLBA data and SED modeling

| Name | Multi-frequency VLBA results (this work) | | | | Published SED model parameters | | | | |
	$R_{43\,GHz}$ [10^{15} cm]	$p_{VLBA}^{a,b}$	B_{VLBA}^{b} [G]	D_{var}^{e}	D_{SED} [10^{15} cm]	R_{SED}	p_{SED}^{a}	B_{SED} [G]	Ref.
AO 0235+16	≤ 5800	0.8	≤ 11	24.0					
B0528+134	≤ 7600	1.4	≤ 1.2	31.2					
S5 0716+714	≤ 2100	$\alpha = 0.4^{d}$		10.9	14	40	2.0	1	(1)
OJ 248	≤ 6300	1.6	≤ 23	13.1					
OJ 287	≤ 2800	$\alpha = 0.7^{d}$		17.0					
W Com	≤ 1700	0.8	≤ 118	1.2	20	3	2.55	0.35	(2)
3C 273	≤ 1800	2.0	≤ 0.2	17.0	9	20	2	12	(3)
3C 279	≤ 4600	1.4	≤ 14	24.0	21.5	25	2.0	1.8	(4)
PKS B1510−089	≤ 3900	$\alpha = 0.2^{d}$		16.7	37	18	1.9	0.09	(5)
4C 38.41	≤ 3500	1.0	≤ 1.8	21.5					
Mrk 501	≤ 470	1.6	≤ 67	$\ldots^{f}$	20	1.03	2	0.3	(6)
NRAO 530	≤ 6200	1.6	≤ 20	10.7					
B1959+650	≤ 510	1.4	≤ 300	$\ldots^{f}$	18	7.3	2	0.25	(7)
B2155−304	≤ 2400	1.0	≤ 745	$\ldots^{f}$	32	150	1.3	0.018	(8)
BL Lac	≤ 590	1.0	≤ 3	7.3					
3C 454.3	≤ 6500	$\alpha = 0.8^{d}$		33.2	26	15	1.1	5.4	(9)
B2344+514	≤ 680	1.2	≤ 57^{c}	$\ldots$					

[a] p is the power law index in the electron energy distribution $N(E) = N_0 E^{-p}$. For the optically thin part of the synchrotron spectrum $p = 1 - 2\alpha$ where α is defined as $S_\nu \sim \nu^\alpha$. [b] The estimates correspond to the parsec-scale radio core. [c] The value is in the observer's frame. [d] The homogeneous synchrotron source model is not applicable for such spectrum. [e] The variability Doppler factor from Hovatta et al. (2009) used to transform the observed magnetic field strength into the source frame. [f] The same Doppler factor as in the corresponding SED model was adopted.

References: 1: Chen et al. (2008); 2: Acciari et al. (2009); 3: Pacciani et al. (2009); 4: Giuliani et al. (2009); 5: this work; 6: Anderhub et al. (2009); 7: Tagliaferri et al. (2008); 8: Aharonian et al. (2009); 9: Bonnoli et al. (2010).

frequency switching between individual VLBI scans. After the initial calibration in *AIPS* (Greisen 1990), the sources were self-calibrated and imaged independently at each frequency using *Difmap* (Shepherd 1994). This software was also used to model the source structure in the *uv*-plane and derive constraints on the core size at 43.2 GHz (Table 1).

A special procedure was developed to improve amplitude calibration of the correlated flux density resulting in a ∼ 5 % accuracy in 4.6-15.4 GHz range and a ∼ 10 % accuracy at 23.8 and 43.2 GHz. Images at different frequencies were aligned with each other using optically thin regions of the jet to compensate for phase center shifts and possible frequency-dependent core position ("core shift", Lobanov 1998, Kovalev et al. 2008). We applied a spectrum extraction technique described by Sokolovsky et al. (2010) which relies on the positions and flux densities of individual CLEAN components as opposed to the use of restored VLBI images in order to suppress spectral artifacts arising from the convolution with a Gaussian beam.

The sources were observed with *Swift* in X-ray and optical-UV bands typically within two days after the VLBA observation. The Swift data were analyzed using standard tools provided in the *HEAsoft*[1] package. Whenever feasible, standard stars within the UVOT field of view were utilized to improve photometry in *UBV* bands. The Galactic correction was applied using the val-

___
[1] http://heasarc.nasa.gov/lheasoft/
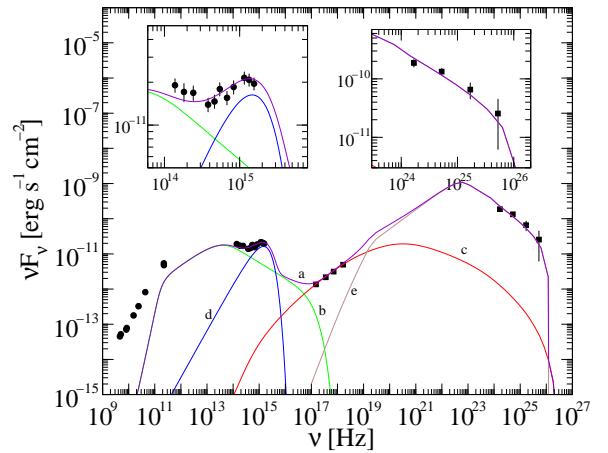
Fig. 1: Quasi-simultaneous SED of PKS B1510−089 constructed using observations with the VLBA, *Swift*, *Fermi*/LAT, NOT, SMA and the 2.1 m telescope Guillermo Haro. The violet curve (a) represents the combined SED model: green curve (b) is the synchrotron component, red (c) is the SSC component, blue (d) is the accretion disk and brown (e) represents EC scattering of the disk radiation (see also Table 2).

ues from Schlegel et al. (1998) and Kalberla et al. (2005) for the optical-UV and X-ray absorption respectively.

To obtain the quasi-simultaneous SED of PKS B1510−089 (Fig. 1) discussed below, the VLBA, *Swift* and *Fermi*/LAT data collected during two days 2009 April 09 – 10 were complemented by $UBVR_c i$ photometry obtained on April 12 with the 2.56 m Nordic Optical Telescope (NOT) and infrared JHK_s photometry obtained on April 07 and 17 with the 2.1 m telescope of Guillermo Haro Observatory in Cananea, México. The Submillimeter Array (SMA) provided flux density measurements at 1 mm from 2009 April 05 and 14. These observations resulted in the most well-sampled quasi-simultaneous SED (containing multi-frequency VLBI data) among all our sources, and for that reason it was the first we chose to construct a model of.

UBV magnitudes of PKS B1510−089 observed by the *Swift*/UVOT are systematically (0^m5–0^m3) brighter then those observed by the NOT two days later. Since both observations were calibrated against the same set of comparison stars from González-Pérez et al. (2001), the difference can be interpreted as a clear sign of optical inter-day variability.

3. Discussion of the first results

Parsec-scale radio emission of all the observed sources (Table 1) is dominated by a bright unresolved core (the apparent origin of the jet, see a discussion by Marscher 2008) which exhibits high-amplitude flux density variability (e.g. Vercellone et al. 2010). The parsec-scale core is a natural candidate to be directly related to the bright variable emission at γ-rays (Kovalev et al. 2009) and other bands.

(a) PKS B1510−089   (b) OJ 248
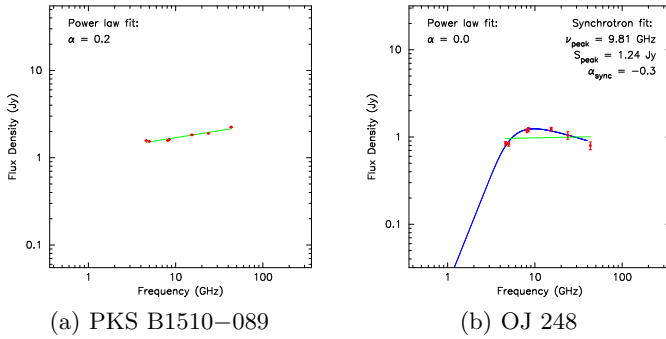
Fig. 2: VLBA spectra of core regions of PKS B1510−089 (a) and OJ 248 (b). The former spectrum is flat while the latter one shows a prominent synchrotron self-absorption peak. The green line is a power law fit. The blue curve is a homogeneous synchrotron source model.

The multi-frequency VLBA observations have detected the synchrotron self-absorption peak in core regions of most of the observed sources with the exception of B0716+714, OJ 287, PKS B1510−089 and 3C 454.3. The latter sources show inverted spectra in the 4.6–43.2 GHz range, characteristic of a partially optically-thick inhomogeneous source. These sources may have a detectable self-absorption turnover at frequencies > 43 GHz. Fig. 2 compares core radio spectra of PKS B1510−089 and OJ 248.

For sources where the self-absorption peak was detected, it was possible to put upper limits on the magnetic field strength using the procedure described by Sokolovsky et al. (2010). The source intrinsic values were computed using variability Doppler factor estimations from Hovatta et al. (2009). The resulting liberal upper limits on the magnetic field strength owe to poor resolution at lower observing frequency (4.6 GHz) which ultimately limits our ability to unambiguously extract spectrum of a given spatial region.

In the case of a bright isolated component, which dominates the emission across the whole observed frequency range, it is possible to estimate its size using the highest observing frequency (43.2 GHz) instead of the lowest one and, therefore, obtain much tighter constrains on the component size and the magnetic field strength. The applicability of this "isolated component" scenario to each individual source is currently being investigated.

Table 1 presents constrains on size ($R_{43\,\mathrm{GHz}}$), magnetic field strength (B_{VLBA}) and electron energy spectral slope (p_{VLBA}) in the radio core region, see Sokolovsky et al. (2010) for a more detailed discussion. These values are compared to the corresponding parameters of SED models (R_{SED}, B_{SED}, p_{SED}) reported in the literature. Doppler factors from SED models (D_{SED}) and those assumed for B_{VLBA} computation (D_{var}) are also listed. The SED model parameters are well within the constraints set by the multi-frequency VLBA data, except for 3C 273 which shows a discrepancy in B_{VLBA}–B_{SED} that may be due to insufficient resolution of our data set. There

is evidence from 86 GHz VLBI data that $B \sim 1\,\mathrm{G}$ in the mm-wavelength core of 3C 273 (Savolainen et al. 2008).

To further test the possible relation between the radio core and the emitting blob implied by single-zone SED models, we have constructed the quasi-simultaneous SED of PKS B1510−089 presented in Fig. 1. The use of the VLBI core flux density (instead of the total flux density obtained by single-dish radio observations) allows us to exclude the emission coming from the parsec-scale jet and larger scales. Our ambition was to check how this will affect the SED modeling.

Table 2: PKS B1510−089 SED model parameters

Minimum e^- Lorentz factor	$\gamma_{\mathrm{min}} = 30$
Brake Lorentz factor	$\gamma_{\mathrm{brk}} = 1.9 \times 10^3$
Maximum e^- Lorentz factor	$\gamma_{\mathrm{max}} = 1.0 \times 10^5$
e^- energy slope below γ_{brk}	$p_1 = 1.9$
e^- energy slope above γ_{brk}	$p_2 = 3.9$
Doppler factor	$D = 37$
Bulk Lorentz factor	$\Gamma = 37$
Magnetic field strength	$B = 0.09$ G
Variability time	$t_{\mathrm{var}} = 2.16 \times 10^4$ sec
Blob radius	$R = 1.8 \times 10^{16}$ cm
Jet power (magnetic field)	$P_{\mathrm{jet,\,B}} = 2.8 \times 10^{43}$ erg/s
Jet power (electrons)	$P_{\mathrm{jet}\,e^-} = 7.5 \times 10^{45}$ erg/s
Black hole mass	$M_{\mathrm{BH}} = 1 \times 10^9 M_\odot$
Accretion efficiency	$\eta = 1/12$
Eddington ratio	$L_{\mathrm{disk}}/L_{\mathrm{Edd}} = 0.06$
Blob distance from disk	$r = 5.1 \times 10^{17}$ cm

Contribution from a hot thermal component, probably the accretion disk, is evident in the optical and UV bands. The SED in the IR to γ-ray range can be explained by the single zone EC model with the Compton scattered accretion disk photons being responsible for the bulk of the observed γ-ray emission. In this model, the blob is close enough to the accretion disk so the accretion disk photons can reach the blob directly, with no need to be scattered back from BLR clouds or dust. Note, that due to relativistic aberration some of the disk photons will be coming to the blob (nearly) head-on. The photons will primarily come from a radius of the disk of $\sqrt{3}r$ where r is the blob's distance from the black hole (Dermer & Schlickeiser 2002). The blob size was constrained by the observed γ-ray variability time scale of the order of a few hours (Abdo et al. 2010). Parameters of the model are summarized in Table 2. We note that the model fit is not unique, single-zone models with a different source of seed photons could probably also produce an acceptable fit (cf. Abdo et al. 2010).

The constructed model (Fig. 1) represents well the IR to γ-ray data, however it dramatically underpredicts the radio emission because of the synchrotron self-absorption occurring in the small blob at a high frequency. A significantly larger blob size would be inconsistent with the observed variability timescale. Even if the variability timescale argument were dismissed, a single-zone SED

model with a larger blob would have difficulties in explaining the observed hard radio spectrum which is inconsistent with the softer X-ray spectrum or optically thick synchrotron radiation from a uniform source. One way to overcome this difficulty would be to introduce a second brake in the electron energy spectrum.

Alternatively, one could abandon the attempt to explain the whole SED with a single-zone model and assume that even the radio emission observed from the cm-mm band core is coming from a larger ($R_{SED} < R < R_{43\ GHz}$) structure downstream of the blob responsible for the IR-to-γ-ray emission. This structure (which cannot be observed separately from the blob due to limited resolution of the available VLBI data) could be a smooth jet (Blandford & Konigl 1979) or a number of distinct jet components (Marscher 1980) – perhaps the blobs which contributed to high-energy emission earlier... One could argue that currently this extended region does not contribute significantly to the optical and γ-ray emission on the basis of the observed short timescale variability in these bands. A more detailed SED modeling is needed to test this scenario.

4. Summary

The program of coordinated multi-frequency (4.6–43.2 GHz) VLBA, *Swift* and *Fermi* observations of selected γ-ray bright blazars is described and the first analysis results are discussed. Constraints on the size ($R_{43\ GHz}$) and magnetic field strength (B_{VLBA}) in the parsec-scale core region derived from the VLBA observations are consistent with the values (R_{SED}, B_{SED}) usually assumed in single-zone SED models (Table 1). However, the single-zone SED model which we tested for PKS B1510−089 has difficulties in explaining the observed level of core radio emission while being consistent with the observed γ-ray and optical variability timescales. The multi-frequency VLBA and SED data analysis for the whole sample is in progress. The SED data on PKS B1510−089 discussed here are available from KVS upon request.

References

Abdo, A. A., Ackermann, M., Ajello, M., et al. 2010, ApJ submitted

Acciari, V. A., Aliu, E., Aune, T., ApJ, 707, 612

Aharonian, F., Akhperjanian, A. G., Anton, G., et al. 2009, ApJ, 696, L150

Anderhub, H., Antonelli, L. A., Antoranz, P., et al. 2009, ApJ, 705, 1624

Blandford R. D., Konigl A. 1979, ApJ, 232, 34

Bonnoli, G., et al. 2010, submitted to MNRAS arXiv:1003.3476

Chen A. W., D'Ammando, F., Villata, M., et al. 2008, A&A, 489, L37

Dermer, C. D., & Schlickeiser, R. 2002, ApJ, 575, 667

Finke J. D., & Dermer C. D. 2010, ApJ, 714, L303

Ghisellini, G., & Maraschi, L. 1989, ApJ, 340, 181

Giuliani, A., D'Ammando, F., Vercellone, S., et al. 2009, A&A, 494, 509

González-Pérez, J. N., Kidger, M. R., & Martín-Luis, F. 2001, AJ, 122, 2055

Greisen E. W. 1990, in *Seminar on Acquisition, Processing and Archiving of Astronomical Images*, 125

Hovatta, T., Valtaoja, E., Tornikoski, M., Lähteenmäki, A. 2009, A&A, 494, 527

Jones, T. W., O'Dell, S. L., Stein, W. A., 1974, ApJ, 188, 353

Kalberla P. M. W., Burton, W. B., Hartmann, D., et al. 2005, A&A, 440, 775

Kovalev, Y. Y., Lobanov, A. P., Pushkarev, A. B., Zensus, J. A. 2008, A&A, 483, 759

Kovalev, Y. Y., Aller, H. D., Aller, M. F., et al., 2009, ApJ, 696, L17

Lobanov, A. P. 1998, A&A, 330, 79

Marscher, A. P. 1980, Nature, 288, 12

Marscher, A. P. 2006, AIP Conf. Ser., 856, 1

Marscher, A. P. 2008, ASP Conf. Ser., 386, 437

Marscher, A. P., 2010, in *The Jet paradigm - From Microquasars to Quasars*, ed. T. Belloni, Lecture Notes in Physics, 794, 173

Napier, P. J. 1994, IAUS, 158, 117

Pacciani, L., Donnarumma, I., Vittorini, V., et al. 2009, A&A, 494, 49

Pacholczyk, A. G. 1970, Radio astrophysics, (San Francisco: Freeman)

Savolainen, T., Wiik, K., Valtaoja, E., Tornikoski, M. 2008, in *Extragalactic Jets: Theory and Observation from Radio to Gamma Ray*, ed. T.A. Rector & D.S. De Young, ASP Conf. Ser. 386, (San Francisco: ASP), p. 451

Schlegel, D. J., Finkbeiner, D. P., Davis, M. 1998, ApJ, 500, 525

Shepherd, M. C., Pearson, T. J., & Taylor, G. B. 1994, BAAS, 26, 987

Sikora, M., Begelman, M. C., & Rees, M. J. 1994, ApJ, 421, 153

Sokolovsky, K. V., Lobanov, A. P., Savolainen, T., et al. 2010, in *2009 Fermi Symposium*, eConf Proceedings C091122, arXiv:1001.2591

Tagliaferri, G., Foschini, L., Ghisellini, G., et al. 2008, ApJ, 679, 1029

Vercellone, S., D'Ammando, F., Vittorini, V., et al. 2010, ApJ, 712, 405

Rapid Variability of Gamma-ray Emission from Sites near the 43 GHz Cores of Blazar Jets

A. P. Marscher and S. G. Jorstad

Institute for Astrophysical Research, Boston University, USA

Abstract. Comprehensive VLBI and multi-waveband monitoring indicate that a single superluminal knot can cause a number of γ-ray flares at different locations. However, the often very rapid variability timescale is a challenge to theoretical models when a given flare (perhaps the majority of those observed) is inferred from observations to lie near the 43 GHz core, parsecs from the central engine. We present some relevant observational results, using the BL Lac object AO 0235+164 as an example. We propose a turbulent cell model leading to a frequency-dependent filling factor of the emission region. This feature of the model can provide a solution to the timescale dilemma and other characteristics of blazar emission.

1. Introduction

There exists a crisis in the interpretation the results of multi-waveband monitoring of blazars. Comparisons of dates of peak γ-ray flux measured by EGRET with epochs of ejections of superluminal radio knots (Jorstad et al. 2001a), onsets of millimeter-wave flares (Lähteenmäki & Valtaoja 2003), and changes in centimeter-wave polarization (Jorstad et al. 2001b) lead to the conclusion that most γ-rays outbursts are coincident with radio events. Yet we know that the jets of blazars are opaque to radio emission within ~ 1 pc or more from the central engine. This is difficult to reconcile with the shortest time scales of GeV variability observed — a few hours in PKS $1622-297$ (Mattox et al. 1997) and 3C 454.3 (Foschini et al. 2010).

However time scales of variability reflect size scales, not distance from the central engine. Furthermore, jets are very narrow, with opening half-angle $\sim 10°/\Gamma$, where Γ is the bulk Lorentz factor of the flow in the jet (Jorstad et al. 2005). Because of this, a jet can have a cross-sectional radius much less than its distance from the central engine. Nevertheless, this does not solve the entire problem. The core on 43 GHz Very Long Baseline Array (VLBA) images of PKS $1510-089$ has been estimated to lie ~ 20 pc from the central engine (Marscher et al. 2010a). Offsets of parsecs are implied for other luminous blazars as well (e.g., Marscher et al. 2008; Chatterjee et al. 2008). The cross-sectional radius of a luminous blazar is ~ 0.1 pc near the 43 GHz core. With a Doppler factor $\delta \sim 20$ and redshift ~ 0.5, the shortest time scale of variability should be ~ 1 week, not a fraction of a day.

Because of this discrepancy, a number of authors have insisted that the γ-ray emitting region lies within $\sim 10^{16}$ cm of the central engine (e.g., Tavecchio et al. 2010). This has the advantage for high-energy emission models that optical-UV photons from the broad emission-line region are available for scattering to γ-ray energies by highly relativistic electrons in the jet. Poutanen & Stern (2010) find that pair production off the UV photon field

can then cause the observed sharp break in the spectrum of some blazars at GeV energies. However, such an interpretation requires that the timing of the radio and γ-ray events is a chance coincidence in every case. This seems unlikely, especially with singular events such as the ultra-high-amplitude optical flare, very sharp γ-ray flare, and passage of a superluminal knot through the 43 GHz core in PKS $1510-089$ at essentially the same time (Marscher et al. 2010a, 2010b). Furthermore, the number of γ-ray outbursts observed with *Fermi* that are either coincident with or follow the passage of a new superluminal knot through the centroid of the core is becoming high enough to conclude that a large fraction of the γ-ray emission originates parsecs away from the central engine (Jorstad et al. 2010 and these proceedings).

We propose to solve this dilemma by developing a model in which much of the optical and high-energy radiation in a blazar is emitted near the 43 GHz core in VLBA images, parsecs from the central engine. The model allows for short time scales of optical and γ-ray variability by restricting the highest-energy electrons radiating at these frequencies to small sub-regions of the jet. That is, in our model the filling factor at high frequencies is relatively low, while that of the electrons radiating at $\sim 10^{10-13}$ Hz is near unity. Such a model is consistent with other prominent features of optical vs. lower frequency emission.

2. Properties of blazar emission to incorporate in the development of a model

We now have at our avail light curves at many frequencies across the electromagnetic spectrum, polarization vs. time data at radio, mm-wave, and optical/near-IR bands, and well-sampled sequences of VLBI images—in both total and polarized intensity—at high radio frequencies for many blazars. This is providing a wealth of information that must be considered when developing models for the non-thermal emission from blazar jets. This information includes the following:
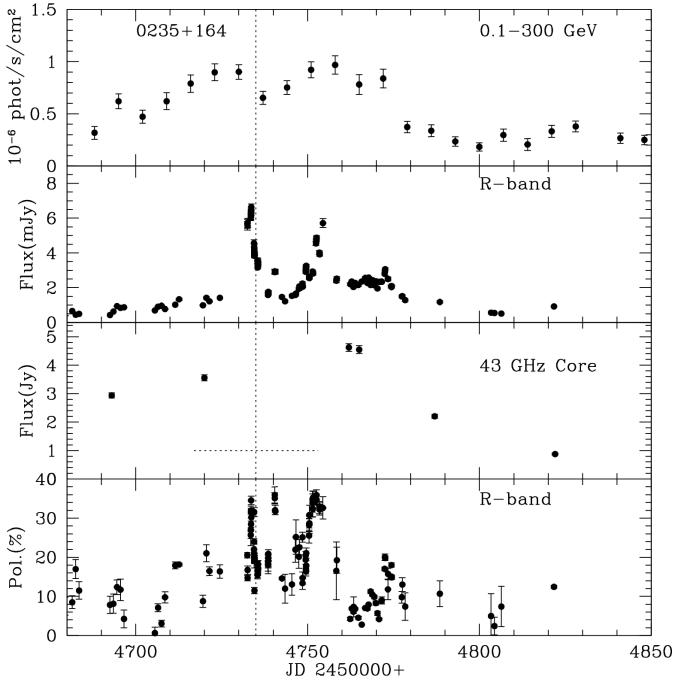
Fig. 1. Multi-waveband light curves of the BL Lac object AO 0235+164 in late 2008. The time when the superluminal knot (see Fig. 2) passed through the core is marked by a vertical line, with the horizontal line in panel 3 indicating the uncertainty in the date of this event.

(1) In most blazars, the detailed properties of the synchrotron emission change gradually as the wavelength of observation decreases from the millimeter to optical range. (a) The spectral index ($\alpha \equiv -d \log F_\nu/d \log \nu$) steepens from a value usually in the range of 0.5-1.0 to > 1; (b) the linear polarization increases on average and becomes more highly variable (D'Arcangelo et al. 2009); and (c) the time scale of flux variability, $[t_{\rm var} \equiv (t_2 - t_1)/|ln(F_2/F_1)|$, where t_1 and t_2 are times when flux densities F_1 and F_2 are measured, respectively] decreases. An example of the latter is the BL Lac object AO 0235+164 ($z = 0.94$) during a multi-waveband outburst in 2008 (Fig. 1). As seen in Figure 2, a bright, extremely superluminal ($\sim 70c!$) knot passed through the core at essentially the same time as the peak of a sharp optical flare during a ~ 80-day γ-ray outburst. During the declining phase of another major flare observed at two optical and two near-IR bands, the shortest measured time scale of flux decrease depended on frequency ν as $t_{\rm var} \propto \nu^{-0.16}$ (see Fig. 3).

(2) The period of elevated optical flux in 0235+164 (see Fig. 1) matches that of the high γ-ray state, but there were no high-amplitude γ-ray flares during the two main optical events. Yet electrons with sufficient energies to emit optical synchrotron radiation for typical magnetic field strengths of ~ 0.5 G (Hagen-Thorn et al. 2008), $E \sim 10^4 mc^2$, should also be able to scatter those photons (or other optical photons from the surroundings) to γ-ray
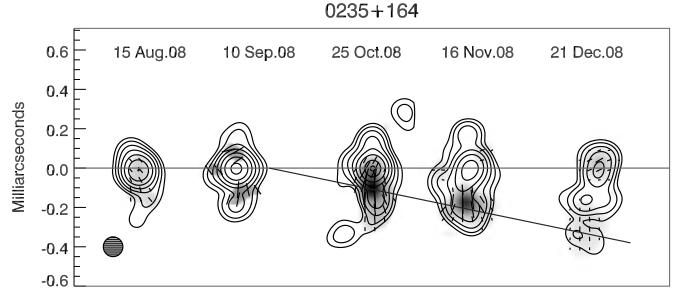

Fig. 2. VLBA images at 43 GHz of 0235+164 in late 2008. Contours (factors of 2 starting at 0.023 Jy/beam) correspond to total intensity and gray scale to polarized intensity. Line segments indicate direction of polarization electric vectors. A circular Gaussian restoring beam is used with FWHM similar to the resolution of the longest VLBA baselines. Motion of the superluminal knot is indicated by the diagonal line.
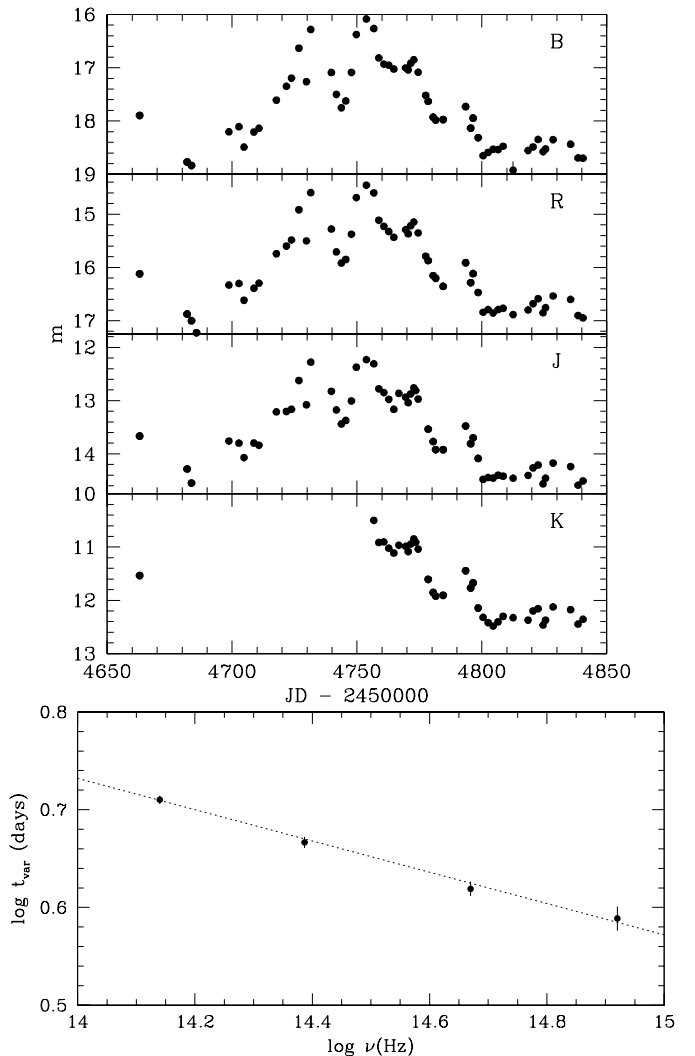

Fig. 3. *Top:* Multi-band optical/near-IR light curves of 0235+164 during the interval displayed in Fig. 1. Magnitudes here are not corrected for extinction. *Bottom:* Time scale of flux variability (as defined in the text) as a function of optical/near-IR frequency of 0235+164 between Julian dates 2454756.7 and 2454758.7. Diagonal line represents a power law with slope -0.16. Data are from the Yale Fermi/SMARTS project, website http://www.astro.yale.edu/smarts/glast/.

energies.

(3) The power spectral density (PSD) of flux variations of the γ-ray bright blazar 3C 279 follows a power law (Chatterjee et al. 2008) without any indication of a break on time scales from ~ 1 day to 12 years.

(4) The 43 GHz core on VLBI images lies at a significant distance from the central engine. This must be the case theoretically based on the self-absorption turnover in the synchrotron F_ν vs. ν spectrum at millimeter wavelengths (Impey & Neugebauer 1988). If emission in the jet continued in a self-similar way down to a size less than about 10^{15} cm, the turnover would occur at much shorter wavelengths. In the radio galaxy 3C 120, time delays between a drop in X-ray flux from the central engine and the passage of a new superluminal knot through the core at 43 GHz led Marscher et al. (2002) and Chatterjee et al. (2009) to conclude that the core lies 0.5 pc from the black hole. In a more powerful source, such as the quasars 3C 279 and PKS 1510−089, timing studies indicate that the core lies tens of parsecs (after de-projection) from the central engine (Marscher et al. 2010a, 2010b; Chatterjee et al. 2008).

3. A turbulent cell model for variability in blazars

The red-noise behavior of the PSD of 3C 279 (Chatterjee et al. 2008) implies that the variations are stochastic in nature. If main events in the light curves associated with bright superluminal knots are caused by shocks, these shocks must be produced randomly with a range of compression ratios. The short-term fluctuations can be understood as the consequence of turbulent ambient jet plasma that passes through the shocks (Marscher, Gear, & Travis 1992). If this is the case, then the multi-wavelength behavior of the emission depends on the range of physical parameters of the turbulence.

We propose a model in which the emission arises from a collection of turbulent cells of similar size, each with strength of the magnetic field B (with random orientation) and density of electrons n_e that follow a probability distribution, with higher values less likely. We imagine that the turbulent cells pass into and out of a disk-shaped primary emission region representing a shock, bounded by the shock front and, probably, a rarefaction. Electrons are injected with a power-law energy distribution at the shock front, after which the cell advects away from the shock. The cooling time of the electrons depends on B. If inverse Compton losses are important, then it will also depend on the energy density of photons n_γ; we defer consideration of this case to a subsequent study.

The key addition to this model over that proposed in Marscher et al. (1992) is that the maximum electron energy E_{max} varies from cell to cell. According to models of energization of particles at relativistic shock fronts (e.g., Baring 2010), the efficiency of particle acceleration depends inversely on the ratio of the gyro-radius to mean free path for pitch-angle scattering. This ratio should be
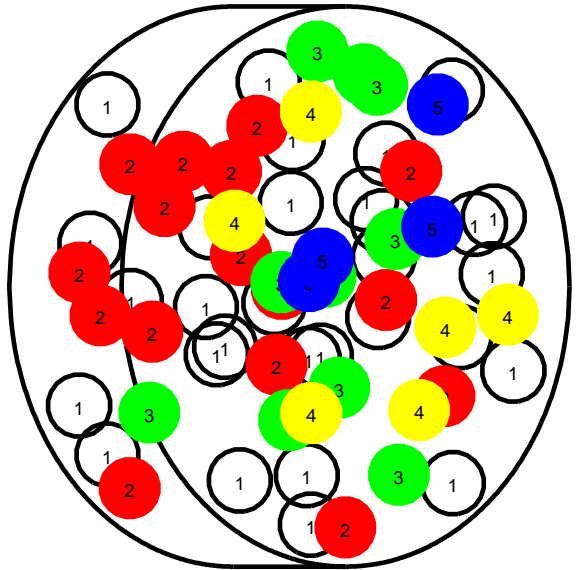

Fig. 4. Sketch of our proposed model consisting of a number of emission cells (circles) inside a disk (representing, for example, a shock wave), each with a different maximum energy of relativistic electrons. All numbered cells have electrons with sufficiently high energies to emit synchrotron radiation at a relatively low frequency, e.g., $< 10^{13}$ Hz. Only the cells marked 2 and higher have electron energies high enough to emit at $> 10^{13.5}$ Hz. Only those marked 3, 4, and 5 can emit at $> 10^{14}$ Hz, only those numbered 4 and 5 can emit at $> 10^{14.5}$ Hz, and only those numbered 5 can emit at $> 10^{15}$ Hz.

larger when B is stronger, so that the amplitude of the magnetic turbulence rises. If the value of B in a cell follows a power-law probability distribution above some minimum value, then we might expect E_{max} to do the same. (Or the slope of the resultant electron energy distribution might be flatter for stronger fields, thereby increasing the relative number of electrons with the highest energies. This would produce a similar effect on the synchrotron spectrum as the case considered here.)

The different values of B, E_{max}, and n_e in different cells, with higher values occurring more rarely, leads to a frequency dependence of the synchrotron emission. Recall that, in the scenario envisioned by Marscher & Gear (1985), the synchrotron spectrum steepens by $1/2$ because the dimension transverse to the shock front, and therefore the volume V, of the emitting region follows $V(\nu) \propto \nu^{-1/2}$. This will still apply at sufficiently high frequencies if electrons are injected only as a cell passes across the shock front. However, we introduce an additional frequency dependence on the volume because only some fraction of the cells contain electrons that can radiate at frequency ν after they cross the shock front. We illustrate the geometry of our model in Figure 4.

We have not yet developed a definite relationship between the electron energy distribution and the power spectrum of the turbulence. Our model therefore does not at this stage predict the slope of the spectrum at frequencies where $V(\nu) < 1$. We can, however, turn to ob-
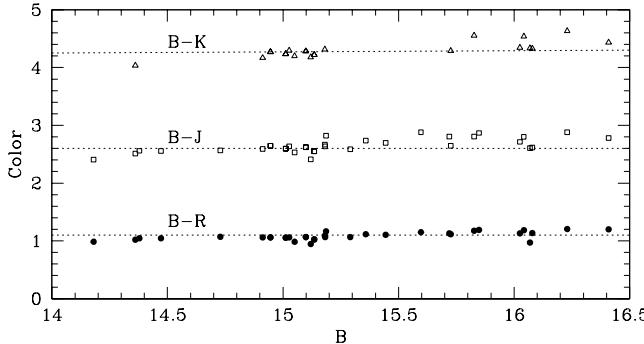
Fig. 5. Optical/near-IR colors vs. B magnitude of 0235+164 during the interval covered in Fig. 1. All magnitudes and colors have been corrected for foreground reddening in both our Galaxy and an intervening galaxy at redshift 0.524 according to Table 5 of 2005. Comparison with the horizontal dotted lines shows the trend of flatter spectra as the flux increases. For example, the $B - J$ color difference between 2.4 at $B = 14.17$ and 2.85 at $B = 2.85$ corresponds to a change in the spectral index from $\alpha = 1.01$ to 1.34. Data source is the same as for Fig. 3.

servations to infer the required functional form of $V(\nu)$. The relationship $t_{var} \propto \nu^{-0.16}$ found above for 0235+164 could correspond to stochastic variations in N cells if $N(\nu) \propto V(\nu) \propto \nu^{-0.32}$, since we expect that the level of fluctuations in flux $\langle \Delta F/F \rangle \propto N^{-1/2}$. This is in agreement with the steepening of the continuum spectrum from far-IR ($\alpha \approx 1.0$) to optical (($\alpha \approx 1.3$) at times when there is no flare. Since 0.32 is less than 0.5, we infer that cells can cross the entire emission region before electrons that radiate at B band suffer significant synchrotron losses in 0235+164.

Since a rapid flare corresponds to one or more new cells with higher than average B or n_e, the spectrum should flatten near the peak of the flare, since the volume of the enhanced emission is roughly the same at all wavelengths within a relatively narrow range (e.g., optical/near-IR). As Figure 5 demonstrates, this indeed occurred during the 80-day γ-ray outburst of 0235+164. The change in spectral index closely matches that required by the model ($\Delta\alpha = 0.32$).

The higher mean level and amplitude of fluctuations of linear polarization at higher frequencies is a natural consequence of the turbulent cell model. In the extreme case of either very little compression at the electron injection front (weak shock) or a shock viewed almost exactly face-on (so that the component of **B** in the plane of the sky remains chaotic), the mean degree of polarization at frequency ν would be $\sim 0.75 N(\nu)^{-1/2}$ (Burn 1966) and the standard deviation $\sim 0.75 [2N(\nu)]^{-1/2}$ (Jones 1988). This becomes more complicated when the compression is substantial and the front lies at an angle to the sky plane. There will still be frequency-dependent polarization, but simulations are needed for a more quantitative analysis.

The time scale of variability $t_{var} \propto \nu^{-0.16}$ in 0235+164 at optical/near-IR frequencies, probably extending down to $\sim 10^{13}$ Hz. If we assume that the volume of emission

at this frequency includes the entire superluminal knot, whose angular diameter was 0.05 mas on JD 2454762 as measured by modeling the feature as a face-on disk and fitting the VLBA data. This corresponds to a radius of 0.2 pc. If we adopt $\delta \approx 70$, the typical time scale of variability at $\nu \sim 10^{13}$ Hz should be ~ 7 days. This becomes ~ 3 days at B band, close to the observed value of 4 days (see Fig. 3).

Inverse Compton emission depends on n_e and n_γ, while the synchrotron flux depends on the former and on the strength and direction of the local magnetic field. We therefore expect correlations between the optical and γ-ray emission, but not exact correspondence of light curves. The geometrical break in the synchrotron spectrum should appear also in the γ-ray spectrum from inverse Compton scattering. We plan to investigate this possibility alongside the detailed time behavior of the multi-waveband emission through numerical simulations of the model in the near future.

References

Baring, M. G. 2010, Adv. Space Res., in press `arXiv: 1002.3848`
Burn, B. J. 1966, MNRAS, 133, 67
Chatterjee, R., et al. 2008, ApJ, 689, 79
Chatterjee, R., et al. 2009, ApJ, 704, 1689
D'Arcangelo, F. D. 2009, Ph.D Thesis, Boston University
Foschini, L., et al. 2010, MNRAS, submitted `arXiv: 1004.4518`
Hagen-Thorn, V. A., et al. 2008, ApJ, 672, 40
Impey, C. D., & Neugebauer, G. 1988, AJ, 95, 307
Jones, T. W.. 1988, ApJ, 332, 678
Jorstad, S. G., et al. 2001a, ApJS, 134, 181
Jorstad, S. G., et al. 2001b, ApJ, 556, 738
Jorstad, S. G., et al. 2005, AJ, 130, 1418
Jorstad, S., Marscher, A., D'Arcangelo, F. & Harrison, B. 2010, 2009 Fermi Symposium, ed. W. N. Johnson & D. J. Thompson (eConference C091122) `arXiv:1002.0806`
Läteenmäki, A., & Valtaoja, E. 2003, ApJ, 590, 95
Marscher, A. P., et al. 2002, Nature, 417, 625
Marscher, A. P., et al. 2008, Nature, 452, 966
Marscher, A. P., et al. 2010a, ApJL, 710, L126
Marscher, A. P., et al. 2010b, 2009 Fermi Symposium, ed. W. N. Johnson & D. J. Thompson (eConference C091122) `arXiv:0912.5230`
Marscher, A. P., & Gear, W. K. 1985, ApJ, 298, 114
Marscher, A. P., Gear, W. K., & Travis, J. P. 1992, in Blazar Variability, ed. E. Valtaoja & M. Valtonen (Cambridge U. Press), 85
Mattox, J. R., et al. 1997, ApJ, 476, 692
Poutanen, J., & Stern, B. 2010, ApJ, submitted `arXiv: 1005.3792`
Raiteri, C. M., et al. 2005, A&A, 438, 39
Tavecchio, F., Ghisellini, G., Bonnoli, G. & Ghirlanda, G. 2010, MNRAS, 405, L94

Radio Flaring Activity of 3C 345 and its Connection to γ-Ray Emission

F. K. Schinzel[1,4]⋆, A. P. Lobanov[1], S. G. Jorstad[3], A. P. Marscher[3], G. B. Taylor[2,4]⋆⋆, and J. A. Zensus[1,4]

[1] Max-Planck-Institut für Radioastronomie, Auf dem Hügel 69, 53121 Bonn, Germany
[2] Department of Physics and Astronomy, University of New Mexico, Albuquerque NM, 87131, USA
[3] Institute for Astrophysical Research, Boston University, 725 Commonwealth Avenue, Boston, MA 02215, USA
[4] On behalf of the *Fermi*/LAT collaboration

Abstract. 3C 345 is one of the archetypical active galactic nuclei, showing structural and flux variability on parsec scales near a compact unresolved radio core. During the last 2 years, the source has been undergoing a period of high activity visible in the broad spectral range, from radio through high-energy bands. We have been monitoring parsec-scale radio emission in 3C 345 during this period at monthly intervals, using the VLBA at 15, 24, and 43 GHz. Our radio observations are compared with gamma-ray emission detected by Fermi-LAT in the region including 3C 345 (1FGL J1642.5+3947). Three distinct gamma-ray events observed in this region are associated with the propagation of relativistic plasma condensations inside the radio jet of 3C 345. We report on evidence for the gamma-rays to be produced in a region of the jet of up to 40 pc (de-projected) in extent. This suggests the synchrotron self-Compton process as the most likely mechanism for production of gamma-rays in the source.

1. Introduction

The quasar 3C 345 is one of the best studied "super-luminal" radio source, with its parsec-scale radio emission monitored over the past 30 years. Substantial variability of the optical (Babadzhanyants & Belokon(1984), Kidger & Takalo(1990)) and radio (Aller et al.(1996), Teraesranta et al.(1998), Lobanov & Zensus(1999)) emission has been observed, with a possible periodicity of 3.5–4.5 years and major flares occurring every 8–10 years. A new cycle of such enhanced nuclear activity has begun in early 2008 (Larionov et al.(2009)).

3C 345 has also been known as a prominent variable source at high energies up to the X-ray band and only in the γ-ray regime it had not been clearly detected (Casandjian & Grenier(2008)), possibly due to low spatial resolution of previous γ-ray instruments and a lack of space instruments during periods of high source activity. The launch of the GLAST satellite (now *Fermi*) equipped with the Large Area Telescope (LAT) survey instrument (Atwood et al.(2009)) enabled continuous monitoring of γ-ray emission originating from the vicinity of 3C 345.

This paper presents first results from analysis of *Fermi*/LAT γ-ray monitoring data, combined with monthly radio observations made at 43.2 GHz (7 mm wavelength) with very long baseline interferometry (VLBI), using the VLBA[1] facility.

⋆ Member of the International Max Planck Research School (IMPRS) for Astronomy and Astrophysics.
⋆⋆ Also an Adjunct Astronomer at the National Radio Astronomy Observatory.
[1] Very Long Baseline Array of the National Radio Astronomy Observatory, Socorro, USA

Throughout this paper, a flat ΛCDM cosmology is assumed, with $H_0 = 71 \, \text{km} \, \text{s}^{-1} \, \text{Mpc}^{-1}$ and $\Omega_M = 0.27$. At the redshift $z = 0.593$ (Schneider et al.(2007)) of 3C 345, this corresponds to a luminosity distance $D_L = 3.47 \, \text{Gpc}$, a linear scale of 6.64 pc mas^{-1}, and a proper motion scale of 1 mas year^{-1} corresponding to 34.5 c.

2. Observations & Data Processing

2.1. Fermi/LAT

The 11-month all-sky γ-ray monitoring by the *Fermi*/LAT instrument lists a strong detection of a γ-ray emitter in the region 1FGL J1642.5+3947 (Abdo et al. (2010a), Abdo et al.(2010b)), which lies in close vicinity of the three quasars 3C 345 (∼6.4′ away from γ-ray localization) CLASS J1641+3935 (∼17′ away) and NRAO 512 (∼31′ away). The three month bright AGN list mentions the source 0FGL J1641.4+3939 (Abdo et al.(2009a)) to be associated with the faint blazar CLASS J1641+3935 with low probability. However, the 1FGL source is now more convincingly associated with 3C 345 and not the faint CLASS source, albeit still formally at a low-probability.

The angular resolution (at a 68% confidence) of the *Fermi*/LAT instrument is about 0.8° for single photons at 1 GeV energy and it is worse at other energies (Atwood et al.(2009)), thus making it difficult to obtain a significant association with any source in this particular field, based on the γ-ray data alone. The statistical analysis shows that the majority of the received photons are closer to 3C 345 than to the other two sources. Contribution by the other two candidates seems to be minor. A firm association of 1FGL J1642.5+3947 with 3C 345 can only be established with the inclusion of
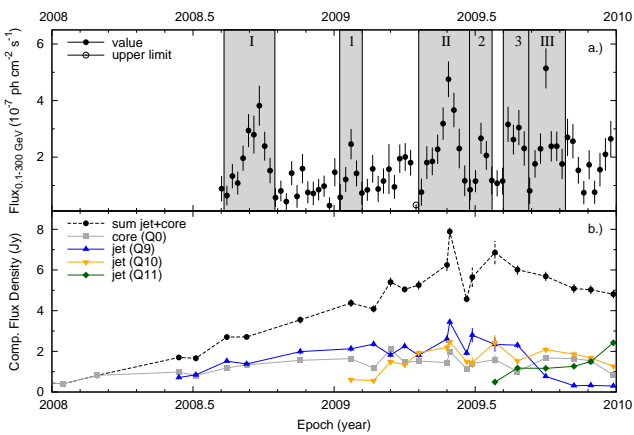
Fig. 1. *a.) top:* *Fermi*-LAT weekly γ-ray light-curve of 3C 345 for the energy range 0.1–300 GeV. The integrated values have a test statistics value of at least 5, corresponding to a $\geq 2.2\sigma$ detection. *b.) bottom:* VLBA 7 mm component flux densities for the model-fitted VLBI core and inner jet, represented by up to four circular Gaussians (Q0, Q11, Q10, Q9). The component labeled Q0 is the eastern-most component (see Fig. 2) and represents the compact "core" or base of the jet. The dashed line plots the sum of the flux densities of all four components.

multi-wavelength observations. A detailed description of the maximum likelihood analysis as well as a thorough discussion of the γ-ray data will be given in a forthcoming *Fermi*/LAT collaboration paper on the γ-ray detection and multi-wavelength identification of 3C 345 (Schinzel et al. (2010)).

From the available *Fermi*/LAT data, a weekly light curve was constructed for the first 14 months of LAT observations using the *Fermi* Science Tools software package release v9r15p2 (08/08/2009). The procedures applied were similar to the one described in Abdo et al.(2009a) using the current instrument response function P6_V3, isotropic background model v02, and Galactic diffuse background models as discussed in Abdo et al.(2009b). The sources Mrk 501 and 4C +38.41 have been included in the source model for the region of interest using a power-law spectral fit with photon spectral energy indices[2] of around 1.79 and 2.66 respectively. For the target source 3C 345, a fixed photon index of 2.46 has been applied to obtain weekly averaged flux values from the model-fits. The resulting 0.1–300 GeV light-curve of 3C 345 is shown in the top panel of Fig. 1.

2.2. VLBA

Following the onset of a new period of flaring activity in 2008, we initiated a dedicated monthly VLBA monitoring of radio emission from 3C 345 at 43.2, 23.8, and 15.4 GHz (VLBA project codes: BS193, BS194). In this paper, only the 43.2 GHz observations are discussed, while the analysis of 15.4 and 23.8 GHz data is continued. The observations

were made with a bandwidth of 32 MHz (total recording bit rate 256 MBit s^{-1}). The total of 12 VLBA observations have been completed, with about 4.5 hours at 43.2 GHz spent on 3C 345 during each observation. Scans on 3C 345 were interleaved with observations of J1310+3233 (amplitude check, EVPA calibrator), J1407+2827 (D-term calibrator), and 3C 279 (amplitude check, EVPA calibrator). The VLBA data were correlated at the NRAO VLBA processor. Analysis was done with NRAO Astronomical Image Processing System (AIPS) and Caltech Difmap (Shepherd et al.(1995)) software for imaging and modeling. Corrections were applied for the parallactic angle and for Earth orientation parameters used by the VLBA correlator. Fringe fitting was applied to calibrate the observations for group delay and phase rate. A summary of all the observations is presented in Table 1. The data from the first 10 epochs of the projects BS193 and BS194 are complemented with 14 VLBA observations from the blazar monitoring program of Marscher et al. (VLBA project codes BM256, BM303, S1136) available online[3]. The combined data (see Table 1) cover a period from January 2008 to December 2009, with observations spaced roughly at monthly intervals.

Brightness distribution of the radio emission was model-fitted by multiple Gaussian components, providing positions, flux densities and sizes of distinct emitting regions in the jet. Fig. 2 illustrates the observed radio structure and its Gaussian model fit representation. Compact emission in the nuclear region (≤ 0.15 mas from the VLBI core) was modelled using two circular Gaussian providing the optimal ratio of χ^2 to the number of model parameters for all epochs.

We interpret the eastern-most component, hereafter labeled Q0, as the base (or "core") of the radio jet at 43.2 GHz, whereas the other features can signify perturbations or shocks developing in the jet. Locations and proper motions of other jet features are then determined with respect to Q0.

3. Results

3.1. Evolution of the radio emission in the nuclear region

A new moving emission region, labeled Q9, was first detected with the VLBA observation on June 16, 2008, followed by detections of another new component on January 24, 2009 (Q10) and a third one on July 27, 2009 (Q11). In the following, the components Q9, Q10, and Q11 observed within on a distance of ≤ 0.3 mas from the core Q0 are referred to as the "jet".

The flux density evolution of the jet is plotted in the lower part of Fig. 1 together with the flux densities of the core and the sum of jet and core. During 2009, the jet (average flux density: 3.6 Jy) was stronger than the core (average flux density: 1.5 Jy) by a factor of 2.4.

Table 1. Summary of 43 GHz VLBA Observations.

Date	S_{tot} [Jy]	D	Beam (bpa) [mas]x[mas] (deg)	Ref.
2008-01-17	1.90	2300	0.31×0.19 (−27.2)	1
2008-02-29	2.02	1600	0.37×0.21 (−29.1)	1
2008-06-12	2.44	2100	0.38×0.16 (−28.2)	1
2008-07-06	2.23	800	0.33×0.15 (−16.6)	1
2008-08-16	3.78	2700	0.41×0.19 (−30.2)	1
2008-09-10	3.67	4300	0.37×0.19 (−32.5)	1
2008-11-16	4.43	300	0.37×0.33 (−1.49)	1
2008-12-21†	2.91	5500	0.39×0.17 (−16.9)	1
2009-01-24	5.04	8900	0.31×0.17 (−20.5)	1
2009-02-19†	3.55	2200	0.37×0.20 (−19.0)	2
2009-02-22	4.63	8800	0.35×0.15 (−19.1)	1
2009-03-16	6.01	2400	0.43×0.30 (9.31)	2
2009-04-01	5.67	8000	0.33×0.16 (−18.7)	1
2009-04-21	5.78	2600	0.33×0.22 (−16.7)	2
2009-05-27	7.00	3500	0.33×0.18 (−15.2)	2
2009-05-30	8.65	6900	0.32×0.16 (−19.8)	1
2009-06-21	5.04	6500	0.28×0.16 (−10.9)	1
2009-06-29	6.43	2600	0.29×0.16 (−11.6)	2
2009-07-27	7.63	2900	0.38×0.16 (−30.8)	1
2009-08-26	6.58	2000	0.32×0.17 (−24.8)	2
2009-10-01	6.67	2300	0.22×0.18 (−21.6)	2
2009-11-07	6.38	1400	0.32×0.16 (−15.3)	2
2009-11-30	5.53	2000	0.29×0.16 (−16.9)	2
2009-12-28	4.95	2400	0.31×0.16 (−8.14)	2

Notes: S_{tot} – total flux density recovered in VLBA image; D – dynamic range measured as a ratio of the image peak flux density to the r.m.s. noise; Beam (bpa) – beam size, major axis vs minor axis with position angle of ellipse in parenthesis; References: 1 – blazar monitoring Marscher et al. (VLBA project code BM256, BM303, S1136); 2 – dedicated monitoring (VLBA project codes BS193, BS194). $\dagger$ – not used for the flux density analysis due to gain calibration problems and bad weather conditions on some of the VLBA antennas.
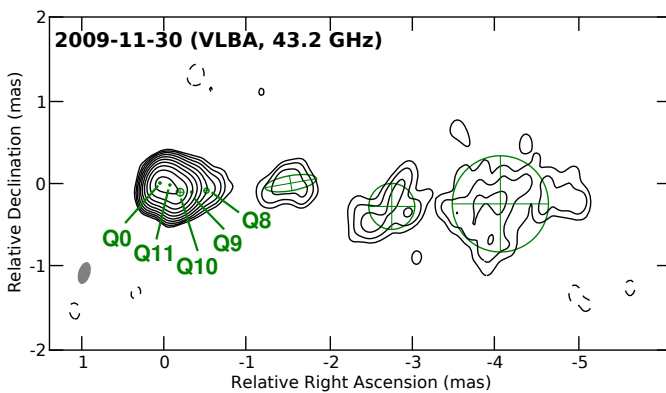

Fig. 2. VLBA image of total intensity of 3C 345 at 43.2 GHz made from observations on Nov. 30, 2009. Open circles show FWHM of eight Gaussian components applied to fit the structure observed. Shaded ellipse represents the FWHM of the restoring beam. The image peak flux density is 2.1 Jy beam^{-1} and the r.m.s. noise is 1 mJy beam^{-1}. The contour levels are (-0.15, 0.15, 0.3, 0.6, 1.2, 2.4, 4.8, 9.6, 19, 38, 77) % of the peak flux density.

Relative positional offsets of the components Q10, Q9, and Q8 are measured with respect to the base of the jet at the component Q0. All three features follow a similar trajectory, however curiously the recently detected Q11 shows a north-ward offset by 0.025 mas ($\sim$1/7th of the beam size) in its trajectory, compared to the previous features. This should be verified by continued radio monitoring of the jet.

All newly ejected jet features show similar apparent acceleration from about 2 - 10 c over a distance of 0.2 mas.

3.2. γ-Ray Emission

The weekly binned light curve plotted in Fig. 1a., shows six distinct events above $2.4 \cdot 10^{-7}\,\mathrm{ph\,cm^{-2}\,s^{-1}}$.

The six events are split into two sub-categories according to their duration. Long events, with durations of 40–60 days, are labeled with roman capitals, shorter events, with durations of 20–35 days, are labeled with arabic numbers. These sub-categories can also be distinguished by their peak fluxes: the long events had peak flux values of $(3.86 - 5.19) \cdot 10^{-7}\,\mathrm{ph\,cm^{-2}\,s^{-1}}$, whereas short events ended up with a lower range of $(2.48 - 3.19) \cdot 10^{-7}\,\mathrm{ph\,cm^{-2}\,s^{-1}}$.

Flare III has been reported on previously in form of two Astronomers Telegrams by the *Fermi*/LAT (Reyes & Cheung(2009)) and GASP collaborations (Larionov et al.(2009)), reporting on mm-wavelength (230 GHz SMA), optical (R-Band) and γ-ray (GeV) activity.

3.3. Radio-γ-ray Correlation

A first look at the γ-ray light curve (Fig. 1 a) gives the impression of a rising underlying trend in the γ-ray emission similar to the one observed in radio.

The radio and γ-ray light curves were de-trended using cubic spline interpolations with 0.5 year bins (Press et al.(1992)). Remarkably as shown in Fig 3, the jet matches the long-term trend of the γ-rays. A mismatch of the first 0.5 year results from absence of γ-ray data before 2008.6 and a secondary weaker γ-ray flare after 2008.7 (see Fig. 1) which contributes to the flux level at 2008.8 causing a slightly higher starting flux. The core showed none to little variation in flux density over this time period, with an average value around 1.5 Jy.

A discrete correlation as described by Edelson & Krolik(1988) was applied on the re-scaled and de-trended light curves. No strong correlation is evident neither for the jet nor for the core after de-trending. However, the jet shows a weak correlation with a coefficient of 0.6 ± 0.3 at time lag 3 ± 15 days and a weak anti-correlation in the following bin of -0.6 ± 0.3.

Sparse sampling of the radio data makes it difficult to obtain firm specific localizations of individual events in the radio jet. Nonetheless, the similarity of the long-term trends observed in the light-curves provides good evidence
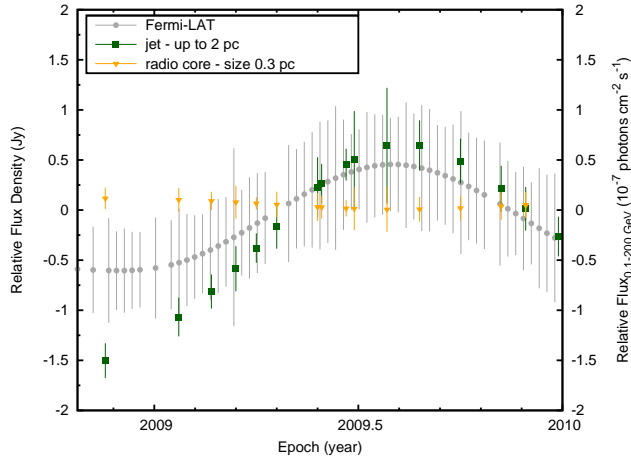
Fig. 3. Long-term trends of the radio jet, radio core flux densities and the γ-ray flux relative to their respective mean values (jet: 3.6 Jy, core: 1.5 Jy, γ: $1.9 \cdot 10^{-7}$ ph cm^{-2} s^{-1}). The trend has been extracted using splines with 0.5 year bins. γ-ray and radio light curves between 2009.8 and 2010.0 have been rescaled. The 0 value represents the respective mean value of 3.60 Jy for the radio flux density of the jet of an apparent size of ≤ 2 pc (excluding the core), 1.5 Jy for the flux density of the core of an apparent size of ~ 0.3 pc and $1.9 \cdot 10^{-7}$ ph cm^{-2} s^{-1} for γ-rays.

for correlated underlying emission between the radio flux density of the jet and the γ-ray flux.

4. Summary & Conclusions

We have found a correspondence between the long-term *Fermi*-LAT light-curve of the region 1FGL J1642.5+3947 and radio emission of 3C 345, establishing the detection of γ-ray emission from 3C 345 by comparison of radio and γ-ray variability.

More importantly, we find γ-ray emission to be related to the pc-scale jet of the source of up to 2 pc (~ 40 pc de-projected adopting a viewing angle of $\theta \sim 2.7°$; Jorstad et al.(2005)). We have been able to trace back the ejection of new superluminally moving and apparently accelerating features in the jet to be linked to γ-ray production. Even though a correspondence between the jet and γ-ray emission was found, there is no evidence for correlation between γ-ray emission and radio core flux density at 43 GHz. The observed radio properties of these features together with the observed γ-ray variability question existing jet models and suggest the synchrotron self-Compton (SSC) process as the most likely mechanism driving the production of γ-ray photons in the source. This conclusion is supported by the spectral energy distribution of 3C 345 being compatible with SSC exhibiting an IC to synchrotron peak ratio of only ~ 5 (for the Oct. 2009 flare).

Continued monitoring and more densely sampled VLBI observations could provide better confirmation of our results and provide an opportunity to localize more accurately the sites of individual flares in the jet. At this writing, the nuclear region of 3C 345 remains at high flux density and γ-ray flux levels are still elevated. The characteristics of the long-term activity of the source as observed over the last 30 years suggest that this continued activity may last for at least another year, giving a unique opportunity to trace this active state.

References

The Fermi-LAT Collaboration 2010a, arXiv:1002.2280, ApJS accepted
Abdo, A. A., et al. 2010b, ApJ, 715, 429
Abdo, A. A., et al. 2009a, ApJ, 700, 597
Abdo, A. A., et al. 2009b, ApJS, 183, 46
Aller, H. D., Aller, M. F., & Hughes, P. A. 1996, Blazar Continuum Variability, 110, 208
Atwood, W. B., et al. 2009, ApJ, 697, 1071
Babadzhanyants, M. K., & Belokon, E. T. 1984, Astrophysics, 20, 461
Casandjian, J.-M., & Grenier, I. A. 2008, A&A, 489, 849
Edelson, R. A., & Krolik, J. H. 1988, ApJ, 333, 646
Jorstad, S. G., et al. 2005, AJ, 130, 1418
Kidger, M., & Takalo, L. 1990, A&A, 239, L9
Press, W. H., et al. 1992, Cambridge: University Press, —c1992, 2nd ed.,
Reyes, L. C., & Cheung, C. C. 2009, ATel, 2226, 1
Schinzel, F. K., et al. for the *Fermi*/LAT collaboration 2010, *in prep.*
Schneider, D. P., et al. 2007, AJ, 134, 102
Shepherd, M. C., Pearson, T. J., & Taylor, G. B. 1995, BAAS, 27, 903
Teraesranta, H., et al. 1998, A&AS, 132, 305
Larionov, V. M., et al. 2009, ATel, 2222, 1
Lobanov, A. P., & Zensus, J. A. 1999, ApJ, 521, 509

The TANAMI Program

Roopesh Ojha[1]*, Matthias Kadler[2,3,4], Moritz Böck[2], Faith Hungwe[5,6], Cornelia Müller[2], Joern Wilms[2], Eduardo Ros[7,8], and the TANAMI Team

[1] NVI/United States Naval Observatory, 3450 Massachusetts Ave, NW, Washington, DC 20392-5420, USA
[2] Dr. Karl Remeis-Sternwarte & ECAP, Sternwartstrasse 7, 96049 Bamberg, Germany
[3] CRESST/NASA Goddard Space Flight Center, Greenbelt, MD 20771, USA
[4] USRA, 10211 Wincopin Circle, Suite 500 Columbia, MD 21044, USA
[5] Department of Physics & Electronics, Rhodes University, PO Box 94, Grahamstown 6140, South Africa
[6] Hartebeesthoek Radio Astronomy Observatory, PO Box 443, Krugersdorp 1740, South Africa
[7] Department d'Astronomia i Astrofisica, Universitat de València, E-46100 Burjassot, Spain
[8] Max-Planck-Institut für Radioastronomie, Auf dem Hügel 69, D-53121 Bonn, Germany

Abstract. The TANAMI (Tracking AGN with Austral Milliarcsecond Interferometry) program provides comprehensive VLBI monitoring of extragalactic gamma-ray sources south of declination -30 degrees. Operating at two radio frequencies (8 and 22 GHz), this program is a critical component of the joint quasi-simultaneous observations with the *Fermi Gamma-Ray Space Telescope* and ground based observatories to discriminate between competing theoretical blazar emission models. We describe the TANAMI program and present early results on the 75 sources currently being monitored.

1. Introduction

Very Long Baseline Interferometry (VLBI) observations play a unique role in unraveling the physics of active galactic nuclei (AGN). They provide the only direct measurements of relativistic motion in AGN, thus measuring jet speeds, Doppler factors, opening and inclination angles of jets. With their unmatched resolution, VLBI observations can allow us to associate γ-ray flaring activity with structural changes on millarcsecond scales (such as jet-component ejections) helping to identify the location and extent of emission regions.

VLBI observations have acquired particular salience in the age of *Fermi*. Data from *Fermi*/LAT in combination with other space and ground-based telescopes have made possible the quasi-simultaneous observations across the electromagnetic spectrum that have long been considered essential to distinguish between different models of AGN emission. The close connection between VLBI and *Fermi* observations is impressively demonstrated by the large number of VLBI-*Fermi* papers published and submitted in the past year, including many from the *Fermi*/LAT collaboration, to which VLBI observations have contributed crucially needed data for the proper interpretation of γ-ray results. With VLBI data we have started to address some of the most crucial questions raised by the association of γ-ray emission with blazars.

2. The TANAMI Program

The indispensable role of parsec-scale monitoring of radio- and γ-ray bright AGN has lead to the establishment of a

number of highly successful VLBI monitoring programs (see Lister et al. 2010 for a review) but all of these programs use northern hemisphere arrays that cannot observe much of the southern hemisphere. The TANAMI program is the only parsec scale monitoring program targeting AGN south of declination $-30°$. Further, uniquely among comparable VLBI programs, TANAMI observations are made at two frequencies (8.4 and 22 GHz). This lets us monitor the parsec-scale spectra of the cores and the brightest jet features, allowing us to contribute radio spectral indices of jet features to *Fermi* multi-wavelength studies (e.g., Abdo et al. 2010a, Chang et al. 2010) besides probing emission processes along AGN jets (e.g., Müller et al. 2010, Hungwe et al. 2010).

Since it covers that third of the sky not observed by other VLBI monitoring programs, TANAMI significantly improves the statistics for jet kinematics and flare-ejection studies. This region of the sky includes many interesting AGN (see below) and newly discovered γ-ray AGN can be followed up, often for the first time, with VLBI (e.g., Abdo et al. 2009). The TANAMI collaboration has also begun work with the ANTARES (Coyle 2010) and KM3NeT (Piattelli 2010) consortia, two neutrino telescopes that target the southern sky. *Fermi* γ-ray variability data and TANAMI-determined jet-ejection epochs will help develop data-filtering techniques to search for extragalactic neutrino point sources. This could usher us into an era of multi-messenger astronomy.

TANAMI observations are made using the telescopes of the Australian Long Baseline Array (LBA[1]; e.g.,

---

* rojha@usno.navy.mil

[1] The Long Baseline Array is part of the Australia Telescope which is funded by the Commonwealth of Australia for operation as a National Facility managed by CSIRO.
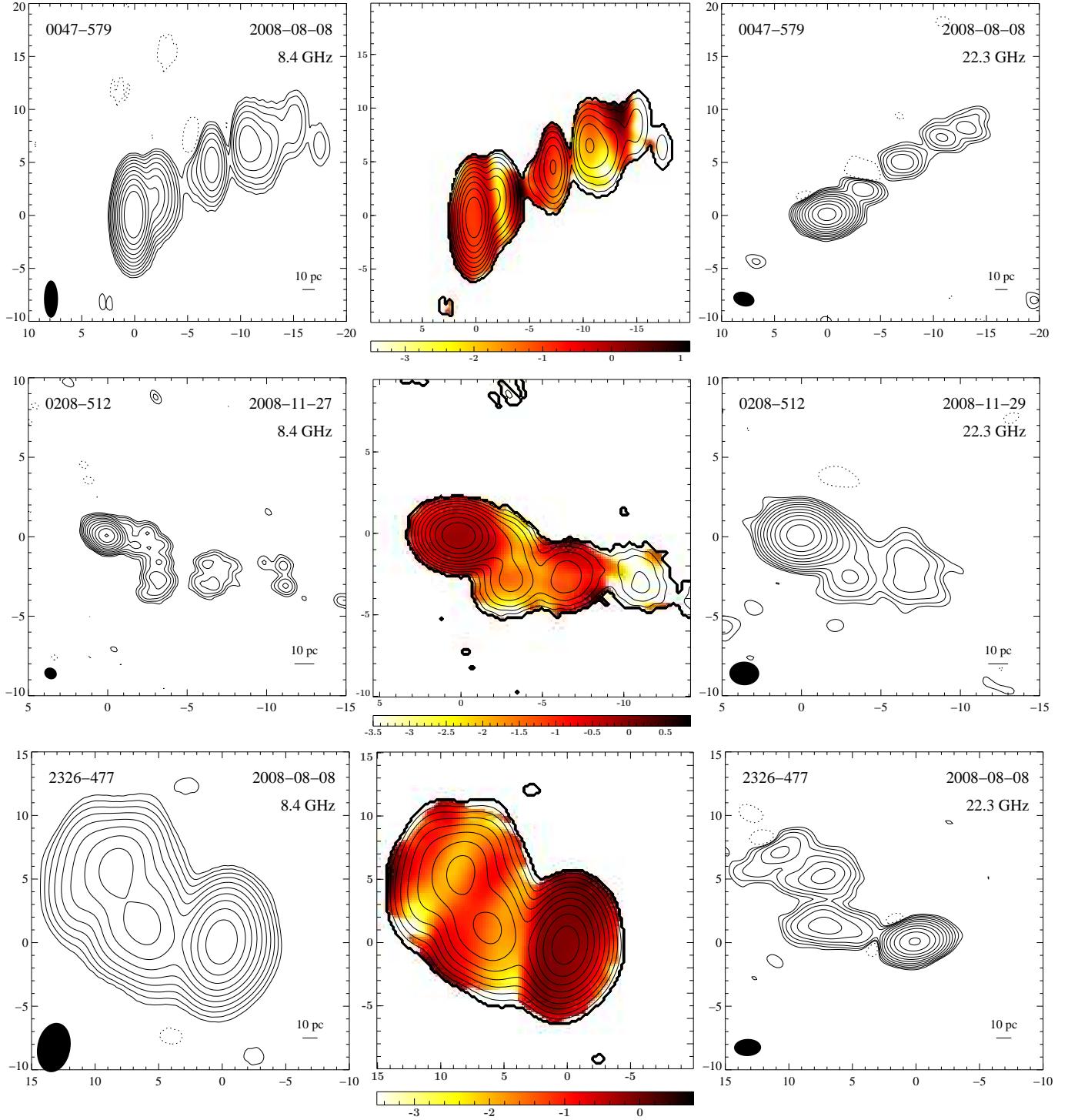
Fig. 1. TANAMI images of four *Fermi* sources. Starting from the top, the four rows show images of 0047−579, 0208−512, and 2326−477 respectively. In each row the left image shows the image at 8 GHz and the image on the right at 22 GHz at the same epoch. In the center of each row is the spectral index image made from the simultaneous images at these two frequencies. Both the axes in all plots are labeled in milliarcseconds from the center of the image. The hatched ellipse at the bottom left of each contour image represents the synthesized beam of the observing array. The color coding in the spectral index image represents the spectral index defined as $F_\nu \sim \nu^+\alpha$.

Ojha et al. 2005) and affiliated telescopes. TANAMI was able to significantly improve the (u, v)-coverage of the LBA by obtaining access to International VLBI Service (IVS) telescopes in Antarctica and Chile as well as Deep Space Network telescopes in Tidbinbilla, Australia. All telescopes that participate in TANAMI observations are listed, along with their diameters, in Table 1. At each epoch and each frequency, every source is typically observed for 6 scans of about 10 minutes each. Typical (u, v)-coverage at both frequencies are shown in Müller et al. 2010. Our augmentation of the LBA has lead to the highest fidelity images for most of the sources observed by TANAMI.

The initial sample of 44 TANAMI sources were selected based on previous (EGRET) γ-ray detection and/or radio flux density and luminosity. Under an MoU (Memorandum of Understanding) with the *Fermi* collaboration TANAMI started monitoring observations of new *Fermi* sources through 2009 adding the new sources to our observing schedule while decreasing the observing cadence of sources showing limited radio-structural variability. The current TANAMI sample includes 75 sources of which 55 have been detected by *Fermi*. 53 TANAMI sources have 1FGL (Abdo et al. 2010c) associations while 2 are tentative new detections (Böck et al. 2010). To date, 12 epochs (most at both frequencies) have been observed. Correlation, processing and imaging are progressing smoothly. Images and other results are available at our website[2] as soon as they are finalized. For further details of the TANAMI program including details of calibration and imaging see Ojha et al. (2010).

3. Results

TANAMI is routinely producing VLBI images of high quality at 8 and 22 GHz (X and K-band respectively). We show examples for three sources in Fig. 1. For each source we show the 8.4 GHz image and the 22 GHz image from the same epoch (on the left and right respectively). In the center of each row is shown the corresponding two-frequency spectral index image. It is important to note that the resolution of the lower frequency image is often *better* than that of the higher frequency image because the trans-oceanic telescopes in Antarctica and Chile cannot observe at 22 GHz.

These spectral index images were made by aligning the brightest pixels in the X and K-band images from the same epoch. The images at both frequencies have been convolved with the larger of the two beams of the individual images. The larger beam has also been used to produce the overlaid contours on these images. The color coding depicts the spectral index defined as $F_\nu \sim \nu^\alpha$ i.e., a positive spectral indicates an inverted spectrum. Thus we are able to measure spectral indices of the cores and individual jet features and we are using these data to measure core shift, localize the central engine, calculate the opac-

---

[2] http://pulsar.sternwarte.uni-erlangen.de/tanami/

Table 1. VLBI array for TANAMI observations.

Telescope	Diameter [m]
Parkes, NSW, Australia	64
Narrabri, NSW, Australia	5×22
Hobart, TAS, Australia	26
Ceduna, SA, Australia	30
Hartebeesthoek, S. Africa[a]	26
DSS43, ACT, Australia[b]	70
DSS45, ACT, Australia[b]	34
O'Higgins, Antarctica[c]	9
TIGO, Concepción, Chile[c]	6

[a] Not available since Sept 2008. Likely return Sept 2010.
[b] Operated by the Deep Space Network of the National Aeronautics and Space Administration, USA
[c] Operated by the German Bundesamt für Kartographie und Geodäsie (BKG) http://www.bkg.bund.de/nn_147094/ EN/Home/homepage__node.html__nnn=true

ity towards the central engine and identify the emission along the jet. In combination with data at other wavelengths we are modeling the SEDs of AGN. Note that the figures shown here are not corrected for coreshift.

For a growing number of sources in our sample we have enough epochs of data to study their kinematics. We are fitting Gaussian components to jet features to track jet trajectories, measure their speeds, and derive their intrinsic parameters. When combined with SED modeling, these kinematic data address the relationship between the Doppler-boosting parameters for the radio and γ-ray emitting regions of the jets.

TANAMI data have been and are being used in a number of studies that can broadly divided into two categories, individual source studies and statistical studies of the full sample or some subset, which are briefly described below.

3.1. Individual Source Studies

Studies of individual TANAMI sources include:
• One of the first *Fermi*/LAT publications addresses a bright γ-ray flare of the poorly studied source PKS 1454-354 (Abdo et al. 2009). TANAMI contributed the first deep 8.4 GHz VLBI image of this source revealing its core-jet structure.
• TANAMI data on nine *Fermi*/LAT sources were used to generate SEDs of the γ-ray selected LBAS blazars and investigate their broadband spectral propeties (Abdo et al. 2010a).
• TANAMI data were used to construct the SED of PKS 2052−47 during a LAT multiwavelength campaign (Chang et al. 2010).
• TANAMI data are being used to study the highly variable BLLac 0537−441 which is one of the most luminous γ-ray blazars detected in the southern sky so far (Hungwe et al. 2010)

• TANAMI data were used to constrain the size of the γ-ray emitting region and for SED modeling of the nearest galaxy Centaurus A (Abdo et al. 2010b). A multi-epoch, dual-frequency analysis of the innermost regions of this source is in progress (Müller et al. 2010)

3.2. First Epoch Results

First epoch 8.4 GHz results for the initial sample of 43 sources have been analyzed and presented in Ojha et al. (2010). Using the classification scheme of Kellermann et al. (1998), the initial sample has 33 single-side (SS) and 5 double-sided (DS) sources with just one example each of the compact (C) and irregular (Irr) morphological types. Three sources do not have an optical identification. All of the quasars and BL Lacertae objects in the sample have an SS morphology while all 5 DS sources are galaxies. The lone C source is optically unidentified while the only Irr source is a GPS galaxy 1718−649.

The core and the total luminosity was calculated for all 38 initial TANAMI sources that had published redshifts, assuming isotropic emission. There is no significant difference in the distribution of luminosities of LBAS and non-LBAS sources. On the other hand, there is a clear relationship between luminosity and optical type with quasars dominating the high luminosity end of the distribution, galaxies dominating the low luminosity end while the BL Lacertae objects fall in between.

The redshift distribution of the quasars and BLLacs in the TANAMI sample is similar to those for the LBAS and EGRET blazars. There does not appear to be any significant difference between the radio- and γ-ray selected subsamples. The core brightness temperature ($T_{\rm B}$) limit of all initial TANAMI sources was calculated. The high end of the distribution of calculated brightness temperatures is dominated by quasars and the low end by BL Lacertae objects and galaxies. Of the 43 sources in the sample, 14 have a maximum $T_{\rm B}$ below the equipartition value of 10^{11} K (Readhead 1994), 30 below the inverse Compton limit of 10^{12} K (Kellermann & Pauliny-Toth 1969), putting about a third of the values above this limit. There is no significant difference in the brightness temperature distribution of LBAS and non-LBAS sources.

A link between γ-ray emission and the parsec scale morphology of AGN has been sought (e.g., Taylor et al. 2007). We fit circular Gaussians to the visibility data and measured the angle at which the innermost jet component appears relative to the position of the core i.e. the opening angle. Of the LAT AGN Bright Sample (LBAS) sources 78% have an opening angle > 30 degrees while only 27% of non-LBAS sources do. This result should be treated with great caution as the sample size for this analysis is currently small but Pushkarev et al. (2009) report similar results.

If confirmed, the above result presents two possibilities: either the LBAS jets have smaller Lorentz factors (since the width of the relativistic beaming cone $\sim 1/\Gamma$) or LBAS jets are pointed closer to the line of sight than γ-ray faint jets. The former scenario appears unlikely, indeed the opposite effect is reported by Lister et al. (2009), Kovalev et al. (2009).

4. Conclusions

Fermi sources in the southern third of the sky are being monitored by the TANAMI program at about every two months. These high quality, dual frequency observations are producing spectral index images at milliarcsecond resolutions which are a crucial element in the multiwavelength study of AGN physics. For a subset of the TANAMI sample, the number of observed epochs is now sufficient for kinematic modeling to begin. When combined with jet-speed measurements, SED modeling across the electromagnetic spectrum will let us probe the relation between the Doppler-boosting parameters for the radio and γ-ray emitting regions of the jet.

Studies of several individual AGN detected by *Fermi* have been enriched by data from the TANAMI program and multiwavelength analysis of a number of interesting sources are in progress. Statistical analysis of the growing TANAMI sample is providing broader insight into the tie between the low- and high-energy radiation from AGN.

References

Abdo, A. A., et al. 2009, ApJ, 697, 934
Abdo, A. A, et al. 2010, ApJ, 716, 30
Abdo, A. A., et al. 2010, ApJ, submitted
Abdo, A. A., et al. 2010, ApJS, 188, 405
Böck et al. 2009, Fermi Symposium, eConf Proc C091122 [arXiv:0912.4192]
Böck, M., et al. 2010, these proceedings, p. 17
Chang, C.-S. et al. 2010, Fermi Symposium, eConf Proc C091122, [arXiv:1001.1563]
Coyle, P. 2010, in Proc. of the 31st Intnl. Cosmic Ray Conf., in press, [arXiv:1002.0754]
Hungwe, F., Ojha. R, et al. 2010, these proceedings p. 199
Kellermann, K. I., Vermeulen, R. C., Zensus, J. A., Cohen, M. H. 1998, AJ 115, 1295
Kellermann, K. I., Pauliny-Toth, I. I. K. 1969, ApJ 155, L71
Kovalev Y. Y., Aller H. D., et al. 2009, ApJ 696, L17
Lister M. L., et al. 2009, AJ 137, 3718
Lister. M. L., et al. 2010, these proceedings, p. 159
Müller, C., et al. 2010, these proceedings, p. 229
Ojha, R, et al. 2005, AJ, 130, 2529
Ojha, R, et al. 2010, A&A, in press, [arXiv:1005.4432]
Piattelli, P. 2010, Earth, Planets and Space, 62, 201
Pushkarev, A. B., Kovalev, Y. Y., Lister, M. L., & Savolainen, T. 2009, A&A, 507, L33
Readhead, A. C. S. 1994, ApJ, 426, 51
Taylor, G. B., et al. 2007, ApJ, 671, 1355

A new sample of faint blazars

F. Mantovani, M. Bondi, and K.-H. Mack

Istituto di Radioastronomia – INAF, Via P. Gobetti, 101, I-40129 Bologna, Italy

Abstract. We report on Effelsberg 100-m telescope multi-frequency observations of a sample of 103 faint blazars. They were extracted from the "Deep X-ray Radio Blazar Survey" selecting objects with Declination > -20 deg. Results on their flux density variability with time, percentage of polarised emission, and spectral index behaviour are given. This sample of blazars is also target of a high resolution campaign aimed at defining their structure at milli-arcsecond resolution. A sub-sample of 18 of them has been observed with the European VLBI Network at 5 GHz, first step of a monitoring programme to check for structural changes and their correlation with *Fermi*-detected AGN. Preliminary results of the data analysis are given.

1. Introduction

Blazars are an extreme class of Active Galactic Nuclei (AGN), characterized by high luminosity, rapid variability, and high polarisation. In the radio band, blazars are core-dominated objects with apparent superluminal speeds along relativistic jets pointed close to the observer's line of sight. Their broadband emission is mainly of non-thermal origin, generated from synchrotron and inverse Compton mechanisms. Blazars have flat spectral indices and they include flat-spectrum radio quasars and BL Lacertae objects, the counterparts of high- and low-luminosity radio galaxies. Due to their orientation with respect to the line of sight, blazars represent less than 5% of all AGNs, a quite rare class of sources.

The available blazar samples were selected at relatively high limiting flux densities in the radio and X-ray band, ~ 1 Jy and a few times 10^{-13} ergs cm^{-2} s^{-1}, respectively. Those samples have small sizes (30–50 objects) making it difficult to statistically derive parameters related to beaming effects. Moreover, the estimate of those parameters is based on bright and intrinsically luminous sources.

A deeper, larger sample of blazars has been constructed by Perlman et al. 1998 and by Landt et al. 2001: the "Deep X-ray Radio Blazar Survey" (DXRBS). The DXRBS has been constructed by cross-correlating all ROSAT sources of the WGCAT catalogue (White, Giommi & Angelini 1995) and radio sources with flat radio spectra. The radio flux densities ($S_{5\,GHz} > 50$ mJy; $S_{1.4\,GHz} > 100$ mJy) have been taken from available catalogues, like GB6 (Gregory et al. 1996), NORTH20CM (White & Becker 1992), and PMN (Griffith & Wright 1993).

1.1. Spectral indices behaviour

The DXRBS sample is currently the faintest, down to ~ 50 mJy at 5 GHz and power $\sim 10^{24}$ W Hz^{-1}, and largest blazar sample with nearly complete optical identifications. It includes both Flat Spectrum Radio Quasars (FSRQs)

and BL Lac sources. Sources have been included in the DXRBS list when their two point spectral index α between 1.4 GHz and 5 GHz is flatter than 0.7 (S $\propto \nu^{-\alpha}$). However, blazars are variable sources. Simultaneous flux density measurements at several frequencies of DXRBS sources to obtain reliable spectral index is needed to better define their classification. Moreover, new flux density measurements will allow us to look for flux density variability through a comparison with previous measurements available in the literature.

Blazars are well known γ-ray sources. EGRET has detected about 130 blazars, likely a lower limit. It is expected that the *Fermi Gamma-Ray Space Telescope*, formerly *GLAST*, ~ 30 times more sensitive than EGRET, will detect more than 20,000 blazars over the whole sky. It is reasonable to expect that the objects in the DXRBS will be possible counterparts of γ-ray sources detected by the *Fermi Gamma-Ray Space Telescope*. For this reason, information on their radio structure is of course fundamental.

We are undertaking an extensive observing investigation of the DXRBS sample. Our goal is to check the completeness of the DXRBS catalogue verifying the spectral index classification of each source and their radio structure at both sub-arcsecond and milli-arcsecond resolution of the listed objects. Finally, we plan for further VLBI monitoring observations of the detected sources looking for relativistic motions.

2. Results from Effelsberg 100-m telescope observations

We have made simultaneous flux density measurements of all DXRBS sources with declination > -20 deg with the Effelsberg 100-m telescope at four independent frequencies, namely 2.64 GHz, 4.85 GHz, 8.35 GHz, and 10.45 GHz. They represent a complete sample of 103 objects with known optical identification and redshift. The main aim was the determination of their radio spectrum, originally defined taking flux density measure-
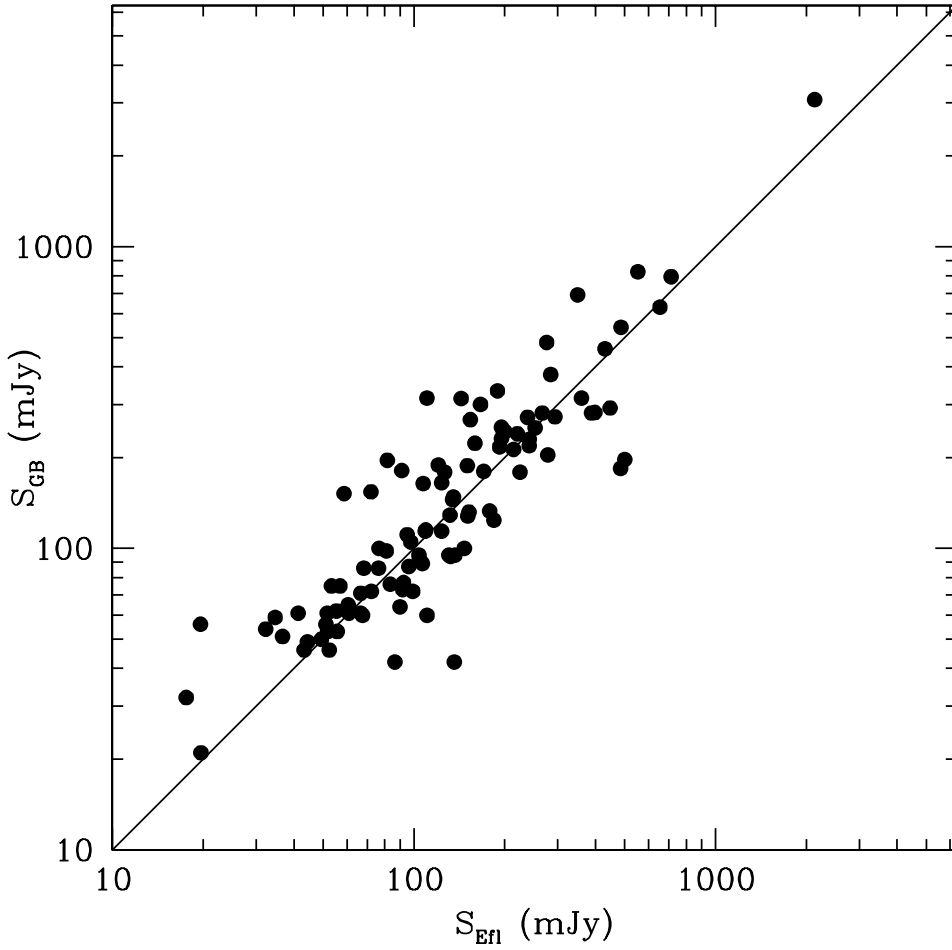
Fig. 1. Effelsberg flux densities *vs* GB6 flux densities at 5 GHz. The straight line means a ratio of 1. The size of a dot represents a flux density error of 10%.

ments at 1.4 GHz and 5 GHz from existing catalogues. Measurements done at 5 GHz have also allowed us to look for any flux density variability through a comparison with the measurements available in the GB6 catalogue (Gregory et al. 1996). The observations were carried out in a few days in July 2009. Since all the target sources are point-like to the Effelsberg telescope beams, we used standard cross-scanning along the azimuth and elevation axes to determine their total intensity and polarisation emission. Details about the observation mode, calibration and evaluation of flux density errors are found in Mantovani et al. (2009).

About 14% of the sources in our DXRBS sub-sample show a clearly inverted spectrum, while about 6% of the sources possess a spectral index steeper than 0.7. Consequently, this last group of sources cannot be classified as FSRQs. The remaining sources do have a more complex spectral index, however with a clear indication of flattening at higher frequencies, sign of the existence of a compact component.

2.1. Polarised emission

The percentage of polarised flux density that we can reliably measure with the observing mode adopted using the Effelsberg 100-m telescope is $\geq$ 3% and $\geq$ 2%

at 2.64 GHz and 4.85 GHz, respectively. At 2.64 GHz we found 25 sources polarised with a median value of the percentage of polarised emission of $4.9\pm^{1.1}_{0.4}$ %. At 4.85 GHz we found 36 sources polarised with a median polarisation degree of 5.8 ± 0.9 %. These values are typical of the class of FSRQs.

2.2. Flux density variability

The flux densities obtained with the 100-m Effelsberg telescope at 5 GHz in July 2009 can be compared with the flux densities listed in the GB6 catalogue. The Green Bank catalogue has been built from observations performed in 1986-87. That catalogue contains sources with $S_{5\,\mathrm{GHz}} > 18\,\mathrm{mJy}$. A 20 mJy source has an error of 4-5 mJy. Both the Effelsberg and GB6 flux density measurements are on the Baars scale (Baars et al. 1977).

In Fig. 1 we plot the Effelsberg flux densities *versus* the GB6 flux densities at 5 GHz. The size of a dot represents a flux density error of 10%. The flux density measurements are well placed around the equal flux line, with a scatter given by the variability. To quantify the number of sources showing significant variations, in Fig. 2 we plot the histogram of the quantity $|S_{\mathrm{Eff}} - S_{\mathrm{GB}}|/S_{\mathrm{GB}}$. About 50% of the sources in our sample exhibit flux density variations larger than 20% on a temporal scale of about 22 years.
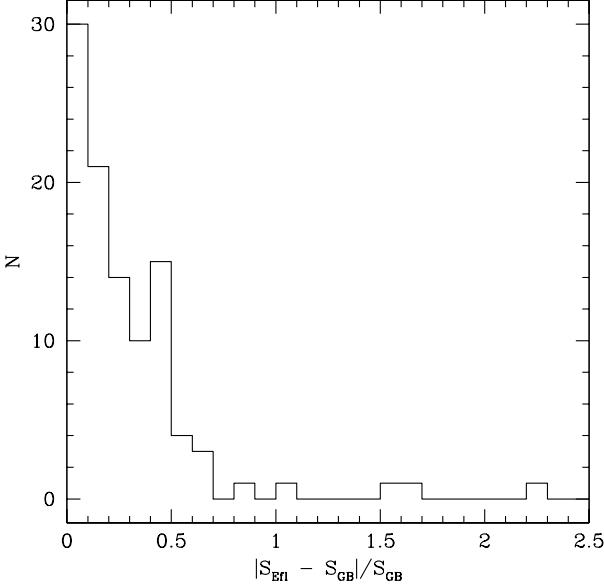
Fig. 2. Cumulative histogram of the ratio between the Effelsberg flux density minus the GB6 flux density module and the GB6 flux density.

3. Results from EVN observations

The high resolution radio structure of the blazars listed in the DXRBS is not known yet. The target objects are blazars and we expect that the large majority of them are very compact and easily detectable by the EVN observations. We have planned to observe with the EVN a subsample of those blazars. We restrict the number of sources in our sample introducing a limit in declination only. Of the 103 target objects, $\sim$ 13% are BL Lacs and $\sim$ 87% FSRQs. We have extracted the positions of those DXRBS objects from the FIRST (Becker et al. 1994) and from the NVSS (Condon et al. 1998) catalogues at 1.4 GHz. Positions for 63 objects are available in the FIRST catalogue with an accuracy better than $0.5''$.

We report here on the results obtained observing 18 objects during the October 2009 EVN session at 5 GHz. A second sub-sample will be observed during the coming May–June 2010 session.

The observations were done with an array of 11 EVN telescopes at a frequency of 5 GHz and single LHC polarisation. The recording bit rate was 512 ,Mbps, with a 2-bit sampling. Each source was observed with 5–6 scans at different hour angles. The data set has been processed with an integration time of 1 second to achieve a wide field of view ($\sim 11''$) with the MPIfR Software Correlator, Bonn.

All the 18 sources observed have been detected and fringes were found at all the baselines. Twelve sources are core dominated with a core-jet structure. The remaining 6 sources are point-like. The resolution achieved with these observations is better than 5 mas along the major axis. As an example of a core-jet source the image of WGA J0829.5+0858 is presented in Fig. 3.

The total flux density measured in the VLBI images is in all cases lower than that measured with single-dish ob-
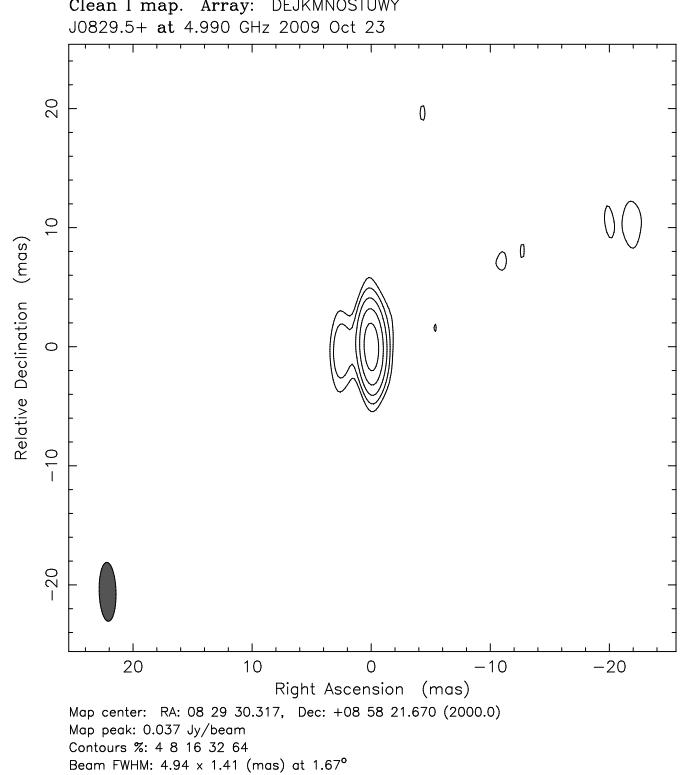

Fig. 3. EVN image at 5 GHz of the source WGA J0829.5+0858.

servations few months earlier. Only WGA J1101.8+6241 shows a ratio around 1, while WGA J0937.1+5008 presents a ratio of 2.3. The former has a core-jet structure, while WGA J0937.1+5008 looks point-like for our observing resolution.

4. Fermi and the DXRBS sample

The list of sources detected by *Fermi* after 1 year of observing activity has been recently made public (Abdo et al. 2010). Eight out of 103 sources in our declination limited complete sub-sample of DXRBS sources have been detected. Two of them, namely WGA J0847.2+1133 and WGA J0937.1+5008, are part of the first set of sources we observed with the EVN at 5 GHz. Both are classified as point-like sources. The source WGA J0847.2+1133 is a BL Lac object at z=0.198 with a steep spectral index between 2.65 GHz and 4.85 GHz and an inverted spectra between 4.85 GHz and 8.35 GHz. The flux density ratio between the VLBI value and the Effelsberg value is of 0.28. It shows a variability as high as 50% comparing the Effelsberg flux density and the GB6 flux density. The source WGA J0937.1+5008, a FSRQ at z=0.275, also exhibits a high degree of variability at 5 GHz, of the order of 60 to 70%. Moreover, it shows an increase in flux density by a factor of 2.3 comparing the Effelsberg flux density with the flux density measured few months later by the EVN at 5 GHz. This object has an inverted spectral index ($\alpha > 1$) from 2.65 GHz and 10.35 GHz. This source is worth to be monitored both for flux density variabil-

ity and for structural changes provided to be observed at sufficiently high resolution.

5. Conclusions

a) We are investigating a sample of 103 faint blazars with the goal of providing a comparison sample to the existing relatively bright samples both in radio and X-ray bands.

b) Multi-frequency observations with the Effelsberg 100-m telescope allowed us to define their one-epoch spectral index behaviour. 6% of them cannot be considered FSRQs any more.

c) About 50% of them show flux density variability greater than 20% comparing measurements done with a time delay of about 22 years.

d) 35% of the sources show polarised emission $\geq$2% at 5 GHz and 24% of them show polarised emission $\geq$3% at 2.65 GHz.

e) All the 18 sources observed so far with the EVN at 6 cm have been detected. Twelve exhibit a core-jet structure and 6 are point-like at a resolution higher than 5 mas.

f) Almost all sources show a VLBI flux density at 5 GHz much smaller than that achieved with single-dish observations performed almost at the same epoch, indication of the existence of extended emission resolved out by the high-resolution observations.

g) One source, WGA J0937.1+5008, point-like at the EVN resolution at 5 GHz, shows an increase in flux density by a factor of 2.3 comparing the VLBI flux density to that measured by single-dish observations few months earlier. WGA J0937.1+5008 presents an inverted spectral index.

h) Eight out of the 103 sources in our sample have been detected by *Fermi*. Two out of the 18 sources observed so far with the EVN are among the 8 detected by *Fermi*. The source WGA J0937.1+5008 is one of the two, deserving further follow-up monitoring observations to check for flux density variability and structural changes.

References

Abdo, A.A., Ackermann, M., Ajello, M. et al. 2010, ApJS 188, 405

Baars, J.W.M., Genzel, R., Pauliny-Toth, I.I.K. & Witzel, A. 1977, A&A 61, 99

Becker et al. 1994, ASP Conference Series, v. 61, eds. Crabtree, Hanisch & Barnes, p. 165

Condon, J.J., Cotton, W.D., Greisen, E.W. et al. 1998 AJ, 115, 1693

Gregory, P.C., Scott, W.K., Douglas, K, et al. 1996 ApJS, 103, 427

Griffith, M.R., & Wright, A.E. 1993 AJ, 105, 1666

Landt, H., Padovani, P., Perlman, E.S. et al. 2001 MNRAS, 323, 757

Mantovani, F., Mack, K.-H., Montenegro-Montes, F.M., et al. 2009 A&A, 512, 61

Perlman, E.S, Padovani, P., Giommi, P, et al. 1998 AJ, 115, 1253

White, N.E., & Becker, R.H. 1992 ApJS, 79, 331

White, N.E., Giommi, P., & Angelini, L. 1995 `http://lheawww.gsfc.nasa.gov/users.white/wgcat.wgcat.html`

The Jet in M 87 from e-EVN Observations

G. Giovannini[1,2], C. Casadio[1,2], M. Giroletti[1], M. Beilicke[3], A. Cesarini[4], and H. Krawczynski[3]

[1] Istituto di Radioastronomia-INAF, via Gobetti 101, 40129 Bologna, Italy
[2] Dipartimento di Astronomia, via Ranzani 1, 40127 Bologna, Italy
[3] Department of Physics, Washington University, St. Louis, MO 63130, USA
[4] School of Physics, National University of Ireland Galway, University Road, Galway, Republic of Ireland

Abstract. One of the most intriguing open questions of today's astrophysics is the one concerning the location and the mechanisms for the production of MeV, GeV, and TeV gamma-rays in AGN jets. M 87 is a privileged laboratory for a detailed study of the properties of jets, owing to its proximity, its massive black hole, and its conspicuous emission at radio wavelengths and above. We started on November 2009 a monitoring program with the e-EVN at 5 GHz, during which two episodes of activity at energy E>100 GeV have occured. We present here results of these multi-epoch observations. The inner jet and HST-1 are both detected and resolved in our datasets. One of these observations was obtained at the same day of the first high energy flare. A clear change in the proper motion velocity of HST-1 is present at the epoch ∼2000.5. In the time range 2003–2005.5 the apparent velocity is sub-luminal, and superluminal (∼2.7 c) after 2005.5.

1. Introduction

The giant radio galaxy Messier 87 (M 87), also known as 3C 274 or Virgo A, is one of the best studied radio sources and a known γ-ray-emitting AGN. It is located at the center of the Virgo cluster of galaxies at a distance of 16.7 Mpc, corresponding to an angular conversion 1 mas = 0.081 pc. The massive black hole at the M 87 center has an estimated mass of $6 \times 10^9\,M_\odot$, with a scale of 1 mas = 140 R_S. The bright jet is well resolved in the X-ray, optical, and radio wave bands.

The jet is characterized by many substructures and knots. In 1999 HST observations revealed a bright knot at about $1''$ from the core, named HST-1. This feature is active in the radio, optical, and X-ray regimes. It was discussed by Perlman et al. (1999), who compared optical and radio images. Biretta et al. (1999) measured in the range 1994-1998 a sub-luminal apparent speed of 0.84 c

Fig. 1. e-EVN image at 5 GHz of the inner jet of M 87, February 10th, 2010 epoch. The HPBW is 8×3.4 mas. Levels are -2 2 4 6 8 10 30 50 100 300 500 1000 1500 mJy/beam

for the brightest structure (HST-1 East), which appears to emit superluminal features moving at 6 c. However this motion was measured in regions on a larger scale with respect to the VLBI structures discussed here.

VLBI observations of the M 87 inner region show a well resolved, edge-brightened jet structure. At very high resolution (43 and 86 GHz) near to the brightest region the jet has a wide opening angle, and we refer to the many published papers which discuss the possible presence of a counter-jet and the location of the radio core (see e.g. Junor et al., 1999; Krichbaum et al., 2005; Ly et al., 2007; Kovalev et al., 2007).

Very High Energy (VHE) γ-ray emission was reported by the High Energy Gamma-Ray Astronomy (HEGRA) collaboration in 1998/99 (Aharonian et al., 2003), confirmed by the High Energy Stereoscopic System (HESS) in 2003-2006 (Aharonian et al., 2006), and by VERITAS in 2007 (Acciari et al., 2008). Coordinated intensive campaigns have permitted to detect the source again in 2008 (Acciari et al., 2009) and as recently as February and April 2010 (Mariotti, 2010; Ong, 2010). Steady emission at MeV/GeV energies has also been detected by *Fermi*/LAT (Abdo et al., 2009).

Various models have been proposed to explain the multi-wavelength emission and in particular to constrain the site of the VHE emission in M 87. The inner jet region was favoured by the observed short TeV variability timescales (Aharonian et al., 2006). The VHE emission could then be produced in the BH magnetosphere (Neronov & Aharonian, 2007) or in the slower jet layer (Tavecchio & Ghisellini, 2008), with the spine accounting for the emission from the radio to the GeV band; this would lead to a complex correlation between the TeV component and the lower energy ones.

However, VLBA observations at 1.7 GHz (Cheung et al., 2007) resolved HST-1 in substructures with superluminal components. Aharonian et al. (2006) discussed that HST-1 cannot be excluded as a source of TeV γ rays, however they conclude that the more promising possibility is that the site of TeV γ-ray production is the nucleus of M 87 itself. Comparing multi-frequency data Harris et al. (2008) suggested that the TeV emission from M 87 was originated in HST-1.

Finally, Acciari et al. (2009) reported rapid TeV flares from M 87 in February 2008, associated by an in increase of the radio flux from the nucleus, while HST-1 was in a low state, thus concluding that the TeV flares originate in the core region.

In this context we started at the end of 2009 a program to observe with the e-EVN M 87 at 5 GHz to study the properties of the M 87 core, jet, and HST-1 structure.

2. Observations and Data Reduction

Our original monitoring schedule included four epochs at 5 GHz, to be carried out before and during the season of visibility from the TeV telescopes, namely on 2009 November 19, 2010 January 27, February 10, and March 28. Following the February (Mariotti, 2010) and April (Ong, 2010) high energy events, three more epochs have been added on 2010 March 6, May 25, and June 9 as Target of Opportunity (ToO) observations.

The observations have been carried out in eVLBI mode, with data acquired by EVN radio telescopes, directly streamed to the central data processor at JIVE, and correlated in real-time. The observing frequency of 5 GHz was chosen to simultaneously grant a large field of view and a high angular resolution. For observations taking advantage of the long baselines provided by the Arecibo and Shanghai telescopes, our clean beam with uniform weights is about 2.0×0.9 mas in PA $-25°$.

As a result of the large bandwidth (a rate of 1 Gbps was sustained by most stations), long exposure (up to 6 hours per epoch), and extended collecting area, the rms noise in our images is mostly dynamic range limited. As an average value, we can quote 0.5–0.8 mJy beam^{-1} in the nuclear region and 0.1–0.2 mJy beam^{-1} in the HST-1 region. We present here preliminary results from the first 5 epochs. The reduction of May 25th data is still in progress.

3. Results

3.1. The inner jet region

In Fig. 1 we show the image obtained on Feb. 10th, 2010 of the core and inner jet region of M 87. The jet orientation and velocity has been discussed in many papers comparing observational data on the jet brightness and proper motion. Recently Acciari et al. (2009) assumed as a likely range $\theta = 15 - 25$ deg.

We used our images to search for evidence of a possible proper motion, comparing different epoch position
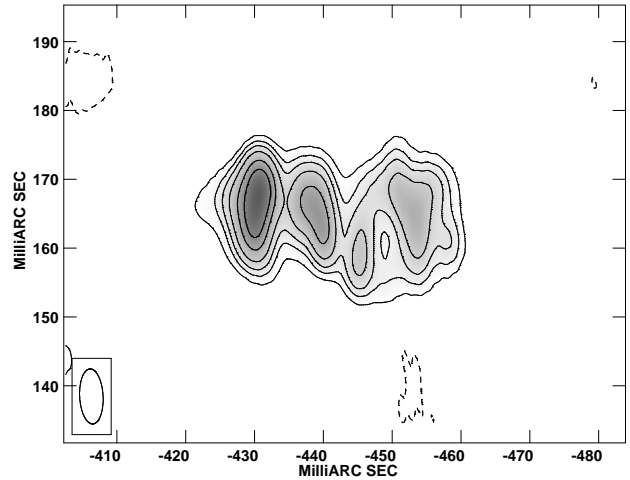
Fig. 2. e-EVN image at 5 GHz of HST-1, January 27th, 2010 epoch. The HPBW is 8×3.4 mas. Levels are -0.3 0.3 0.5 0.7 1 1.5 2 3 mJy/beam
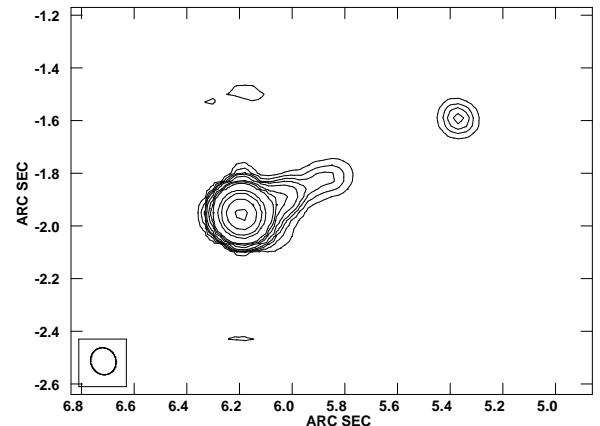

Fig. 3. VLA image at 5 GHz of the inner jet of M 87 obtained on November 2008. The HPBW is 0.10 arcsec. Levels are 5 10 15 20 30 50 70 100 300 500 1000 2000 mJy/beam

of jet substructures and subtracting images at different epochs (with the same grid, angular resolution and similar (u, v)-coverage) to look for possible systematic trends. No evidence was found in any case.

From the jet/counter-jet brightness ratio we derive that $\beta \cos \theta > 0.82$ which implies $\theta < 35°$.

To better constrain the jet velocity and orientation we assume that the jet limb-brightened structure is due to a velocity structure: a fast inner spine and a relatively slow external shear layer. In a range of θ it is possible that the Doppler factor of the slower external regions is higher than the Doppler factor of the fast spine. Therefore the apparent brightness of the spine can appear fainter than that of the shear layer. We estimated different Doppler factors using reasonable velocities and jet orientation. We found that if the orientation angle θ is in the range $20°$–
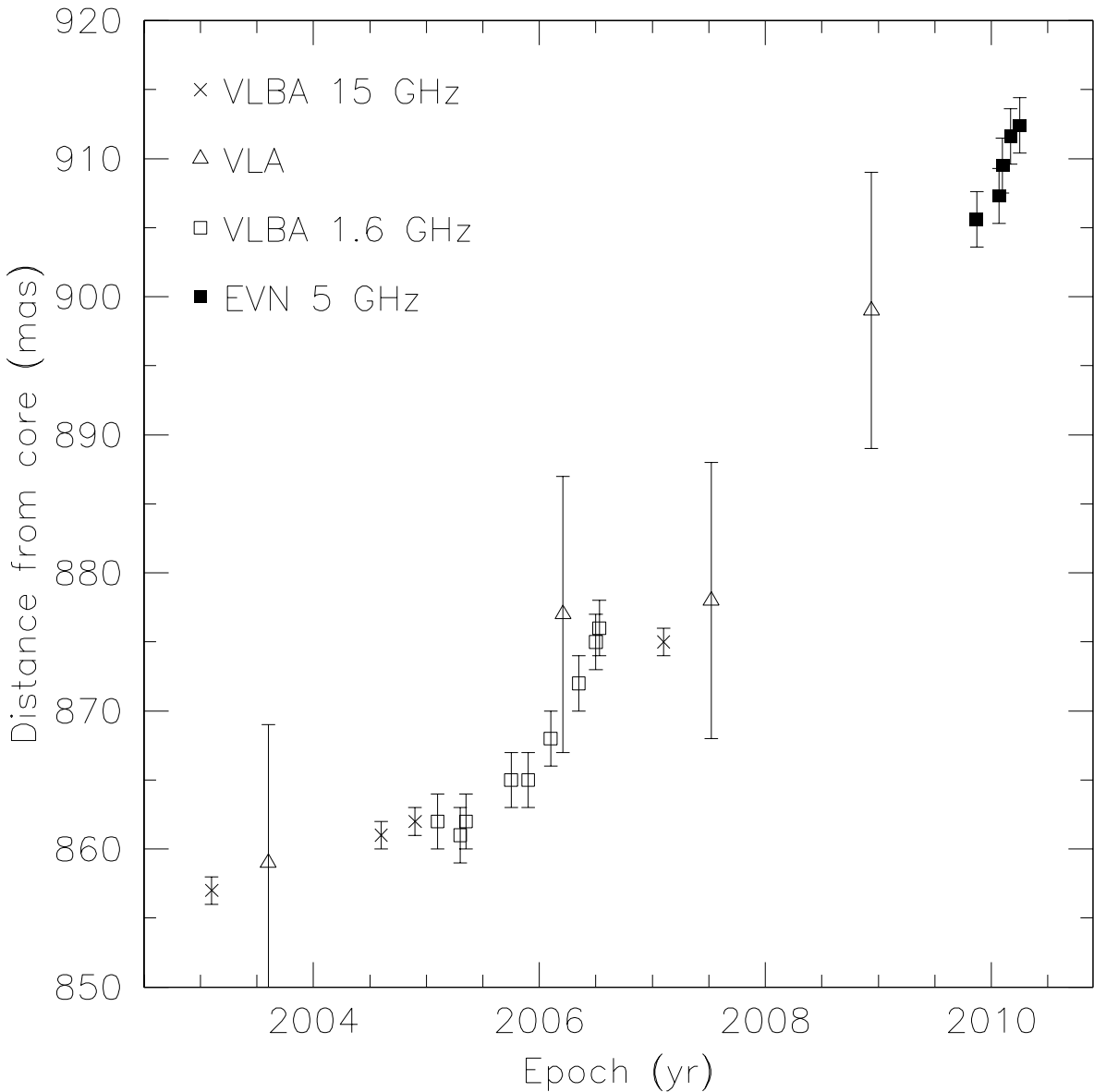
Fig. 4. Distance of HST-1 brightest peak from the M 87 core at different epochs

Table 1. e-EVN Results

Epoch [yr]	S_{core} [mJy]	HST-1 peak [mas beam^{-1}]	Distance [mas]
2009.87	1806	3.5	905.6
2010.07	1810	2.7	907.3
2010.11	1798	3.0	909.5
2010.17	1891	4.6	911.6
2010.25	2013	3.4	912.4

S_{core} uncertainty is ~ 30 mJy; Distance is between the HST-1 peak flux and the core, with an uncertainty of ~ 2 mas

30° the limb-brightened structure can be due to a different Doppler factor.

In Table 1 we report the nuclear flux density measured in images at the same angular resolution (8×3.4 mas). We find a marginal evidence of a nuclear flux density increasing in the last two epochs, and of a high HST-1 peak flux on 2010.17.

3.2. HST-1

In our observations HST-1 is clearly resolved (Fig. 2). Comparing different epochs we are able to individuate the brightest knot and to measure its proper motion (Table 1). Other features appear to move at about the same velocity, but because of the low brightness and complex morphology we discuss here only the position of the brightest knot inside HST-1.

To better study the dynamic of this structure we searched archive VLA data at high resolution (A configuration) and high frequency (X, U, and Q bands). We refer to Harris et al. (2009) for a discussion of the flux density variability. Here we only want to compare different epochs to derive the HST-1 dynamic.

We started to analyze data from 2003.6 since, as shown in Harris et al. (2009), in previous epochs few data are available, moreover the HST-1 flux density was very low. A better analysis with a larger time range will be presented in a future paper.

Starting from 2003.6 the HST-1 structure is well evident (see e.g., Fig. 3 obtained on November 2008) and well separated by the jet structure near the core. From VLA multi-frequency observations at the same time we find that the total spectrum for HST-1 is moderately steep: on 2006.21 is $\alpha_{15}^{8.4} = 0.68$ and $\alpha_{22}^{15} = 0.82$ The high frequency steepening is not always present, on 2007.52 $\alpha_{15}^{8.4}$ is the same but $\alpha_{22}^{15} = 0.36$. This variability and trend of the radio spectrum is in agreement with the substructures and variability visible in VLBI images of HST-1.

We estimated from e-EVN and VLA data the distance of HST-1 from the core. In e-EVN data we measured the distance between the core and the brightest knot in HST-1, in VLA images we used the HST-1 peak, being this structure unresolved. Adding the values obtained at 1.5 and 15 GHz by Cheung et al. (2007) and Chang et al. (2010), respectively, we can study the HST-1 proper motion with a good statistic from 2003 to present epoch. The apparent proper motion of HST-1 is shown in Fig. 4. Unfortunately in the time range 2006.5–2007.5 there are only a few points not completely in agreement, however taking into account the different observing frequency, angular resolution and radio telescopes, the proper motion looks well defined.

A clear change in the proper motion velocity is present at the epoch $\sim$2000.5, coincident with the TeV γ-ray activity and the maximum radio/X-ray flux density of HST-1. In the time range 2003–2005.5 the apparent velocity is 0.5 c–0.6 c; in the time range 2005.5–2010.25 the apparent velocity is ~ 2.7 c. Assuming a jet orientation angle of 25°, a proper motion of 2.7 c corresponds to an intrinsic velocity of 0.94 c.

4. Summary

With our new e-EVN data obtained in the time range 2009.87–2010.25 we have obtained images of the nuclear region of M 87 and of the jet substructure HST-1.

The radio core flux density is constant in the first three epochs with an average flux density ~ 1805 mJy and slightly increasing in the last two epochs: 2013 mJy in 2010.25.

The inner jet is transversally resolved and assuming that the limb-brightened structure is due to a different Doppler factor because of the jet velocity structure we derive a source orientation angle $\theta = 20$–30 degree.

The HST-1 structure is well resolved in many substructures. A proper motion is clearly present. Comparing e-EVN data with archive VLA data and published VLBA data at 1.7 and 15 GHz we find a strong evidence that in 2005.5 HST-1 increased its velocity from an apparent velocity of 0.5–0.6 c to 2.7 c. With present data it is not possible to discuss if this change in velocity is related to the M 87 VHE activity and/or to the maximum radio/X-ray flux density of HST-1 at this epoch. A more regular and longer monitor and a multi-frequency comparison is necessary to clarify this point.

References

Abdo, A. A., Ackermann, M., Ajello, M., et al. 2009, ApJ, 707, 55

Acciari, V. A., Aliu, E., Arlen, T., et al. 2009, Sci, 325, 444

Acciari, V. A., Beilicke, M., Blaylock, G., et al. 2008, ApJ, 679, 397

Aharonian, F., Akhperjanian, A., Beilicke, M., et al. 2003, A&A, 403, L1

Aharonian, F., Akhperjanian, A. G., Bazer-Bachi, A. R., et al. 2006, Sci, 314, 1424

Biretta, J. A., Sparks, W. B., & Macchetto, F. 1999, ApJ, 520, 621

Chang, C. S., Ros, E., Kovalev, Y. Y., & Lister, M. L. 2010, A&A 535, A38

Cheung, C. C., Harris, D. E., & Stawarz, L., 2007, ApJ, 663, L65

Harris, D. E., Cheung, C. C., & Stawarz, L., & al. 2008, in ASP Conf. Ser. 386, 80

Harris, D. E., Cheung, C. C., Stawarz, L., Biretta, J. A., & Perlman, E. S. 2009, ApJ, 699, 305

Junor, W., Biretta, J. A., & Livio, M. 1999, Nature, 401, 891

Kovalev, Y. Y., Lister, M. L., Homan, D. C., & Kellermann, K. I. 2007, ApJ, 668, L27

Krichbaum, T. P., Zensus, J. A., & Witzel, A. 2005, AN, 326, 548

Ly, C., Walker, R. C., Junor, W. 2007, ApJ, 660, 200

Marconi, A., Axon, D. J., Macchetto, F. D., Capetti, A., Sparks, W. B., & Crane, P. 1997, MNRAS, 289, L21

Mariotti, M. 2010, ATel, 2431, 1

Neronov, A. & Aharonian, F. A., 2007 ApJ 671, 85

Ong, R. A. 2010, ATel, 2443, 1

Perlman, E. S., Biretta, J. A., Zhou, F., Sparks, W. B., & Macchetto, F. D. 1999, AJ, 117, 2185

Tavecchio, F. & Ghisellini, G. 2008, MNRAS, 385, 98

Revealing the jets of the faintest BL Lacs

M. Giroletti[1], E. Massaro[2], G. Tosti[3,4], M. Kadler[5,6,7,8], G. B. Taylor[9],
on behalf of the *Fermi*/LAT collaboration
and G. Giovannini[1,10], C. Casadio[1,10], E. Liuzzo[1,10], S. Tamburri[1,10]

[1] INAF Istituto di Radioastronomia, via Gobetti 101, I-40129 Bologna, Italy
[2] Università di Roma "La Sapienza", I-00185 Roma, Italy
[3] Istituto Nazionale di Fisica Nucleare, Sezione di Perugia, I-06123 Perugia, Italy
[4] Dipartimento di Fisica, Università degli Studi di Perugia, I-06123 Perugia, Italy
[5] Dr. Remeis-Sternwarte Bamberg, Sternwartstrasse 7, D-96049 Bamberg, Germany
[6] Center for Research and Exploration in Space Science and Technology (CRESST), NASA Goddard Space Flight Center, Greenbelt, MD 20771, USA
[7] Erlangen Centre for Astroparticle Physics, D-91058 Erlangen, Germany
[8] Universities Space Research Association (USRA), Columbia, MD 21044, USA
[9] University of New Mexico, MSC07 4220, Albuquerque, NM 87131, USA
[10] Dipartimento di Astronomia, Università di Bologna, I-40127 Bologna, Italy

Abstract. BL Lac objects, particularly high-energy peaked ones (HBLs), made up only a fraction of the known extragalactic gamma-ray source population. With the advent of *Fermi*, and thanks to its large sensitivity up to several GeV, they have become the most numerous population. However, since they are relatively weak radio sources, most of them are poorly known as far as their parsec scale structure is concerned. Independently of their gamma-ray properties, we have selected a complete sample of low redshift BL Lacs to study with a multi-wavelength (radio, optical, X-ray, gamma-ray) approach. Here, we present the preliminary results of new VLBA observations at 8 and 15 GHz of 24 BL Lacs, most of which never observed before, carried out in 2009/2010. The detection rate is as high as 85% at both frequencies, even for the faintest sources. The detection rate at gamma-rays is only slightly lower (75%); almost all the sources detected by *Fermi*/LAT after 18 months are also VLBA detection; conversely, the sources not revealed by the VLBA are also gamma-quiet.

1. Introduction

Unidentified sources and Flat Spectrum Radio Quasars (FSRQ) have dominated the census of the extragalactic gamma-ray sky during the EGRET era: in the 3rd EGRET catalog, 96/181 of the high galactic latitude ($|b| > 10°$) sources remained unidentified and FSRQ accounted for 77% of the high confidence blazar associations (Hartman et al., 1999). In total, only 15 BL Lacs had been found, corresponding to just 8% of the high latitude gamma-ray sources.

By contrast, the Large Area Telescope (LAT) on board the *Fermi* Gamma-Ray Space Telescope launched on 2008 June 11 is radically changing this status. Indeed, among the large legacy of results delivered with the LAT Bright AGN Sample (LBAS, Abdo et al., 2009) and the First LAT AGN Catalog (1LAC, Abdo et al., 2010b), a couple of extremely relevant discoveries concern the blazar population. In short, they can be summarized as follows: (1) BL Lacs have now become the most numerous population of gamma-ray sources, surpassing FSRQs and with a net count of 300/671 in the 1LAC; (2) the gamma-ray properties of the two population are markedly distinct, with average photon indices of 1.99 ± 0.22 and 2.40 ± 0.17 for BL Lacs and FSRQs, respectively (see also Abdo et al., 2010a). As long as some theoretical works has somehow

anticipated these results (e.g. Mücke & Pohl, 2000; Lott et al., 2007), it is nonetheless striking to see how clearly they have emerged from the data collected by *Fermi*/LAT.

At lower energy, all known BL Lacs are radio sources. They exhibit the characteristic treats of the blazar population, with a high core dominance, large degrees of variability and polarization, and one-sided Doppler beamed parsec-scale jets. However, their properties are in some cases quite different from those of FSRQs; for example, the apparent velocities measured in BL Lac objects are generally lower than in jets associated with quasars (Gabuzda et al., 1994; Jorstad et al., 2001; Kellermann et al., 2004). This effect becomes particularly prominent when the most extreme BL Lacs are considered, i.e., TeV BL Lacs. In these sources, such as Mrk 501 (Giroletti et al., 2004a), jet component proper motions are hardly revealed, and in any case they are generally consistent with being subluminal (e.g. Piner et al., 2008).

Moreover, the distribution of the radio luminosity of BL Lacs extends down to $10^{23.5}$ W Hz^{-1}, implying de-beamed values intermediate between those of radio quiet objects and powerful radio galaxies (Giroletti et al., 2004b). Indeed, many LAT BL Lacs are high-synchrotron-peaked (HSP) sources, discovered at X-rays and generally dim radio sources. BL Lac studies with VLBI up to now have generally been affected by small numbers, high flux

density limits, incompleteness, and/or other various selection effects (Wu et al., 2007; Giroletti et al., 2004b, 2006; Rector et al., 2003; Cassaro et al., 2002). Even the large dataset provided by MOJAVE (Lister et al., 2009), being selected on the basis of a large correlated flux ($S > 200$ mJy), is somewhat unsuited to systematically study the properties of the radio jets in BL Lacs.

In the present paper, we introduce a new complete sample of low redshift BL Lacs (Sect. 2) and present VLBA observations recently performed for a number of its members (Sect. 3). Preliminary results and a discussion are given in Sect. 4, in which we also discuss the γ-ray emission properties of the sources, as provided by the *Fermi*/LAT data. Finally, a summary of the current status and an outlook on the future plans are given in Sect. 5.

We adopt a ΛCDM cosmology with $h = 0.71$, $\Omega_m = 0.27$, and $\Omega_\Lambda = 0.73$ (Komatsu et al., 2009). The radio spectral index α is defined such that $S(\nu) \propto \nu^{-\alpha}$.

2. The sample

The sample presented in this paper has been extracted from the ASDC Catalog of known blazars[1] (Roma-BZCat, Massaro et al., 2009). In order to perform a systematic study, we only applied the basic criterion of a measured redshift $z < 0.2$, which grants a good linear resolution (1 pc $\sim$ 0.5 mas at $z = 0.1$) and the possibility to study also the least powerful sources, such as the weak population of HSP BL Lacs. Moreover, the starting selection is independent of the discovery of gamma-ray emission from *Fermi*, so the sample is unbiased and suitable for a statistical study.

The only additional selection is the location of the sources within the sky area covered by the Sloan Digital Sky Survey (SDSS, Abazajian et al., 2009). This criterion does not introduce any significant bias and permits a good characterization of the optical properties of the sources, while keeping the sample to a reasonable size. Moreover, since the FIRST radio surveys has covered this field, there is an additional resource available for our study, which permits to compare nuclear and extended radio properties. In total, the number of sources in this sample is 42. The list of sources is given in Table 1.

One of the main goals for our study is to constrain the broad band energy distributions and variability, and to detect episodes of strong activity. For this, multi-band photometry of the sample is being carried out with several facilities across the electromagnetic spectrum: *Fermi*/LAT, SWIFT, Chandra, XMM-Newton, INTEGRAL; optical ground based observations are performed with the telescope of the Vallinfreda Astronomical Station, in addition to the photometry available from the SDSS. In the present paper, we report on the preliminary results of VLBA observations in the radio band.

---

[1] Available on-line at `http://www.asdc.asi.it/bzcat`

3. VLBA Observations

We have so far obtained time to observe 24 sources, out of the total 42 objects in the sample. Observations of the remaining sources are currently queued in the VLBA dynamic schedule. Each target was observed at 8 and 15 GHz for about one hour in total, with roughly a 1:3 ratio between the low and high frequency total integration time. Targets weaker than 30 mJy at 8 GHz and 50 mJy at 15 GHz have been observed in phase referencing mode. Indeed, most sources had not been observed before and the phase referencing technique has also provided the possibility to obtain absolute coordinates for them.

The observations were carried out using 9 VLBA telescopes, since the Saint-Croix antenna was not available. Severe weather conditions also affected part of the observations at North Liberty, resulting in a loss of 15 GHz data for several hours. However, the quality of the data is overall good and permits to achieve with a 256 Mbps recording rate a noise levels of ~ 0.2 mJy beam^{-1}, i.e., comparable to the theoretical one. The restoring beam is the typical one of the VLBA at our frequencies, i.e., $\sim 1.2 \times 1.8$ mas at 8 GHz and $\sim 0.6 \times 0.9$ mas at 15 GHz, for sources at intermediate declination and with natural weights.

4. Results and discussion

At a preliminary analysis, most of the sources are detected with a good significance, either at the fringe fitting stage for the brightest targets or directly in the image plane after applying phase corrections from the reference calibrator source. Only a couple of sources do not seem revealed at either 8 and 15 GHz (J1201−0007 and J1201−0011), while in another couple of cases the visibility data suggest there might be a detection but it has not yet been possible to reveal it in the image plane.

The total radio flux densities for the detected sources range over a quite broad interval, from as little as a few milliJanskys to almost 1 Jy. However, the bulk of the population has a total integrated flux density below ~ 30 mJy. It has to be noted that such comparatively low flux densities and small observing bandwidth do not allow to perform self calibration with short solution intervals, therefore it is difficult to constrain the final flux density of the targets. This affects also the estimate of the spectral index, which in general appears to be moderately steep.

A moderately steep spectral index is however in agreement with the presence of a fair amount of extended emission, which we clearly detect in a few cases. Keeping in mind the short integration at our disposal and the overall weakness of the targets, the detection of jet features in our images is certainly remarkable and somewhat surprising. We show in Fig. 1 some of these objects, selected among the faintest ones to show jet structure.

Finally, it is interesting to start to have a look at the gamma-ray properties of these sources and how they compare to the radio ones. First, the detection rate in gamma-rays is of about 58% for the sources observed so far, while

Table 1. List of sources in the sample. Data are taken from the BZCat master list archives (Massaro et al., 2009); in particular, the reported 1.4 GHz radio flux densities were obtained from the NVSS. The last column reports on the detection in the 1-year *Fermi* catalog (Abdo et al., 2010c). Sources in the upper part of the table have been observed at the VLBA as of May 2010.

Name	RA(J2000) (hh mm ss)	Dec(J2000) (° ′ ″)	R band (mag)	$S_{1.4\ \mathrm{GHz}}$ (mJy)	F X-ray (10^{-11}cgs)	z	1FGL source (y/n)
BZB J0754+3910	07 54 37.08	+39 10 47.6	12.8	58	0.44	0.096	n
BZB J0809+3455	08 09 38.89	+34 55 37.3	12.6	223	4.07	0.083	y
BZB J0809+5218	08 09 49.15	+52 18 58.7	14.6	182	8.26	0.138	y
BZB J0847+1133	08 47 12.93	+11 33 50.1	16.6	33	11.01	0.199	y
BZB J0850+3455	08 50 36.18	+34 55 22.8	14.3	35	0.65	0.145	y
BZB J0903+4055	09 03 14.72	+40 55 59.7	15.8	36	2.00	0.188	n
BZB J0916+5238	09 16 51.94	+52 38 28.4	15.0	73	3.83	0.190	n
BZB J0930+4950	09 30 37.57	+49 50 25.6	17.3	21	16.7	0.187	n
BZB J1053+4929	10 53 44.13	+49 29 56.0	13.8	64	0.82	0.140	y
BZB J1120+4212	11 20 48.06	+42 12 12.4	16.9	24	7.81	0.124	y
BZB J1136+6737	11 36 30.08	+67 37 04.4	15.3	45	14.8	0.136	y
BZB J1201−0007	12 01 06.19	−00 07 01.6	15.7	70	1.05	0.165	n
BZB J1201−0011	12 01 43.66	−00 11 14.0	16.7	28	0.56	0.164	n
BZB J1217+3007	12 17 52.08	+30 07 00.6	14.5	572	24.9	0.130	y
BZB J1221+0821	12 21 32.06	+08 21 44.2	16.3	176	1.14	0.132	n
BZB J1221+3010	12 21 21.94	+30 10 37.1	15.7	71	16.3	0.182	y
BZB J1253+0326	12 53 46.99	+03 26 30.1	12.7	107	1.67	0.066	y
BZB J1341+3959	13 41 05.11	+39 59 45.4	14.9	41	5.15	0.172	y
BZB J1419+5423	14 19 46.60	+54 23 14.8	13.8	788	0.81	0.153	n
BZB J1427+5409	14 27 30.27	+54 09 23.7	11.8	44	0.38	0.106	n
BZB J1428+4240	14 28 32.66	+42 40 20.6	14.4	58	35.5	0.129	y
BZB J1436+5639	14 36 57.80	+56 39 25.0	17.6	20	1.67	0.150	y
BZB J1442+1200	14 42 48.28	+12 00 40.3	15.2	69	7.82	0.163	y
BZB J1516+2918	15 16 41.59	+29 18 09.5	14.6	134	1.27	0.130	n
BZB J0751+1730	07 51 25.08	+17 30 51.1	18.2	10	1.78	0.185	n
BZB J0751+2913	07 51 09.57	+29 13 35.5	16.9	10	0.21	0.194	n
BZB J0753+2921	07 53 24.61	+29 21 31.9	15.7	4	1.29	0.161	n
BZB J0810+4911	08 10 54.60	+49 11 03.7	13.5	11	0.20	0.115	n
BZB J1012+3932	10 12 58.37	+39 32 39.0	16.0	20	0.65	0.171	n
BZB J1022+5124	10 22 12.62	+51 24 00.3	16.7	5	3.44	0.142	n
BZB J1058+5628	10 58 37.73	+56 28 11.2	14.0	228	3.13	0.143	y
BZB J1145−0340	11 45 35.11	−03 40 01.7	16.2	18	4.10	0.167	n
BZB J1156+4238	11 56 46.56	+42 38 07.4	15.6	14	0.69	0.172	n
BZB J1215+0732	12 15 10.98	+07 32 04.7	14.8	137	3.27	0.136	n
BZB J1221+2813	12 21 31.69	+28 13 58.5	14.3	732	1.30	0.102	y
BZB J1231+6414	12 31 31.39	+64 14 18.3	14.3	58	2.49	0.163	n
BZB J1257+2412	12 57 31.93	+24 12 40.1	15.7	14	7.22	0.141	n
BZB J1427+3908	14 27 45.92	+39 08 32.3	18.0	7	0.16	0.165	n
BZB J1510+3335	15 10 41.18	+33 35 04.5	15.1	8	2.53	0.114	n
BZB J1534+3715	15 34 47.20	+37 15 54.8	16.3	22	0.23	0.143	n
BZB J1604+3345	16 04 46.52	+33 45 21.8	18.0	7	0.72	0.177	n
BZB J1647+2909	16 47 26.85	+29 09 49.9	13.4	390	0.43	0.132	n

it goes down to 38% when the remaining sources – which are generally fainter – are considered. The photon indices of the detected sources are typical of BL Lacs, i.e., quite hard, and even as hard as $\Gamma = 1.3$ for the TeV source J1428+4240, while no source has a photon index in excess of $\Gamma = 2$.

Interestingly, all the γ-ray detected sources are revealed as compact radio sources by our VLBA observations. This makes somewhat more interesting the fact that

the VLBA non detection occur for sources that are not detected by *Fermi* either (with the only possible exception of J0847+1133). While additional analysis of the VLBA and LAT data could possibly change this status, it is nonetheless a remarkable fact and poses questions as to the classification of these apparently elusive sources.
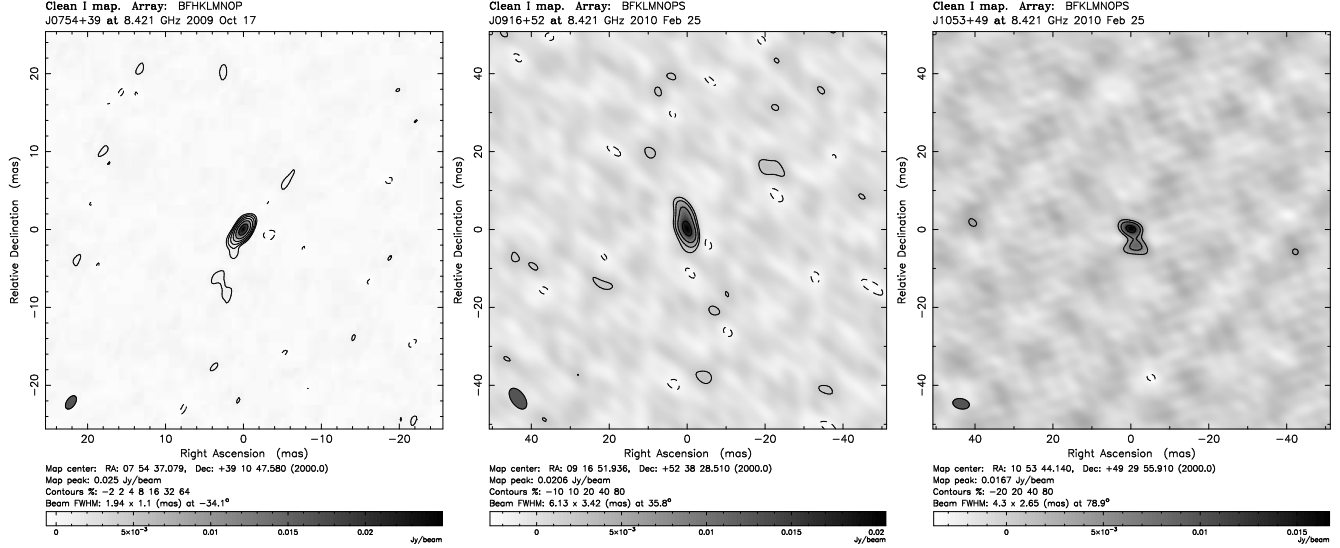
Fig. 1. VLBA 8 GHz images of three BL Lacs in the range $S_8 \sim 10 - 30$ mJy displaying jet like features beside a compact core. More prominent jets are found in brighter sources.

5. Summary and outlook

The current observations have revealed that compact cores are detected in a very high fraction of the sources in the current sub-sample, and basically always when the BL Lac is also a gamma-ray source. Observations of the remaining 18 targets are currently ongoing; since the observing strategy has left the weakest sources last, it will be interesting to see how they complete the picture sketched by the comparatively brighter targets observed thus far. We will then be able to compare our results with the broad band spectral properties for all the sample. We also remind that the calibrated data will be made available at a web site that will be announced at a later stage.

References

Abazajian, K. N., Adelman-McCarthy, J. K.; Agüeros, M. A.; et al. 2009, ApJS, 182, 543

Abdo, A. A., Ackermann, M., Ajello, A., et al. 2009, ApJ, 700, 597

Abdo, A. A., Ackermann, M., Ajello, A., et al. 2010a, ApJ, 710, 1271

Abdo, A. A., Ackermann, M., Ajello, A., et al. 2010b, ApJ, 715, 429

Abdo, A. A., Ackermann, M., Ajello, A., et al. 2010c, ApJS, 188, 405

Cassaro, P., Stanghellini, C., Dallacasa, D., Bondi, M., & Zappalà, R. A. 2002, A&A, 381, 378

Gabuzda, D. C., Mullan, C. M., Cawthorne, T. V., Wardle, J. F. C., & Roberts, D. H., 1994, ApJ, 435, 140

Giroletti, M., Giovannini, G., Feretti, L., et al. 2004a, ApJ, 600, 127

Giroletti, M., Giovannini, G., Taylor, G. B., & Falomo, R., 2004b, ApJ, 613, 752

Giroletti, M., Giovannini, G., Taylor, G. B., & Falomo, R. 2006, ApJ, 646, 801

Hartman, R. C., Bertsch, D. L., Bloom, S. D., et al. 1999, ApJS, 123, 79

Jorstad, S. G., Marscher A.P., Mattox J. R., et al. 2001, ApJS, 134, 181

Kellermann, K. I., Lister M. L., Homan D. C. et al. 2004, ApJ, 609, 539

Komatsu, E., Dunkley, J., Nolta, M. R., et al. 2009, ApJS, 180, 330

Lister, M. L., Cohen, M. H., Homan, D. C., et al. 2009, AJ, 138, 1874

Lott, B., Carson, J., Ciprini, S., et al. 2007, AIPC, 921, 347

Mücke, A., & Pohl, M. 2000, MNRAS, 312, 177

Massaro, E., Giommi, P., Leto, C., et al. 2009, A&A, 495, 691

Piner, B. G., Pant, N., & Edwards, P. G. 2008, ApJ, 678, 64

Rector, T. A., Gabuzda, D. C., & Stocke, J. T. 2003, AJ, 125, 1060

Wu, Z., Jiang, D. R., Gu, M., Liu, Y., 2007, A&A, 466, 63

Gamma-ray duty cycle in the bright parsec-scale AGN jets

T. Hovatta[1], M. L. Lister[1], Y. Y. Kovalev[2,3], and A. B. Pushkarev[3,4,5]

[1] Department of Physics, Purdue University, 525 Northwestern Avenue, West Lafayette, IN 47907, USA
[2] Astro Space Center of Lebedev Physical Institute, Profsoyuznaya 84/32, 117997 Moscow, Russia
[3] Max-Planck-Institute für Radioastronomie, Auf dem Hügel 69, 53121 Bonn, Germany
[4] Pulkovo Observatory,Pulkovskoe Chaussee 65/1, 196140 St. Petersburg, Russia
[5] Crimean Astrophysical Observatory, 98409 Nauchny, Crimea, Ukraine

Abstract. Thanks to the excellent quality of the *Fermi*/LAT data, during the past year, there have been many studies showing evidence of a radio–γ-ray connection in AGN. The MOJAVE program (Monitoring Of Jets in Active galactic nuclei with VLBA Experiments) uses the Very Long Baseline Array (VLBA) at 15 GHz to monitor the changes in the structure, flux density and polarization of parsec-scale jets in a large sample of highly-beamed AGN. We have calculated a γ-ray flux distribution for each of the 82 sources in the MOJAVE-1 sample that were detected by the LAT during its first 11 months of operation. We define a 95% maximum γ-ray photon flux statistic for each source from the distributions and correlate it with various parsec-scale jet properties. We find a strong positive correlation between the γ-ray photon flux and the 15 GHz total VLBA flux density, core total and linearly polarized flux density and Doppler boosting factor. The best correlation is achieved when VLBA data from the LAT-era are used.

1. Introduction

The extragalactic γ-ray sky as observed by the *Fermi* Large Area Telescope (LAT) is dominated by radio-loud AGN (Abdo et al. 2010d, 2010c). Within the first two years of the launch of the *Fermi* satellite, several studies have shown correlations between the radio and γ-ray properties of these sources. Soon after the release of the *Fermi* 3-month catalog of bright AGN (LBAS, Abdo et al. 2009), Kovalev et al. (2009) found the γ-ray photon flux to be correlated with the radio flux density from MOJAVE observations. The differences between LAT-detected and non-detected sources showed that the γ-ray sources were found in higher radio activity states. A significant correlation was also found between non-simultaneous VLBI flux density and γ-ray photon flux by Kovalev (2009b). The LBAS sources were shown to have higher apparent speeds (Lister et al. 2009b), higher Doppler boosting factors (Savolainen et al. 2010) and smaller viewing angles (Pushkarev et al. 2009) than the non-detected MOJAVE sources.

Evidence for a correlation between the strong γ-ray flares and parsec-scale radio events has been found for a few individual well-monitored sources (e.g., Abdo et al. 2010a, 2010b, Aller et al. 2009, Jorstad et al. 2009, 2010 and Marscher et al. 2009). In this paper we will further study this connection by using weekly binned LAT lightcurves and deriving a maximum γ-ray photon flux to be compared with the parsec scale jet properties.

2. The sample and data

In our analysis we use the flux-density-limited MOJAVE-1 sample of highly beamed AGN (Lister et al. 2009). The sample consists of all AGN at declinations $\delta > -20°$ which have had a 15 GHz flux density of at least 1.5 Jy (2 Jy at $\delta < 0°$) at any epoch between 1994.0 and 2004.0. Here we restrict our sample to the 82 sources that are listed as associations in the 1FGL catalog (Abdo et al. 2010d).

2.1. VLBA data

The radio data used in the analysis are from the MOJAVE (Lister et al. 2009) and archival observations between 1994 and 2010. We calculate the maximum total VLBA flux density, maximum core flux density and maximum core polarized flux density for all the sources for the whole time period, the time period before the launch of *Fermi* in August 2008 (hereafter pre-LAT), and for August 2008 until January 2010 (hereafter LAT-era).

2.2. LAT light curves

The LAT light curves from August 2008 to January 2010 were produced from the publicly available data using Fermi Science Tools[1] and the instrument response functions given by `P6_V3_DIFFUSE`. We binned the data into weekly bins and in each time bin, we used the energy range from 0.1 to 100 GeV and selected good, diffuse events, and used a zenith angle cut of 105° to avoid times with high background levels from the Earth albedo. For all the sources we used a region of interest (ROI) of 10° centered at the position of the source. After calculating the live time and exposure cubes, the photon fluxes were computed using the tool gtlike. We modeled all the point sources within a source region of 15° and took the galactic diffuse com-

---

[1] http://fermi.gsfc.nasa.gov/ssc/data/analysis/
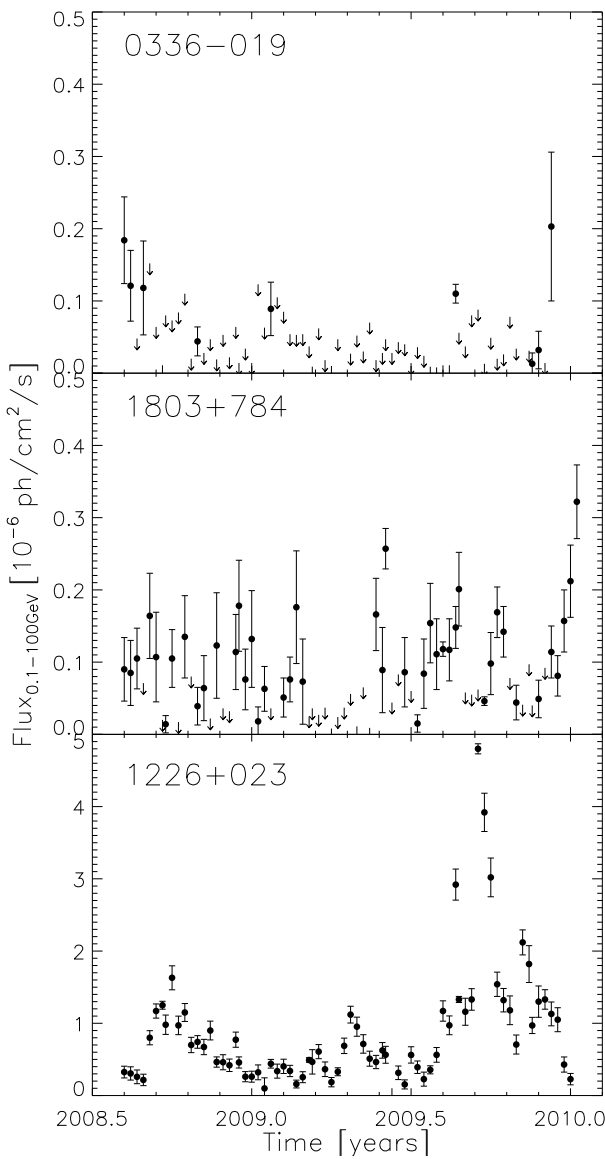
Fig. 1. LAT lightcurves of three sources. The downward arrows indicate upper limits.

ponent (using `gll_iem_v02.fit`) and the isotropic extragalactic background (using `isotropic_iem_v02.txt`) into account. The source models were made using the user-provided python tool `make1FGLxml.py`[2] which reads the 1FGL catalog to insert sources within a region of radius ROI + 5° and their parameters into the source model file. The flux and photon index were left as free parameters. If the test statistics (TS, Mattox et al. 1996) in a bin were less than 10 (corresponding to $\sim 3\sigma$) an upper limit was calculated. In some bins the fit from the gtlike tool did not converge and neither a flux or upper limit was calculated. This happened usually in 0–4 bins of a source. Examples of three light curves are shown in Fig. 1.

It is clear that the weekly binning is not sufficient for 0336−019 (Fig. 1 top panel) as majority of the points are

upper limits. By using longer bins, we would, however, lose time resolution in sources like 1226+023 (3C 273) (Fig. 1 bottom panel) in which even daily binning would produce a light curve with majority of points being detections. In 1803+784 (Fig. 1 middle panel) the weekly binning seems to work well as about 60% of the points are detections. This creates complications when studying large samples as it would be beneficial to use different time resolution for different sources. However, the brightness of the source is not the only factor affecting the TS value but sources in more complex background regions (e.g., near to the galactic plane) may have lower TS values even if they are as bright as sources in less crowded regions. This matter requires further investigation which is beyond the scope of this paper.

2.3. γ-ray flux distributions

Using the LAT light curves, we calculate the differential and integral γ-ray flux distributions for all the sources as introduced by Tavecchio et al. (2010) for PKS 1510−089 and 3C 454.3. These should be representative of the γ-ray duty cycle. As for many sources in our sample most of the points are upper limits, instead of defining the integral distribution as number of points above a certain flux value, we define it to be number of points which have not exceeded the flux value, which should properly account for the upper limits. For calculation of the differential distribution, we bin the data into 0.16 wide bins in the log-space. It is clear that the differential distribution is not well-defined if there are many upper limits in a bin, and therefore we have only decided to use the high-end tail of the distributions to determine a maximum γ-ray photon flux as a point where 95% of the points are below it. If there were upper limits within the highest 5% of the points, we define the maximum flux as an upper limit. All our statistical tests are conducted using the `ASURV` package (Lavalley et al. 1992) suitable for censored data.

Examples for the same three sources are shown in Fig. 2, where it is easy to see that the example sources are in general in very different flux states. The lightcurve of 0336−019 (Fig. 1 top panel) consists mainly of upper limits and the few detections are shown as a tail in the differential distribution (Fig. 2 left panel). 1803+784 has only a slightly higher maximum γ-ray photon flux but is detected in more bins and the distribution is better defined. The final example is 1226+023 (3C 273), which was detected in all but one bin (Fig. 1 bottom panel). Its typical γ-ray state is much higher than in the two other sources and the extreme flaring fluxes are seen as a tail in the differential distribution (Fig. 2 right panel).

In Fig. 3 we have compared the maximum photon fluxes obtained from the distributions to the maximum photon flux of the 11 monthly observations in the same energy range (Abdo et al. 2010d). Spearman rank correlation test gives a coefficient of $\rho = 0.80$ with a probability of the correlation occuring by chance p<0.0001. Even

---
[2] http://fermi.gsfc.nasa.gov/ssc/data/analysis/user/
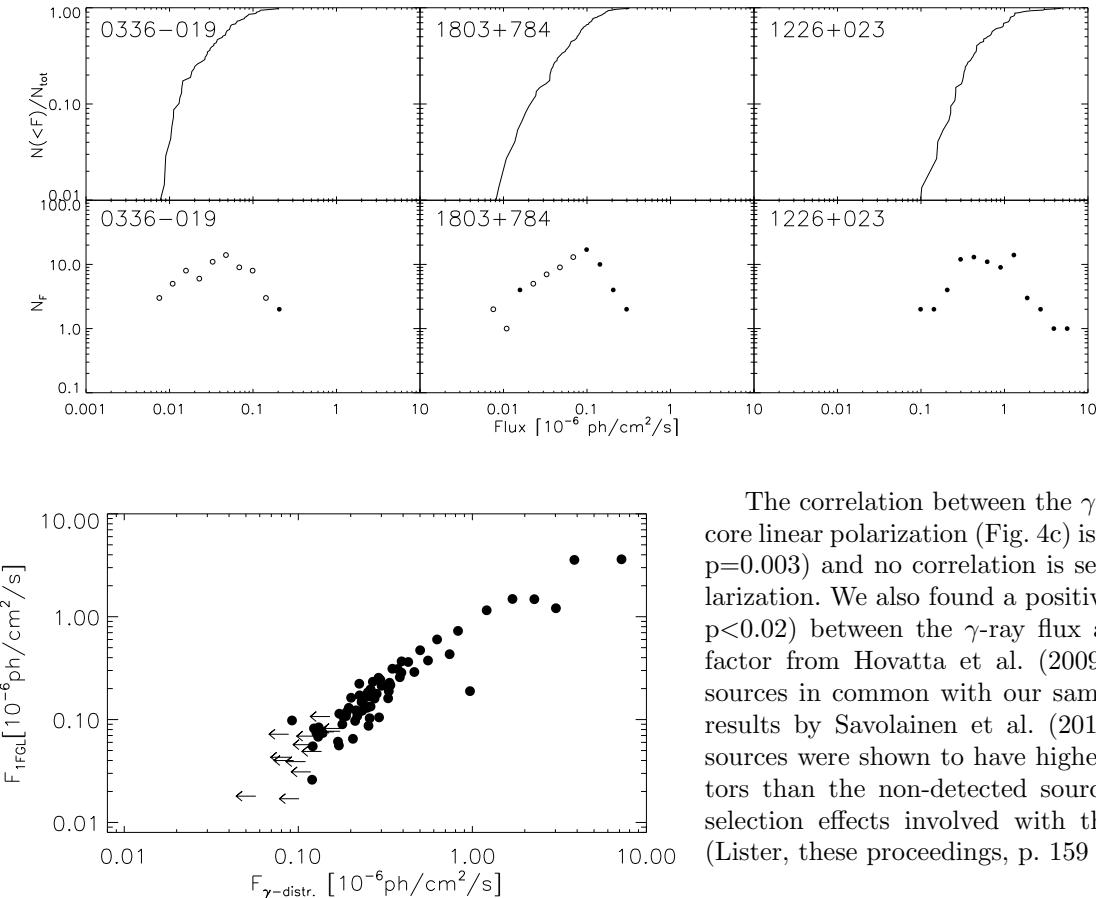
Fig. 2. Integrated (top panel) and differential (bottom panel) γ-ray photon flux distributions of three sources. Open circles indicate bins which contain more than 50% upper limits.
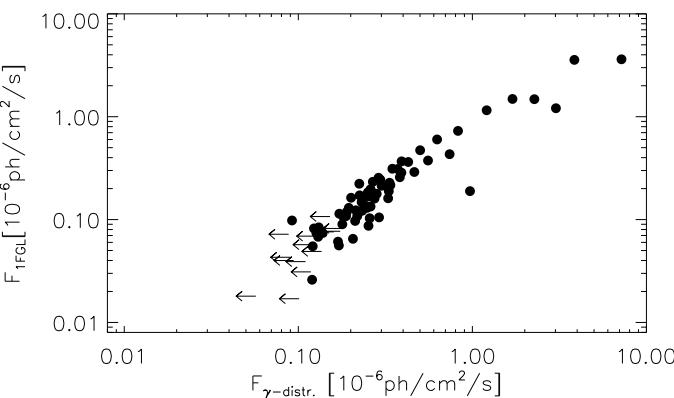

Fig. 3. Correlation between the maximum γ-ray photon flux from the 11 monthly bins in the 1FGL catalog and maximum from the γ-ray distribution. Left-pointing arrows indicate upper limits in the photon flux from the γ-ray distribution.

though the correspondence between the values is good, the values from the γ-ray distribution are higher than in the 1FGL catalog because we use weekly binning and longer datasets.

3. Radio - γ-ray correlations

We have defined a maximum photon flux from the γ-ray flux distributions and checked for correlations with several parsec-scale jet properties. We find a significant positive correlation between the γ-ray flux and maximum total VLBA flux density (Fig. 4a). The best correlation ($\rho = 0.49$, p<0.0001) is achieved when VLBA data from the LAT-era (as defined in Sect. 2.1) is used. A similar correlation ($\rho = 0.54$, p<0.0001) is present with the maximum VLBA core flux density (Fig. 4b). Also in this case the best correlation occurs using data from the LAT-era. These findings support what has been found previously using the LAT 3-month catalog and MOJAVE data (Kovalev et al. 2009). In particular, the fact that we see the best correlation using simultaneous data also enhances our result that the delay between γ-ray and cm radio data is of the order of a few months (Pushkarev et al. these proceedings, p. 163).

The correlation between the γ-ray flux and maximum core linear polarization (Fig. 4c) is not as strong ($\rho = 0.33$, p=0.003) and no correlation is seen in the fractional polarization. We also found a positive correlation ($\rho = 0.36$, p<0.02) between the γ-ray flux and variability Doppler factor from Hovatta et al. (2009) (Fig. 4d) for the 47 sources in common with our samples. This confirms the results by Savolainen et al. (2010) in which the LBAS sources were shown to have higher Doppler boosting factors than the non-detected sources. Note, however, the selection effects involved with this radio-bright sample (Lister, these proceedings, p. 159).

4. Discussion

The correlations obtained between radio and γ-ray flux imply a connection between the two emission regions, which is not surprising considering that both are expected to emerge in the relativistic jet. The location of the γ-ray emitting region is not clear and connections to radio properties will help in solving the problem. Our VLBA sampling density is, however, too sparse to constrain the emission region for individual sources. The correlation between core VLBA flux and γ-ray photon flux implies that the γ-rays are emitted somewhere within the optically thick 15 GHz core confirming early findings by Kovalev et al. (2009). A statistical study of the delay between γ-ray and radio flux levels shows that the typical observed delay is from 3 to 6 months with γ-rays leading the radio (Pushkarev et al. these proceedings, p. 163).

The situation is further complicated when the Doppler-boosting is taken into account. As is shown in Fig. 4d, there is a significant positive correlation between the γ-ray photon flux and Doppler boosting factor. We do not know, however, if the amount of Doppler boosting is the same in the γ-ray and radio regimes. Lyutikov & Lister (2010) propose that the high-energy GeV and TeV emission in blazars is produced by a faster moving edge of the emission region, while the radio emission is produced in the slower-moving bulk flow. This would result in a higher Doppler boosting factor in the γ-ray regime, which in turn would smear any intrinsic linear correlation of un-beamed radio
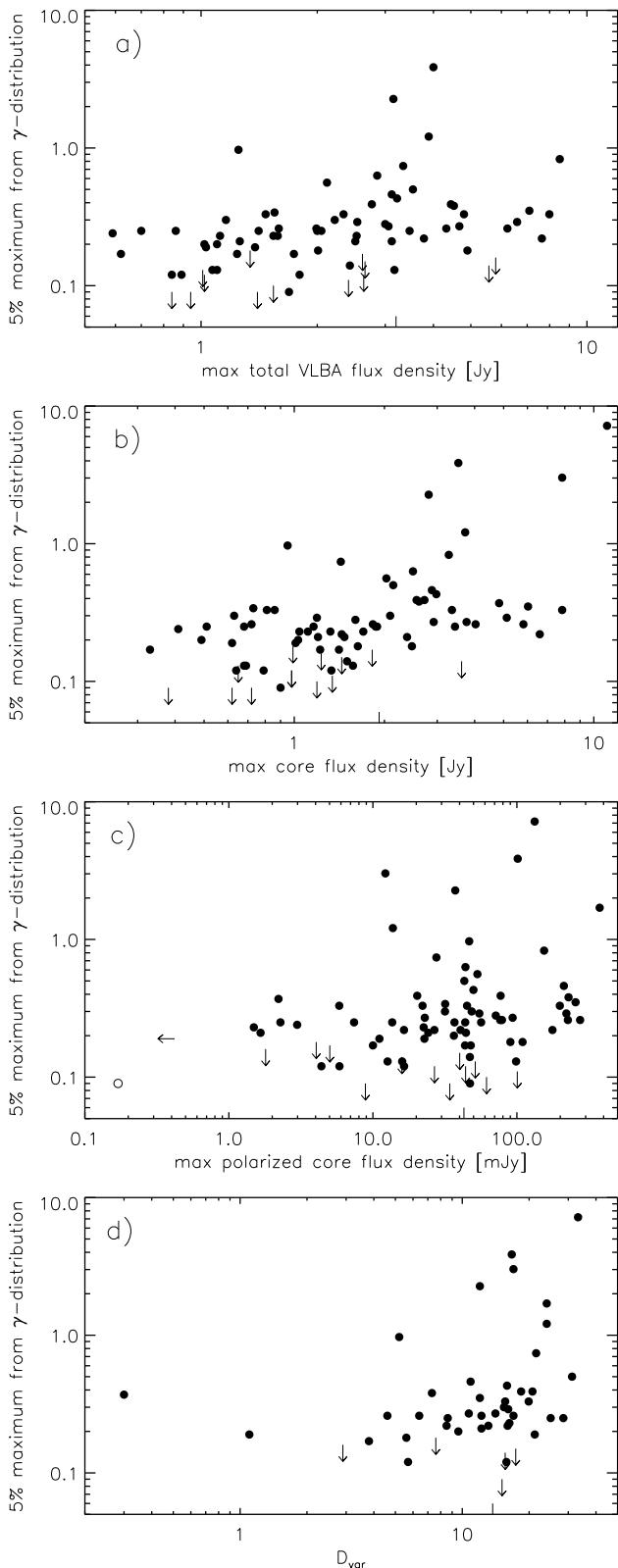
Fig. 4. Correlations between the maximum from the γ-ray flux distributions and a) maximum total 15 GHz VLBA flux density in the LAT-era, b) maximum 15 GHz core flux density in the LAT-era, c) maximum 15 GHz core linear polarization in the LAT-era, and d) variability Doppler factor. Filled circles are detections, arrows indicate upper limits and the open circle an upper limit both in the γ-ray flux and polarized flux density.

emission and γ-ray emission in any flux-flux plot. Indeed, our correlation between γ-ray and VLBA flux has a lot of scatter Fig. 4 (top two panels). The model also predicts that γ-bright sources should have larger Doppler boosting factors which is also seen in our analysis. Similarly, if the γ-ray emission is produced by external inverse Compton mechanism, the beaming cone is narrower for the γ-ray emission than for the synchrotron emission, producing different amounts of Doppler boosting at these two regimes (Dermer 1995).

References

Abdo, A. A., Ackermann, M., Ajello, M., et al. 2009, ApJS, 183, 46

Abdo, A .A., Ackermann, M., Ajello, M., et al. 2010a, ApJ, 699, 31

Abdo, A. A., Ackermann, M., Ajello, M., et al. 2010b, ApJ, 710, 810

Abdo, A. A., Ackermann, M., Ajello, M., et al. 2010c, ApJ, 715, 429

Abdo, A. A., Ackermann, M., Ajello, M., et al. 2010d, ApJS, 188, 405

Aller, M. F., Aller, H. D., & Hughes, P. A. 2009, Fermi Symposium eConf Proceedings C091122, arXiv:0912.3176

Dermer, C.D. 1995, ApJL, 446, 63

Hovatta, T., Tornikoski, M. Valtaoja, E., & Lähteenmäki, A. 2009, A&A, 494, 527

Jorstad, S., Marscher, A., D'Arcangelo, F., & Harrison, B. 2009, Fermi Symposium eConf Proceedings C091122, arXiv:0912.5230

Jorstad, S. G., Marscher, A. P., Larionov, V. M., et al. 2010, ApJ, 715, 362

Kovalev, Y. Y., Aller, H. D., Aller, M. F., et al. 2009, ApJ, 696, L17

Kovalev, Y. Y. 2009, ApJ, 707, L56

LaValley, M, Isobe T., & Feigelson, F. D. 1992, BAAS, 24, 839

Lister, M. L., Aller, H. D., Aller, M. F., et al. 2009, AJ, 137, 3718

Lister, M. L., Homan, D. C., Kadler, M., et al. 2009b, ApJ, 696, L22

Lyutikov, M., & Lister, M. L. 2010, eprint arXiv:1004.2430

Marscher, A. P., Jorstad, S. G., Larionov, V. M. 2009, ApJ, 710, L126

Mattox, J. R., Bertsch, D. L., Chiang, J., et al. 1996, ApJ, 461, 396

Pushkarev, A. B., Kovalev, Y. Y., Lister, M. L., & Savolainen, T. 2009, A&A, 507, 33

Savolainen, T., Homan, D. C., Hovatta, T., et al. 2010, A&A, 512, A24

Tavecchio, F., Ghisellini, G., Bonnoli, G., & Ghirlanda, G. 2010, MNRAS, 405, L94

VLBI Monitoring of the bright γ-ray blazar PKS 0537−441

F. Hungwe[1,4] R. Ojha[2], M. Kadler[3,6,7], R. Booth[4], J. Blanchard[5], J. Lovell[5], C. Müller[3], M. Böck[3] and the TANAMI team

[1] Department of Physics & Electronics, Rhodes University, PO Box 94, Grahamstown 6140, South Africa
[2] NVI/United States Naval Observatory, 3450 Massachusetts Ave, NW, Washington, DC 20392-5420
[3] Dr. Remeis-Sternwarte & ECAP, Universität Erlangen-Nürnberg, Sternwartstr. 7, 96049 Bamberg, Germany
[4] Hartebeesthoek Radio Astronomy Observatory, PO Box 443, Krugersdorp 1740, South Africa
[5] School of Mathematics & Physics, Private Bag 37, University of Tasmania, Hobart TAS 7001, Australia
[6] CRESST/NASA Goddard Space Flight Center, Greenbelt, MD 20771, USA
[7] Universities Space Research Association, 10211 Wincopin Circle, Suite 500 Columbia, MD 21044, USA

Abstract. One of the defining characteristics of BL Lacertae objects is their strong variability across the electromagnetic spectrum. PKS 0537−441 is one such object and is one of the most luminous blazars from radio to γ-ray wavelengths. It was detected as a strong and highly variable source by EGRET and has been reported several times to be in an active state by *Fermi*. It is one of the brightest γ-ray blazars detected in the southern sky so far. The TANAMI (Tracking Active Galactic Nuclei with Austral Milliarcsecond Interferometry) program is monitoring PKS 0537−441 at VLBI resolutions. We present 8.4 GHz and 22 GHz images of the milliarcsecond scale structure. We also present our ongoing analysis of the spectral and temporal changes in this object.

1. Introduction

PKS 0537−441 is a strongly variable BL Lacertae object and is one of the brightest γ-ray blazars detected in the southern sky to date. The source is known to be a strong intra-day variable and is sometimes classified as a highly polarised quasar (Treves et al. (1993)). It has been a candidate for gravitational micro-lensing (Romero et al. (1995)) but Heidt et al. (2003) disprove this and suggest it might be part of binary quasar.

Using the Australian Long Baseline Array (LBA) and affiliated telescopes, the Tracking Active Galactic Nuclei with Austral Milliarcsecond Interferometry (TANAMI) program (Ojha et al. (2010)) has been monitoring southern sky blazars such as PKS 0537−441 at VLBI resolutions. TANAMI began observing known and possible γ-ray loud extragalactic sources south of −30 degrees about a year before the launch of *Fermi*. TANAMI observations at 8.4 GHz and 22 GHz are made about every 2 months at milliarcsecond resolution. The TANAMI sample is modified to include sources within this declination range that are detected by the Large Area Telescope (LAT) on board *Fermi Gamma-Ray Space Telescope*.

Studying Active Galactic Nuclei (AGN) at different wavelengths is crucial in order to understand AGN-jets and differentiate between different models explaining the jets. TANAMI observations of PKS 0537−441 complement ongoing observations at other wavelengths. This source is on the *Fermi*/LAT monitored source list and is also in the LAT 1-year Point Source Catalog (Abdo et al. (2010c)).

PKS 0537−441 has been reported by *Fermi*/LAT to be active about four times in the past two years. In October 2008 and July 2009, the *Fermi*/LAT observed an increase in γ-ray activity in the source (Tosti (2008);
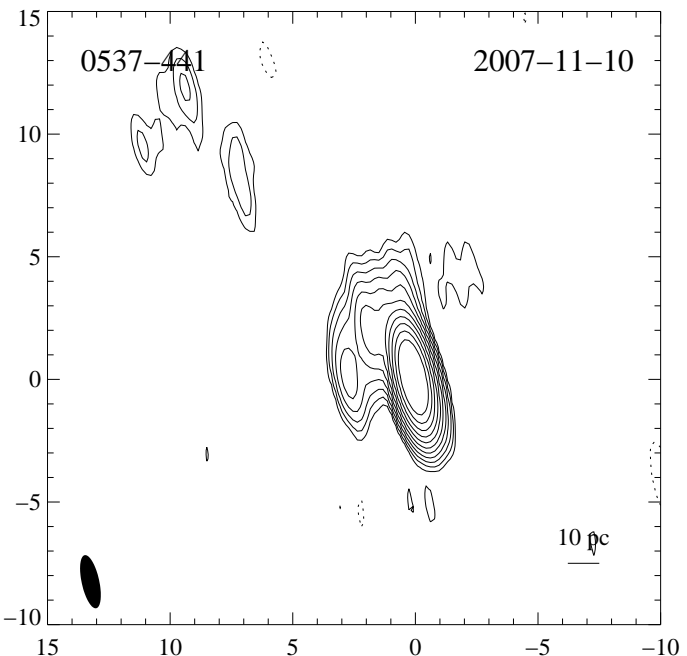

Fig. 1. 8.4 GHz radio images for PKS 0537−441 for observations done in Nov 2007. x- and y-axis are labeled in milliarcseconds and the hatched ellipse on the bottom left represents the beam of the observing array.

Bastieri (2009)). In February of 2010, *AGILE* detected 'enhanced γ-ray emission above 100 MeV from a source positionally consistent with the blazar PKS 0537−441' (Lucarelli et al. (2010)). Most recently (April 2010) the *Fermi*/LAT observed increased γ-ray activity in this source.
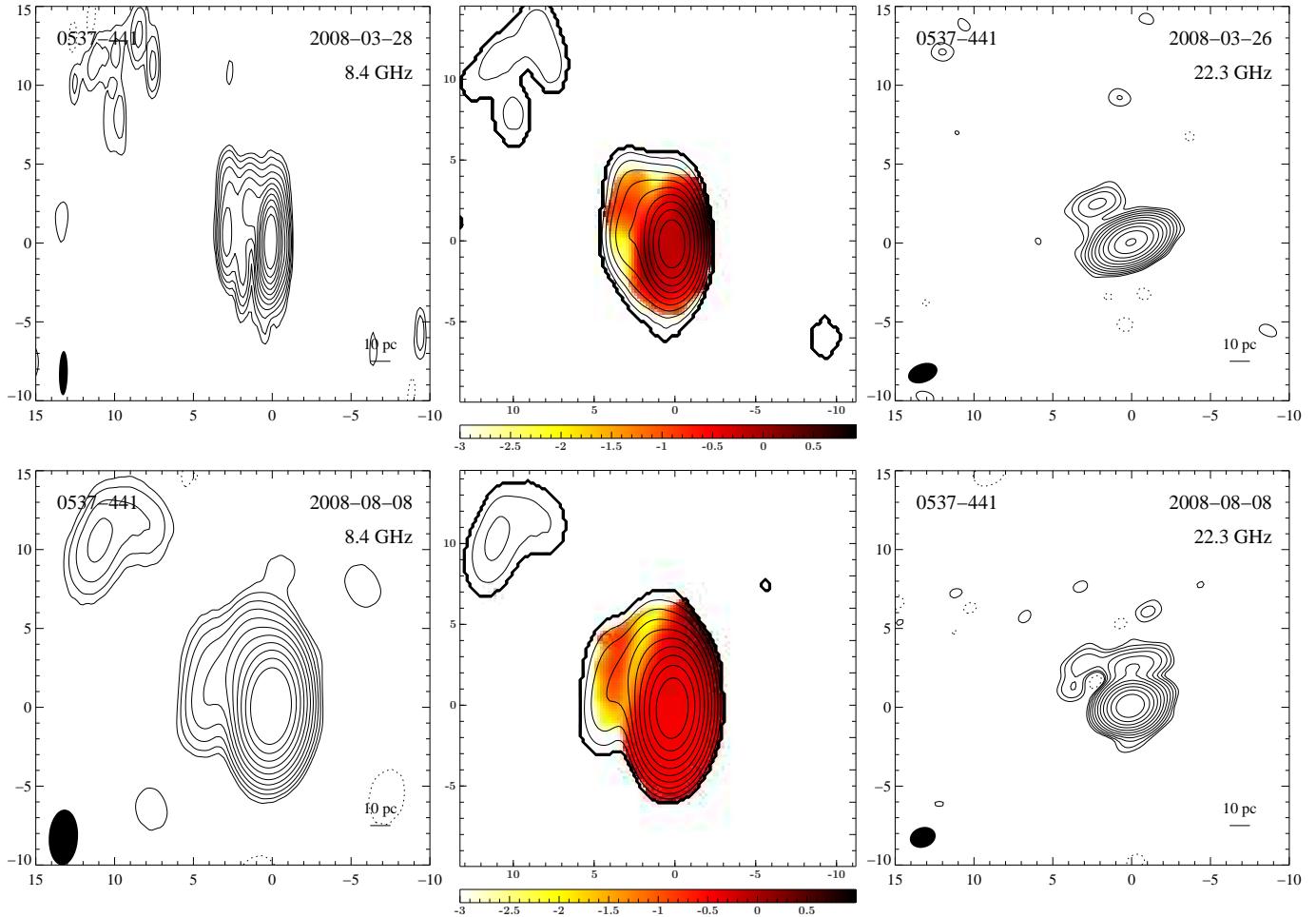
Fig. 2. Images from 2 epochs of dual frequency observations of PKS 0537$-$441. x- and y-axis are labeled in milliarcseconds and the hatched ellipse on the bottom left represents the beam of the observing array. In each row, the left and right images are observations at 8.4 GHz and 22 GHz respectively. The image at the centre of each row is the spectral index map made from the images on either side. The colour coding shows the spectral index as defined in the text.

2. Observations and Data Reduction

VLBI observations for the epochs presented were made using the Australian Long Baseline Array (LBA[1]) together with the Hartebeesthoek 26m dish in South Africa. The LBA consists of five telescopes, namely, Parkes (64 m), Narrabri (5x22 m), Ceduna (30 m), Hobart (26 m) and Mopra (22 m). In addition, TANAMI sometimes has access to two other telescopes within Australia, the 70 m and 34 m telescopes belonging to NASA's Deep Space Network at Tidbinbilla. These observations were made at 8.4 GHz and 22 GHz. Each observing run is 24 hours long with every source being observed for about an hour. The observations are made approximately every 2 months. The data were correlated at the Swinburne University Correlator. The radio data were calibrated using AIPS and the radio images were made using the CLEAN algorithm in DIFMAP interactive mode (Shepherd (1997)). For details of the observations, calibration and imaging see Ojha et al. (2010).

Here we present VLBI images from three epochs of observations two of which have data both at 8.4 and 22 GHz.

The data used for the radio light curve was taken using the University of Tasmania's 30 m telescope. This dish, together with the 26 m dish at Hobart, have since August 2007, been monitoring TANAMI sources (PI: Jim Lovell). Hobart observes at 2.3 GHz and 6.4 GHz while Ceduna observes at 6.7 GHz. Weekly, 48 hour observations are done with about one hour spent observing a single source for every epoch.

The γ-ray observations were made using the LAT. The *Fermi*/LAT has a number of observing modes but spends most of its time in survey modes where the whole sky is scanned once every two orbits. For each event, the *Fermi*/LAT measures 3 quantities, the arrival direction, the energy and the arrival time. All *Fermi*/LAT data shown here were downloaded from the public website[2].

---

[1] The Long Baseline Array is part of the Australia Telescope which is funded by the Commonwealth of Australia for operation as a National Facility managed by CSIRO.

[2] http://fermi.gsfc.nasa.gov/cgi-bin/ssc/LAT/
LATDataQuery.cgi

The data were reduced using *Fermi* science tools[3] using monthly time bins and an energy range of 100 MeV to 300 GeV. GTSELECT was used to specify the time (in mission elapsed time) and energy range and the region of interest. To make good time intervals, removing data when the *Fermi* spacecraft was over the South Atlantic Anomaly, GTMKTIME was used. Lifetime cubes were calculated using GTLTCUBE while GTEXPMAP was used to generate exposure maps for the region of interest. GTLIKE was then used to perform the likelihood analysis of the *Fermi*/LAT data. The output of GTLIKE gives the integrated flux and the test statistic among other parameters.

3. TANAMI images of PKS 0537−441

Figure 1 shows an 8.4 GHz image from November 2007. Figure 2 shows 8.4 GHz and 22 GHz radio images from observations at two additional epochs (March and August 2008). In each row the 8.4 and 22 GHz images are shown at the left and right, respectively. The corresponding spectral index map made using these images is shown at the central panels. Details of all these images are summarized in Table 1.

The 8.4 GHz images show a radio core and extended emission to the east. The images show more extended emission in March 2008 and even more in August 2008. This is the time leading to the γ-ray flare observed weeks leading to October 2008. The core is unresolved at 22 GHz for both epochs. Observations at the two frequencies allow calculations of the spectral indices which, when used together with indices from other energy bands, e.g., γ-ray, give the broadband Spectral Energy Distribution (SEDs) needed to understand Active Galactic Nuclei.

The mean flux density $\bar{S}$ at the 8.4 GHz epochs is $\bar{S}_{\text{peak}} \approx 4.3$ Jy beam^{-1} while $\bar{S}_{\text{total}} \approx 4.75$ Jy. The peak flux density S_{peak} at 8.4 GHz shows significant variability in the flux density with a standard deviation of 0.80 Jy beam^{-1}, while the total flux density S_{total} has a standard deviation of 0.45 Jy. At 22 GHz, there is a slight decrease in the flux density from the March 2008 epoch to the August 2008 epoch.

Figure 2 shows the spectral index maps derived from the two observing frequencies, 8.4 GHz and 22 GHz. The spectral index is defined as $F_\nu \sim \nu^{+}\alpha$. The spectral index maps of PKS 0537−441 were calculated according to this definition where $S_{8.4\text{GHz}} \geq 5\sigma_{8.4\text{GHz}}$ and $S_{22\text{GHz}} \geq 5\sigma_{22\text{GHz}}$. The color coding shows the changing of the spectral index from optically thin to optically thick emission regions. The overlaid contours show the flux density distribution at 8.4 GHz folded with the beam of the corresponding 22 GHz image. The core of the source has an almost perfectly flat spectrum, while the jet has an optically thin spectrum with a hint of steepening with time. As we have not modeled any optically thin components, we have not been able to calculate a core shift for PKS 0537−441 yet.

[3] *Fermi* science tools can be downloaded from `http://fermi.gsfc.nasa.gov/ssc/data/analysis/software/`
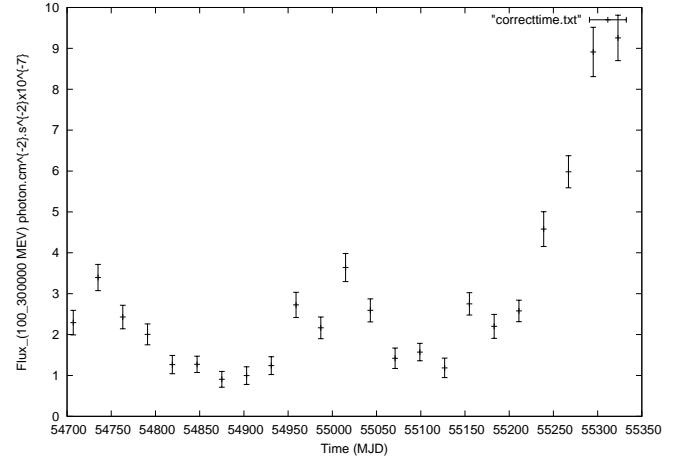
Fig. 3. Gamma-ray light curve for PKS 0537−441 spanning ~21 months from August 2008 to May 2010.

4. Radio and γ-ray Light Curves of PKS 0537-441

Figures 3 and 4 show the γ-ray light curve for data from August 2008 to May 2010 and the radio light curve for the period 14 April to 28 May 2010, respectively. The points on the γ-ray light curve represent monthly bin sizes. Photons with energies from 100 MeV to 300 GeV were considered.

PKS 0537−441 has been reported by the Astronomer's Telegram to be in an active state in October 2008, July 2009, February 2010 and April 2010. The γ-ray light curve shows the source to be active in September 2008, July 2009 and April 2010. When reducing the data, we used monthly bin sizes and this is a possible source of the disparity. Also, most telegrams are sent at the onset of increased activity and not necessarily the peak of such activity.
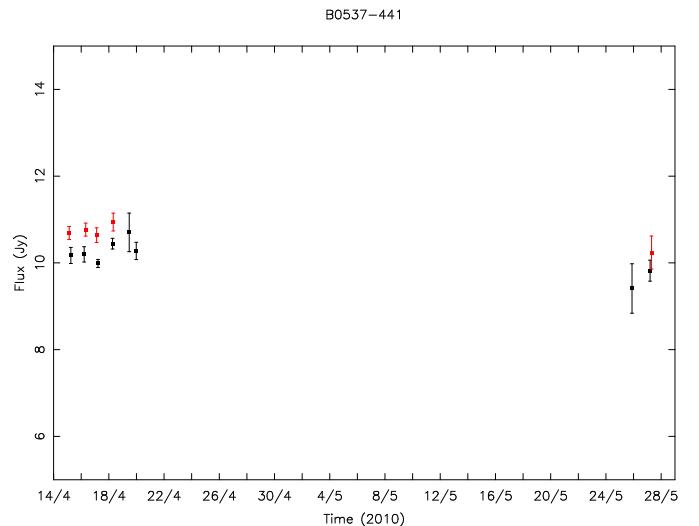

Fig. 4. Radio light curve for PKS 0537−441. Note that these data cover a much shorter time compared to the gamma-ray light curve.

Table 1. Image parameters and observation characteristics

Frequency [GHz]	Epoch yyyy-mm-dd	RMS [mJy beam^{-1}]	S_{peak} [Jy beam^{-1}]	S_{total} [Jy]	θ_{maj} [mas]	θ_{min} [mas]	P.A. [°]
8.4	2007-11-10	0.37 ± 0.40	4.85	5.10	2.2	0.7	12
8.4	2008-03-28	0.58 ± 0.11	3.38	4.24	2.8	0.6	−1
8.4	2008-08-08	0.39 ± 0.35	4.67	4.91	3.5	1.9	−3
22.3	2008-03-26	0.47 ± 0.99	3.12	3.43	1.9	1.2	−70
22.3	2008-08-08	0.47 ± 0.36	3.00	3.21	1.7	1.3	−72

The data for the radio light curve was taken at 6.7 GHz using the University of Tasmania's 30m telescope at Ceduna outside of Adelaide, Australia. This (when not observing as part of the LBA and other VLBI observations) monitors 15 sources continuously, with an additional 50 observed once every two weeks. The continuous monitoring is split into two groups, a southern group and a northern group, which are alternated in two week blocks (though there is some overlap).

Data is taken in four scan blocks, two scans in RA, and two in DEC and fit with a Gaussian on a 2nd order polynomial baseline. The two scans in each direction are merged, and cross checked. If the amplitudes do not match, the entire four scan block is rejected. A pointing offset and correction is then calculated and applied in both RA and DEC. The resulting RA and DEC, pointing corrected, scans are also then cross checked and merged. Again the entire block is rejected if the RA and DEC amplitudes don't match.

The resulting amplitude is then corrected for gain-elevation effects and calibrated. The northern group uses 3C 227 as a calibrator and the southern B1934−638. Data finally is binned into one-day bins (unless intra-day scintillation observations are being made).

The radio light curve covers a much shorter time period than the γ-ray curve and does not show evidence for variability. We will continue to monitor this source in the radio to look for possible connections between the radio and γ-ray light-curves.

5. Conclusion

Multi-epoch TANAMI observations of the highly luminous blazar PKS 0537−441 at two radio frequencies and single dish monitoring data from the Ceduna radio telescope are presented here in addition to a γ-ray light curve from *Fermi*/LAT. We have used simultaneous observations at 8.4 and 22 GHz to produce a spectral index map that appears to be the first for this source at these resolutions. These data are being combined with simultaneous data from *Fermi* to construct SEDs and understand the behaviour of this interesting object. Modeling of multiple epochs of data in order to understand the kinematic behaviour is also in progress.

References

Abdo, A. A., Ackermann, M., Ajello, M., et al. 2010, ApJS, 188, 405
Bastieri, D. 2009, ATel, 2124
Heidt, J., Jäger, K., Nilsson, K., et al., 2003, A&A, 406, 565-577
Lucarelli, F., Striani, E., D'Ammando, F., et al., 2010, ATel 2454
Ojha, R., Kadler, M., Böck, M., et al. 2010, A&A, in press, arXiv:1005.4432
Romero, G. E., Surpi, G. & Vucetich, H. 1995, A&A, 301, 641
Shepherd, M. C. 1997, Astronomical Society of the Pacific Conference Series, 125, 77
Tosti, G. 2008, ATel, 1759
Treves, A., Belloni, T., Falomo, R., et al. 1993, ApJ, 406, 447-450

Superluminal Motion in AGNs and GRBs

Zhi-Bin Zhang[1,2]

[1] Department of Physics, College of Sciences, Guizhou University, Huaxi district, Guiyang, Guizhou 550025, China.
[2] The NAOC-GZU Joint Research Center for Astronomy, China. Email: sci.zbzhang@gzu.edu.cn

Abstract. In this paper, I have investigated the differences in superluminal motion between AGNs and GRBs, two classes of objects with large differences in their lifetimes, sizes and features. In addition, the properties of the superluminal motion between different sub-classes of AGNs (e.g., radio galaxies, BL Lac objects, and quasars) are also compared in detail. The apparent transverse velocity ($\beta_{\rm app}$) of *Swift* and pre-*Swift* GRBs are tightly correlated with the Doppler factor δ as $\beta_{\rm app} \propto \delta^{1/2}$, while all AGNs are distributed around the line of $\beta_{\rm app} = \delta$, showing a weak correlation of $\beta_{\rm app}$ with δ. $\beta_{\rm app}$ exhibits an apparent positive correlation with $1 + z$ for both AGNs and GRBs, showing a cosmological effect of evolution with redshift. The superluminal properties of GRBs are significantly different from those of AGNs, but, there are no obvious differences between radio galaxies, BL Lac objects, and quasars.

1. Introduction

The apparent superluminal phenomenon – that the transverse velocity of an object moving (ultra-)relativistically in some special directions may appear to exceed the speed of light – was first predicted by Rees (1966). At first glance such a motion is quite counter-intuitive although it does not violate special relativity. It is essentially a geometric and light travel-time effect (Chodorowski 2005).

This motion was initially confirmed and discovered in quasars and radio galaxies by using the technique of Very Long Baseline Interferometry (VLBI) (Whitney et al. 1971, Cohen et al. 1971). Superluminal motion is not unique to quasars and radio galaxies, but is also found in other sources, including micro-quasars and BL Lac objects (e.g., Mirabel & Rodríguez 1994, Fan et al. 1996, Jorstad et al. 2001, Kellermann et al. 2004, etc). This may be because jets or jet-like outflows are common among various kinds of astrophysical phenomena with different scales, such as the Sun, proto-stellar systems, isolated neutron stars, neutron star and black hole binaries, supermassive black holes (or active galactic nuclei, AGNs) and gamma-ray bursts (GRBs) (Zhang 2007). Measurement of the apparent velocity provides a constraint on the geometry and underlying physics of the formation, ejection and acceleration of jets (Ghisellini & Celotti 2002).

AGNs are generally thought to be associated with supermassive black holes located in their centers. Classification is a very important strategy to comprehend their basic physics. They can be classified into several groups or subgroups by means of some diagnostic diagrams, e.g., Seyfert I and II galaxies, quasars, blazars (BL Lac objects and OVVs), radio galaxies, and LINERs. On the whole, blazars, radio galaxies and some quasars are radio-loud, while the remainder are radio-quiet. The radio-loud AGNs typically exhibit strong radio radiation, variable and jetted outflows, X-ray emission and UV ex-cess. This is surprisingly similar to what is observed in GRBs. Moreover, these radio-loud sources, together with GRBs, have a common property that the ejecta from their cores move outwards at very close to the speed of light, and both of them exhibit violent outbursts. This motivates me to make a comparative study between GRBs and radio-loud AGNs of superluminal motion. In addition, GRBs in the pre-*Swift* and *Swift* eras have also been compared to check the dependence of the apparent transverse velocity on different instruments.

2. Superluminal motion

By considering the geometry of ejecta relative to the observer, the apparent transverse velocity $\beta_{\rm app}$ is given by

$$\beta_{\rm app} = \frac{\beta \sin \theta}{1 - \beta \cos \theta} \tag{1}$$

in units of the speed of light c, where β represents the real speed of ejecta and θ is the viewing angle between the line of sight and the bulk outward velocity. Note that β is also in units of c and is associated with a Lorentz factor γ where $\beta = (1 - \gamma^{-2})^{0.5}$. For a given γ, one can make a plot of $\beta_{\rm app}$ versus θ, which shows a profile with a single peak at $\theta \approx 1/\gamma$ (Cohen, Lister & Vermeulen 2004, Kellermann et al. 2007).

In addition to $\beta_{\rm app}$, a Doppler factor δ is also associated with θ and γ, and is given by

$$\delta = \frac{1}{\gamma(1 - \beta \cos \theta)} \tag{2}$$

Eqs. (1) and (2) involve four variables ($\beta_{\rm app}$, β, θ and δ) but if two independent variables are known the others can be deduced. For radio observations of AGNs with measured redshift (z), $\beta_{\rm app}$ is in general measurable and given by

$$\beta_{\rm app} = \frac{\mu D_{\rm A}}{c}, \tag{3}$$
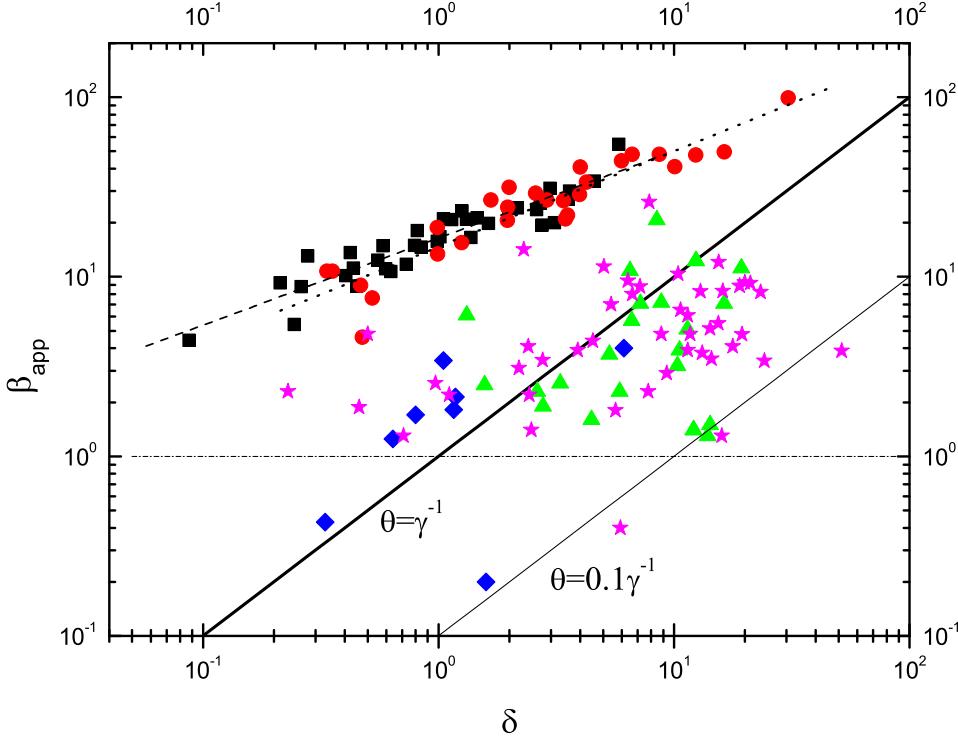
Fig. 1. The apparent transverse velocity β_{app} vs. the Doppler factor δ for AGNs and GRBs in our samples. *Circles:Swift* GRBs; *squares:*pre-*Swift* GRBs; *stars:*quasars; *triangles:*BL Lac objects; *diamonds:* Radio galaxies. Thick, thin and dash-dotted lines denote the relations of $\beta_{\mathrm{app}} = \delta$, $\beta_{\mathrm{app}} = 0.1\delta$ and $\beta_{\mathrm{app}} =$ constant, respectively. The dotted and dashed lines correspond to their best fits to the GRB data. All the symbols defined here are the same as those in the other two Figs.

where μ is the observed proper motion and D_{A} denotes the angular diameter distance of the source. In practice, the luminosity distance, D_{L} defined by the expression for flux, $f = L(4\pi D_{\mathrm{L}})^{-1}$, is usually used for cosmological studies. D_{A} and D_{L} are related to each other by

$$D_{\mathrm{L}} = (1+z)^2 D_{\mathrm{A}} \,, \tag{4}$$

Hence β_{app} can also be expressed as

$$\beta_{\mathrm{app}} = \frac{\mu D_{\mathrm{L}}}{c(1+z)^2} \tag{5}$$

The Doppler factor δ can be estimated (Ghisellini et al. 1993) using

$$\delta = f(\alpha)S_m[\frac{\log(\nu_b/\nu_m)}{S_x\phi_d^{6+4\alpha}\nu_x^{\alpha}\nu_m^{5+3\alpha}}]^{1/(4+2\alpha)} \cdot (1+z) \,, \tag{6}$$

where $f(\alpha) \simeq 0.08\alpha + 0.14$ is a function of the spectral index α, S_m is the maximum radio flux (in Jy) at frequency ν_m (in GHz), S_x (Jy) represents the flux in the X-ray (or optical) band ν_x (in keV), ν_b is the synchrotron high energy cutoff frequency and ϕ_d is the angular size of the core (in mas). For AGNs of known redshift β_{app} and δ can be derived from radio observations, and hence β and θ can be deduced.

In principle, the superluminal phenomenon can be seen as long as the viewing angle θ is small enough in comparison with the cone angle $\sim 1/\gamma$ of the outflow, due to the beaming action. For a given source, the cone angle is generally knowable in a direct or indirect way, which make Eq. (1) reduce to the following three cases of θ as:

1. In the case of $\theta \ll \gamma^{-1}$, the observer is within the jet cone angle. Some simplified forms of $\sin\theta \sim \theta$ and $\cos\theta \sim 1$ lead Eq. (1) to be rewritten as

$$\beta_{\mathrm{app}} \simeq 2\gamma^2\theta \tag{7}$$

2. In the case of $\theta \sim \gamma^{-1}$, one can just see the edge of the outflow under the assumption that the jet does not have a significant sideways expansion. Relations of $\cos\theta \sim 1 - \gamma^{-2}/2$, $\sin\theta \sim \gamma^{-1}$ and $\beta = 1 - \gamma^{-2}/2$ are derived. In this way, β_{app} is reduced and reaches its maximum as

$$\beta_{\mathrm{app}} \simeq \gamma \simeq \delta \simeq \csc\theta \tag{8}$$

3. In the case of $\theta \gg \gamma^{-1}$, the observer is located outside the jet cone angle, which means $\sin\theta \sim \theta$, $\cos\theta \sim 1 - \theta^2/2$ and $\beta \sim 1$, thus

$$\beta_{\mathrm{app}} \simeq 2/\theta \tag{9}$$

3. Samples

In view of the above considerations, 8 radio galaxies, 24 BL Lac objects, and 46 quasars with superluminal observations by VLBI have been chosen from the literature (Hong et al. 1995, Jorstad et al. 2001, Kellermann et al. 2004), to constitute three independent AGN samples.

For GRBs, current observations of radio afterglows hiding superluminal motion are very rare. Up to now, only GRB 030329 and GRB 980425 have been suggested to be potential candidates (e.g., Dar & De Rujula 2000; Dado et al. 2004). The reason is that the angular resolution of current telescopes is still too low to measure the proper motion of GRB afterglows, except for GRB 030329 (Taylor
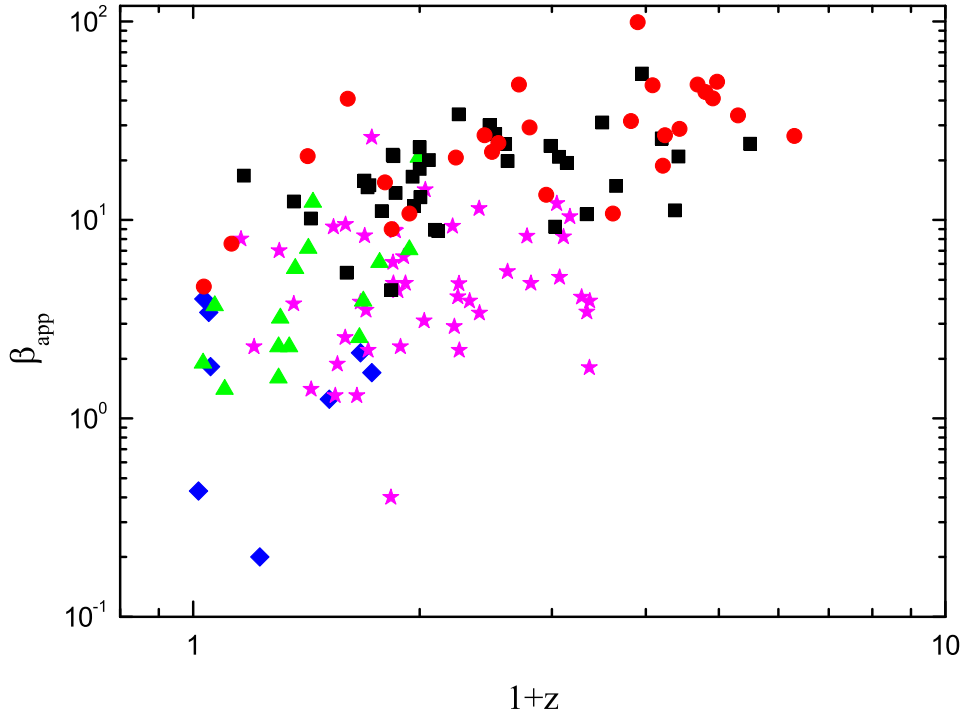
Fig. 2. The apparent transverse velocity β_{app} vs. cosmological inflation factor of $1+z$ on a logarithmic scale.

et al. 2004). It is more difficult to quantify superluminal motion in the phase of prompt emission, due to the lack of much higher resolution. This results in Eq. (3) being unusable for deriving β_{app}. Alternatively, Eq. (1) can be used to investigate superluminal motion during the prompt γ-ray emissions if only the viewing angle θ can be conveniently measured provided the Lorentz factors of GRBs are roughly estimated by

$$\Gamma \approx 240 \times E_{\mathrm{iso},52}^{1/8} n_1^{-1/8} (T_{90}/10s)^{-3/8}\,, \qquad (10)$$

as suggested by Rees & Mészáros (1992). Here, it has been assumed that the jet opening angle θ_j is equivalent to the viewing angle θ since the jetted outflow from us is much farther than that from its central engine. Based on these considerations, the apparent superluminal motion of GRBs in their prompt phase have been studied. For the sake of comparison, 27 *Swift* and 37 pre-*Swift* long GRBs with known redshift, duration time and jet break time have been selected.

4. Results

In this section the main results related to superluminal motion are presented for different sorts of cosmological sources. I pay special attention to the comparison between AGNs and GRBs for both radio and γ energy bands.

Figure 1 shows a largely different behaviour between GRBs and AGNs in the plane of β_{app} versus δ. Pre-*Swift* and *Swift* long GRBs, however, exhibit a similar positively correlated tendency. The dotted and dashed lines correspond to their best fits to the GRB data, following a very close power-law of $\beta_{app} \sim \delta^{0.5}$. Unlike GRBs, most AGNs are located within the range of $\theta \geq 0.1\gamma^{-1}$ and are roughly

distributed along the line of $\beta_{app} \propto \delta$ with large dispersion.

A linear correlation analysis gives a correlation coefficient of 0.6 for all AGNs with a very small chance probability of $P < 0.0001$.

Another interesting phenomenon seen in Fig. 2 is that the combination of AGNs and GRBs seems to be much better than either alone in respect of probing the cosmological evolution of β_{app}. β_{app} shows a clear positive trend with $1 + z$, showing a visible evolution of superluminal motion with z from the low redshift to the higher redshift universe.

As seen from Eqs. (7)–(9) and Fig. 3, I obtain $\beta_{app} \sim \gamma$ and $\beta_{app} \sim 2/\theta$ when $\theta \sim 1/\gamma$ and $\theta > 1/\gamma$, respectively. Here, the former is for AGNs with a tight positive correlation. The latter for GRBs shows no relation because β_{app} becomes only dependent on θ when $\theta > 1/\gamma$.

5. Conclusions

On the basis of the above analysis, one can state the following four conclusions:

Outflows of *Swift* and pre-*Swift* GRBs are found to be extremely superluminal in their prompt γ-ray emission phase. Meanwhile the superluminal motion is instrument-independent.

There is no significant difference in superluminal motion between distinct AGN sub-classes. However, radio galaxies exhibit slightly smaller β_{app}, z, δ and γ, in comparison with quasars and BL Lac objects.

As suggested by Kellermann et al. (2004), radio jets associated with strong gamma-ray sources detected by EGRET appear to have significantly faster speeds than non-EGRET sources, consistent with the idea that
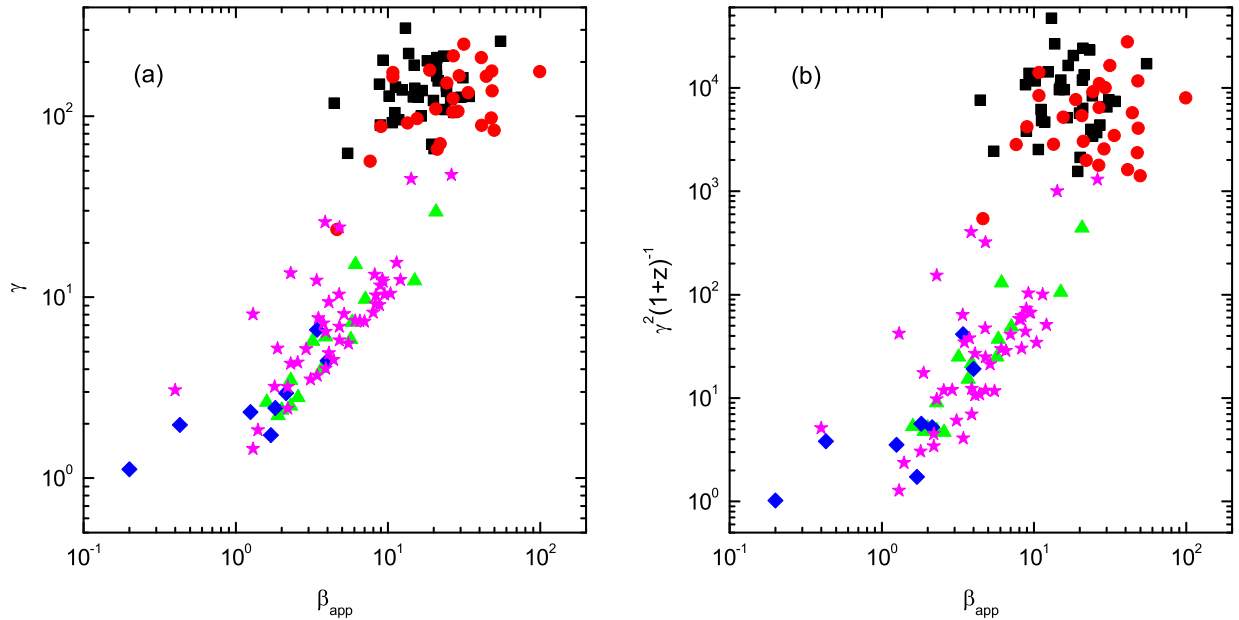
Fig. 3. Correlations of the apparent velocity β_{app} with the Lorentz factor γ in panel (a) and the modifying factor $\gamma^2(1 + z)^{-1}$ for the effects of Doppler boosting and cosmological expansion in panel (b), respectively.

gamma-ray sources have larger Doppler factors than non-gamma-ray sources. For GRBs the radio jets should have much larger speeds than those without gamma-ray detections.

It has been found that the apparent velocity shows a systematic decrease with increasing wavelength from Figs 1, 2, and 3, as Kellermann et al. (2004) pointed out. However, the probable interpretation that observations at different wavelengths sample different parts of the jet structure needs to be further confirmed.

References

Chodorowski, M.J. 2005, AmJPh, 73, 639

Cohen, M.H., Cannon, W., Purcell, G.H., et al. 1971, ApJ, 170, 207

Cohen, M.H., Lister, M.L., & Vermeulen, R.C., 2004, in Radio Astronomy at 70: from Karl Jansky to microjansky, L. Gurvits, S. Frey & S. Rawlings (eds.), EAS Publ. Ser., 15, p. 93

Dado, S., Dar, Arnon, De Rujula, A., 2004, arXiv:astro-ph/0402374

Dar, S., Dar, A., De Rujula, A., 2000, CERN Rep. 2000–257, arXiv:astro-ph/0008474

Ghisellini G., Celotti A., 2002, in Blazar Astrophysics with *Beppo SAX* and Other Observatories, P. Giommi, E. Massaro & G. Palumbo (eds.), ESA-ESRIN, p. 257

Ghisellini, G., 1993, ApJ, 407, 65

Hong,X.Y., Jiang,D.R., Wan, T.S., 1995, Acta Astronomica Sinica, 36, 147

Fan, J. H., Xie, G. Z., Wen, S. L., 1996, A&AS, 116, 409

Fan, J.-H., Wang, Y.-J., Yang, J.-H., & Su, C.-Y., 2004, ChJAA, 4, 533

Jorstad S.G., Marscher A.P., Mattox J.R. et al., 2001, ApJS, 134, 181

Kellermann K.I., Lister M.L., Homan D.C. et al., 2004, ApJ, 609, 539

Kellermann K.I., Kovalev, Y.Y., Lister, M.L. 2007, Ap&SS, 311, 231

Mirabel I.F. & Rodríguez L.F., 1994, Nature 371, 46

Rees, M.J., 1966, Nature, 211, 468

Rees, M.J. & Mészáros, P., 1992, MNRAS, 258, 41

Taylor, G.B., Frail, D.A., Berger, E., Kulkarni, S.R., ApJ, 2004, 609, L1

Whitney, A.R., Shapiro, I.I., Rogers, A.E.E., et al., 1971, Science, 173, 225

Zhang, S.N., 2007, in 26th IAU GA Prague, K.A. van der Hucht (ed.), Highlights of Astronomy, 14, 41

M 87 and the Dynamics and Microphysics inside the Blazar Zone

P. Hardee

Department of Physics & Astronomy, Gallalee Hall, The University of Alabama, Tuscaloosa, AL 35487, USA

Abstract. The blazars provide a considerable opportunity to peer into the workings within a few tens of parsecs of the central engine in AGN. This considerable opportunity involves significant challenges as different macroscopic dynamical processes and microscopic physical processes operating at different locations can be responsible for the observed emission. In this proceedings article I review recent theoretical and numerical results relevant to dynamics inside the blazar zone, review the particle acceleration processes capable of producing the high energy particles required by the observed emission, discuss some of the progress made at the microphysical level, and consider what recent TeV and radio observations of M 87 can tell us about the blazar zone.

1. Introduction

The deepest parts of AGN jets are explored by studying the properties of blazars. The spectrum from the radio to the TeV gamma-rays is characterized by two peaks and typically modeled as synchrotron plus inverse Compton emission, e.g., Ghisellini et al. (1998); Sikora (2001). Rapid non-thermal particle acceleration, often assumed to be associated with ejection event driven shocks, is required to generate the synchrotron emission.

Tremendous progress has been made during the past decade on reproducing the spectral energy distributions (SEDs) of blazars. The *Fermi*/LAT has filled in an important frequency gap between coverage provided by *Swift* and that provided by ground based Cherenkov arrays. Radio and optical flux, polarization, and timing information along with proper motions, have made it possible to construct likely scenarios for the dynamics and location of emission in the various different wavebands. Nevertheless, much remains to be understood.

The fundamental question is: How is the emission from blazars shaped by (a) the central engine properties, (b) the jet properties, (c) the external environment properties, and (d) in what mixture. Here an ultimate understanding requires that we know: (1) How relativistic jets are launched from the vicinities of super massive black holes (SMBHs). (2) How do the jet structure and composition change along the outflow. (3) What are the particle acceleration processes that produce the TeV particle energies required by the observed emission.

Marscher and coworkers' multi-wavelength campaigns provide revealing probes into the structure of the blazar zone (Marcher et al. 2008; Marscher et al. 2010). Here VLBI proper motions supply an estimate of Lorentz factors that link observed timescales to intrinsic timescales and distances between the central engine and the mm-radio core. The observed rotation of the optical polarization vector indicates helical twisting of the flow and magnetic field between the central engine and the radio core.

The multi-wavelength observations suggest one or more ejection events resulting in emission from moving jet shocks. The emission comes from internal synchrotron and synchrotron self-Compton (SSC) processes and inverse Compton (IC) processes involving photons from outside the moving zone of emission, e.g., Sikora et al. (1994); Dermer et al. (2009). The SEDs and timing signatures of internal shocks have been considered in some detail by Böttcher & Dermer (2010) for flat-spectrum radio quasars (FSRQs) or low-frequency peaked BL Lac objects (LBLs) where gamma-ray production is dominated by Comptonization of external radiation. For some sources these models may satisfactorily explain timing lags.

Observations suggesting ejection events challenge the assumption of a fixed location for the blazar zone. Still strong outbursts, e.g., 3C 454.3 (Sikora et al. 2008) suggest a blazar zone coincident with a recollimation shock as this fixed structure is more efficient at dissipating energy than internal shocks. Sikora et al. (2008) suggest that a recollimation shock could be located at 3–9 pc from the central engine and nearly co-spatial with the mm-wavelength radio core, e.g., as in Marscher et al. (2008, 2010). Nevertheless, the emission from blazars is likely produced over a broad range of distances from the central engine.

Fitting the SEDs of sources with one-zone homogeneous SSC models makes it possible to find a unique set of parameters for the emitting region (Tavecchio et al. 1998). Application of these models to TeV sources typically requires a Doppler factor, $\delta \equiv [\Gamma(1 - v/c \cos \theta)]^{-1}$, that ranges from 10–20 (Katarzynski et al. 2003) up to 50 (Konopelko et al. 2003) depending on the absorption of TeV photons by the IR background. However, these large Doppler and associated Lorentz factors are problematic (Henri & Saugé 2006) because VLBI studies indicate slow moving pc-scale emission features in strong TeV BL Lacs (Lister 2006; Piner, Pant & Edwards 2008).

The slow pc-scale motions led Georganopoulos & Kazanas (2003) to propose that fast moving material at the jet base relativistically boosts radiation produced by slow moving material at the end of a deceleration zone. Alternatively Ghisellini et al. (2005) proposed a fast jet

spine slow jet sheath configuration. In both scenarios the synchrotron and inverse Compton emission come from different regions and this allows reduced Doppler factor values compared to pure one-zone SSC models.

The electron-synchrotron origin of the low frequency emission is well established but the high energy emission could be dominated by cascades if protons are accelerated to pγ pion production energies. Such hadronic blazar models in which high magnetic fields are needed for proton acceleration and synchrotron radiation from protons and associated secondaries, e.g., Krawczynski (2007), have not received as much attention as leptonic blazar models. Still there is evidence that leptonically dominated blazar jet models are energetically dominated by protons with Poynting flux to kinetic flux conversion taking place very close to the central engine (Sikora et al. 2005).

Rapid observed variability timescales, Δt, pose severe constraints on the particle acceleration timescale, $\sim \delta \Delta t$ and the emission region size, $\sim \delta c \Delta t$. Correlated X-ray/TeV gamma-ray flares with timescales from 15 minutes (Mrk 421) to a few hours (Mrk 501 & 1ES 1959+650) have been observed. Interestingly a similar correlation of the radio-to-optical emission with the X-ray or TeV gamma-ray emission is not found, e.g., Krawczynski (2007) and references therein. Thus flares may come from small, a few Schwarzschild radii in size, fast moving "needles" within a slower jet or "jet-in-a-jet" (Levinson 2007; Begelman, Fabian & Rees 2008; Ghisellini & Tavecchio 2008; Giannios, Uzdensky & Begelman 2009).

The X-ray/TeV flares also require very rapid particle acceleration. Fermi acceleration processes are claimed capable of providing the needed acceleration (Henri et al. 1999; Tammi & Duffy 2009), but require large velocity differences combined with turbulent scattering, e.g., shocks or velocity shear along flow boundaries (Stawarz & Ostrowski 2002). Accretion disk shear and turbulence followed by centrifugal acceleration out to the light cylinder is also capable of accelerating protons to 10^{20} eV and electrons to the 10–100 TeV required (Istomin & Sol 2009). Fermi processes can take place in super-Alfvénic flow regions but are not likely in the sub-Alfvénic magnetically dominated jet production and acceleration region from which TeV flares might originate. In the absence of Fermi acceleration, acceleration may be provided by vacuum gap electric fields in the black hole magnetosphere (Blandford & Znajek 1977; Krawcznski 2007) or by current driven instability and magnetic reconnection leading to conversion of Poynting flux to kinetic flux (Sikora et al. 2005).

Of course, escape of TeV photons depends on the ambient photon field (Ghisellini & Tavecchio 2009). Here TeV photons might escape from the center of BL Lacs as a result of a reduced ambient photon field that might accompany the reduced accretion rate compared to the FSRQs (Ghisellini et al. 2009) .

2. MHD dynamics inside the blazar zone

The location of blazar emission in different wavebands could stretch from the black hole ergosphere to over ten parsecs along the relativistic jets produced by the central engine. Thus, how relativistic jets are launched from the vicinities of SMBHs, and how the jet structure and composition change along the outflow are critical issues for blazars. Theoretically we need to study RMHD processes beginning at scales smaller than the gravitational radius of the accreting black hole, where magnetic and electric fields likely dominate the jet dynamics, out to distances where kinetic effects likely dominate the jet dynamics.

GRMHD codes are used to study the extraction of rotational energy from a spinning black hole, i.e., Blandford-Znajek mechanism (Komissarov 2005; McKinney 2005), and from the accretion disk (Meier 2005), i.e., Blandford-Payne mechanism (Blandford & Payne 1982). Jet generation simulations (Hawley & Krolik 2006; McKinney 2006) show development of angular momentum transfer in the accretion disk, leading to diffusion of matter and magnetic field inwards, and unsteady outflows near a centrifugally supported "funnel" wall (Hawley & Krolik 2006). In general, GRMHD simulations with spinning black holes indicate jet production with a Poynting-flux high Lorentz factor spine with $v \sim c$ and $\Gamma \sim 10$, and a matter dominated sheath with $v \sim c/2$ possibly embedded in a lower speed, $v \ll c$, disk/coronal wind. This basic result suggests the fast jet spine and slower jet sheath type structure advocated to reduce the need for very high Lorentz and Doppler boost factors. We note however that the transverse profile of the Lorentz factor can achieve a maximum in a tenuous boundary layer between a Poynting-flux spine and a dense low speed kinetically dominated sheath (Mizuno et al. 2008; Aloy & Mimica 2008).

Until recently simulation work considered only axisymmetric systems. As a result the efficiency of this mechanism has been questioned because the magnetic configurations are susceptible to a disruptive current driven (CD) kink instability (Begelman 1998). Even so, the outflow may be well collimated by the large-scale poloidal magnetic field of the accretion disk (Spruit, Foglizzo & Stehle 1997). In this scenario the CD kink instability still comes into play because the poloidal field declines in the expanding flow faster than the toroidal field, but the instability develops in the already collimated flow so the jet preserves its directionality. Poynting energy flux should be converted into plasma energy. Gradual acceleration by magnetic forces (Vlahakis 2004; Vlahakis & König 2004a,b; Beskin & Nokhrina 2006; Komissarov et al. 2007) as well as dissipation of alternating magnetic fields (Levinson & van Putten 1997; Levinson 1998; Heinz & Begelman 2000) have also been proposed. While these processes could play a role in jets, magnetic energy release via the CD kink instability is inherent in narrow Poynting dominated jets. This instability disrupts the regular structure of the magnetic field to liberate magnetic energy (Lyubarskii 1992, 1999; Spruit et al. 1997; Begelman 1998;

Giannios & Spruit 2006), and naturally could result in flaring activity like that observed from the blazars.

3D RMHD simulations designed to investigate the properties of the CD kink instability of a static plasma column and more recently incorporating a sub-Alfvénic velocity shear surface (Mizuno et al. 2009; and work in progress) show that on the order of 100 Alfvén crossing times are required to reach the non-linear stages of kink development. In the SMBH jet collimation and acceleration environment an Alfvén crossing time is comparable to a light crossing time of the Poynting-flux spine. Of particular interest in the blazar context is the finding that a velocity shear surface inside some critical magnetic radius results in helically twisted flow within a growing and slowly moving kink as opposed to a kink embedded within and moving with the flow.

Jet expansion will significantly slow the spatial growth of a developing kink as the Alfvén crossing time increases. In this regard a recent fully 3D GRMHD simulation (McKinney & Blandford 2009) reveals that the jets generated by rotating, accreting black holes can be relatively stable structures out to 10^3 gravitational radii and reach Lorentz factors of $\Gamma \sim 10$. Some mild twisting associated with a kink mode is evident in the simulation but no significant disruption or dissipation occurs. Beyond the Alfvén surface where the jet is super-Alfvénic there is a possibility of coupling between the CD kink and the Kelvin-Helmholtz (KH) velocity shear driven helical instability. Theory and simulations (Hardee 2007; Mizuno et al. 2007) have indicated that strong magnetic fields combined with a spine-sheath morphology can also slow the spatial growth of this mode. Thus, it should be possible for a jet to maintain a relatively strong and ordered helical magnetic field and flow structure through the blazar zone as needed to explain the Marscher et al. (2008, 2010) polarization results. Once the flow is super-magnetosonic, internally driven and externally driven shocks could form in the flow.

3. Microphysics inside the blazar zone

Inside the black hole magnetosphere and in the near jet generation zone the dominant particle acceleration processes should be associated with vacuum gap electric fields and magnetic reconnection. Electromagnetic models have been discussed by Levinson (2000), Maraschi & Tavecchio (2003), and Kundt & Gopal- Krishna (2004), and the consequences for emission by Krawczynski (2007). These particle acceleration processes cannot be studied on a fundamental level by MHD type numerical simulations but ultimately can be investigated on the microphysical level using general relativistic particle-in-cell (GRPIC) codes, e.g., Watson & Nishikawa (2009).

When the jet becomes super-Alfvénic and subsequently super-magnetosonic (location depending on magnetic reconnection at various scales, associated particle heating/acceleration and mass loading of the Poynting-flux spine) shocks can form. Typically we assume Fermi

acceleration in the shock region, but shock models, e.g, Böttcher & Dermer (2010), have to assume an electron injection energy spectrum, a fraction, ϵ_B, of the energy density in the shocked plasma contained in the magnetic field, and a fraction, ϵ_e, of the shocked plasma kinetic energy transferred into relativistic electrons. These assumed microphysics parameters, whose values are usually fitted from the data, reflect our lack of understanding of the microphysics (Waxman 2006).

The microphysics, e.g., Spitkovsky (2008) and Nishikawa et al. (2009) from relativistic shocks is now being investigated using relativistic particle-in-cell (RPIC) codes. Computational constraints have limited the majority of simulations to shocks in electron-positron pair plasmas and 2D simulations are used to cover parameter space combined with a few fully 3D simulations. In relativistic shocks the most rapid acceleration is provided in situ by the filamentation instability, so named as the interpenetrating plasmas form current filaments and associated magnetic fields. Particle acceleration occurs rapidly on electron plasma frequency timescales. For electron-proton plasmas the protons respond on proton plasma frequency timescales that are much longer than the electron plasma frequency timescales.

A 3D simulation of a Lorentz factor 15 unmagnetized pair jet penetrating an unmagnetized ambient pair plasma achieved partial development of a a hydrodynamic-like trailing shock, contact discontinuity, and leading shock structure. The strongest electromagnetic fields appeared in the nearly fully developed trailing shock with $\epsilon_B \sim 0.3$ (Nishikawa et al. 2009). 2.5D and 3D pair plasma shocks have been investigated in the contact discontinuity frame over a broad range of magnetic obliquities (Sironi & Spitkovsky 2009a). Fermi type particle acceleration was observed but with particle acceleration and spectral index sensitive to the magnetic obliquity and no "suprathermal" power law tail developed for magnetic fields not sufficiently oblique to the shock surface as significant self-generated shock turbulence could not develop upstream of the shock. However, very recent simulations investigating the effect of increasing the positive particle mass (private communication) indicate significant differences at sufficiently large "proton" masses, $m_p/m_e > 20$. Ultimately we may be able to tell the difference between pair plasma shocks and pair/proton plasma shocks and confirm or refute the one-zone blazar model requirement that jets are dynamically dominated by cold protons.

Other recent developments include the self-consistent computation of emission from pair plasma shocks (Sironi & Spitkovsky 2009b). In RPIC simulations, emission can be calculated self-consistently from the particle accelerations in the turbulent electric and magnetic fields accompanying the shock. These 2D based self-consistent pair plasma simulation results carried out in the reference frame of the shock contact discontinuity reveal synchrotron like self-absorbed spectra at lower frequencies, a thermal component, and higher frequency supra-thermal emission over a six orders of magnitude frequency range.

Ultimately it is hoped that magnetized RMHD shock simulations on macroscopic scales can provide the global shock properties that can be inserted into coupled RPIC simulations to investigate the microphysics on much smaller scales. The results could provide a firm physical basis for magnetization and particle acceleration inputs into existing blazar shock models.

4. The case of M 87

4.1. The TeV-Radio Connection

The radio galaxy M 87 is a Fanaroff-Riley Type I source, the SED is similar to that of an LBL, and this suggests that M 87 is a misaligned BL Lac. The luminosity distance is D = 16.7 Mpc (Mei et al. 2007), so 1 mas corresponds to 0.081 pc = 2.5×10^{17} cm in the sky plane. The mass of the central black hole is $(6.0 \pm 0.5) \times 10^9 \, M_\odot$ (Gebhardt & Thomas 2009), at the above distance. The Schwarzschild radius $R_s \sim 1.8 \times 10^{15}$ cm and 1 mas $\sim 140 R_s$. The most rapid optical proper motion is observed at HST-1 (~ 1 arc-sec from the radio/optical core) with superluminal speed $\beta_{obs} \sim 6$ (Biretta, Sparks & Macchetto 1999). The most rapid radio proper motion at HST-1 indicates $\beta_{obs} \sim 4$ (Cheung, Harris, & Stawarz 2007). The limb brightened radio structure and proper motion difference has been interpreted as evidence for velocity shear.

The highest observed superluminal speed requires a jet viewing angle of $\theta < 19^o$ and the assumption of $\theta \sim 15^o$ seems reasonable. With this choice the intrinsic distance along the jet is $r_{\rm int} \sim 3.86 \, r_{\rm obs}$, and 1 mas $\sim 540 R_s$ along the jet. The optical and radio proper motions then indicate Lorentz factors of ~ 7.5 and ~ 4.5, respectively at HST-1 at $\sim 5.3 \times 10^5 R_s$ along the jet.

VLBA observations at 43 GHz show a limb brightened jet to within 0.5 mas (270 R_s along the jet) of the core. Wider opening angles are observed closer to the core (Junor et al. 1999; Walker et al. 2008; Kovalev et al. 2007). At 86 GHz the core is no larger than $25 \times 7 \, R_s$ (Krichbaum et al. 2006). The opening angle morphology and the observation of a faint counter-jet (Kovalev et al. 2007) are consistent with the jet converging at the central engine.

VHE gamma-ray emission was first reported by HEGRA in 1998/99 (Aharonian et al. 2003). The emission was confirmed by H.E.S.S. in 2003-2006 (Aharonian, et al. 2006a) with gamma-ray flux variability on time scales of days. During 50 nights between January and May 2008 H.E.S.S. (Aharonian et al. 2006b), MAGIC (Albert et al. 2008) and VERITAS (Acciari et al. 2008) found day scale variability in the energy range between 0.1 and 10's of TeV, and the flux reached the highest level ever observed from M 87, > 10% of the Crab Nebula.

Leptonic (Georganopoulos, Perlman & Kazanas 2005; Lenain 2008) and hadronic (Reimer, Protheroe & Donea 2004) VHE gamma-ray models have been proposed. The nucleus (Neronov & Aharonian 2007; Rieger & Aharonian 2008), the inner jet (Tavecchio & Ghisellini 2008) or HST-1, have been discussed as possible sites (Cheung, Harris & Stawarz 2007).

At X-ray frequencies during 2008 HST-1 is found in a low state, but the nucleus was found in its highest X-ray flux state since 2000 (Harris, Cheung & Stawarz 2009). This is in contrast to the 2005 VHE gamma-ray flares (Aharonian et al. 2006), which happened after a several year increase in the X-ray flux of HST-1 (Harris et al. 2006). Given its low X-ray flux in 2008, HST-1 is an unlikely site for the 2008 VHE flaring activity.

Throughout 2007 the VLBA observed M 87 at 43 GHz roughly every three weeks (Walker et al. 2008, 2009) and every 5 days from January to April 2008, see Acciari et al. (2009) with a resolution of 0.21×0.43 mas (resolution $\sim 230 R_s$ along the jet at a viewing angle of 15°). An initial radio flux density increase was located in the unresolved core. The radio peak occurred about 50 days after the onset of the VHE flare. Over this time the jet base brightened and extended about 0.77 mas, implying an average apparent velocity of 1.1 c, and Lorentz and Doppler factors of ~ 1.8 and ~ 2.8, respectively at $\theta = 15^o$.

4.2. Implications for the Blazar Zone

The observed emission can be explained by an ejection event in the central region associated with the VHE flare. Synchrotron self-absorption or the time needed to cool the electrons causes a delay of the observed radio peak. The radio structural change along with the timing of the VHE activity, imply that the VHE emission came from a region closer to the central engine than the VLBA resolution along the jet, $\sim 230 R_s$. The day scale variability implies an intrinsic timescale, $\Delta t_{\rm int} << \delta_{\rm max} \Delta t_{\rm obs} \sim 15 \times 10^5$ sec, and acceleration and emission region size $<< 25 R_s = 4.5 \times 10^{16}$ cm $= c \Delta t_{\rm int}$ where $\delta_{\rm max} = 2\Gamma$ with $\Gamma = 7.5$.

TeV gamma-ray photons can escape the central region of M 87 without being heavily absorbed through $e^+ e^-$ pair production (Neronov & Aharonian 2007; Rieger & Aharonian 2008) with either photons from the accretion disk (Cheung, Harris & Stawarz 2007) or infrared photons as M 87 harbors a low luminosity accretion disk (Rieger & Aharonian 2008) and lacks a source of infrared radiation close to the central black hole (Perlman et al. 2007).

Acceleration by vacuum gap electric fields in the black hole magnetosphere (Neronov & Aharonian 2007) or due to centrifugal acceleration in an active plasma-rich environment, where the parallel electric field is screened (Rieger & Aharonian 2008) are definite possibilities. Synchrotron and curvature radiation of the charged particles, and inverse Compton scattering of thermal photons can produce VHE gamma-ray photons (Krawczynski 2007). An alternative scenario could be that the primary photons create a pair cascade whose leakage produces the observed gamma-ray emission (Bednarek 1997).

In an hadronic M 87 model (Reimer et al. 2004), a primary relativistic electron population is injected together with high-energy protons into a highly magnetized emission region. The VHE emission is dominated by either $\mu^\pm / \pi^\pm$ synchrotron radiation or by proton synchrotron

radiation. The low-energy component is explained by the synchrotron emission of the electron population. The requirement of magnetic fields $\sim 10^3$ Gauss is inconsistent with the low accretion flow, low density and low magnetic field environment inferred for M 87 (see Neronov & Aharonian 2007), although not ruled out during short episodes. This makes an hadronic origin for the TeV emission unlikely.

Neronov & Aharonian (2007) demonstrate that the TeV emission from M 87 can be explained as IC emission of ultra-relativistic e^+e^- pairs produced in an electromagnetic cascade in the black hole magnetosphere with acceleration and radiation occurring in the magnetospheric vacuum gap. With acceleration and emission processes occurring on spatial scales on the order of R_s, the day scale TeV variability that requires $c\Delta t \sim R_s$ for a stationary acceleration and emission region is satisfied. Thus, a magnetospheric vacuum gap model for the TeV emission remains a definite possibility for M 87.

One-zone blazar models would appear to require unrealistic Doppler factors in the M 87 jet beyond the radio core (Tavecchio & Ghisellini 2007). This difficulty is remedied by the adoption of a spine-sheath structure such as is suggested by proper motions at HST-1, implied by the limb brightened sub-parsec scale jet, and on the basis of theoretical arguments (e.g., Henri & Pelletier 1991) and GRMHD numerical simulations (e.g., Hawley & Krolik 2006; McKinney 2006). Tavecchio & Ghisellini (2007) are able to produce reasonable fits to the M 87 SED using spine-sheath Lorentz factors and a viewing angle not significantly different from those appropriate to optical and radio proper motions at HST-1.

The rapid time variability of the TeV emission poses a difficulty if a spine-sheath model is applied to the jet as a whole. A similar problem arises if particle acceleration is the result of magnetic reconnection applied to the jet as a whole. With a reconnection timescale on the order of 100 Alfvén-light crossing times (Mizuno et al. 2009), particle acceleration can only be associated with reconnection occurring on spatial scales $<< 25R_s/100$.

Thus, smaller scale "needles" within the jet seem needed to account for rapid time variability and particle acceleration by magnetic reconnection. In this regard Lenain et al. (2008) showed that a high-energy emission region (X-rays up to VHE) could consist of small blobs ($\sim 10^{14}$ cm) moving within the large opening angle jet base [similar in spirit to the needles within a jet model] and radiating at distances just beyond the Alfvén surface, $\sim 100R_s$. The fast, compact blobs could contribute to X-rays and gamma-rays through the synchrotron self-Compton mechanism, and be embedded in an extended, diluted and slower jet emitting synchrotron radiation from radio to optical frequencies. A slow rise of radio emission is expected because the emission volume is synchrotron self-absorbed at radio frequencies. Here it should be noted that TeV emission coming from within $\sim 230R_s$ along the jet can come from the broad jet base, full intrinsic opening angel of $\sim 17^o$ at $\theta = 15^o$, where part of flow could lie at

less than 7° to the line of sight with the jet axis at 15° to the line of sight.

The "jet-in-a-jet" model of Giannios et al. (2009) remains a possibility for the fast TeV variability as in this model high Lorentz factor structures within the Poynting flux region could lie within $230R_s$ along the jet and could again come from the broad jet base. A rapid jet deceleration model also remains a possibility as the proposed jet deceleration zone lies within $230R_s$ along the jet (Georganopoulos et al. 2005) and the background radiation field is of the correct order to give rise to the required deceleration but still be transparent enough to TeV gamma-rays (Levinson 2007). In these models the large scale flow Lorentz factor beyond $230R_s$ along the jet need not significantly exceed the Lorentz factor at HST-1.

The mm radio core in M 87 seems to be nearly coincident with the central engine and well inside the radio core distance from the central engine in PKS 1510−089 (Marscher et al. 2010) or even BL Lac (Marcher et al. 2008). This may be a result of the relatively large viewing angle and reduced synchrotron self absorption. However, we note that the jet is highly structured out to large distances from the core and there is evidence for helically twisted filaments along the kiloparsec jet (Lobanov et al. 2003). This provides circumstantial evidence for helically ordered flow and magnetic fields on the parsec scales suggested by the multi-wavelength studies of PKS 1510−089 and BL Lac. On the other hand, there is no evidence for a recollimation shock in the M 87 jet downstream from the radio core. This fact may simply mean that recollimation shocks are not always present in AGN jets or coincident with the radio core.

5. Conclusions

The results from GRMHD jet generation simulations along with the limb brightened radio structure of M 87 at sub-parsec and kiloparsec scales suggests that a high speed spine and lower speed sheath morphology is likely to exist within the blazar zone. These results suggest that we can decouple the synchrotron and IC regions and reduce the Doppler factors required by simple homogeneous one-zone blazar models. GRMHD simulation results along with theoretical and numerical CD and KH jet instability work indicate that a jet can be sufficiently stable but at the same time contain helically organized flow and magnetic fields within the blazar zone.

For M 87, observed proper motions at sub-parsec to a few hundred parsec (HST-1) scales indicate superluminal sheath motions from 1–2 c (sub-parsec) to 4 c (HST-1) and superluminal spine motions of 6 c (HST-1). At a viewing angle $\theta = 15^o$ these results suggest sheath Lorentz factors from 2 (sub-parsec) to 4.5 (HST-1) and, at least at HST-1, a BL Lac like spine Lorentz factor of 7.5. At $\theta = 15^o$ these Lorentz factors imply only modest de-boosting of the spine relative to the sheath. Higher spine Lorentz factors and/or an intrinsically radio faint spine are required to

achieve the observed radio limb brightening. Higher spine Lorentz factors cannot be ruled out on the sub-parsec jet.

The VLBI jet collimation morphology and faint counter-jet suggest that the radio core is nearly coincident with the central black hole. Here the broad jet base allows a part of the jet flow to be pointed within 7° of the line of sight.

Outside the M 87 radio core the jet expands uniformly all the way to knot A (a few kiloparsecs). This indicates that conversion of Poynting flux to kinetic flux occurs inside $230R_s$ along the jet. CD instability driven jet spine magnetic reconnection and reconfiguration remains a possibility on these spatial scales. This is consistent with an Alfvén point on the order of $100R_s$ from the central black hole, and the uniformity of the radio structure from sub-parsec to kiloparsec scales indicates that a recollimation shock need not exist within the blazar zone.

The observed SED for M 87 seems adequately described by leptonic models and hadronic models for emission coming from inside $230R_s$ along the jet are unlikely. This result can likely be extended to BL Lacs with low accretion rates and correspondingly weak magnetic fields.

Like other TeV blazars the TeV variability requires relatively small acceleration and emission regions. In the case of M 87 this suggests vacuum gap electric field particle acceleration in the black hole magnetosphere, local magnetic reconnection driven particle acceleration on the small scale size of the "jet-in-a-jet" model, or rapid shock acceleration in the "needle" type model.

At least for M 87 there appears to be a definite connection between the TeV, possibly X-ray, and radio events associated with a central engine ejection episode.

References

Acciari, V. et al. 2008, ApJ, 679, 1427
Acciari, V. et al. 2009, Science 325, 444
Aharonian, F. et al. 2003, A&A, 403, L1
Aharonian, F. et al. 2006a, Science, 314, 1424
Aharonian, F. et al. 2006b, A&A 457, 899
Albert, J. et al. 2008, ApJ, 674, 1037
Aloy, M., & Mimica, P. 2008, ApJ, 681, 84
Bednarek, W. 1997, MNRAS, 285, 69
Begelman, M.C., 1998, ApJ, 493, 291
Begelman, M., & Fabian, A. 2008, MNRAS, 384, L19
Beskin, V.S., & Nokhrina, E.E. 2006, MNRAS, 367, 375
Biretta, J., Sparks, W., & Macchetto, F. 1999, ApJ, 520, 621
Blandford, R., & Znajek, R. 1977, MNRAS, 179, 433
Blandford, R.D., & Payne, D.G. 1982, MNRAS, 199, 883
Böttcher, M., & Dermer, C. 2010, ApJ, 711, 445
Cheung, C., Harris, D., & Stawarz, L. 2007, ApJ, 663, L65
Dermer, C. et al. 2009, ApJ, 692, 32
Gebhardt, K., & Thomas, J. 2009, ApJ, 700, 1690
Georganopoulos, M. & Kazanas, D. 2003, ApJ, 594, L27
Georganopoulos, M. et al. 2005, ApJ, 634, L33
Ghisellini, G. et al. 2005, A&A, 432, 401
Ghisellini, G., & Tavecchio, F. 2008, MNRAS, 386, L28

Ghisellini, G., & Tavecchio, F. 2009, MNRAS, 397, 985
Ghisellini, G. et al. 2009, MNRAS, 396, L105
Giannios, D., & Spruit, H. C. 2006, A&A, 450, 887
Giannios, D. et al. 2009, MNRAS, 395, 29
Hardee, P.E. 2007, ApJ, 664, 26
Harris, D. et al. 2006, ApJ, 640, 211
Harris, D., Cheung, C., & Stawarz, L. 2009, ApJ, 699, 305
Hawley, J.F., & Krolik, J.H. 2006, ApJ, 614, 103
Heinz, S., & Begelman, M.C. 2000, ApJ, 535, 104
Henri G. et al. 1999, Astroparticle Physics II, 347
Henri, G., & Pelletier, G. 1991, ApJ, 383, L7
Henri, G., & Saugé, L. 2006, ApJ, 640, 185
Istomin Y., & Sol, H. 2009, Ap&SS, 321, 57
Junor, W., Biretta, J., & Livio, M. 1999, Nature, 401, 891
Katarzynski, K., Sol, H., & Kus, A. 2003, A&A, 410, 101
Konopelko, K. et al. 2003, ApJ, 597, 851
Komissarov, S.S. 2005, MNRAS, 359, 801
Komissarov, S. et al. 2007, MNRAS, 380, 51
Kovalev, Y. et al. 2007, ApJ, 668, L27
Krawczynski, H. 2007, ApJ, 659, 1063
Krichbaum, T.P. et al. 2006, JPhys: Conf. Series 54, 328
Kundt, & Gopal-Krishna 2004, J.Astrophys&Astron., 25, 115
Lenain, J.-P. et al. 2008, A&A, 478, 111
Levinson, A. 2000, Phys. Rev. Lett., 85, 912
Levinson, A. 2007, ApJ, 671, L29
Levinson, A., 1998, ApJ, 507, 145
Levinson, A., & van Putten, M. 1997, ApJ, 488, 69
Lister, M. 2006, ASPCS, 350, eds. Miller, Marshall, Webb, &
    Aller (San Francisco : ASP), 139
Lovanov, A. et al. 2003, New Science Reviews, 47, 629
Lyubarskii, Y.E. 1992., Sov.Astron.Lett., 18, 356
Lyubarskii, Y.E. 1999, MNRAS, 308, 1006
Maraschi, L., & Tavecchio, F. 2003, ApJ, 593, 667
Marscher, A. et al. 2008, Nature, 452, 966
Marscher, A. et al. 2010, ApJ, 710, L126
McKinney, J.C. 2005, ApJ, 630, L5
McKinney, J.C. 2006, MNRAS, 368, 1561
McKinney, J., & Blandford, R. 2009, MNRAS, 394, L126
Mei, S., et al. 2007, ApJ, 655, 144
Meier, D.L. 2005, Ap&SS, 300, 55
Mizuno, Y., Hardee, P., & Nishikawa, K. 2007, ApJ, 662, 835
Mizuno, Y. et al. 2008, ApJ, 672, 72
Mizuno, Y. et al. 2009, ApJ, 700, 684
Neronov, A., & Aharonian, F. 2007, ApJ, 671, 85
Nishikawa et al. 2009, ApJ, 697, L1
Perlman, E. et al. 2007, ApJ, 663, 808
Piner, B., Pant, N., & Edwards, P. 2008, ApJ, 678, 64
Reimer, A. et al. 2004, A&A, 419, 89
Rieger, F., & Aharonian, F. 2008, IJMPD, 17, 1569
Sikora, M., Begelman, M., & Rees, M. 1994, ApJ, 421, 153
Sikora, M. et al. 2005, ApJ, 625, 72
Sikora, M., Moderski, R., & Madejski, G. 2008, ApJ, 675, 71
Sironi, L., & Spitkovsky, A. 2009a, ApJ, 698, 1523
Sironi, L., & Spitkovsky, A. 2009b, ApJ, 707, L92
Spitkovsky, A. 2008, ApJ, 682, L5
Spruit, H. et al. 1997, MNRAS, 288, 333
Stawarz, L., & Ostrowski, M. 2002, ApJ, 578, 763
Tammi, J. & Duffy, P. 2009, MNRAS, 393, 1063
Tavecchio, F. et al. 1998, ApJ, 509, 608
Tavecchio, F., & Ghisellini, G. 2008, MNRAS, 385, L98
Vlahakis, N. 2004, ApJ, 600, 324
Vlahakis, N., & Königl, A. 2004a, ApJ, 596, 1104
Vlahakis, N., & Königl, A. 2004b, Ap&SS, 293, 67
Walker, R. et al. 2008, JPhCS, 131, 012053
Walker, R. et al. 2009, ASPCS, 402, eds. Hagiwara, Fomalont,
    Tsuboi & Murata, (San Francisco, ASP) 227
Watson, M., & Nishikawa, K.-I. 2009, `arXiv:0904.0232`
Waxman, E. 2006, PP&CF, Vol. 48, Issue 12B, 137

Resolving the Doppler-factor crisis in AGNs: non-steady magnetized outflows

M. Lyutikov[1] and M. L. Lister[1]

Department of Physics, Purdue University, 525 Northwestern Avenue, West Lafayette, IN 47907-2036, USA

Abstract. Magnetically-driven non-stationary acceleration of jets in AGNs results in the leading parts of the flow being accelerated to much higher Lorentz factors than in the case of steady state acceleration with the same parameters. The higher Doppler-boosted parts of the flow may dominate the high energy emission of blazar jets. We suggest that highly variable GeV and TeV emission in blazars is produced by the faster moving leading edges of highly magnetized non-stationary ejection blobs, while the radio data trace the slower-moving bulk flow. Model predictions compare favorably with the latest *Fermi* γ-ray and MOJAVE radio VLBI results.

1. Variability and Doppler factors crisis in blazars

One of the defining characteristics of AGNs is the flux variability in all spectral bands (Krolik, 1999). Short times scale, of the order of minutes, may be explained if the emission region is part of a jet that is moving towards Earth with high bulk Lorentz factor Γ. In this case time dilation and propagation effects combine to greatly increase the jet frame variability. For this reason short variability is one of the characteristic properties of blazars, which are known to have relativistic AGN jets directed close to the line of sight.

An important problem that short variability poses is known as the compactness problem (Guilbert et al., 1983). If variability is detected in gamma-ray photons of energies exceeding the electron rest mass energy, then the emission region contains photons which can pair produce. If the number density of these photons is too high, then none of the photons will escape the region. The solution to this problem is, again, bulk relativistic motion towards the observer, which reduces the intrinsic luminosity, decreases energy of photons and increases the effective source of size R.

Recent observations of AGNs in GeV and TeV energy range have raised new questions regarding the parameters of the central engine, and the location and kinematics of the high energy γ-ray, as well as X-ray and radio emission zones. In particular, the rapid flares reported for Mrk 501 and PKS 2155−304, on timescales of 3-5 minutes (Albert, 2007; Aharonian, 2007) imply an emitting size smaller than the gravitational radius $t_{lc} \sim$ hours of the supermassive black holes of these blazars. This indicates very high Doppler factors δ, exceeding $\delta = 100$. A similar estimate also comes from the requirement that the TeV photons escape the production region.

While highly relativistic motion may appear to be a cure-all, the bulk Lorentz factor Γ can be directly constrained by VLBI observations of bright blobs moving with apparent speeds on the sky, β_{app}, that appear to be super-luminal (Rees, 1966). The maximum β_{app} can reach is $\beta_\Gamma \Gamma$ when $\theta_{\mathrm{ob}} \cong 1/\Gamma$. Thus, if the blob motion corresponds to the underlying bulk motion of the jet , measuring β_{app} can constrain the possible bulk Lorentz factor, Γ.

The MOJAVE survey of radio-loud AGN has analyzed the motion of emitting blobs in 127 jets and found the that the observed superluminal speed distribution peaks at $\beta_{\mathrm{app}} \sim 10c$ and tapers off at $\beta_{\mathrm{app}} \sim 50c$ (Lister et al., 2009a). This suggests that the bulk Lorentz factors of such objects are typically around ~ 10, and extend up ~ 50, making the estimated for PKS 2155−304 and Mrk 501 of $\Gamma \geq 50$ rather difficult to reconcile with the radio data. Further, direct VLBI observations of these sources on parsec scales have not even detected superluminal motion (Piner & Edwards, 2004; Giroletti, 2004). Thus, the latest MOJAVE results do support the interpretation of moving features as physical entities, as opposed to patterns (Lister et al., 2009b). In short, observations of bidirectional motions, absence of inward moving features, ejections of multiple blobs in the same jet with the same speed and tight correlations of jet speeds with other properties, like gamma ray emission, apparent γ-ray luminosity, brightness temperature, and even optical classification, all support the notion that the blob motion typically reflects the underlying flow.

VLBI observations of blazars such as PKS 2155−304 and Mrk 501 are not the only data which imply a low Γ. Another way of investigating blazars is to search for their AGN counterparts whose jets are not directed along the line of sight, which are presumed to be radio galaxies. There are actually two distinct types of radio galaxies, FRI and FRII, that are thought to correspond to the two categories of blazars, BL Lacs and optically violent variables; Urry & Padovani (1995). However, studies comparing the relative fluxes and numbers of radio galaxies and blazars point towards Lorentz factors of $\Gamma < 10$ (Henri & Saugé, 2006). Indeed, preliminary results of MOJAVE observations of low luminosity jets from radio galaxies imply speeds of c or less.

Thus, there is apparent contradiction between measured superluminal velocities and bulk Lorentz factors required by radiation modeling. This is known as the *"Blazars' Bulk Lorentz Factor Crisis"* (Henri & Saugé, 2006).

2. Acceleration in non-stationary outflows

Following Blandford & Rees (1974), models of AGN jets typically assume steady-state injection conditions. This is based on the fact that the sonic time over the black hole horizon is typically shorter than any observed times scales of variability of black hole systems (except for such subtle effects as quasi-periodic oscillations in Galactic binaries, e.g., van der Klis 2005). By consequence, it is argued, a system reaches a quasi-equilibrium state. On the other hand, both Galactic black hole candidates, as well as AGN jets show a wide variety of non-stationary behavior. This non-stationarity is driven by various disk instabilities, occurring, presumably, on the viscous time scale of (inner) accretion disk.

The efficiency of the BH-powered jet depends (e.g., in a Blandford & Znajek, 1977, paradigm of jet launching) both on the parameters of the black hole (mass and spin) as well as on the magnetic field supplied by the disk. An important assumption here is time stationarity. In contrast, it is well known from conventional hydrodynamics that the maximum velocity of non-stationary flows $v_{\mathrm{max,non-stat}} = 2/(\Gamma - 1)c_s$ (here Γ is the polytropic index and c_s is initial sound speed) is typically larger than those of stationary ones $v_{\mathrm{max,stat}} = \sqrt{2/\Gamma - 1}c_s$ (e.g. Stanyukovich, 1955, this is true for fluid obeying polytropic equation of state with index $\Gamma < 3$). For relativistic outflows it is then expected (and confirmed by calculations Lyutikov, 2010) that the maximum Lorentz factor of non-stationary flows exceeds the one that can be obtained in stationary flows.

Lyutikov (2010) found exact non-linear solutions for expansion of magnetized gas into a vacuum[1]. The solutions indeed show that magnetically-driven non-stationary acceleration results in the leading parts of the flow being accelerated to much higher Lorentz factors than in the case of steady state acceleration with the same parameters. If the initial plasma had magnetization $\sigma = B^2/(4\pi\rho c^2)$ (here B is the magnetic field and ρ is the plasma density; σ is twice the ratio of magnetic to plasma rest mass energy), then the maximum Lorentz factor for expansion of plasma starting from rest is $\gamma_{\mathrm{max}} = 1 + 2\sigma$, while the bulk flow is moving with $\gamma_{\mathrm{bulk}} \sim \sigma^{1/3}$.

---

[1] Exact, explicit, non-linear solutions of relativistic fluid equations, and especially relativistic MHD equations, are difficult to obtain and, thus, are rare. Many modern computational algorithms are based on the solution of Riemann problems (e.g. Toro, 1999); exact solutions are then absolutely necessary for code testing and for benchmark estimates of the overall dynamical behavior in numerical simulations of relativistic flows and strongly magnetized outflows in particular.

The acceleration is driven by magnetic pressure gradients and, qualitatively, is similar to acceleration experienced by pressurized gas expanding into a low pressure medium, except that what drives the acceleration in this case is magnetic, not kinetic pressure.

3. Breaking through the corona

One expects that accretion onto the black hole may change on a time scale of the order of viscous time scale of the inner part of the disk, which may be weeks to months to years for a typical AGN (e.g., if we associate blob ejection time scales as being due to the inner disk instability). As the relativistic jet propagates away from the central black hole it expands sideways, reaching a transverse scale of a fraction of parsec at the distance of the order of a parsec. Close to the black hole, the corona of the accretion disk is hot, with a nearly relativistic speed of sound: the sonic time scale of the magnetosphere across the black hole is much shorter than the viscous time scale of the inner accretion disk. Further out, the variability time scale of the jet will be shorter than the dynamical time scale of the corona across the jet.

In a static corona the local sound speed is close to the virial velocity and decreases outward form the central BH. On the other hand, for a conical jet the transverse linear scale increase outward form the central BH. Thus, for a given variability times scale, at large distances the jet variability proceeds on time scales shorter than the dynamical time scale across the jet, so the external medium does not have time to react to changing jet conditions. A newly created jet will then propagate along a nearly empty channel, cleared by the previous jet activity. Thus, we expect that initially, close to the black hole, the non-stationary injected jet propagates through a relaxed corona and will have to "bore" its way through. At sufficiently large distances the leading edge of the jet will break out into low density medium created by the previous jet activity. What are the consequences of this non-stationary behavior for jet acceleration?

Let us assume that a jet with an opening angle of $\Theta_j \sim 0.1$ is propagating through a corona, which is in hydrostatic equilibrium with the local sound speed c_s close to the virial velocity, $c_s = \sqrt{GM_{\mathrm{BH}}/r}$. Relating the disk variability time scale to the Keplerian period near the black hole, $t_d = \xi r_{\mathrm{BH}}/c \approx 10\,\mathrm{days}\, M_{\odot,9}\xi_2,\ \xi \gg 1$, where the sound crossing time across the jet is longer than the variability time scale for

$$r_{\mathrm{breakout}} \geq \left(\frac{\xi}{\Theta_j}\right)^{2/3} r_{\mathrm{BH}} = 2\times10^{16} M_{\odot,9}\xi_2^{2/3}\Theta_{j,-1}^{-2/3}\,\mathrm{cm}\,.(1)$$

where the notation X_a implies $(X/10^a)$ (e.g., $\xi_2 = \xi/100$, $\Theta_{j,-1} = \Theta_j/0.1$). At distances larger than (1), the jet variability on a time scale of a hundred Keplerian periods near the black hole, $\xi_2 = 1$ proceeds on time scales shorter than the dynamical time scale across the jet, so the external medium does not have time to react to changing jet
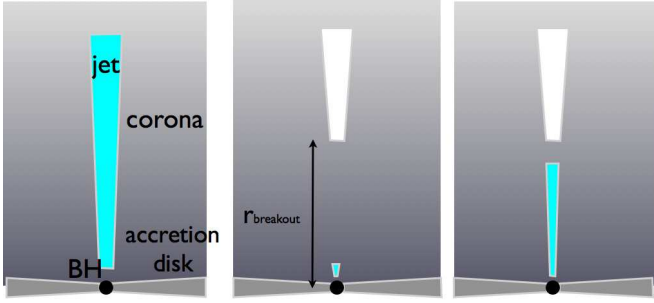
Fig. 1. Cartoon of the model. Accretion onto the black hole generates a non-stationary jet. During the "off" stage, the hot corona quickly fills in the jet channel near the black hole. At the distances larger than r_{breakout} the corona does time to fill-in the jet channel. After reactivation, the jet breaks out into low density medium after reaching r_{breakout}.

conditions. It is also required that the jet travel time to r_{breakout} be smaller than the the sound crossing time at r_{breakout}. This requires $\xi < 1/\Theta_j^2$.

Thus, we expect that initially, close to the black hole, the non-stationary injected jet propagates through a relaxed corona and will have to "bore" its way through. After reaching the distance (1), the leading edge of the jet will break out into low density medium created by the previous jet activity.

At the confined stage, $r < r_{\mathrm{break}}$, the jet can reach a relativistic Lorentz factor γ_w:

$$\gamma_w = \left(\frac{L}{\rho_{\mathrm{ex}} c^3} \right)^{1/4} r^{-1/2} = 20 L_{j,46}^{1/4} \Theta_{j,-1} n^{-1/4} , \qquad (2)$$

where we have assumed $\xi = 1/\Theta_j$ and typical parameters of AGN outflows.

After breakout, at $r > r_{\mathrm{break}}$, the total Lorentz factor in the observer frame will be $2\sigma^{1/3}$ times larger for the bulk flow, $\sim 2\gamma_w \sigma^{1/3}$, and 4σ times larger for the leading edge, $\sim 4\gamma_w \sigma$:

$$\gamma_{\mathrm{bulk}} = 40 \, \sigma^{1/3} L_{j,46}^{1/4} \Theta_{j,-1} n^{-1/4}$$
$$\gamma_{\mathrm{vac}} = 80 \, \sigma L_{j,46}^{1/4} \Theta_{j,-1} n^{-1/4}. \qquad (3)$$

For values of σ exceeding unity, the difference between Lorentz factors of the bulk flow and that of the leading edge is even greater.

4. Implications

The higher Doppler-boosted parts of the flow may dominate the high energy emission of blazar jets. We suggest that highly variable GeV and TeV emission in blazars is produced by the faster moving leading edges of highly magnetized non-stationary ejection blobs, while the radio data trace the slower-moving bulk flow. Model predictions compare favorably with the latest *Fermi* γ-ray and MOJAVE radio VLBI results (Lyutikov & Lister, 2010)

There are a number of correlations that we would expect in the model. First of all, we expect some correlation between the γ-ray and radio core fluxes, and this has already been seen by Fermi and MOJAVE (Kovalev, 2009).

Since the γ-rays are produced in a faster moving part of the flow, we expect that the jets of γ-ray selected AGNs are more aligned than those in radio-selected samples. This effect should be reflected in a flux-flux plot of a well-defined flux-limited blazar sample, due to the different degrees of Doppler beaming in the radio versus γ-ray regimes. For example, a tight linear correlation of intrinsic (i.e., unbeamed) radio vs. γ-ray jet luminosity will be greatly smeared out in the flux-flux plot, although an upper envelope will still be present (see, e.g., simulations by Lister 2007). Indeed, the form and scatter of the observed radio-γ-ray correlation in blazars (Kovalev, 2009) does support the notion that the γ-ray emission is likely boosted by a higher Doppler factor than the radio emission. This is also reflected in the superluminal speeds and apparent jet opening angles, which suggest higher Doppler factors and smaller viewing angles for Fermi-detected AGN (Lister et al., 2009c; Pushkarev et al., 2009)

A radio-γ-correlation depends crucially on the fact that the cores of AGN jets are optically thick to synchrotron emission up to the frequency-dependent radius (Blandford & Konigl, 1979, Eq. 28)

$$r_{\mathrm{core}} \approx 1.4 \mathrm{pc} \zeta_R^{2/3} L_{46}^{2/3} \gamma_{w,1}^{-1/3} \nu_9^{-1} . \qquad (4)$$

where ζ_R parameterizes the observed radio luminosity in terms of the total jet power $L_R = \zeta_R L$, with $\zeta_R \sim 0.01$; we also assumed here (and in the estimates below) that $\Theta_j \sim 1/\gamma_j$, $\xi = 1/\Theta_j^2$. The core radius (4) is typically much larger than the breakout radius (1). Thus, typically, the jet breakout will occur while the jet is still optically thick in the radio. In this case the high energy emission will not be accompanied by the simultaneous increase of radio flux (at least at low frequencies). At sufficiently high radio frequencies, the radius where the jet becomes optically thin (4) may become comparable to the breakout radius (1).

We expect that *a γ-ray event should precede the radio blob ejection* by

$$\Delta t_{\gamma-R} \sim \frac{r_{\mathrm{core}}/c}{2\gamma_w^2} \sim 8 \, \zeta_R^{2/3} L_{46}^{2/3} \gamma_w^{-7/3} \nu_9^{-1} \, \mathrm{days} . \qquad (5)$$

These are typical time scales between variability at radio, optical and γ-ray bands (Marscher, 2010). Also, since this timescale (Eq. 5) is fairly long, we expect occasional γ-ray flares without radio blob ejection; this appears to be the case in TeV flares associated with high-energy peaked AGN such as Mrk 421, and Mrk 501, in which no major changes in VLBI radio structure are seen (MOJAVE program; Ros *et al.* in prep). Furthermore, the *γ-ray events should be better correlated with with radio blob ejection at high radio frequencies.* Higher resolution monitoring of MOJAVE sources by the Boston University group (Jorstad, 2005) at 43 GHz has revealed instances of jet features moving at higher speeds than those seen at 15 GHz

(Lister et al., 2009b) that fade out very rapidly close to the core region. The extensive VLBA & *Fermi* data currently being gathered on these AGN should provide a useful test of this prediction.

The above correlations assume that the γ-ray photons produced at the breakout radius (1) do not suffer from absorption. This depends on the compactness parameter corresponding to the bulk motion of the jet (since γ-ray photons can pair produce on a lower moving bulk plasma):

$$l \sim \frac{1}{\gamma_w^6} \frac{\sigma_T}{m_e c^3} \frac{L_\gamma}{r_{\text{breakout}}} = 10^{-7} L_{\gamma,44} \Theta_{j,-1}^8 \,. \tag{6}$$

On the other hand, the γ-ray variability time scale depends on the Lorentz factor of the leading edge

$$\Delta t \sim \frac{r_{\text{breakout}}}{c} \frac{1}{32\gamma_j^2 \sigma^2} = 150 \sec \frac{1}{\sigma^2} \Theta_{j,-1} \,. \tag{7}$$

Thus, *the model is able to accommodate both the requirement of small optical depth for γ-ray photons and the short time-scale variability, down to few minutes.*

The jets of lower power FRI sources and higher power FRII sources have somewhat different morphology on mass-scales. Relatively low power blazar jets in the MOJAVE program like Mrk 421 or Mrk 501 show a very smooth fall-off in radio intensity with distance from the core, and have maintained this structure over more than a decade of VLBI monitoring. In contrast, higher power blazars such as 3C 279 display jet morphologies dominated by individual bright knots that continually emerge from the core and move downstream at superluminal speeds.

One possible explanation for the dichotomy of jet properties is that the emitted blobs merge, creating smooth large scale profiles. If the blobs are ejected on a time scale $t_d = \xi r_{\text{BH}}/c$, they will merge at distance (in the observer frame the time of merger is determined by the Lorentz factor of the trailing edge of the preceding injection $\gamma \sim \gamma_j/(4\sigma)$):

$$r_{\text{merge}} \sim 2ct_d \left(\frac{\gamma_j^2}{16\sigma^2} \right) \approx 3 \times 10^{20} \text{cm} \frac{1}{\sigma^2} \Theta_{j,-1}^{-2} \,. \tag{8}$$

Thus, at linear scales ≥ 100 pc, the jet is expected to be mostly smooth. Note, that since in blazars the angle between the jet direction and the line of sight are small, the projected distance corresponding to (8) are small. For example, with the jets in Mrk 421 or Mrk 501 at z=0.03 oriented at a few degrees to the line of sight, this corresponds to a few milliarcseconds projected on the sky. In addition, since the radius r_{merge} depends sensitively on the assumed bulk Lorentz factor, our model predicts that in powerful FR-II jets, the jet may remain knotty up to the kiloparsec scale.

Can the observed morphology of the jets be used to determine intrinsic jet properties, like bulk Lorentz factor and magnetization? High-frequency peaked blazars (HBLs) are under-represented in the MOJAVE sample; in fact, there are no HBLs in the complete radio-selected sample (Lister & Homan, 2005). On the other hand, HBLs

are well represented in the *Fermi* sample (Abdo, 2009). In the framework of our model, this can be due to their lower bulk Lorentz factors, but high magnetization (see Eq. (10)). It would then imply relatively smaller merging distances (15) and smoother jet structures, consistent with observations. An obvious caveat in this argument is that HBLs have flatter γ-ray spectra and are more likely to be seen by the *Fermi* LAT. Further careful analysis of beaming and instrumental selection effects is needed to explore these possibilities more fully.

References

Abdo, A. A., et al. 2009, eprint arXiv:0912.2040
Aharonian, F., et al. 2007, ApJ, 664, L71
Albert, J., et al. 2007, ApJ, 669, 862
Blandford, R. D. & Königl, A. 1979, ApJ, 232, 34
Blandford, R. D. & Rees, M. J. 1974, MNRAS, 169, 395
Blandford, R. D. & Znajek, R. L. 1977, MNRAS, 179, 433
Giroletti, M., et al. 2004, ApJ, 600, 127
Guilbert, P. W., Fabian, A. C., & Rees, M. J. 1983, MNRAS, 205, 593
Henri, G. & Saugé, L. 2006, ApJ, 640, 185
Jorstad, S. G., et al. 2005, AJ, 130, 1418
Kovalev, Y. Y., et al. 2009, ApJ, 696, L17
Krolik, J. H. 1999, Active galactic nuclei : from the central black hole to the galactic environment, Princeton University Press
Lister, M. L. 2007, in American Institute of Physics Conference Series, Vol. 921, The First GLAST Symposium, ed. S. Ritz, P. Michelson, & C. A. Meegan, 345–346
Lister, M. L., et al. 2009a, AJ, 138, 1874
—. 2009b, AJ, 138, 1874
—. 2009c, ApJ, 696, L22
Lister, M. L. & Homan, D. C. 2005, AJ, 130, 1389
Lyutikov, M. 2010, eprint arXiv:1004:2428
Lyutikov, M. & Lister, M. 2010, eprint arXiv:1004:2430
Marscher, A. P., et al. 2010, ApJ, 710, L126
Piner, B. G. & Edwards, P. G. 2004, ApJ, 600, 115
Pushkarev, A. B., Kovalev, Y. Y., Lister, M. L., & Savolainen, T. 2009, A&A, 507, L33
Rees, M. J. 1966, Nat, 211, 468
Stanyukovich, K. 1955, Non-Stationary Motion in Continuous Medium (Russian) (State Publ., Moscow)
Toro, E. F. 1999, Riemann Solvers and Numerical Methods for Fluid Dynamics: A Practical Introduction
Urry, C. M. & Padovani, P. 1995, PASP, 107, 803
van der Klis, M. 2005, Astronomische Nachrichten, 326, 798

Gamma-ray emission from mini-jets

K. Nalewajko⋆

Nicolaus Copernicus Astronomical Center, ul. Bartycka 18, 00-716 Warsaw, Poland; `knalew@camk.edu.pl`

Abstract. Mini-jets are perpendicular flows within Poynting-flux-dominated jets, driven by relativistic magnetic reconnection. They may arise during brief episodes of magnetic polarity reversal and have been proposed to explain the extremely fast variability of TeV blazars. We present a semi-analytical model based on relativistic Petschek reconnection to calculate the broad-band non-thermal emission from these structures and the radiative effects on their dynamics. We show that the observed properties of the July 2006 flare in PKS 2155−304 can be best described in a scenario including radiative interaction between two opposite mini-jet systems in the absence of a guide field.

1. Introduction

Relativistic jets produced in Active Galactic Nuclei (AGNs) are thought to be launched as cold and highly-magnetized outflows, whose energetics are dominated by Poynting flux. Energy dissipation in this region can be provided by relativistic magnetic reconnection. This idea lead to the development of the mini-jets model, which has been proposed to explain the extremely fast variability observed in TeV blazars (Giannios et al., 2009) and the radio galaxy M 87 (Giannios et al., 2010). Mini-jets are perpendicular relativistic flows within a relativistic jet and as such obtain very high Lorentz factors $\Gamma > 50$ required to circumvent the gamma-ray opacity problem (Begelman et al., 2008). Given a magnetization parameter $\sigma \sim 100$, magnetic reconnection will accelerate both the electrons and the bulk outflow to Lorentz factors high enough to place the Klein-Nishina limit for observed photon energy in TeV band.

Extremely fast TeV flares have been observed in only two BL Lac objects: PKS 2155−304 (Aharonian et al., 2007) and Mrk 501 (Albert et al., 2007). Long-term monitoring of PKS 2155−304 by *H.E.S.S.* indicates that the July 2006 flaring state had a flux distribution distinct from the quiescent states (Abramowski et al., 2010), which suggests a different underlying mechanism. This high activity episode lasted for only a few days and was unique over a time span of several years. Simultaneous X-ray and optical monitoring (Aharonian et al., 2009) indicates strong Compton dominance and almost cubic correlation between TeV and X-ray flux. This poses additional severe constraint on flare models, in addition to large TeV luminosity, the few-minute variability timescale and low $\gamma\gamma$ opacity.

In previous work, the mini-jet emitting region has been treated as a compact blob propagating out of the mini-jet region. Here we investigate a stationary outflow fuelled by steady relativistic Petschek reconnection. As the fluid is eventually slowed down by a terminal shock separat-
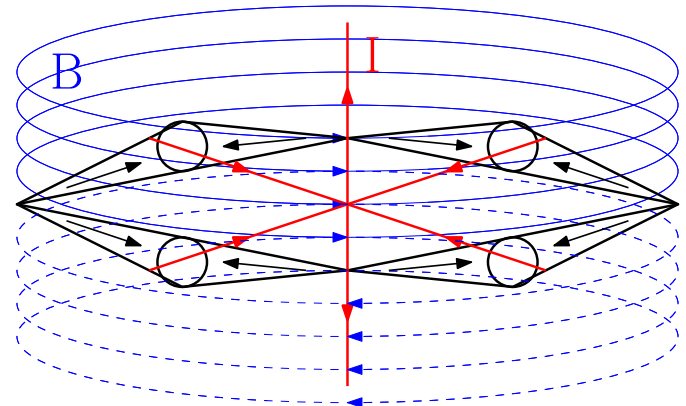
Fig. 1. Schematic representation of the current sheet separating two opposite magnetic domains. The current sheet is unstable and fragments into a ring of alternating O-points and X-points, where relativistic magnetic reconnection drives perpendicular outflow called mini-jets *(solid black arrows)*.

ing it from the so-called magnetic islands, two emitting regions which are relativistically boosted with respect to each other form, greatly enhancing the relative importance of the inverse-Compton (IC) process. In addition, a radiative interaction of two opposite mini-jet systems can be investigated, providing even higher Compton ratio. We study the effects of the presence of a weak guide field, radiative cooling, Compton drag and pair-production opacity, as they all become significant under observational constraints.

2. Model description

Magnetic fields dominate the energy flux in the inner parts of AGN jets (Sikora et al., 2005) and hence they preserve an order imprinted at the jet formation region. To launch a relativistic outflow from an accreting black hole system, a strong poloidal magnetic field component is required. This could be either produced locally within an accretion disc by the magneto-rotational instability or advected from the galactic environment. The topology of magnetic fields permeating the outer regions of the accretion disk

---

⋆ Collaborators in this project: M. C. Begelman, D. Giannios, M. Sikora and D. Uzdensky
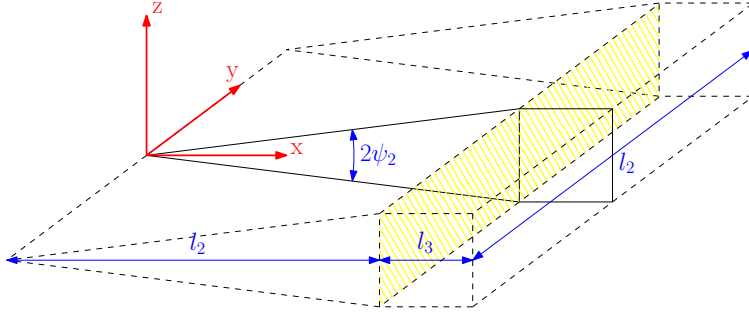
Fig. 2. Geometry of a single mini-jet model. The X-point is aligned with y axis and the mini-jet plasma flows along x-axis towards a stationary shock *(shaded)* separating the mini-jet region of length l_2 from the island region of length l_3.

has to be preserved into the innermost region (Beckwith et al., 2008). As there is no evidence for a uniform polarity of magnetic fields in the immediate surroundings of AGNs, a number of regions (domains) of opposite magnetic polarity could appear in the accreted material.

In the simplest scenario, two such domains are separated radially in the accretion disk and then consecutively pass through the jet formation region (Lovelace et al., 1997). This will result in two magnetic domains in the inner jet separated by a current sheet (Sikora et al., 2003). As the magnetic fields of either domain are quickly stretched in the toroidal direction by lateral expansion of the jet (Begelman et al., 1984), the current sheet can approach a toroidal, disk-like shape. It will then separate along the azimuthal angle into a sequence of X-points (where reconnection takes place) and O-points (magnetic islands), see Fig. 1. Mini-jets will form as coherent flows from the X-points to the O-points. If the magnetization parameter of the jet is large, the mini-jets will be relativistic in the frame co-moving with the current-sheet. They would be directed mainly in the toroidal direction, and thus perpendicular to the jet propagation. For an external observer, they would be much more strongly boosted than the jet itself (Giannios et al., 2009).

We adopt the scenario of relativistic Petschek reconnection with a guide field studied analytically by Lyubarsky (2005) and numerically by Zenitani et al. (2009). The dynamical model allows one to calculate the parameters of the reconnected outflow (mini-jet) from the jet parameters: magnetization $\sigma_1 \sim 100$, magnetic field $B_1 \sim 10$ G and Lorentz factor $\Gamma_1 \sim 10$.[1] The mini-jet Lorentz factor is estimated as $\Gamma_2 \sim \sqrt{\sigma_1} \sim 10$, and typical electron random Lorentz factors as $\langle \gamma_2 \rangle \sim \sqrt{\sigma_1}(m_p/m_e) \sim 10^4$.

Figure 2 shows the geometry of a single mini-jet model. The mini-jet region of length l_2 ends in a perpendicular stationary shock arising from the interaction between the mini-jet outflow with a magnetic island. The shock severely slows down the enthalpy-dominated mini-jet flow, increasing its magnetization and energy density. We follow the post-shock flow over a so-called island region of length $l_3 \sim 2\psi_2 l_2$, where ψ_2 is the opening angle of the mini-jet region. We seed the mini-jet and island regions with initial electron distributions in the form of a rela-

tivistic Maxwellian with a high-energy power-law tail of index $p = 3.4$, which is necessary to reproduce the measured high-energy spectrum. The normalization factor and average energy are determined from the values of pressure and particle number density. We assume a proton-electron plasma, as an addition of pairs would decrease the average electron Lorentz factor. We divide both the mini-jet and island regions into a 1D grid of several sectors to account for evolution of the electron distribution and (in the mini-jet region) of the Lorentz factor, pressure, magnetic field and particle density. We calculate the radiation emitted by these electrons, taking into account the following effects:

- Synchrotron emission is calculated in every sector, according to the local electron distribution and magnetic field value.
- In every sector we calculate the energy density of synchrotron radiation produced both locally and in all other sectors of both regions, taking into account the Lorentz transformations between the elements of a 2D geometrical grid.
- Both local and external synchrotron photons are Comptonized and (in the mini-jet region) used for calculation of the mini-jet deceleration due to the Compton drag effect (Sikora et al., 1996), which affects the values of magnetic field and particle number densities.
- Evolution of the electron distribution takes into account radiative cooling from both synchrotron and IC processes, adiabatic heating due to flow deceleration and mixing of evolved electrons with new injections from oblique boundaries of the mini-jet region. Pressure is recalculated at every step to match the evolving electron distribution and adiabatically scaled proton energy density.
- Final evolved values of mini-jet pressure, Lorentz factor, density and magnetic field are being matched with the initial parameters in the island region via jump conditions at the stationary shock.
- Pair-production opacity for high-energy radiation is calculated by tracking sample photons emitted towards an observer, taking into account contributions from individual elements from the 2D geometrical grid.
- In one case, radiative interaction between two identical mini-jet-island systems located on opposite sides of a magnetic island is investigated. Radiation from the op-

---

[1] Subscripts denote quantities measured either in the jet (1), in the mini-jet region (2) or in the island region (3).
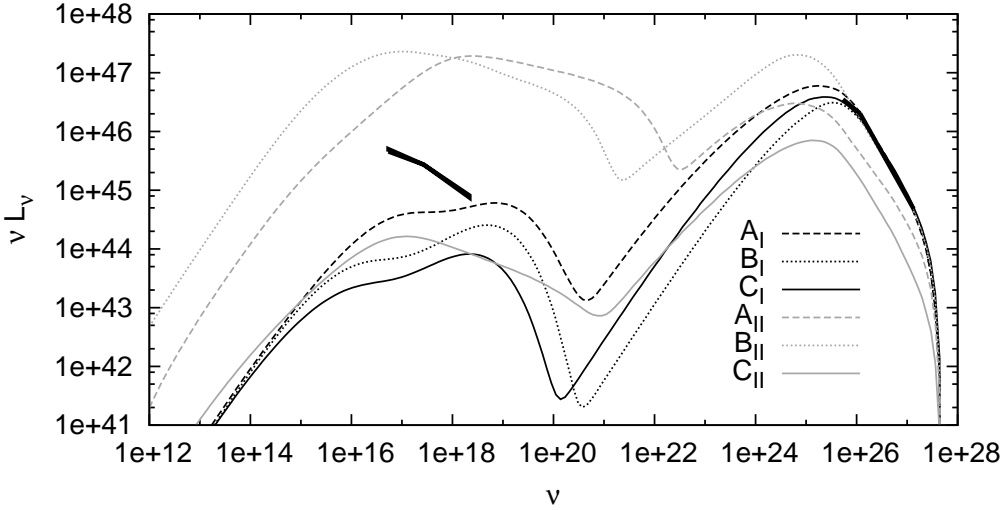
Fig. 3. Spectral energy distributions (SEDs) of total radiation emitted from a single mini-jet system compared with *H.E.S.S* and *Chandra* simultaneously observed spectra (Aharonian et al., 2009). See main text for description of the line types.

posite mini-jet is used for calculations of IC emission, Compton drag and $\gamma\gamma$ opacity.

The relations between various parameters are very tight, and in fact we have only two free parameters: l_2 as a measure of the system size and B_1 as a measure of energy density.[2]

3. Results

Preliminary results of our modelling are shown in Fig. 3. We consider two classes of models: I – without guide field (shown with black lines) and II – with a weak guide field with $\alpha = B_{1,G}/B_1 \sim 1/(2\sqrt{\sigma_1}) \sim 0.05$ (shown with grey lines). Dashed lines mark models (A) with a fixed size of the mini-jet region $l_2 \sim 10^{14}$ cm, corresponding to a crossing timescale of ~ 5 minutes and magnetic field strengths $B_1 = 75$ G in case I and $B_1 = 150$ G in case II. As these values are much larger than those estimated in Giannios et al. (2009), we calculated a second set of models (B), shown with dotted lines, fixing the magnetic field strength at $B_1 = 10$ G. In order to match the TeV spectrum, we increased the size of mini-jet region to $l_2 = 7 \times 10^{14}$ cm in case I and $l_2 = 3.5 \times 10^{15}$ cm in case II. Note that the larger size doesn't necessarily violate the variability timescale requirement as TeV emissivity is strongly concentrated in the immediate vicinity of the stationary shock (last $\sim 10\%$ of the mini-jet region length). A third set of models (C), shown with solid lines, also had fixed B_1, but radiation from the opposite mini-jet was taken into account. The relative boost between opposite mini-jet regions is much stronger than the relative boost between the mini-jet and island regions within the same system; thus the resulting SEDs are more Compton-dominated. By assuming that these mini-jet systems are identical and located as closely as possible, we didn't increase the number of free parameters. To match the TeV data, we increased the size of the mini-jet regions to $l_2 = 6 \times 10^{14}$ cm.

Fig. 4. Pair-production opacity for high-energy photons emitted from a sector of the mini-jet region located close to the stationary shock, where the bulk of VHE emission is produced. Line types match those in Fig. 3

We could match the spectrum observed by *H.E.S.S.* for all models without guide field (I) and for model B_{II}. However, models A_{II} and B_{II} strongly overproduce X-ray emission and are inconsistent with *Chandra* results. The X-ray spectra of all models in case I are significantly harder than observed spectra; this is because the hard X-ray (10–100 keV) peak produced in the island region is higher than the soft X-ray component produced in the mini-jet region. Model A_I is only marginally consistent with observations and would be excluded, if contributions from misaligned mini-jets were taken into account.[3]

Figure 4 shows pair-production opacity for high-energy photons. The main source of opacity is synchrotron emission from the island region and, for models C, emission from the opposite mini-jet system. As we see, the models without guide field show low opacity ($\tau < 1$), while the models including a guide field are affected by absorption. In particular, model B_{II} shows the highest opacity ($\tau \sim 2$)

---

[2] They are not really free, as they are related to variability timescale and energetics.

[3] There are two reasons why misaligned mini-jets should be important contributors to ~ 10 keV flux: 1) we expect many misaligned mini-jets for every aligned one; 2) the island regions are only weakly boosted, with typically $\Gamma_3 < 2$.
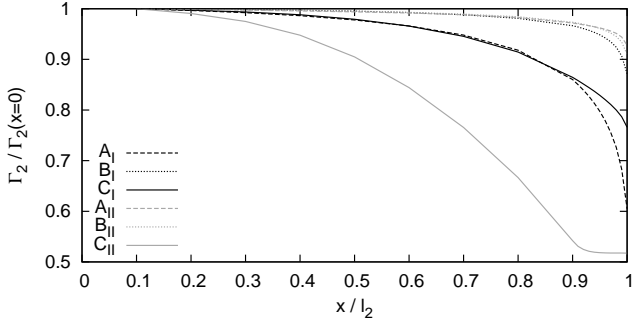
Fig. 5. Evolution of Lorentz factor Γ_2 along the mini-jet region between the X-point ($x = 0$) and the stationary shock ($x = l_2$). Line types match those in Fig. 2.

at TeV energies. This is the reason why we couldn't match the TeV spectrum for this model by increasing B_1 to arbitrarily large values; opacity sets an upper limit on observed high-energy luminosity. Models $A_{\rm II}$ and $C_{\rm II}$ have opacity approaching $\tau = 1$ at photon energy ~ 1 TeV.

Figure 5 shows the evolution of mini-jet Lorentz factor Γ_2 due to the Compton drag effect. It is seen that the strongest drag takes place for $x > 0.9 l_2$, just before reaching the stationary shock. The drag is relatively weak for models B and $A_{\rm II}$, medium for models $A_{\rm I}$ and $C_{\rm I}$ and strong for model $C_{\rm II}$. In this last case, the mini-jet region is weakly boosted and further increasing of the mini-jet region size will lead to a catastrophic Compton drag which will prevent an increase of high-energy luminosity.

4. Discussion

Of the 6 particular scenarios for fast TeV flares observed in PKS 2155−304, presented in the previous section, the most promising are models $B_{\rm I}$ and $C_{\rm I}$. In fact, these models have very similar parameters (in particular B_1 and l_2) and lowest opacities. The effect of a strong additional source of photons in model $C_{\rm I}$ has been partially balanced with more effective Compton drag (see Fig. 5), which decreased the boosting factor of the critical region around the location of the stationary shock. The $C_{\rm I}$ model produces the highest Compton/synchrotron luminosity ratio, allowing for quite a large number of misaligned mini-jets forming one or more rings, visualized in Fig. 1.

It is interesting that a luminosity of $\sim 10^{46}$ erg is close to the limit imposed by both opacity and Compton drag arguments. Our most effective models reproduce this luminosity, with opacity at TeV energies of $\tau \sim 0.1$. There is not much room for a different parameter choice, especially if we adopt the new estimates of variability timescale for PKS 2155−304 of about 2 min (Abramowski et al., 2010).

Our models produce IC components peaking at ~ 100 GeV and the spectral region corresponding to the *Fermi*/LAT sensitivity range is not different from classical SSC models of High-frequency-peaked BL Lacs (HBLs). If similar structures of reversed magnetic polarity arise in bright blazars (FSRQs), intense external radiative fields would dominate local synchrotron radiation and produce emission peaking at ~ 1 GeV, while absorbing the bulk of TeV emission. During the extremely bright December 2009 flare of 3C 454.3, short substructures of doubling timescale of ~ 3 hours were detected by LAT (Tavecchio et al., 2010; Fermi Collaboration, 2010). In a pointed mode, LAT can probe variability timescales as short as ~ 30 minutes (Foschini et al., 2010). However it is not clear how short variability timescales are achievable with luminosities as high as 10^{49} erg s^{-1}.

It can also be speculated that since several outbursts in blazars have been connected to ejections of new superluminal radio knots (e.g., Jorstad et al., 2010), magnetic polarity reversals may form 'seeds' for these features. If this is the case, information about the rate of ejections could be used to constrain the topology of the magnetic fields permeating the accretion systems in radio-loud AGNs.

References

Aharonian, F., Akhperjanian, A. G., Bazer-Bachi, A. R., et al., 2007, ApJ, 664, L71

Aharonian, F., Akhperjanian, A. G., Bazer-Bachi, A. R., et al., 2009, A&A, 502, 749

Abramowski, A., Acero, F., Aharonian, F., et al., 2010, A&A(in press), e-print arXiv:1005.3702

Albert, J., Aliu, E., Anderhub, H., et al., 2007, ApJ, 669, 862

Beckwith, K., Hawley, J. F., & Krolik, J. H., 2008, ApJ, 678, 1180

Begelman, M. C., Blandford, R. D., Rees, M. J., 1984, RvMP, 56, 255

Begelman, M. C., Fabian, A. C., Rees, M. J., 2008, MNRAS, 384, L19

Fermi Collaboration, 2010, in preparation

Foschini, L., Tagliaferri, G., Ghisellini, et al., 2010, MNRAS, in press, e-print arXiv:1004.4518

Giannios, D., Uzdensky, D. A. & Begelman, M. C., 2009, MNRAS, 395, L29

Giannios, D., Uzdensky, D. A., & Begelman, M. C., 2010, MNRAS, 402, 1649

Jorstad, S. G., Marscher, A. P., Lariono, V. M., et al., 2010, ApJ, 715, 362

Lovelace, R. V. E., Newman, W. I., & Romanova, M. M., 1997, ApJ, 484, 628

Lyubarsky, Y. E., 2005, MNRAS, 358, 113

Sikora, M., Sol, H., Begelman, M. C. & Madejski, G. M., 1996, MNRAS, 280, 781

Sikora, M., Begelman, M. C., Coppi, P., & Proga, D., 2003, submitted to ApJ, e-print arXiv:astro-ph/0309504

Sikora, M., Begelman, M. C., Madejski, G. M., & Lasota, J.-P., 2005, ApJ, 625, 72

Tavecchio, F., Ghisellini, G., Bonnoli, G., & Ghirlanda, G., 2010, MNRAS, L68

Zenitani, S., Hesse, M. & Klimas, A., 2009, ApJ, 705, 907

VLBI Monitoring of 3C 84 in Gamma-ray Active Phase

H. Nagai[1], K. Suzuki[2], K. Asada[3], M. Kino[4], S. Kameno[5], A. Doi[1], M. Inoue[3], and U. Bach[6]

1. Institute of Space and Astronautical Science, Japan Aerospace Exploration Agency, 3-1-1 Yoshinodai, Chuo-ku, Sagamihara 252-5210, Japan
2. Institute of Astronomy, University of Tokyo, 2-21-1 Osawa, Mitaka, Tokyo 181-0015, Japan
3. Institute of Astronomy and Astrophysics, Academia Sinica, P.O. Box 23-141, Taipei 10617, Taiwan, R.O.C.
4. National Astronomical Observatory, 2-21-1 Osawa, Mitaka, Tokyo 181-8588, Japan
5. Faculty of Science, Kagoshima University, 1-21-35 Korimoto, Kagoshima, Kagoshima 890-0065, Japan
6. Max-Planck-Institute für Radioastronomie, Auf dem Hügel 69, 53121 Bonn, Germany

Abstract. We report on a multi-epoch Very Long Baseline Interferometry (VLBI) study of the innermost jet of 3C 84. We carried out 14-epoch VLBI observations during 2006-2009 with the Japanese VLBI Network (JVN) and the VLBI Exploration of Radio Astrometry (VERA), immediately following the radio outburst that began in 2005. A comparison between VLBI and single-dish light curves indicates that the outburst was associated with the central ~ 1 pc core. We found that this outburst accompanied the emergence of a new component, and the projected speed of this new component was $0.23c$ from 2007/297 (2007 October 24) to 2009/114 (2009 April 24). We discuss the site of γ-ray emission detected by *Fermi*/LAT and jet kinematics in connection with the γ-ray emission mechanism.

1. Introduction

NGC 1275 is a nearby Seyfert galaxy, the dominant member of the Perseus cluster. At the radio wavelengths, it is also known as the strong radio source 3C 84. The radio structure of 3C 84 is complex, consisting of multiple lobe-like features (radio bubbles) on many different angular scales. In the innermost region there is a pair of lobes, probably formed by the jet activity originating in the 1959 outburst (e.g., Asada et al. 2006), extending to ~ 5 pc from the core along the north-south direction. The northern counter-jet becomes brighter and extends closer to the core with increasing frequency, suggesting free-free absorption by an accretion disc, rather than Doppler dimming (Romney et al. 1995). Detection of the northern counter jet implies a jet viewing angle of 30°-55°, with jet speed of 0.3-0.5c (Walker et al. 1994).

The LAT of *Fermi Gamma-Ray Space Telescope* found GeV γ-ray emission from NGC 1275 (Abdo et al. 2009, hereafter A09). The *Fermi* γ-ray flux is about 10 times higher than the upper limit constrained by EGRET. This indicates that the source is variable on timescales of years to decades, and therefore the size of the γ-ray emission region is likely to be smaller than ~ 10 pc. Interestingly, University of Michigan Radio Astronomy Observatory (UMRAO) monitoring shows a radio flare starting in 2005. MOJAVE observations also found radio brightening in the central ~ 1 pc core between 2007 and 2008. This coincidence of radio and γ-ray flares may indicate that the γ-ray emission is associated with the radio core. Thanks to its proximity, 3C 84 is an excellent laboratory to study the jet physics very close to the core in connection with the γ-ray emission mechanism. We report here the results from VLBI data and long-term single dish monitoring.

2. Observations and Data Reduction

2.1. Archival Data

We used archival data of VLBI Exploration of Radio Astrometry (VERA) from 2006 May to 2008 May (2006/134, 2006/143, 2006/346, 2007/142, 2007/258, 2007/297, 2007/324, 2007/361, 2008/035, 2008/063, 2008/106, 2008/141[1]). Observations were carried out with four VERA stations at 22.2 GHz, where 3C 84 was being used as a bandpass calibrator or a fringe finder. Typically five scans of 5-minutes duration were obtained. Left hand circular polarization (LHCP) was received and sampled with 2-bit quantization, and filtered using the VERA digital filter unit (Iguchi et al. 2005). The data were recorded at a rate of 1024 Mbps, providing a bandwidth of 256 MHz in which 14 IF-channels from a total of 16 IF-channels of 16 MHz bandwidth were assigned to 3C 84. For 2006/134, 2006/143, and 2007/297 data, only 1 IF-channel with 8 MHz bandwidth was assigned, and for 2007/142 data, 2 IF-channels with 8 MHz bandwidth were assigned. Correlation processes were performed with the Mitaka FX correlator (Chikada et al. 1991).

2.2. New Observations with VERA and JVN

The Japanese VLBI Network (JVN: Fujisawa 2008) observations were carried out on 2008/354 using the four VERA stations at 22.2 GHz, and on 2008/356 using the Yamaguchi 32-m telescope, the Tsukuba 32-m telescope, and the four VERA stations at 8.4 GHz. The VERA observation was carried out on 2009/114 at 22.2 GHz. Right hand circular polarization was received at 8.4 GHz, and

---

[1] Observing sessions are denoted by year/(day of the year).

LHCP was received at 22.2 GHz. The data were recorded at a rate of 128 Mbps. Data correlation was performed with the Mitaka FX correlator. VERA observations were performed in dual-beam phase referencing mode, but in the present paper we report the analysis using one-beam data.

2.3. Single-Dish Monitoring with Effelsberg

The flux density measurements at the Effelsberg 100-m telescope of the Max-Planck-Institut für Radioastronomie (MPIfR) were obtained during regular calibration and pointing observations at 22 GHz. The measurements were made using cross-scans in azimuth and elevation direction. The data reduction was done in the standard manner as described by Kraus et al. (2003). The measured antenna temperatures were linked to the flux-density scale using primary calibrators like NGC 7027, 3C 286, and 3C 48 (Ott et al. 1994; Baars et al. 1977).

2.4. VLBI Data Reduction

Data reduction was performed using the NRAO Astronomical Imaging Processing System (AIPS). A priori amplitude calibration and fringe fitting were performed in the usual manner. For JVN observation at 8.4 GHz, amplitude calibration was performed by scaling the correlated flux to the flux obtained with single dish observation. For a more detailed description, see Nagai et al. (2010).

3. Results

Figure 1 shows total intensity images of the central ~ 1 pc region at 22.2 GHz. In the first 4 epochs, component C2 was visible at a position separated by ~ 1 mas from the central core (C1) in a position angle of $-141°$. The alignment of these components was similar to that in the γ-ray quiet phase (Dhawan et al. 1998). During the first 4 epochs, component C2 showed no significant motion relative to component C1. Remarkably, a new component (C3) suddenly emerged to the south of the central core on 2007/258 (Fig. 1(e)) despite only 4 months having passed since the previous observation (Fig. 1(d)). Moreover, component C3 was clearly resolved on 2007/297 (Fig. 1(f)), separated by only one month from the previous epoch observation in which component C3 was blended with the other components. In later epochs, component C3 appeared more significant.

In Figure 2 we show the light curve monitored with the Effelsberg 100-m telescope and total CLEANed flux at 22.2 GHz with VERA as a function of time. The trend of flux increase in the central 1-pc core resembles the total flux increase. The difference between them, probably the emission from the extended feature, is almost constant (~ 5 Jy). In order to look for any change of the extended feature, we also analyzed 8 GHz data observed with JVN, which has better coverage of short interferometer baselines compared to the 22 GHz data. No significant change of the
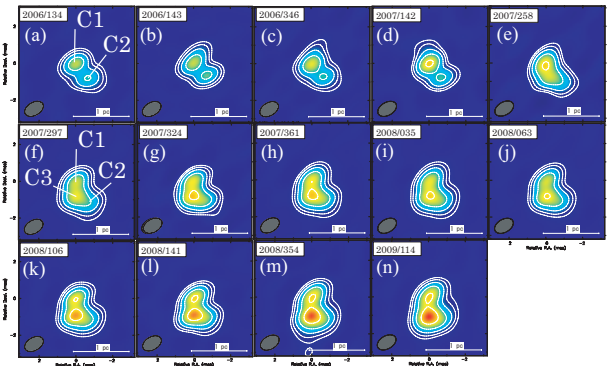
Fig. 1. VERA images of 3C 84 at 22 GHz. All images are aligned using the northern component (component C1) as a reference. The contours are plotted at levels of 4.18, 8.36, 16.72, 33.44, and 66.88 % of the peak intensity (4.989 Jy/beam) on 2009 April 24. The restoring beam (1.1×0.7 mas, position angle of $-60°$) was fixed to make the images uniform.

extended feature is seen compared to that in the γ-ray quiet phase (see Nagai et al. 2010). It is obvious that the flux increase starting in 2005 originated in the central 1-pc core. The flux density of each component is also plotted in Figure 2. Component C3 showed the most significant increase in flux.

Figure 3 shows the separation between components C1 and C3 as a function of time. The positions of components C1 and C3 were derived from a two-dimensional Gaussian fit in the interferometric (u, v)-plane using the "modelfit" task in Difmap. It is difficult to measure the positional error of each component quantitatively from the interferometric data in each epoch independently. We thus employed the method described in Homan et al. (2001). We initially set the uncertainty for each data point equal to unity, and then performed a linear fit to the data assuming the motion with constant speed to obtain a preliminary χ^2. Taking this preliminary χ^2, we then uniformly rescaled the uncertainty of each data point such that the reduced-χ^2 became unity. Finally, the positional error of each data point is estimated to be 0.013 mas. This error is typically two times larger than that estimated from the signal-to-noise ratio (SNR), i.e., $\theta_{beam}/$SNR, where θ_{beam} is the beam size. This fit results in an apparent speed of 0.20±0.01 mas/yr (projected speed of $0.23 \pm 0.01c$) towards the south. This is approximately consistent with the jet speeds in the γ-ray quiet phase (Dhawan et al. 1998). The direction of motion of the new component differs from the alignment of components C1 and C2 by $\sim 40°$ on the projected plane. We note that we did not include the data on 2007/258 in this fit because component C3 might have moved faster before 2007/297 (see §4).

4. Discussion

In this section, we first discuss the intrinsic speed of the new component (C3), and then compare the jet speed expected from SED modeling including GeV γ-ray data with
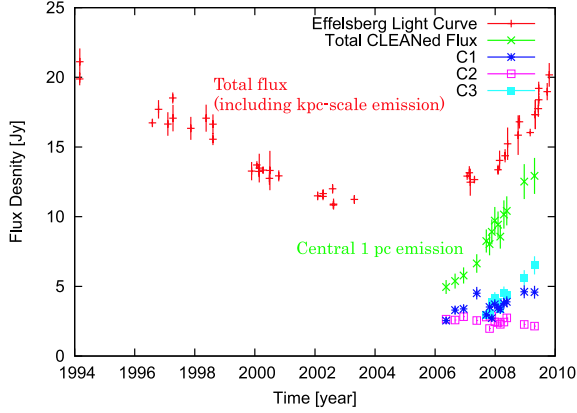
Fig. 2. Radio light curve of 3C 84. Pluses: The Effelsberg light curve of 3C 84 at 22 GHz. Crosses: total CLEANed flux of VERA observation at 22.2 GHz. Asterisks: The light curve of component C1. Open squares: The light curve of component C2. Filled squares: The light curve of component C3.
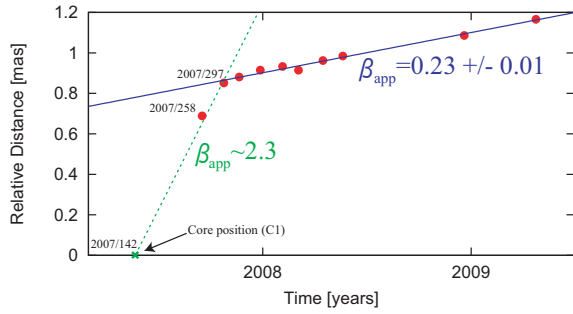

Fig. 3. Plot of the separation between component C3 and component C1. The error bar is smaller than the size of each symbol. The blue solid line represents a linear fit to the data from 2007/297 to 2009/114. The green broken line represents that from 2007/142 to 2007/297, assuming that component C3 was ejected from the position of component C1 on 2007/142 (see §4.2).

that measured using VLBI. Finally, we discuss the possible site of GeV γ-ray emission.

4.1. Constraints on the Speed of C3

Under the simple beaming model for a symmetric jet system with equal and constant speeds, the apparent speed of the approaching jet is

$$\beta_{app} = \frac{\beta \sin \theta}{1 - \beta \cos \theta}. \qquad (1)$$

where β is the intrinsic jet speed and θ is the angle to the line of sight. The ratio of brightness of the jet and counter-jet components is

$$R = \left(\frac{1 + \beta \cos \theta}{1 - \beta \cos \theta} \right)^{\eta} \qquad (2)$$

where η can be $(2 - \alpha)$ or $(3 - \alpha)$, depending on whether the jet is continuous or a single component (α is the spectral index; $S \propto \nu^{-\alpha}$). In Figure 4 the curve for $\beta_{app} = 0.23$

is represented by the red solid line and the region for $R > 91$ is represented by the gray-shaded region. (The region for $R > 91$ is the lower limit constrained by the non-detection of counter-jet in Figure 1.) Here we assumed a single component with $\alpha = 0.5$. For these two conditions, the jet speed and the angle to the line of sight are about $\beta > \sim 0.72$ and $\theta < \sim 5°$. This constraint on the jet viewing angle is much smaller than the angle to the line of sight estimated for ~ 10 mas scale jets (30-55°; Walker, Romney, & Vermeulen 1994). Such a change in angle can occur if the jet is precessing. The change in the jet direction in Figure 1 might be also explained by jet precession.

A very small angle to the line of sight is not required under the free-free absorption model (e.g., Walker, Romney, & Vermeulen 1994). The pc-scale northern counter-jet has a strongly inverted spectral index, which is consistent with free-free absorption by ionized material along the line of sight to the counter-jet. Spectral fits to multi-frequency VLBI data showed that the opacity increases closer to the core (Walker et al. 2000). The new jet components originating in the recent outburst still reside very close to the core (~ 1 pc), and therefore the counter-jet component must suffer from very strong absorption. The brightness ratio between the jet and counter-jet can be smaller if we remove the absorption effect. If we adopt a brightness ratio between the jet and counter-jet on a 10 mas scale of $R = 3.7$ (Walker et al. 2000), the jet speed and the angle to the line of sight are about $0.3c$ and $\theta = 30°$.

4.2. Discrepancies of jet speeds

Modeling of the broad-band SED including *Fermi* data, in a blazar scenario with moderate beaming, requires a bulk Lorentz factor of $\Gamma = 1.8$ ($\beta = 0.83$) and a viewing angle (θ) of 25° (A09). Our observed apparent speed of $\beta_{app} = 0.23$ would imply that $\beta = 0.83$ can only be achieved for $\theta < \sim 3°$. This disagrees with not only the jet viewing angle derived from the SED modeling but also $R = 3.7$ derived from the jet-counter-jet ratio on a 10 mas scale. If our non-detection of the counterjet is solely due to relativistic beaming ($R > 91$), $\beta = 0.83$ and $\theta = 25°$ can be reproduced. However, this is not consistent with our observed apparent motion ($\beta_{app} = 0.23$). In any case, under the simple beaming model, the observed jet speed and jet-counterjet ratio are not consistent with the jet speed and viewing angle derived from the SED modeling.

A similar apparent slow-moving jet, in spite of strong γ-ray emission, is seen in some BL Lac objects and the radio galaxy M 87 (e.g., Giroletti et al. 2004; Edwards & Piner 2002; Kovalev et al. 2007). A spine sheath model has been suggested to ease this problem: a fast spine jet produces the strong TeV emission by inverse Compton scattering of the radio photons from a surrounding slow layer (Ghisellini et al. 2005). Limb-brightening structure seen in Mrk 501 and M 87 is consistent with the spine-sheath model (e.g., Giroletti et al. 2008; Kovalev et al.

2007). However, it is difficult to test limb-brightening in 3C 84 even with VLBA observations at 43 GHz (Dhawan et al. 1998), due to lack of resolution. The upcoming higher resolution telescope VSOP-2 (Tsuboi et al. 2009) would be valuable in this respect.

A decelerating jet model is also able to solve this problem (Georganopoulos & Kazanas 2003). We note that there is one data point which does not fit on the regression line of $0.23c$ in Figure 3. This could be the signature of a deceleration. However, we need further careful study due to lack of resolution and possible absorption effects (see Nagai et al. (2010)).

4.3. Implication for the site of γ-ray emission

It is of great interest whether γ-ray emissions come from the close vicinity of the core or a component more distant from the core in AGNs. For example in M 87, which is another low power (FRI) radio galaxy known to be a γ-ray source, there is a prominent component separated by $\sim$ 100 pc from the central core, the so-called HST-1. In 2005 a significant flux increase was observed at radio and X-ray bands in HST-1 (Cheung et al. 2007). During this flare a TeV excess was also confirmed, allowing the speculation that HST-1 might be the site of the γ-ray flare. In contrast to the 2005 flare, a TeV flare in 2008 was accompanied by a strong increase of the radio flux from the core but no obvious radio brightening in HST-1 (Acciari et al. 2009).

Due to the lack of γ-ray data between the EGRET era and *Fermi* era, we do not know exactly when the GeV γ-ray flare started in NGC 1275. However, it is clear that the γ-ray emission of NGC 1275 is now in an active phase compared to the EGRET era, and this γ-ray variability is very similar to the radio flux increase (A09). Moreover, the radio flux increase is likely to originate in the central 1-pc core. This allows us to expect that the γ-ray emission might be associated within the central 1-pc core.

Although there is a long-term correlation between radio and γ-ray light curves, the problem of no exact correlation between γ-ray and radio on a timescale within a year remains; while the radio flux continuous to increase, the γ-ray emission shows no significant time variation except for a small flare in April-May 2009. There is room for further investigation in this respect.

References

Abdo, A. A., Ackermann, M., Ajello, M., et al. 2009, ApJ, 699, 31 (A09)

Acciari, V. A., Aliu, E., Arlen, T., et al. 2009, Science, 325, 444

Asada, K., Kameno, S., Shen, Z.-Q., et al. 2006, PASJ, 58, 261

Fig. 4. Constraints on the speed and the angle to the line of sight. Red solid line represents $\beta = 0.23$. Blue dotted line represents $R = 3.7$. Green broken line represents $R = 91$. Gray shaded region represents the condition required from non-detection of the counterjet.

Baars, J. W. M., Genzel, R., Pauliny-Toth, I. I. K., & Witzel, A. 1977, A&A, 61, 99

Cheung, C. C., Harris, D. E., & Stawarz, Ł. 2007, ApJ, 663, L65

Chikada, Y., Kawaguchi, N., Inoue, M., 1991, Frontiers of VLBI, 79

Dhawan, V., Kellermann, K. I., & Romney, J. D. 1998, ApJ, 498, L111

Edwards, P. G., & Piner, B. G. 2002, ApJ, 579, L67

Fujisawa, K. 2008, The role of VLBI in the Golden Age for Radio Astronomy

Georganopoulos, M., & Kazanas, D. 2003, ApJ, 594, L27

Ghisellini, G., Tavecchio, F., & Chiaberge, M. 2005, A&A, 432, 401

Giroletti, M., Giovannini, G., Feretti, L., et al. 2004, ApJ, 600, 127

Giroletti, M., Giovannini, G., Cotton, W. D., et al. 2008, A&A, 488, 905

Homan, D. C., Ojha, R., Wardle, J. F. C., et al. 2001, ApJ, 549, 840

Iguchi, S., Kurayama, T., Kawaguchi, N., & Kawakami, K. 2005, PASJ, 57, 259

Kataoka, J., Stawarz, Ł, Cheung, C. C., et al. 2010, ApJ, 715, 554

Kovalev, Y. Y., Lister, M. L., Homan, D. C., & Kellermann, K. I. 2007, ApJ, 668, L27

Kraus, A., Krichbaum, T. P., Wenger, R., et al. 2003, A&A, 401, 161

Nagai, H., Suzuki, K., Asada, K., et al. 2010, PASJ, 62, L11

Ott, M., Witzel, A., Quirrenbach, A., et al. 1994, A&A, 284, 331

Pedlar, A., Ghataure, H. S., Davies, R. D., et al. 1990, MNRAS, 246, 477

Romney, J. D., Benson, J. M., Dhawan, V., et al. 1995, PNAS 92, 11360

Tsuboi, M., & VSOP-2/ASTRO-G Project Team 2009, ASP Conf. Ser., 402, 30

Vermeulen, R. C., Readhead, A. C. S., & Backer, D. C. 1994, ApJ, 430, L41

Walker, R. C., Romney, J. D., & Benson, J. M. 1994, ApJ, 430, L45

Walker, R. C., Dhawan, V., Romney, J. D., Kellermann, K. I., & Vermeulen, R. C. 2000, ApJ, 530, 233

Centaurus A as a Cosmic Ray Accelerator

R.J. Protheroe

Department of Physics, School of Chemistry & Physics, The University of Adelaide, SA 5005, Australia.

Abstract. We consider the maximum energy of cosmic-ray nuclei in the radiation/magnetic environments found in active galactic nuclei (AGN) and apply our results to the case of Centaurus A. We also discus the propagation of ultra-high energy (UHE) cosmic rays (CR) from Centaurus A and investigate whether the UHE CR observed by Auger from the general direction of Cen A could be due to acceleration in the jets and hot-spots as they are now, or if they could have been accelerated several Myr ago, when Cen A's jets were more powerful, and are only now arriving.

1. Introduction

Arrival directions of the UHE CR detected by the Pierre Auger experiment above 5.6×10^{19} eV have been found to be statistically correlated with positions of nearby AGN (Abraham et al. 2007), and a few of the arrival directions appear to be clustered around Centaurus A, our nearest active galactic nucleus at a distance of ~ 3.8 Mpc. This has led to speculation that Centaurus A may be responsible for some of the UHE CR. We consider the acceleration of such cosmic-ray protons and nuclei in astrophysical environments which may be found in and around AGN, taking into account all the relevant interaction processes with photon backgrounds.

Protons and nuclei being accelerated in or propagating through the intergalactic medium interact mainly with the cosmic microwave background (CMB), and infrared, optical and ultraviolet (IR/Opt/UV) photon backgrounds. These interactions produce features in the propagated UHE CR spectrum such as the "GZK cutoff" (Greisen, 1966; Zatsepin & Kuzmin, 1966). Nuclei suffer Bethe-heitler pair production, but more importantly suffer photo-disintegration (Puget et al., 1976).

With Centaurus A only 3.8 Mpc away, and with the pion photo-production energy-loss distance on the CMB minimizing at ~ 12 Mpc above 10^{11} GeV (e.g. Protheroe 2004) for rectilinear propagation one would observe UHE CR protons almost unattenuated by pion photo-production interactions on the CMB. Rieger & Aharonian (2009) suggest that shear acceleration along the kpc jet may accelerate protons beyond 5×10^{19} eV. See also Kachelriess et al. (2009a, 2009b). The magnetic field of Centaurus A's giant lobes (Feain et al. 2009) may also provide an environment suitable for acceleration of UHE CR (Benford & Protheroe 2008; Hardcastle et al. 2009).

GeV energy gamma-rays have been observed from Cen A at GeV energies by Fermi-LAT (2010) and by HESS at TeV energies (Aharonian et al. 2009). A summary of neutrino flux limits for Cen A over the energy range above 10^{17} eV is given by James et al. (2010), although they are not yet sensitive enough to seriously constrain models.

2. Attenuation of protons and nuclei in background radiation

To model interactions with radiation we use the SOPHIA event generator for pion photo-production (Mücke et al., 2000), continuous energy loss for Bethe-Heitler (BH) pair production (Rachen 1996) and the photon-nucleus interaction event generator developed by Allard et al. (2005, 2006, 2007, 2008) – see these papers for references to the original data compilations and fits. For the photon backgrounds in the infra-red, optical and ultra-violet window, we use an estimate by Stecker et al. (2005).
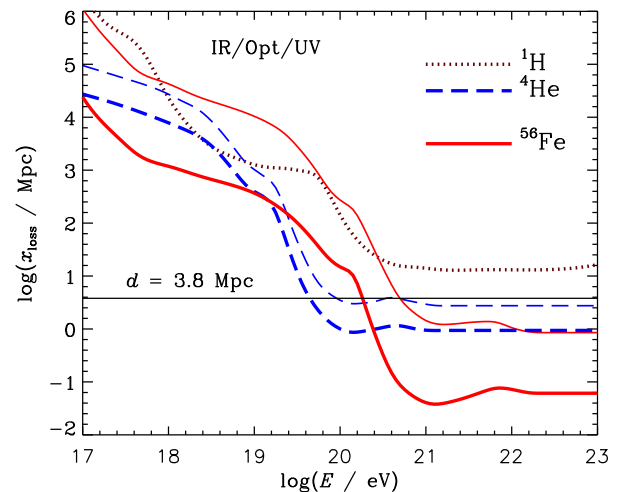
Fig. 1. Loss distances (upper curves) and mean free paths (lower curves) for helium and iron nuclei in the CMB plus IR/Opt/UV radiation fields (from Allard & Protheroe 2009) plotted against energy. Loss distance of protons is also shown. The distance to Cen A is indicated.

In Fig. 1 we show the dependence of the loss (or attenuation) length for cosmic-ray protons, helium and iron
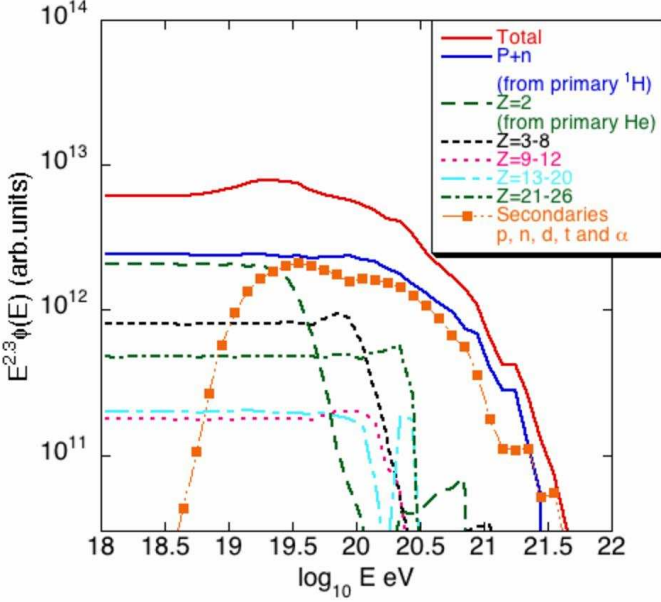
Fig. 2. Propagation of a galactic mixed composition with an $E^{-2.3}$ spectrum and $E_{\max} = Z \times 10^{21}$ eV over 3.8 Mpc (D. Allard, private communication)


Fig. 3. The ρ—l_c space is divided into regions in which the propagation can be described as diffusion, rectilinear or deflection for $B = 10^{-4}$ G (solid lines), $B = 10^{-5}$ G (long dashed lines), ... $B = 10^{-9}$ G (dotted lines).

nuclei, and the mean free paths of helium nuclei and iron nuclei in the CMB plus intergalactic IR/Opt/UV background as a function of energy. The loss length for CR protons is $x_{\mathrm{loss}}(E) = cE/[dE/dt]$ where dE/dt and is an effective energy loss rate for Bethe-Heitler pair production and pion photo-production on the ambient radiation field. The loss length for nuclei of atomic mass $A > 1$ is $x_{\mathrm{loss}}(E) = cA/[dA/dt]$ where dA/dt is the average rate of loss of nucleons from the nucleus by photo-disintegration, and is somewhat longer than the mean free path by a factor slightly less than A. In determining the survival probability of compound nuclei the mean free path is relevant, and we see immediately that for rectilinear propagation over 3.8. Mpc, no iron nuclei will survive above an energy of 1.8×10^{20} eV, and no helium nuclei will survive above an energy of 4×10^{19} eV. However where the path-length is only a few mean free paths heavy nuclei resulting from photo-disintegration of iron would be present.

As an example of a full calculation propagation of nuclei over 3.8 Mpc we show in Fig. 2 we show the result of the propagation for $B = 0$ of a galactic mixed composition with an $E^{-2.3}$ spectrum and $E_{\max} = Z \times 10^{21}$ eV. One can see that the cut off for the heaviest component (arbitrarily as $Z > 20$) occurs before the crossing on the loss length plot. This is because the notion of "survival" of a nucleus is somewhat arbitrary.

The presence of an intergalactic magnetic field increases the travel-times of CR from Cen A, either as a result of magnetic deflection at high energies, or at lower energies by diffusive propagation. Propagation in a magnetic field with a domain-like structure will have a different rigidity dependence to that of diffusion. Sigl et al. (2003) estimate the travel time for UHE CR from distance
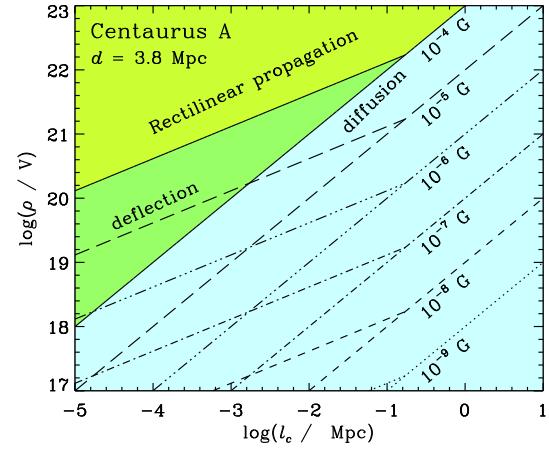
d through the intergalactic field to be

$$c\,t_{\mathrm{defl}}(\rho, d) = 0.045 \left(\frac{\rho}{10^{20}\,\mathrm{V}}\right)^{-2}$$
$$\times \left(\frac{d}{1\,\mathrm{Mpc}}\right)^2 \left(\frac{l_c}{\mathrm{Mpc}}\right) \left(\frac{B}{10^{-7}\,\mathrm{G}}\right)^2 \mathrm{Mpc}$$

where l_c is the coherence length of the magnetic field, which is a few tens of kpc in clusters (Kotera et al. 2009). Ryu et al. (2008) estimate the magenetic field to be a few microgauss in clusters and groups. At rigidities above

$$\rho_{\mathrm{rect}} = 2.1 \times 10^{19} \left(\frac{d}{1\,\mathrm{Mpc}}\right)^{1/2} \left(\frac{l_c}{\mathrm{Mpc}}\right)^{1/2} \left(\frac{B}{10^{-7}\,\mathrm{G}}\right) \mathrm{V}$$

cosmic ray propagate almost rectilinearly. At rigidities below

$$\rho_{r_g - l_c} = 10^{20} \left(\frac{l_c}{\mathrm{Mpc}}\right)^{1/2} \left(\frac{B}{10^{-7}\,\mathrm{G}}\right) \mathrm{V}$$

the gyro-radius is less than the coherence length and cosmic rays propagate diffusively, and in this region

$$c\,t_{\mathrm{diff}}(\rho, d) = ct_{\mathrm{defl}}(\rho_{r_g - l_c}, d) \left(\frac{\rho}{\rho_{r_g - l_c}}\right)^{-1/3}.$$

Fig. 3 maps the ρ—l_c space for propagation from Cen A and shows which type of propagation will occur for the magnetic fields indicated.

In Fig. 4 we plot the loss distance of protons, and mean free paths of helium and iron nuclei in the CMB plus IR/Opt/UV radiation fields against rigidity $\rho \approx E/Ze$ where E is the total energy and Z is the atomic number. The propagation time, multiplied by c, for $B = 1\,\mu$G and $B = 1\,$nG, and l_c in the 10—100 kpc range. We see that the survival probability of iron nuclei, and even helium nuclei, is quite sensitive to the extragalactic magnetic field and it's structure. For example, if $B = 1\,\mu$G and $l_c = 1$
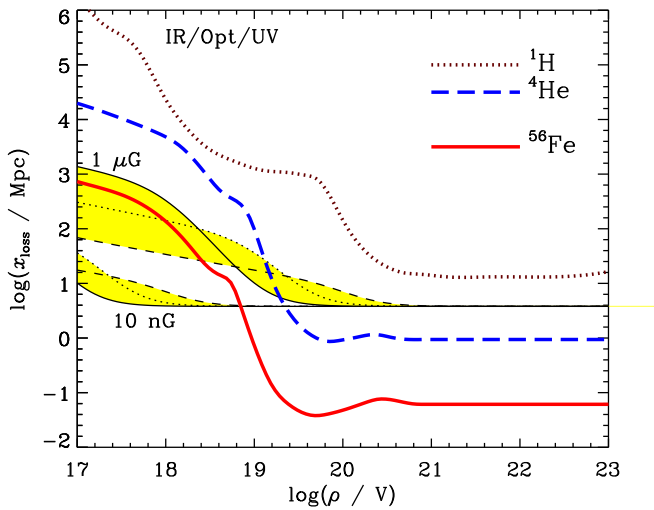
Fig. 4. Loss distance of protons, and mean free paths of helium and iron nuclei in the CMB plus IR/Opt/UV radiation fields (from Allard & Protheroe 2009) plotted against rigidity. The propagation time, multiplied by c, is shown for $B = 1\,\mu$G and $B = 1\,$nG by the thin curves for $l_c = 1\,$kpc (thin solid curves), $l_c = 10\,$kpc (thin dotted curves), and $l_c = 100\,$kpc (thin dashed curves).

kpc then no UHE CR Fe nuclei will survive at any energy. If $B = 1\,\mu$G and $l_c = 10$ kpc all Fe nuclei above 2.6×10^{19} eV will be photo-disintegrated, and if $B = 1\,\mu$G and $l_c = 100$ kpc all Fe nuclei above 6.5×10^{19} eV will be photo-disintegrated. Again, one should note that heavy nuclei from photo-disintegration of iron may be present at some level. In the case of He nuclei, if $B = 1\,\mu$G and $l_c = 10\,$kpc then above 2.7×10^{19} eV He nuclei will be photo-disintegrated, i.e. at an energy only marginally lower than for rectilinear propagation.

3. Acceleration

By plotting magnetic field vs. size of various astrophysical objects, Hillas (1984) identified possible sites of acceleration of UHE CR based on whether or not the putative source could contain the gyro-radius of the accelerated particles, and on the likely velocity of scattering centers in these sites, and narrowed the field of possible sources to radio galaxy lobes and galaxy clusters. In general, the maximum rigidity gain rate of relativistic particles can be written $r_{\rm gain}(\rho) \equiv (1/\rho)(d\rho/dt) = \xi(\rho)c^2 B\rho^{-1}$ where $\xi(\rho) < 1$ is the acceleration rate parameter which depends on the details of the acceleration mechanism, with $\xi = 1$ corresponding to the highest posible gain rate for any mechanism (see Protheroe 1998).

From the gain and the loss rates for proton or nucleus-photon interactions and synchrotron radiation, together with the maximum time available for acceleration, we can estimate the maximum energies of accelerated particles by solving

$$r_{\rm gain}(E_{\rm max}) - r_{\rm loss}(E_{\rm max}) - r_{\rm synch}(E_{\rm max}) - 1/t_{\rm max} = 0.$$

This has been done for three values of ξ in Fig. 5 for proton for the standard IR/Opt/UV radiation field. For each ξ-value we show the result for $ct_{\rm max}$=0.4 Mpc, 3.2 Mpc, and 32 Mpc.

For an acceleration rate 10^{-4} times the maximum possible, pion photo-production, finite size or maximum time available cuts off the spectrum for fields below $\sim 100\,\mu$G and synchrotron losses cut off the spectrum for higher fields. In order to accelerate protons above 10^{20} eV the ideal sources have acceleration region sizes (magnetic field) between 1 kpc (~ 1 mG) and 1 Mpc ($\sim 1\,\mu$G) such that the gyro-radius can be contained within the accelerator. These parameters allow the spectrum to extent beyond 10^{20}eV. This makes radio galaxies and clusters of galaxies probable sites of UHE CR acceleration (see Fig. 6 of Protheroe 2004) in agreement with the conclusion of Hillas. Indeed, in a recent review, Biermann et al. (2008) concluded that the most promising contenders are radio galaxies and gamma-ray bursts (GRB). However, if the whole acceleration region is moving relativistically, Doppler boosting in energy of neutrons (produced by pion photo-production) escaping from such sources allows blazar jets (Protheroe et al. 2003) and GRB (Waxman 2006 and references therein) to remain possible sites of UHE CR acceleration, and in these cases proton synchrotron losses are likely to cut off the spectrum. Large-scale cosmic shocks in the Universe may also be sites of UHE CR acceleration (Kang & Jones 2002, Inoue et al. 2007) as well as colossal magneto-hydrodynamic fossil AGN structures (Benford & Protheroe 2008), AGN jets and cocoons surrounding AGN jets (Schopper et al. 2002, Norman et al. 1995) and hot spots in radio lobes of powerful radio galaxies (Rachen & Biermann 1993). In these cases pion photo-production, the finite size of the accelerator or the time available for acceleration may cause the cut-off in the spectrum of protons at acceleration.

4. Acceleration in the past when Cen A was more powerful

While now Cen A is now only a very weak AGN with a short jet just a few kpc long, it has a giant radio relic indicating that in the past it was probably a more powerful AGN, possibly a powerful radio galaxy as the radio relic extends several hundreds of kpc from the source with of comparable length in the past. Das et al. (2008) have simulated propagation of UHE CR through magnetized large scale structure and conclude that for observers located inside groups of galaxies like ours, about 70% and 35% of UHECR events above 60 EeV arrive within 15° and 5°, respectively, of the source position with time delays of less than 10^7 yr. So any CR we see now could have been accelerated 1 My earlier than the images in radio and optical we see now, i.e. when Cen A was probably a powerful radio galaxy (even though now Cen A is relatively weak). The magnetic field conditions at the far end of a historic more-powerful jet Cen A, may have been similar to FR II radio galaxies we see now with $B = 0.3\,$mG and
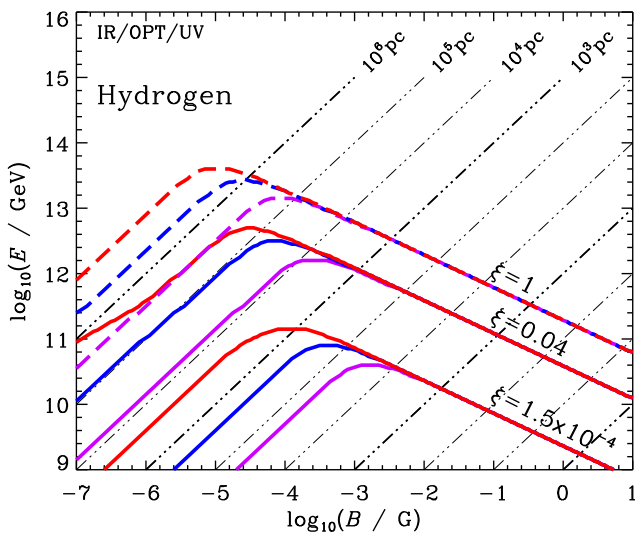
Fig. 5. Maximum energy of protons in the CMB plus IR/Opt/UV radiation vs magnetic field for ct_{max}=0.4 Mpc (lower curves), 3.2 Mpc (middle curves), and 32 Mpc (upper curves) for each ξ value indicated.

$v_{shock} = 0.3c$, and this would have given a high acceleration rate. Looking at Fig. 5 for acceleration in our standard IR/Opt/UV radiation we see that for $B = 0.3$ mG and $\xi = 0.04$ acceleration of protons to 10^{21} eV in a ~ 3 kpc size hot-spot at the end of a ~ 300 kpc jet somewhere near the edge of the current giant lobes could have been possible. For the same parameters, iron nuclei would have been accelerated to about 2.5×10^{22} eV.

From Fig. 4 that delays of the order of a few Mpc are possible, and so, protons and Fe nuclei will have very different travel times. If Cen A was very active long ago but has not been as powerful over the past few Myr, then: (i) if B is small we should see no protons from Cen A, but we should see Fe nuclei from Cen A but not tightly correlated with Cen A direction; (ii) if B is large we should see both protons and Fe, but not tightly correlated with Cen A direction.

5. Conclusion

UHE CR protons should reach us almost unattenuated from Cen A, while compound nuclei will suffer photo-disintegration on the CMB and IR/Opt/UV background radiation fields. No iron nuclei should survive above 1.8×10^{20} eV. However, as a result of magnetic deflection or diffusion, depending on the magnetic field and it's coherence length travel times may be extended such that this maximum energy for survival of iron, and to a lesser extent other nuclei, may be significantly reduced. The presence or absence of iron nuclei in the energy range below 1.8×10^{20} eV may therefore provide some constraints on the magnetic structure if the intergalactic medium. Finally, the longer travel times (than the light-travel time) mean that in cosmic rays we see Cen A as it was at earlier

times than we see Cen A in the optical, when Cen A was possibly a more powerful AGN able accelerate cosmic rays to well above 10^{20} eV with sufficient cosmic ray luminosity to explain a substantial fraction of the observed UHE CR.

References

Abraham J. et al. (Auger Collaboration), 2007, Science, 318, 938
Aharonian, F., et al. 2009, ApJ, 695, L40
Allard, D., et al. 2005, A&A, 443, L29
Allard, D., et al. 2006, Journal of Cosmology and Astro-Particle Physics, 9, 5
Allard, D., Olinto, A. V., & Parizot, E. 2007, A&A, 473, 59
Allard, D., et al. 2008, Journal of Cosmology and Astro-Particle Physics, 10, 33
Allard, D. & Protheroe, R. J. 2009, A&A, 502, 803
Benford, G. & Protheroe, R. J. 2008, MNRAS, 383, 663
Biermann, P. L., et al. 2008, proceedings for "Origin, Mass, Composition and Acceleration Mechanisms of UHECRs (CRIS 2008)", arXiv:0811.1848
Das, S., Kang, H., Ryu, D., & Cho, J. 2008, ApJ, 682, 29
Engel R., Seckel D., Stanev T., 2001, Phys. Rev. D 64, 093010
Feain I. J., et al., 2009, ApJ, 707, 114
Fermi-LAT Collaboration, 2010, Science, 328, 725
Greisen, K. 1966, Phys. Rev. Lett., 16, 748
Hardcastle M. J., et al., 2009, MNRAS, 393, 1041
Hillas, A.M. 1984, Ann. Rev. Astron. Astrophys., 22, 425
Inoue, S., et al. 2007, Proceedings of the 30th ICRC, Merida, Mexico, arXiv:0711.1027
James, C. W., et al., 2010, arXiv:0906.3766
Kachelriess M., et al. 2009, New J. of Phys., 11, 065017
Kachelriess M., et al. 2009, Int. J. Mod. Phys. D18, 1591
Kang, H. & Jones, T. W. 2002, Journal of Korean Astronomical Society, 35, 159
Kotera, K., et al. 2009, ApJ, 707, 370
Mücke, et al. 2000, Comp. Phys. Com., 124, 290
Norman, C.A., et al. 1995, ApJ, 454, 60
Protheroe, R.J. 2000, in "Topics in cosmic-ray astrophysics" ed. M. A. DuVernois, Nova Science Publishing: New York, 2000, pp 258–298
Protheroe, R.J. 2004, Astropart. Phys., 21, 415
Protheroe, R. J., et al. 2003, Astroparticle Physics, 19, 559
Puget, J. L., et al. 1976, ApJ. 205, 638
Rachen, J. P. 1996, Interaction processes and statistical properties of the propagation of cosmic-rays in photon backgrounds, PhD thesis, Bonn University.
Rachen, J.P. & Biermann, P.L. 1993, Astron. Astrophys., 272, 161
Rieger F. M. & Aharonian F. A., 2009, A&A, 506, L41
Ryu, D., et al., 2008, Science, 320, 909
Schopper, R., et al. 2002, Astroparticle Physics, 17, 347
Sigl, G., et al. 2003, Phys. Rev. D, 68, 043002
Stecker, F. W., et al. 2006, ApJ, 648, 774
Tavecchio, F., et al. 2002, ApJ, 575, 137
Waxman, E. 2006, Nuclear Physics B Proceedings Supplements 151, 46
Zatsepin, G.T. & Kuzmin, V.A. 1966, Sov. Phys. JETP Lett., 4, 78

Sub-parsec scale imaging of Centaurus A

Cornelia Müller[1], M. Kadler[1,2,3], R.Ojha[4,5], M. Böck[1], C. M. Fromm[7], E. Ros[6,7], R. E. Rothschild[8] and J. Wilms[1]

[1] Dr. Remeis-Sternwarte & ECAP, Sternwartstrasse 7, 96049 Bamberg, Germany
[2] CRESST/NASA Goddard Space Flight Center, Greenbelt, MD 20771, USA
[3] USRA, 10211 Wincopin Circle, Suite 500 Columbia, MD 21044, USA
[4] United States Naval Observatory, 3450 Massachusetts Ave., NW, Washington DC 20392, USA
[5] NVI,Inc., 7257D Hanover Parkway, Greenbelt, MD 20770, USA
[6] Departament d'Astronomia i Astrofisica, Universitat de València, E-46100 Burjassot, Spain
[7] Max-Planck-Institut für Radioastronomie, Auf dem Hügel 69, 53121 Bonn, Germany
[8] Center for Astrophysics and Space Sciences, University of California, San Diego, 9500 Gilman Drive, La Jolla, CA 92093-0424, USA

Abstract.

At a distance of about 3.4 Mpc, the radio galaxy Centaurus A is the closest active galaxy. Therefore it is a key target for studying the innermost regions of active galactic nuclei (AGN). VLBI observations conducted within the framework of the TANAMI program enable us to study the central region of the Cen A jet with some of the highest linear resolutions ever achieved in an AGN. This region is the likely origin of the γ-ray emission recently detected by the *Fermi* Large Area Telescope (LAT). TANAMI monitors a sample of radio and γ-ray selected extragalactic jets south of $-30°$ declination at 8.4 GHz and 22.3 GHz with the Australian Long Baseline Array (LBA) and the transoceanic antennas Hartebeesthoek in South Africa, the 6 m Transportable Integrated Geodetic Observatory (TIGO) in Chile and the 9 m German Antarctic Receiving Station (GARS) in O'Higgins, Antarctica. The highest angular resolution achieved at 8.4 GHz in the case of Cen A is 0.59 mas × 0.978 mas (natural weighting) corresponding to a linear scale of less than 16 milliparsec.

We show images of the first three TANAMI 8.4 GHz observation epochs of the sub-parsec scale jet-counterjet system of Cen A. With a simultaneous 22.3 GHz observation in 2008 November, we present a high resolution spectral index map of the inner few milliarcseconds of the jet probing the putative emission region of γ-ray-photons.

1. Introduction

Centaurus A (PKS 1322−427) is the closest active radio galaxy at a distance of 3.42 ± 0.18 Mpc (Ferrarese et al. 2007), where an angular resolution of one milliarcsecond (mas) corresponds to ~ 0.016 pc. The optical counterpart of Cen A is a giant elliptical galaxy (NGC 5128) which hosts a supermassive black hole with a mass $M = 5.5 \pm 3.0 \times 10^7 M_\odot$ (Israel 1998, Neumayer et al. 2010).

Due to its proximity, Cen A is an exceptionally good laboratory for studying the innermost regions of active galactic nuclei (AGN). Cen A can be seen over the whole range of the electromagnetic spectrum up to highest energies. Recently, the γ-ray detection by *CGRO*/EGRET was confirmed by *Fermi*/LAT (Hartman et al. 1999, Abdo et al. 2010). In the TeV range, Cen A was detected by H.E.S.S. (Aharonian et al. 2009).

The radio source Cen A is usually classified as a Fanaroff-Riley type I (FR I) radio galaxy (Fanaroff & Riley 1974). The spectrum of the core ($\leq$ 4 mas) is inverted, indicating synchrotron or even free-free self absorption (Tingay et al. 1998). On sub-parsec scales, the radio jet-counterjet system was clearly resolved with the VLBI Space Observatory Program (VSOP) by

Horiuchi et al. (2006) at 5 GHz. As part of the TANAMI program[1], we produce images of Cen A at comparable resolution with only ground based telescopes. Here we give an overview of all TANAMI observations of Cen A prior to November 2008 and first results of the ongoing analysis.

2. Observations and Data reduction

The Very Long Baseline Interferometry (VLBI) observations of Cen A presented here were made in the framework of the TANAMI program (Ojha et al. 2010). The participating telescopes in this southern-hemisphere VLBI project are the Australian Long Baseline Array (LBA), with antennas in Narrabri (5×22 m), Ceduna (30 m), Hobart (26 m), Mopra (22 m), Parkes (64 m), the 70 m and 34 m telescopes of NASA's Deep Space Network (DSN) located at Tidbinbilla, the 26 m South-African Hartebeesthoeck antenna, the 9 m German Antarctic Receiving Station (GARS) in O'Higgins, Antarctica, and the 6 m Transportable Integrated Geodetic Observatory (TIGO) in Chile. The TANAMI source list consists currently of 75 extragalactic jets. Observations are conducted

---

[1] Tracking Active Galactic Nuclei with Austral Milliarcsecond Interferometry
http://pulsar.sternwarte.uni-erlangen.de/tanami
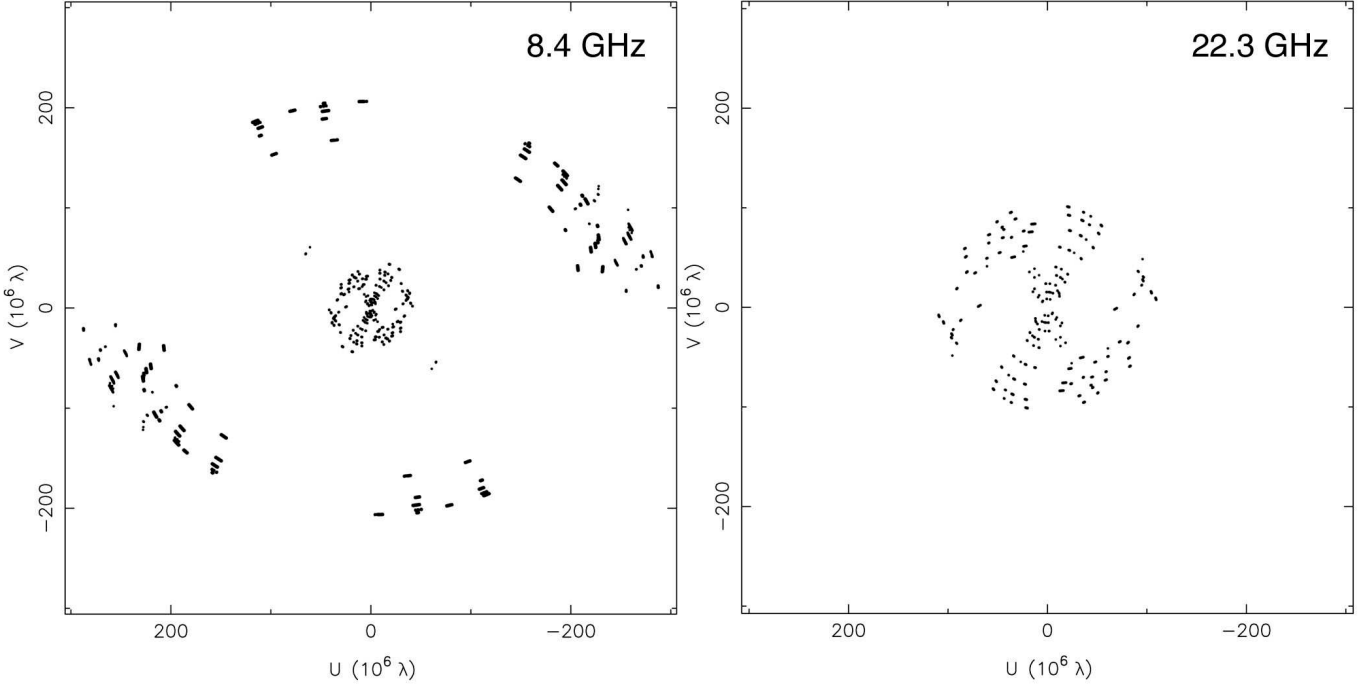
Fig. 1. (u-v)-coverage at 8.4 GHz (left) and 22.3 GHz (right) for Centaurus A

Table 1. Image parameters and observation characteristics (natural weighting)

Frequency [GHz]	Epoch yyyy-mm-dd	RMS * [mJy beam^{-1}]	S_{peak} [Jy beam^{-1}]	S_{total} [Jy]	θ_{maj} [mas]	θ_{min} [mas]	P.A. [°]
8.4	2007-11-10	0.37 ±0.04	0.60	2.6 ±0.1	1.64	0.41	7.9
8.4	2008-06-09	0.58 ±0.05	1.06	3.1 ±0.1	2.86	1.18	−12.7
8.4	2008-11-27	0.39 ±0.02	0.74	3.9 ±0.1	0.98	0.59	31.4
22.3	2008-11-29	0.47 ±0.03	1.77	3.4 ±0.1	2.01	1.27	87.9

* RMS values are determined in a region of the final map without significant source flux.

at 8.4 GHz and 22.3 GHz (for more details see Ojha et al., these proceedings p. 179). The γ-ray properties of the sample including Cen A are presented by Böck et al. in these proceedings, p. 17 .

Fig. 1 shows the (u-v)-coverage for Cen A at 8.4 GHz (left) and 22.3 GHz (right) for the November 2008 TANAMI observation. The radial (u-v)-coverage at 170–290 Mλ is provided by baselines involving the TIGO and O'Higgins antennas. This results in an angular resolution of 0.59 mas × 0.978 mas (natural weighting) at 8.4 GHz.

Since the transoceanic antennas O'Higgins and TIGO do not support observations at 22.3 GHz, at this frequency the resolution is lower (2.01 mas × 1.27 mas).

Data calibration and hybrid imaging were performed by using standard techniques as described by Ojha et al. (2010).

3. Results

The image parameters and observation characteristics of the three 8.4 GHz and the one 22.3 GHz TANAMI observations of Cen A are listed in Table 1. Imaging was performed with the program DIFMAP (Shepherd 1997), using the CLEAN algorithm and making use of phase and amplitude self-calibration.

TANAMI monitored Cen A until November 2008 three times at 8.4 GHz and one time simultaneously at 22.3 GHz. Figs. 2 and 3 show the resulting naturally weighted 8.4 GHz and 22.3 GHz images. With only ground based telescopes, we achieve highest angular resolution observations of Cen A, which can be compared with earlier space-VLBI observations (Horiuchi et al. 2006). The smallest resolved structures are on the scale of 12 light-days.

We resolve the core region of Cen A into several jet components. At both frequencies and at all epochs, a well collimated jet at a mean position angle (P.A.) of $\sim 50°$ and a fainter counterjet (P.A.$\sim -130°$) with an emission gap in between is seen. The significant features within the sub-parsec scale jet observed in the November 2007 image at 8.4 GHz of TANAMI observations (2010) are in good agreement with those of the following epochs. This result can be used to set constraints on the position of the core.

In the highest resolution image of 2008 November, a widening of the jet at about 25 mas (≈ 0.4 pc) downstream and a subsequent recollimation are observed. These features appear also in the November 2007 and June 2008
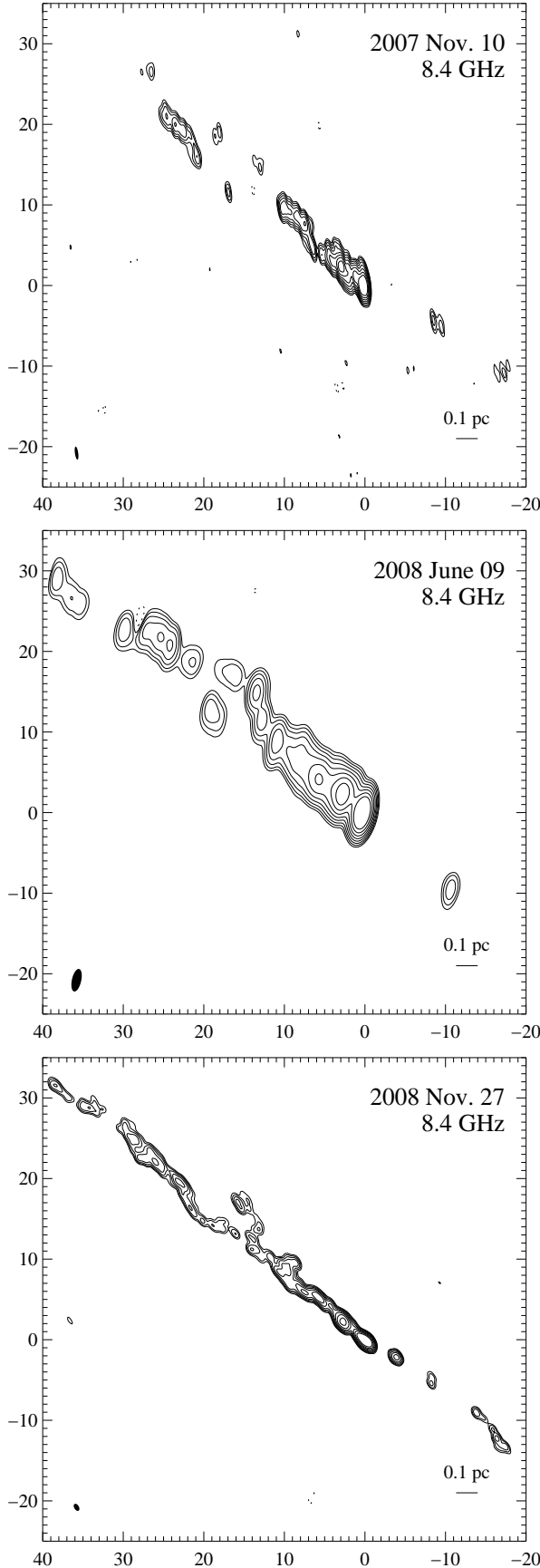
Fig. 2. 8.4 GHz images of Cen A of November 2007 (top), June 2008 (middle) and of November 2008 (bottom). The lowest contours are at 3σ.

images as well as in the 22.3 GHz map at lower resolution (see Figs. 2 & 3).

The November 2008 image reveals a small counterjet displacement from the jet line, which can also be seen in the image of Horiuchi et al. (2006).

Both, the peak and the total flux densities at the 8.4 GHz epochs show only moderate variability with a mean of $S_{\text{peak}} \sim 0.71 \, \text{Jy beam}^{-1}$ and $S_{\text{total}} \sim 3.5 \, \text{Jy}$. At 22.3 GHz, the flux density is higher indicating an inverted core spectrum (see below).

By analyzing ~ 8 years of observations at multiple frequencies Tingay et al. (1998) measured a jet speed of $0.1 \, c$. Our three 8.4 GHz jet images (separated by 0.5 years each) can be fitted with a self-consistent model of Gaussian components within the inner 25 mas. At least one more observation epoch is required to measure robust component velocities.

Despite a larger synthesized beam at the higher frequency, the jet structures at 8.4 GHz and 22.3 GHz in the simultaneous measured November 2008 images match well within the inner 30 mas ($\approx 0.5 \, \text{pc}$) of the jet. We modeled the core at both frequencies with three Gaussian components. The comparison of the optically thin components reveals a shift of the 22.3 GHz core with respect to the 8.4 GHz core in the direction of the central black hole of $\Delta\alpha \approx 0.2 \, \text{mas}$ and $\Delta\delta \approx 0.15 \, \text{mas}$. Taking this alignment correction into account, we obtained the spectral index distribution along the jet shown in Fig. 4. Both images were restored with a common beam (80% of synthesized beam at 22.3 GHz; $1.61 \times 1.016 \, \text{mas}$, P.A. 88°). The overlaid contours correspond to the 8.4 GHz image folded with this common beam. The core region has an inverted spectrum which changes from flat to steep downstream. The highest spectral indices with values $\alpha \leq 1$ are found in the core, indicating synchrotron self-absorption.

Recently, the *Fermi* Large Area Telescope detected γ-ray emission from the Cen A lobes (Fermi-LAT Collaboration 2010), as well as from its core (Abdo et al. 2010b, submitted). Flat spectrum regions in the sub-parsec scale radio jet are possible production regions of high energetic photons (Marscher 2010). We identify the inner few milliarcseconds ($\sim 0.2 \, \text{pc}$) at 8.4 GHz of the Cen A radio jet as possible sources of γ-ray emission with the strongest inverted-spectral emission coming from the jet core on scales of $\leq 0.1 \, \text{pc}$.

4. Conclusions

We presented the first TANAMI observations of Cen A at 8.4 GHz and 22.3 GHz including the highest resolved image of Cen A ever made with ground based telescopes. With a simultaneous observation in November 2008 we were able to produce a spectral index map of the milliparsec-scale jet of Cen A identifying the putative γ-ray emission regions.

Further analysis of the following TANAMI observations of Cen A will try to test the previously determined jet speeds.
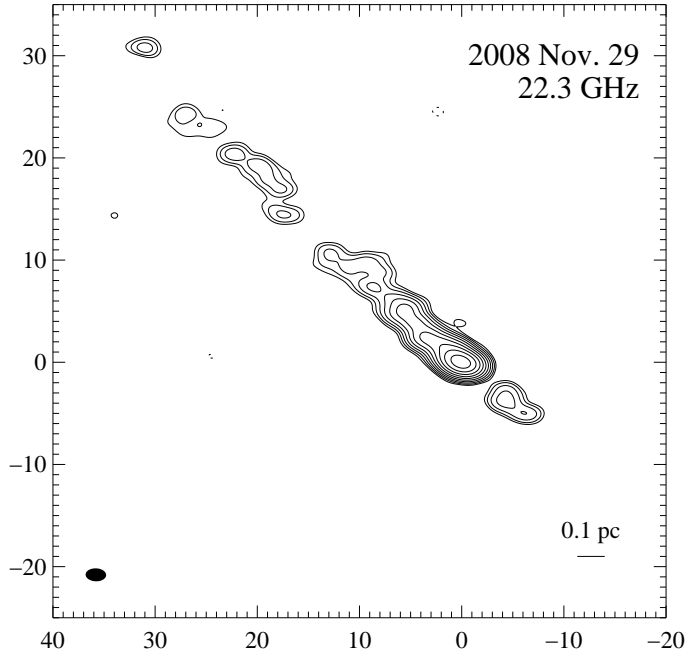
Fig. 3. 22.3 GHz image of November 2008
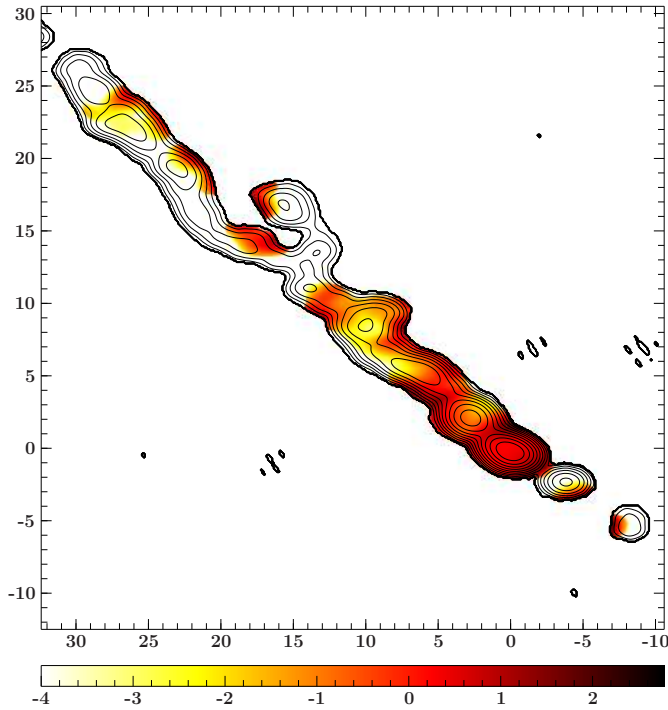
Fig. 4. Spectral index map as calculated for $S_{8.4\,\mathrm{GHz}} \geq 3\sigma_{8.4\,\mathrm{GHz}}$ and $S_{22.3\,\mathrm{GHz}} \geq 2\sigma_{22.3\,\mathrm{GHz}}$. The overlaying contours show the flux density distribution at 8.4 GHz folded with a common beam of 1.61×1.02 mas (P.A. $= 88°$). The spectral index is defined as $F_\nu \sim \nu^{+\alpha}$.

References

Fermi-LAT Collaboration 2010, Science, 328, 725
Abdo, A. A., et al. 2010, submitted to ApJ, arXiv:1005.2626
Abdo, A. A., et al. 2010, ApJS, 188, 405
Aharonian, F., et al. 2009, ApJ, 695, L40
Fanaroff, B. L. & Riley, J. M. 1974, MNRAS, 167, 31P
Ferrarese, L., Mould, J. R., Stetson, et al. 2007, ApJ, 654, 186
Hartman, R. C., et al. 1999, ApJS, 123, 79
Horiuchi, S., Meier, D. L., Preston, R. A., & Tingay, S. J. 2006, PASJ, 58, 211
Israel, F. P. 1998, A&A Rev., 8, 237
Marscher, A. P., 2010, in *The Jet paradigm - From Microquasars to Quasars*, ed. T. Belloni, Lecture Notes in Physics, 794, 173
Neumayer, N., Cappellari, M., van der Werf, et al. 2010, The Messenger, 139, 36
Ojha, R., Kadler, M., Böck, M. et al. 2010, in press (arXiv:1005.4432)
Shepherd, M. C. 1997, Astronomical Data Analysis Software and Systems VI, 125, 77
Tingay, S. J., Jauncey, D. L., Reynolds, J. E., et al. 1998, AJ, 115, 960

Author Index